

NOVEMBER 2020

AJNR

VOLUME 41 • PP 1963-2171

AJNR

AMERICAN JOURNAL OF NEURORADIOLOGY

NOVEMBER 2020
VOLUME 41
NUMBER 11
WWW.AJNR.ORG

THE JOURNAL OF DIAGNOSTIC AND
INTERVENTIONAL NEURORADIOLOGY

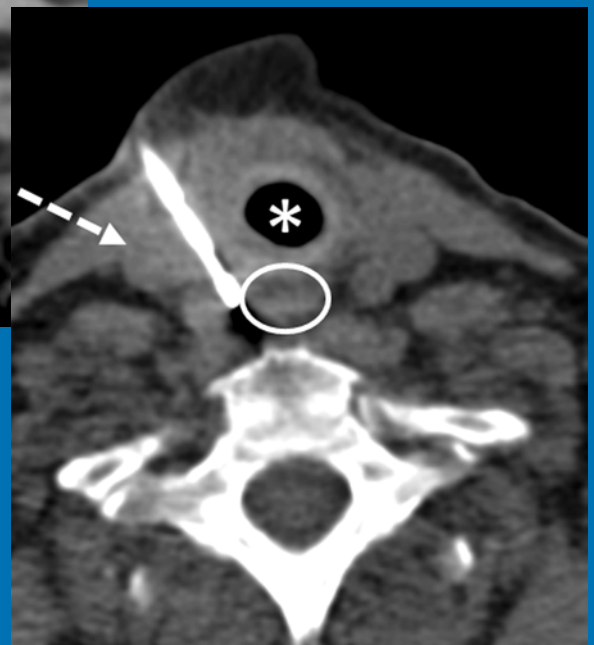
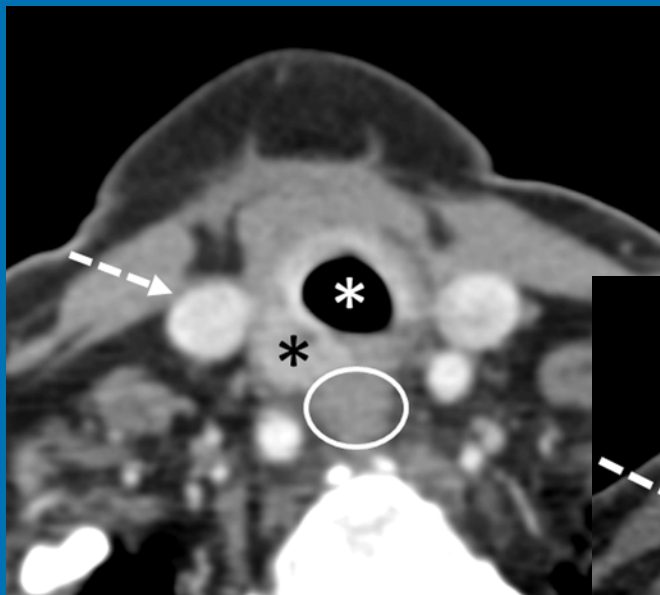
CT-guided core needle biopsies of head and neck masses

Brain imaging of patients with COVID-19

Diffusion for differentiation between treatment-related lesions and glioma

Tumefactive primary CNS vasculitis

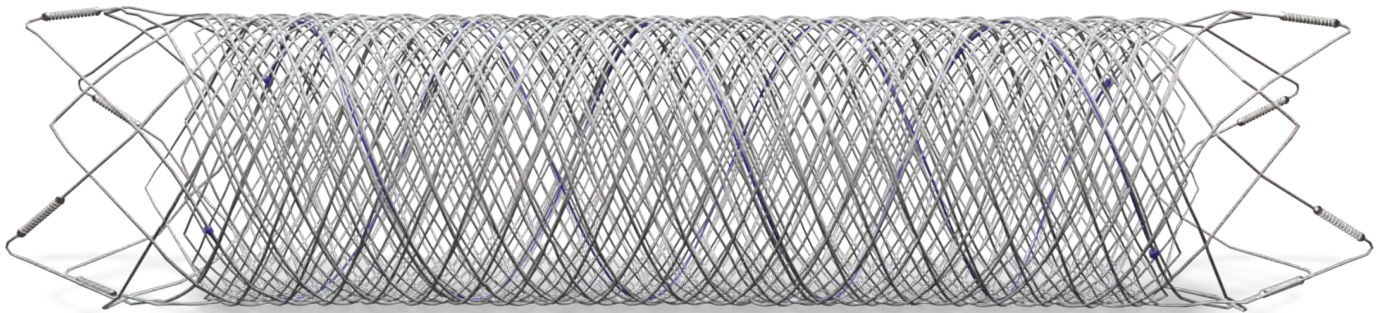
Official Journal ASNR • ASFNR • ASHNR • ASPNR • ASSR



FRED™

Flow Re-Direction
Endoluminal Device

FLOW DIVERSION.



SIMPLIFIED.



MicroVention Worldwide
Innovation Center
35 Enterprise
Aliso Viejo, CA 92656 USA
MicroVention UK Limited
MicroVention Europe S.A.R.L.
MicroVention Deutschland GmbH
Web

PH +1 714.247.8000

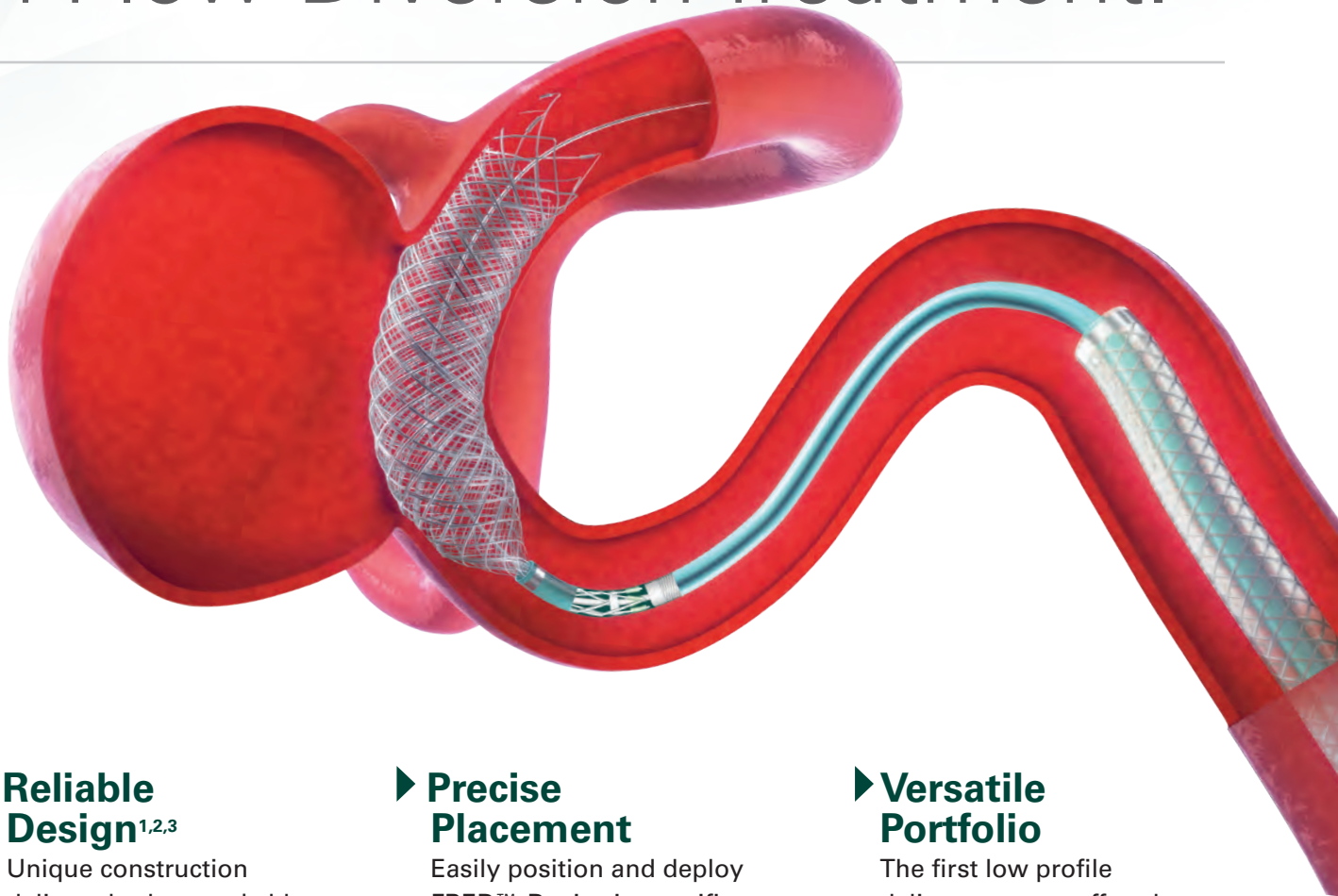
PH +1 44 (0) 191 258 6777

PH +33 (1) 39 21 77 46

PH +49 211 210 798-0

microvention.com

The New Standard of **Ease and Simplicity** in Flow Diversion Treatment.



► **Reliable Design**^{1,2,3}

Unique construction delivers both remarkable ease of use and excellent flow diversion^{1,2,3}

► **Precise Placement**

Easily position and deploy FRED™ Device in specific, targeted locations^{4,5,6}

► **Versatile Portfolio**

The first low profile delivery system offered in combination with large diameter and long length options

References:

1. TR11-211 2. TR13-171 3. TR15-055 4. TR13-192 5. TR15-072 6. TR19-145

The Flow Re-Direction Endoluminal Device (FRED™) System is indicated for use in the internal carotid artery from the petrous segment to the terminus for the endovascular treatment of adult patients (22 years of age or older) with wide-necked (neck width ≥ 4 mm or dome-to-neck ratio < 2) saccular or fusiform intracranial aneurysms arising from a parent vessel with a diameter ≥ 2.0 mm and ≤ 5.0 mm.

Use of the FRED™ System is contraindicated under these circumstances: Patients in whom anticoagulant, anti-platelet therapy, or thrombolytic drugs are contraindicated. Patients with known hypersensitivity to metal such as nickel-titanium and metal jewelry. Patients with anatomy that does not permit passage or deployment of the FRED™ System. Patients with an active bacterial infection. Patients with a pre-existing stent in place at the target aneurysm. Patients in whom the parent vessel size does not fall within the indicated range. Patients who have not received dual anti-platelet agents prior to the procedure. For complete indications, contraindications, potential complications, warnings, precautions, and instructions, see instructions for use (IFU provided in the device).

RX Only: Federal (United States) law restricts this device to sale by or on the order of a physician.

MICROVENTION™ and FRED™ are registered trademarks of MicroVention, Inc. in the United States and other jurisdictions. © 2020 MicroVention, Inc. 04/2020.

stryker

We
make the
solutions.

**You
make the
difference.**



Looking for customizable
fracture care? Stryker puts
the possibilities in your hands.

strykerIVS.com/VCF

Stryker or its affiliated entities own, use, or have applied for the following trademarks or service marks: AVAllex, IVAS, SpineJack and Stryker. All other trademarks are trademarks of their respective owners or holders.

The absence of a product, feature, or service name, or logo from this list does not constitute a waiver of Stryker's trademark or other intellectual property rights concerning that name or logo.

170000033896
Copyright © 2020 Stryker

AJNR *go green*

***AJNR* urges American Society of Neuroradiology members to reduce their environmental footprint by voluntarily suspending their print subscription.**

The savings in paper, printing, transportation, and postage directly fund new electronic enhancements and expanded content.

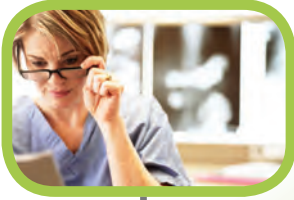
The digital edition of *AJNR* presents the print version in its entirety, along with extra features including:

- Publication Preview
- Case Collection
- Podcasts
- The *AJNR* News Digest
- The *AJNR* Blog

It also reaches subscribers much faster than print. An electronic table of contents will be sent directly to your mailbox to notify you as soon as it publishes.

Readers can search, reference, and bookmark current and archived content 24 hours a day on www.ajnr.org.

ASNR members who wish to opt out of print can do so by using the *AJNR* Go Green link on the *AJNR* Website (<http://www.ajnr.org/content/subscriber-help-and-services>). Just type your name in the email form to stop print and spare our ecosystem.



Simplify the MOC Process



Manage your CME Credits Online

CMEgateway.org

Available to Members of Participating Societies

American Board of Radiology (ABR)
American College of Radiology (ACR)
American Roentgen Ray Society (ARRS)
American Society of Neuroradiology (ASNR)
Commission on Accreditation of Medical
Physics Educational Programs, Inc. (CAMPEP)
Radiological Society of North America (RSNA)
Society of Interventional Radiology (SIR)
SNM
The Society for Pediatric Radiology (SPR)

It's Easy and Free!

Log on to CME Gateway to:

- View or print reports of your CME credits from multiple societies from a single access point.
- Print an aggregated report or certificate from each participating organization.
- Link to SAMs and other tools to help with maintenance of certification.

American Board of Radiology (ABR) participation!

By activating ABR in your organizational profile, your MOC-fulfilling CME and SAM credits can be transferred to your own personalized database on the ABR Web site.

Sign Up Today!

go to CMEgateway.org

We're Inside Every Great Neuroradiologist!

ASNR MEMBERS RECEIVE

American Journal of Neuroradiology (AJNR)

The leading neuroradiology research journal, published monthly

Neurographics

Bimonthly educational journal with CME for members

ASNR Annual Meeting

Discounts for members on the field's premier conference

eCME

Online collection of lectures and articles with SA-CME and Category 1 credit

Advocacy

Coding/reimbursement, quality standards and practice guidelines; demonstrating neuroradiology's value!

Networking

Access to 5,000 peers

... And More!

Join the leaders in neuroradiology today!

Learn more at www.asnr.org/join

ASNR

American Society of Neuroradiology

800 Enterprise Dr., Suite 205, Oak Brook, IL 60523 • (630)574-0220 • membership@asnr.org • www.asnr.org

PS Form 3526 Statement of Ownership, Management, and Circulation (All Periodicals Publications Except Requester Publications)

1. Publication Title AMERICAN SOCIETY OF NEURORADIOLOGY/ AJNR-AMERICAN JOURNAL OF NEURORADIOLOGY			2. Publication Number 532630		ISSN		3. Filing Date 09/24/2020	
4. Issue Frequency MONTHLY			5. Number of Issues Published Annually 12			6. Annual Subscription Price		
7. Complete Mailing Address of Known Office of Publication 800 ENTERPRISE DRIVE SUITE 205 OAK BROOK, DU PAGE, IL 60523						Contact Person KAREN HALM Telephone (630) 574-1487 Ext. 238		
8. Complete Mailing Address of Headquarters or General Business Office of Publisher AMERICAN SOCIETY OF NEURORADIOLOGY 800 ENTERPRISE DRIVE, SUITE 205 OAK BROOK, IL 60523								
9. Full Names and Complete Mailing Addresses of Publisher, Editor, and Managing Editor								
Publisher (Name and complete mailing address) AMERICAN SOCIETY OF NEURORADIOLOGY 800 ENTERPRISE DRIVE, SUITE 205 OAK BROOK, IL 60523								
Editor (Name and complete mailing address) JEFFREY S. ROSS 800 ENTERPRISE DRIVE, SUITE 205 OAK BROOK, IL 60523								
Managing Editor (Name and complete mailing address) KAREN E. HALM 800 ENTERPRISE DRIVE, SUITE 205 OAK BROOK, IL 60523								
10. Owner (Do not leave blank. If the publication is owned by a corporation, give the name and address of the corporation immediately followed by the names and addresses of all stockholders owning or holding 1 percent or more of the total amount of stock. If not owned by a corporation, give names and addresses of the individual owners. If owned by a partnership or other unincorporated firm, give its name and address as well as those of each individual owner. If the publication is published by a nonprofit organization, give its name and address.)								
Full Name AMERICAN SOCIETY OF NEURORADIOLOGY			Complete Mailing Address 800 ENTERPRISE DRIVE, SUITE 205, OAK BROOK, IL 60523					
11. Known Bondholders, Mortgagees, and Other Security Holders Owning or Holding 1 Percent or More of Total Amount of Bonds, Mortgages, or Other Securities. If none, check box <input checked="" type="checkbox"/> None								
Full Name			Complete Mailing Address					

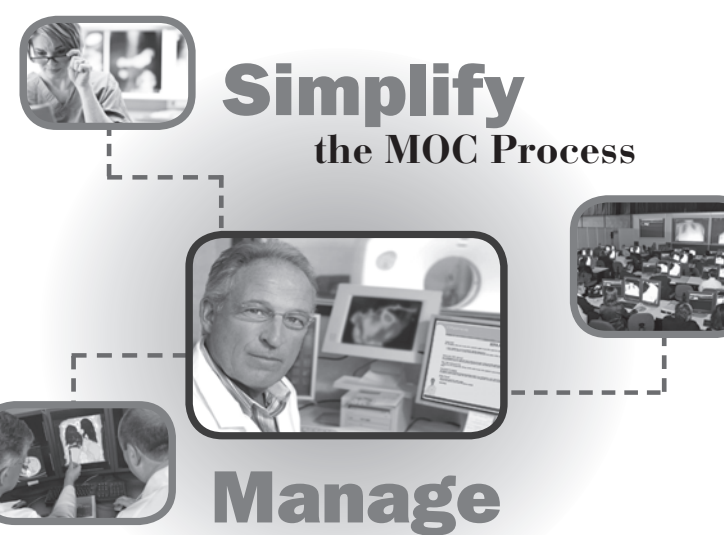
PS Form 3526, September 2007 (Page 1)

PRIVACY NOTICE: See our privacy policy on www.usps.com

13. Publication Title AMERICAN SOCIETY OF NEURORADIOLOGY/AJNR-AMERICAN JOURNAL OF NEURORADIOLOGY		14. Issue Date for Circulation Data Below 09/14/2020	
15. Extend and Nature of Circulation		Average No. Copies Each Issue During Preceding 12 Months	No. Copies of Single Issue Published Nearest to Filing Date
a. Total Numbers of Copies (Net press run)		2808	2737
b. Paid Circulation (By Mail and Outside the Mail)	(1) Mailed Outside County Paid Subscriptions Stated on PS Form 3541 (include paid distribution above nominal rate, advertiser's proof copies, and exchange copies)	2267	2236
	(2) Mailed In-County Paid Subscriptions Stated on PS Form 3541 (include paid distribution above nominal rate, advertiser's proof copies, and exchange copies)	0	0
	(3) Paid Distribution Outside the Mails Including Sales Through Dealers and Carriers, Street Vendors, Counter Sales, and Other Paid Distribution Outside USPS	212	200
	(4) Paid Distribution by Other Classes of Mail Through the USPS (e.g. First-Class Mail)	96	0
c. Total Paid Distribution (Sum of 15b (1), (2), (3), (4))		2575	2436
4. Free or Nominal Rate Distribution (By Mail and Outside the Mail)	(1) Free or Nominal Rate Outside County Copies included on PS Form 3541	36	32
	(2) Free or Nominal Rate In-County Copies included on PS Form 3541	0	0
	(3) Free or Nominal Rate Copies Mailed at Other Classes Through the USPS (e.g. First-Class Mail)	0	0
	(4) Free or Nominal Rate Distribution Outside the Mail (Carriers or other means)	0	0
e. Total Free or Nominal Rate Distribution (Sum of 15d (1), (2), (3), (4))		36	32
f. Total Distribution (Sum of 15c and 15e)		2611	2468
g. Copies not Distributed		197	269
h. Total (Sum of 15f and 15g)		2808	2737
i. Percent Paid ((15c / 15f) times 100)		98.62 %	98.70 %
16. If total circulation includes electronic copies, report that circulation on lines below.			
a. Paid Electronic Copies		0	0
b. Total Paid Print Copies (Line 15c) + Paid Electronic Copies		0	0
c. Total Print Distribution (Line 15f) + Paid Electronic Copies		0	0
d. Percent Paid (Both Print and Electronic Copies)		0.00 %	0.00 %
<input type="checkbox"/> I certify that 50% of all my distributed copies (Electronic and Print) are paid above a nominal price.			
17. Publication of Statement of Ownership			
<input checked="" type="checkbox"/> If the publication is a general publication, publication of this statement is required. Will be printed in the 11/15/2020 issue of this publication.		<input type="checkbox"/> Publication not required.	
18. Signature and Title of Editor, Publisher, Business Manager, or Owner		Title	Date
Karen E. Halm		Managing Editor	09/24/2020 09:43:14 AM
I certify that all information furnished on this form is true and complete. I understand that anyone who furnishes false or misleading information on this form or who omits material or information requested on the form may be subject to criminal sanctions (including fines and imprisonment) and/or civil sanctions (including civil penalties).			

PS Form 3526, September 2007 (Page 2)

PRIVACY NOTICE: See our privacy policy on www.usps.com



Simplify the MOC Process

Manage your CME Credits Online

CMEgateway.org

It's Easy and Free!

Log on to CME Gateway to:

- View or print reports of your CME credits from multiple societies from a single access point.
- Print an aggregated report or certificate from each participating organization.
- Link to SAMs and other tools to help with maintenance of certification.

American Board of Radiology (ABR) participation!

By activating ABR in your organizational profile, your MOC-fulfilling CME and SAM credits can be transferred to your own personalized database on the ABR Web site.

Sign Up Today!
go to CMEgateway.org

Available to Members of Participating Societies

American Board of Radiology (ABR)	Radiological Society of North America (RSNA)
American College of Radiology (ACR)	Society of Interventional Radiology (SIR)
American Roentgen Ray Society (ARRS)	SNM
American Society of Neuroradiology (ASNR)	The Society for Pediatric Radiology (SPR)
Commission on Accreditation of Medical Physics Educational Programs, Inc. (CAMPEP)	

IMPORTANT SAFETY INFORMATION¹

WARNING: NEPHROGENIC SYSTEMIC FIBROSIS (NSF)

Gadolinium-based contrast agents (GBCAs) increase the risk for NSF among patients with impaired elimination of the drugs. Avoid use of GBCAs in these patients unless the diagnostic information is essential and not available with non-contrasted MRI or other modalities. NSF may result in fatal or debilitating fibrosis affecting the skin, muscle and internal organs.

- The risk for NSF appears highest among patients with:
 - Chronic, severe kidney disease (GFR < 30 mL/min/1.73m²), or
 - Acute kidney injury.
- Screen patients for acute kidney injury and other conditions that may reduce renal function. For patients at risk for chronically reduced renal function (e.g. age > 60 years, hypertension, diabetes), estimate the glomerular filtration rate (GFR) through laboratory testing.
- For patients at highest risk for NSF, do not exceed the recommended DOTAREM dose and allow a sufficient period of time for elimination of the drug from the body prior to any re-administration.

INDICATIONS AND USAGE

DOTAREM[®] (gadoterate meglumine) injection is a prescription gadolinium-based contrast agent indicated for intravenous use with magnetic resonance imaging (MRI) in brain (intracranial), spine and associated tissues in adult and pediatric patients (including term neonates) to detect and visualize areas with disruption of the blood brain barrier (BBB) and/or abnormal vascularity.

CONTRAINDICATIONS

History of clinically important hypersensitivity reactions to DOTAREM.

WARNINGS AND PRECAUTIONS

- Hypersensitivity Reactions: Anaphylactic and anaphylactoid reactions have been reported with DOTAREM, involving cardiovascular, respiratory, and/or cutaneous manifestations. Some patients experienced circulatory collapse and died. In most cases, initial symptoms occurred within minutes of DOTAREM administration and resolved with prompt emergency treatment.
- Before DOTAREM administration, assess all patients for any history of a reaction to contrast media, bronchial asthma and/or allergic disorders. These patients may have an increased risk for a hypersensitivity reaction to DOTAREM.
- Administer DOTAREM only in situations where trained personnel and therapies are promptly available for the treatment of hypersensitivity reactions, including personnel trained in resuscitation.
- Gadolinium Retention: Gadolinium is retained for months or years in several organs. The highest concentrations have been identified in the bone, followed by brain, skin, kidney, liver and spleen. The duration of retention also varies by tissue, and is longest in bone. Linear GBCAs cause more retention than macrocyclic GBCAs.
- Consequences of gadolinium retention in the brain have not been established. Adverse events involving multiple organ systems have been reported in patients with normal renal function without an established causal link to gadolinium retention.
- Acute Kidney Injury: In patients with chronically reduced renal function, acute kidney injury requiring dialysis has occurred with the use of GBCAs. The risk of acute kidney injury may increase with increasing dose of the contrast agent; administer the lowest dose necessary for adequate imaging.
- Extravasation and Injection Site Reactions: Ensure catheter and venous patency before the injection of DOTAREM. Extravasation into tissues during DOTAREM administration may result in tissue irritation.

ADVERSE REACTIONS

- The most common adverse reactions associated with DOTAREM in clinical trials were nausea, headache, injection site pain, injection site coldness and rash.
- Serious adverse reactions in the Postmarketing experience have been reported with DOTAREM. These serious adverse reactions include but are not limited to: arrhythmia, cardiac arrest, respiratory arrest, pharyngeal edema, laryngospasm, bronchospasm, coma and convulsion.

USE IN SPECIFIC POPULATIONS

- **Pregnancy:** GBCAs cross the human placenta and result in fetal exposure and gadolinium retention. Use only if imaging is essential during pregnancy and cannot be delayed.
- **Lactation:** There are no data on the presence of gadoterate in human milk, the effects on the breastfed infant, or the effects on milk production. However, published lactation data on other GBCAs indicate that 0.01 to 0.04% of the maternal gadolinium dose is present in breast milk.
- **Pediatric Use:** The safety and efficacy of DOTAREM at a single dose of 0.1 mmol/kg has been established in pediatric patients from birth (term neonates \geq 37 weeks gestational age) to 17 years of age based on clinical data. The safety of DOTAREM has not been established in preterm neonates. No cases of NSF associated with DOTAREM or any other GBCA have been identified in pediatric patients age 6 years and younger.

You are encouraged to report negative side effects of prescription drugs to the FDA. Visit www.fda.gov/medwatch or call 1-800-FDA-1088.

Please see the full Prescribing Information, including the patient Medication Guide, for additional important safety information.

References: 1. Dotarem [package insert]. Princeton, NJ: Guerbet LLC; Oct 2019. 2. Maravilla K et al. Comparison of Gadoterate Meglumine and Gadobutrol in the Diagnosis of Primary Brain Tumors: A Double-Blind Randomized Controlled Intraindividual Crossover Study (the REMIND Study). 2017 June 29. doi: 10:3174/ajnr.A5316. [Epub ahead of print]. 3. de Kerviler E et al. Adverse reactions to gadoterate meglumine: review of over 25 years of clinical use and more than 50 million doses. Invest Radiol 2016;51:544–51 CrossRef Medline. 4. Endrikat J et al. Safety of gadobutrol: results from 42 clinical phase II to IV studies and postmarketing surveillance after 29 million applications. Invest Radiol 2016;51: 537–43 CrossRef Medline. 5. Port M et al. Efficiency, thermodynamic and kinetic stability of marketed gadolinium chelates and their possible clinical consequences: a critical review. Biometals. 2008;21:469-90. 6. Frenzel T et al. Stability of gadolinium-based magnetic resonance imaging contrast agents in human serum at 37°C. Invest Radiol. 2008;43:817-828.

DOTAREM[®] is a registered trademark of Guerbet LLC, and is available by prescription only.

Gadavisit[®] is a registered trademark of the Bayer group of companies, and is available by prescription only.

DOTAREM[®] (gadoterate meglumine) Injection

MR

Comparison of Dotarem[®] to Gadavist[®] for Overall Visualization and Characterization in the MRI Diagnosis of Primary Brain Tumors



Despite the difference in relaxivity between these 2 GBCAs



There Is No Measurable Difference in Clinical Benefit Observed Between Dotarem[®] and Gadavist^{®2}



as demonstrated by the **REMIND Study**, a multicenter, double-blind, randomized, controlled intraindividual crossover study.²

This study “demonstrates the non-inferiority of gadoterate meglumine [Dotarem[®]] versus gadobutrol [Gadavist[®]] for overall visualization and characterization of primary brain tumors”.² Additionally, there was no preference of the readers for either contrast agent, in most cases, regarding border delineation, internal morphology, and the qualitative degree of contrast enhancement, despite quantitative mean lesion percentage enhancement being higher with gadobutrol.²

- For all readers in the REMIND Study, more than 90% of patients presented with good or excellent overall lesion visualization and characterization with either Dotarem[®] or Gadavist^{®2}.
- The REMIND Study also demonstrated a low incidence of immediate reported AEs with Dotarem[®] and with Gadavist[®], as shown in multiple previous studies.^{2,3,4}
- Dotarem[®] is the first imaging contrast with a macrocyclic and ionic structure for high thermodynamic and kinetic stability.^{5,6}
- Dotarem[®] is not only trusted for high molecular stability^{5,6}; the REMIND Study demonstrates that it is as effective as Gadavist[®] for MRI diagnosis of primary brain tumors.²

Please see Important Safety information on opposite page. For more information on Dotarem[®], please see Full Prescribing Information including Boxed Warning and Medication Guide.

Guerbet | 

COMMITTED

Learn more at
RemindStudy.com



Introducing
Eclipse 2L
DUAL LUMEN BALLOON CATHETER



Balt's Access Portfolio Delivers Unique Solutions



Visit www.balt-usa.com to learn more

AJNR

AMERICAN JOURNAL OF NEURORADIOLOGY

NOVEMBER 2020
VOLUME 41
NUMBER 11
WWW.AJNR.ORG

Publication Preview at www.ajnr.org features articles released in advance of print. Visit www.ajnrblog.org to comment on AJNR content and chat with colleagues and AJNR's News Digest at <http://ajnrdigest.org> to read the stories behind the latest research in neuroimaging.

1963 **PERSPECTIVES** *B. Thomas*

EDITORIAL

1964 **Imaging for Menière Disease** *E. Kay-Rivest, et al.*

HEAD & NECK

REVIEW ARTICLES

  1966 **Cross-Sectional Imaging of Third Molar–Related Abnormalities**
R.M. Loureiro, et al.

HEAD & NECK

  1975 **The Perplexity Surrounding Chiari Malformations – Are We Any Wiser Now?** *S.B. Hiremath, et al.*

ADULT BRAIN

 1982 **Neuro-Oncology and Radiogenomics: Time to Integrate?** *A. Lasocki, et al.*

ADULT BRAIN

PATIENT SAFETY

 1989 **Fetal Exposure to MR Imaging: Long-Term Neurodevelopmental Outcome** *E. Zvi, et al.*

PEDIATRICS

RADIOLOGY-PATHOLOGY CORRELATION

  1993 **COVID-19-Associated Carotid Atherothrombosis and Stroke** *C. Esenwa, et al.*

EXTRACRANIAL
VASCULAR

PRACTICE PERSPECTIVES

1996 **Evolving Use of fMRI in Medicare Beneficiaries** *S. Asnafi, et al.*

FUNCTIONAL

GENERAL CONTENTS

 2001 **Brain Imaging of Patients with COVID-19: Findings at an Academic Institution during the Height of the Outbreak in New York City** *E. Lin, et al.*

ADULT BRAIN

  2009 **A Double-Edged Sword: Neurologic Complications and Mortality in Extracorporeal Membrane Oxygenation Therapy for COVID-19–Related Severe Acute Respiratory Distress Syndrome at a Tertiary Care Center** *J. Masur, et al.*

ADULT BRAIN

 2012 **Stroke Thrombectomy in Patients with COVID-19: Initial Experience in 13 Cases** *R. Pop, et al.*

INTERVENTIONAL

 2017 **Cytotoxic Lesion of the Corpus Callosum in an Adolescent with Multisystem Inflammatory Syndrome and SARS-CoV-2 Infection** *J. Lin, et al.*

PEDIATRICS

AJNR (Am J Neuroradiol ISSN 0195–6108) is a journal published monthly, owned and published by the American Society of Neuroradiology (ASNR), 800 Enterprise Drive, Suite 205, Oak Brook, IL 60523. Annual dues for the ASNR include approximately 21% for a journal subscription. The journal is printed by Cadmus Journal Services, 5457 Twin Knolls Road, Suite 200, Columbia, MD 21045; Periodicals postage paid at Oak Brook, IL and additional mailing offices. Printed in the U.S.A. POSTMASTER: Please send address changes to American Journal of Neuroradiology, P.O. Box 3000, Denville, NJ 07834, U.S.A. Subscription rates: nonmember \$410 (\$480 foreign) print and online, \$320 online only; institutions \$470 (\$540 foreign) print and basic online, \$935 (\$1000 foreign) print and extended online, \$380 online only (basic), \$825 online only (extended); single copies are \$35 each (\$40 foreign). Indexed by PubMed/MEDLINE, BIOSIS Previews, Current Contents (Clinical Medicine and Life Sciences), EMBASE, Google Scholar, HighWire Press, Q-Sensei, RefSeek, Science Citation Index, SCI Expanded, Meta/CZI, ReadCube, and Semantic Scholar. Copyright © American Society of Neuroradiology.

-   2020 **Location-Specific ASPECTS Paradigm in Acute Ischemic Stroke: A Systematic Review and Meta-Analysis** *S.M. Seyedsaadat, et al.* **ADULT BRAIN**
-  2027 **Maximum Ambiguity Distance for Phase Imaging in Detection of Traumatic Cerebral Microbleeds: An Improvement over Current Imaging Practice** *K. Nael, et al.* **ADULT BRAIN FUNCTIONAL**
-  2034 **Dynamic CTA-Derived Perfusion Maps Predict Final Infarct Volume: The Simple Perfusion Reconstruction Algorithm** *C.C. McDougall, et al.* **ADULT BRAIN FUNCTIONAL**
-  2041 **Comparison of Dynamic Contrast-Enhancement Parameters between Gadobutrol and Gadoterate Meglumine in Posttreatment Glioma: A Prospective Intraindividual Study** *J.E. Park, et al.* **ADULT BRAIN FUNCTIONAL**
-   2049 **Centrally Reduced Diffusion Sign for Differentiation between Treatment-Related Lesions and Glioma Progression: A Validation Study** *P. Alcaide-Leon, et al.* **ADULT BRAIN**
-  2055 **Monro-Kellie Hypothesis: Increase of Ventricular CSF Volume after Surgical Closure of a Spinal Dural Leak in Patients with Spontaneous Intracranial Hypotension** *T. Dobrocky, et al.* **ADULT BRAIN FUNCTIONAL**
-  2062 **Sensitive Detection of Infratentorial and Upper Cervical Cord Lesions in Multiple Sclerosis with Combined 3D FLAIR and T2-Weighted (FLAIR3) Imaging** *R.E. Gabr, et al.* **ADULT BRAIN**
-   2068 **MR Imaging Features of Middle Cranial Fossa Encephaloceles and Their Associations with Epilepsy** *D.R. Pettersson, et al.* **ADULT BRAIN**
-  2075 **Tumefactive Primary Central Nervous System Vasculitis: Imaging Findings of a Rare and Underrecognized Neuroinflammatory Disease** *S. Suthiphosuwana, et al.* **ADULT BRAIN**
-  2082 **Detailed Arterial Anatomy and Its Anastomoses of the Sphenoid Ridge and Olfactory Groove Meningiomas with Special Reference to the Recurrent Branches from the Ophthalmic Artery** *M. Hiramatsu, et al.* **ADULT BRAIN INTERVENTIONAL**
-  2088 **Carotid Stenting and Mechanical Thrombectomy in Patients with Acute Ischemic Stroke and Tandem Occlusions: Antithrombotic Treatment and Functional Outcome** *V. Da Ros, et al.* **INTERVENTIONAL**
-  2094 **Use of Cangrelor in Cervical and Intracranial Stenting for the Treatment of Acute Ischemic Stroke: A “Real Life” Single-Center Experience** *A. Cervo, et al.* **INTERVENTIONAL**
- 2100 **Transarterial Treatment of Cranial Dural Arteriovenous Fistulas: The Role of Transarterial and Transvenous Balloon-Assisted Embolization** *J.O. Zamponi Jr, et al.* **INTERVENTIONAL**
-  2107 **Computational Fluid Dynamics Using a Porous Media Setting Predicts Outcome after Flow-Diverter Treatment** *M. Beppu, et al.* **INTERVENTIONAL**
- 2114 **Efficacy of Asahi Fubuki as a Guiding Catheter for Mechanical Thrombectomy: An Institutional Case Series** *L. Rinaldo, et al.* **INTERVENTIONAL**
-  2117 **Percutaneous CT-Guided Core Needle Biopsies of Head and Neck Masses: Technique, Histopathologic Yield, and Safety at a Single Academic Institution** *T.J. Hillen, et al.* **HEAD & NECK**
- 2123 **Commentary**
Image-Guided Biopsies in the Head and Neck: Practical Value and Approach *A.H. Aiken* **HEAD & NECK**
-  2126 **Diagnostic Yield and Therapeutic Impact of Face and Neck Imaging in Patients Referred with Otolgia without Clinically Overt Disease** *E. Ainsworth, et al.* **HEAD & NECK**

EDITOR-IN-CHIEF

Jeffrey S. Ross, MD

Professor of Radiology, Department of Radiology,
Mayo Clinic College of Medicine, Phoenix, AZ

SENIOR EDITORS

Harry J. Cloft, MD, PhD

Professor of Radiology and Neurosurgery,
Department of Radiology, Mayo Clinic College of
Medicine, Rochester, MN

Christopher G. Filippi, MD

Professor and Vice Chair of Biomedical and
Translational Science,
Donald and Barbara Zucker School of Medicine at
Hofstra/Northwell,
Lenox Hill Hospital and Greenwich Village
Healthplex, New York, NY

Thierry A.G.M. Huisman, MD

Radiologist-in-Chief, Texas Children's Hospital,
Houston, TX

Yvonne W. Lui, MD

Associate Professor of Radiology,
Chief of Neuroradiology,
New York University School of Medicine,
New York, NY

C.D. Phillips, MD, FACR

Professor of Radiology, Weill Cornell Medical
College, Director of Head and Neck Imaging,
New York-Presbyterian Hospital, New York, NY

Lubdha M. Shah, MD, MS

Professor of Radiology and Director of Spine
Imaging, University of Utah Department of
Radiology and Imaging Sciences, Salt Lake City, UT

STATISTICAL SENIOR EDITOR

Bryan A. Comstock, MS

Senior Biostatistician,
Department of Biostatistics,
University of Washington, Seattle, WA

ARTIFICIAL INTELLIGENCE DEPUTY EDITOR

Peter D. Chang, MD

Assistant Professor-in-Residence,
Departments of Radiological Sciences,
Computer Sciences, and Pathology,
Director, Center for Artificial Intelligence in
Diagnostic Medicine (CAIDM),
University of California, Irvine, Irvine, CA

EDITORIAL BOARD

Ashley H. Aiken, Atlanta, GA

Lea M. Alhilali, Phoenix, AZ

Mohammed A. Almekhlafi, Calgary, Alberta,
Canada

Joachim Berkefeld, Frankfurt, Germany

Aashim Bhatia, Pittsburgh, PA

Waleed Brinjikji, Rochester, MN

Judah Burns, New York, NY

Danielle Byrne, Dublin, Ireland

Federico Cagnazzo, Montpellier, France

J. Levi Chazen, New York, NY

James Y. Chen, San Diego, CA

Gloria C. Chiang, New York, NY

Daniel Chow, Irvine, CA

Kars C.J. Compagne, Rotterdam, The Netherlands

Arturo Consoli, Suresnes, France

Seena Dehkharghani, New York, NY

Nilesh K. Desai, Houston, TX

Yonghong Ding, Rochester, MN

Birgit Ertl-Wagner, Toronto, Ontario, Canada

Clifford J. Eskey, Hanover, NH

Massimo Filippi, Milan, Italy

Nils D. Forkert, Calgary, Alberta, Canada

Ana M. Franceschi, New York, NY

Frank Gaillard, Melbourne, Australia

Joseph J. Gemmete, Ann Arbor, Michigan

Wende N. Gibbs, Phoenix, AZ

Philipp Göltz, Erlangen, Germany

Brent Griffith, Detroit, MI

Joseph M. Hoxworth, Phoenix, Arizona

Raymond Y. Huang, Boston, MA

Gábor Janiga, Magdeburg, Germany

Christof Karmonik, Houston, TX

Timothy J. Kaufmann, Rochester, MN

Hillary R. Kelly, Boston, MA

Toshibumi Kinoshita, Akita, Japan

Alexander W. Korutz, Chicago, IL

Stephen F. Kralik, Houston, TX

Alexander Lerner, Los Angeles, CA

Yinsheng Li, Madison, WI

Franklin A. Marden, Chicago, IL

Markus A. Möhlenbruch, Heidelberg, Germany

Kambiz Nael, Los Angeles, CA

Renato Hoffmann Nunes, Sao Paulo, Brazil

Sasan Partovi, Cleveland, OH

Johannes A.R. Pfaff, Heidelberg, Germany

Laurent Pierot, Reims, France

Alireza Radmanesh, New York, NY

Prashant Raghavan, Baltimore, MD

Eytan Raz, New York, NY

Paul M. Ruggieri, Cleveland, OH

Sebastian Schafer, Madison, WI

Maksim Shapiro, New York, NY

Timothy Shepherd, New York, NY

James Shin, New York, NY

Mark S. Shiroishi, Los Angeles, CA

Bruno P. Soares, Baltimore, MD

Jason F. Talbott, San Francisco, CA

Ruth Thiex, Everett, Washington

Vincent Thijs, Melbourne, Victoria, Australia

Anderanik Tomasian, Los Angeles, CA

Fabio Triulzi, Milan, Italy

Anja G. van der Kolk, Utrecht, the Netherlands

Arastoo Vossough, Philadelphia, PA

Elysa Widjaja, Toronto, Ontario, Canada

Leonard Yeo, Singapore

Woong Yoon, Gwangju, South Korea

David M. Yousem, Evergreen, CO

Carlos Zamora, Chapel Hill, NC

Chengcheng Zhu, Seattle, WA

EDITORIAL FELLOW

Matthew D. Alvin, Baltimore, MD

SPECIAL CONSULTANTS TO THE EDITOR

AJNR Blog Editor

Neil Lall, Denver, CO

Case of the Month Editor

Nicholas Stence, Aurora, CO

Case of the Week Editors

Juan Pablo Cruz, Santiago, Chile

Matylda Machnowska, Toronto, Ontario, Canada

Sapna Rawal, Toronto, Ontario, Canada

Classic Case Editor

Sandy Cheng-Yu Chen, Taipei, Taiwan

Health Care and Socioeconomics Editor

Pina C. Sanelli, New York, NY

Physics Editor

Greg Zaharchuk, Stanford, CA

Podcast Editor

Wende N. Gibbs, Phoenix, AZ

Twitter Editor

Roger Jordan, Houston, TX

Official Journal:

American Society of Neuroradiology

American Society of Functional Neuroradiology

American Society of Head and Neck Radiology

American Society of Pediatric Neuroradiology

American Society of Spine Radiology

Founding Editor

Juan M. Taveras

Editors Emeriti

Mauricio Castillo, Robert I. Grossman,

Michael S. Huckman, Robert M. Quencer

Managing Editor

Karen Halm

Assistant Managing Editor

Laura Wilhelm

Editorial Assistant

Margaret B. Sabato

Executive Director, ASNR

Mary Beth Hepp



Title: Yonge Street, Toronto, a Decade Back. Memories of My Fellowship Days. Acrylic on handmade paper, 17" × 12".
Bejoy Thomas, MD, DNB, PDCC, Trivandrum, Kerala, India

Imaging for Menière Disease

 E. Kay-Rivest,  D.R. Friedmann, and  J.T. Roland

Menière disease is an inner ear problem that manifests with the symptoms of ear fullness, hearing loss, tinnitus, and vertigo attacks. Typically, the fullness, hearing loss, and tinnitus manifest first and are followed by vertigo attacks. The typical episode of vertigo lasts a few hours and is usually accompanied by nausea and vomiting but may persist for days. Menière disease is most commonly unilateral but can affect patients in both ears. The pathognomonic anatomic finding in Menière disease relates to increased endolymphatic fluid volume resulting in distension of the Reissner membrane into the scala vestibuli of the cochlea. Presently, endolymphatic hydrops can only be confirmed with postmortem examination of temporal bone specimens.

Thus, the diagnosis of definite Menière disease is based on clinical criteria and requires the observation of an episodic vertigo syndrome associated with low- to midfrequency sensorineural hearing loss and fluctuating aural symptoms (hearing loss, tinnitus, and/or fullness) in the affected ear. Probable Menière disease is a broader concept defined by episodic vestibular symptoms (vertigo or dizziness) associated with fluctuating aural symptoms occurring for 20 minutes to 24 hours.¹ With astute history-taking and clinical observation, Menière disease can be differentiated from other inner ear or neurologic disorders that cause similar symptoms.

As neurotologists with a large practice in a metropolitan area, we treat many patients with endolymphatic hydrops. We have often requested MR imaging of the cerebellar pontine angle when we are contemplating a more aggressive intervention in patients who do not obtain relief with medical intervention, such as endolymphatic sac decompression, vestibular nerve section, and labyrinthectomy. We request imaging to rule out other pathologies on the affected and the contralateral sides. We do not consider imaging to be absolutely necessary for the initial diagnosis of Meniere disease.

Other physiologic tests have been used to evaluate and diagnose the patient with Menière disease. The audiogram is important because Menière disease preferentially affects the lower and middle frequencies and is one of the only inner ear pathologies to cause fluctuating low-frequency sensorineural hearing loss. With progression of disease, the patient may also lose high-frequency hearing and even completely lose hearing. Electrocochleography (ECoG) has been used as a diagnostic tool. Clinical evaluation of cochlear function using ECoG has focused on the amplitude ratio of the summing potential (SP) and action potential (AP). An elevated SP/AP ratio is thought to reflect endolymphatic hydrops in patients with suspected Menière disease. Results from a survey of otologist and neurotologist professional society members suggested low clinical utility of ECoG in diagnosis/management of Menière disease. For approximately half of respondents, ECoG had no role in their

clinical practice. ECoG was used routinely by only 1 in 6 respondents. Those who used ECoG differed widely in electrode placement and type of stimulus paradigm used.² Vestibular-evoked myogenic potentials have also been investigated as a means of diagnosing Menière disease, but their clinical accuracy and utility are not evident at this time.³

Imaging of the inner ear can now detect endolymphatic hydrops.⁴ Different techniques such as delayed imaging after intravenous administration of a double dose of gadolinium and imaging after intratympanic gadolinium administration have been used. Several studies, including one of our own, have validated a strong correlation with a symptomatic ear and positive imaging findings of dilated endolymphatic spaces in the inner ear.⁵

Although no cost analysis has been performed evaluating MR imaging in the diagnosis of Menière disease, its use certainly incurs higher costs. As stated, these studies can be performed with either intratympanic (IT) or IV injection of gadolinium. The IT route requires an individual qualified in injecting into the middle ear through the tympanic membrane. Furthermore, the MR imaging is performed 24 hours after the IT injection, involving 2 hospital or clinic visits. If bilateral Menière disease is suspected, the patient requires bilateral injections. There are risks to IT injections of any sort, including further hearing loss, tympanic membrane perforation, and infection. The IV route is less labor-intensive; however, patients are still required to wait 4–6 hours before MR imaging.

Other inner ear findings may mimic Meniere symptoms, such as a dural-based tumor adjacent to the endolymphatic sac. Some reports support a high-riding jugular bulb, impinging on the endolymphatic sac, that can be associated with a higher incidence of Menière disease along with other causes of “secondary” endolymphatic hydrops.⁶ In addition, other diagnoses such as vestibular migraine and vestibular neuronitis, for example, may mimic symptoms associated with endolymphatic hydrops. MR imaging shows promise in helping to better differentiate these entities.⁷

However, can imaging absolutely rule out Menière disease? In complex situations in which Workers’ Compensation insurance or malpractice litigation are involved, can imaging be of use? Imaging of the inner ear, with the ability to reliably detect dilation of the endolymphatic spaces, might satisfy those who are making legal and financial decisions. Additionally, we do not know the incidence of positive radiographic findings in ears of patients without symptoms. Is an ear with the appearance of hydrops on imaging likely to develop into a symptomatic ear? Can imaging predict the severity of the associated hearing loss or the likelihood of recovery? Can we use imaging to regulate medical management, such as knowing when to stop or reduce a medication that has been effective? Can imaging predict which patient might develop bilateral Menière disease and therefore help determine the aggressiveness of interventions?⁸

In summary, we think that imaging of the inner ear with advanced MR imaging techniques, while interesting, is not essential for the diagnosis and management of the overwhelming majority of patients with Menière disease. There are some questions that might be answered with well-designed clinical studies in

asymptomatic patients, in unilateral symptomatic patients, in patients in whom the diagnosis of Menière disease is questioned, and in patients in whom the cessation of medical therapy is under consideration. Furthermore, patients with so-called “cochlear hydrops” may manifest only auditory symptoms with characteristic low-frequency sensorineural hearing loss but without vertigo. It is unclear whether this symptom complex represents a spectrum of Menière disease with the same histopathologic findings or a distinct entity. There is the potential for imaging to clarify this question. Undoubtedly, high-resolution imaging of the inner ear is of great interest and importance to neurotologists for many other reasons. Pursuing Menière imaging technology might lead eventually to visualizing the spiral ganglion cell count or accurately measuring the cross-sectional area of the cochlear nerve.

REFERENCES

1. Lopez-Escamez JA, Carey J, Chung WH, et al; Korean Balance Society. **Diagnostic criteria for Menière's disease.** *J Vestib Res* 2015;25:1–7 CrossRef Medline
2. Nguyen LT, Harris JP, Nguyen QT. **Clinical utility of electrocochleography in the diagnosis and management of Ménière's disease: AOS and ANS membership survey data.** *Otol Neurotol* 2010;31:455–59 CrossRef Medline
3. Maheu M, Alvarado-Umanzor JM, Delcenserie A, et al. **The clinical utility of vestibular-evoked myogenic potentials in the diagnosis of Ménière's disease.** *Front Neurol* 2017;8:415 CrossRef Medline
4. Lopez-Escamez JA, Attyé A. **Systematic review of magnetic resonance imaging for diagnosis of Meniere disease.** *J Vestib Res* 2019;29:121–29 CrossRef Medline
5. Hagiwara M, Roland JT Jr, Wu X, et al. **Identification of endolymphatic hydrops in Ménière's disease utilizing delayed postcontrast 3D FLAIR and fused 3D FLAIR and CISS color maps.** *Otol Neurotol* 2014;35:e337–42 CrossRef Medline
6. Ferster AP, Cureoglu S, Keskin N, et al. **Secondary endolymphatic hydrops.** *Otol Neurotol* 2017;38:774–79 CrossRef Medline
7. Sun W, Guo P, Ren T, et al. **Magnetic resonance imaging of intratympanic gadolinium helps differentiate vestibular migraine from Ménière disease.** *Laryngoscope* 2017;127:2382–88 CrossRef Medline
8. Attyé A, Barma M, Schmerber S, et al. **The vestibular aqueduct sign: magnetic resonance imaging can detect abnormalities in both ears of patients with unilateral Meniere's disease.** *J Neuroradiol* 2020;47:174–79 CrossRef

Cross-Sectional Imaging of Third Molar–Related Abnormalities

 R.M. Loureiro,  D.V. Sumi,  H.L.V.C. Tames,  S.P.P. Ribeiro,  C.R. Soares,  R.L.E. Gomes, and  M.M. Daniel



ABSTRACT

SUMMARY: Third molars may be associated with a wide range of pathologic conditions, including mechanical, inflammatory, infectious, cystic, neoplastic, and iatrogenic. Diagnosis of third molar–related conditions can be challenging for radiologists who lack experience in dental imaging. Appropriate imaging evaluation can help practicing radiologists arrive at correct diagnoses, thus improving patient care. This review discusses the imaging findings of various conditions related to third molars, highlighting relevant anatomy and cross-sectional imaging techniques. In addition, key imaging findings of complications of third molar extraction are presented.

ABBREVIATIONS: CBCT = cone-beam CT; MDCT = multidetector-row CT

Third molars, or wisdom teeth, are a more common source of pathologic conditions than other teeth. They are the last teeth to develop and usually fail to erupt correctly. Impacted third molars have been associated with inflammatory and infectious conditions as well as development of cysts and tumors.¹ Furthermore, third molar extraction is a widespread procedure in clinical practice with the potential for multiple complications.²

Although dedicated dental images are not performed in some radiology services, the teeth are often included in examinations of the head and neck. Third molar–related abnormalities can be incidental findings or the cause of a patient’s symptoms. This review discusses the imaging findings of various pathologies related to third molars, highlighting the relevant anatomy and describing cross-sectional imaging techniques. Finally, key imaging findings of complications of third molar extraction are presented.

ANATOMY

The third molar is the most distal tooth located in each quadrant of the permanent dentition and is absent in the primary dentition (the deciduous dentition or temporary “baby teeth”).³ Third

molars usually erupt between 18 and 25 years of age.⁴ Every tooth is anatomically divided into a crown and a root by the cementoenamel junction. The crown is the outer portion exposed in the oral cavity, and the root is the portion covered by the alveolar ridge (Fig 1).³ Each crown has 5 free surfaces. In the case of the molars, the surfaces are named as follows: mesial, distal, buccal, lingual, and occlusal, referring to the anterior, posterior, lateral, medial, and biting surfaces, respectively.⁴ Third molars have a square-shaped crown with a large and irregular occlusal surface suitable for shearing and grinding food and usually have 3 roots, though the number is variable.⁵

The maxillary third molars can have a close anatomic relationship with the maxillary sinus floor, depending on the length and divergence of their roots and the degree of pneumatization of the maxillary sinus. This close relationship increases the risk of developing odontogenic sinusitis as well as an oroantral fistula after dental extraction.⁶

The mandibular third molars are the teeth closest to the mandibular canal, which contains the inferior alveolar neurovascular bundle. This close relationship poses a risk of injury to the inferior alveolar nerve during dental procedures, particularly mandibular third molar extraction.⁷

CROSS-SECTIONAL IMAGING METHODS

Cone-beam CT (CBCT) and multidetector-row CT (MDCT) are able to evaluate the teeth and adjacent bone with submillimeter spatial resolution, allowing for multiplanar reformatting and 3D reconstruction.^{8,9}

CBCT uses a pulsed conic or pyramidal x-ray beam and a flat panel detector and performs a single rotation in a circular path around an isocenter to obtain images.⁸ CBCT involves less radiation

Received April 7, 2020; accepted after revision June 19.

From the Department of Radiology, Hospital Israelita Albert Einstein, São Paulo, SP, Brazil.

Previously presented in part at: Jornada Paulista de Radiologia, May 2-5, 2019; São Paulo, Brazil.

Please address correspondence to Rafael Maffei Loureiro, MD, Hospital Israelita Albert Einstein, Department of Radiology, Av. Albert Einstein, 627/701, 05652-900 São Paulo, SP, Brazil, e-mail: rafael.loureiro@einstein.br; @RMaffeiLoureiro

 Indicates open access to non-subscribers at www.ajnr.org

 Indicates article with supplemental on-line photos.

<http://dx.doi.org/10.3174/ajnr.A6747>

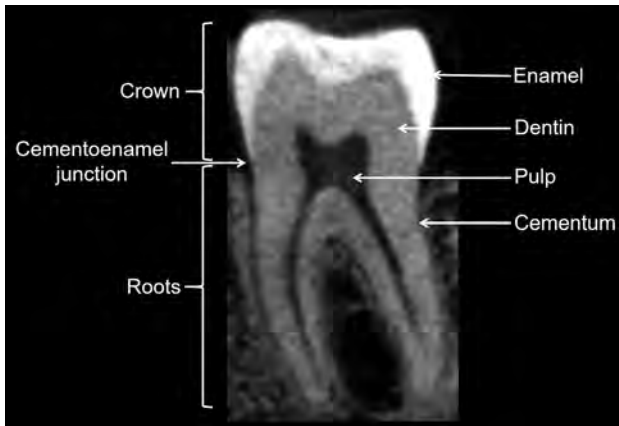


FIG 1. Anatomy of a normal molar tooth. Sagittal CBCT image shows the 3 mineralized hard tissues (enamel, dentin, cementum) and the pulp. The enamel is the outermost layer of the crown, and the root is enveloped by a thin layer of cementum. The dentin is isoattenuating to the cementum and hypoattenuating to the enamel. The pulp contains the neurovascular elements.

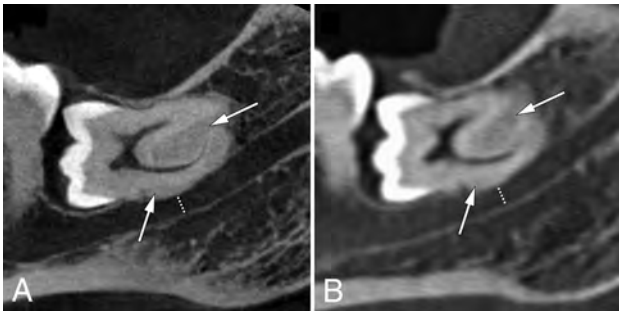


FIG 2. Horizontal unerupted impacted third molar. Sagittal CBCT (A) and MDCT (B) images show an unerupted third molar impacted in the second molar. A close relationship between the third molar and the roof of the mandibular canal, hypercementosis around the roots (arrows), and mild reduction of the caliber of this canal (dotted lines) are observed. The CBCT image (A) has considerably higher spatial resolution than the MDCT image (B) (voxel size, 0.09 mm versus 0.625 mm).



FIG 3. Pericoronitis. Axial contrast-enhanced CT (A) image shows thickening and enhancement of pericoronar tissues around the left mandibular third molar (long arrow), thickening of the adjacent buccinator-buccal mucosa complex (short arrow), and stranding of the left buccal space (arrowheads). Coronal CT (B) image shows that this tooth is partially erupted and covered by thickened gingiva (star). The “puffed-cheek” technique distends the oral cavity with air, helping to detect these abnormalities more accurately.

exposure and has higher spatial resolution than MDCT (Fig 2).¹⁰ Whereas MDCT produces images of the entire part of the body under examination, CBCT typically provides a small set of different field-of-view sizes, ranging from 4 cm (ideal for a few teeth) to >20 cm in diameter according to the clinical indication.¹¹ CBCT is more suitable for patients who are claustrophobic because it has an open design and is generally performed with the patient in an upright position (seated or standing), but MDCT is performed with the patient lying down.⁸ However, CBCT has the disadvantage of poor image quality for soft tissues.¹²

By contrast, MDCT uses a fan-shaped beam that performs several rotations around the patient to obtain images, commonly in a continuous spiral over the axial plane. MDCT has a shorter acquisition time, thus reducing motion artifacts, such as those caused by breathing and swallowing. A distinctive feature of MDCT is that it affords superior characterization of soft tissue. It is also possible to administer an iodinated-based contrast agent when using this method, which is especially helpful when an infection or tumor is under investigation.⁹ However, compared with CBCT, MDCT has some drawbacks, including a higher cost, a greater amount of space needed to house the equipment, and generation of more metal artifacts.¹³

Postprocessing dental software packages are available for both CBCT and MDCT, though they are usually purchased at an additional cost for MDCT. These software packages produce reformatted panoramic and multiple cross-sectional images along the dental arches and are particularly helpful when planning dental implants.¹⁴

On MDCT examination, some dynamic maneuvers can be performed to provide more image detail and enhanced accuracy. When evaluating the soft tissues adjacent to the teeth, the “puffed-cheek” technique is of considerable value. In this maneuver, the patient distends the oral cavity with air, separating the gingival and buccal mucosal surfaces, which helps to better depict mucosal lesions (Fig 3).¹⁵ Metal artifacts from dental hardware can be avoided by acquiring images with the mouth closed and open, moving the artifacts to a different area in the second acquisition.¹⁶ An alternative strategy is to perform a second acquisition through the oral cavity with the neck flexed or extended (or with the gantry angled)¹⁷ to cast these artifacts into a different plane.

Metal artifact reduction algorithms can improve the quality of images obtained by CBCT and MDCT,^{8,18} though they may introduce new artifacts into the images. Therefore, images obtained with and without application of these algorithms should always be reviewed together to avoid misinterpretation.¹⁸

MR imaging is a useful radiation-free tool for evaluation of dentoalveolar disease in selected cases and provides superior soft-tissue contrast. It is the ideal imaging choice for assessment of early bone marrow abnormalities in suspected osteomyelitis, soft tissue infections, and both cystic and solid components of jaw tumors.¹⁹⁻²¹ Moreover, MR imaging neurography can assess the terminal branches of the trigeminal nerve that are in close proximity to the mandibular third molars.²² However, MR imaging is an expensive and time-consuming technique that has lower spatial resolution than CT.²¹

THIRD MOLAR IMPACTION

Tooth impaction is a pathologic condition in which complete eruption into a normal functional position is prevented because

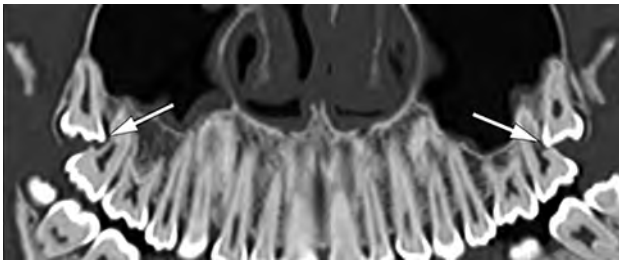


FIG 4. Panoramic reformatted CT image shows impacted unerupted maxillary third molars causing external root resorption of the maxillary second molars (*arrows*).

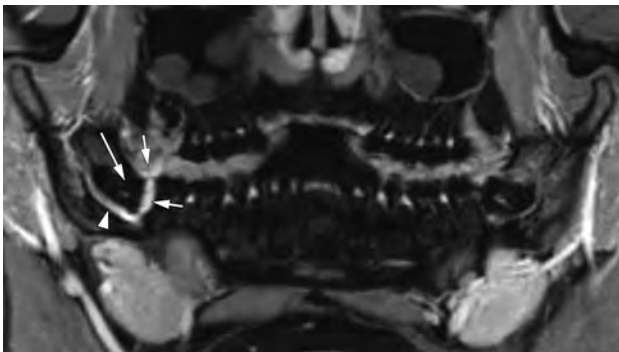


FIG 5. Pericoronitis. Panoramic reformatted contrast-enhanced T1-weighted MR image shows enhancement of the soft tissues (*short arrows*) around the crown of the horizontally impacted right mandibular third molar (*long arrow*) as well as in the right mandibular canal (*arrowhead*).



FIG 6. Odontogenic sinusitis. Oblique sagittal CT image shows mucosal thickening of the maxillary sinus associated with a bone defect (*short arrow*) that communicates the sinus floor with periapical disease of a third molar with a carious lesion (*long arrow*).

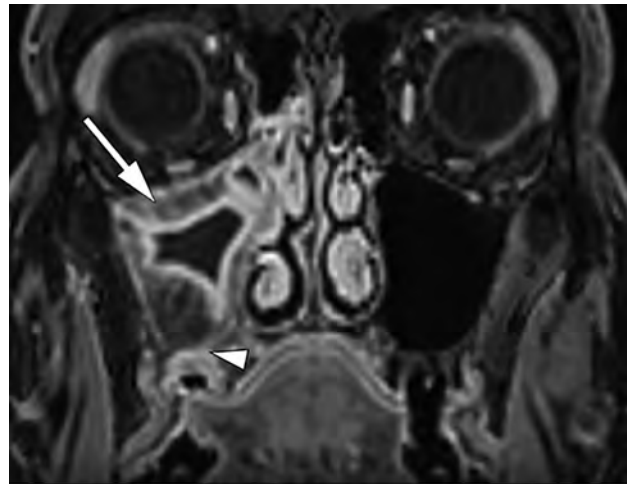


FIG 7. Odontogenic sinusitis following maxillary third molar extraction. Coronal contrast-enhanced T1-weighted MR image shows complete opacification of the right maxillary sinus with mucosal thickening and enhancement (*arrow*) associated with a bone defect in its floor (third molar socket) (*arrowhead*).



FIG 8. Dentigerous cyst. Oblique sagittal CT image shows an expansile well-defined lesion surrounding an unerupted mandibular third molar that is partially attached in the cemento-enamel junction (*arrow*). Hypercementosis is observed around the roots of this tooth (*arrowhead*).

of a lack of space, obstruction by another tooth, malposition, or other impediment (Fig 2).¹ Third molars are the teeth most commonly impacted, with an estimated worldwide prevalence of 24.4%.²³ Third molar impaction is more frequent in the mandible and has a female predominance.²⁴

Impacted third molars can be classified according to their inclination to the long axis of the second molar (eg, mesioangular, distoangular, or horizontal) based on the Archer classification for maxillary third molars and on the Winter classification for mandibular third molars (On-line Figs 1 and 2).²⁵

Complete tooth impaction is considered to have occurred when the tooth is entirely covered by bone, soft tissue, or both. A partial tooth impaction is deemed to have occurred when the tooth is visible on oral inspection but has not erupted into a normal functional position. In most cases, impaction occurs when second molars block the path of eruption of third molars.¹

Partially impacted third molars are prone to development of several pathologies, including pericoronitis, carious lesions, and periodontal bone loss, often because of difficulties in reaching them during routine oral hygiene.^{24,26} External root resorption and carious lesions are usually observed on the distal surface of the adjacent second molars as a result of the pressure exerted by impacted third molars (Fig 4). This leads to inflammation and triggers resorption, ultimately resulting in pulp necrosis and loss of the second molars.^{27,28} Conversely, entirely unerupted impacted third molars are more likely to be associated with development of cysts and tumors.²⁹

When reporting an impacted third molar, it is important to assess the relationship with the adjacent second molar, the

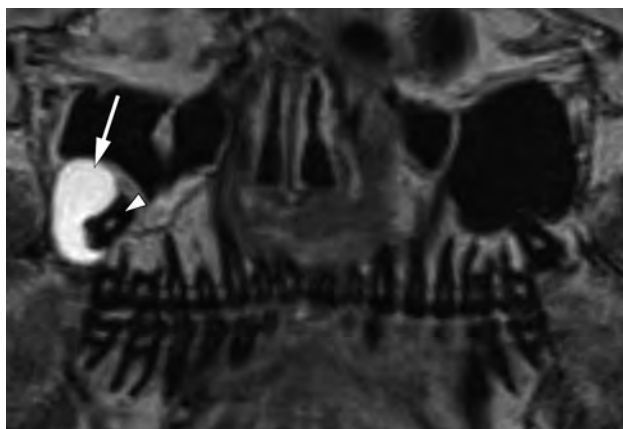


FIG 9. Dentigerous cyst. Panoramic reformatted FLAIR MR image shows an expansile and homogeneous well-defined lesion (arrow) surrounding the crown of the unerupted right maxillary third molar (arrowhead), superiorly displacing the maxillary sinus floor.

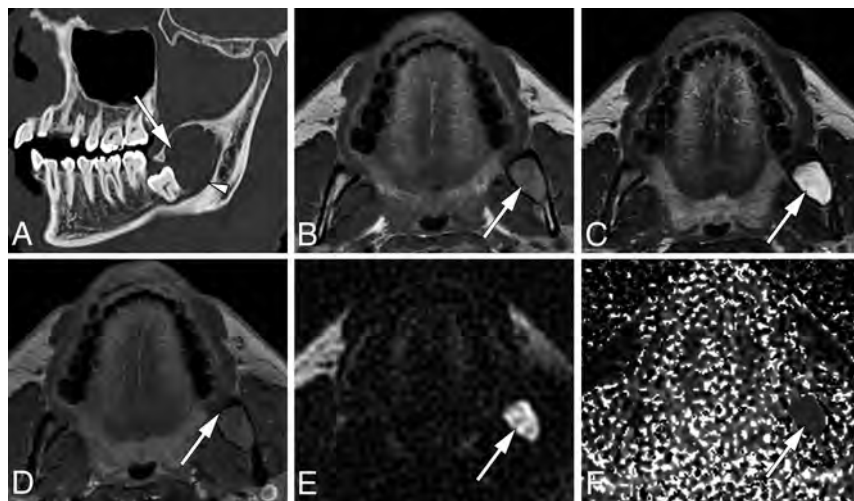


FIG 10. Odontogenic keratocyst. Oblique sagittal CT (A) image shows an expansile, well-defined lesion (arrow) in the left mandibular angle in contact with the distal surface of the unerupted third molar, inferiorly displacing the mandibular canal (arrowhead). Axial T1-weighted (B) and T2-weighted (C) MR images of the same patient show the lesion to be heterogeneous but predominantly isointense to hyperintense on T1WI and hyperintense on T2WI (arrows). Axial contrast-enhanced T1-weighted (D) image shows thin peripheral enhancement (arrow). Diffusion-weighted image (E) and the corresponding ADC map (F) reveal restricted diffusion (arrows).

number of roots and their morphology (convergent, divergent, and/or fused), and in particular the relationship between the tooth and the mandibular canal or maxillary sinus floor. The status of the surrounding bone and any associated pathologies, such as periapical lesions and coronal or pericoronal lucencies, should also be described.³⁰ In some cases, hypercementosis may be observed. Hypercementosis refers to excessive deposition of cementum around the roots of a tooth (Fig 2); it does not alter tooth vitality but can pose difficulties during dental procedures such as extraction and endodontic treatment.³¹

PERICORONITIS

Pericoronitis is an infection of the soft tissue surrounding the crown of a partially erupted tooth, usually the mandibular third molar, which is frequently impacted and partially covered by gingiva. Food debris lodges beneath the overlying gingiva, which is subsequently infected by bacteria.^{3,20} Infection might spread to the surrounding tissue, including the alveolar bone and deep neck spaces, potentially evolving into an abscess. On imaging, pericoronitis typically appears as thickening and enhancement of the pericoronal tissues of a partially erupted tooth (Figs 3 and 5).¹⁶ Contrast-enhanced CT and MR imaging are able to evaluate the spread of infection to surrounding tissues.²⁰ Dynamic maneuvers, such as the “puffed-cheek” technique, can enhance accuracy when evaluating the gingiva.¹⁵

ODONTOGENIC SINUSITIS

Maxillary third molars can be a source of odontogenic sinusitis. For practical purposes, their etiologies can be divided into dental disease (mainly periapical) and iatrogenic. Iatrogenic sources include postdental extraction, inadequate positioning of dental implant fixtures, infected retained roots, and foreign bodies (eg, extruded root canal fillings).^{6,32}

CT is the best imaging method for diagnosis of odontogenic sinusitis. CT demonstrates maxillary sinus disease with a bone defect in the maxillary sinus floor, which is typically associated with dental disease or complications of dental procedures (Figs 6 and 7). Maxillary sinus disease begins as an asymptomatic mucosal thickening in the floor and can evolve to subtotal or total sinus opacification, potentially occluding the ostiomeatal complex and ultimately leading to frontal and anterior ethmoidal sinusitis. Unilateral sinusitis involving the maxillary sinus or the anterior sinuses should raise suspicion for an odontogenic process; therefore, the maxillary sinus floor, posterior maxillary teeth, and alveolar process should be investigated carefully for abnormalities.^{6,33}

CYSTS AND TUMORS

Unrupted impacted third molars are prone to development of odontogenic cysts and tumors, particularly dentigerous cysts, odontogenic keratocysts, and ameloblastomas.²⁹



FIG 11. Ameloblastoma. Oblique sagittal (A) and axial contrast-enhanced (B) CT images show a unilocular, expansile lesion in the right mandibular angle (*arrow*) with marked cortical thinning, buccolingual expansion, and internal solid mural nodules (*arrowheads*). (Case courtesy of Eloisa S. Gebrim, MD, PhD, InRad, University of São Paulo, Brazil.)

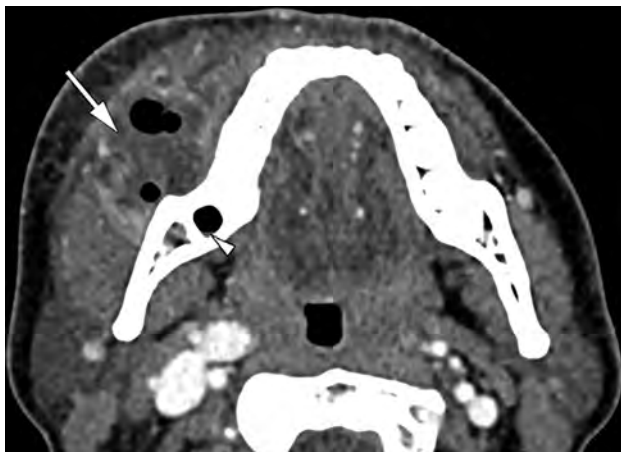


FIG 12. Abscess after dental extraction. Axial contrast-enhanced CT image shows an abscess (*arrow*) near the right mandibular third molar socket (*arrowhead*).

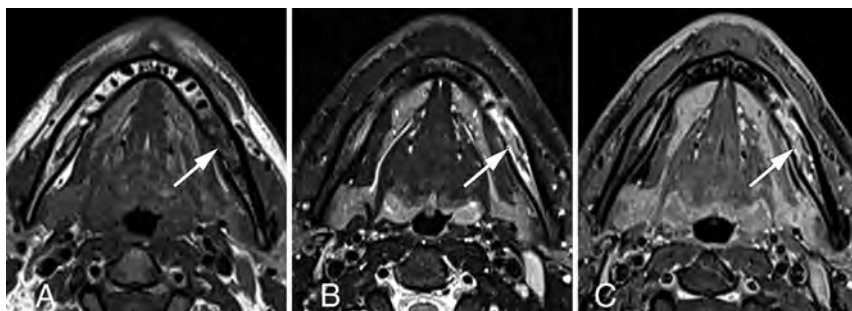


FIG 13. Acute osteomyelitis of the mandible after extraction of the left first and third molars. Axial T1-weighted (A), fat-saturated T2-weighted (B), and contrast-enhanced T1-weighted (C) MR images show signal intensity abnormalities and enhancement of the bone marrow in the left mandibular body (*arrows*).

Dentigerous cysts, also called follicular cysts, are the most common noninflammatory odontogenic cysts, arising around the crown of an unerupted or impacted tooth, most frequently the mandibular third molar.³⁴ On CT, the classic presentation of a dentigerous cyst is a unilocular radiolucent lesion attached to the cemento-enamel junction of an unerupted or impacted tooth.²⁹ On MR imaging, dentigerous cysts typically show low signal intensity on T1-weighted images and high signal intensity on T2-weighted images with a thin enhancing ring (Figs 8 and 9). However, they may appear hyperintense on T1-weighted images because of the presence of cholesterol crystals or proteinaceous material.³⁴

Odontogenic keratocysts are lesions constituted by a cystic space containing desquamated keratin and occur more frequently in the mandible, mainly in the posterior regions. Although they are histologically benign lesions, they are usually locally aggressive with a relatively high recurrence rate.³⁵ On CT, odontogenic keratocysts typically appear as radiolucent, unilocular, expansile lesions with smooth and often scalloped margins. In the mandible, they tend to grow along the length of the bone, causing relatively minimal buccolingual expansion. If associated with the crown of an unerupted tooth, an odontogenic keratocyst can mimic a dentigerous cyst. Large odontogenic keratocysts can present as septate or multiloculated lesions that may simulate ameloblastoma. On MR imaging, odontogenic keratocysts usually show diffuse heterogeneous signal intensity on T1- and T2-weighted images (ranging from low to high) with a thin enhancing ring.^{19,34,36} DWI has proved to be a useful adjuvant tool for differentiating odontogenic lesions; odontogenic keratocysts tend to have lower ADC values because of their high level of desquamated keratin, especially compared with ameloblastomas (Fig 10).^{36,37}

Ameloblastoma is a benign but locally aggressive odontogenic tumor that is more common in the posterior mandible. CT features include a uniloculated or multiloculated expansile lesion, commonly with a “soap-bubble” or honeycombed pattern accompanied by remodeling and cortical thinning. Resorption of the roots of adjacent teeth is also common. Unlike odontogenic keratocysts, ameloblastomas have a propensity for buccolingual expansion in the mandible.^{35,38} MR imaging typically reveals high signal intensity on T2-weighted images. Both contrast-enhanced CT and MR imaging show enhancing septations, mural nodules, or both in classic cases; these enhancing components are more easily detectable on MR imaging scans, which are also useful for evaluating extraosseous components, including involvement of neurovascular structures (Fig 11 and On-line Fig 3).^{19,38} Unicystic ameloblastoma is a subtype encountered less often and can mimic a dentigerous cyst or odontogenic keratocyst.²⁹

COMPLICATIONS OF THIRD MOLAR EXTRACTION

Complications of third molar extraction occur in 3.5% to 14.8% of patients² and are more common in the

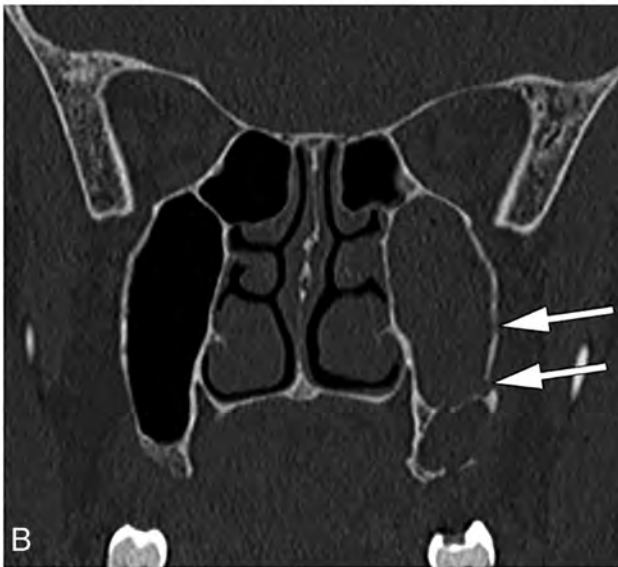
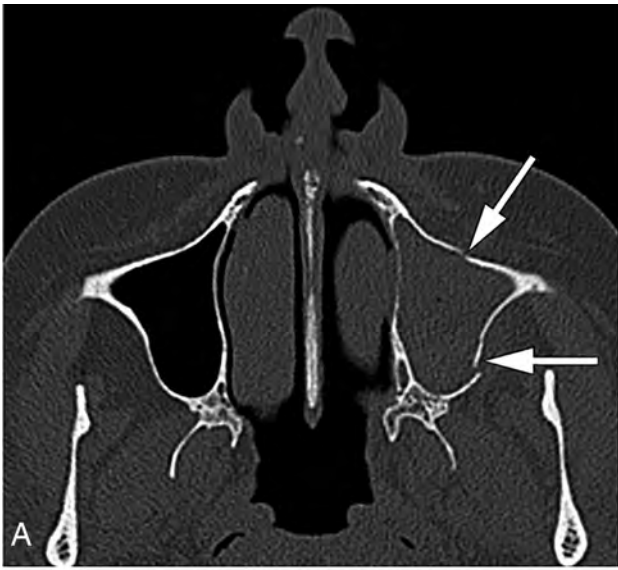


FIG 14. Fracture of the maxillary sinus walls after third molar extraction. Axial (A) and coronal (B) CT images show fractures of the anterior and lateral walls of the left maxillary sinus (arrows) with complete opacification of the sinus.

mandibular third molars.³⁹ Many of these complications are related to a greater degree of tooth impaction.^{2,40} Complications of dental extraction range from mild local discomfort to serious conditions requiring hospitalization or resulting in sequelae.⁴¹

Infection is one of the most frequent complications after third molar removal⁴¹ and often starts at the surgical site.⁴⁰ It can extend to the adjacent soft tissue, leading to cellulitis, myositis, and abscess. Contrast-enhanced CT is the first-line imaging technique for a suspected abscess, which appears as a fluid collection with rim enhancement near the tooth socket, sometimes with gas bubbles, and is frequently associated with surrounding inflammatory changes (Fig 12). Immediate post-procedural soft tissue emphysema is a common finding unless other infectious findings such as abscess or cellulitis are also present. CT is also useful for assessing the bone status

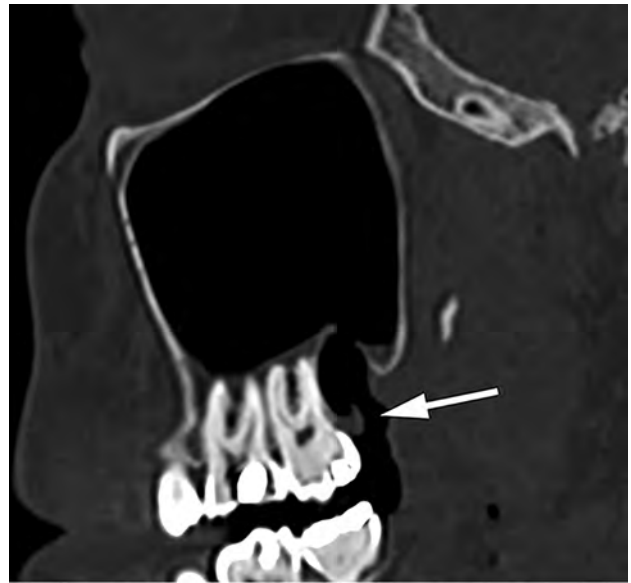


FIG 15. Oroantral fistula after third molar extraction. Sagittal CT image shows an air-filled gap (arrow) between the maxillary sinus and the oral cavity through the tooth socket.

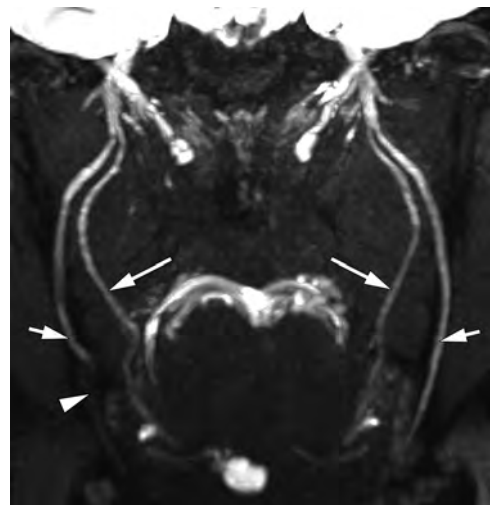


FIG 16. Right inferior alveolar nerve injury after third molar extraction. Coronal MR neurography image of the lingual (long arrows) and inferior alveolar (short arrows) nerves shows a discontinuity in the right inferior alveolar nerve (arrowhead). The remaining nerves have a normal caliber and signal intensity.

in the surgical site and may depict other complications, such as retained tooth fragments and osteomyelitis.⁴²

Osteomyelitis develops when an infection reaches the bone marrow. In the acute phase, MR imaging is the best method for detection of early bone marrow signal abnormalities, observed as low signal on T1-weighted images and high signal on T2-weighted images with enhancement on postcontrast sequences (Fig 13). CT is ideal for depicting bone erosion and periosteal reaction. In the chronic phase, bone sclerosis and sequestrum can be observed. Soft tissue edema, cellulitis, and abscess are common findings in both phases.²⁰



FIG 17. Active bleeding in the tooth socket. Coronal contrast-enhanced CT image shows a focus of active extravasation of contrast material in the tooth socket after extraction (*arrow*). The patient is biting a gauze pad (*arrowhead*).

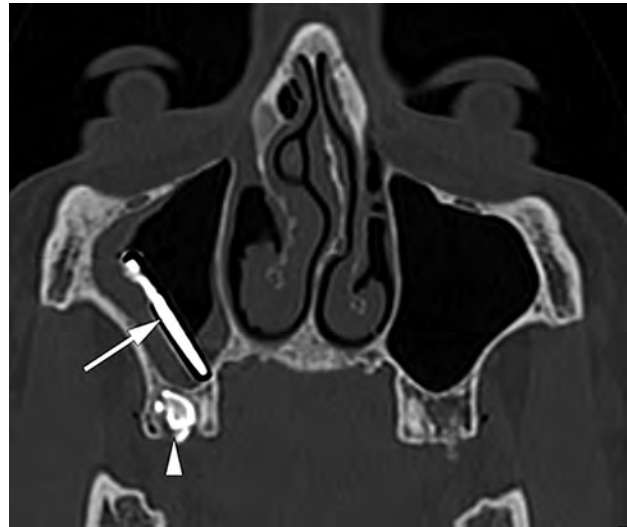


FIG 19. Accidental displacement of a foreign body into the maxillary sinus. Coronal CT image shows a dental bur (*arrow*) displaced into the right maxillary sinus. Fragmentation of the right maxillary third molar is also observed (*arrowhead*).



FIG 18. Accidental third molar displacement into the maxillary sinus. Oblique sagittal CT image shows a third molar displaced into the maxillary sinus (*arrow*) and rupture of the maxillary sinus floor (*arrowhead*) with nearby small bone fragments.

Alveolar osteitis, also called “dry socket,” is a clinical diagnosis characterized by development of intense throbbing pain several days after dental extraction and is often associated with halitosis. Alveolar osteitis is a frequent complication of tooth removal and is related to partial or complete loss of the blood clot in the tooth socket.^{40,41} Oral examination findings include a cryptlike socket with exposed bone and erythematous borders, food debris, and other detritus in the socket. Imaging examinations are useful for exclusion of other complications, such as a residual tooth fragment and fracture.⁴³

Fractures may affect the alveolar processes of the maxilla and mandible; the body, angle, and ramus of the mandible; the maxillary tuberosity; and the floor and walls of the maxillary sinus. CT is the criterion standard imaging method for evaluation of

fractures, which appear as lucent noncorticated lines with variable deviation and angulation of the fragments (Fig 14).^{40,44}

Communication between the maxillary sinus and tooth socket can occur during extraction of a maxillary third molar. If this connection is smaller than 2 mm, it generally closes spontaneously⁴⁵; however, if this communication becomes epithelialized (which takes ~7 days), it becomes an oroantral fistula.⁶ CT is the best imaging technique to diagnose oroantral fistula, which appears as an air connection between the maxillary sinus and the oral cavity (Fig 15). The “puffed-cheek” technique (described earlier) may help detect this air passageway.¹⁶

Mandibular third molar extraction may cause injuries to the peripheral branches of the trigeminal nerve, particularly the inferior alveolar and lingual nerves. Abnormalities can be accurately diagnosed by MR neurography as areas of increased T2 signal intensity, changes in the caliber of the nerve, or discontinuities (Fig 16).^{22,46} Unerupted teeth, horizontal impaction, and root apices inside or in contact with the mandibular canal are associated with an increased risk of inferior alveolar nerve injury, whereas unerupted teeth, distoangular impaction, and the lingual bone split surgical technique are considered risk factors for lingual nerve injury.^{47,48}

Hemorrhage may occur during or after third molar removal; rarely, foci of active bleeding can appear as contrast-material extravasation inside or near the tooth socket (Fig 17).¹⁶

Accidental displacement of the third molar into adjacent spaces, such as the parapharyngeal space or maxillary sinus (Fig 18), is another possible complication after extraction attempts. Foreign bodies, such as root fragments and dental instruments, may also be introduced into the maxillary sinus during extraction (Fig 19).⁴⁹⁻⁵¹

Rarely, emphysema in the subcutaneous and deep neck spaces can result from forced injection of pressurized air

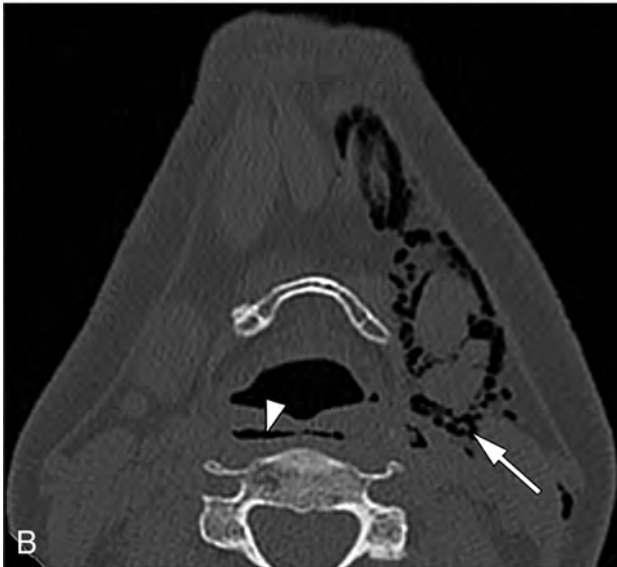


FIG 20. Emphysema following a dental procedure. Axial CT images show extensive deep emphysema in the left face and neck (arrows) as well as in the retropharyngeal or danger space (arrowheads).

from dental drills into the surgical site (Fig 20).^{52,53} Finally, overeruption of the opposing third molar is considered a late adverse event, which can lead to tooth misalignment and occlusal disability (Fig 21).⁵⁴

CONCLUSIONS

The increasing sophistication of cross-sectional imaging techniques plays a pivotal role in diagnosing third molar-related conditions, which can be challenging for radiologists who are inexperienced in dental imaging. Comprehensive knowledge of the imaging characteristics of these abnormalities helps the practicing radiologist arrive at a correct diagnosis, thus improving patient care.

ACKNOWLEDGMENT

The authors thank Rodrigo Tonan for the tooth illustrations.



FIG 21. Sagittal CT image shows overeruption of the maxillary third molar (arrow) caused by previous extraction of the opposing third molar.

REFERENCES

- Ghaemina H, Perry J, Nienhuijs ME, et al. **Surgical removal versus retention for the management of asymptomatic disease-free impacted wisdom teeth.** *Cochrane Database Syst Rev* 2016;CD003879 CrossRef Medline
- Miclote I, Agbaje JO, Spaey Y, et al. **Incidence and treatment of complications in patients who had third molars or other teeth extracted.** *Br J Oral Maxillofac Surg* 2018;56:388–93 CrossRef Medline
- Scheinfeld MH, Shifteh K, Avery LL, et al. **Teeth: what radiologists should know.** *Radiographics* 2012;32:1927–44 CrossRef Medline
- Husain MA. **Dental anatomy and nomenclature for the radiologist.** *Radiology Clin North Am* 2018;56:1–11 CrossRef Medline
- Zohrabian VM, Poon CS, Abrahams JJ. **Embryology and anatomy of the jaw and dentition.** *Semin Ultrasound CT MR* 2015;36:397–406 CrossRef Medline
- Whyte A, Boeddinghaus R. **Imaging of odontogenic sinusitis.** *Clin Radiol* 2019;74:503–16 CrossRef Medline
- Aksoy U, Aksoy S, Orhan K. **A cone-beam computed tomography study of the anatomical relationships between mandibular teeth and the mandibular canal, with a review of the current literature.** *Microsc Res Tech* 2018;81:308–14 CrossRef
- Nasseh I, Al-Rawi W. **Cone beam computed tomography.** *Dent Clin North Am* 2018;62:361–91 CrossRef Medline
- Gohel A, Oda M, Katkar AS, et al. **Multidetector row computed tomography in maxillofacial imaging.** *Dent Clin North Am* 2018;62:453–65 CrossRef Medline
- Nardi C, Talamonti C, Pallotta S, et al. **Head and neck effective dose and quantitative assessment of image quality: a study to compare cone beam CT and multislice spiral CT.** *Dentomaxillofac Radiol* 2017;46:20170030 CrossRef Medline
- Schulze RK, Drage NA. **Cone-beam computed tomography and its applications in dental and maxillofacial radiology.** *Clin Radiol* 2020;May 23 [Epub ahead of print] CrossRef Medline
- Miracle AC, Mukherji SK. **Conebeam CT of the head and neck, part 1: physical principles.** *AJNR Am J Neuroradiol* 2009;30:1088–95 CrossRef Medline

13. Chindasombatjaroen J, Kakimoto N, Murakami S, et al. **Quantitative analysis of metallic artifacts caused by dental metals: comparison of cone-beam and multi-detector row CT scanners.** *Oral Radiology* 2011;27:114–20 CrossRef Medline
14. Scarfe WC, Toghiani S, Azevedo B. **Imaging of benign odontogenic lesions.** *Radiol Clin North Am* 2018;56:45–46 CrossRef Medline
15. Weissman JL, Carrau RL. **“Puffed-cheek” CT improves evaluation of the oral cavity.** *AJNR Am J Neuroradiol* 2001;22:741–44 Medline
16. Loureiro RM, Naves EA, Zanello RF, et al. **Dental emergencies: a practical guide.** *Radiographics* 2019;39:1782–95 CrossRef Medline
17. Barrett JF, Keat N. **Artifacts in CT: recognition and avoidance.** *Radiographics* 2004;24:1679–91 CrossRef Medline
18. Katsura M, Sato J, Akahane M, et al. **Current and novel techniques for metal artifact reduction at CT: practical guide for radiologists.** *Radiographics* 2018;38:450–61 CrossRef Medline
19. Meyer KA, Bancroft LW, Dietrich TJ, et al. **Imaging characteristics of benign, malignant, and infectious jaw lesions: a pictorial review.** *AJR Am J Roentgenol* 2011;197:W412–21 CrossRef Medline
20. Mardini S, Gohel A. **Imaging of odontogenic infections.** *Radiol Clin North Am* 2018;56:31–44 CrossRef Medline
21. Demirturk Kocasarac H, Geha H, Gaalaas LR, et al. **MRI for dental applications.** *Dent Clin North Am* 2018;62:467–80 CrossRef Medline
22. Dessouky R, Xi Y, Zuniga J, et al. **Role of MR neurography for the diagnosis of peripheral trigeminal nerve injuries in patients with prior molar tooth extraction.** *AJNR Am J Neuroradiol* 2018;39:162–69 CrossRef Medline
23. Carter K, Worthington S. **Predictors of third molar impaction: a systematic review and meta-analysis.** *J Dent Res* 2016;95:267–76 CrossRef Medline
24. Shoshani-Dror D, Shilo D, Ginini JG, et al. **Controversy regarding the need for prophylactic removal of impacted third molars: an overview.** *Quintessence Int* 2018;49:653–62 CrossRef Medline
25. Miclotte A, Grommen B, Cadenas de Llano-Pérula M, et al. **The effect of first and second premolar extractions on third molars: a retrospective longitudinal study.** *J Dent* 2017;61:55–66 CrossRef Medline
26. Steed MB. **The indications for third-molar extractions.** *J Am Dent Assoc* 2014;145:570–73 CrossRef Medline
27. Tassoker M. **What are the risk factors for external root resorption of second molars associated with impacted third molars? A cone-beam computed tomography study.** *J Oral Maxillofac Surg* 2019;77:11–17 CrossRef Medline
28. Consolaro A, Bittencourt G. **Why not to treat the tooth canal to solve external root resorptions? Here are the principles!** *Dental Press J Orthod* 2016;21:20–22 CrossRef Medline
29. Mortazavi H, Baharvand M. **Jaw lesions associated with impacted tooth: a radiographic diagnostic guide.** *Imaging Sci Dent* 2016;46:147–57 CrossRef Medline
30. Matzen LH, Wenzel A. **Efficacy of CBCT for assessment of impacted mandibular third molars: a review—based on a hierarchical model of evidence.** *Dentomaxillofac Radiol* 2015;44:20140189 CrossRef Medline
31. Patil SR, Araki K, Yadav N, et al. **Prevalence of hypercementosis in a Saudi Arabian population: a cone beam computed tomography study.** *J Oral Res* 2018;7:94–97 CrossRef Medline
32. Kim SM. **Definition and management of odontogenic maxillary sinusitis.** *Maxillofac Plast Reconstr Surg* 2019;41:13 CrossRef Medline
33. Little RE, Long CM, Loehrl TA, et al. **Odontogenic sinusitis: a review of the current literature.** *Laryngoscope Investig Otolaryngol* 2018;3:110–14 CrossRef Medline
34. Mosier KM. **Lesions of the jaw.** *Semin Ultrasound CT MR* 2015;36:444–50 CrossRef Medline
35. Bilodeau EA, Collins BM. **Odontogenic cysts and neoplasms.** *Surg Pathol Clin* 2017;10:177–222 CrossRef Medline
36. Borghesi A, Nardi C, Giannitto C, et al. **Odontogenic keratocyst: imaging features of a benign lesion with an aggressive behaviour.** *Insights Imaging* 2018;9:883–97 CrossRef Medline
37. Sumi M, Ichikawa Y, Katayama I, et al. **Diffusion-weighted MR imaging of ameloblastomas and keratocystic odontogenic tumors: differentiation by apparent diffusion coefficients of cystic lesions.** *AJNR Am J Neuroradiol* 2008;29:1897–901 CrossRef Medline
38. Oren N, Vaysberg A, Ginat DT. **Updated WHO nomenclature of head and neck lesions and associated imaging findings.** *Insights Imaging* 2019;10:72 CrossRef Medline
39. Contar CM, de Oliveira P, Kanegusuku K, et al. **Complications in third molar removal: a retrospective study of 588 patients.** *Med Oral Patol Oral Cir Bucal* 2010;15:e74–78 CrossRef Medline
40. Deliverska EG, Petkova M. **Complications after extraction of impacted third molars—literature review.** *J IMAB* 2016;22:1202–11 CrossRef
41. Bouloux GF, Steed MB, Perciaccante VJ. **Complications of third molar surgery.** *Oral Maxillofac Surg Clin North Am* 2007;19:117–28 CrossRef Medline
42. Capps EF, Kinsella JJ, Gupta M, et al. **Emergency imaging assessment of acute, nontraumatic conditions of the head and neck.** *Radiographics* 2010;30:1335–52 CrossRef Medline
43. Susarla SM, Smart RJ, Dodson TB. **Complications associated with den-toalveolar surgery.** In: Andersson L, Kahnberg KE, Pogrel MA, eds. *Oral and Maxillofacial Surgery.* Blackwell; 2010:155–63
44. Chrcanovic BR, Custódio AL. **Considerations of mandibular angle fractures during and after surgery for removal of third molars: a review of the literature.** *Oral Maxillofac Surg* 2010;14:71–80 CrossRef Medline
45. Kretzschmar DP, Kretzschmar JL. **Rhinosinusitis: review from a dental perspective.** *Oral Surg Oral Med Oral Pathol Oral Radiol Endod* 2003;96:128–35 CrossRef Medline
46. Cox B, Zuniga JR, Panchal N, et al. **Magnetic resonance neurography in the management of peripheral trigeminal neuropathy: experience in a tertiary care centre.** *Eur Radiol* 2016;26:3392–400 CrossRef Medline
47. Juodzbalys G, Daugela P. **Mandibular third molar impaction: review of literature and a proposal of a classification.** *J Oral Maxillofac Res* 2013;4:e1 CrossRef Medline
48. Leung YY, Cheung LK. **Risk factors of neurosensory deficits in lower third molar surgery: a literature review of prospective studies.** *Int J Oral Maxillofac Surg* 2011;40:1–10 CrossRef Medline
49. Iwai T, Chikumaru H, Shibasaki M, et al. **Safe method of extraction to prevent a deeply-impacted maxillary third molar being displaced into the maxillary sinus.** *Br J Oral Maxillofac Surg* 2013;51:e75–6–e76 CrossRef Medline
50. Hara Y, Shiratsuchi H, Tamagawa T, et al. **A large-scale study of treatment methods for foreign bodies in the maxillary sinus.** *J Oral Sci* 2018;60:321–28 CrossRef Medline
51. Di Nardo D, Mazzucchi G, Lollobrigida M, et al. **Immediate or delayed retrieval of the displaced third molar: a review.** *J Clin Exp Dent* 2019;11:e55–61 CrossRef Medline
52. Romeo U, Galanakis A, Lerario F, et al. **Subcutaneous emphysema during third molar surgery: a case report.** *Braz Dent J* 2011;22:83–86 CrossRef Medline
53. Tay YBE, Loh WS. **Extensive subcutaneous emphysema, pneumo-mediastinum, and pneumorrhachis following third molar surgery.** *Int J Oral Maxillofac Surg* 2018;47:1609–12 CrossRef Medline
54. Craddock HL. **An investigation of overeruption of posterior teeth with partial occlusal contact.** *J Oral Rehabil* 2007;34:246–50 CrossRef Medline

The Perplexity Surrounding Chiari Malformations – Are We Any Wiser Now?

 S.B. Hiremath,  A. Fitsiori,  J. Boto,  C. Torres,  N. Zakhari,  J.-L. Dietemann,  T.R. Meling, and  M.I. Vargas



ABSTRACT

SUMMARY: Chiari malformations are a diverse group of abnormalities of the brain, craniovertebral junction, and the spine. Chiari 0, I, and 1.5 malformations, likely a spectrum of the same malformation with increasing severity, are due to the inadequacy of the para-axial mesoderm, which leads to insufficient development of occipital somites. Chiari II malformation is possibly due to nonclosure of the caudal end of the neuropore, with similar pathogenesis in the rostral end, which causes a Chiari III malformation. There have been significant developments in the understanding of this complex entity owing to insights into the pathogenesis and advancements in imaging modalities and neurosurgical techniques. This article aims to review the different types and pathophysiology of the Chiari malformations, along with a description of the various associated abnormalities. We also highlight the role of ante- and postnatal imaging, with a focus on the newer techniques in the presurgical evaluation, with a brief mention of the surgical procedures and the associated postsurgical complications.

ABBREVIATION: CM = Chiari malformation

Chiari malformations (CMs) are a group of rhombencephalic abnormalities, initially described by Hans Chiari, traditionally classified into 4 types.¹⁻³ Types I to III are associated with a varying degree of caudal displacement of the contents of the posterior fossa, along with cerebellar tonsillar herniation through the foramen magnum. Type IV is characterized by cerebellar hypoplasia or aplasia and an occipital encephalocele.¹⁻³ Because of the complex nature of the associated abnormalities, CMs can present with diverse clinical manifestations, secondary to the involvement of the cerebellum, brain stem, spinal cord, lower cranial nerves, and altered CSF flow dynamics. Recent advances in imaging techniques, such as phase-contrast imaging, cine MR imaging, and DTI, with frequent imaging and surgical management of these

malformations, necessitate a re-evaluation of this classification because some forms do not conform well to the previously described categories. We present herein a review of the existing literature on the newer types of CMs, their etiopathogenesis, associated abnormalities, and postsurgical evaluation.

Types and Prevalence of CMs

Chiari I malformation (CM-1) is characterized by caudal migration of the cerebellar tonsils below the foramen magnum by >5 mm (Fig 1).^{1,2,4-6} The prevalence of CM-1 was previously estimated to be <1%, with a mild female preponderance.⁷ However, with the frequent use of neuroimaging, incidental identification of CM-1 is estimated to range between 1% and 4% in individuals undergoing MR imaging of the brain and cervical spine.⁸ An advanced form of CM-1, associated with caudal migration of the obex beyond the foramen magnum, and elongation of the medulla and fourth ventricle, is described as CM-1.5 (Fig 2).^{3,4,9} Tubbs et al¹⁰ described a prevalence of CM-1.5 in 17% of individuals initially diagnosed as CM-1.⁹ The higher rates of revision surgery for persistent syringohydromyelia after posterior fossa decompression in CM-1.5 highlight the need to distinguish between the 2 variants.^{4,9} Individuals who present with typical clinical symptoms of CM-1 and syringohydromyelia but lack tonsillar and brain stem herniation are classified as CM-0. Milhorat et al^{11,12} described the occurrence of mild tonsillar herniation (<5 mm), along with syringohydromyelia and clinical features

Received May 10, 2020; accepted after revision June 23.

From the Division of Diagnostic and Interventional Neuroradiology (S.B.H., A.F., J.B., M.I.V.) and the Division of Neurosurgery (T.R.M.), Department of Clinical Neurosciences, Geneva University Hospitals, Geneva, Switzerland; Division of Neuroradiology (S.B.H., C.T., N.Z.), Department of Radiology, University of Ottawa, The Ottawa Hospital Civic Campus, Ottawa, Ontario, Canada; University of Strasbourg (J.-L.D.), Strasbourg, France; and Faculty of Medicine (T.R.M., M.I.V.), University of Geneva, Geneva, Switzerland.

Please address correspondence to Maria Isabel Vargas, MD, Division of Diagnostic and Interventional Neuroradiology, Department of Diagnostics, Geneva University Hospitals, Rue Gabrielle-Perret-Gentil 4, 1211 Genève 14, Switzerland; e-mail: maria.i.vargas@hcuge.ch; @maiva96

 Indicates open access to non-subscribers at www.ajnr.org

 Indicates article with supplemental on-line tables.

 Indicates article with supplemental on-line photos.

<http://dx.doi.org/10.3174/ajnr.A6743>

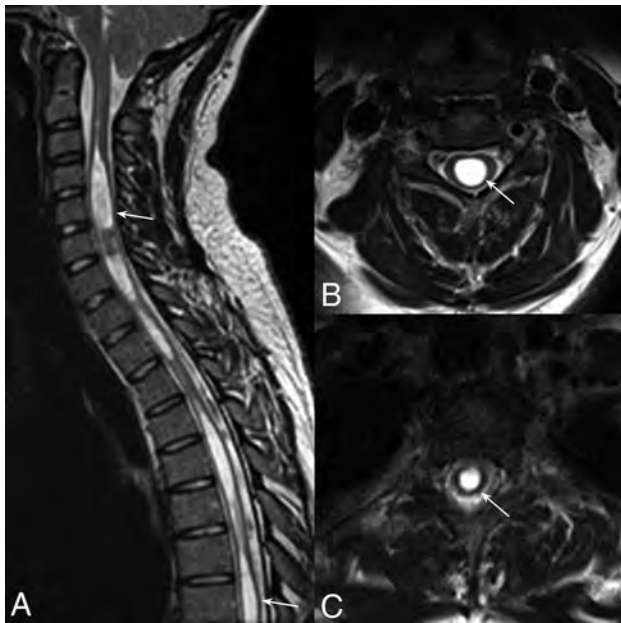


FIG 1. CM-1. Sagittal T2WI of the cervical and upper thoracic spine (A) shows cerebellar tonsillar herniation below the foramen magnum, with syringohydromyelia (arrows). Axial T2WI at C4 (B) and T5 (C) levels demonstrate syringohydromyelia.



FIG 2. CM-1.5. Sagittal T1WI and T2WI of the cervical and upper thoracic spine (A and B) show obex herniation below the foramen magnum, with medullary kink (arrowhead).

typical for CM-1 in 8.7% of patients who are symptomatic, calling it low-lying cerebellar tonsil syndrome.

CM-2 is characterized by caudal migration of the brain stem, cerebellum, and fourth ventricle through the foramen magnum, along with inferior displacement of the cervical

spinal cord (Fig 3).^{1,2,13} The occurrence of low occipital or high cervical encephalocele with signs of CM-2 other than lumbar meningocele and/or myelomeningocele is described as a CM-3.^{1,2} Since the initial description of CM-3, there have only been approximately 60 reported cases.^{3,14} The only reported case of occipitocervical encephalocele communicating with the foregut has been referred to as CM-3.5.^{3,15,16} CM-4, currently termed “primary cerebellar agenesis” or “severe cerebellar hypoplasia,” was initially described as cerebellar hypoplasia with occipital encephalocele.^{2,3} CM 5 is the coexistence of lumbar meningocele and/or myelomeningocele (CM-2), with a low occipital or high cervical myelomeningocele (CM-3).¹⁷

Pathophysiology of CMs

The exact etiopathogenesis of CM-1 is not entirely understood. There is no single hypothesis that can explain the occurrence of CM and all the associated abnormalities. CM-1 is thought to be due to the inadequacy of paraxial mesoderm after the closure of the neural tube, leading to insufficient development of occipital somites.^{18,19} Although a small posterior fossa is not necessarily seen in all patients with CM-1, individuals with a small posterior fossa tend to be symptomatic at an earlier age, present with syringohydromyelia, and show a better response to suboccipital decompression.²⁰⁻²³ CM-0, CM-1, and CM-1.5 share a common pathophysiologic basis and could likely represent a spectrum of the same malformation, with increasing severity, rather than distinct entities.

CM-2 is believed to be due to nonclosure of the caudal end of the neuropore, leading to the egress of CSF from the CNS.^{24,25} The ventricular distension acts as a scaffold for neurodevelopment, primarily of the supratentorial cerebral parenchyma and surrounding mesenchyme, which form the skull vault and base.^{25,26} The absence of adequate ventricular fluid and the failure of distension of the developing ventricles lead to disorganized development of the CNS, which results in abnormalities, including callosal dysgenesis, anomalous neural migration, and falx defects. Secondary effects include mesenchymal maldevelopment and a small posterior fossa, which proves inadequate to contain the developing hindbrain. This leads to caudal descent of the cerebellar vermis, the tonsils, and the fourth ventricle through the foramen magnum into the cervical spinal canal and also to obstruction of CSF flow, with resultant hydrocephalus. CM-3 shares a similar pathophysiology with the defect that involves the rostral end of the neuropore. In fetal life, the neurenteric canal establishes a temporary communication between the yolk sac and the amniotic cavity, and possibly maintains equal pressures in the 2 cavities.²⁷ CM-3.5 may be due to the persistence of the neurenteric canal with resultant abnormal communication between the yolk sac and the amniotic cavity.¹⁵

Associated Abnormalities

The associated abnormalities in CM can be categorized based on their anatomic location into those that involve the brain and spinal cord, skull and vertebral column, ventricles, and meninges, as described in On-line Table 1.

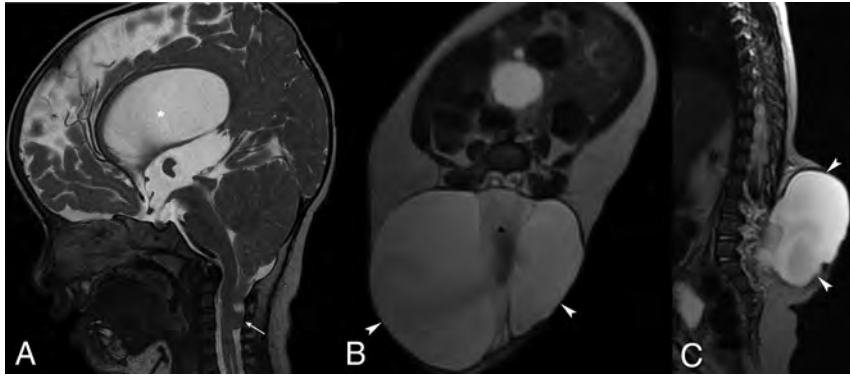


FIG 3. CM-2. Sagittal T2WI of the brain (A) shows cerebellar tonsillar herniation below the level of the foramen magnum (arrow), hydrocephalus (asterisk), tectal beaking, and towering of the cerebellum. Axial and sagittal T2WIs of the lumbar spine (B and C) show myelomeningocele with neural placode exposure (arrowheads) and CSF flow artifacts (asterisk).

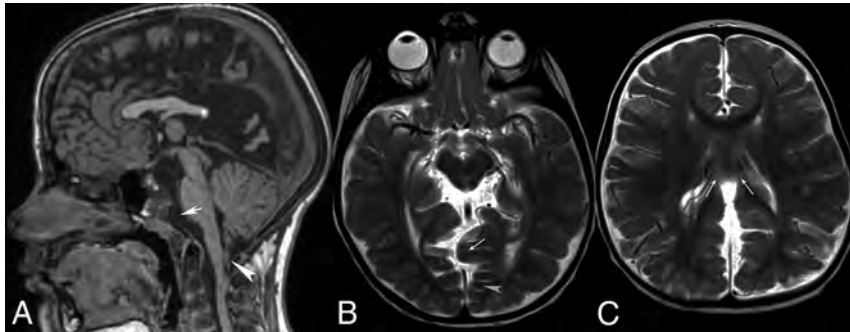


FIG 4. CM-2. Sagittal T1WI of the brain (A) shows hypoplasia of the splenium of corpus callosum (asterisk) and tonsillar parenchymal loss secondary to the herniation (arrowhead), scalloping of the clivus (short arrow), and dysplastic sella (gray asterisk). Axial T2WIs (B and C) show interdigitating gyri (white arrows in B) due to fenestrated falx, stenogryria (gray arrowhead), and hypoplasia of the splenium of the corpus callosum (white arrows in C).

Brain. In CM-1, the brain is usually normal except for asymmetrical tonsillar herniation with a peglike configuration, showing loss of folial pattern.²⁸ CM-1 is associated with anterior flattening of the midbrain, pons, and medulla, and rarely hydrocephalus.²⁹ Although rare, spontaneous resolution of CM-1 is known to occur in children and adults, possibly related to an increased posterior fossa volume, cerebellar tonsillar atrophy, and spontaneous disruption of arachnoid adhesions (On-line Fig 1).⁸

CM-2 is associated with cerebellar hypoplasia and caudal herniation of the cerebellar tonsils, which wrap around the medulla, ie, the so-called banana sign, along with towering of the cerebellum.³⁰ Other cerebellar abnormalities include heterotopic and dysplastic gray matter. In a retrospective study, 2 of 17 patients with cerebellar dysplasias had associated CMs.³¹ The brain stem, especially the midbrain, is elongated, with the fusion of the colliculi and tectal beaking. There is elongation and stenosis of the cerebral aqueduct with hypoplasia or aplasia of cranial nerves.²⁸ The massa intermedia is enlarged and anteriorly displaced in approximately 75%–90% of patients, along with elongation of the habenular commissure and pineal gland.^{28,32} Approximately 90% of patients with CM-2 have associated hydrocephalus and

disproportionate enlargement of the atria and occipital horns, ie, colpocephaly.³³ The corpus callosum may show partial or complete agenesis with the absence of the septum pellucidum (Fig 4). The cerebral cortex may show multiple small gyri, ie, stenogryria, with a partial or complete absence of the olfactory bulbs and tracts. In approximately one-third of the patients with CM-2, ventricular margins may show a nodular appearance due to subependymal nodular heterotopia.^{28,34}

In CM-3, there is cerebellar or low occipital encephalocele in association with herniation of the sagittal sinus or torcular herophili and the brain stem. Partial or complete agenesis of the corpus callosum may also be seen in CM-3.

Spinal Cord. Syringomyelia is a fluid-filled cavity formed by CSF dissecting the spinal cord, as opposed to hydro-myelia, which represents dilation of the ependymal-lined central canal. Because the distinction between these entities is often not possible on imaging, the term syringohydromyelia is used. The filiform or fusiform dilation of the central ependymal canal up to 2–3 mm is termed prominent central canal and >3 mm as syringomyelia.^{17,35} It typically involves the lower cervical or upper thoracic spinal cord; seen in approximately 50%–75% of

individuals with CM-1 and 25%–45% of patients with CM-2, and may also be seen in CM-3.^{36–38} The extent of the abnormality may vary from a small segment of spinal cord to an elongated (holocord) syringohydromyelia. Rarely, syringohydromyelia may contain internal septations and affect the entire length of the spinal cord.

Neuroimaging of the syrinx is essential for presurgical planning for associated scoliosis and craniovertebral junction abnormalities.³⁹ The aim of imaging is to assess the size, extent, and level of cord involvement. It is essential to identify the presyrinx state, ie, an abnormal spinal cord signal intensity adjacent to the syrinx, and the presence of flow voids within the syrinx on T2-weighted MRI because these features are potential predictors of a good response after correction of the CSF obstruction.^{40–42} Open spinal dysraphism, ie, lumbar meningocele and/or myelomeningocele, is associated with CM-2 in >90% of cases.^{1,2,13,17} The global birth prevalence of spina bifida aperta is between 3.4 and 4.8 per 10,000 live births, and nearly all cases are associated with CM-2.^{43–45} Approximately 8% of patients with open spinal dysraphism have an associated diastematomyelia, ie, split cord malformation.⁴⁶

Skull and Vertebral Column. CM-1 is associated with skull base and craniovertebral junction abnormalities, including concave clivus, basilar invagination, and platybasia, in approximately 50% of patients.³⁶ There also is hypoplasia of the basiocciput and foramen magnum widening. The associated bony abnormalities are severe in CM-2. Luckenschadel, or lacunar skull, along with bone scalloping in the frontal region, ie, lemon sign, is usually seen in CM-2. Scalloping of the clivus, petrous temporal bone, and jugular tubercles leads to a shortening of the internal auditory canals. In CM-2, the posterior vertebral defects often affect the lumbar spine and, less commonly, the thoracic spine, compared with CM-3, which involves the cervical spine, predominantly in the upper cervical vertebrae; however, there could be involvement up to the level of C7. Various vertebral segmentation and fusion abnormalities, such as hemivertebrae, block vertebrae, and Klippel-Feil syndrome, can be associated with CM. Other vertebral abnormalities include atlanto-occipital assimilation, the retroflexed odontoid process, and scoliosis.⁴⁷

Meninges. In CM-1, the tentorium cerebelli shows increased sloping, there is arachnoid thickening and adhesions in approximately 70% of patients at the level of the foramen magnum, and outlet of the fourth ventricle can be seen.^{28,48,49} In CM-2, however, the tentorium is low-lying, hypoplastic, V-shaped, and widened, and there is tectal beaking and towering of the cerebellum. The straight sinus is more vertical due to tentorial sloping. The falx cerebri may show fenestrations or hypoplasia with interdigitating gyri in approximately 30% of patients (Fig 4B).⁵⁰ CM-3 shows findings similar to CM-2.

Imaging Modalities and Clinical Utility

Antenatal Imaging. Sonography is currently the imaging technique of choice for the assessment of fetal abnormalities. Fetal MR imaging, a level III diagnostic tool, has increased sensitivity and diagnostic confidence, and provides additional findings that may affect prognosis and management.^{51,52} Fetal MR imaging may accurately demonstrate the level of the defect in open spinal dysraphism but has a limited ability to reveal split cord malformations compared with postnatal MR imaging.⁴⁶ Recent studies indicate improved cerebellar herniation and a decreased need for ventriculoperitoneal CSF shunting, along with improved mental and motor function in patients who underwent in utero repair of open spinal dysraphism compared with those who underwent postnatal repair.^{45,53} Prenatal MR imaging of patients with open spinal dysraphism has shown an association between decreased head circumference and effaced extra-axial CSF spaces in higher grades of CM. However, there was no significant difference in postnatal ventricular size between the prenatal and postnatal repair groups.⁵³

Postnatal Imaging. Radiographic evaluation by using a lateral projection of the skull is used to assess platybasia, retroflexion of the odontoid process, basilar invagination, and atlanto-occipital assimilation. A decreased clival canal angle $<125^\circ$ and a posterior margin of the odontoid process located >9 mm beyond the pB-C2 line indicate a potential risk for occipitocervical fusion, along with posterior cervical decompression.^{54,55} Evaluation of the

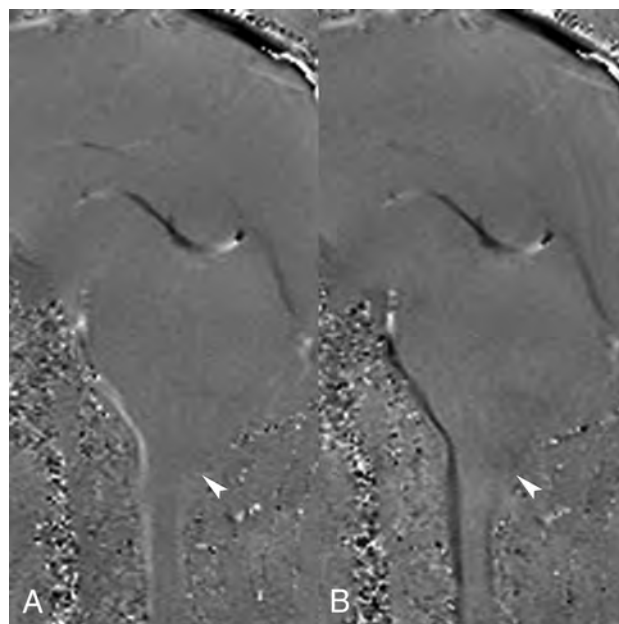


FIG 5. Phase-contrast MR imaging: CSF flow study. Phase images in systole and diastole (A and B) show decreased CSF flow posterior to the cerebellum and the dorsal subarachnoid space (arrowheads).

spine is performed on anteroposterior, upright, and lateral views. The assessment for acute idiopathic scoliosis includes the coronal Cobb angle to look for hyperscoliosis, and Risser scores to look for residual growth potential. The presence of hyperscoliosis may point to an associated neural axis abnormality and syringohydromyelia.

A volumetric CT aids in the optimal evaluation of the bony abnormalities of the skull base, craniocervical junction, and vertebral anomalies. CT is also helpful in the assessment of the posterior fossa volume and cerebellar tonsillar herniation. MR imaging is the most sensitive imaging technique for the evaluation of intracranial abnormalities in CM. The conventional and advanced MR imaging sequences useful in the morphologic assessment of the brain and spine, CSF flow dynamics, tonsillar motion, and the microstructural alterations of the brain stem are as detailed in On-line Table 2.

The evaluation of CSF flow by phase-contrast MR imaging in the presurgical period may serve as a guide for surgical planning and predict surgical outcomes in CM.^{56,57} The salient findings on CSF flow studies include obstruction of CSF flow at the level of the foramen magnum, which results in increased flow in the anterior and decreased flow in the posterior subarachnoid space along the proximal cervical cord (Fig 5). Other findings on CSF flow studies include increased flow in the anterior subarachnoid space and increased CSF flow velocity. Based on the involved regions, the CSF flow abnormalities are classified into 3 different patterns: 1) CSF flow obstruction posterior to the cerebellum and tonsils; 2) CSF flow obstruction posterior to the cerebellum, tonsils, and through the fourth ventricle and cerebral aqueduct; and 3) CSF flow obstruction posterior to the cerebellum and the tonsils, through the fourth ventricle, and the cerebral aqueduct, and ventral to the brain stem.⁵⁸ In pattern 1, “bone only” craniocervical decompression is usually performed and the subarachnoid

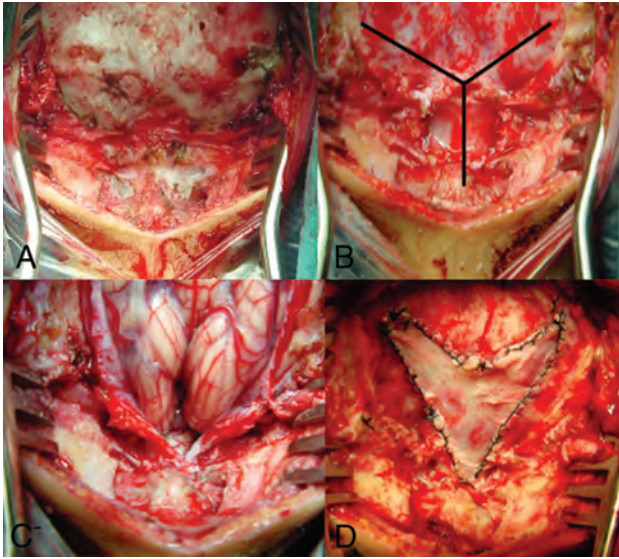


FIG 6. Intraoperative photographs show posterior fossa decompression in a patient with CM-1. *A*, After a midline incision in the occipito-cervical region, the occipital bone, the atlanto-occipital membrane, and the C1 lamina are exposed. *B*, A suboccipital craniectomy and removal of the posterior arch of C1 has been performed, and the dura mater will be opened in a Y-shaped fashion. *C*, After opening of the dura mater and the arachnoid overlying the cisterna magna, the 2 cerebellar hemispheres with their respective cerebellar tonsils can be visualized. *D*, A duraplasty has been performed, wherein a dural graft has been inserted and sutured in a watertight fashion to enlarge the cistern.

manipulation, ie, bone decompression with duraplasty with or without dissection of the arachnoid adhesions, is reserved for patients with pattern 3.⁵⁸ The surgical management in pattern 2 is based on the extent of the CSF flow restoration on intraoperative sonography.

In healthy individuals, cine MR imaging demonstrates a slight inferior motion of the cerebellar tonsils, followed by the medulla and the spinal cord. Also, there is a mild anteroposterior motion of the tonsils, medulla, and the spinal cord. In CM, there is increased craniocaudal displacement of the tonsils and the medulla. There may be impaired passive recoil, with a decreased upward motion, which may contribute to syrinx formation. DTI is a sensitive technique to assess microstructural changes in the brain stem and cerebellar peduncles. In CM-2, antenatal DTI demonstrated increased fractional anisotropy values in the mid-brain, which may aid in the prenatal diagnosis of open neural tube defects.⁵⁹ Presurgical MR imaging in CM-1 showed elevated fractional anisotropy values in the anterior pons, which reduced after decompression surgery.⁶⁰ DTI studies demonstrate parenchymal alterations and may contribute to the diagnosis and management of CM in the future.^{59,60}

Posterior Fossa Decompression for CM-1

The decision to treat CM-1 surgically is based on the severity and progression of symptoms and signs, in conjunction with the MR imaging findings. Indications for surgery are typically symptoms that affect daily life or any degree of symptomatic syringohydromyelia.⁶¹ The goals of surgery are to stop the

progression of symptoms, relieve the brain stem and spinal cord compression, restore the normal flow of CSF through the foramen magnum, and stop the progression of syringohydromyelia. If warranted, posterior fossa decompression consists of surgical enlargement of the posterior cranial fossa, with a “bone-only” craniocervical decompression (typically a small suboccipital craniectomy above the foramen magnum with removal of the posterior arch of C1) or bone decompression, with an expanding duraplasty, ie, opening of the dura mater over the cisterna magna, and insertion and suturing of allogenic and xenogenic connective tissue dura graft in a watertight fashion to enlarge the cistern (Fig 6). Intraoperative sonography may be performed to determine if a dura mater opening is necessary because bone removal alone may sometimes not suffice to restore normal CSF flow. Dissection of arachnoid adhesions is frequently performed in patients with a syrinx. Tonsillopexy, ie, limited resection of the cerebellar tonsils with bipolar cautery, may also be performed when the surgeon is unable to adequately superiorly mobilize herniated tonsils that severely impinge on the foramen magnum.

Postsurgical Imaging in CM

MR imaging is generally the technique of choice for evaluation of the expected postoperative imaging findings (On-line Fig 2) and the associated complications in patients with CMs.

Complications in CM-1 Surgery. Pseudomeningoceles are subcutaneous fluid collections that are more likely in patients undergoing posterior fossa decompression with duraplasty versus without duraplasty (18.5% versus 1.8%).⁶² Wound infections are either superficial, ie, cellulitis involving the postoperative bed, or deep in the form of subcutaneous abscesses or meningitis. The incidence rates of postsurgical infections range from 1% to as high as 11%.⁶³ Abscesses appear as rim-enhancing fluid collections with restricted diffusion. Meningitis typically demonstrates leptomeningeal enhancement that predominantly involves the posterior fossa.

Anterior and posterior circulation strokes are rare complications of CM surgery, occurring in 0.5% of patients.⁶² The posterior inferior cerebellar artery territory is usually involved, possibly due to injury to its distal branches during revision surgeries. Arachnoid adhesions complicate approximately 0.5% of cases with allogenic and xenogenic connective tissue grafts.⁶⁴ They may obstruct the normal flow of CSF owing to tethering of the parenchyma to the overlying dura, leading to hydrocephalus and symptomatic recurrence. Inferior migration of the cerebellum, ie, cerebellar slumping, is an unlikely event due to excessive bony decompression of the foramen magnum ($>4 \times 4$ cm). It may result in treatment failure or even mass effect on the brain stem and spinal cord.⁶⁵

Complications in CM-2 Surgery. Postoperative complications in CM-2 include wound dehiscence and shunt infection (7.6%), CSF leaks and postoperative fluid collections (32.8%), and inclusion cysts and intraspinal arachnoid cysts (3.4%).^{45,46}

CONCLUSIONS

CMs are a diverse group of abnormalities that involve the brain, the craniocervical junction, and the spine. They present with a multitude of clinical manifestations, depending on the affected regions, and altered CSF flow dynamics. Because of the increasing performance of neuroimaging for optimal therapeutic guidance, we need to be aware of common and uncommon types of CM, associated abnormalities, and common imaging findings.

REFERENCES

- Chiari H. Ueber Veränderungen des Kleinhirns infolge von Hydrocephalie des Grosshirns I [About changes in the cerebellum as a result of hydrocephalus of the cerebrum]. *Dtsch Med Wochenschr* 1891;17:1172–75 CrossRef
- Chiari H. Ueber Veränderungen des Kleinhirns, der Pons und der Medulla oblongata infolge von congenitaler Hydrocephalie des Grosshirns [About changes in the cerebellum, the pons and the medulla oblongata as a result of congenital hydrocephalus of the cerebrum]. *Denkschr Akad Wiss Wien* 1895;63:71–115
- Haddad FA, Qaisi I, Joudeh N, et al. The newer classifications of the Chiari malformations with clarifications: an anatomical review. *Clin Anat* 2018;31:314–22 CrossRef Medline
- Tubbs RS, Iskandar BJ, Bartolucci AA, et al. A critical analysis of the Chiari 1.5 malformation. *J Neurosurg* 2004;101:179–83 CrossRef Medline
- Chiapparini L, Saletti V, Solero CL, et al. Neuroradiological diagnosis of Chiari malformations. *Neurol Sci* 2011;32(suppl 3):S283–86 CrossRef Medline
- Doberstein CA, Torabi R, Klinge PM. Current concepts in the pathogenesis, diagnosis, and management of type I Chiari malformations. *R I Med J (2013)* 2017;100:47–49 Medline
- Speer MC, Enterline DS, Mehlretter L, et al. Review article: Chiari type I malformation with or without syringomyelia: prevalence and genetics. *J Genet Couns* 2003;12:297–311 CrossRef Medline
- Briganti F, Leone G, Briganti G, et al. Spontaneous resolution of Chiari type I malformation. A case report and literature review. *Neuroradiol J* 2013;26:304–09 CrossRef Medline
- Kim I-K, Wang K-C, Kim I-O, et al. Chiari 1.5 malformation: an advanced form of Chiari I malformation. *J Korean Neurosurg Soc* 2010;48:375–79 CrossRef Medline
- Tubbs RS, McGirt MJ, Oakes WJ. Surgical experience in 130 pediatric patients with Chiari I malformations. *J Neurosurg* 2003;99:291–96 CrossRef Medline
- Milhorat TH, Chou MW, Trinidad EM, et al. Chiari I malformation redefined: clinical and radiographic findings for 364 symptomatic patients. *Neurosurgery* 1999;44:1005–17 CrossRef Medline
- Milhorat TH, Bolognese PA, Nishikawa M, et al. Association of Chiari malformation type I and tethered cord syndrome: preliminary results of sectioning filum terminale. *Surg Neurol* 2009;72:20–35 CrossRef Medline
- Cama A, Tortori-Donati P, Piatelli GL, et al. Chiari complex in children—neurological diagnosis, neurosurgical treatment and proposal of a new classification (312 cases). *Eur J Pediatr Surg* 1995;5(suppl 1):35–38 CrossRef Medline
- Ivashchuk G, Loukas M, Blount JP, et al. Chiari III malformation: a comprehensive review of this enigmatic anomaly. *Childs Nerv Syst* 2015;31:2035–40 CrossRef Medline
- Fisahn C, Shoja MM, Turgut M, et al. The Chiari 3.5 malformation: a review of the only reported case. *Childs Nerv Syst* 2016;32:2317–19 CrossRef Medline
- Muscatello G. Ueber die angeborenen Spalten des Schädels und der Wirbelsäule [About the congenital clefts of the skull and the spine]. *Archiv f kiln Chir Bd* 1984;47:162–301
- Osborn AG, Hedlund GL. Posterior fossa malformations. In: *Osborn's Brain: Imaging, Pathology, and Anatomy*. 2nd ed. Osborn AG (ed). Elsevier: Philadelphia, 2018:1169–94
- Müller F, O'Rahilly R. The human chondrocranium at the end of the embryonic period, proper, with particular reference to the nervous system. *Am J Anat* 1980;159:33–58 CrossRef Medline
- Marin-Padilla M, Marin-Padilla TM. Morphogenesis of experimentally induced Arnold-Chiari malformation. *J Neurol Sci* 1981;50:29–55 CrossRef Medline
- Tubbs RS, Hill M, Loukas M, et al. Volumetric analysis of the posterior cranial fossa in a family with four generations of the Chiari malformation type I. *J Neurosurg Pediatr* 2008;1:21–24 CrossRef Medline
- Sgouros S, Kountouri M, Natarajan K. Posterior fossa volume in children with Chiari malformation type I. *J Neurosurg* 2006;105(suppl):101–06 CrossRef Medline
- Badie B, Mendoza D, Batzdorf U. Posterior fossa volume and response to suboccipital decompression in patients with Chiari I malformation. *Neurosurgery* 1995;37:214–18 CrossRef Medline
- Taylor DG, Mastorakos P, Jane JA, et al. Two distinct populations of Chiari I malformation based on presence or absence of posterior fossa crowding on magnetic resonance imaging. *J Neurosurg* 2017;126:1934–40 CrossRef Medline
- McLone DG, Knepper PA. The cause of Chiari II malformation: a unified theory. *Pediatr Neurosci* 1989;15:1–12 CrossRef Medline
- McLone DG, Nakahara S, Knepper PA. Chiari II malformation: pathogenesis and dynamics. *Concepts Pediatr Neurosurg* 1991:1–17 CrossRef Medline
- Pexieder T, Jelinek R. Pressure of the CSF and the morphogenesis of the CNS. II. Pressure necessary for normal development of brain vesicles. *Folia Morphol (Praha)* 1970;18:181–92 Medline
- Birinyi PV, Bieser S, Reis M, et al. Impact of DTI tractography on surgical planning for resection of a pediatric pre-pontine neurenteric cyst: a case discussion and literature review. *Childs Nerv Syst* 2015;31:457–63 CrossRef Medline
- Tubb RS, Pugh JA, Oakes WJ. Chiari Malformations. In: *Youmans Neurological Surgery*, Winn HR (ed). Elsevier Saunders: Philadelphia, 2011:1918–27
- Cai C, Oakes WJ. Hindbrain herniation syndromes: the Chiari malformations (I and II). *Semin Pediatr Neurol* 1997;4:179–91 CrossRef Medline
- Van den Hof MC, Nicolaidis KH, Campbell J, et al. Evaluation of the lemon and banana signs in one hundred thirty fetuses with open spina bifida. *Am J Obstet Gynecol* 1990;162:322–27 CrossRef Medline
- Soto-Ares G, Delmaire C, Deries B, et al. Cerebellar cortical dysplasia: MR findings in a complex entity. *AJNR Am J Neuroradiol* 2000;21:1511–19 Medline
- Gooding CA, Carter A, Hoare RD. New ventriculographic aspects of the Arnold-Chiari malformation. *Radiology* 1967;89:626–32 CrossRef Medline
- Rauzzino M, Oakes WJ. Chiari II malformation and syringomyelia. *Neurosurg Clin N Am* 1995;6:293–309 CrossRef Medline
- Hino-Shishikura A, Niwa T, Aida N, et al. Periventricular nodular heterotopia is related to severity of the hindbrain deformity in Chiari II malformation. *Pediatr Radiol* 2012;42:1212–17 CrossRef Medline
- Petit-Lacour MC, Lasjaunias P, Iffenecker C, et al. Visibility of the central canal on MRI. *Neuroradiology* 2000;42:756–61 CrossRef Medline
- Menezes AH. Chiari I malformations and hydromyelia—complications. *Pediatr Neurosurg* 1991;17:146–54 CrossRef Medline
- Alai A, Reddy CG, Amrami KK, et al. Charcot arthropathy of the shoulder associated with typical and atypical findings. *Clin Anat* 2013;26:1017–23 CrossRef Medline
- Sgouros S. Chiari II malformation and syringomyelia. In: Memet Özek M, Cinalli G, Maixner WJ, eds. *The Spina Bifida: Management and Outcome*. Springer-Verlag: Milan, 2008: 237–48

39. Milhorat TH. **Classification of syringomyelia.** *Neurosurg Focus* 2000;8:E1 CrossRef Medline
40. Fischbein NJ, Dillon WP, Cobbs C, et al. **The “presyrinx” state: a reversible myelopathic condition that may precede syringomyelia.** *AJNR Am J Neuroradiol* 1999;20:7–20. Accessed April 26, 2020. <http://www.ajnr.org/content/20/1/7> Medline
41. Goh S, Bottrell CL, Aiken AH, et al. **Presyrinx in children with Chiari malformations.** *Neurology* 2008;71:351–56 CrossRef Medline
42. Sen A. **Flow comp off: an easy technique to confirm CSF flow within syrinx and aqueduct.** *Indian J Radiol Imaging* 2013;23:97–100 CrossRef Medline
43. Atta CAM, Fiest KM, Frolkis AD, et al. **Global birth prevalence of spina bifida by folic acid fortification status: a systematic review and meta-analysis.** *Am J Public Health* 2016;106:e24–34 CrossRef Medline
44. Boulet SL, Yang Q, Mai C, et al. **Trends in the postfortification prevalence of spina bifida and anencephaly in the United States.** *Birth Defects Res Part A Clin Mol Teratol* 2008;82:527–32 CrossRef Medline
45. Adzick NS, Thom EA, Spong CY, et al. **A randomized trial of prenatal versus postnatal repair of myelomeningocele.** *N Engl J Med* 2011;364:993–1004 CrossRef Medline
46. Nagaraj UD, Bierbrauer KS, Stevenson CB, et al. **Spinal imaging findings of open spinal dysraphisms on fetal and postnatal MRI.** *AJNR Am J Neuroradiol* 2018;39:1947–52 CrossRef Medline
47. Cesmebasi A, Loukas M, Hogan E, et al. **The Chiari malformations: a review with emphasis on anatomical traits.** *Clin Anat* 2015;28:184–94 CrossRef Medline
48. Dlouhy BJ, Dawson JD, Menezes AH. **Intradural pathology and pathophysiology associated with Chiari I malformation in children and adults with and without syringomyelia.** *J Neurosurg Pediatr* 2017;20:526–41 CrossRef Medline
49. Menezes AH, Greenlee JDW, Dlouhy BJ. **Syringobulbia in pediatric patients with Chiari malformation type I.** *J Neurosurg Pediatr* 2018;22:52–60 CrossRef Medline
50. Geerdink N, van der Vliet T, Rotteveel JJ, et al. **Essential features of Chiari II malformation in MR imaging: an interobserver reliability study—part I.** *Childs Nerv Syst* 2012;28:977–85 CrossRef Medline
51. Gonçalves LF, Lee W, Mody S, et al. **Diagnostic accuracy of ultrasonography and magnetic resonance imaging for the detection of fetal anomalies: a blinded case-control study.** *Ultrasound Obstet Gynecol* 2016;48:185–92 CrossRef Medline
52. Griffiths PD, Bradburn M, Campbell MJ, et al. **Use of MRI in the diagnosis of fetal brain abnormalities in utero (MERIDIAN): a multicentre, prospective cohort study.** *Lancet* 2017;389:538–46 CrossRef Medline
53. Nagaraj UD, Bierbrauer KS, Zhang B, et al. **Hindbrain herniation in Chiari II malformation on fetal and postnatal MRI.** *AJNR Am J Neuroradiol* 2017;38:1031–36 CrossRef Medline
54. Bollo RJ, Riva-Cambrin J, Brockmeyer MM, et al. **Complex Chiari malformations in children: an analysis of preoperative risk factors for occipitocervical fusion.** *J Neurosurg Pediatr* 2012;10:134–41 CrossRef Medline
55. Grabb PA, Mapstone TB, Oakes WJ. **Ventral brain stem compression in pediatric and young adult patients with Chiari I malformations.** *Neurosurgery* 1999;44:520–27; discussion 527–28 CrossRef Medline
56. McGirt MJ, Nimjee SM, Fuchs HE, et al. **Relationship of cine phase-contrast magnetic resonance imaging with outcome after decompression for Chiari I malformations.** *Neurosurgery* 2006;59:140–46; discussion 140–46 CrossRef Medline
57. Lee A, Yarbrough CK, Greenberg JK, et al. **Comparison of posterior fossa decompression with or without duraplasty in children with type I Chiari malformation.** *Childs Nerv Syst* 2014;30:1419–24 CrossRef Medline
58. Fan T, Zhao H, Zhao X, et al. **Surgical management of Chiari I malformation based on different cerebrospinal fluid flow patterns at the cranial-vertebral junction.** *Neurosurg Rev* 2017;40:663–70 CrossRef Medline
59. Woitek R, Prayer D, Weber M, et al. **Fetal diffusion tensor quantification of brainstem pathology in Chiari II malformation.** *Eur Radiol* 2016;26:1274–83 CrossRef Medline
60. Eshetu T, Meoded A, Jallo GI, et al. **Diffusion tensor imaging in pediatric Chiari type I malformation.** *Dev Med Child Neurol* 2014;56:742–48 CrossRef Medline
61. Bolognese PA, Brodbelt A, Bloom AB, et al. **Professional profiles, technical preferences, surgical opinions, and management of clinical scenarios from a panel of 63 international experts in the field of Chiari I malformation.** *World Neurosurg* 2020;S1878-8750:30590-98 CrossRef Medline
62. Klekamp J. **Surgical treatment of Chiari I malformation—analysis of intraoperative findings, complications, and outcome for 371 foramen magnum decompressions.** *Neurosurgery* 2012;71:365–80; discussion 380 CrossRef Medline
63. Arnaoutovic A, Splavski B, Boop FA, et al. **Pediatric and adult Chiari malformation type I surgical series 1965–2013: a review of demographics, operative treatment, and outcomes.** *J Neurosurg Pediatr* 2015;15:161–77 CrossRef Medline
64. Parizek J, Měrická P, Husek Z, et al. **Detailed evaluation of 2959 allogeneic and xenogeneic dense connective tissue grafts (fascia lata, pericardium, and dura mater) used in the course of 20 years for duraplasty in neurosurgery.** *Acta Neurochir (Wien)* 1997;139:827–38 CrossRef Medline
65. Duddy MJ, Williams B. **Hindbrain migration after decompression for hindbrain hernia: a quantitative assessment using MRI.** *Br J Neurosurg* 1991;5:141–52 CrossRef Medline

Neuro-Oncology and Radiogenomics: Time to Integrate?

A. Lasocki, M.A. Rosenthal, S.J. Roberts-Thomson, A. Neal, and K.J. Drummond



ABSTRACT

SUMMARY: Radiogenomics aims to predict genetic markers based on imaging features. The critical importance of molecular markers in the diagnosis and management of intracranial gliomas has led to a rapid growth in radiogenomics research, with progressively increasing complexity. Despite the advances in the techniques being examined, there has been little translation into the clinical domain. This has resulted in a growing disconnect between cutting-edge research and assimilation into clinical practice, though the fundamental goal is for these techniques to improve patient care. The goal of this review, therefore, is to discuss possible clinical scenarios in which the addition of radiogenomics may aid patient management. This includes facilitating patient counseling, determining optimal patient management when complete molecular characterization is not possible, reclassifying tumors, and overcoming some of the limitations of histologic assessment. The review also discusses considerations for selecting relevant radiogenomic features based on the clinical setting.

ABBREVIATIONS: *IDH* = isocitrate dehydrogenase; *IDH^{mut}* = *IDH* mutant; *IDH^{wt}* = *IDH* wild-type; WHO = World Health Organization; HG = 2-hydroxyglutarate; nCET = non-contrast-enhancing tumor; cIMPACT-NOW = Consortium to Inform Molecular and Practical Approaches to CNS Tumor Taxonomy

Radiogenomics, also known as imaging genomics, aims to predict genetic markers based on imaging features. An important change in the 2016 update to the World Health Organization (WHO) Classification of Tumors of the CNS was the addition of molecular markers to the diagnosis of diffuse gliomas, providing an integrated phenotypic and genetic classification.¹ In particular, diffuse gliomas of all grades (II–IV) are now classified according to *isocitrate dehydrogenase* (*IDH*) status as either *IDH* mutant (*IDH^{mut}*) or *IDH* wild-type (*IDH^{wt}*), and grade II and III gliomas with an *IDH* mutation are further classified based on the presence or absence of 1p/19q-codeletion (with codeletion representing combined loss of both the short arm of chromosome 1 and the long arm of chromosome 19).² The greater importance of genetic markers has led to a rapid growth in radiogenomics research in

gliomas, with progressively increasing complexity, including the incorporation of artificial intelligence techniques.

Most radiogenomics research has focused on MR imaging, though a small minority of studies have considered CT (in particular in relation to the presence of calcification^{3,4}), and there is also a growing interest in PET, in particular using amino acid tracers such as ¹⁸F-FDOPA (fluorine-18-fluoro-L-dihydroxyphenylalanine).^{5,6} MR imaging studies have examined both conventional MR imaging sequences (eg, pre- and postcontrast T1WI, T2WI, and FLAIR) and widely used advanced sequences (eg, DWI and MR imaging perfusion techniques). Notably, in addition to standard MR imaging spectroscopy⁷, novel spectroscopic assessment targeting 2-hydroxyglutarate (2HG)—an oncometabolite that accumulates in *IDH^{mut}* gliomas caused by catalysis of alpha-ketoglutarate to 2HG⁸—has been shown to have high sensitivity for detecting *IDH* mutations.^{9,10} Newer MR imaging techniques such as chemical exchange-dependent saturation transfer imaging have also been examined¹¹ but currently largely lie outside the clinical domain. A multiparametric approach improves accuracy,^{12,13} though a greater number of variables requires larger cohorts to provide a robust algorithm.

There has also been increasing interest in harnessing the power of a variety of computational techniques. Radiomics describes a range of computational methods to extract quantitative features from radiographic images¹¹—most commonly MR imaging in the case of brain tumors—providing quantitative assessment of features that include signal intensity, shape, volume, and heterogeneity.¹⁴ These features, with the aid of machine learning methods, can in

Received April 29, 2020; accepted after revision June 27.

From the Departments of Cancer Imaging (A.L.) and Medical Oncology (M.A.R.), Peter MacCallum Cancer Centre, Melbourne, Australia; Sir Peter MacCallum Department of Oncology (A.L.), and Department of Surgery (K.J.D.), The University of Melbourne, Parkville, Australia; Departments of Anatomical Pathology (S.J.R.-T.), Neurology (A.N.), and Neurosurgery (K.J.D.), The Royal Melbourne Hospital, Parkville, Australia; and Department of Neuroscience, Faculty of Medicine (A.N.), Nursing and Health Sciences, Central Clinical School, Monash University, Melbourne, Australia.

Arian Lasocki was supported by a Peter MacCallum Cancer Foundation Discovery Partner Fellowship.

Please address correspondence to Arian Lasocki, Department of Cancer Imaging, Peter MacCallum Cancer Centre, Grattan St, Melbourne, Victoria 3000, Australia; e-mail: arian.lasocki@petermac.org

Indicates open access to non-subscribers at www.ajnr.org

<http://dx.doi.org/10.3174/ajnr.A6769>

turn be mined to detect correlations with genomic markers.¹¹ More recently, deep learning (a subset of machine learning¹⁵) using convolutional neural networks has further improved radiogenomic prediction.^{13,16} Initial concerns regarding the uninterpretable “black box” nature of neural networks are being overcome by more recent work; for example, Chang et al¹⁶ applied principal component analysis to the final feature vector to demonstrate the appearances most strongly correlating with a particular genomic marker.

Despite the rapid advances and growth in the complexity of the techniques being examined, there has been little translation into the clinical domain. This has resulted in a growing disconnect between cutting-edge research and assimilation into clinical practice, though the fundamental goal is for these techniques to improve patient care. Therefore, it is important to take a step back and discuss possible ways in which radiogenomics could be incorporated into clinical practice, with a multidisciplinary focus. By identifying relevant clinical scenarios, we also hope to encourage research into the clinical impact of radiogenomics, ideally prospectively. Being the key genetic markers in the current WHO classification, our discussion focuses on *IDH* and 1p/19q status, though similar principles generally apply also to other genetic markers. Our focus is on possible clinical scenarios rather than a detailed discussion on the specific imaging features.

CLINICAL APPLICATIONS OF RADIOGENOMICS

Definitive histopathologic and genetic assessment based on histologic specimens remains the criterion standard for the diagnosis of brain tumors, but imaging has several advantages. The most obvious limitation of histology is that it requires surgery—and its associated morbidity—to obtain the specimen, but imaging is noninvasive. Thus, radiogenomics has value before surgery or in situations when there may be a preference for or a possibility of avoiding surgery. A further advantage of imaging is its ability to image the entire tumor, which is of particular value for gliomas given their inherently diffuse and heterogeneous nature. Finally, radiogenomics can be tailored toward the clinical question, by the appropriate selection of imaging modalities, the optimal use of the given technique (eg, in the selection of MR imaging sequences or PET tracers), and even in the application of computational techniques. Possible clinical uses of radiogenomics are discussed, including the advantages and disadvantages of radiogenomics and a brief description of specific imaging features that could be used. The scenarios discussed include:

- Providing a “virtual biopsy.”
- Aiding patient counseling.
- Guiding perioperative management.
- The prediction of “noncanonical” *IDH* mutations.
- Considerations in centers with limited access to genetic testing methods.
- Tumor reclassification.
- Overcoming the limitations of histologic assessment.
- Posttreatment follow-up.

“Virtual Biopsy”

The ultimate vision is, perhaps, for imaging genomics to deliver a “virtual biopsy,” by providing—noninvasively—a sufficiently confident prediction of genetic status to guide clinical management.

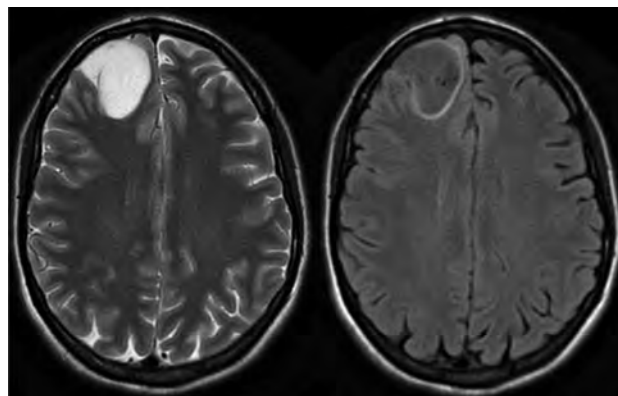


FIGURE. Axial T2WI (left) and FLAIR (right) image of a right frontal lobe WHO grade III, *IDH*-mutant, 1p/19q noncodeleted glioma demonstrating the T2-FLAIR mismatch sign.

Arguably, the T2-FLAIR mismatch sign, when present, already provides a confident prediction of an *IDH*^{mut}, 1p/19q noncodeleted tumor, having been shown to have a 100% positive predictive value in several different cohorts, with moderate to near-perfect interobserver agreement ($\kappa = 0.56\text{--}0.88$)^{4,12,17,18} (Figure). False-positive results can occur in the case of enhancing tumors or pediatric patients,^{19,20} but exceptions are rare in the case of nonenhancing tumors in an adult population,¹⁹ and this sign remains highly specific of an *IDH*^{mut}, 1p/19q noncodeleted tumor in this context. The main limitation of this sign, however, is its sensitivity, being present in 22%–51% of *IDH*^{mut}, 1p/19q noncodeleted lower-grade gliomas in different cohorts.^{12,17,18}

Even if imaging genomics were able to approach 100% accuracy more widely, however, surgery not only provides a diagnosis (both histologic and genetic) but is also a key therapeutic technique in diffuse gliomas of all grades.^{21,22} Indeed, the importance of surgery may increase because of the push toward extending resection beyond the enhancing component of gliomas to the nonenhancing tumor component.^{23–25} Furthermore, there has been an increasing push toward early functional-guided resection for lower-grade gliomas to optimize both oncologic and functional long-term outcomes.²⁶ As such, other than for tumors in locations that are challenging surgically or in patients with a gliomatosis-like pattern in whom even subtotal resection is not feasible,²⁶ resection cannot practically be avoided unless medical treatments improve dramatically.

Nevertheless, there are clinical scenarios when the differential diagnosis of a brain lesion includes non-neoplastic etiologies that do not require immediate surgery, in particular when the lesion is nonenhancing. A radiogenomic approach can aid decision making in such cases. The presence of imaging features that have been shown to correlate with a particular glioma genotype supports a diagnosis of a glioma, and thus a need for surgery, but the lack of such features gives clinicians greater confidence in managing the lesion as nongliomatous. Possible scenarios include focal lesional epilepsy caused by isolated amygdala enlargement with associated T2 hyperintensity²⁷ and unilateral mesial temporal FLAIR hyperintensity that is suspected to be caused by autoimmune encephalitis.²⁸

Patient Counseling

Radiogenomics is relevant for counseling patients before surgery. A “watch-and-wait” approach may have been used in the past for patients suspected on imaging of having a low-grade glioma but is going out of favor because of the importance of genetic markers and a recognition of the effect of extent of resection on survival.²¹ Patients may nevertheless wish to adopt such a strategy, for example, because of fear, logistic difficulties, or medical comorbidities, and the ability to predict the genetic status with MR imaging allows a more informed decision-making process. If MR imaging suggests an *IDH*^{wt} tumor, this provides further support for recommending surgery because tumor progression is likely to be more rapid, and it is important to confirm *IDH*^{wt} status to institute appropriate management. Even if the patient remains hesitant, imaging follow-up should occur at a shorter interval. In contrast, if an *IDH* mutation can be confidently predicted based on the preoperative imaging (eg, because of the presence of a T2-FLAIR mismatch sign^{4,17,18} or high ADC values),²⁹ this may provide greater confidence that active surveillance is a feasible alternative. Such considerations already occur to some extent (eg, based on the presence or absence of enhancement), but the addition of radiogenomics data would further optimize personalized care.

Perioperative Management

Seizures are common in diffuse gliomas, particularly grade II–III tumors.^{30–32} *IDH* mutations have been proposed as a potential biomarker of glioma-associated epilepsy, being associated with increased rates of seizures in both the pre- and postoperative settings.^{30,31,33} 2HG is structurally similar to the excitatory neurotransmitter glutamate and is hypothesized to activate excitatory N-Methyl-D-aspartate receptors.³⁰ Radiogenomic identification of an *IDH*^{mut} tumor thus suggests that patients could benefit from preoperative prophylactic antiepileptic treatment.

Prediction of Noncanonical *IDH* Mutations

After histology has confirmed a diffuse glioma, *IDH* testing is the next step in the molecular characterization of both grade II or III gliomas and glioblastomas.² Traditionally, *IDH* testing has started with immunohistochemistry, and this remains the practice in most centers. An inherent limitation of this technique is that it is specific to the R132H mutation in the *IDH1* gene and is thus unable to detect “noncanonical” *IDH* mutations, namely, non-R132H-*IDH1* mutations and all *IDH2* mutations.³⁴ The possibility of a noncanonical mutation is sufficiently high in grade II and III tumors³⁴ that the WHO mandates definitive *IDH* testing for these tumors.² Definitive *IDH* testing is not required for older patients (55 years of age and older) with a glioblastoma and negative *IDH1* immunohistochemistry because of the very low likelihood of a noncanonical mutation.³⁵ Chen et al³⁶ have created and described an on-line tool that predicts, with high accuracy, the likelihood of a noncanonical *IDH* mutation based on patient age; tumor grade; and, if a glioblastoma, whether there was a prior history of a grade II or III tumor (ie, whether the glioblastoma is “primary” or “secondary”). This allows a determination as to whether a noncanonical mutation is sufficiently likely to warrant definitive *IDH* testing, and such a threshold can vary

between individuals and departments. Radiogenomics has the potential to add to such a system, either based on simple criteria (eg, the likelihood of an *IDH* mutation is very low if a glioblastoma is located outside of the frontal lobes and demonstrates little non-contrast-enhancing tumor [nCET])³⁷ or on more comprehensive radiomic assessment.

Limited Access to Genetic Testing Methods

Similar considerations are even more relevant if a center does not have ready access to all the testing methods required for complete characterization according to the WHO guidelines. *IDH1* immunohistochemistry is relatively accessible, but testing for 1p/19q status and, in particular, noncanonical *IDH* mutations is not as widely available. Even if there is a possibility of sending specimens to another institution for testing, this adds to costs (to either the institution or the patient). Although the cost of performing any given test can be expected to decrease over time, there is likely to be a growth in the number of genetic markers incorporated into future diagnostic classifications. Arguably, this is less of an issue in glioblastoma because *IDH* status currently provides important prognostic information but does not alter standard management (beyond the clinical trial setting). In the case of grade II and III gliomas, however, there is the potential for changes to management. For example, if chemotherapy is considered, whereas temozolomide is typically used for astrocytomas (whether *IDH*^{mut} or *IDH*^{wt}), procarbazine, lomustine, and vincristine chemotherapy may be preferred for oligodendrogliomas,³⁸ and 1p/19q status is important for this distinction. Even if chemotherapy is not considered at the initial diagnosis, it is likely to be warranted at progression.

Radiogenomics has the potential to provide complementary information in such a setting and may more accurately predict the molecular subtype than the histologic phenotype if certain MR imaging features are present.⁴ It is rare for tumor operations to occur without preoperative MR imaging; therefore, radiogenomic information, at the very least involving a neuroradiologist’s interpretation of conventional sequences, is likely to be available. This may be particularly useful for a smaller institution requesting advice from a quaternary center because the transfer of data is facilitated by the digital nature of modern imaging, especially compared with sending pathologic specimens for further analysis.

Tumor Reclassification

Many patients currently living with gliomas—in particular, with lower-grade gliomas—will have been diagnosed before the 2016 WHO update. Such patients may have an outdated pathologic diagnosis, which could change if the histology were to be reviewed. This is most common in tumors previously labeled oligoastrocytomas—a diagnosis that is now obsolete except in rare cases—with molecular markers allowing a definitive diagnosis as either an astrocytoma or oligodendroglioma.³⁹ Also, an astrocytoma may occasionally be reclassified as an oligodendroglioma or vice versa.³⁹ If tumor progression occurs and a change to the treatment is being considered, there is an opportunity to re-evaluate the diagnosis. Even if there is insufficient histologic material for retrospective testing, review of the patient’s preoperative MR imaging may allow prediction of the molecular subtype without the need for repeat

surgery. At the least, radiogenomics may suggest that the molecular subtype is different from what would be suspected from the histologic testing and thus provide a triaging role.

Such considerations can be expected to become more prevalent in the future as further genetic markers with prognostic and therapeutic implications are identified and potentially incorporated into subsequent classification systems. Indeed, the rapid growth—both recent and continuing—in our understanding of the molecular characteristics of CNS tumors has also led to the development of cIMPACT-NOW (Consortium to Inform Molecular and Practical Approaches to CNS Tumor Taxonomy).⁴⁰ Given that the 2016 WHO update occurred 9 years after the preceding classification,⁴¹ this initiative acknowledges a need to evaluate classification progress faster than can occur for a complete update to the WHO classification and thus provides consensus recommendations for proposed changes to future classifications.⁴⁰ For example, cIMPACT-NOW has recommended that in the case of a phenotypic grade II or III astrocytoma with an *IDH* mutation, loss of nuclear *ATRX* expression, or diffuse p53 immunopositivity is adequate to label the tumor an *IDH*^{mut} astrocytoma according to the current WHO guidelines without definitive 1p/19q testing.⁴² Another important recommendation is the addition of the entity diffuse astrocytic glioma, *IDH*^{wt}, with molecular features of glioblastoma.⁴³ This suggests patients be treated as having glioblastoma even when the formal histologic criteria have not been met.⁴³ This diagnosis requires an additional finding of high-level *epidermal growth factor receptor (EGFR)* amplification, whole-chromosome 7 gain and whole-chromosome 10 loss, or a *TERT* promoter mutation.⁴³ Thus, markers beyond just *IDH* and 1p/19q status have become clinically relevant, providing new avenues for radiogenomics research and subsequent clinical integration before the next WHO update.

It is worthwhile noting that changes to classification systems also have implications for the relevance of previous research. For example, previously, grade III and IV gliomas were often grouped together as high-grade gliomas, with grade II gliomas considered low-grade gliomas. Now, grade II and III tumors are often considered together, sometimes referred to together as lower grade gliomas. As such, the value of previous studies comparing grade II and grade III/IV tumors is much diminished. If, for example, future iterations of the WHO classification were to put all emphasis on genotype, removing histologic grade entirely, current radiogenomic literature—which typically distinguishes between grade II/III and IV tumors, as per the current WHO classification—would need to be reassessed. An advantage of radiogenomics, however, is its ability to reanalyze previous data based on the most up-to-date information, and computational techniques are making such processes easier and faster.

Overcoming Limitations of Histology

Despite remaining the criterion standard for glioma diagnosis, histopathology has some limitations. 1p/19q testing methods have been shown to occasionally provide false-positive results, for example, in the case of partial- rather than whole-arm deletion.⁴⁴ Sampling error is a well-recognized issue in gliomas because of their heterogeneous nature, and this is particularly relevant to determining the grade⁴⁵ but also potentially relevant to the determination of the genotype. Even advanced *IDH* testing methods

may produce false-negative results if there is a limited number of tumor cells within the sample being analyzed.^{34,46} In addition, although *IDH* status is generally considered to be consistent throughout a glioma, some heterogeneity can be observed. For example, Preusser et al⁴⁶ reported that only a fraction of tumor cells exhibited immunostaining in approximately 15% of their glioma cohort, with some of these cases demonstrating biphasic immunostaining patterns. As such, there is the potential for MR imaging to provide genetic information when there is some reason to suspect inaccuracy of genetic testing. For example, if the pathologist acknowledges the possibility of a false-negative test result because of a small sample, imaging may be able to provide a confident prediction of the molecular status without the morbidity of repeat surgery. Equally, if a highly specific imaging feature is present but is at odds with the genetic testing result, in particular if genetic testing results are negative, more comprehensive histologic assessment may be warranted.

There are 2 *IDH* alleles, and mutation in 1 is sufficient for a tumor to be considered *IDH*^{mut}.³⁴ Occasions exist, however, when tumors express only 1 of the 2 alleles, known as monoallelic gene expression.³⁴ This can occur in *IDH*^{mut} gliomas, with an incidence of 15% in 1 study.⁴⁷ Most commonly, only the *IDH*^{wt} allele is expressed, resulting in a worse prognosis.⁴⁷ Similarly, *IDH*^{mut} gliomas may rarely lose their *IDH*^{mut} allele.⁴⁸ As such, there is the potential for *IDH*^{mut} gliomas to be or become functionally *IDH*^{wt}, and this may not be readily identifiable by genetic testing methods.³⁴ Radiogenomics could have value in such situations, potentially identifying an MR imaging appearance more in keeping with an *IDH*^{wt} rather than *IDH*^{mut} tumor, and thus suggesting a more aggressive treatment approach. Interestingly, deletion of the wild-type allele in *IDH*^{mut} gliomas also results in decreased 2HG production, showing that both wild-type and mutant alleles are necessary for 2HG production in glioma cells.⁴⁹ Thus, although 2HG spectroscopy has typically been studied in the preoperative setting,^{9,50} it may also be able to quantitatively demonstrate such changes in *IDH* expression and 2HG production as the tumor evolves.

Similar considerations are also relevant to mixed tumors. Although an important role of the new WHO classification is to largely remove the diagnostic uncertainty of tumors with a mixed histologic phenotype (in particular oligoastrocytomas), true genetically mixed tumors—with 2 genetically distinct components—do occasionally occur.^{51,52} Genetic testing is typically performed in a single portion of the tumor, so the incidence of true mixed tumors may be underappreciated.⁵¹ Radiogenomics therefore has the potential to identify distinct appearances in different portions of the tumor, suggesting value in repeating testing in a different portion.

It has become critical for medical oncologists and neurosurgeons treating patients with gliomas to have a strong understanding of the molecular subtypes of gliomas and the histologic testing methods. This knowledge is also becoming increasingly important for neuroradiologists, and it may be worthwhile not only stating the likely diagnosis in the radiologic report but also the likely molecular subtype if there are indicative features. Similarly, there is value in neuropathologists having some knowledge of the growing field of radiogenomics, at least the imaging

features most sensitive or specific for a particular molecular subtype. This may allow neuropathologists to appropriately temper their confidence if relevant radiologic features are present and there is some doubt as to the validity of the histologic assessment, facilitating optimal multidisciplinary care.

Posttreatment Follow-Up

As discussed, resection is a key part of the patient's management at diagnosis, which somewhat decreases the value of radiogenomics at this time. Posttreatment follow-up could therefore be a more useful clinical context for radiogenomics because further surgery may not be otherwise warranted. This is particularly relevant given that the newly understood genetic landscape of gliomas has progressed to the therapeutic domain, for example, with the advent of *IDH* inhibitors, which have now entered clinical trials.⁵³ Intuitively, knowledge of the imaging appearance associated with the genetic mutation being targeted therapeutically has value. For example, features associated with an *IDH* mutation in glioblastoma include the presence of nCET,⁵⁴ a masslike morphology of nCET,⁵⁵ and a minimally invasive phenotype on diffusion-tensor imaging.⁵⁶ Targeted therapies have produced dramatic responses in some extracranial malignancies, but the plasticity of tumor cells can result in resistance to these treatments through a variety of mechanisms,⁵⁷ and similar mechanisms can be expected in gliomas. The imaging changes related to targeted treatments such as *IDH* inhibitors are as yet unknown, but given that gliomas have strategies to circumvent *IDH* mutation as outlined earlier, one would expect that these strategies would occur more commonly on treatment with a targeted agent. Again, if the appearance of the tumor were to change, for example, by developing a more infiltrative imaging phenotype, this could suggest the development of resistance to the therapeutic agent.

Of note, much of the research in this field focuses on preoperative imaging and cannot necessarily be extrapolated to the posttreatment setting. A further difficulty with the posttreatment context is that a variety of additional confounders are introduced. There are differences in the extent of resection and postsurgical changes, and imaging changes after radiation therapy can also vary between patients. These complexities are most pronounced with medical therapies, including conventional chemotherapy (in particular temozolomide), antiangiogenics agents (the most commonly used being bevacizumab), and less established treatments such as immunotherapy, vaccine therapy, and, increasingly, targeted agents. These treatments have revealed challenging imaging patterns, well demonstrated by the phenomena of pseudoprogression and pseudoresponse, and one would expect that emerging and future therapies may provide similar conundrums. With the greater number of potential variables in the posttreatment setting, development of a robust radiogenomic algorithm requires a much larger number of testing cases, providing an opportunity for automated computational techniques. Advanced artificial intelligence techniques such as deep learning are also able to identify features not readily discernible to the human eye, of particular relevance given that important clinical scenarios such as pseudoprogression are notoriously difficult for neuroradiologists.

CHOOSING APPROPRIATE RADIOGENOMIC FEATURES

The way in which radiogenomic data are incorporated into clinical practice may vary depending on the specific scenario. For example, if the hope is to confidently diagnose a specific mutation or molecular subtype, specificity is important. The T2-FLAIR mismatch sign is the best example of such a feature, being able to predict a *IDH*^{mut}, 1p/19q noncodeleted grade II/III tumor with high confidence.^{4,12,17,18} If this feature is absent, however, its sensitivity is insufficient to exclude an *IDH*^{mut}, 1p/19q noncodeleted tumor.^{4,17,18} In contrast, although the presence of nCET is associated with *IDH* mutations in glioblastoma,⁵⁴ it is not sufficiently specific to confidently predict an *IDH* mutation,³⁷ rather, the moderate sensitivity of this feature means that a glioblastoma without substantial nCET is unlikely to have an *IDH* mutation (ie, it is likely *IDH*^{wt}).³⁷ Thus, to confidently predict a particular genetic marker, specificity is important, but if the goal is to exclude a genetic marker, sensitivity is more important.

The specific clinical scenario has implications for the use of the results of radiogenomics research. Because there is usually a degree of overlap in the imaging features between molecular subtypes, many studies aim to maximize the overall accuracy by using area under the curve analysis, but this may not be optimal for a given patient. If such a model were to predict a given genetic marker in a specific patient, it would be important to know not just the likely result but also the degree of confidence in this result because this would greatly impact the value of this information for any given patient. Some continuous variables, such as ADC, can potentially be thresholded in different ways depending on how they are to be used. *IDH*^{wt} gliomas are associated with lower ADC values, but there is overlap with *IDH*^{mut} gliomas, in particular at intermediate ADC values.^{29,58,59} An appropriate threshold can be selected depending on whether there is a desire to more confidently diagnose or exclude a particular mutation. For example, if the goal were to confidently diagnose an *IDH* mutation, a higher ADC threshold would be preferable, with ADC values above this being particularly suggestive of an *IDH*^{mut} tumor. Multivariate methods such as radiomics have even greater potential for being targeted toward optimizing sensitivity or specificity depending on the clinical scenario.

Here, it is important to recognize that whether a feature can be used and how this could be done depends on the grade of the tumor. For example, the T2-FLAIR mismatch sign and the presence of calcifications (predictive of an *IDH*^{mut}, 1p/19q codeleted tumor) are only relevant to grade II and III tumors.^{3,4,12,17,18} In contrast, a frontal lobe location is associated with *IDH* mutations in both grade II and III gliomas and glioblastomas,^{37,54,60} but the positive predictive value varies between grades because of the much lower incidence of *IDH* mutations in glioblastoma compared with grade II and III gliomas.³⁴

CONCLUSIONS

The field of radiogenomics has advanced rapidly in recent times because of the increased understanding of the importance of molecular markers and the development of computational techniques. The clinical implementation of these techniques is lagging behind the research, however, and this disconnect warrants further

consideration. Possible roles for radiogenomics include determining the likely molecular subtype in gliomas when complete genetic characterization is not practical, reclassifying tumors diagnosed before the current classification systems, and optimizing discussion with patients when conservative management is being considered. With the advent of targeted therapies for glioma, there is also the potential to identify features suggestive of resistance to treatment.

Disclosures: Arian Lasocki—RELATED: Grant: Peter MacCallum Cancer Foundation, Comments: Supported by a Peter MacCallum Cancer Foundation Discovery Partner Fellowship.* *Money paid to the institution.

REFERENCES

- Louis DN, Perry A, Reifenberger G, et al. **The 2016 World Health Organization Classification of Tumors of the Central Nervous System: a summary.** *Acta Neuropathol* 2016;131:803–20 CrossRef Medline
- Louis DO, Wiestler OD, Cavenee WK. *World Health Organization Histological Classification of Tumours of the Central Nervous System.* International Agency for Research on Cancer; 2016
- Saito T, Muragaki Y, Maruyama T, et al. **Calcification on CT is a simple and valuable preoperative indicator of 1p/19q loss of heterozygosity in supratentorial brain tumors that are suspected grade II and III gliomas.** *Brain Tumor Pathol* 2016;33:175–82 CrossRef Medline
- Lasocki A, Gaillard F, Gorelik A, et al. **MRI features can predict 1p/19q status in intracranial gliomas.** *AJNR Am J Neuroradiol* 2018;39:687–92 CrossRef Medline
- Cicone F, Carideo L, Scaringi C, et al. **(18)F-DOPA uptake does not correlate with IDH mutation status and 1p/19q co-deletion in glioma.** *Ann Nucl Med* 2019;33:295–302 CrossRef Medline
- Verger A, Metellus P, Sala Q, et al. **IDH mutation is paradoxically associated with higher (18)F-FDOPA PET uptake in diffuse grade II and grade III gliomas.** *Eur J Nucl Med Mol Imaging* 2017;44:1306–11 CrossRef Medline
- Nakae S, Murayama K, Sasaki H, et al. **Prediction of genetic subgroups in adult supra tentorial gliomas by pre- and intraoperative parameters.** *J Neurooncol* 2017;131:403–12 CrossRef Medline
- Dang L, White DW, Gross S, et al. **Cancer-associated IDH1 mutations produce 2-hydroxyglutarate.** *Nature* 2009;462:739–44 CrossRef Medline
- Choi C, Ganji SK, DeBerardinis RJ, et al. **2-hydroxyglutarate detection by magnetic resonance spectroscopy in IDH-mutated patients with gliomas.** *Nat Med* 2012;18:624–29 CrossRef Medline
- Suh CH, Kim HS, Jung SC, et al. **Imaging prediction of isocitrate dehydrogenase (IDH) mutation in patients with glioma: a systemic review and meta-analysis.** *Eur Radiol* 2019;29:745–58 CrossRef Medline
- Jiang S, Zou T, Eberhart CG, et al. **Predicting IDH mutation status in grade II gliomas using amide proton transfer-weighted (APT_w) MRI.** *Magn Reson Med* 2017;78:1100–09 CrossRef Medline
- Batchala PP, Muttikkal TJE, Donahue JH, et al. **Neuroimaging-based classification algorithm for predicting 1p/19q-codeletion status in IDH-mutant lower grade gliomas.** *AJNR Am J Neuroradiol* 2019;40:426–32 CrossRef Medline
- Li Z, Wang Y, Yu J, et al. **Deep learning based radiomics (DLR) and its usage in noninvasive IDH1 prediction for low grade glioma.** *Sci Rep* 2017;7:5467 CrossRef Medline
- Gillies RJ, Kinahan PE, Hricak H. **Radiomics: images are more than pictures, they are data.** *Radiology* 2016;278:563–77 CrossRef Medline
- Rudie JD, Rauschecker AM, Bryan RN, et al. **Emerging applications of artificial intelligence in neuro-oncology.** *Radiology* 2019;290:607–18 CrossRef Medline
- Chang P, Grinband J, Weinberg BD, et al. **Deep-learning convolutional neural networks accurately classify genetic mutations in gliomas.** *AJNR Am J Neuroradiol* 2018;39:1201–07 CrossRef Medline
- Patel SH, Poisson LM, Brat DJ, et al. **T2-FLAIR mismatch, an imaging biomarker for IDH and 1p/19q status in lower-grade gliomas: a TCGA/TCIA project.** *Clin Cancer Res* 2017;23:6078–85 CrossRef Medline
- Broen MPG, Smits M, Wijnenga MMJ, et al. **The T2-FLAIR mismatch sign as an imaging marker for non-enhancing IDH-mutant, 1p/19q-intact lower-grade glioma: a validation study.** *Neuro-Oncol* 2018;20:1393–99 CrossRef Medline
- Johnson DR, Kaufmann TJ, Patel SH, et al. **There is an exception to every rule—T2-FLAIR mismatch sign in gliomas.** *Neuroradiology* 2019;61:225–27 CrossRef Medline
- Juratli TA, Tummala SS, Riedl A, et al. **Radiographic assessment of contrast enhancement and T2/FLAIR mismatch sign in lower grade gliomas: correlation with molecular groups.** *J Neurooncol* 2019;141:327–35 CrossRef Medline
- Schiff D, van den Bent M, Vogelbaum MA, et al. **Recent developments and future directions in adult lower-grade gliomas: Society for Neuro-Oncology (SNO) and European Association of Neuro-Oncology (EANO) consensus.** *Neuro Oncol* 2019;21:837–53 CrossRef
- Weller M, van den Bent M, Hopkins K, European Association for Neuro-Oncology (EANO) Task Force on Malignant Glioma, et al. **EANO guideline for the diagnosis and treatment of anaplastic gliomas and glioblastoma.** *Lancet Oncol* 2014;15:e395–403 CrossRef Medline
- Li YM, Suki D, Hess K, et al. **The influence of maximum safe resection of glioblastoma on survival in 1229 patients: can we do better than gross-total resection?** *J Neurosurg* 2016;124:977–88 CrossRef Medline
- Pessina F, Navarra P, Cozzi L, et al. **Maximize surgical resection beyond contrast-enhancing boundaries in newly diagnosed glioblastoma multiforme: is it useful and safe? A single institution retrospective experience.** *J Neurooncol* 2017;135:129–39 CrossRef Medline
- Lasocki A, Gaillard F. **Non-contrast-enhancing tumor: a new frontier in glioblastoma research.** *AJNR Am J Neuroradiol* 2019;40:758–65 CrossRef Medline
- Duffau H. **Diffuse low-grade glioma, oncological outcome and quality of life: a surgical perspective.** *Curr Opin Oncol* 2018;30:383–89 CrossRef Medline
- Beh SMJ, Cook MJ, D'Souza WJ. **Isolated amygdala enlargement in temporal lobe epilepsy: a systematic review.** *Epilepsy Behav* 2016;60:33–41 CrossRef Medline
- Graus F, Titulaer MJ, Balu R, et al. **A clinical approach to diagnosis of autoimmune encephalitis.** *Lancet Neurol* 2016;15:391–404 CrossRef Medline
- Thust SC, Hassanein S, Bisdas S, et al. **Apparent diffusion coefficient for molecular subtyping of non-gadolinium-enhancing WHO grade II/III glioma: volumetric segmentation versus two-dimensional region of interest analysis.** *Eur Radiol* 2018;28:3779–88 CrossRef Medline
- Chen H, Judkins J, Thomas C, et al. **Mutant IDH1 and seizures in patients with glioma.** *Neurology* 2017;88:1805–13 CrossRef Medline
- Neal A, Kwan P, O'Brien TJ, et al. **IDH1 and IDH2 mutations in postoperative diffuse glioma-associated epilepsy.** *Epilepsy Behav* 2018;78:30–36 CrossRef Medline
- Neal A, Morokoff A, O'Brien TJ, et al. **Postoperative seizure control in patients with tumor-associated epilepsy.** *Epilepsia* 2016;57:1779–88 CrossRef Medline
- Liubinas SV, D'Abaco GM, Moffat BM, et al. **IDH1 mutation is associated with seizures and protoplasmic subtype in patients with low-grade gliomas.** *Epilepsia* 2014;55:1438–43 CrossRef Medline
- Horbinski C. **What do we know about IDH1/2 mutations so far, and how do we use it?** *Acta Neuropathol* 2013;125:621–36 CrossRef Medline
- Louis DN, Wesseling P, Paulus W, et al. **cIMPACT-NOW update 1: not otherwise specified (NOS) and not elsewhere classified (NEC).** *Acta Neuropathol* 2018;135:481–84 CrossRef Medline

36. Chen L, Voronovich Z, Clark K, et al. **Predicting the likelihood of an isocitrate dehydrogenase 1 or 2 mutation in diagnoses of infiltrative glioma.** *Neuro Oncol* 2014;16:1478–83 CrossRef Medline
37. Lasocki A, Tsui A, Gaillard F, et al. **Reliability of noncontrast-enhancing tumor as a biomarker of IDH1 mutation status in glioblastoma.** *J Clin Neurosci* 2017;39:170–75 CrossRef Medline
38. Weller M, van den Bent M, Tonn JC, et al. **European Association for Neuro-Oncology (EANO) guideline on the diagnosis and treatment of adult astrocytic and oligodendroglial gliomas.** *Lancet Oncol* 2017;18:e315–29 CrossRef Medline
39. Rogers TW, Toor G, Drummond K, et al. **The 2016 revision of the WHO Classification of Central Nervous System Tumours: retrospective application to a cohort of diffuse gliomas.** *J Neurooncol* 2018;137:181–89 CrossRef Medline
40. Louis DN, Aldape K, Brat DJ, et al. **Announcing cIMPACT-NOW: the Consortium to Inform Molecular and Practical Approaches to CNS Tumor Taxonomy.** *Acta Neuropathol* 2017;133:1–3 CrossRef Medline
41. Louis DN, Wiestler OD, Cavanee WK. *World Health Organization histological classification of tumours of the central nervous system.* International Agency for Research on Cancer, Lyon; 2007
42. Louis DN, Giannini C, Capper D, et al. **cIMPACT-NOW update 2: diagnostic clarifications for diffuse midline glioma, H3 K27M-mutant and diffuse astrocytoma/anaplastic astrocytoma, IDH-mutant.** *Acta Neuropathol* 2018;135:639–42 CrossRef Medline
43. Brat DJ, Aldape K, Colman H, et al. **cIMPACT-NOW update 3: recommended diagnostic criteria for “Diffuse astrocytic glioma, IDH-wildtype, with molecular features of glioblastoma, WHO grade IV.”** *Acta Neuropathol* 2018;136:805–10 CrossRef Medline
44. Horbinski C, Nikiforova MN, Hobbs J, et al. **The importance of 10q status in an outcomes-based comparison between 1p/19q fluorescence in situ hybridization and polymerase chain reaction-based microsatellite loss of heterozygosity analysis of oligodendrogliomas.** *J Neuropathol Exp Neurol* 2012;71:73–82 CrossRef Medline
45. Lasocki A, Tsui A, Tacey MA, et al. **MRI grading versus histology: predicting survival of World Health Organization grade II–IV astrocytomas.** *AJNR Am J Neuroradiol* 2015;36:77–83 CrossRef Medline
46. Preusser M, Wohrer A, Stary S, et al. **Value and limitations of immunohistochemistry and gene sequencing for detection of the IDH1-R132H mutation in diffuse glioma biopsy specimens.** *J Neuropathol Exp Neurol* 2011;70:715–23 CrossRef Medline
47. Walker EJ, Zhang C, Castelo-Branco P, et al. **Monoallelic expression determines oncogenic progression and outcome in benign and malignant brain tumors.** *Cancer Res* 2012;72:636–44 CrossRef Medline
48. Pusch S, Sahn F, Meyer J, et al. **Glioma IDH1 mutation patterns off the beaten track.** *Neuropathol Appl Neurobiol* 2011;37:428–30 CrossRef Medline
49. Jin G, Reitman ZJ, Duncan CG, et al. **Disruption of wild-type IDH1 suppresses D-2-hydroxyglutarate production in IDH1-mutated gliomas.** *Cancer Res* 2013;73:496–501 CrossRef Medline
50. Tietze A, Choi C, Mickey B, et al. **Noninvasive assessment of isocitrate dehydrogenase mutation status in cerebral gliomas by magnetic resonance spectroscopy in a clinical setting.** *J Neurosurg* 2018;128:391–98 CrossRef Medline
51. Huse JT, Diamond EL, Wang L, et al. **Mixed glioma with molecular features of composite oligodendroglioma and astrocytoma: a true “oligoastrocytoma”?** *Acta Neuropathol* 2015;129:151–53 CrossRef Medline
52. Wilcox P, Li CC, Lee M, et al. **Oligoastrocytomas: throwing the baby out with the bathwater?** *Acta Neuropathol* 2015;129:147–49 CrossRef Medline
53. Huang J, Yu J, Tu L, et al. **Isocitrate dehydrogenase mutations in glioma: from basic discovery to therapeutics development.** *Front Oncol* 2019;9:506 CrossRef Medline
54. Carrillo JA, Lai A, Nghiemphu PL, et al. **Relationship between tumor enhancement, edema, IDH1 mutational status, MGMT promoter methylation, and survival in glioblastoma.** *AJNR Am J Neuroradiol* 2012;33:1349–55 CrossRef Medline
55. Lasocki A, Gaillard F, Tacey M, et al. **Morphologic patterns of non-contrast-enhancing tumor in glioblastoma correlate with IDH1 mutation status and patient survival.** *J Clin Neurosci* 2018;47:168–73 CrossRef Medline
56. Price SJ, Allinson K, Liu H, et al. **Less invasive phenotype found in isocitrate dehydrogenase-mutated glioblastomas than in isocitrate dehydrogenase wild-type glioblastomas: a diffusion-tensor imaging study.** *Radiology* 2017;283:215–21 CrossRef Medline
57. Ramos P, Bentes-Alj M. **Mechanism-based cancer therapy: resistance to therapy, therapy for resistance.** *Oncogene* 2015;34:3617–26 CrossRef Medline
58. Leu K, Ott GA, Lai A, et al. **Perfusion and diffusion MRI signatures in histologic and genetic subtypes of WHO grade II–III diffuse gliomas.** *J Neurooncol* 2017;134:177–88 CrossRef Medline
59. Xing Z, Yang X, She D, et al. **Noninvasive assessment of IDH mutational status in World Health Organization grade II and III astrocytomas using DWI and DSC-PWI combined with conventional MR imaging.** *AJNR Am J Neuroradiol* 2017;38:1138–44 CrossRef Medline
60. Darlix A, Deverdun J, Menjot de Champfleury N, et al. **IDH mutation and 1p19q codeletion distinguish two radiological patterns of diffuse low-grade gliomas.** *J Neurooncol* 2017;133:37–45 CrossRef Medline

Fetal Exposure to MR Imaging: Long-Term Neurodevelopmental Outcome

E. Zvi, A. Shemer, S. toussia-Cohen, D. Zvi, Y. Bashan, L. Hirschfeld-dicker, N. Oselka, M.-M. Amitai, O. Ezra, O. Bar-Yosef, and E. Katorza



ABSTRACT

BACKGROUND AND PURPOSE: Very few studies have investigated long-term neurodevelopment of children exposed to MR imaging antenatally. Thus, the purpose of our study was to evaluate long-term neurodevelopmental outcomes of children exposed to MR imaging during pregnancy.

MATERIALS AND METHODS: We conducted a historical prospective cohort study in a single tertiary medical center. Women exposed to 1.5T noncontrast MR imaging for maternal or fetal indications were matched to unexposed controls. Long-term neurodevelopmental outcomes were evaluated of their children, 2.5 to 6 years of age, according to the Vineland-II Adaptive Behavior Scale. The Vineland-II Adaptive Behavior Scale assesses communication, daily living skills, socialization, and motor skills. A composite score summarizes these 4 domains.

RESULTS: A total of 131 exposed women matched our inclusion criteria and were included in the study group, and 771 unexposed women, in the control group. No difference was identified in the Vineland-II Adaptive Behavior Scale composite score between the children of the study and control groups (mean, 110.79 versus 108.18; $P = .098$). Differences were also not observed between the children of the 2 groups in 3 of the 4 questionnaire domains: communication (108.84 versus 109.10; $P = .888$), daily living skills (109.51 versus 108.28; $P = .437$), and motor skills (105.09 versus 104.42; $P = .642$). However, the socialization score was favorable for the study group (112.98 versus 106.47; $P < .001$).

CONCLUSIONS: Exposure to 1.5T noncontrast MR imaging during pregnancy had no harmful effects on long-term neurodevelopmental outcomes. This study contributes to understanding the safety of MR imaging during pregnancy.

ABBREVIATION: VABS = Vineland-II Adaptive Behavior Scale

MR imaging has become commonly used when higher resolution imaging is needed for fetuses and pregnant women. The consensus is to avoid ionizing radiation whenever possible due to adverse effects on fetal development.^{1,2} Therefore, clinicians prefer to use nonionizing imaging such as sonography and MR imaging during pregnancy.³

Currently, MR imaging is used for fetal and maternal indications in pregnant women with selected conditions.^{4,5} Animal studies have shown associations of some adverse effects with long-term exposure to MR imaging, including hearing impairment, skeletal malformations, and fetal weight abnormalities.⁶⁻⁸ Human studies did not show similar results but concluded that more research needs to be conducted.⁹⁻¹¹

The American College of Radiology practice guidelines state that there is no conclusive evidence of harmful effects on a developing fetus exposed to 1.5T MR imaging.¹² However, concerns about MR imaging safety during pregnancy, especially during organogenesis, have been raised due to loud noise, heating caused by absorption of radio waves, and exposure to high-power electromagnetic fields.¹³⁻¹⁶ Two recent studies with large cohorts helped shed light on the subject. One retrospective study compared hearing screening results of 751 neonates exposed to MR imaging in utero with those of 10,042 unexposed neonates. The respective rates of hearing impairment or deafness at birth were

Received May 25, 2020; accepted after revision July 14.

From the Antenatal Diagnostic Unit (E.Z., S.t.-C., O.E., E.K.), Department of Obstetrics and Gynecology, and Department of Diagnostic Radiology (M.-M.A.), Chaim Sheba Medical Center, Tel-Hashomer, Israel; Sackler School of Medicine (E.Z., A.S., S.t.-C., D.Z., Y.B., L.H.-d., N.O., M.-M.A., O.E., O.B.-Y., E.K.), Tel Aviv University, Tel Aviv, Israel; and Pediatric Neurology Unit (O.B.-Y.), Sheba Medical Center, Ramat-Gan, Israel.

Paper previously presented as a poster at: Sackler Faculty of Medicine 13th Medical Research Fair, April 16, 2019; Tel Aviv, Israel.

Please address correspondence to Elad Zvi, MD, Chaim Sheba Medical Center, Tel-Hashomer 52621, Ramat Gan, Israel; e-mail: elad.zvi@gmail.com

Indicates article with supplemental on-line tables.

<http://dx.doi.org/10.3174/ajnr.A6771>

0% and 0.34%. Long-term outcomes were not assessed. The median gestational age at MR imaging was 37 weeks, with the earliest at 16 weeks.¹⁷ The second study compared 1737 fetuses exposed to MR imaging during the first trimester versus 1,418,451 unexposed fetuses. A follow-up at 4 years of age was performed using diagnosis billing codes. Five outcomes were evaluated: 1) stillbirth after 20 weeks' gestational age, 2) congenital anomaly, 3) neoplasm, 4) vision loss, and 5) hearing loss. The risk for these outcomes was not significantly higher in the exposed compared with the unexposed group.¹⁸ To the best of our knowledge, studies of long-term neurodevelopmental assessments are scarce. Thus, the objective of our study was to examine the long-term neurodevelopmental outcomes of fetuses exposed to MR imaging during pregnancy.

MATERIALS AND METHODS

This is a historical prospective cohort study, conducted in a single tertiary medical center (Chaim Sheba Medical Center) between 2011 and 2017. Demographic and clinical data were collected from the electronic records of each patient. The study included all women who gave birth at our medical center and underwent a noncontrast 1.5T MR imaging during pregnancy due to fetal or maternal indications. Maternal indications for MR imaging included suspected appendicitis, cholecystitis, multiple sclerosis, back pain, severe headaches, and trauma. Fetal indications for MR imaging included suspected mild ventricular dilation or asymmetry,¹⁹ microcephaly, or macrocephaly and a previous pregnancy with CNS malformations. All the fetuses included in the study had normal MR imaging findings and were without evidence of chromosomal abnormalities or cytomegalovirus infection during pregnancy. No contrast materials were used during the MR imaging. Women with substance abuse, including tobacco and alcohol, were excluded from the study. We created a control group that consisted of women who gave birth at the same medical center on the same days. All the women in the control group met the inclusion and exclusion criteria of the study, apart from exposure to MR imaging during pregnancy.

For the neurodevelopmental assessment, we selected women from the control group and matched them according to date of birth and mode of delivery at the ratio of 1:1 with the study group. Four neurodevelopmental long-term aspects were assessed using the Vineland-II Adaptive Behavior Scale (VABS): communication, daily living skills, socialization, and motor skills. These provide a composite score that summarizes the individual's performance across all 4 domains.^{20,21} Telephone interviews were conducted between February 2017 and July 2017. All the children were between 2.5 and 6 years of age at the time of the interviews. The VABS is standardized by age. The mean score for all ages is 100 ± 15 . Scores of <70 are considered in the abnormal range.

Categoric variables were described using frequencies and percentages. Continuous variables were evaluated for normal distribution using histograms and quartile-quartile plots. Normally distributed continuous variables were described as means and SDs, and skewed variables were expressed as medians and interquartile ranges. The ANOVA, independent-samples *t* test, Kruskal-Wallis test, and the Mann-Whitney test

were used, as appropriate, to compare continuous variables among categories within the exposed group. Categoric variables were compared using the χ^2 test or Fisher exact test. Study and control-matched women were compared using the paired-samples *t* test, Wilcoxon signed rank test, McNemar test, generalized estimating equations, or conditional logistic regression, as appropriate.

The sample size was calculated by using WINPEPI software (<http://www.brixtonhealth.com/pepi4windows.html>). Significance level and power were set to 5% and 80%, respectively. To identify a 5-point difference in the VABS composite score, 73 matched pairs of patients were needed.

All the statistical tests were 2-tailed. $P < .05$ was considered statistically significant. All the statistical analyses were performed using SPSS Statistics software, Version 24 (IBM).

The study was approved by the institutional review board (No. 1902-15-SMC). The authors obtained both informed consent and ethics committee approval for accessing data from patient records and conducting a telephone questionnaire.

RESULTS

Demographic and Clinical Characteristics of the Study Population

One hundred thirty-one pregnant women who were exposed to MR imaging during pregnancy, between 2011 and 2015 met the inclusion criteria of the study. The excluded cases were mainly due to fetal anomalies or chromosomal aberrations, twin pregnancy, cytomegalovirus infection during pregnancy, and delivery in a different medical center. Of 131 deliveries, 58 (44.3%) were girls; the mean gestational age at birth was 39 weeks. Eight women were exposed to MR imaging during the first trimester; 28, during the second; and 95, during the third. During pregnancy, 114 women were exposed once to MR imaging scans, and 17 were exposed ≥ 2 times. Seventy-two MR imaging scans were for fetal indications (68 CNS and 4 body), and 62 were for maternal indications (20 CNS and 42 body) as shown in On-line Table 1.

Comparison between the Study and Control Groups

During the same study period, 771 women met our criteria for the control group. Of them, 392 fetuses were girls (50.8%). The mean gestational age at birth was 39 weeks. Compared with the control group, for the study group, parity was higher (1.68 versus 1.14), as was the prevalence of pregestational diabetes mellitus (6.1% versus 1.3%), the use of anticoagulation (8.4% versus 3.9%) and antihypertensive medications during pregnancy (6.9% versus 1.2%), and cesarean delivery (37% versus 22.8%). In contrast, thrombocytopenia was more prevalent in the control than in the study group (16% versus 3.8%). Statistically significant differences were not found between the groups in maternal age during delivery or in the mode of conception, as shown in On-line Table 2.

The neonatal characteristics and outcomes for the study and control groups are presented in On-line Table 3. Compared with the study group, for the control group, the mean gestational age at delivery was higher (39.01 versus 38.41 weeks, $P < .001$) and the birth weight was higher (3216.6 versus 3069.95 g, $P = .002$). The weight percentiles did not differ significantly between the

groups. The mean APGAR scores after 5 minutes were higher in the control than the study group (9.96 versus 9.86, $P = .04$). APGAR 1-minute scores and hearing test results after birth did not differ between the groups.

Neurodevelopmental Outcome

One hundred ninety-two women responded to the VABS in a 1:1 ratio of exposed and unexposed cases, matched according to the birth date and mode of delivery (96 in each group). No statistically significant difference was found in the VABS composite score between the children of the study and control groups (110.79 versus 108.18, $P = .098$). None of the children (exposed or nonexposed) had abnormal VABS composite scores. However, analyzing each domain separately (communication, daily living skills, socialization, and motor skills), a statistically significant difference was noticed between the groups only in the socialization score in favor of the study group (112.98 ± 13.28 versus 106.47 ± 11.08 , $P < .001$) (On-line Table 4).

In an analysis that stratified by the trimester of MR imaging exposure (On-line Table 5), the mean motor skills score of the VABS was significantly lower among those exposed in the first compared with the second and third trimesters (94.5 ± 10.71 , 106.28 ± 11.03 , and 105.91 ± 10.31 , respectively, $P = .037$). Notably, despite the statistically significant difference, all the scores were within the normal range. No other differences in fetal outcome (birth weight, APGAR score, hearing screening) were found according to the trimester of exposure, the number of MR imaging exposures during the same pregnancy, and the MR imaging protocols.

DISCUSSION

Our study evaluated long-term neurodevelopmental outcomes of children exposed to MR imaging during pregnancy, according to VABS, as assessed by telephone interviews.

We showed no difference in the adaptive behavior composite score between the exposed and the unexposed groups.

However, the socialization score of the study group was significantly higher than that of the control group (112.98 versus 106.47 ; $P < .001$). This finding probably does not have any clinical significance because all the scores are within the normal range. Our results suggest that exposure to MR imaging does not have a harmful long-term effect on the child's neurodevelopment between 2.5 and 6 years of age. This result is in agreement with those in smaller studies that evaluated long-term effects of fetal MR imaging exposure.^{22,23}

Recommendations that have been published for MR imaging safety during pregnancy do not contraindicate the use of this technique according to the trimester of pregnancy.^{3,14,24} Other studies have suggested that MR imaging is safe during all trimesters of pregnancy in regard to neonatal normal hearing and vision and the risks for neoplasm, stillbirth, and congenital anomalies.^{17,18} No other study evaluated long-term neurodevelopment of MR imaging-exposed fetuses or compared the MR imaging exposure effects in different trimesters and protocols. The lack of long-term adverse effects demonstrated in our study corroborates previous reports and supports the use of MR imaging in prenatal imaging.

We found that children who were exposed to MR imaging in the first trimester had lower scores on the motor skills domain of

the VABS than those exposed in the second and third trimesters. This is probably without any clinical manifestation because all the scores were within the normal range and all the neonates were delivered at term with normal APGAR scores. However, only 8 fetuses were exposed in the first trimester.

None of the outcomes examined differed between children whose mothers underwent a CNS protocol MR imaging during pregnancy and children whose mothers underwent other MR imaging protocols. Notably, in mothers with CNS protocols, the distance of the fetus from the center of the MR imaging is farther than with other protocols; therefore, the exposure is lower.²⁵ A similar result was demonstrated when comparing the fetal CNS protocol, in which the MR imaging is focused on the fetal brain, with the rest of the protocols. Thus, according to these findings, the fetus is not affected by MR imaging, regardless of the protocol used.

The proportion of cesarean deliveries was higher in the study than in the control group. A possible explanation may relate to close monitoring of most of the pregnancies of women who underwent MR imaging due to the particular circumstances involved. No statistically significant differences were noticed between the groups regarding birth weight, weight percentile, and 5-minute APGAR scores, concurring with previous reports.²⁶ Regarding birth weight and gestational age at delivery, we showed similar results to those in a previous study.²⁷

The strengths of this study include the long-term evaluation of motor skills, socialization, daily living skills, and communication obtained by the VABS. In addition, to avoid any confounders that could affect the results, we set strict inclusion and exclusion criteria that were achieved by reviewing all the medical files. All information regarding prenatal evaluation before the MR imaging exposure was collected, together with potential teratogens such as medication, alcohol use, and maternal morbidity. Furthermore, all the MR imaging protocols are known and were grouped by anatomic region of the mother and fetus. To further reduce any confounders, we matched 96 women in the study and control groups by day and mode of delivery.

Our study has a number of limitations. First, only a small number of women were exposed to MR imaging during the first trimester, thus limiting the power of this study to assess the risk of MR imaging exposure during this trimester. Second, the main indication of MR imaging in this study was for the fetal CNS (35.3%), which may cause a selection bias.

CONCLUSIONS

Exposure to 1.5T noncontrast MR imaging during pregnancy had no harmful effects on long-term neurodevelopmental outcomes, regardless of gestational age, the number of MR imaging scans during pregnancy, and the use of various MR imaging protocols. This study contributes to the understanding of the safety of MR imaging during pregnancy and may benefit prenatal counseling.

REFERENCES

1. Fazel R, Krumholz HM, Wang Y, et al. Exposure to low-dose ionizing radiation from medical imaging procedures. *N Engl J Med* 2009;361:849–57 CrossRef Medline

2. Chen MM, Coakley FV, Kaimal A, et al. **Guidelines for computed tomography and magnetic resonance imaging use during pregnancy and lactation.** *Obstet Gynecol* 2008;112:333–40 CrossRef Medline
3. ACOG Committee on Obstetric Practice. **ACOG Committee Opinion: Number 299, September 2004 (replaces No. 158, September 1995)—guidelines for diagnostic imaging during pregnancy.** *Obstet Gynecol* 2004;104:647–51 CrossRef Medline
4. Rapp EJ, Naim F, Kadivar K, et al. **Integrating MR imaging into the clinical workup of pregnant patients suspected of having appendicitis is associated with a lower negative laparotomy rate: single-institution study.** *Radiology* 2013;267:137–44 CrossRef Medline
5. Spalluto LB, Woodfield CA, DeBenedictis CM, et al. **MR imaging evaluation of abdominal pain during pregnancy: appendicitis and other nonobstetric causes.** *Radiographics* 2012;32:317–34 CrossRef Medline
6. Mevissen M, Buntenkötter S, Löscher W. **Effects of static and time-varying (50-Hz) magnetic fields on reproduction and fetal development in rats.** *Teratology* 1994;50:229–37 CrossRef Medline
7. Yip YP, Capriotti C, Talagala SL, et al. **Effects of MR exposure at 1.5 T on early embryonic development of the chick.** *J Magn Reson Imaging* 1994;4:742–48 CrossRef Medline
8. Gerhardt KJ, Pierson LL, Huang X, et al. **Effects of intense noise exposure on fetal sheep auditory brain stem response and inner ear histology.** *Ear Hear* 1999;20:21–32 CrossRef Medline
9. Rocha EB, Frasson de Azevedo M, Ximenes Filho JA. **Study of the hearing in children born from pregnant women exposed to occupational noise: assessment by distortion product otoacoustic emissions.** *Braz J Otorhinolaryngol* 2007;73:359–69 CrossRef Medline
10. Reeves MJ, Brandreth M, Whitby EH, et al. **Neonatal cochlear function: measurement after exposure to acoustic noise during in utero MR imaging.** *Radiology* 2010;257:802–09 CrossRef Medline
11. Choi JS, Ahn HK, Han JY, et al. **A case series of 15 women inadvertently exposed to magnetic resonance imaging in the first trimester of pregnancy.** *J Obstet Gynaecol* 2015;35:871–72 CrossRef Medline
12. American College of Radiology. **ACR-SPR Practice Guideline for the Safe and Optimal Performance of Fetal Magnetic Resonance Imaging (MRI).** American College of Radiology; 2015. <https://www.acr.org/-/media/ACR/Files/Practice-Parameters/mr-fetal.pdf>. Accessed November 13, 2016
13. Patenaude Y, Pugash D, Lim K, et al; Society of Obstetricians and Gynaecologists of Canada. **The use of magnetic resonance imaging in the obstetric patient.** *J Obstet Gynaecol Can* 2014;36:349–63 CrossRef Medline
14. Kanal E, Barkovich AJ, Bell C, et al; ACR Blue Ribbon Panel on MR Safety. **ACR guidance document for safe MR practices: 2007.** *AJR Am J Roentgenol* 2007;188:1447–74 CrossRef Medline
15. Hartwig V, Giovannetti G, Vanello N, et al. **Biological effects and safety in magnetic resonance imaging: a review.** *Int J Environ Res Public Health* 2009;6:1778–98 CrossRef Medline
16. Kikuchi S, Saito K, Takahashi M, et al. **Temperature elevation in the fetus from electromagnetic exposure during magnetic resonance imaging.** *Phys Med Biol* 2010;55:2411–26 CrossRef Medline
17. Strizek B, Jani JC, Mucyo E, et al. **Safety of MR imaging at 1.5 T in fetuses: a retrospective case-control study of birth weights and the effects of acoustic noise.** *Radiology* 2015;275:530–37 CrossRef Medline
18. Ray JG, Vermeulen MJ, Bharatha A, et al. **Association between MRI exposure during pregnancy and fetal and childhood outcomes.** *JAMA* 2016;316:952–61 CrossRef Medline
19. Barzilay E, Bar-Yosef O, Dorembus S, et al. **Fetal brain anomalies associated with ventriculomegaly or asymmetry: an MRI-based study.** *AJNR Am J Neuroradiol* 2017;38:371–75 CrossRef Medline
20. Limperopoulos C, Majnemer A, Steinbach CL, et al. **Equivalence reliability of the Vineland Adaptive Behavior Scale between in-person and telephone administration.** *Phys Occup Ther Pediatr* 2006;26:115–27 CrossRef Medline
21. Sparrow SS, Balla DA, Cicchetti DV. **PsycTESTS dataset.** In: Sparrow SS, Balla DA, Cicchetti DV. *Vineland Adaptive Behavior Scales.* 2nd ed. American Psychological Association; 2005
22. Clements H, Duncan KR, Fielding K, et al. **Infants exposed to MRI in utero have a normal paediatric assessment at 9 months of age.** *Br J Radiol* 2000;73:190–94 CrossRef Medline
23. Kok RD, de Vries MM, Heerschap A, et al. **Absence of harmful effects of magnetic resonance exposure at 1.5 T in utero during the third trimester of pregnancy: a follow-up study.** *Magn Reson Imaging* 2004;22:851–54 CrossRef Medline
24. Jaffe TA, Miller CM, Merkle EM. **Practice patterns in imaging of the pregnant patient with abdominal pain: a survey of academic centers.** *AJR Am J Roentgenol* 2007;189:1128–34 CrossRef Medline
25. Padiaditis M, Leitgeb N, Cech R. **RF-EMF exposure of fetus and mother during magnetic resonance imaging.** *Phys Med Biol* 2008;53:7187–95 CrossRef Medline
26. Dollberg S, Haklai Z, Mimouni FB, et al. **Birth weight standards in the live-born population in Israel.** *Isr Med Assoc J* 2005;7:311–14 Medline
27. Myers C, Duncan KR, Gowland PA, et al. **Failure to detect intrauterine growth restriction following in utero exposure to MRI.** *Br J Radiol* 1998;71:549–51 CrossRef Medline

COVID-19-Associated Carotid Atherothrombosis and Stroke

C. Esenwa, N.T. Cheng, E. Lipsitz, K. Hsu, R. Zampolin, A. Gersten, D. Antoniello, A. Soetanto, K. Kirchoff, A. Liberman, P. Mabie, T. Nisar, D. Rahimian, A. Brook, S.-K. Lee, N. Haranhalli, D. Altschul, and D. Labovitz



ABSTRACT

SUMMARY: We present a radiology-pathology case series of 3 patients with coronavirus disease 2019 (COVID-19) with acute ischemic stroke due to fulminant carotid thrombosis overlying mild atherosclerotic plaque and propose a novel stroke mechanism: COVID-associated carotid atherothrombosis.

ABBREVIATIONS: ACE2 = angiotensin-converting enzyme 2; CCA = common carotid artery; COVID-19 = coronavirus disease 2019; RT-PCR = reverse-transcriptase polymerase chain reaction; SARS-CoV-2 = Severe Acute Respiratory Syndrome coronavirus 2

Carotid plaque size is a predictor of ischemic stroke and guides treatment strategies.¹ However, since 1952, when C. Miller Fisher associated carotid atherosclerosis with stroke, there remained an unresolved question: Why did the plaque become symptomatic when it did?² Inflammation has been proposed as the main mediator³ of carotid disease, and with the emergence of the coronavirus disease 2019 (COVID-19), we may have entered a new era of large-vessel atherothrombotic disease with a unique opportunity to address Fisher's question.

COVID-19 causes acute cardiovascular events with unusual manifestations.⁴ Reports of patients with intracranial large-vessel occlusion implicates cerebrocervical vessel involvement as part of the spectrum of cardiovascular events in COVID-19.^{5,6} One mechanism under investigation is related to the binding of Severe Acute Respiratory Syndrome coronavirus 2 (SARS-CoV-2) on the human angiotensin-converting enzyme 2 (ACE2) receptor.⁷ ACE2 is highly expressed in the endothelium and has been directly implicated in mediating vessel wall inflammation, oxidative stress, and atherosclerosis.⁸ Evidence of viral infection with endothelial inflammation and apoptosis in bowel and lung tissue of patients with COVID-19 has been termed "endotheliitis."⁹

We describe 3 patients with COVID-19 with acute ischemic stroke due to fulminant carotid thrombosis overlying mild atherosclerotic plaque. We review the clinical course, advanced imaging, and pathologic examination and propose a previously undescribed COVID-19-related stroke mechanism.

Case Series Description

From April 9 to 23, 2020, a 2-week period when COVID-19 peaked in New York City, we encountered 3 patients with COVID-19 and partially occlusive cervical carotid thrombosis. Patients 1 and 3 presented to our tertiary-care hospital and comprehensive stroke center (Montefiore Medical Center - Moses Campus) with acute stroke, while patient 2 developed stroke as an inpatient. The patients shared comorbid conditions, biomarker profiles, and radiographic features (On-line Table). CT angiography showed nonocclusive thrombus adherent to the distal common carotid artery (CCA) and carotid bifurcation on CTA of the head and neck (Fig 1), with cortical acute ischemic strokes ipsilateral to the carotid lesion in all patients. Patient 1 also had an incidental aortic arch thrombus adherent to the vessel wall. All 3 patients demonstrated peripheral ground-glass pulmonary findings consistent with COVID-19 infection. Patients 1 and 3 were diagnosed with COVID-19 on the basis of the clinical course, pulmonary findings, and a positive reverse-transcriptase polymerase chain reaction test (RT-PCR) for SARS-CoV-2. Patient 2 presented with signs and symptoms of COVID-19 pneumonia, had profound pulmonary findings consistent with COVID-19 pneumonia on imaging, and while RT-PCR results were negative, the patient tested positive for the SARS-CoV-2 antibody. The patients were treated with apixaban or intravenous unfractionated heparin without resolution of the thrombus. Two were also on antiplatelet therapy before undergoing

Received May 30, 2020; accepted after revision June 26.

From the Departments of Neurology (C.E., N.T.C., D. Antoniello, A.S., K.K., A.L., P.M., T.N., D.R., D.L.), Radiology (K.H., R.Z., A.B., S.-K.L.), Pathology (A.G.), Neurosurgery (N.H., D. Altschul), and Cardiothoracic and Vascular Surgery (E.L.), Montefiore Medical Center/Albert Einstein College of Medicine, Bronx, New York.

Drs Esenwa and Cheng contributed equally as primary authors.

Please address correspondence to Charles Esenwa, MD, MS, Montefiore Medical Center, 3316 Rochambeau Ave, 4th floor, Bronx, NY 10467; e-mail: cesenwa@montefiore.org

 Indicates open access to non-subscribers at www.ajnr.org

 Indicates article with supplemental on-line table.

<http://dx.doi.org/10.3174/ajnr.A6752>

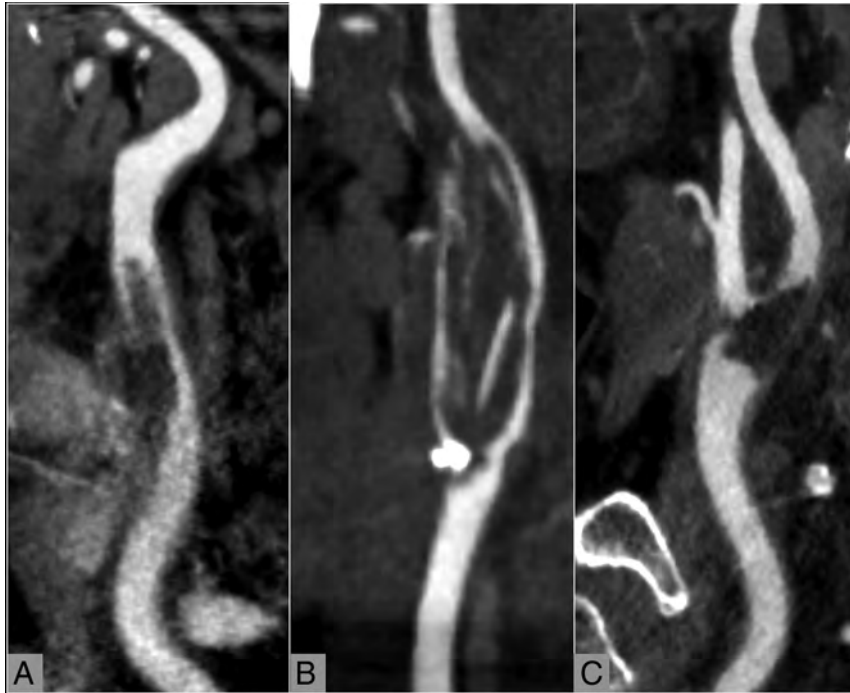


FIG 1. CT angiogram of cervical vessels showing thrombosis. Curved planar reformatted CTA neck images demonstrate adherent thrombus in the left mid-common carotid artery (patient 1) (A). The thrombus appears to start from the right carotid bifurcation and extend toward both the internal and external carotid arteries (patient 2) (B), and the left carotid bifurcation shows wedge-shaped intraluminal thrombus (patient 3) (C). Note the relatively minor mineralized and nonmineralized atherosclerotic plaque adjacent to the thrombus in each patient.

open thrombectomy and carotid endarterectomy. Surgical intervention was chosen to facilitate complete clot removal and perform endarterectomy as needed, as well as to minimize embolic risk from the intraluminal thrombus.

Open exploration in patient 1 revealed an organized thrombus moderately adherent to the wall of the CCA over a length of approximately 1 cm and encompassing approximately 70% of its circumference. A free-floating tail of thrombus extended distally to the level of the carotid bifurcation. Moderate plaque with marked inflammatory changes at the area of clot adherence did not cause considerable plaque-related luminal stenosis. Microscopic examination confirmed thrombus adherent to the wall. The intima had inflammatory infiltrates as well as some degenerative cellular debris consistent with apoptosis (Fig 2C).

Open exploration in patient 2 identified a small, moderately adherent organized thrombus in the carotid bulb with a smaller contiguous portion adjacent to an area of calcified plaque extending into the external carotid artery. Gross examination found only mild inflammatory changes at the level of clot adherence. Microscopically, the intima was thickened with evolving calcification consistent with atherosclerotic disease. A portion of the intima contained mononuclear inflammatory cells (Fig 2A, -B).

Patient 3 had organized, nearly occlusive thrombus, extending into the proximal internal carotid artery, with moderate plaque and

an approximate 6 × 6 mm area of ulceration in the carotid bulb at the area of adhesion. Considerable inflammation was noted in the area of the bulb. The specimen showed mild-to-moderate atherosclerotic disease with intimal thickening, plaque, and mural calcification. There were scattered mononuclear cells in an area of thickened intima.

DISCUSSION

We propose a novel stroke mechanism, COVID-19-associated carotid atherothrombosis, and review the imaging and pathologic findings. While still not fully understood, it is believed that an overwhelming innate immune response to SARS-CoV-2 results in 1) systemic inflammation, 2) associated coagulopathy, and 3) local endotheliitis, in some.^{9,10} In the patients described herein, SARS-CoV-2 endotheliitis may have destabilized mild chronic atherosclerotic plaque to initiate thrombosis, with subsequent propagation due to a prothrombotic state broadly termed “COVID-19-associated coagulopathy.”¹¹ Reports of SARS-CoV-2-mediated endotheliitis support this possible mechanism because local inflammation might alter endothelial functions.^{12,13} Pathologic reports of multiorgan thrombotic microangiopathy in patients with COVID-19 support our theory that COVID-19-associated coagulopathy may have additionally and perhaps synergistically contributed to the disproportionately high intraluminal thrombus burden relative to the mild underlying atherosclerotic plaque.^{14,15} On the basis of our limited case observation and the available literature, we further suggest the possibility that thromboinflammation related to COVID-19 may preferentially affect areas of atheromatous disease. Thus, our clinical impression in each of the described cases was that medical therapy with anticoagulation or antiplatelets alone was not sufficient to minimize the embolic risk; therefore, we recommended surgical intervention to facilitate complete clot and atheroma removal.

From this radiology-pathology case series, we deduce that areas of mild carotid atherosclerosis may be particularly prone to thrombus formation in patients with COVID-19 because of the unique combination of endotheliitis and COVID-19-associated coagulopathy. In the face of this pandemic, we may have coincidentally come closer to answering Fisher’s question and are poised to address the next: How do we prevent COVID-19-associated carotid atherothrombosis?

Disclosures: Ava Liberman—RELATED: Grant: National Institutes of Health, Comments: The Mentored Patient-Oriented Research Career Development Award (K23).* Seon-Kyu Lee—UNRELATED: Consultancy: GraftWorks; Grants/

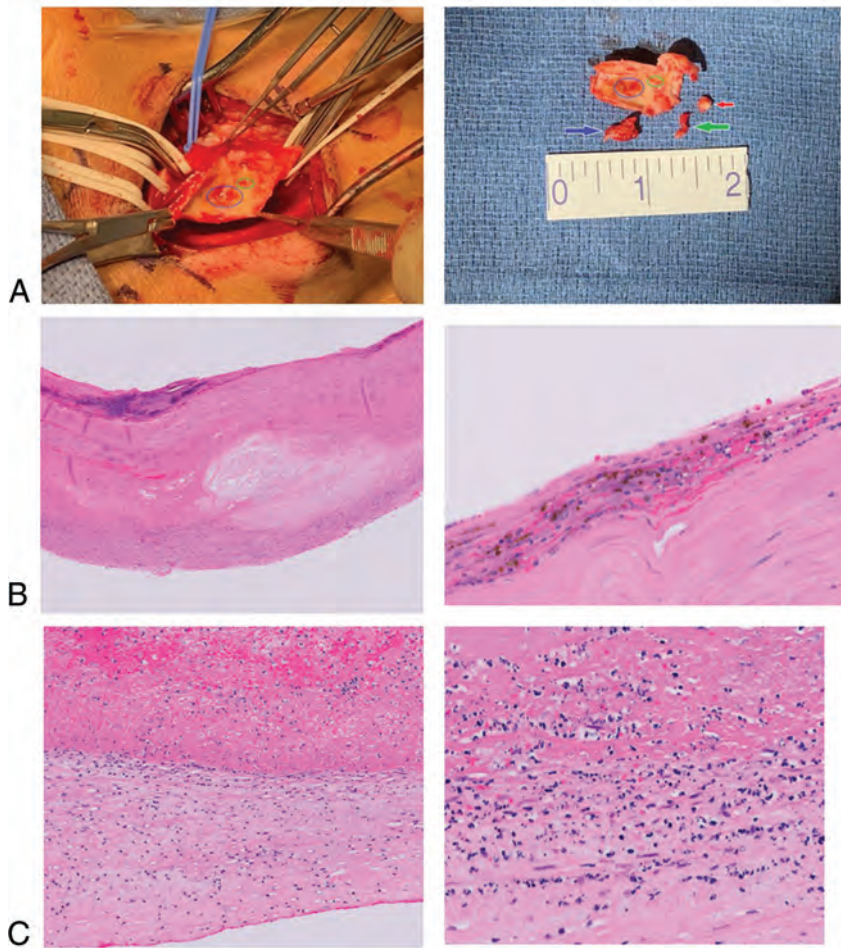


FIG 2. Gross and microscopic pathology. *A*, Surgical view in patient 2. The *blue circle* indicates the area to which the thrombus was adherent, and the *green circle* indicates the area to which the contiguous portion of the thrombus was adherent. *Arrows* represent the larger portion of thrombus (*blue*), smaller portion of thrombus (*green*), and calcified plaque at the external carotid origin (*red*). *B*, Microscopic examination of a specimen from patient 2. Hematoxylin-eosin stain shows intimal thickening, plaque formation, and calcification. Higher magnification shows an area of intima with mononuclear inflammatory cells and evolving plaque formation. *C*, Microscopic examination of a specimen from patient 1. Low-power hematoxylin-eosin stain shows the thrombus adherent to the wall (upper portion is thrombus; lower portion is the wall). Higher-power view of an area of adherent thrombus shows the intima with inflammatory infiltrate as well as some degenerating cellular debris that may indicate apoptosis.

Grants Pending: National Institutes of Health grants. Comments: 1 R21 CA205892-01, 1 R21 EB022291-01. David Altschul—UNRELATED: Consultancy: MicroVenton. *Money paid to the institution.

REFERENCES

1. Barnett HJ, Taylor DW, Haynes RB, et al; North American Symptomatic Carotid Endarterectomy Trial Collaborators. **Beneficial effect of carotid endarterectomy in symptomatic patients with high-grade carotid stenosis.** *N Engl J Med* 1991;325:445–53 CrossRef Medline
2. Fisher CM. **Transient monocular blindness associated with hemiplegia.** *AMA Arch Ophthalmol* 1952;47:167–203 CrossRef Medline

3. Esenwa CC, Elkind MS. **Inflammatory risk factors, biomarkers and associated therapy in ischaemic stroke.** *Nat Rev Neurol* 2016;12:594–604 CrossRef Medline
4. Clerkin KJ, Fried JA, Raikhelkar J, et al. **Coronavirus disease 2019 (Covid-19) and cardiovascular disease.** *Circulation* 2020;141:1648–55 CrossRef
5. Oxley TJ, Mocco J, Majidi S, et al. **Large-vessel stroke as a presenting feature of Covid-19 in the young.** *N Engl J Med* 2020;382:e60 CrossRef Medline
6. Wang A, Mandigo GK, Yim PD, et al. **Stroke and mechanical thrombectomy in patients with COVID-19: technical observations and patient characteristics.** *J Neurointerv Surg* 2020;12:648–53 CrossRef Medline
7. Hoffmann M, Kleine-Weber H, Schroeder S, et al. **SARS-CoV-2 cell entry depends on ACE2 and TMPRSS2 and is blocked by a clinically proven protease inhibitor.** *Cell* 2020;181:271–80.e278 CrossRef Medline
8. Tikellis C, Thomas MC. **Angiotensin-converting enzyme 2 (ACE2) is a key modulator of the renin angiotensin system in health and disease.** *Int J Pept* 2012;2012:256294 CrossRef Medline
9. Varga Z, Flammer AJ, Steiger P, et al. **Endothelial cell infection and endotheliitis in Covid-19.** *Lancet* 2020;395:1417–18 CrossRef Medline
10. Buja LM, Wolf DA, Zhao B, et al. **The emerging spectrum of cardiopulmonary pathology of the coronavirus disease 2019 (COVID-19): report of 3 autopsies from Houston, Texas, and review of autopsy findings from other United States cities.** *Cardiovasc Pathol* 2020;48:107233 CrossRef Medline
11. Connors J, Levy J. **Covid-19 and its implications for thrombosis and anticoagulation.** *Blood* 2020;135:2033–40 CrossRef Medline
12. Magro C, Mulvey JJ, Berlin D, et al. **Complement associated microvascular injury and thrombosis in the pathogenesis of severe COVID-19 infection: a report of five cases.** *Transl Res* 2020;220:1–13 CrossRef Medline
13. Carsana L, Sonzogni A, Nasr A, et al. **Pulmonary post-mortem findings in a series of COVID-19 cases from northern Italy: a two-centre descriptive study.** *Lancet Infect Dis* 2020 June 8. [Epub ahead of print] CrossRef Medline
14. Connors JM, Levy JH. **Thromboinflammation and the hypercoagulability of COVID-19.** *J Thromb Haemost* 2020;18:1559–61 CrossRef Medline
15. Jackson SP, Darbousset R, Schoenwaelder SM. **Thromboinflammation: challenges of therapeutically targeting coagulation and other host defense mechanisms.** *Blood* 2019;133:906–18 CrossRef Medline

Evolving Use of fMRI in Medicare Beneficiaries

 S. Asnafi,  R. Duszak,  J.M. Hemingway,  D.R. Hughes, and  J.W. Allen

ABSTRACT

SUMMARY: Using the Medicare Physician-Supplier Procedure Summary Master File, we evaluated the evolving use of fMRI in Medicare fee-for-service beneficiaries from 2007 through 2017. Annual use rates (per 1,000,000 enrollees) increased from 17.7 to 32.8 through 2014 and have remained static since. Radiologists have remained the dominant specialty group from 2007 to 2017 (86.4% and 88.6% of all services, respectively), and the outpatient setting has remained the dominant place of service (65.4% and 65.4%, respectively).

ABBREVIATIONS: CPT = Current Procedural Terminology; MEG = magnetoencephalography

First introduced in 1991 for mapping the visual cortex, fMRI relies on detecting small changes in the blood oxygen level-dependent MR imaging signal as a result of neuronal activity following specific tasks.¹ Since its introduction, fMRI has been widely used in neuroimaging research and increasingly incorporated into clinical practice. Currently, fMRI has value in the neurosurgical planning of conditions such as brain tumors or epilepsy, diagnosis and management of Alzheimer disease, and better understanding of psychiatric conditions.²

In January 2007, three distinct Current Procedural Terminology (CPT) codes were introduced to report fMRI services.³ Several studies have examined changing use of various radiologic modalities and procedures across various time periods,^{4,5} but no similar study has been performed to assess the nationwide adoption of fMRI. Given the relatively new translation of fMRI into clinical practice and the possibility that the high costs of fMRI might not be adequately reimbursed by current payor schemes,⁶ such information could potentially inform clinical practice guidelines and payer-coverage decisions. For these reasons and focusing on Medicare beneficiaries, we aimed to investigate the use patterns of fMRI with regard to both specialty groups and places of service since the introduction of unique CPT codes.

MATERIALS AND METHODS

The Annual Medicare Physician-Supplier Procedure Summary Master File from 2007 through 2017 was obtained from the Centers for Medicare & Medicaid Services. These files contain aggregated, submitted national Part B Medicare claims for all beneficiaries in the traditional Medicare fee-for-service program. These data are classified by codes for procedures, places of service, and provider specialties, along with the number of services both billed and denied. Physician-Supplier Procedure Summary files include no individual patient, diagnosis, or other encounter-specific information. Thus, their use does not constitute human subject research, and no institutional review board oversight was required for this study.

For this study, fMRIs were identified using the following service-specific CPT codes: 70554, 70555, and 96020 (Table 1).³ Analysis was performed as previously described using SPSS Statistics 25.0 (IBM) and Excel 2016 (Microsoft).^{4,5,7} fMRI use rates were calculated per 1,000,000 Medicare enrollees per year. Provider specialties and sites of service were grouped using relevant Medicare codes (Table 2).

RESULTS

Between 2007 and 2014, use rates for fMRI studies performed on Medicare fee-for-service beneficiaries increased 85% (from 17.7 to 32.8) but have since stabilized (32.8, 32.6, 32.7, and 33.3 from 2014 to 2017, respectively). In 2007, radiology was the dominant specialty group, with a rate of 15.3 (versus 2.4 for all other specialties), which has continued to be the case since (Fig 1). The specialties with the second and the third highest rates were neurology and neurosurgery, respectively, with considerable year-to-year variability. Radiology, neurology, and neurosurgery accounted for overall

Received April 9, 2020; accepted after revision June 22.

From the Departments of Radiology and Imaging Sciences (S.A., R.D., J.W.A.) and Neurology (J.W.A.), Emory University School of Medicine, Atlanta, Georgia; Harvey L. Neiman Health Policy Institute (J.M.H., D.R.H.), Reston, Virginia; and School of Economics (D.R.H.), Georgia Institute of Technology, Atlanta, Georgia.

Please address correspondence to Jason W. Allen, MD, PhD, Emory University School of Medicine, Emory University Hospital, 1364 Clifton Rd Northeast, Atlanta, GA 30322; e-mail: jason.w.allen@emory.edu
<http://dx.doi.org/10.3174/ajnr.A6845>

Table 1: CPT Codes for fMRI

CPT Code	Description
70554	fMRI; including test selection and administration of repetitive body part movement and/or visual stimulation, not requiring physician or psychologist administration
70555	fMRI; requiring physician or psychologist administration; this is to be always reported with CPT code 96020
96020	Neurofunctional testing selection and administration during noninvasive imaging functional brain mapping, with test administered entirely by a physician or psychologist, with review of test results and report

Table 2: Site of service and specialty groups studied with the corresponding codes

Site Group/Specialty Group	Sites (Code)
Outpatient	Office (11), outpatient hospital (19 and 22), independent clinic (49)
Inpatient	Inpatient hospital (21)
Emergency department	Emergency department (23)
Other	Other: independent laboratory (81), skilled nursing facility (31), temporary lodging (16), mobile unit (15), home (12), and other place of service (99)
Radiology	Diagnostic radiology (30), interventional radiology (94), and nuclear medicine (36)
Neurology	Neurology (13)
Neurosurgery	Neurosurgery (14)
Others	All other identifiable groups
Unidentified	Unidentified: independent diagnostic testing facility (47), single or multispecialty clinic or group practice (70), unknown physician specialty (99)

use rates of 280.4, 11.2, and 3.4, respectively, during the entire time period.

Separate analysis of the CPT codes billed by radiology showed that the code 70554 (test selection/administration not requiring physician or psychologist administration) billing rate increased from 12.3 in 2007 to 20.7 in 2017 (Fig 1). Code 70555 (requiring physician or psychologist administration) radiology billing also increased from 3.0 in 2007 to 8.8 in 2017 (Fig 1). Code 96020 must always be accompanied by code 70555 during billing, though 96020 may be billed by a separate provider. For radiology, the rate of billing 96020 was 0.25 in 2007 and 5.18 in 2017. From 2007 through 2017, the rate of billing 96020 for radiology was always lower than for code 70555. However, the percentage of cases in which code 70555 was billed with 96020 by radiology has increased from 2007 to 2017.

Most of the fMRI studies were performed in the outpatient (office, outpatient hospital, or independent clinic) setting, accounting for 65.4% in 2007

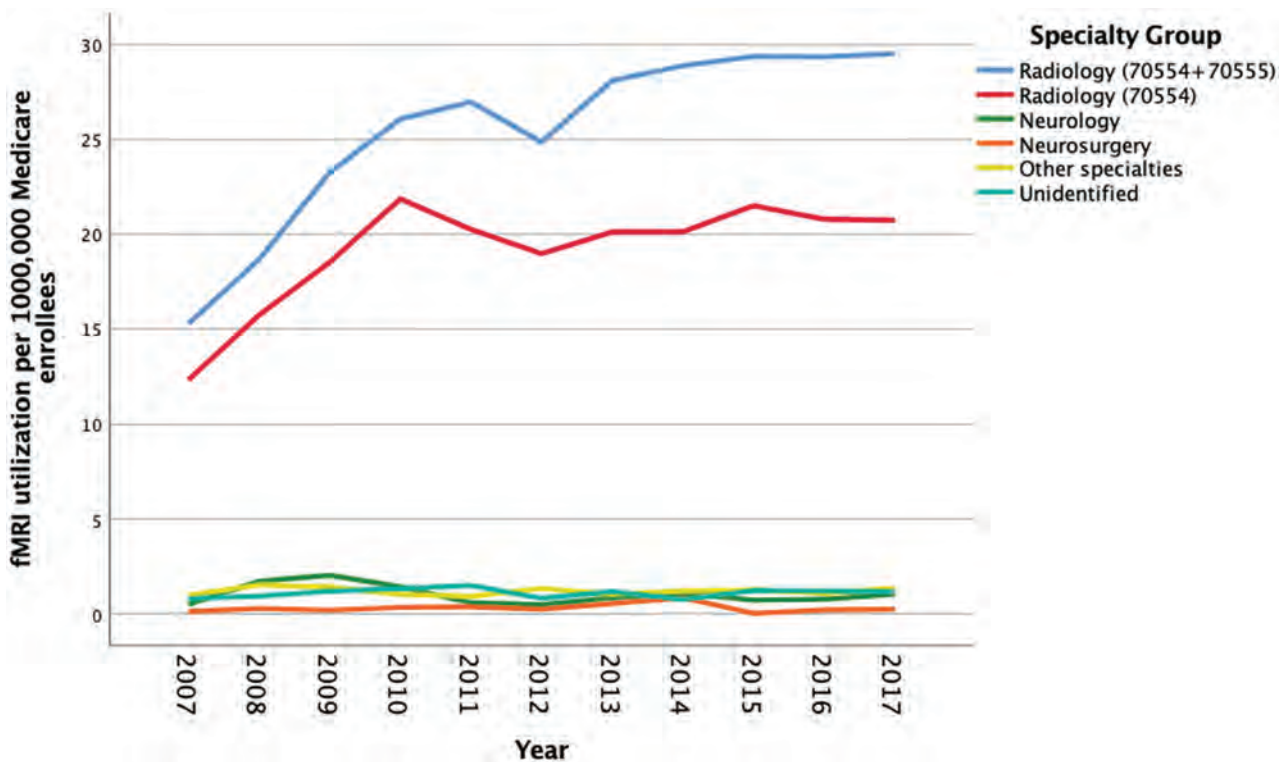


FIG 1. Functional MR imaging use in Part B Medicare beneficiaries from 2007 to 2017 by physician specialty group. Radiology (70554 + 70555) refers to the total billing of fMRI by this specialty. Radiology (70554) refers only to the 70554 CPT code. All other specialties reflect total billing.

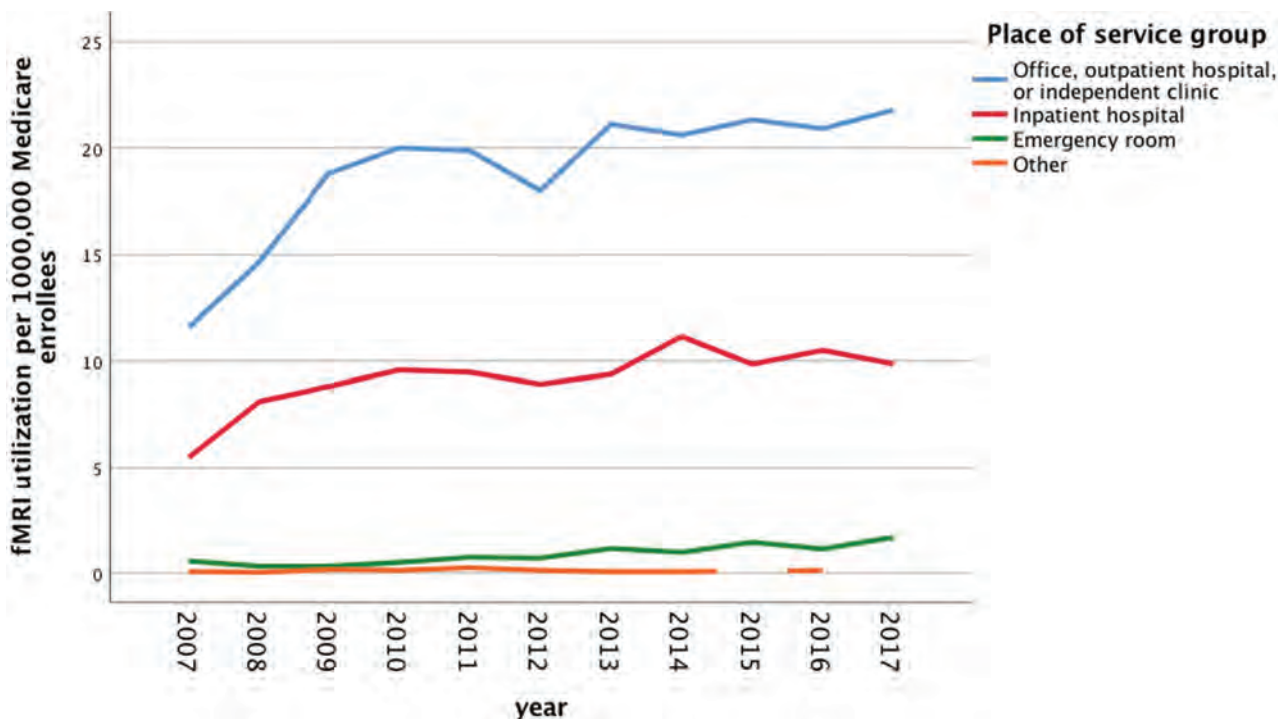


FIG 2. Functional MR imaging use in Part B Medicare beneficiaries from 2007 to 2017 by place of a service group.

and 65.4% in 2017. The second and the third most common sites were inpatient hospital (31.1 in 2007 and 29.6 in 2017) and emergency department (3.1% in 2007, and 5.0% in 2017). fMRI use with regard to place of service is illustrated in Fig 2.

DISCUSSION

Using annual aggregate Medicare fee-for-service claims files for all years for which unique CPT code data were currently available, we studied nationwide use of fMRI and found an increased adoption in the first 7 years after CPT codes became available, with a plateau in use thereafter. fMRI has consistently been performed predominantly by radiologists and predominantly in the outpatient setting, not dissimilar to patterns previously described for nonfunctional brain CT and MR imaging.⁸

Preoperative planning is one of the widely accepted applications of fMRI, which is commonly used in brain tumor surgery and in surgical resection of epileptic foci for certain patients.² A recent study on national trends in brain tumor management during a relatively similar time period to our study (2004 to 2015) reported a total of 464,856 brain and other nervous system cancers among patients with a median age of 60 years, with an overall 56% rate of surgical procedures performed.⁹ In that study, 260,317 surgical procedures were performed on patients with brain cancer during the 11-year period. Not every neurosurgical procedure for brain cancer requires preoperative fMRI. However, given the benefit of fMRI in selected patients¹⁰⁻¹² and the difference between this number of surgical studies performed and the 10,056 fMRI studies billed during the similar 10-year period of our study, there may be a gap between potential ideal and actual fMRI use rates. Moreover, the prevalence and incidence of primary brain tumors in the United States are thought to be rising due to a combination of an

aging population and improved diagnosis and therapies.^{9,13} Thus, it may be expected that the rate of brain surgery for these tumors will increase as well, particularly because the extent of tumor resection positively correlates with improved patient outcomes,¹⁴ and the need for preoperative fMRI should also increase.

Despite the increase in the use rates of fMRI, it is possible that barriers exist to furthering expansion of fMRI services and that current levels of fMRI use among Medicare beneficiaries might not be meeting the population-level clinical needs. Decreasing Medicare reimbursement (\$618 in 2007 to \$455 in 2017 for CPT code 70554¹⁵) is potentially a factor leading to the slowing of fMRI adoption. In addition, competing technologies for presurgical evaluation of refractory focal epilepsy and functional brain mapping, such as magnetoencephalography (MEG), have also grown.¹⁶ Increased expertise in the field of clinical MEG might also contribute to blunting the curve of fMRI use in recent years. However, despite the accepted clinical value of MEG,^{17,18} its accessibility is still low, with only 21 clinical MEG sites in 14 states listed by the American Clinical MEG Society.¹⁹ Future comparisons of MEG use with fMRI trends as well as regional use of MEG and fMRI are warranted.

Another potential barrier to fMRI adoption is likely related to the hardware, software, level of experience, and dedicated time required for acquisition, postprocessing, and interpretation of this study. Not surprisingly, radiologists have consistently performed the major share of the fMRIs for Medicare beneficiaries, and have experienced the largest growth since the introduction of dedicated CPT codes. In contrast, other specialties billed a relatively small number of fMRI services and showed no increases in use with time. Considering that 3 of the 4 main applications of fMRI concern neurology and neurosurgery (presurgical planning in brain tumors and epilepsy, more precise study of the level of

consciousness in altered level of consciousness, and in follow-up of patients with traumatic brain injury and stroke), it is expected that those specialists participated as well in the provision of fMRI services. A secondary clinical application of fMRI is in diagnosis and efficacy assessment of certain psychiatric disease treatments.²⁰ We identified no cases of fMRI billed by psychiatrists, possibly reflecting the low rate at which psychiatrists perform any imaging services.

A separate analysis of the CPT codes in this study showed that for radiology, both the number of billings for 96020 and the percentage of cases of simultaneous billing of codes 70555 and 96020 have increased from 2007 to 2017. This increase suggests that radiologists have become more comfortable across time acting as the physician who selects and administers fMRI paradigms, in addition to interpreting these studies. Alternatively, this may reflect an increased awareness of correct CPT billing practices. Regardless, despite the overall increase in radiology billing of 96020, the rate of billing of this code has always been lower than the rate of 70555, indicating that other specialties continue to perform and bill fMRI in conjunction with radiologists. Another possibility is that radiologists are performing both roles but incorrectly billing Medicare for this service.

The clinical use of resting-state fMRI, which is performed without an explicit task, has been advocated recently.²¹⁻²³ Once standardized clinical protocols are established, the use of resting-state fMRI may drive increased overall use of fMRI. The currently available fMRI CPT codes assume that a task is administered and there is no separate CPT code for isolated resting-state fMRI at this time. Therefore, it is not currently possible to assess the use of resting-state fMRI using national databases, so the impact of resting-state fMRI on overall fMRI use cannot be determined at this time.

Our study has limitations similar to those in other studies investigating the changing use of physician services. Most important, we studied only Medicare fee-for-service enrollees. Thus, our findings cannot necessarily be generalized to the population more broadly. However, considering that on the basis of the Surveillance, Epidemiology, and End Results Program data, approximately 40% of new national cases of brain and central nervous system cancers are associated with the older-than-65-year age group,²⁴ our findings are, nonetheless, quite relevant. Additionally, we were constrained because certain Medicare provider codes did not allow identification of specific provider specialties (these were grouped as “unidentified specialty”). Moreover, we were not able to compare our findings on fMRI use trends with those of other advanced imaging techniques such as diffusion tensor imaging because there are no separate CPT codes for them. Future studies would benefit from the inclusion of both private and public payers as well as a larger age range of patients, particularly because presurgical fMRI is also used in the pediatric population.

In summary, fMRI use among the Medicare beneficiary population has markedly increased between 2007 and 2014 but has since plateaued. In this population, fMRI is primarily performed by radiologists in the outpatient setting.

Disclosures: Richard Duszak—RELATED: Grant: Harvey L. Neiman Health Policy Institute.* Danny R. Hughes—RELATED: Grant: Harvey L. Neiman Health Policy Institute.* Jason W. Allen—UNRELATED: Grants/Grants Pending: NIH R21 NS114603 (PI); NIH R01 MH111682 (Co-I); Radiological Society of North America Resident Grant

(Mentor/Co-I), Comments: Hemodynamics, Thrombosis, and Stroke Risk in Patients With Carotid Webs, Impact of Trauma Exposure on Critical Periods in Brain Development, Functional and Structural Brain Connectivity Alterations in Visual Vertigo Syndrome: A prospective MRI Study of Central Vestibular Impairment in Mild Traumatic Brain Injury.* *Money paid to the institution.

REFERENCES

- Ogawa S, Lee TM, Kay AR, et al. **Brain magnetic resonance imaging with contrast dependent on blood oxygenation.** *Proc Natl Acad Sci U S A* 1990;87:9868–72 CrossRef Medline
- Matthews PM, Honey GD, Bullmore ET. **Applications of fMRI in translational medicine and clinical practice.** *Nat Rev Neurosci* 2006;7:732–44 CrossRef Medline
- Hart J Jr, Rao SM, Nuwer M. **Clinical functional magnetic resonance imaging.** *Cogn Behav Neurol* 2007;20:141–44 CrossRef Medline
- Duszak R Jr, Bilal N, Picus D, et al. **Central venous access: evolving roles of radiology and other specialties nationally over two decades.** *J Am Coll Radiology* 2013;10:603–12 CrossRef Ref
- Duszak R Jr, Walls DG, Wang JM, et al. **Expanding roles of nurse practitioners and physician assistants as providers of nonvascular invasive radiology procedures.** *J Am Coll Radiol* 2015;12:284–89 CrossRef Medline
- Yousem DM. **The economics of functional magnetic resonance imaging: clinical and research.** *Neuroimaging Clin N Am* 2014;24:717–24 CrossRef Medline
- Morris E, Duszak R Jr, Sista AK, et al. **National trends in inferior vena cava filter placement and retrieval procedures in the Medicare population over two decades.** *J Am Coll Radiol* 2018;15:1080–86 CrossRef Medline
- Babiarz LS, Yousem DM, Parker L, et al. **Utilization rates of neuroradiology across neuroscience specialties in the private office setting: who owns or leases the scanners on which studies are performed?** *AJNR Am J Neuroradiol* 2012;33:43–48 CrossRef Medline
- Garcia CR, Slone SA, Dolecek TA, et al. **Primary central nervous system tumor treatment and survival in the United States, 2004–2015.** *J Neurooncol* 2019;144:179–91 CrossRef Medline
- Al-Okaili RN, Krejza J, Wang S, et al. **Advanced MR imaging techniques in the diagnosis of intraaxial brain tumors in adults.** *Radiographics* 2006;26(Suppl 1):S173–89 Medline
- Brodbeck A. **Clinical applications of imaging biomarkers, Part 2: the neurosurgeon’s perspective.** *Br J Radiol* 2011;84(Spec No 2):S205–08 CrossRef Medline
- Mabray MC, Barajas RF Jr, Cha S. **Modern brain tumor imaging.** *Brain Tumor Res Treat* 2015;3:8–23 CrossRef Medline
- Feigin VL, Abajobir AA, Abate KH, et al. **Global, regional, and national burden of neurological disorders during 1990–2015: a systematic analysis for the Global Burden of Disease Study 2015.** *Lancet Neurol* 2017;16:877–97 CrossRef Medline
- Sanai N, Berger MS. **Glioma extent of resection and its impact on patient outcome.** *Neurosurgery* 2008;62:753–64; discussion 264–66 CrossRef Medline
- Center for Medicare & Medicaid Services. **Medicare Physician Fee Schedule (MPFS).** <https://www.cms.gov/apps/physician-fee-schedule/overview.aspx>. Accessed June 10, 2020
- Bagic A, Funke ME, Ebersole J; ACMEGS Position Statement Committee. **American Clinical MEG Society (ACMEGS) position statement: the value of magnetoencephalography (MEG)/magnetic source imaging (MSI) in noninvasive presurgical evaluation of patients with medically intractable localization-related epilepsy.** *J Clin Neurophysiol* 2009;26:290–93 CrossRef Medline
- RamachandranNair R, Otsubo H, Shroff MM, et al. **MEG predicts outcome following surgery for intractable epilepsy in children with normal or nonfocal MRI findings.** *Epilepsia* 2007;48:149–57 CrossRef Medline
- Knowlton RC, Shih J. **Magnetoencephalography in epilepsy.** *Epilepsia* 2004;45(Suppl 4):61–71 CrossRef Medline

19. American Clinical MEG Society. **Clinical MEG Locations**. <https://www.acmegs.org/membership/clinical-meg-locations>. Accessed June 9, 2020
20. Greicius MD, Srivastava G, Reiss AL, et al. **Default-mode network activity distinguishes Alzheimer's disease from healthy aging: evidence from functional MRI**. *Proc Natl Acad Sci USA* 2004;101:4637–42 CrossRef Medline
21. Lee MH, Smyser CD, Shimony JS. **Resting-state fMRI: a review of methods and clinical applications**. *AJNR Am J Neuroradiol* 2013;34:1866–72 CrossRef Medline
22. Lee MH, Miller-Thomas MM, Benzinger TL, et al. **Clinical resting-state fMRI in the preoperative setting: are we ready for prime time?** *Top Magn Reson Imaging* 2016;25:11–18 CrossRef Medline
23. Greicius M. **Resting-state functional connectivity in neuropsychiatric disorders**. *Curr Opin Neurol* 2008;21:424–30 CrossRef Medline
24. National Cancer Institute. **Cancer Stat Facts: Brain and Other Nervous System Cancer**. <https://seer.cancer.gov/statfacts/html/brain.html>. Accessed January 20, 2020

Brain Imaging of Patients with COVID-19: Findings at an Academic Institution during the Height of the Outbreak in New York City

E. Lin, J.E. Lantos, S.B. Strauss, C.D. Phillips, T.R. Campion, Jr., B.B. Navi, N.S. Parikh, A.E. Merkle, S. Mir, C. Zhang, H. Kamel, M. Cusick, P. Goyal, and A. Gupta



ABSTRACT

BACKGROUND AND PURPOSE: A large spectrum of neurologic disease has been reported in patients with coronavirus disease 2019 (COVID-19) infection. Our aim was to investigate the yield of neuroimaging in patients with COVID-19 undergoing CT or MR imaging of the brain and to describe associated imaging findings.

MATERIALS AND METHODS: We performed a retrospective cohort study involving 2054 patients with laboratory-confirmed COVID-19 presenting to 2 hospitals in New York City between March 4 and May 9, 2020, of whom 278 (14%) underwent either CT or MR imaging of the brain. All images initially received a formal interpretation from a neuroradiologist within the institution and were subsequently reviewed by 2 neuroradiologists in consensus, with disputes resolved by a third neuroradiologist.

RESULTS: The median age of these patients was 64 years (interquartile range, 50–75 years), and 43% were women. Among imaged patients, 58 (21%) demonstrated acute or subacute neuroimaging findings, the most common including cerebral infarctions (11%), parenchymal hematomas (3.6%), and posterior reversible encephalopathy syndrome (1.1%). Among the 51 patients with MR imaging examinations, 26 (51%) demonstrated acute or subacute findings; notable findings included 6 cases of cranial nerve abnormalities (including 4 patients with olfactory bulb abnormalities) and 3 patients with a microhemorrhage pattern compatible with critical illness–associated microbleeds.

CONCLUSIONS: Our experience confirms the wide range of neurologic imaging findings in patients with COVID-19 and suggests the need for further studies to optimize management for these patients.

ABBREVIATIONS: ACE2 = angiotensin converting enzyme 2; COVID-19 = coronavirus disease 2019; MFS = Miller Fisher syndrome; PRES = posterior reversible encephalopathy syndrome; SARS-CoV-2 = Severe Acute Respiratory Syndrome coronavirus 2

Since the introduction of Severe Acute Respiratory Syndrome coronavirus 2 (SARS-CoV-2) to the human population in December 2019, coronavirus disease 2019 (COVID-19) has rapidly become a global pandemic. While pulmonary manifestations remain its hallmark, COVID-19 is gaining recognition as a multi-system disease,^{1–6} and there is increasing recognition of frequent neurologic manifestations, which reportedly may affect up to

36.4% of patients with COVID-19.^{7,8} While there is growing literature describing neurologic symptoms in patients with COVID-19, little has been published about neuroimaging findings outside of case reports and smaller case series. Our objective was to present the yield of neuroimaging and report the neuroimaging findings in a large cohort of patients with COVID-19 at NewYork-Presbyterian/Weill Cornell Medical Center and NewYork-Presbyterian Lower Manhattan Hospital in New York City.

Received June 11, 2020; accepted after revision July 17.

From the Department of Radiology (E.L., J.E.L., S.B.S., C.D.P., A.G.), Department of Population Health Sciences (T.R.C., Jr., M.C.), Clinical and Translational Neuroscience Unit (B.B.N., N.S.P., A.E.M., S.M., C.Z., H.K., A.G.), Feil Family Brain and Mind Research Institute and Department of Neurology, and Department of Medicine (P.G.), Weill Cornell Medicine, New York, New York.

E. Lin and J.E. Lantos contributed equally to this article as co-first authors.

This study was supported by National Institutes of Health grants K23NS091395 and R01HL144541. It also received support from NewYork-Presbyterian Hospital and Weill Cornell Medical College, including the Clinical and Translational Science Center (UL1 TR000457) and Joint Clinical Trials Office.

No funding organization had a role in the design and conduct of the study; collection, management, analysis, and interpretation of the data; preparation, review, or approval of the manuscript; or the decision to submit the manuscript for publication.

MATERIALS AND METHODS

A retrospective cohort study was performed at an academic quaternary-care center and an affiliated community hospital, both in New York City. Using automated systems for electronic capture

Please address correspondence to Eaton Lin, MD, Department of Radiology, Weill Cornell Medicine, 525 East 68th St, New York, NY 10065; e-mail: eal9007@med.cornell.edu

Indicates open access to non-subscribers at www.ajnr.org

<http://dx.doi.org/10.3174/ajnr.A6793>

Characteristics of patients with COVID-19^a

Characteristic	Patients with COVID-19 Undergoing CT or MR Imaging of the Brain (n = 278)	Patients with COVID-19 without Brain Imaging (n = 1776)
Age (yr) ^b	71.8 (15.4)	60.6 (18.1)
Male	165 (59%)	1009 (57%)
Race		
Asian	42 (15%)	222 (13%)
Black	37 (13%)	231 (13%)
White	84 (30%)	524 (30%)
Other	58 (21%)	400 (23%)
Unknown	57 (21%)	399 (22%)
Medical comorbidities		
Atrial fibrillation	79 (28%)	244 (14%)
Hypertension	214 (77%)	1030 (58%)
Hyperlipidemia	115 (41%)	515 (29%)
Diabetes	144 (52%)	709 (40%)
Coronary artery disease	93 (33%)	421 (24%)
Chronic kidney disease	58 (21%)	267 (15%)
COPD	40 (14%)	150 (8%)
Mechanical ventilation	53 (19%)	292 (16%)
ICU admission	92 (33%)	399 (22%)
Death	61 (22%)	213 (12%)

Note:—COPD indicates chronic obstructive pulmonary disease; ICU, intensive care unit.

^a Data are reported as number (%) except where otherwise noted.

^b Age is presented as mean age, with SD in parentheses.

of laboratory data, we identified all patients with an active COVID-19 infection with an emergency department visit or hospitalization between March 4, 2020, and May 9, 2020. All COVID-19 diagnoses were confirmed via detection of SARS-CoV-2 RNA in nasopharyngeal swab specimens by real-time reverse transcription polymerase chain reaction. The study population was then narrowed to adults (18 years of age or older) who underwent cranial neuroimaging (either CT or MR imaging of the brain) during this period. The racial demographics of our cohort were included given the disproportionate burden of COVID-19 among racial minorities and to assess the generalizability of our findings. Weill Cornell Medicine's COVID-19 Research Data Repository automated data capture feature was also used to collect data on performed imaging studies, demographics, medical comorbidities, presenting symptoms, and the use of mechanical ventilation.⁹ Our institutional review board approved this study and waived the requirement for informed consent.

CT imaging was performed on 1 of 3 scanners: HD Discovery 750, Optima 660, or Revolution EVO (GE Healthcare) with 0.625-mm section thickness, 22-cm FOV, 120 kV(peak), and 250–300 mA. Coverage was from the foramen magnum to the vertex. Images were reconstructed in the axial plane at 2.5- and 5-mm intervals and in the coronal and sagittal planes at 2-mm intervals. MR imaging was performed on 1 of 3 machines: SIGNA Architect (3T), Discovery 750 (3T), or SIGNA Artist (1.5T) (GE Healthcare). Postcontrast MR imaging was performed using intravenous gadobutrol, 0.1 mmol/kg (Gadavist; Bayer Schering Pharma). Although there was some variability in MR imaging protocols, all MRIs included diffusion-weighted imaging, SWI, T2 FLAIR, and T1-weighted sequences.

Neuroimaging was reviewed by 2 Certificate of Added Qualification–certified neuroradiologists, each with 10 years of

experience. A third Certificate of Added Qualification–certified neuroradiologist was available for resolving discrepancies, but none arose. Neuroimaging findings were documented, including acute or subacute infarctions, posterior reversible encephalopathy syndrome (PRES), and acute or subacute hemorrhage. PRES was determined by the presence of confluent T2-FLAIR hyperintensity or CT hypoattenuation, as described in prior literature.¹⁰ The burden of microhemorrhage seen on SWI sequences was also recorded. Chronic findings, including chronic infarcts and white matter changes deemed likely of microvascular origin based on age and expected findings, were considered incidental to the event and not recorded. Special attention was directed toward the presence or absence of previously reported COVID-19-related neuroimaging findings,

including acute hemorrhagic necrotizing encephalopathy,¹¹ leptomeningeal enhancement,¹² cortical T2 hyperintensity,¹³ cranial nerve abnormalities,¹⁴ and olfactory cleft obstruction.¹⁵

Stroke mechanisms and etiologies of parenchymal hematomas were determined by 2 study neurologists as per established criteria and classification systems.^{16–18} We used descriptive statistics to characterize the patient cohort and to estimate the yield of neuroimaging. We used STATA (Version 15.1; StataCorp) to perform statistical analyses.

RESULTS

Our 2 hospitals treated 2054 adult patients with laboratory-confirmed COVID-19 between March 4, 2020, and May 9, 2020, including 263 patients with emergency department visits and 1791 hospitalized patients. Among the total cohort of patients, the age range was 18–101 years, median age was 64 years (interquartile range, 50–75 years), and 43% were women. Among the cohort, 491 (24%) were admitted to the intensive care unit and 345 (17%) were mechanically ventilated. Patient demographics and medical comorbidities are further detailed in the Table. Cross-sectional neuroimaging of the brain was performed for 278 (14%) patients, with 269 (13%) patients undergoing CT, 51 (2.5%) patients undergoing MR imaging, and 42 (2.0%) patients undergoing both CT and MR imaging. For 17 of the 51 patients undergoing an MR imaging examination, imaging was performed both before and after intravenous administration of gadobutrol.

Among the 278 patients with neuroimaging, 58 (21%) demonstrated acute or subacute neuroimaging findings. There were 31 cerebral infarctions (11%), 10 parenchymal hematomas (3.6%), 6 cases of cranial nerve abnormalities (2.2%), 3 cases of PRES (1.1%), 3 cases of probable critical illness–associated microhemorrhage (1.1%), 3 nontraumatic subdural hemorrhages (1.1%), and 2

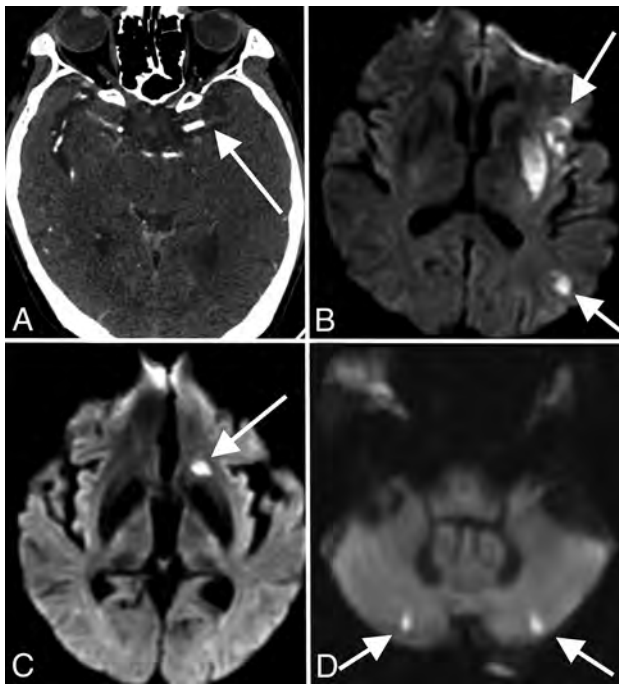


FIG 1. Stroke. A 53-year-old man with COVID-19 with an axial CTA image (A) demonstrating an abrupt cutoff of the proximal M1 segment of the left MCA (arrow), consistent with thrombosis. The patient later underwent MR imaging, with a DWI sequence (B) demonstrating acute infarctions in the left MCA territory (arrows). An 85-year-old woman with COVID-19 and MR imaging with a DWI sequence (C and D) demonstrating acute infarctions in both the anterior (arrow, C) and posterior (arrows, D) circulations, consistent with central embolic etiology. Most patients in our cohort had stroke of either embolic or cryptogenic etiology.

nonaneurysmal subarachnoid hemorrhages (0.7%). The yield of neuroimaging was higher among the 51 patients undergoing MR imaging, with 26 (51%) patients having acute or subacute findings, including 13 cerebral infarctions (26%), 6 cranial nerve abnormalities (12%), 3 cases of suspected critical illness-associated microhemorrhage (5.9%), 2 cases of PRES (3.9%), and 1 subarachnoid hemorrhage (2.0%). Individual findings are discussed in more detail below.

Cerebral Infarction

Acute and subacute infarctions were the most common imaging finding in our cohort (Fig 1). Of 31 patients with cerebral infarctions, the median age was 69 years (interquartile range, 66–78 years) and 13 (42%) were women. Mechanisms of infarction, as determined by our study neurologists, were mostly cryptogenic ($n = 16$, 52%) or cardioembolic ($n = 13$, 42%), with 8 (26%) cases resulting from large-vessel occlusion. Of the cryptogenic infarctions, multiple cerebrovascular territories were involved for 11 (69%) patients. Of the patients determined to have cardioembolic strokes, 10 had atrial fibrillation, 4 had low ejection fraction heart failure, and 1 was found to have a moderate-to-large patent foramen ovale on an echocardiogram during admission; multiple mechanisms were identified in 2 patients. Aside from the frequency of multiterritory infarctions, no particularly unique imaging characteristics were noted among infarctions in our patients with COVID-19.

Intracranial Hemorrhage

All except 1 patient with acute parenchymal hematomas in our cohort were men, with a median age of 68 years (interquartile range, 67–74 years). Of the 10 hematomas, 6 (60%) were >5 cm, all with intraventricular extension, surrounding edema, midline shift, and downward herniation. All 6 of these patients died soon after initial imaging, without follow-up examinations. All 6 patients were on anticoagulation, and 1 had an underlying thrombocytopenia, but only 2 patients demonstrated a hematocrit level on imaging. The remaining 4 cases of parenchymal hematomas either resolved or decreased in size on follow-up imaging. Our study neurologists attributed 6 (60%) cases to anticoagulation, 2 (30%) to indeterminate mechanisms, 1 (10%) to trauma, and 1 (10%) to hypertension. One case of subarachnoid hemorrhage arose from an incidental dural arteriovenous fistula, while the other was posttraumatic. There were also 3 cases of spontaneous subdural hemorrhage.

Microhemorrhages

Twenty-six (51%) of the patients having undergone MR imaging had foci of age-indeterminate microhemorrhage. Most ($n = 17$) of these patients had 1–3 foci of microhemorrhage, a number that did not allow further characterization. Seven (14%) of the patients had a greater burden of microhemorrhage (>15 foci). Of these patients, 1 had a cortical and subcortical distribution sparing the deep gray matter structures in a pattern compatible with cerebral amyloid angiopathy; 1 had predominant involvement of the basal ganglia and cerebellum, with both the microhemorrhage distribution and clinical history compatible with a hypertensive etiology; and 1 had foci attributable to previously treated widespread metastatic disease. Another patient had a nonspecific pattern possibly associated with multiple chronic infarcts but also had a history of hypertension.

The 3 remaining patients with a greater burden of microhemorrhage had innumerable foci, predominantly involving the splenium of the corpus callosum, along with several foci along the remainder of the corpus callosum, internal capsules, and juxtacortical white matter (Fig 2). There were no foci involving the cortex, deep gray matter, brain stem, or cerebellum. The distribution in these 3 patients was atypical for both cerebral amyloid angiopathy and hypertensive microhemorrhage and, instead, was most compatible with critical illness-associated microhemorrhage.^{19,20} All 3 patients had prolonged intensive care unit courses with intubation and mechanical ventilation, but none were treated with extracorporeal membrane oxygenation. Two of the 3 had a history of hypertension, and none of the 3 had a history of seizures or antiepileptic medication use. One patient was receiving therapeutic enoxaparin (Lovenox) for deep vein thrombosis, while the other 2 patients were receiving prophylactic Lovenox at the time of imaging. Initial radiology reporting for 2 of these patients raised the possibility of diffuse axonal injury, but none of these patients had a trauma history. Following extubation, all 3 patients had clinical courses complicated by prolonged delirium and altered mental status. Of the patients with fewer than 15 foci of microhemorrhage, 2 additional patients also demonstrated foci only within the splenium of the corpus callosum.

PRES. There were 3 patients with imaging findings typical of PRES, with acute development of occipital subcortical white

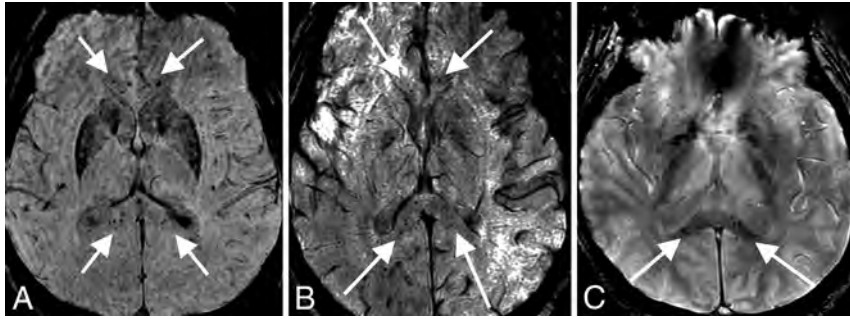


FIG 2. Corpus callosum microhemorrhages. A 65-year-old woman (A), a 44-year-old woman (B), and a 69-year-old man (C) all demonstrate microhemorrhages on SWI, with a similar distribution, preferentially involving the corpus callosum (arrows in A–C), particularly the splenium. All patients had undergone mechanical ventilation before imaging. The distribution is similar to that previously described in critically ill, ventilated patients as well as in those with high-altitude cerebral edema.

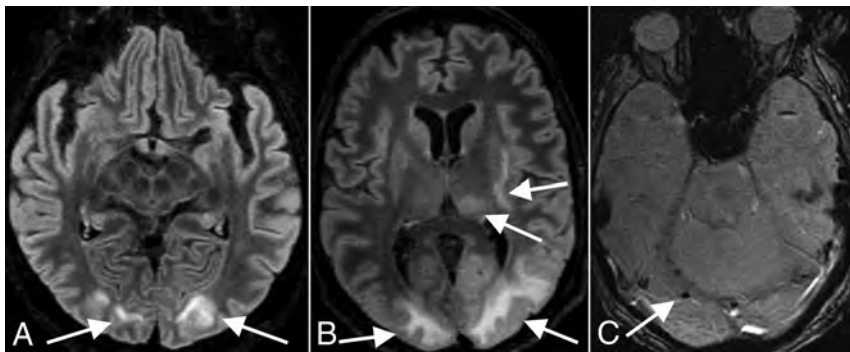


FIG 3. PRES. A 65-year-old woman (A, same patient as in Fig 2A) and 63-year-old man (B and C) demonstrate a typical imaging appearance of PRES on T2-FLAIR images (arrows in A and B), with bilateral subcortical occipital white matter hyperintense signal, as well as more pronounced involvement of the patient in B with thalamic and internal and external capsule involvement. This patient also has evidence of associated right occipital microhemorrhage (arrow in C). Both patients had the typical risk factors for PRES of acute kidney injury and hypertension.

matter edema. One patient, a 72-year-old man, was diagnosed solely on the basis of the CT examination. He was intubated for hypoxic respiratory failure and also developed acute kidney injury. The patient was initially hypotensive, requiring pressors, but afterward was intermittently hypertensive. He had follow-up CT showing resolution of occipital white matter edema. The other 2 patients, a 65-year-old woman (Fig 3A) and a 63-year-old man (Fig 3B, -C), both underwent CT and MR imaging and had evidence of associated acute microhemorrhage on susceptibility-weighted MR imaging sequences. Both of these patients also had complications of hypoxic respiratory failure requiring intubation, acute renal failure, and acute hypertension. The 65-year-old woman did not have follow-up imaging, but the 63-year-old man had follow-up CT showing resolution of edema. None of these 3 patients were septic or hyperammonemic, and no cases of PRES were attributable to medications such as various immunosuppressive or chemotherapeutic agents.

Cranial Neuropathies

Six patients had cranial nerve abnormalities on MR imaging. Four of these patients had olfactory bulb abnormalities and will be discussed separately. The remaining 2 patients are discussed below.

The first patient presented with diplopia, ataxia, and areflexia typical of Miller Fisher syndrome (MFS), the cranial nerve variant of Guillain-Barré syndrome. MR imaging of the brain with dedicated orbital sequences showed an enlarged, T2-hyperintense left oculomotor nerve with marked nerve enhancement after intravenous gadobutrol administration (Fig 4). This patient had negative serum anti-ganglioside testing, and symptoms improved after intravenous immunoglobulin treatment. Another patient presented with painless diplopia and right abducens palsy, with MR imaging demonstrating enhancement of the bilateral optic nerve sheaths and posterior Tenon capsules. The patient was treated with hydroxychloroquine, and diplopia and abducens palsy resolved after 2 weeks.

Olfactory Bulb Abnormality

Given the prevalence of anosmia in patients with COVID-19,²¹⁻²³ our department added thin-section coronal T2 imaging through the olfactory bulbs to brain MRIs for all patients with COVID-19 in whom clinical status allowed the additional scan time. A total of 13 examinations (12 patients; mean age, 58 years; 6 women) included both diagnostic olfactory bulb sequences and high-resolution 3D-T2 FLAIR sequences; these studies were included in a separate systematic review (S.B. Strauss, unpublished data, May 2020). Briefly, no patient demonstrated changes in olfactory bulb volume. However, 4 of 12 patients demonstrated abnormally increased olfactory bulb signal on postcontrast T2 FLAIR, which may reflect intrinsic T2 prolongation or, potentially, contrast enhancement (Fig 5). No abnormalities were identified along the olfactory clefts within this cohort to correlate with findings reported in a prior case report of olfactory cleft obstruction in a patient with COVID-19 with anosmia.¹⁵ One of the 4 patients with olfactory bulb signal abnormality had documented anosmia, but for the other 3 patients, there was no clinical documentation addressing either the presence or absence of anosmia.

Pertinent Negatives

None of the 51 MR imaging examinations performed in our cohort demonstrated the abnormal cortical T2-FLAIR hyperintensity described in a recent case series.¹³ There were no cases of hemorrhagic encephalitis in our cohort. There were also no cases with abnormal leptomeningeal enhancement among the 17 patients undergoing postcontrast MR imaging.

DISCUSSION

COVID-19 is the disease caused by the novel coronavirus SARS-CoV-2, which emerged in December 2019. As the disease has spread, neurologic manifestations have been increasingly described as a contributor to morbidity and mortality. One review of 214 patients found neurologic symptoms, including headache, ataxia, cognitive impairment, anosmia, and stroke, in 36.4%.⁷ Kandemirli et al¹³ studied 235 patients who were admitted to the intensive care unit for complications of COVID-19 and found that 21% had neurologic symptoms. Of the symptomatic patients in that study, 54% underwent MR imaging of the

brain, almost half (44%) of whom had acute findings. Mahammedi et al²⁴ found that 16% of 725 patients had acute neurologic symptoms and underwent neuroimaging.

At our institution, a review of 2054 patients with COVID-19 presenting during the height of the pandemic in New York City found that 278 patients (14%) underwent cranial neuroimaging with either CT, MR imaging, or both. Of our imaged patients, 21% had acute or subacute findings, with a higher yield on MR imaging (51%). Ischemic stroke (11%) was the most common acute finding, and most were multifocal and determined to be either cryptogenic or cardioembolic in origin. Potential pathogenesis of stroke in COVID-19 may be from the development of a coagulopathy or endothelial dysfunction.²⁵ Coagulopathy may be attributable to the thrombophilic effects of systemic inflammation; the presence of lupus anticoagulant and antiphospholipid antibodies has also been reported.^{5,25,26} Despite reported elevated D-dimer levels and a high incidence of deep vein thrombosis in COVID-19,²⁷ we did not find evidence of cerebral venous thrombosis in our cohort. Parenchymal hematomas were found in 10 (3.6%) patients, most ($n = 6$) of whom had hemorrhages attributed to anticoagulation, a finding that highlights the risks of initiating anticoagulant therapy in response to the prothrombotic features of patients with COVID-19.

Microhemorrhages were found in 26 of 51 patients, with 3 patients demonstrating extensive microhemorrhages predominantly involving the corpus callosum, similar to those shown in a recent case report of a patient with COVID-19 and PRES²⁸ and also in keeping with another recent observational study describing 4 patients with COVID-19 with microhemorrhage in the corpus callosum.²⁹ This pattern of microhemorrhage involving the corpus callosum has also been described in critically ill patients, including those mechanically ventilated for acute respiratory distress syndrome, as well as in patients with high-altitude cerebral edema.^{19,30} High-altitude cerebral edema microhemorrhages are thought to be due to increased cerebral venous pressure, and positive pressure ventilation may impair cerebral venous return secondary to raised intrathoracic pressure, perhaps explaining the common finding in these 2 distinct patient populations.¹⁹ All 3 of our patients with callosal microhemorrhage received mechanical ventilation before MR imaging. Therefore, callosal microhemorrhage in COVID-19 is potentially attributable to mechanical

ventilation rather than a direct effect from the virus. These 3 patients did not receive extracorporeal membrane oxygenation, which has previously been reported with callosal microhemorrhages.³¹ We agree with Radmanesh et al²⁹ that these callosal hemorrhages resemble those seen with diffuse axonal injury, but, as in their study, the clinical history of our patients excludes post-traumatic etiology.

Our review found 2 types of cases in which neural tissue was involved. The first is a patient previously reported¹⁴ who presented with clinical MFS and had imaging confirming

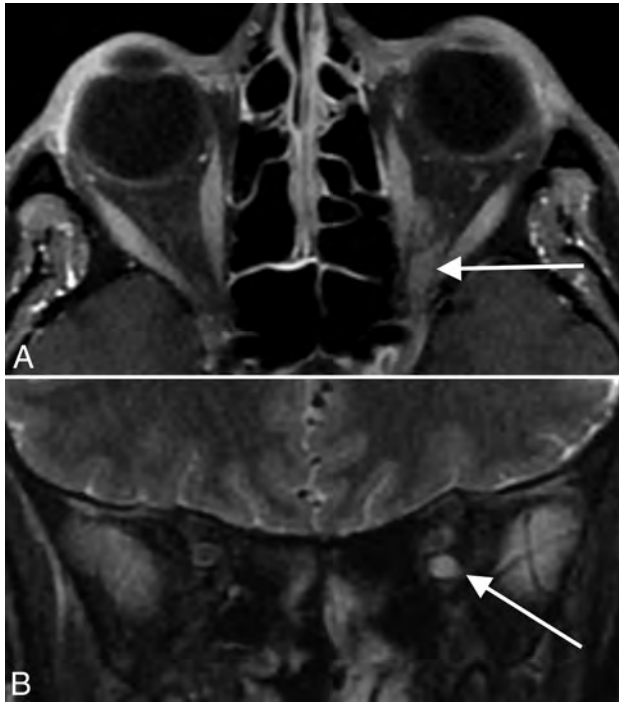


FIG 4. Miller Fisher syndrome. A 36-year-old male patient with a history of COVID-19 and diplopia, ataxia, and areflexia. Axial T1 postcontrast (A) and coronal T2 fat-suppressed (B) MR images through the orbits demonstrate striking enlargement, enhancement, and T2 hyperintense signal of cranial nerve III (arrows in A and B). The patient was clinically diagnosed with Miller Fisher syndrome and improved with intravenous immunoglobulin treatment.

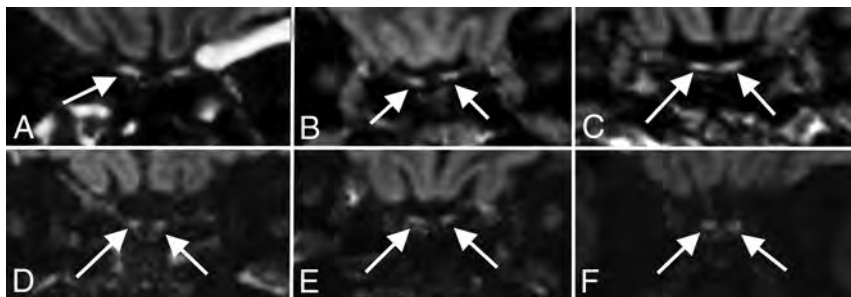


FIG 5. Olfactory neuritis. Six patients with COVID-19 with coronal T2-FLAIR postcontrast images. A 48-year-old woman (A) demonstrates hyperintense signal in the right (arrow) greater than left olfactory bulbs. A 52-year-old woman (B) and a 62-year-old man (C) demonstrate symmetric hyperintense signal in the olfactory bulbs (arrows). For comparison, 3 different patients (D–F) in our cohort with normal olfactory bulbs (arrows) are included.

oculomotor nerve abnormality. Serum ganglioside testing was negative in this patient, leaving open the possibility that there was direct inoculation of the nerve by SARS-CoV-2, rather than a cross-reactive immune response induced by molecular mimicry, as is more typical of MFS. MFS is the cranial nerve variant of Guillain-Barré syndrome, which has also been described in COVID-19 in prior case reports, also with negative serum ganglioside testing.³² Furthermore, our patient presented with MFS and then tested positive for SARS-CoV-2, indicating that MFS may be a parainfectious rather than postinfectious process, similar to that reported with the Zika virus.^{33,34} Parainfectious Guillain-Barré syndrome has also been recently reported in association with COVID-19.³⁵ Whether COVID-19 has the propensity to cause cranial neuropathies more or less than other viruses is an area of potential future investigation and may depend on various factors, including, but not limited to, viral load, neurotropism, and systemic inflammation.

We also found that 4 of our patients with COVID-19 had evidence of an olfactory neuritis, with hyperintensity of the olfactory bulb on postcontrast T2 FLAIR images, potentially a biomarker of disease and an imaging correlate of the anosmia commonly experienced by patients. Recently, it has been shown that sustentacular cells of the olfactory epithelium (technically part of the peripheral nervous system) express the angiotensin converting enzyme 2 (ACE2) receptor,³⁶ providing a potential entry point to the CNS via synapses with the olfactory bulbs. Extension to the brain may occur via further trans-synaptic spread, as has been shown to occur in other coronaviruses.³⁷ For example, transnasal exposure in mice to the related coronavirus SARS-CoV resulted in detection of the virus in regions with direct neuronal connection to the olfactory bulb: the piriform and infralimbic cortices, basal ganglia, and midbrain.³⁸ Another coronavirus, Middle East respiratory syndrome coronavirus, has also been shown to invade the brain of mice when administered intranasally.³⁹ Trans-synaptic spread may also allow coronaviruses to gain access to the CNS via other parts of the peripheral nervous system.³⁷

Hematogenous spread to the CNS is proposed to be due to viral binding to ACE2 receptors in the capillary endothelium, resulting in damage to the endothelial lining. This could lead to increased permeability of the blood-brain barrier and loss of hemostatic regulation, with resultant cerebral edema. This mechanism could explain the PRES cases that we observed, as has been recently proposed in 2 other cases of PRES with COVID-19.²⁸ However, each of our 3 patients with PRES also had the typical risk factors of acute kidney injury and elevated blood pressure. Endothelial damage could also allow the SARS-CoV-2 spike protein to bind directly with neural ACE2 receptors. However, Li et al³⁷ believed that the related virus SARS-CoV is highly unlikely to spread to the brain by the hematogenous or lymphatic route because almost no viral particles have been detected in nonneuronal cells of infected brain areas in multiple studies. By implication, the same could be true of SARS-CoV-2.

Poyiadji et al¹¹ were the first to describe acute hemorrhagic necrotizing encephalitis in the setting of COVID-19 infection. We did not have a similar case in our relatively large cohort,

indicating that this may be an uncommon neuroimaging finding, but further investigation is required to assess the incidence in association with COVID-19. Our study did not confirm the cortical T2-FLAIR signal abnormality recently reported in 10 of 27 patients admitted to the intensive care unit for COVID-19.¹³ We also did not observe abnormal leptomeningeal enhancement in any of our patients undergoing postcontrast imaging, despite prior reports of this finding in COVID-19.¹²

Limitations of this study include those inherent in a retrospective, observational design. In addition, our patients are from 2 centers during the height of the pandemic in New York City and may not represent the true spectrum of neuroimaging findings in COVID-19, especially more chronic, long-term findings. Some of our patients with relatively mild neurologic symptoms may not have undergone imaging due to regulatory constraints imposed during the pandemic, and on the contrary, some patients with more pronounced neurologic impairment may have been too unstable to undergo imaging. Furthermore, it is uncertain whether the observed findings are directly related to SARS-CoV-2 infection rather than to coincident conditions, particularly because the patients undergoing imaging had more medical comorbidities than the overall cohort. Given the retrospective design and the critically ill conditions of many of these patients, it was also difficult to obtain full clinical correlation for many of the patients.

Finally, our study was not comprehensive and omitted a few potential areas of interest. For example, we did not include pediatric patients in our cohort, but with the emergence of pediatric COVID-19 manifestations such as multisystem inflammatory syndrome, neuroimaging findings in this population may be of interest. Also, with growing speculation that COVID-19 may be a vascular disease with manifestations in various highly perfused organs,⁴⁰ intracranial vasculitis would be a plausible manifestation of infection; however, due to the limited number and quality of MR angiographic studies performed with a vessel wall imaging protocol in our cohort, we were unable to confidently assess the prevalence of intracranial vasculitis.

CONCLUSIONS

Understanding of the novel coronavirus SARS-CoV-2 is still in its infancy. Neurologic complications are increasingly recognized, and familiarity with imaging findings is important for radiologists as the pandemic spreads. Of our patients with COVID-19 undergoing neuroimaging, 21% had acute or subacute findings, including 51% of the patients undergoing MR imaging. We observed ischemic strokes and intracranial hemorrhages that are similar in appearance to those in patients without COVID-19, though seemingly more common in this patient population. We also observed microhemorrhages with a predilection for the corpus callosum, similar to those previously described in high-altitude cerebral edema and severely ill, ventilated patients. A small subset of our patients had abnormal olfactory nerves, a possible imaging correlate to frequently reported anosmia. Our experience indicates a wide range of neuroimaging findings in COVID-19 and suggests the need for further studies to optimize management of patients with COVID-19 with neurologic manifestations.

Disclosures: Eaton Lin—RELATED: Grant: National Institutes of Health, Comments: grants K23NS091395 and R01HL144541, awarded to one of our authors.* Thomas R. Campion, Jr—RELATED: Grant: National Center for Advancing Translational Sciences, Comments: The Clinical and Translational Science Center (UL1 TR000457) provided funding for the informatics infrastructure that supported this study.* Babak B. Navi—UNRELATED: Expert Testimony: medicolegal consulting on stroke; Grants/Grants Pending: National Institutes of Health grants K23NS091395 and R01HL144541; Other: Data Safety and Monitoring Board Member for Patient-Centered Outcomes Research Institute-funded TRAVERSE trial. Neal S. Parikh—RELATED: Grant: Leon Levy Foundation, Florence Gould Foundation, New York State Empire Clinical Research Investigator Program, Comments: The funding was not specific to this project but provides salary support for my research time.* Alexander E. Merkler—UNRELATED: Expert Testimony: medicolegal consulting on neurological disorders; Grants/Grants Pending: American Heart Association, Comments: American Heart Association grant 18CDA34110419. Hooman Kamel—OTHER RELATIONSHIPS: Dr Kamel serves as co-Principal Investigator for the National Institutes of Health-funded ARCADIA trial (National Institute of Neurological Disorders and Stroke U01NS095869), which receives an in-kind study drug from the Bristol Myers Squibb-Pfizer Alliance for Eliquis and ancillary study support from Roche Diagnostics; serves as Deputy Editor for *JAMA Neurology*; serves as a steering committee member of the Medtronic Stroke AF trial (uncompensated); serves on an endpoint adjudication committee for a trial of empagliflozin for Boehringer Ingelheim; and has served on an advisory board for Roivant Sciences related to factor XI inhibition. Ajay Gupta—RELATED: Grant: National Institutes of Health*; UNRELATED: Travel/Accommodations/Meeting Expenses Unrelated to Activities Listed: GE Healthcare and Siemens USA. *Money paid to the institution.

REFERENCES

- Oudkerk M, Büller HR, Kuijpers D, et al. **Diagnosis, prevention, and treatment of thromboembolic complications in COVID-19: report of the National Institute for Public Health of the Netherlands.** *Radiology* 2020 Apr 23. [Epub ahead of print] CrossRef Medline
- Goyal P, Choi JJ, Pinheiro LC, et al. **Clinical characteristics of Covid-19 in New York City.** *N Engl J Med* 2020;382:2372–74 CrossRef Medline
- Zheng YY, Ma YT, Zhang JY, et al. **COVID-19 and the cardiovascular system.** *Nat Rev Cardiol* 2020;17:259–60 CrossRef Medline
- Klok FA, Kruip M, van der Meer NJM, et al. **Incidence of thrombotic complications in critically ill ICU patients with COVID-19.** *Thromb Res* 2020 Apr 10. [Epub ahead of print] CrossRef Medline
- Helms J, Tacquard C, Severac F, et al. CRICS TRIGGERSEP Group (Clinical Research in Intensive Care and Sepsis Trial Group for Global Evaluation and Research in Sepsis). **High risk of thrombosis in patients with severe SARS-CoV-2 infection: a multicenter prospective cohort study.** *Intensive Care Med* 2020;46:1089–98 CrossRef Medline
- Fukuhara S, Rosati CM, El-Dalati S. **Acute type A aortic dissection during COVID-19 outbreak.** *Ann Thorac Surg* 2020 Apr 22. [Epub ahead of print] CrossRef Medline
- Mao L, Jin H, Wang M, et al. **Neurologic manifestations of hospitalized patients with coronavirus disease 2019 in Wuhan, China.** *JAMA Neurol* 2020;77:683. Apr 10. [Epub ahead of print] CrossRef Medline
- Wu Y, Xu X, Chen Z, et al. **Nervous system involvement after infection with COVID-19 and other coronaviruses.** *Brain Behav Immun* 2020;87:18–22 CrossRef Medline
- Sholle ET, Kabariti J, Johnson SB, et al. **Secondary use of patients' electronic records (SUPER): an approach for meeting specific data needs of clinical and translational researchers.** *AMIA Annu Symp Proc* 2017;2017:1581–88 Medline
- Schweitzer AD, Parikh NS, Askin G, et al. **Imaging characteristics associated with clinical outcomes in posterior reversible encephalopathy syndrome.** *Neuroradiology* 2017;59:379–86 CrossRef Medline
- Poyiadji N, Shahin G, Noujaim D, et al. **COVID-19-associated acute hemorrhagic necrotizing encephalopathy: CT and MRI features.** *Radiology* 2020;296:E119–20 CrossRef Medline
- Helms J, Kremer S, Merdji H, et al. **Neurologic features in severe SARS-CoV-2 infection.** *N Engl J Med* 2020;382:2268–70 CrossRef Medline
- Kandemirli SG, Doagn I, Sarikaya ZT, et al. **Brain MRI findings in patients in the intensive care unit with COVID-19 infection.** *Radiology* 2020 May 8. [Epub ahead of print] CrossRef Medline
- Lantos JE, Strauss SB, Lin E. **COVID-19 associated Miller Fisher syndrome: MRI findings.** *AJNR Am J Neuroradiol* 2020;41:1184–86 CrossRef Medline
- Eliezer M, Hautefort C, Hamel A, et al. **Sudden and complete olfactory loss function as a possible symptom of COVID-19.** *JAMA Otolaryngol Head Neck Surg* 2020 Apr 8. [Epub ahead of print] CrossRef Medline
- Adams HP, Bendixen BH, Kappelle LJ, et al. **Classification of subtype of acute ischemic stroke; definitions for use in a multicenter clinical trial—TOAST. Trial of Org 10172 in Acute Stroke Treatment.** *Stroke* 1993;24:35–41 CrossRef Medline
- Hart RG, Diener HC, Connolly SJ. **Embolic strokes of undetermined source: support for a new clinical construct—authors' reply.** *Lancet Neurol* 2014;13:967 CrossRef Medline
- Meretoja A, Strbian D, Putaala J, et al. **SMASH-U: a proposal for etiologic classification of intracerebral hemorrhage.** *Stroke* 2012;43:2592–97 CrossRef Medline
- Riech S, Kallenberg K, Moerer O, et al. **The pattern of brain microhemorrhages after severe lung failure resembles the one seen in high-altitude cerebral edema.** *Crit Care Med* 2015;43:e386–89 CrossRef Medline
- Fanou EM, Coutinho JM, Shannon P, et al. **Critical-illness associated cerebral microbleeds.** *Stroke* 2017;48:1085–87 CrossRef Medline
- Vaira LA, Salzano G, Deiana G, et al. **Anosmia and ageusia: common findings in COVID-19 patients.** *Laryngoscope* 2020;130:1787 CrossRef Medline
- Gane SB, Kelly C, Hopkins C. **Isolated sudden onset anosmia in COVID-19 infection: a novel syndrome?** *Rhinology* 2020;58:299–301 CrossRef Medline
- Hopkins C, Surda P, Kumar BN. **Presentation of new onset anosmia during the COVID-19 pandemic.** *Rhinology* 2020;58:295–98 CrossRef Medline
- Mahammedi A, Saba L, Vagal A, et al. **Imaging in neurological disease of hospitalized COVID-19 patients: an Italian multicenter retrospective observational study.** *Radiology* 2020 May 21. [Epub ahead of print] CrossRef Medline
- Becker RC. **COVID-19 update: Covid-19-associated coagulopathy.** *J Thromb Thrombolysis* 2020;50:54–67 CrossRef Medline
- Zhang Y, Xiao M, Zhang S, et al. **Coagulopathy and antiphospholipid antibodies in patients with Covid-19.** *N Engl J Med* 2020;382:e38 CrossRef Medline
- Tang N, Li D, Wang X, et al. **Abnormal coagulation parameters are associated with poor prognosis in patients with novel coronavirus pneumonia.** *J Thromb Haemost* 2020;18:844–47 CrossRef Medline
- Franceschi AM, Ahmed O, Giliberto L, et al. **Hemorrhagic posterior reversible encephalopathy syndrome as a manifestation of COVID-19 infection.** *AJNR Am J Neuroradiol* 2020;41:1173–76 CrossRef Medline
- Radmanesh A, Derman A, Liu YW, et al. **COVID-19-associated diffuse leukoencephalopathy and microhemorrhages.** *Radiology* 2020 May 21. [Epub ahead of print] CrossRef Medline
- Kallenberg K, Dehnert C, Dörfler A, et al. **Microhemorrhages in nonfatal high-altitude cerebral edema.** *J Cereb Blood Flow Metab* 2008;28:1635–42 CrossRef Medline
- Shah J, Armstrong MJ. **Extracorporeal membrane oxygenation: uncommon cause of corpus callosal microhemorrhage.** *Neurology* 2015;84:630 CrossRef Medline
- Toscano G, Palmerini F, Ravaglia S, et al. **Guillain-Barré syndrome associated with SARS-CoV-2.** *N Engl J Med* 2020;382:2574–76 CrossRef Medline
- Parra B, Lizarazo J, Jiménez-Arango JA, et al. **Guillain-Barré syndrome associated with Zika virus infection in Colombia.** *N Engl J Med* 2016;375:1513–23 CrossRef Medline
- Brasil P, Sequeira PC, Freitas AD, et al. **Guillain-Barré syndrome associated with Zika virus infection.** *Lancet* 2016;387:1482 CrossRef Medline

35. Zhao H, Shen D, Zhou H, et al. **Guillain-Barre syndrome associated with SARS-CoV-2 infection: causality or coincidence?** *Lancet Neurol* 2020;19:383–84 CrossRef Medline
36. Bilinska K, Jakubowska P, Von Bartheld CS, et al. **Expression of the SARS-CoV-2 entry proteins, ACE2 and TMPRSS2, in cells of the olfactory epithelium: identification of cell types and trends with age.** *ACS Chem Neurosci* 2020;11:1555–62 CrossRef Medline
37. Li Y, Bai W, Hashikawa T. **The neuroinvasive potential of SARS-CoV2 may play a role in the respiratory failure of COVID-19 patients.** *J Med Virol* 2020;92:552–55 CrossRef Medline
38. Netland J, Meyerholz DK, Moore S, et al. **Severe acute respiratory syndrome coronavirus infection causes neuronal death in the absence of encephalitis in mice transgenic for human ACE2.** *J Virol* 2008;82:7264–75 CrossRef Medline
39. Li K, Wohlford-Lenane C, Perlman S, et al. **Middle East respiratory syndrome coronavirus causes multiple organ damage and lethal disease in mice transgenic for human dipeptidyl peptidase 4.** *J Infect Dis* 2016;213:712–22 CrossRef Medline
40. Varga Z, Flammer AJ, Steiger P, et al. **Endothelial cell infection and endotheliitis in COVID-19.** *Lancet* 2020;395:1417–18 CrossRef Medline

A Double-Edged Sword: Neurologic Complications and Mortality in Extracorporeal Membrane Oxygenation Therapy for COVID-19–Related Severe Acute Respiratory Distress Syndrome at a Tertiary Care Center

J. Masur, C.W. Freeman, and S. Mohan



ABSTRACT

SUMMARY: In this clinical case series, we report our experience to date with neurologic complications of extracorporeal membrane oxygenation therapy for COVID-19 Acute Respiratory Distress Syndrome. We have found an unexpectedly increased rate of complications as demonstrated by neuroimaging compared with meta-analysis data in extracorporeal membrane oxygenation therapy for all Acute Respiratory Distress Syndrome etiologies over the past few decades and compared with the most recent baseline data describing the incidence of neurologic complication in all patients with COVID-19. For our 12-patient cohort, there was a rate of intracranial hemorrhage of 41.7%. Representative cases and images of devastating intracranial hemorrhage are presented. We hypothesize that the interplay between hematologic changes inherent to extracorporeal membrane oxygenation and inflammatory and coagulopathic changes that have begun to be elucidated as part of the COVID-19 disease process are responsible. Continued analysis of extracorporeal membrane oxygenation therapy in this disease paradigm is warranted.

ABBREVIATIONS: ARDS = Acute Respiratory Distress Syndrome; COVID-19 = coronavirus disease 2019; ECMO = extracorporeal membrane oxygenation; MERS = Middle East respiratory syndrome; vv = venovenous

The data regarding all aspects of coronavirus disease 2019 (COVID-19) continue to evolve. As the number of patients treated with specific paradigms grows, continuous reevaluation of the outcomes must be undertaken. Extracorporeal membrane oxygenation (ECMO) has been a mainstay of therapy in multiple treatment strategies related to respiratory failure for several decades, including Acute Respiratory Distress Syndrome (ARDS) refractory to conventional therapy. More recently and specifically, ECMO was shown to have mortality reduction benefit in refractory ARDS secondary to the Middle Eastern Respiratory Syndrome coronavirus (MERS-CoV).¹ As the COVID-19 pandemic has progressed, review of the most recent literature has shown that the ECMO treatment paradigm was thus initiated for severe COVID-19–related ARDS at many institutions. However, as the number of patients

treated with various measures including ECMO grows, continuous reevaluation of the outcomes must be undertaken.

Several initial analyses have found that the ECMO paradigm for refractory ARDS in patients with COVID-19 has not shown the same benefit as seen with MERS-CoV.^{2–4} High mortality rates are being reported in these patients compared with those treated with conventional therapy. Although this is undoubtedly multifactorial and small sample sizes have precluded scientifically sound conclusions to date, the early findings are alarming. For example, a recent pooled retrospective analysis of 4 studies in China comprising 567 patients with COVID-19 and ARDS of whom 17 were treated with ECMO found a mortality rate of 94% in the ECMO subgroup compared with 70% for those treated with conventional therapy alone.⁴

In our group, we are trying to understand the etiopathogenesis and mechanisms of CNS involvement in patients who are positive for COVID-19. Specifically, we are aiming to study the prevalence of neurologic complications and complications of supportive treatments including ECMO. A recent meta-analysis of patients treated with ECMO for respiratory failure of all causes from 1992 to 2015 showed a neurologic complication rate of 7.1%;^{5,6} this included a 3.6% incidence of cerebral hemorrhage and a 1.7% incidence of stroke. Additionally, a recent observational study from a large academic center reported a rate of intracranial hemorrhage of 4.5% in

Received May 28, 2020; accepted after revision June 22.

From the Department of Radiology, Hospital of the University of Pennsylvania, Philadelphia, Pennsylvania.

Please address correspondence to Jonathan Masur, MD, Department of Radiology, Hospital of the University of Pennsylvania, 3400 Spruce St., Philadelphia, PA 19104; e-mail: jonmasur@gmail.com

Indicates open access to non-subscribers at www.ajnr.org

Indicates article with supplemental on-line table.

<http://dx.doi.org/10.3174/ajnr.A6728>

admitted patients who are positive for COVID-19.⁷ Although there are small case series in the literature regarding ECMO therapy and intracranial hemorrhage in patients with COVID-19,⁸ the data regarding ECMO therapy as it relates to the neurologic sequelae and outcomes of COVID-19 remain sparse. Our larger case series aims to elucidate this relationship.

MATERIALS AND METHODS

An observational study design was performed with approval from our institutional review board. The number of inpatients admitted to a tertiary health care system between March 1, 2020, and May 19, 2020, with confirmed infection status of “COVID-19 positive” was determined by using the “Reports” function of the electronic medical record system (Epic Systems). A list of inpatients with an infection status of “COVID-19 positive” and with neuroimaging of the head performed during the same time period, including CT/CTA and MRI/MRA, was subsequently generated.

The medical records of these participants were examined, and the age, sex, utilization of ECMO, either venovenous (VV) or venoarterial, and duration of ECMO therapy during their admissions were recorded. The rationale for initiation of ECMO in these patients was at the discretion of the treating pulmonologist and according to institutional guidelines. The presence of potentially contributory medical comorbidities in this cohort, including autoimmune conditions, immunosuppression, hypertension, diabetes mellitus, asthma, and structural lung disease, was documented. Additionally, the anticoagulation method used during ECMO as well as the patients’ platelet counts at the time of imaging were recorded.

The clinical examination findings prompting neuroimaging in the ECMO cohort were recorded. The images and reports for patients on ECMO with brain imaging were reviewed for critical findings, which we defined as acute or subacute intracranial hemorrhage, acute or subacute infarction, vascular occlusion, findings of infection or inflammation, herniation, hydrocephalus, and evidence of hypoxic-ischemic encephalopathy.

RESULTS

Between March 1, 2020, and May 19, 2020, we identified 12 patients on VV-ECMO at the time of neuroimaging and none on VA-ECMO. The demographics, comorbidities, anticoagulation therapy, ECMO duration, platelet counts, clinical examination findings prompting neuroimaging, and imaging findings are all presented in the On-line Table.

The most common comorbid conditions in the cohort were hypertension (5 of 12; 41.7%), type 2 diabetes mellitus (4 of 12, 33%), and asthma (4 of 12, 33%). Additional pre-existing conditions that could have predisposed patients to vascular phenomena were present: 1 patient had systemic lupus erythematosus, another had sickle cell trait, and a third had rheumatoid arthritis.

The mean duration of ECMO therapy in our cohort at the time of imaging was 230.3 hours. This is similar to the duration of therapy in the referenced meta-analysis, in which the mean duration of therapy in both the CNS complication and non-CNS complication groups was approximately 258 hours.⁵

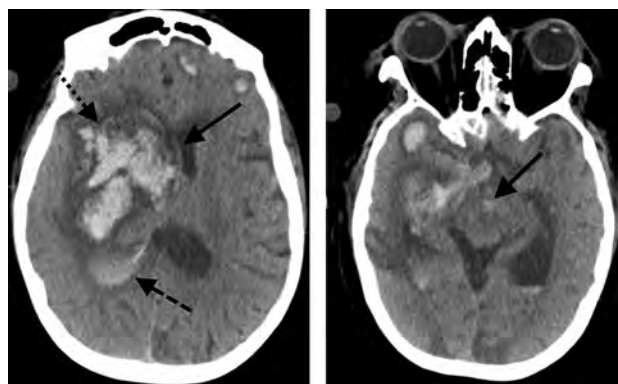


FIG 1. A 65-year-old female patient with a history of rheumatoid arthritis and type 2 diabetes mellitus presented to an outside hospital with fevers and was found to be positive for COVID-19, with pneumonia on chest imaging. The patient’s respiratory status declined despite ventilation, prompting transfer and initiation of VV-ECMO. One day after initiation of ECMO, the patient’s right pupil was fixed on neurologic examination, prompting emergent head CT. This showed a large mixed-attenuation intraparenchymal hemorrhage centered in the right basal ganglia (*dotted arrow*) with intraventricular extension (*dashed arrow*) and right-to-left midline shift or subfalcine herniation (*solid arrow*). Additional intraparenchymal hemorrhages are seen throughout the supratentorial brain (*dotted arrow*) as well as ventricular dilation and right uncal herniation. Subarachnoid hemorrhage was also seen, such as in the interpeduncular cistern (*solid arrow*).

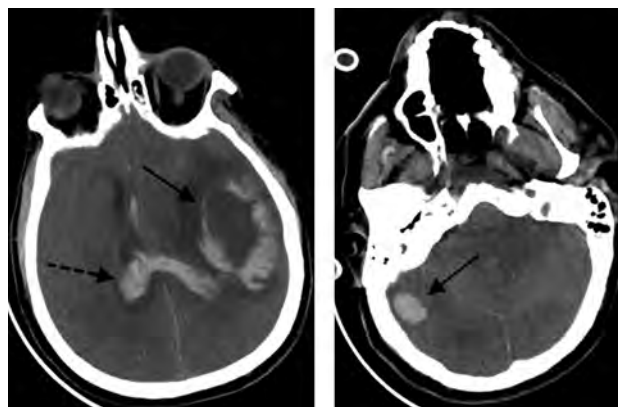


FIG 2. A 60-year-old male patient with a history of asthma and hypertension presented to an outside hospital with fever, dyspnea, and chest imaging demonstrating multifocal pneumonia. The patient tested positive for COVID-19. The patient was intubated, but his condition worsened despite mechanical ventilation, and he was subsequently placed on VV-ECMO. Three days later, the patient demonstrated anisocoria on physical examination, prompting a CT scan of the head. There was diffuse cerebral edema with sulcal and cisternal effacement and multiple intraparenchymal hemorrhages (*solid arrows*) resulting in left-to-right midline shift, intraventricular extension (*dotted arrow*), and subfalcine and uncal herniations.

Critical findings meeting our criteria were identified on neuroimaging studies from 6 of the 12 (50%) participants on ECMO. The most common critical findings were intracranial hemorrhage (5 of 12; 41.7%) with associated herniation in 4 of 5 patients (Figs 1 and 2). All 5 patients had subarachnoid hemorrhage, 4 of 5 had intraparenchymal hemorrhage, and 3 of 5 had intraventricular

hemorrhage. Evidence of ischemic infarctions were seen in 2 of 6, both with concomitant intracranial hemorrhage. Three patients had findings of hydrocephalus. All 4 patients with parenchymal hemorrhage and herniation seen on neuroimaging died from the complications. The fifth patient had isolated small-volume subarachnoid hemorrhage that subsequently resolved, but this patient died from ongoing respiratory complications. The sixth patient had findings suggestive of communicating hydrocephalus without a clear cause. One of the 12 patients had vascular imaging with CTA of the head and neck, which did show multiple intracranial large-vessel occlusions; this patient also had multicompartmental intracranial hemorrhages.

DISCUSSION

Our analysis of the subset of patients with COVID-19–related ARDS treated with ECMO at our institution demonstrates an unexpectedly increased rate (50%) of devastating neurologic events, specifically intracranial hemorrhage (41.7%), as demonstrated by emergently performed neuroimaging. Comparatively, a recent meta-analysis of patients treated with ECMO for respiratory failure from 1992 to 2015 showed a neurologic complication rate of 7.1%, including an incidence of cerebral hemorrhage of 3.6%.⁵ Moreover, a recent similarly designed cohort study of 246 consecutive patients who were positive for COVID-19 with neuroimaging at a large tertiary care center showed an incidence of intracranial hemorrhage of 4.5%.⁷ Although the statistical significance of this difference cannot be definitely determined at this time, the results of our analysis do show a trend toward a significantly increased rate of devastating neurologic events manifested on neuroimaging.

Despite the mortality benefit of ECMO demonstrated in patients with MERS-CoV ARDS, we hypothesize that the interplay between the novel COVID-19–related coagulopathy, pre-existing conditions, and the hematologic alterations inherent to continuous VV-ECMO could be responsible for the increased risk of neurologic complications in this cohort. This is in keeping with similar mechanisms suggested in the most recent literature.⁹

The main limitation of our analysis is the small sample size to date of patients at our institution treated with ECMO for COVID-19–related ARDS. Given the scope of the coronavirus pandemic and international expert predictions that outbreaks could be experienced for at least the next couple of years, an accelerated prospective clinical trial of the risk versus benefit of ECMO therapy in patients with COVID-19–related ARDS should be considered as feasible. Regardless, continuous retrospective analysis of the available data regarding all aspects of this

treatment paradigm is warranted, such that future pooled analyses could add to our work and assess statistical significance of neurologic complications.

CONCLUSIONS

The evidence continues to mount that ECMO should be used with extreme caution in patients with COVID-19–related ARDS. Very close neurologic monitoring and a low threshold for neuroimaging in this cohort should be used because our findings show a concerning trend toward an increased rate of neurologic complications.

Disclosures: Colbey Freeman—UNRELATED: Grants/Grants Pending: RSNA, NVIDIA, Comments: RSNA resident grant 2020-2021 to institution, NVIDIA GPU grant 2019 provided to me.* Suyash Mohan—UNRELATED: Consultancy: Northwest Biotherapeutics; Grants/Grants Pending: Novocure, Galileo.* *Money paid to the institution.

REFERENCES

1. Alshahrani MS, Sindi A, Alshamsi F, et al. **Extracorporeal membrane oxygenation for severe Middle East respiratory syndrome coronavirus.** *Ann Intensive Care* 2018;8:3 CrossRef Medline
2. Sultan I, Habrtheuer A, Usman AA, et al. **The role of extracorporeal life support for patients with COVID-19: preliminary results from a statewide experience.** *J Card Surg* 2020;5:1410–13 CrossRef Medline
3. Jacobs JP, Stammers AH, St Louis J, et al. **Extracorporeal membrane oxygenation in the treatment of severe pulmonary and cardiac compromise in COVID-19: experience with 32 patients.** *ASAIO J* 2020;66:722–30 CrossRef Medline
4. Henry BM, Lippi G. **Poor survival with extracorporeal membrane oxygenation in acute respiratory distress syndrome (ARDS) due to coronavirus disease 2019 (COVID-19): pooled analysis of early reports.** *J Crit Care* 2020;58:27–28 CrossRef Medline
5. Lorusso R, Gelsomino S, Parise O, et al. **Neurologic injury in adults supported with veno-venous extracorporeal membrane oxygenation for respiratory failure: findings from the Extracorporeal Life Support Organization Database.** *Crit Care Med* 2017;45:1389–97 CrossRef Medline
6. Peek GJ, Mugford M, Tiruvoipati R, et al. **Efficacy and economic assessment of conventional ventilatory support versus extracorporeal membrane oxygenation for severe adult respiratory failure (CESAR): a multicentre randomised controlled trial.** *Lancet* 2009;374:1351–63 CrossRef Medline
7. Radmanesh A, Raz E, Zan E, et al. **Brain imaging findings in COVID-19: a single academic center experience in the epicenter of disease in the United States.** *AJNR Am J Neuroradiol* 2020;41:1179–83 CrossRef Medline
8. Heman-Ackah SM, Su S, Spadola M, et al. **Neurologically devastating intraparenchymal hemorrhage in COVID-19 patients on extracorporeal membrane oxygenation: a case series.** *Neurosurgery* 2020;87:E147–51 CrossRef Medline
9. Kowalewski M, Fina D, Słomka A, et al. **COVID-19 and ECMO: the interplay between coagulation and inflammation—a narrative review.** *Crit Care* 2020;24:205 CrossRef Medline

Stroke Thrombectomy in Patients with COVID-19: Initial Experience in 13 Cases

R. Pop, A. Hasiu, F. Bolognini, D. Mihoc, V. Quenardelle, R. Gheoca, E. Schluck, S. Courtois, M. Delaitre, M. Musacchio, J. Pottecher, T.-N. Chamaraux-Tran, F. Sellal, V. Wolff, P.A. Lebedinsky, and R. Beaujeux



ABSTRACT

SUMMARY: We performed a retrospective review in both comprehensive stroke units of a region affected early by the coronavirus disease 2019 (COVID-19) pandemic, between March 1 and April 26, 2020, including patients with COVID-19 who underwent mechanical thrombectomy for ischemic stroke. We identified 13 cases, representing 38.2% of 34 thrombectomies performed during this period. We observed increased mortality and a high incidence of thrombotic complications during hospitalization. Given the high rate of infected patients, systematic use of full personal protection measures seems justified.

ABBREVIATIONS: COVID-19 = coronavirus disease 2019; SARS-CoV-2 = Severe Acute Respiratory Syndrome coronavirus 2

The coronavirus disease (COVID-19) pandemic is an ongoing pandemic caused by Severe Acute Respiratory Syndrome coronavirus 2 (SARS-CoV-2). The outbreak was identified in China in December 2019 and then spread to Europe in January 2020. The first 3 cases in Europe were reported in France on January 24.¹ Epidemic response measures were triggered in France on March 1 and gradually developed until March 17, when a nationwide lockdown was enforced, with strict home confinement of the entire population.

Alsace was the first French region affected by the outbreak. It is a region in the East of France with a population of approximately 1.9 million people. The peak of the epidemic was registered on April 2, with 2142 hospitalized patients diagnosed with COVID-19 (of whom 433 were in intensive care units). On April 26, there were 1153 reported in-hospital deaths.²

We aimed to describe baseline characteristics, procedural metrics, and outcomes of stroke thrombectomies in patients diagnosed with COVID-19, performed at the 2 comprehensive stroke centers (Strasbourg University Hospital and Colmar Hospital) in the Alsace region during the first 2 months of the outbreak.

MATERIALS AND METHODS

We performed a retrospective review in both comprehensive stroke units in the Alsace region, between March 1 and April 26, 2020. Patients were included in the study if they underwent mechanical thrombectomy for acute ischemic stroke and were diagnosed with SARS-CoV-2 infection either before or after the endovascular procedure (during the same hospitalization). Endovascular procedures for cerebral venous sinus thrombosis were not included in this study. Patient files were reviewed to extract demographics, comorbidities, procedural metrics, and complications, as well as clinical follow-up information. In addition, we collected protocols of personal protection measures in the angiography suites and the number of documented contamination cases among medical personnel.

Brief Description of the Stroke Pathway in the Alsace Region

There are 3 hospitals (Strasbourg University Hospital, Colmar Hospital, and Moulhouse Hospital) with stroke units in the region, of which 2 have endovascular treatment facilities (Strasbourg University Hospital and Colmar Hospital). Two additional hospitals (Saverne Hospital and Haguenau Hospital) without stroke units are equipped with telemedicine facilities in the emergency department and are connected to one of the comprehensive stroke centers. Patients are accepted as with stroke alerts following a telephone consultation between the paramedic/physician in the field and the on-call neurologist if there are symptoms suggestive of stroke dating 6 hours from last seen well (up to 24 hours in selected cases). Patients with stroke alerts bypass the emergency department and are seen directly by the on-call neurologist in the radiology department before imaging.

Received May 17, 2020; accepted after revision June 26.

From the Interventional Neuroradiology Department (R.P., A.H., D.M., R.B.), Stroke Unit (V.Q., R.G., V.W.), and Department of Anesthesia (J.P., T.-N.C.-T.), Strasbourg University Hospitals, Strasbourg, France; Institut de Chirurgie Minimale Invasive Guidée par l'Image (R.P., R.B.), Strasbourg, France; Diagnostic and Interventional Neuroradiology Department (F.B., M.D., M.M., P.A.L.) and Neurology Department (F.S.), Hôpitaux Civils de Colmar, Colmar, France; and Neurology Department (E.S., S.C.), Emile Muller Hospital, Mulhouse, France.

Please address correspondence to Raoul Pop, MD, Interventional Neuroradiology Department, Strasbourg University Hospitals, Strasbourg, France, 1 Ave Molière, 67098 Strasbourg, France; e-mail: pop.raoul@gmail.com; @RaoulPop25

Indicates open access to non-subscribers at www.ajnr.org

<http://dx.doi.org/10.3174/ajnr.A6750>

Table 1: Baseline characteristics

	Thrombectomies in Patients with COVID-19 (n = 13)
Age (median) (IQR) (yr)	78 (71–79)
Male sex (No.) (%)	5 (38.4%)
Risk factors (No.) (%)	
Hypertension	8 (61.5%)
Dyslipidemia	3 (23.0%)
Diabetes	2 (15.3%)
Smoking	3 (23.0%)
Baseline mRS score >2	0 (0%)
Baseline NIHSS score (median) (IQR)	13 (7–15)
Symptom onset to femoral puncture (median) (IQR) (min)	244 (232–290)
IV thrombolysis (No.) (%)	4 (30.7%)
Initial imaging type (No.) (%)	
MR imaging	11 (84.6%)
CT	2 (15.3%)
Initial APECTS ^a	
ASPECTS <5 (n/N) (%)	0/12 (0%)
ASPECTS score (median) (IQR)	8 (5.7–9)
Occlusion site at angiography (No.) (%)	
M1 segment	8 (61.5%)
M2 segment	3 (23.0%)
Tandem occlusion	1 (7.6%)
Basilar trunk	1 (7.6%)

Note:—IQR indicates interquartile range; n/N, n - number of cases with ASPECTS <5/N - number of cases with anterior circulation strokes.

^a For anterior circulation strokes.

Table 2: Thrombectomy procedure metrics: clinical and radiologic outcomes

	Thrombectomies in Patients with COVID-19 (n = 13)
Anesthesia method (No.) (%)	
General anesthesia	9 (69.2%)
Conscious sedation	4 (30.7%)
Initial treatment approach (No.) (%)	
Stent retriever	4 (30.7%)
ADAPT technique	6 (46.1%)
Combined distal aspiration and stent retriever	3 (23.0%)
Timing of intervention (median) (IQR) (min)	
Femoral puncture to recanalization	34.5 (23–45)
Symptom onset to recanalization	298.5 (261–324)
Angiographic outcome (No.) (%)	
TICI 2b–3	10 (76.9%)
TICI 2c–3	9 (69.2%)
TICI 3	7 (53.8%)
Procedural complications (No.) (%)	
Neurologic	0 (0%)
Non-neurologic (femoral artery occlusion)	1 (7.6%)
Imaging outcome (No.) (%)	
All hemorrhagic transformation	3 (23.0%)
Symptomatic ICH	0 (0%)
HI1–HI2	2 (15.3%)
PH 1	1 (7.6%)
PH 2	0 (0%)
Clinical outcome	
In-hospital mortality (No.) (%)	2 (15.3%)
Last available NIHSS (median) (IQR) ^a	5 (0.5–12.5)
NIHSS drop (median) (IQR) ^a	2 (0.5–5)

Note:—ADAPT indicates direct aspiration first pass technique; ICH, intracerebral hemorrhage; PH, parenchymal hematoma; HI, petechial hemorrhage.

^a n = 10 (excluding 2 deceased patients).

All 3 centers use MR imaging for patient selection. During the COVID-19 outbreak, all hospitals were able to maintain around-the-clock care for stroke emergencies.

Statistical Analysis

Given the small sample size, the analysis was mainly performed using descriptive statistics. Continuous variables are presented as median with interquartile range. Categorical variables are presented as numbers with percentages. Comparisons of time delays were performed using the Mann-Whitney *U* test after the normality of the distributions was assessed graphically and using the Shapiro-Wilk test. Analyses were performed using GraphPad Prism, Version 6.0 (GraphPad Software).

RESULTS

We identified 13 patients with SARS-Cov-2 infection, representing 38.2% of a total of 34 thrombectomies performed in the 2 centers during the study period. Apart from 1 case, recorded on March 12, all other cases were recorded after March 25.

Baseline characteristics are detailed in Table 1. The median patient age was 78 years, and the median time from symptom onset to groin puncture was 244 minutes. Most cases were anterior circulation strokes (8/13; 61.5%). The median ASPECTS was 8, and none of the patients had ASPECTS < 5.

Procedural metrics and outcomes are detailed in Table 2. The median time from groin puncture to recanalization was 34.5 minutes, and TICI 2b–3 recanalization was obtained in 10/13 (76.9%) cases. No symptomatic hemorrhagic transformation was observed on 24-hour CT scans. In 1 case (7.6%), 9 hours after successful recanalization of a middle cerebral artery occlusion, we observed early arterial re-occlusion of both internal carotid arteries and of the basilar trunk.

Three patients (23.0%) were diagnosed with deep vein thrombosis, and 1 (7.6%), with a pulmonary embolism during hospitalization. Two patients died, accounting for a mortality rate of 15.3%.

Table 3: Influence of COVID-19 epidemic on mechanical thrombectomy volumes and procedural time metrics

	March 1 to April 26, 2019	March 1 to April 26, 2020	Variation/P Value
Volume of mechanical thrombectomies	43	34	–21%
Symptom onset to brain imaging (median) (IQR) (min)	141 (102–189)	135 (100–171)	.568
Symptom onset to IV thrombolysis ^a (median) (IQR) (min)	167 (141–188)	162 (150–180)	.992
Imaging to femoral puncture (median) (IQR) (min)	102 (82–137)	113 (96–138)	.316
Symptom onset to femoral puncture (median) (IQR) (min)	257 (207–298)	258 (211–293)	.919
Femoral puncture to recanalization (median) (IQR) (min)	48 (39–71)	43 (25–58)	.363

^a For patients who received IV thrombolysis before thrombectomy.

COVID-19 Diagnosis

Only 1 patient had been diagnosed with COVID-19 before thrombectomy, and the patient was already hospitalized at the time of the stroke. In the remaining 12/13 (92.3%) cases, patients presented to the hospital primarily for symptoms of acute stroke. On initial examination and history, there were symptoms suggestive of COVID-19 in only 4/12 (33.3%) cases.

Infection with SARS-Cov-2 was confirmed by reverse transcription polymerase chain reaction in 10/13 patients. In 3 of these cases, the results of the first oropharyngeal swab were negative. Subsequently, 2 patients had a second oropharyngeal swab positive for COVID-19, while for the third patient, the reverse transcription polymerase chain reaction was positive for COVID-19 in a sputum sample.

In the remaining 3/13 cases with negative findings with oropharyngeal swabs, the diagnosis was made due to association of typical clinical symptoms and chest CT findings.

Personal Protection Measures

Both centers used personal protection measures during the study period. In 1 center, measures to prevent contamination of personnel were used systematically for all cases, even in the absence of suggestive clinical symptoms. This center (Strasbourg University Hospital) already used systematic general anesthesia for all thrombectomies, and this practice was continued. Orotracheal intubation was performed in the angiography suite, which is equipped with an ISO 7 air-handling unit (capable of clearing 90% of 0.5- μ m particles in less than 6 minutes; Unit model RM09/09, manufacturer ROBATHERM, Jettingen-Scheppach, Germany). All personnel in the angiography suite wore enhanced personal protection equipment, including surgical cap, goggles, full gown/gloves, shoe covers, and a filtering face-piece 3 mask. Extubation was performed in the angiography suite; then, the patient was transferred directly to the stroke unit.

The second center continued their usual practice of thrombectomy with the patient under local anesthesia/conscious sedation. Enhanced personal protective equipment was used only for cases with symptoms suggestive of COVID-19 disease.

During the study period, 1 interventional neuroradiologist developed mild respiratory symptoms suggestive of COVID-19. Subsequent CT of the chest revealed unilateral small ground glass opacities compatible with mild COVID-19 pneumonia. Findings of nasopharyngeal swabs 10 days apart were negative, there was full resolution of symptoms without specific treatment, and the physician resumed activity after 14 days of home confinement. One radiology technician developed respiratory symptoms, tested positive on the first nasopharyngeal swab, and was also able to

resume activity after 14 days of home confinement. There were no other documented cases of contamination in physicians or angiography suite staff (7 interventional neuroradiologists and 29 radiology technicians).

Comparison with Prepandemic Activity

Compared with the same time period in 2019, we observed a 21% decrease in stroke thrombectomy volume. Procedural time metrics compared with the prepandemic period are outlined in Table 3. There was no significant difference in prehospital or in-hospital delays, but this comparison is obviously limited by the small sample size.

DISCUSSION

During the first 2 months of the COVID-19 outbreak, more than one-third of the patients who underwent stroke thrombectomies had SARS-Cov-2 infection. In most cases, patients did not have a COVID-19 diagnosis or suspicion before the acute presentation with stroke symptoms. Moreover, only 1 of 3 patients had suggestive symptoms at the moment of the acute presentation.

These results underline the importance of personal protection measures for all stroke centers in areas touched by the COVID-19 pandemic. An important proportion of cases were not suspected of having COVID-19 at presentation. This scenario can be explained, on one hand, by the high rate of asymptomatic infections and, on the other hand because the initial examination and history are performed in an expedited fashion in the context of stroke alerts because of time constraints and impaired communication due to neurologic deficits. Consequently, it seems justified to systematically apply full personal protection measures for all stroke thrombectomies, for the entire duration of the epidemic. Recent guidance issued by the Society of NeuroInterventional Surgery³ also recommends that patients with undocumented COVID-19 status should be treated as high risk, provided institutional resources are available. However, the high rate of patients positive for COVID-19 observed in our series might not be applicable in other geographic areas. Moreover, the definition of appropriate personal protection measures may vary among facilities and practitioners. This is reflected in the recommendations of the European Society of Minimally Invasive Neurological Therapy,⁴ which state that clinical management should be conducted according to local hospital protocols.

Baseline characteristics among treated cases, as well the duration of procedures and recanalization rates, are comparable with those in previously published literature.⁵ Two recent reports^{6,7} of

10 thrombectomies in relatively young patients (5 cases in each report) suggested that SARS-Cov-2 infection might lead to increased rates of stroke in the younger population. We did not observe this tendency in our cohort. The youngest patient was 62 years of age, and the median age was 78 years, which is above the average age in recent thrombectomy trials. Escalard et al⁸ recently published their experience of thrombectomy in patients with COVID-19 in a high-volume center in Paris, France. They treated 10 patients positive for COVID-19, representing 27% of the total 37 thrombectomies performed during the study period; most patients (70%) had mild or no respiratory signs at the time of stroke. These findings are comparable with the results in our cohort.

With regard to clinical outcomes, despite the obvious limitations pertaining to the small sample size and short follow-up, our initial results suggest an increase in the in-hospital mortality rate (15.3%) and a high rate of thrombotic complications during hospitalization (23.0% with deep vein thrombosis, 7.6% with pulmonary embolism, and 7.6% with early arterial re-occlusion). In the cohort of Escalard et al,⁸ these rates were even higher; 40% of cases had early cerebral re-occlusion and 60% mortality. This finding is concordant with recent reports indicating a hypercoagulable state in patients with COVID-19. Multiple groups have observed high levels of thrombosis and inflammation serum markers such as D-dimers, fibrinogen, and C-reactive protein.^{9–11} Similarly, a recent study¹² found that pulmonary embolism is frequent and is seen in almost 1 of 4 patients with severe clinical features of COVID-19 infection.

Given this physiopathologic evidence, we should be seeing an increase in the incidence of ischemic stroke. Initial reports seem to point in the opposite direction: Two centers in northern Italy^{13,14} observed a reduction in the number of acute presentations, stroke admissions, and the proportion of patients treated with intravenous thrombolysis or mechanical thrombectomy. In our region, compared with the same period in 2019, between March 1 and 31, 2020, there were 39.6% fewer stroke alerts and 33.3% fewer acute revascularization treatments (intravenous thrombolysis and/or mechanical thrombectomy), with a relatively stable number of stroke unit admissions (−0.6%).¹⁵ This finding suggests that the overall stroke incidence remained the same, but fewer patients presented within the therapeutic time window and were thus eligible for intravenous thrombolysis or mechanical thrombectomy.

The incidence of ischemic stroke among patients with COVID-19 remains unknown. In our center,¹⁶ brain MR imaging was performed in 13 patients hospitalized in the intensive care unit with severe COVID-19 infection and acute respiratory distress syndrome. Three cases (23%) had evidence of acute or subacute ischemic stroke. Of note, these patients did not have focal signs suggestive of stroke; they underwent MR imaging because of unexplained encephalopathic features. These findings suggest that ischemic stroke might be frequent in patients with severe COVID-19 infection, but a large proportion of cases are not detected because clinical symptoms are masked by the severity of respiratory features and sedation.

The main limitations of this study are the small sample size and the absence of a comparative cohort. However, the aim of this study was primarily to describe our initial experience of stroke thrombectomy in this particular context and discuss possible implications for clinical practice.

CONCLUSIONS

More than one-third of patients who underwent stroke thrombectomies during the epidemic had SARS-Cov-2 infection. Most patients had not been diagnosed or suspected before the acute stroke presentation, and often they did not have suggestive symptoms on initial examination. In view of these results, it seems justified to systematically apply full personal protection measures for all stroke thrombectomies performed during this epidemic. Patient characteristics and thrombectomy metrics were comparable with those in recent clinical trials; however, initial data on clinical outcomes suggest increased mortality and a high incidence of thrombotic complications during hospitalization.

Disclosures: Julien Pottecher—UNRELATED: Consultancy: LFB BIOMEDICAMENTS; Payment for Development of Educational Presentations: Baxter. Thiën-Nga Chamarau-Tran—UNRELATED: Grants/Grants Pending: Société Française d'Anesthésie de et Réanimation. Comments: research grant; Payment for Lectures Including Service on Speakers Bureaus: Merck Sharp & Dohme, LFB. Francois Sellal—UNRELATED: Payment for Lectures Including Service on Speakers Bureaus: Novartis Pharmaceuticals, Sanofi, Crédit Mutuel.

REFERENCES

1. Bernard Stoecklin S, Rolland P, Silue Y, et al; Investigation Team. **First cases of coronavirus disease 2019 (COVID-19) in France: surveillance, investigations and control measures, January 2020.** *Euro Surveill* 2020;25:200009 CrossRef Medline
2. **COVID-19—France.** <https://www.gouvernement.fr/info-coronavirus/carte-et-donnees>. Accessed April 17, 2020
3. Fraser JF, Arthur AS, Chen M, et al. **Society of NeuroInterventional Surgery recommendations for the care of emergent neurointerventional patients in the setting of COVID-19.** *J Neurointerv Surg* 2020;12:539–41 CrossRef Medline
4. Aggour M, White P, Kulcsar Z, et al. **European Society of Minimally Invasive Neurological Therapy (ESMINT) recommendations for optimal interventional neurovascular management in the COVID-19 era.** *J Neurointerv Surg* 2020;12:542–44 CrossRef Medline
5. Goyal M, Menon BK, van Zwam WH, et al; HERMES collaborators. **Endovascular thrombectomy after large-vessel ischaemic stroke: a meta-analysis of individual patient data from five randomised trials.** *Lancet* 2016;387:1723–31 CrossRef Medline
6. Oxley TJ, Mocco J, Majidi S, et al. **Large-vessel stroke as a presenting feature of Covid-19 in the young.** *N Engl J Med* 2020;382:e60 CrossRef Medline
7. Wang A, Mandigo GK, Yim PD, et al. **Stroke and mechanical thrombectomy in patients with COVID-19: technical observations and patient characteristics.** *J Neurointerv Surg* 2020;12:648–53 CrossRef Medline
8. Escalard S, Maier B, Redjem H, et al. **Treatment of acute ischemic stroke due to large vessel occlusion with COVID-19: experience from Paris.** *Stroke* 2020;51:2540–43 CrossRef Medline
9. Li Y, Wang M, Zhou Y, et al. **Acute cerebrovascular disease following COVID-19: a single center, retrospective, observational study.** *Stroke Vasc Neurol* 2020 Jul 2. [Epub ahead of print] CrossRef Medline
10. Madjid M, Safavi-Naeini P, Solomon SD, et al. **Potential effects of coronaviruses on the cardiovascular system: a review.** *JAMA Cardiology* 2020 March 27. [Epub ahead of print] CrossRef Medline

11. Mehta P, McAuley DF, Brown M, et al; HLH Across Speciality Collaboration, UK. **COVID-19: consider cytokine storm syndromes and immunosuppression.** *Lancet* 2020;395:1033–34 CrossRef Medline
12. Grillet F, Behr J, Calame P, et al. **Acute pulmonary embolism associated with covid-19 pneumonia detected by pulmonary CT angiography.** *Radiology* 2020 April 23. [Epub ahead of print] CrossRef Medline
13. Baracchini C, Pieroni A, Viaro F, et al. **Acute stroke management pathway during Coronavirus-19 pandemic.** *Neurol Sci* 2020;41:1003–05 CrossRef Medline
14. Morelli N, Rota E, Terracciano C, et al. **The baffling case of ischemic stroke disappearance from the casualty department in the COVID-19 era.** *Eur Neurol* 2020;83:213–15 CrossRef Medline
15. Pop R, Quenardelle V, Hasiu A, et al. **Impact of the Covid-19 outbreak on acute stroke pathways - Insights from the Alsace region in France.** *Eur J Neurol* 2020 May 12. [Epub ahead of print] CrossRef Medline
16. Helms J, Kremer S, Merdji H, et al. **Neurologic features in severe SARS-CoV-2 infection.** *N Engl J Med* 2020;382:2268–70 CrossRef Medline

Cytotoxic Lesion of the Corpus Callosum in an Adolescent with Multisystem Inflammatory Syndrome and SARS-CoV-2 Infection

J. Lin, E.C. Lawson, S. Verma, R.B. Peterson, and R. Sidhu



ABSTRACT

SUMMARY: Multisystem inflammatory syndrome in children is a recently described complication in the late phase of Severe Acute Respiratory Syndrome coronavirus 2 (SARS-CoV-2) infection involving systemic hyperinflammation and multiorgan dysfunction. The extent of its clinical picture is actively evolving and has yet to be fully elucidated. While neurologic manifestations of SARS-CoV-2 are well-described in the adult population, reports of neurologic complications in pediatric patients with SARS-CoV-2 infection are limited. We present a pediatric patient with SARS-CoV-2 infection with development of multisystem inflammatory syndrome and acute encephalopathy causing delirium who was found to have a cytotoxic lesion of the corpus callosum on neuroimaging. Cytotoxic lesions of the corpus callosum are a well-known, typically reversible entity that can occur in a wide range of conditions, including infection, seizure, toxins, nutritional deficiencies, and Kawasaki disease. We hypothesized that the cytotoxic lesion of the corpus callosum, in the index case, was secondary to the systemic inflammation from SARS-CoV-2 infection, resulting in multisystem inflammatory syndrome in children.

ABBREVIATIONS: CLOCC = cytotoxic lesion of the corpus callosum; COVID-19 = coronavirus disease 2019; IVIG = intravenous immunoglobulin; MIS-C = multisystem inflammatory syndrome in children; PCR = polymerase chain reaction; SARS-CoV-2 = Severe Acute Respiratory Syndrome coronavirus 2

Severe Acute Respiratory Syndrome coronavirus 2 (SARS-CoV-2) infection in the pediatric population is not well-understood and has, until recently, been thought of as a relatively mild disease compared with that in adults. Most reported symptoms in children are fever, respiratory tract infection, or asymptomatic infection.¹ More recent reports in the pediatric population, however, describe a multisystem inflammatory syndrome in children (MIS-C).²⁻⁶ In the adult population, neurologic manifestations of coronavirus disease 2019 (COVID-19) are being reported with increasing frequency, including seizure, Guillain-Barré syndrome, vasculitis, stroke, cranial nerve palsy, and general encephalopathy.⁷⁻¹¹ Cases of neurologic manifestations in pediatric patients have been limited.

We report the case of a pediatric patient positive for COVID-19 who presented with fever, vomiting, diarrhea, cough, difficulty walking, and delirium.

Case Presentation

A 13-year-old previously healthy girl, who relocated from New York to Georgia a month prior, presented to the emergency department after 3 days of fever, vomiting, diarrhea, cough, dizziness, and gait instability. The only medications given before admission were aspirin and ibuprofen. On presentation to Egleston Hospital of Children's Healthcare of Atlanta, she had a fever of 39.2°C, hypotension initially requiring pressor support, normal white blood cell count (9780 cells/ μ L) with increased neutrophils (88%) and lymphopenia (7%), thrombocytopenia (121,000 cells/ μ L), hyponatremia (128 mmol/L), elevated transaminases (aspartate aminotransferase = 292 U/L, alanine aminotransferase = 336 U/L), acute kidney injury (creatinine = 1.09 mg/dL), elevated inflammatory markers (C-reactive protein = 10.9 mg/dL, erythrocyte sedimentation rate = 63 mm/h, interleukin 6 = 65 pg/mL), and elevated cardiac markers (troponin = 18.2 ng/mL, brain natriuretic peptide = 561 pg/mL). She was admitted to the pediatric intensive care unit for presumed bacterial sepsis and started on ceftriaxone and vancomycin.

Received June 2, 2020; accepted after revision July 8.

From the Department of Pediatric Neurology (J.L., E.C.L., S.V., R.S.), Children's Healthcare of Atlanta, Atlanta, Georgia; Department of Radiology and Imaging Sciences (R.B.P.), Division of Neuroradiology, Department of Neurology (E.C.L.), and Department of Pediatrics (J.L., S.V., R.S.), Division of Neurology, Emory University School of Medicine, Atlanta, Georgia.

J. Lin and E.C. Lawson contributed equally as co-first authors.

Please address correspondence to Reet Sidhu, MD, 1400 Tullie Rd NE, 4th Floor Atlanta, GA 30329; e-mail: reet.sidhu@emory.edu; @RyanBPetersonMD

Indicates open access to non-subscribers at www.ajnr.org

<http://dx.doi.org/10.3174/ajnr.A6755>

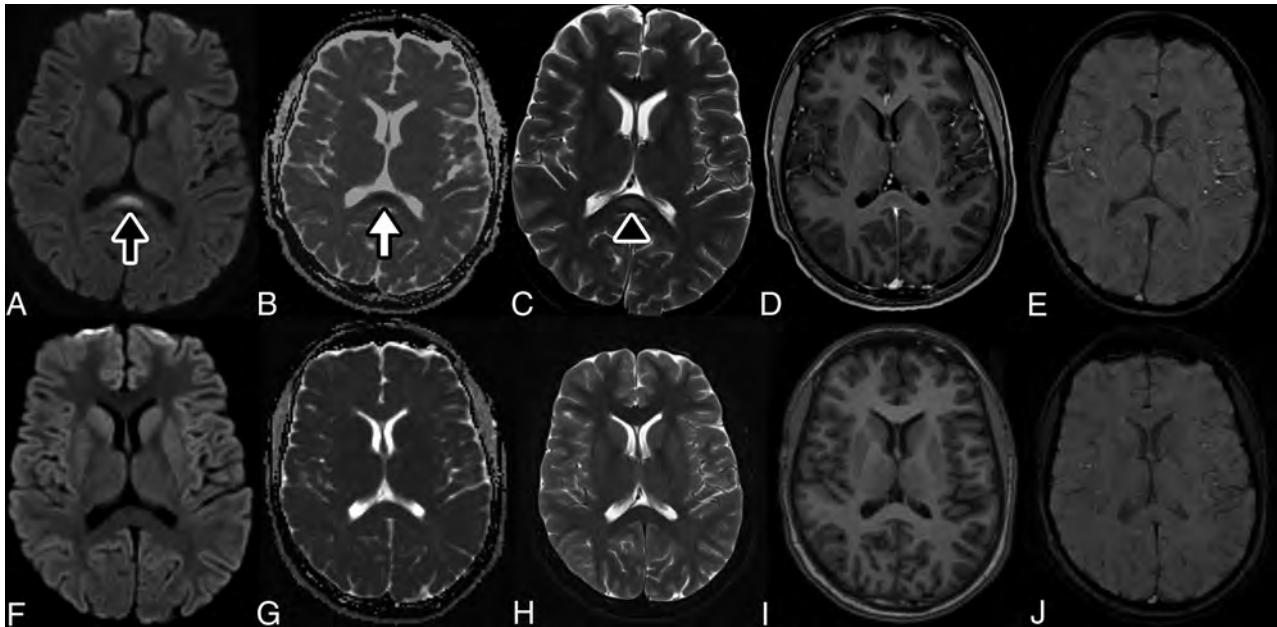


FIGURE. CLOCC in an adolescent with MIS-C and SARS-CoV-2. MR image of the brain demonstrates a nonspecific focus of increased signal in the splenium of the corpus callosum on DWI sequences at $b=1000 \text{ s/mm}^2$ (black arrow, A) with associated loss of signal on apparent diffusion coefficient maps (white arrow, B) corresponding to restricted diffusion. The apparent diffusion coefficient for the lesion is $0.44 \times 10^{-3} \text{ mm}^2/\text{s}$. This lesion corresponds to a faint focus of abnormal increased signal on T2WI spin-echo sequences (black arrowhead, C). The lesion also demonstrates a lack of contrast enhancement on T1WI postcontrast thin-section image (D) and absent susceptibility, suggesting absent hemorrhage on SWI (E). The imaging findings suggest a cytotoxic lesion of the corpus callosum. Follow-up DWI (F) and ADC maps (G) with T2WI (H), T1WI (I), and SWI sequences (J) after 2.5 months demonstrate resolution of the lesion after therapy.

On hospital day 1, she began to have hallucinations in addition to urinary retention, prompting neurology consultation. On neurologic examination, she was agitated and combative with a variable rate of speech. She had intermittent auditory hallucinations. Her attention fluctuated. She was able to follow 1- but not 2-step directions. Cranial nerve function was normal without clinical evidence of anosmia. Muscle tone was decreased with symmetric antigravity movement of all extremities. Sensation to light touch was intact throughout. Deep tendon reflexes were 1+ with absent ankle jerks. Contrast-enhanced MR imaging of the brain (Magnetom Avanto, 1.5T; Siemens) on hospital day 1 demonstrated an abnormal focal nonenhancing lesion with increased intensity on T2-weighted sequences and restricted diffusion in the splenium of the corpus callosum (Figure). Findings on MR imaging of the spine were normal. CSF studies were unremarkable (4 white blood cells (WBC)/ μL , glucose = 83 mg/dL, protein = 32 mg/dL). The electroencephalogram showed diffuse slowing without epileptiform discharges or seizures. On hospital day 2, the patient developed tachypnea requiring escalation of respiratory support to bilevel positive airway pressure, though no desaturation or hypoxemia was noted. The echocardiogram revealed depressed cardiac function with a left ventricular ejection fraction of 38%. Intravenous immunoglobulin (IVIG), 2 g/kg, was administered on hospital day 2, given concerns for atypical Kawasaki-like multisystem inflammatory state.

Extensive infectious and autoimmune investigations were performed. Respiratory viral panel and initial SARS-CoV-2 polymerase chain reaction (PCR) findings on admission were negative. The remainder of infectious evaluation was negative (CSF meningitis

panel, CSF and serum arboviral panels, serum viral studies including coxsackie A9 antibody, West Nile virus antibodies, human immunodeficiency virus antigen and antibody, enterovirus PCR, parvovirus B19 PCR, adenovirus PCR, and Epstein-Barr virus PCR). The serum autoimmune encephalopathy panel had a mildly elevated glutamic acid decarboxylase antibody (0.17 nmol/L) in the setting of recent IVIG administration and was thought to likely be a false-positive. Antinuclear antibody titer was elevated to 1:320 with a negative antibody reflex panel. The remainder of autoimmune work-up had negative findings (CSF oligoclonal bands, immunoglobulin G index, CSF autoimmune encephalopathy panel, serum thyroglobulin and antithyroid peroxidase antibodies, myelin oligodendrocyte glycoprotein antibody, aquaporin-4 antibody). Given the high level of suspicion, SARS-CoV-2 PCR was repeated on hospital day 3 and found to be positive. Qualitative COVID-19 immunoglobulin G in serum drawn on hospital day 2 before IVIG administration was also positive.

During the next few days, the patient's mental status improved gradually; however, she remained weak and tendon reflexes were persistently absent in the ankles. Creatine kinase was elevated (3600 U/L, normal = 50–275 U/L), and the electrodiagnostic study performed on hospital day 5 was unremarkable with no evidence of polyneuropathy or myopathy. On hospital day 6, respiratory support was weaned to nasal cannula, and she was able to stand unassisted. The repeat echocardiogram demonstrated return to normal cardiac function, and laboratory markers normalized. She was transferred out of the intensive care unit and discharged home 12 days following the initial presentation with follow-up in the pediatric neurology clinic scheduled. Furthermore, subsequent

research laboratory studies on the CSF did not detect the presence of SARS-CoV-2 by PCR. An indirect enzyme-linked immunosorbent assay for CSF showed increased levels of immunoglobulin M (1:64) for SARS-CoV-2 S1 and E (envelope) proteins (90% sensitivity, 89% specificity; courtesy of the Dr. William Hu Laboratory, Emory University).

DISCUSSION

We describe a pediatric case of a cytotoxic lesion of the corpus callosum (CLOCC) in the setting of MIS-C due to SARS-CoV-2 infection. CLOCCs have been well-described in a wide variety of conditions, including infection, seizure, toxins, nutritional deficiencies, and Kawasaki disease.^{12,13} Clinically, these lesions can manifest in a wide variety of nonspecific symptoms, such as cognitive impairment, seizures, hallucinations, delirium, dysarthria, and motor weakness.^{12,13} Clinically, the CLOCC may have contributed to her acute encephalopathy, causing delirium with prominent auditory hallucinations. MR imaging features of CLOCCs include increased signal intensity on FLAIR sequences and decreased signal intensity on T1-weighted sequences. Diffusion is reduced, and there is no contrast enhancement.¹³

CLOCCs associated with classic Kawasaki disease are a well-known entity. In hyperinflammatory states, macrophage activation leads to cytokine release that subsequently results in T-cell recruitment and breakdown of the blood-brain barrier. As the cytokine cascade invades the CNS, astrocytes are triggered to release excess glutamate, precipitating further cytokine release from microglia. The corpus callosum is especially vulnerable to this attack due to its high concentration of cytokine and glutamate receptors.¹³ In the index case, a CSF cytokine assay is pending.

SARS-CoV-2 has recently been demonstrated to result in MIS-C.²⁻⁶ This post or peri-infectious immune-mediated disorder leads to persistent fever, gastrointestinal symptoms, lymphadenopathy, and left-heart dysfunction often requiring inotropic support, such as seen in Kawasaki disease.³

The study patient developed MIS-C characterized by elevated serum interleukin 6 and cardiac enzymes, acutely reduced cardiac function, and neurologic dysfunction with neuroimaging showing CLOCC. Most interesting, this is similar to previously reported Kawasaki disease associated with CLOCCs.¹² We hypothesize that the SARS-CoV-2 postor peri-infectious immune-mediated disorder leads to MIS-C with neurologic dysfunction and CLOCC. This concept is further supported by absent SARS-CoV-2 PCR findings and elevated cytokines in the CSF as shown by Benameur et al.¹⁴ In this case, clinical improvement was noted with supportive care and IVIG. Repeat MR imaging 3 months following the initial illness demonstrated resolution of CLOCC, with no residual signal abnormality.

Reports continue to emerge of severe manifestations of COVID-19 in children, despite previous reports of mild illness. This case of MIS-C associated with COVID-19 highlights the potential of MR imaging abnormalities resulting in acute

encephalopathy causing delirium and emphasizes the need for careful consideration of possible neurologic complications of SARS-CoV-2 infection.

ACKNOWLEDGMENTS

We thank the patient and her family along with the physicians and nurses who provided clinical excellence and compassionate care.

REFERENCES

1. CDC COVID-19 Response Team. **Coronavirus disease 2019 in children—United States, February 12–April 2, 2020.** *MMWR Morb Mortal Wkly Rep* 2020;69:422–26 CrossRef Medline
2. Riphagen S, Gomez X, Gonzalez-Martinez C, et al. **Hyperinflammatory shock in children during COVID-19 pandemic.** *Lancet* 2020;395:1607–08 CrossRef Medline
3. Belhadjer Z, Meot M, Bajolle F, et al. **Acute heart failure in multisystem inflammatory syndrome in children (MIS-C) in the context of global SARS-CoV-2 pandemic.** *Circulation* 2020 May 17. [Epub ahead of print] CrossRef Medline
4. Licciardi F, Pruccoli G, Denina M, et al. **SARS-CoV-2-induced Kawasaki-like hyperinflammatory syndrome: a novel COVID phenotype in children.** *Pediatrics* 2020 May 21. [Epub ahead of print] CrossRef Medline
5. Dufort EM, Koumans EH, Chow Ej, et al; New York State and Centers for Disease Control and Prevention Multisystem Inflammatory Syndrome in Children Investigation Team. **Multisystem inflammatory syndrome in children in New York State.** *N Engl J Med* 2020;383:347–58 CrossRef Medline
6. Cheung EW, Zachariah P, Gorelik M, et al. **Multisystem inflammatory syndrome related to COVID-19 in previously healthy children and adolescents in New York City.** *JAMA* 2020 June 8. [Epub ahead of print] CrossRef Medline
7. Mao L, Jin H, Wang M, et al. **Neurologic manifestations of hospitalized patients with coronavirus disease 2019 in Wuhan, China.** *JAMA Neurol* 2020;77:683 CrossRef Medline
8. Dinkin M, Gao V, Kahan J, et al. **COVID-19 presenting with ophthalmoparesis from cranial nerve palsy.** *Neurology* 2020 May 1. [Epub ahead of print] CrossRef Medline
9. Scullen T, Keen J, Mathkour M, et al. **Coronavirus 2019 (COVID-19)-associated encephalopathies and cerebrovascular disease: the New Orleans Experience.** *World Neurosurg* 2020 May 28. [Epub ahead of print] CrossRef Medline
10. Hanafi R, Roger PA, Perin B, et al. **COVID-19 neurologic complication with CNS vasculitis-like pattern.** *AJNR Am J Neuroradiol* 2020 June 8. [Epub ahead of print] CrossRef Medline
11. Nicholson P, Alshafai L, Krings T. **Neuroimaging findings in patients with COVID-19.** *AJNR Am J Neuroradiol* 2020 June 11. [Epub ahead of print] CrossRef Medline
12. Takanashi J, Shirai K, Sugawara Y, et al. **Kawasaki disease complicated by mild encephalopathy with a reversible splenic lesion (MERS).** *J Neurol Sci* 2012;315:167–69 CrossRef Medline
13. Starkey J, Kobayashi N, Numaguchi Y, et al. **Cytotoxic lesions of the corpus callosum that show restricted diffusion: mechanisms, causes, and manifestations.** *Radiographics* 2017;37:562–76 CrossRef Medline
14. Benameur K, Agarwal A, Auld S, et al. **Encephalopathy and encephalitis associated with cerebrospinal fluid cytokine alterations and coronavirus disease, Atlanta, Georgia, USA.** *Emerg Infect Dis* 2020 June. [Epub ahead of print] CrossRef Medline

Location-Specific ASPECTS Paradigm in Acute Ischemic Stroke: A Systematic Review and Meta-Analysis

 S.M. Seyedsaadat,  A.A. Neuhaus,  J.M. Pederson,  W. Brinjikji,  A.A. Rabinstein, and  D.F. Kallmes



ABSTRACT

BACKGROUND: Weighting neuroimaging findings based on eloquence can improve the predictive value of ASPECTS, possibly aiding in informed treatment decisions for acute ischemic stroke.

PURPOSE: Our aim was to study the contribution of region-specific ASPECTS infarction to acute ischemic stroke outcomes.

DATA SOURCES: We searched MEDLINE and EMBASE for reports on ASPECTS in patients with acute ischemic stroke from 2000 to March 2019.

STUDY SELECTION: Two investigators independently reviewed articles and extracted data. Three-month poor functional outcome defined as mRS >2 was the primary end point.

DATA ANALYSIS: A random-effects meta-analysis was performed to compare the association between infarct and mRS >2 among ASPECTS regions. Subanalyses included the following: laterality of stroke (left/right), imaging technique (NCCT or advanced imaging with DWI, CTP, or CTA), and interventional technique (IV-tPA/conservative management or mechanical thrombectomy).

DATA SYNTHESIS: M6 infarct was most associated with poor functional outcome (OR = 3.26; 95% CI, 2.21–4.80; $P < .001$). Pair-wise comparisons of ASPECTS regions regarding the association between infarct and mRS >2 were not significant, with the exception of M6 versus lentiform ($P = .009$). However, pair-wise comparisons among ASPECTS regions were not significant among subgroup analyses.

LIMITATIONS: Limitations were the heterogeneity of time points, neuroimaging modalities, and interventional techniques; limited studies for inclusion; publication bias among some comparisons; and the retrospective nature of included studies.

CONCLUSIONS: Our study indicated an unequal impact of some ASPECTS subregions in predicting outcomes of patients with acute ischemic stroke. Stroke laterality, imaging technique, and interventional technique subgroup analyses showed no differences among ASPECTS regions in predicting outcome. Investigation in larger cohorts is required to assess the association of ASPECTS with acute ischemic stroke outcome.

ABBREVIATIONS: AIS = acute ischemic stroke; M1 = anterior inferior frontal lobe; M2 = temporal lobe; M3 = inferior parietal and posterior temporal lobe; M4 = anterior superior frontal lobe; M5 = precentral and superior frontal lobe; M6 = superior parietal lobe; MT = mechanical thrombectomy; PRISMA = Preferred Reporting Items for Systematic reviews and Meta-Analysis

Despite advances in endovascular therapy, patients with acute ischemic stroke (AIS) often have disabilities following treatment,

indicating the importance of continued refinement in patient-selection criteria.¹ Patient selection for reperfusion therapy is based on brain neuroimaging and time windows; however, standardized guidelines for establishing strict inclusion and exclusion criteria have not been established.^{2,3} Following recent findings from multiple landmark randomized clinical trials that established the advantages of endovascular therapy over medical therapy, the American Heart Association Guidelines recommended ASPECTS ≥ 6 as a cut-off point for treatment.⁴⁻⁹ However, recent studies have indicated that not only would most patients with baseline ASPECTS ≥ 6 achieve good functional outcome but also that up to 42% of successfully recanalized patients with low baseline ASPECTS (ASPECTS

Received January 21, 2020; accepted after revision July 7.

From the Departments of Radiology (S.M.S., W.B., D.F.K.), and Neurology (A.A.R.), Mayo Clinic, Rochester, Minnesota; Medical School (A.A.N.), University of Oxford, Oxford, England; Department of Veterinary and Biomedical Sciences (J.M.P.), University of Minnesota, Minneapolis, Minnesota; and Superior Medical Experts (J.M.P.), St. Paul, Minnesota.

Please address correspondence to John M. Pederson, MD, 1430 Avon St N, Saint Paul, MN 55117; e-mail: jpederson@supedit.com

 Indicates article with supplemental on-line tables.

 Indicates article with supplemental on-line photo.

<http://dx.doi.org/10.3174/ajnr.A6847>

≤5) can achieve good functional outcome.¹⁰ Conversely, patients with relatively high ASPECTS scores may have poor outcomes even after recanalization, highlighting the limited utility of this prognostic tool. These limitations may lead to withholding the criterion standard treatment from patients eligible for reperfusion therapy or may result in treating patients in whom endovascular therapy is unwarranted.

The occlusion site and the resulting ischemic regions are the most important predictors of anterior circulation AIS outcome.^{11,12} The limited predictive value of ASPECTS might be explained by the lack of consideration of functional eloquence across the 10 prespecified brain regions included in the scale. For example, the lentiform nucleus on the nondominant side and M2 on the dominant side contribute equally to the composite ASPECTS, though their functional roles are distinct. By addressing this limitation, better evidence-based clinical decision-making for patients with AIS could be achieved. Indeed, a growing number of studies are supporting the consideration of infarct location and stroke laterality for stroke-outcome prediction in addition to the total DWI or CT ASPECTS score.¹²⁻¹⁵ Consequently, we performed this systematic review and meta-analysis to study the relationship between infarct topography on individual ASPECTS regions and AIS outcomes.

MATERIALS AND METHODS

Literature Search

This study is reported according to the Preferred Reporting Items for Systematic reviews and Meta-Analysis (PRISMA) guidelines. We searched Ovid MEDLINE, Epub Ahead of Print, In-Process, and Other Non-Indexed Citations, Ovid EMBASE, Scopus EMBASE, PubMed, and Google Scholar using predefined keywords and synonyms for studies reporting ASPECTS scores in patients with AIS from 2000 (when ASPECTS was published) to the end of March 2019. An experienced librarian designed and performed the search strategy with input from the principal and senior investigators. We searched for key terms including “Alberta Stroke Program Early CT Score,” “ASPECTS,” and “ischemic stroke.” We also reviewed the reference lists of potentially included articles searching for additional relevant studies.

Study Eligibility

Human studies that reported 90-day clinical outcomes related to each individual ASPECTS score were included. We excluded studies with the following criteria: 1) case reports; 2) review articles; 3) technical notes, editorial comments, or letters; 4) non-English language; 5) conference abstracts with no separated results for each ASPECTS region; and 6) nonrelevant to the study topic. The primary outcomes of interest were associations between poor neurologic outcomes (mRS >2) and deficits in each ASPECTS region.

Data Extraction, Baseline Variables, and Outcome

Studies that were included on the basis of titles and abstracts were screened by a postdoctoral research fellow experienced in neurointerventional medicine. Subsequently, 2 medical doctors with 10 and 3 years of research experience in neuroradiology independently extracted and verified data from the full text of eligible articles. Disagreements were resolved by consensus or consulting with a senior coauthor. The following baseline information was collected

from each study: title, first author, year of publication, patient demographics, study design, number of patients, comorbidities, baseline NIHSS score, stroke laterality, ASPECTS, imaging technique, imaging time, and type of treatment. The primary end point of this study was poor functional outcome, defined as a mRS >2 at 3 months.

Risk of Bias Assessment

The Quality in Prognosis Studies (QUIPS; <https://abstracts.cochrane.org/2017-global-evidence-summit/systematic-reviews-prognostic-studies-ii-assessing-bias-studies>) tool was used to assess the risk of bias of the included studies.¹⁶ Using this risk-of-bias tool, we assessed each study on the basis of 6 criteria under 3 main categories, including 1) selection of study groups; 2) comparability of the study groups; and 3) ascertainment of the outcome. The risk of bias was classed as high, moderate, or low.

Studies with an unclear risk of bias were considered as moderate risk. The full risk-of-bias assessment can be found in On-line Table 1.

Statistical Analysis

ORs with 95% CIs were estimated for each study outcome. ORs were pooled across studies using a random-effects meta-analysis.¹⁷ Heterogeneity across studies that was not attributable to chance was assessed using the I^2 statistic, with $I^2 >50\%$ suggesting substantial heterogeneity.¹⁸ Publication bias across included studies was explored by funnel plots and testing their symmetry by using the Egger regression.¹⁹ Subgroup analyses were categorized by follow-up time, type of neuroimaging, stroke laterality, and mechanical thrombectomy (MT) versus tPA/conservative management subgroups. Brain topography maps indicating correlations between infarct in individual ASPECTS regions and poor neurologic outcome (mRS >2) are represented as β -coefficients from pooled ORs that were normalized to a maximum value of 1.0; thus, the ASPECTS region most strongly associated with poor neurologic outcome was assigned a value of 1.0, and the remaining regions were assigned values relative to the maximum and according to their respective β -coefficients. The analysis was performed using Excel for Office 365 (Version 1909; Microsoft) for basic summary statistics and data organization and Comprehensive Meta-Analysis, Version 3.3 (Biostat) for calculating odds ratios.

RESULTS

Literature Search

Among 1035 search results, 923 articles were duplicates, nonoriginal, or irrelevant to the aim of our study and were thus excluded after reviewing the title and abstracts alone. Of the remaining 112 eligible articles for full-text review, 103 were excluded because they did not provide the outcome for each individual ASPECTS region. Ultimately, 9 articles with 2249 unique patients were included in the random-effects meta-analysis.^{12-15,20-24} Figure 1 shows the PRISMA flow diagram of the process of screening and selection of the eligible studies.

Study and Patient Characteristics

Of the 9 included studies (On-line Table 1), 5 studies were multicenter and 4 were single-center. Three studies were retrospective, and 6 were prospectively designed. The mean age of patients was 67 years, with a slight male preponderance (50.5%). Six studies

evaluated patients using NCCT, while 2 used DWI and 1 used CTP for scoring ASPECTS. Six studies used admission neuroimaging reports, while 3 used images within 12–72 hours after stroke onset. Baseline characteristics of patients and studies are summarized in On-line Table 1.

Outcome

Region-Specific ASPECTS and Infarct Distribution. Overall, infarction was most frequent in the insula (52%) and lentiform nucleus (51.5%) and least frequent in the internal capsule (23.6%) and

M3 (27.9%). A summary of the overall distribution of infarction within ASPECTS regions is shown in On-line Table 2.

Publication Bias and Study Heterogeneity. The risk of bias was not significant (P value $> .05$) for pooled analyses of the M1–M6 and the caudate brain regions; however, the Egger regression showed significant publication bias regarding pooled assessments of the internal capsule, lentiform nucleus, and insula regions. Heterogeneity with regards to poor functional outcome among was low to moderate for all ASPECTS regions ($I^2 < 50\%$; Table).

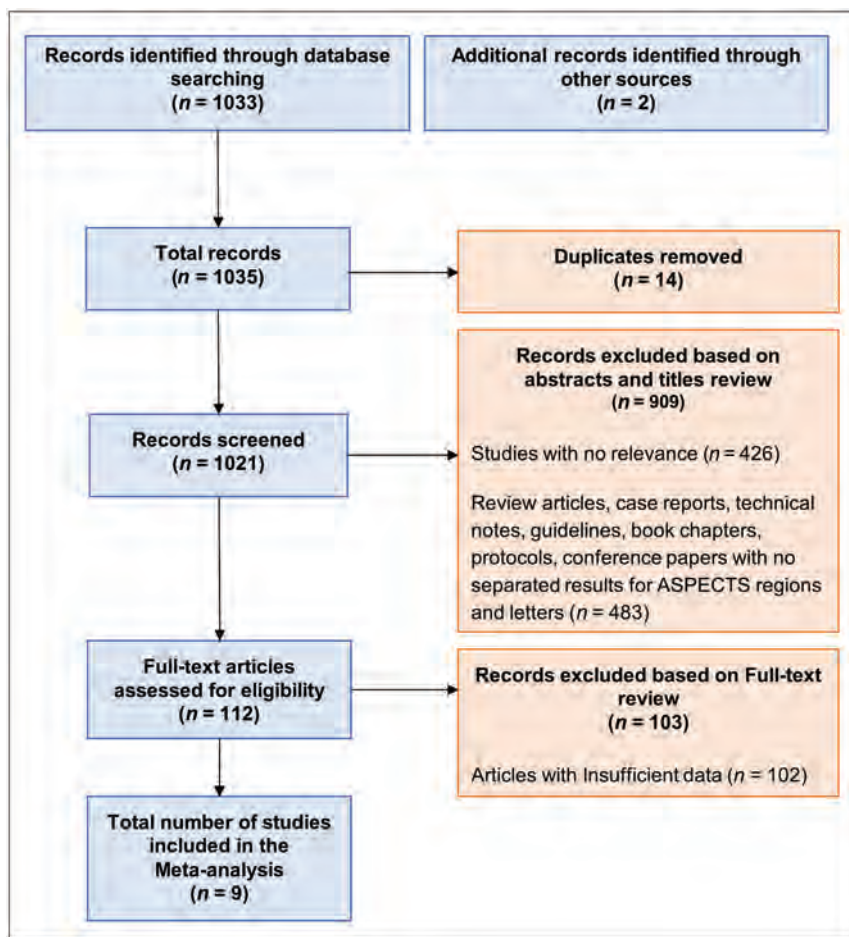


FIG 1. Flow diagram depicting the literature review, search strategy, and selection process using the PRISMA guidelines.

Region-Specific ASPECTS and Outcome.

Figure 2 shows a heat map that indicates the weight of each individual ASPECTS region infarct in predicting outcome, based on the β -coefficients from pooled ORs from included studies. A forest plot of pooled results for the effect of per-region ASPECTS on outcome is provided in Fig 3 (see the On-line Figure for forest plots showing both study-level and pooled results from each ASPECTS region). Across different time points (baseline versus follow-up) and among different modalities (NCCT, CTP, MR imaging), the strongest contribution to long-term outcome was from infarction of M6 (OR = 3.26; 95% CI, 2.21–4.80; $P < .001$). This was followed by M3 (OR = 2.42; 95% CI, 1.45–4.04; $P < .001$) and M2 (OR = 2.40; 95% CI, 1.56–3.66; $P < .001$). ORs from cortical areas were higher than those of subcortical regions in all cases. Overall, caudate (OR = 1.48; 95% CI, 0.94–2.33; $P = .092$) and lentiform (OR = 1.41; 95% CI, 0.98–2.02; $P = .065$) infarcts had the weakest association with poor outcome. Pair-wise comparisons between individual ASPECTS regions regarding the association between infarct and poor neurologic outcome were not significant, with the exception of M6 versus the lentiform nucleus ($P = .009$).

I^2 Statistics and the Egger weighted regression statistics

Region	I^2	I^2 Interpretation	Egger Intercept	Interpretation
M1	0.00%	Low heterogeneity	0.308 ($P = .372$)	Publication bias not significant
M2	19.56%	Low heterogeneity	0.532 ($P = .309$)	Publication bias not significant
M3	32.84%	Moderate heterogeneity	-0.026 ($P = .491$)	Publication bias not significant
M4	11.44%	Low heterogeneity	-0.207 ($P = .414$)	Publication bias not significant
M5	2.85%	Low heterogeneity	0.211 ($P = .373$)	Publication bias not significant
M6	18.21%	Low heterogeneity	-0.066 ($P = .468$)	Publication bias not significant
C	17.36%	Low heterogeneity	-1.290 ($P = .085$)	Publication bias not significant
IC	5.89%	Low heterogeneity	-1.372 ($P = .031$)	Significant publication bias
L	14.91%	Low heterogeneity	-1.406 ($P = .018$)	Significant publication bias
I	40.55%	Moderate heterogeneity	-1.670 ($P = .023$)	Significant publication bias

Note:—C indicates caudate; IC, internal capsule; L, lentiform; I, insula.

Sensitivity Analysis

NCCT versus Advanced Imaging (DWI, CTP, and CTA). Regarding the weights of individual ASPECTS regions in predicting outcome when ischemic, M6 (OR = 3.29; 95% CI, 1.68–6.45; $P < .001$) and M3 (OR = 2.75; 95% CI, 1.19–6.39; $P = .001$) infarctions on NCCT were stronger predictors of poor functional outcome than other ASPECTS regions (Fig 4). For NCCT ASPECTS, the caudate nucleus and insula had the weakest association with poor outcome. For DWI ASPECTS studies, M6 (OR 3.38; 95% CI, 2.07–5.50; $P < .001$) and M4 (OR 3.02; 95% CI, 1.82–5.00; $P < .001$) were more strongly associated with poor functional outcome than other regions (Fig 5). On DWI ASPECTS, lentiform and M3 infarctions had the weakest contribution to long-term function. Pair-wise comparisons among individual ASPECTS regions regarding the association between infarct and poor neurologic outcome were not significant in all cases when

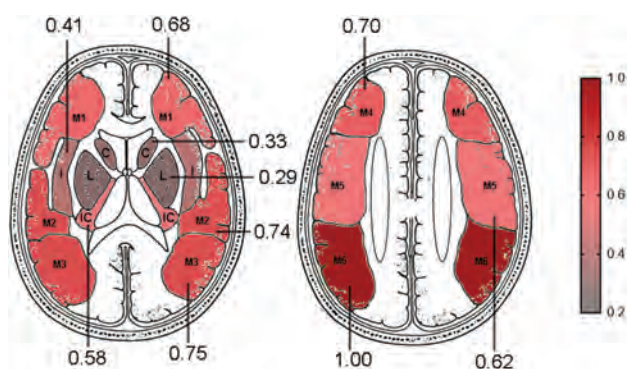


FIG 2. Topography and outcome brain map generated using the β -coefficients from pooled ORs for each region based on the random-effects model, indicating the relative weight of each ASPECTS region to M6, which was determined to be the region with greatest significant association with poor outcomes. The ASPECTS region most strongly associated with poor neurologic outcome was assigned a value of 1.0, and the remaining regions were assigned values relative to the maxima and according to their respective β -coefficients. Reprinted with permission from Barber et al.³⁴ C indicates caudate nucleus; L, lentiform nucleus; IC, internal capsule; I, insula.

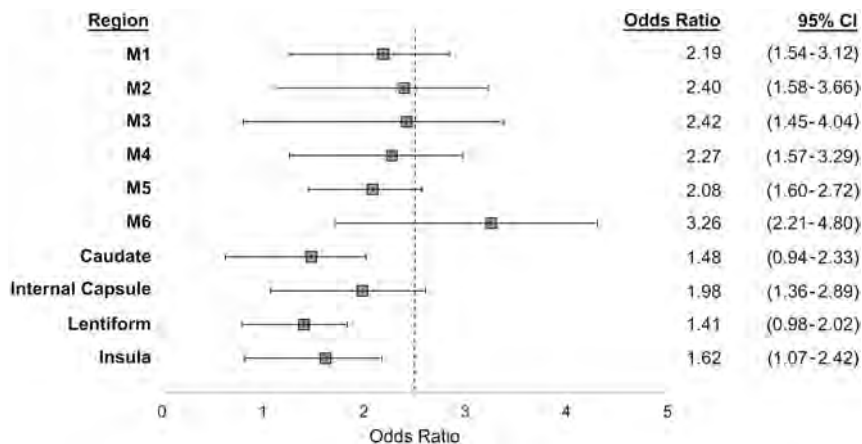


FIG 3. Forest plots demonstrating the contribution of individual ASPECTS regions, with 90-day functional outcome based on collective data of the 9 included studies.

categorizing by imaging technique. The results of pooled analyses from studies measuring region-specific infarcts in ASPECTS locations via CT or MR imaging and associated clinical outcome can be found in On-line Tables 3 and 4, respectively.

Laterality of Stroke. The pooled analysis of studies that evaluated infarcts by laterality showed that only M1, M5, and M6 were significantly associated with poor outcome on the right side (On-line Table 5). A brain topography map indicating the association between infarct in individual ASPECTS regions for right-sided strokes is presented in Fig 6. On the left side, the pooled analysis of observed data demonstrated that only the M1, M2, M4, M5, M6, and the lentiform nucleus were significantly associated with poor outcome (On-line Table 5). A brain topography map indicating the association among infarcts in individual ASPECTS regions for left-sided strokes is also presented in Fig 6. Pair-wise comparisons among individual ASPECTS regions regarding the association between infarct and poor neurologic outcome were not significant in all cases when categorizing by laterality.

MT versus tPA/Conservative Management. The pooled analysis of 4 studies that evaluated infarcts in patients who were treated with only MT showed that M4 (OR = 2.78; 95% CI, 1.75–4.4; $P < .001$) and M6 (OR = 2.59; 95% CI, 1.37–4.9; $P = .003$) were the strongest predictors of poor outcome (On-line Table 6). The pooled analysis of 2 studies that assessed infarcts in patients who were treated with only IV tPA/conservative management demonstrated that M6 (OR = 2.88; 95% CI, 1.4–5.91; $P = .004$) and M3 (OR = 2.76; 95% CI, 1.18–3.65; $P = .011$) were the strongest predictors of poor outcome (On-line Table 7).

DISCUSSION

The collective findings of the 9 studies in the current meta-analysis showed that infarcts in M6 were the strongest predictors of AIS outcome compared with other ASPECTS regions; however, these findings were only statistically significant with respect to infarcts in the lentiform nucleus. When analyzed by technique, infarction in M6 and M2 on NCCT and M6 and M4 on DWI had the greatest relative association with poor AIS outcome. In addition,

infarction in M6 and M2 on the right and M5 and M4 on the left side were associated with worse functional outcome. However, pair-wise comparisons among individual ASPECTS regions regarding the association between infarct and poor neurologic outcome were not statistically significant when categorizing by imaging technique or laterality. Sub-group analyses were performed to separately evaluate the association of ASPECTS location and outcome in the MT group versus IV tPA/conservative management groups. As shown in On-line Tables 6 and 7 for MT and tPA/conservative management, there were no substantial differences for

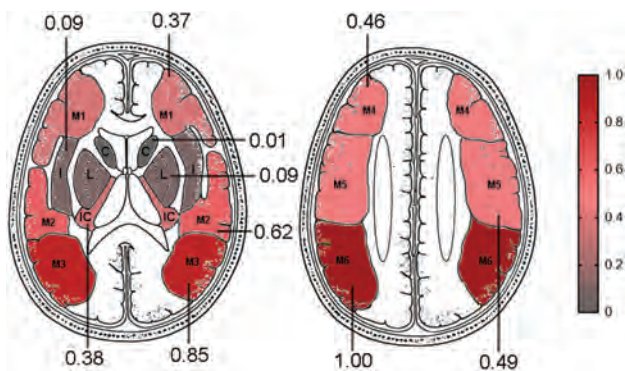


FIG 4. Topography and outcome brain map generated using the β -coefficients from pooled ORs for each region based on NCCT ASPECTS studies. Note that data shown are calculated from both hemispheres but are displayed unilaterally for clarity. The ASPECTS region most strongly associated with poor neurologic outcome was assigned a value of 1.0, and the remaining regions were assigned values relative to the maxima and according to their respective β -coefficients. Reprinted with permission from Barber et al.³⁴ C indicates caudate nucleus; L, lentiform nucleus; IC, internal capsule; I, insula.

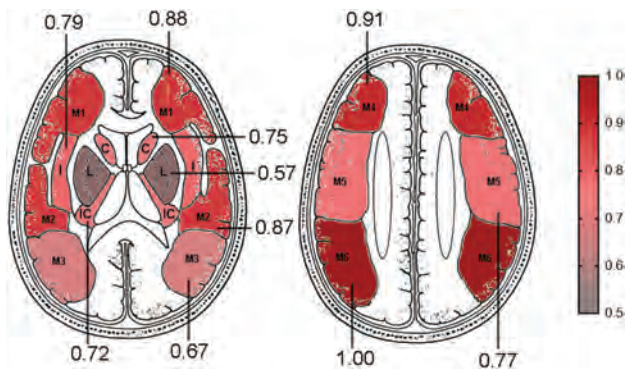


FIG 5. Topography and outcome brain map generated using the β -coefficients from pooled ORs for each region based on DWI ASPECTS studies. Note that data shown are calculated from both hemispheres but are displayed unilaterally for clarity. The ASPECTS region most strongly associated with poor neurologic outcome was assigned a value of 1.0, and the remaining regions were assigned values relative to the maxima and according to their respective β -coefficients. Reprinted with permission from Barber et al.³⁴ C indicates caudate nucleus; L, lentiform nucleus; IC, internal capsule; I, insula.

individual ASPECTS regions both within and between the subgroups.

Previous studies showed that proximal MCA occlusion is associated with worse outcome and worse recanalization than distal MCA occlusion;²⁵ and the corona radiata, internal capsule, and insula have a high influence on 30-day functional outcome following AIS.²⁶ In contrast, our results suggest that cortical areas may have a greater influence on long-term outcome.

In all 3 studies^{14,20,21} that used admission CT, the insula and lentiform nucleus were the 2 most frequently infarcted regions. However, among the 4 studies^{12,13,15,24} that used advanced neuroimaging modalities, insula followed by M5 were the most frequent regions. Most interesting, among all 10 ASPECTS regions, the internal capsule (10.4%) was the least common site of infarction on either admission or 12- to 72-hour CT or DWI.

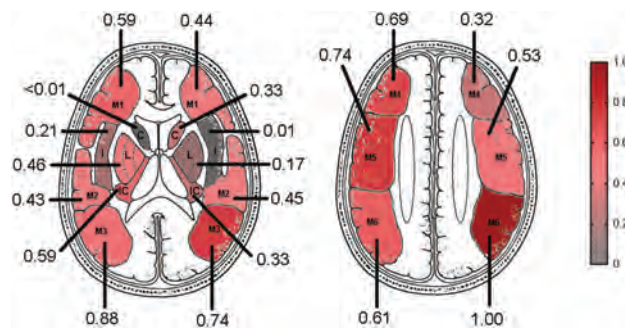


FIG 6. Topography and outcome brain map generated using the β -coefficients from pooled ORs for each region based on the laterality of the stroke. The ASPECTS region most strongly associated with poor neurologic outcome was assigned a value of 1.0, and the remaining regions were assigned values relative to the maxima and according to their respective β -coefficients. Reprinted with permission from Barber et al.³⁴ C indicates caudate nucleus; L, lentiform nucleus; IC, internal capsule; I, insula.

Although NCCT is easy-to-use, time-saving, and the most commonly accessible imaging technique for the evaluation of the extent of early ischemic change,^{4,27} early ischemic changes might not be readily apparent on CT.¹³ The lower sensitivity and interrater reliability of NCCT ASPECTS, compared with DWI ASPECTS, has led to the use of advanced neuroimaging tools with higher reliability and reproducibility, such as MR imaging and CTP in recent trials.^{23,28} The insula was the only region that was consistently associated with poor outcome in the 2 studies^{22,23} that used advanced imaging modalities on admission. The insula is the most vulnerable region to ischemia, and its infarction is associated with delayed recovery from aphasia and paralysis.^{29,30} M6 was not associated with poor outcome in advanced imaging studies on admission; however, with posttreatment DWI ASPECTS, M6 infarction was significantly associated with poor outcomes.^{15,24} In particular, the right-hemisphere M6 was significantly associated with poor clinical outcome, perhaps due to its association with neglect syndromes. This finding has potential implications for the treatment of patients with established M6 infarction because their outcome may be comparatively poor for a given total ASPECTS value.

A few previous studies^{12,13,15,24,31} have evaluated the association of ischemic involvement of different ASPECTS brain regions with functional outcome of patients with AIS separately in each hemisphere using laterality as a surrogate of hemispheric dominance. While the right M6 infarction and preservation were the most associated with poor and good outcome, respectively, no ASPECTS regions distributed by laterality were significantly different in terms of ischemic involvement. There was no specific location in the left hemisphere that was consistently associated with AIS outcome in any of these 4 studies.^{12,13,15,24}

Most interesting, despite our assumptions regarding the functional importance of the internal capsule, its infarction was significantly associated with poor outcomes in only 1 study after adjustment for other potential covariates. Furthermore, the posterior limb of the internal capsule is generally only infarcted in the setting of ICA occlusions involving the anterior choroidal artery origin, and ICA occlusions were found in only a minority of patients included in this study.³²

Tan et al³³ did not investigate infarction directly but analyzed CTA source images, defined as having equal (scoring 2), less prominent (scoring 1), or poor collaterals (scoring 0) compared with the contralateral side, resulting in a 20-point scale on the ASPECTS template. Having excluded the subcortical regions due to poor interrater reliability (see below), they found M5 collaterals to be the only significant predictor of good functional outcome. These results are supported with the poor outcome associated with M5 infarction that was reported by Haranhalli et al.²³

To date, few studies have evaluated the combined effects of per-region ASPECTS infarction on the outcome of patients with AIS. While our meta-analysis did not show significant differences for most pair-wise comparisons for individual ASPECTS regions in terms of meaningful contribution to ischemic change, we suspect that this was due to limited data and a high degree of heterogeneity within the available data. Nevertheless, the results of this meta-analysis could extend the findings of previous studies with relatively small sample sizes. By elucidating the association of each ASPECTS region with long-term outcome after infarction, it could be possible to devise an adjusted ASPECTS scale that weights each region in accordance with these correlations. Such a clinical scale could potentially enhance prognostication as well as inform treatment decisions for patients with AIS. However, future investigations with large cohorts are required to assess the association of ASPECTS with AIS outcome.

One potential limitation of our meta-analysis is that previous studies have not separately reported the relationship of individual ASPECTS regions with outcome based on the recanalization rate and extension of the infarct. Therefore, we were unable to evaluate the influence of the ASPECTS location in relation to the recanalized-versus-unrecanalized vessel and extension of the infarct subgroups. Future studies are recommended to evaluate the relationship of ASPECTS location with AIS outcome in different subgroups, including recanalization status and extent of the primary infarct.

CONCLUSIONS

Our review of 9 articles provided valuable pooled data regarding the importance of location-specific infarct in each ASPECTS region for AIS prognostication. The results of previous studies included in this review article indicate an uneven distribution of infarction in different ASPECTS regions and suggest that ASPECTS regions may be unequally weighted in predicting the outcome of patients with AIS. With regard to stroke location, right M6 infarction was the strongest predictor of poor outcome; however, there was no consensus regarding the most important prediction of stroke outcome in the left hemisphere. Creating and validating eloquence-weighted ASPECTS, taking into account the different neurologic functions of each ASPECTS region, could improve the prediction of prognosis and patient selection for embolectomy.

Data Sharing Statement

Data can be made available by contacting the corresponding author via email.

Disclosures: Seyed Mohammad Seyedasadat—RELATED: Grant: American Heart Association, Comments: I was awarded a 2-year postdoctoral research fellowship

grant by American Heart Association. Ain A. Neuhaus—RELATED: Grant: Oxford University Clinical Academic Graduate School, Comments: academic grant to support travel and living expenses as a visiting scholar at the Mayo Clinic. John M. Pederson—RELATED: Consulting Fee or Honorarium: Superior Medical Experts*; Fees for Participation in Review Activities Such as Data Monitoring Boards, Statistical Analysis, Endpoint Committees, and the Like: Superior Medical Experts*; Payment for Writing or Reviewing the Manuscript: Superior Medical Experts*; Provision of Writing Assistance, Medicines, Equipment, or Administrative Support: Superior Medical Experts*; UNRELATED: Board Membership: Superior Medical Experts*; Employment: Superior Medical Experts and Marblehead Medical*; Payment for Manuscript Preparation: Superior Medical Experts*; Patents (Planned, Pending or Issued): Nested Knowledge*; Stock/Stock Options: Superior Medical Experts, Nested Knowledge.* Alejandro A. Rabinstein—UNRELATED: Royalties: Elsevier, Wolters Kluwer, Springer Publishing, David F. Kallmes—RELATED: Grant: American Heart Association, Comments: Postdoctoral Fellow Award*; UNRELATED: Grants/Grants Pending: Medtronic, MicroVention, NeuroSigma, Neurogami Medical, Inc., Inera Therapeutics*; Patents (Planned, Pending or Issued): Patents related to balloon-guided technology*; Stock/Stock Options: Marblehead Medical, Superior Medical Experts. *Money paid to the institution.

REFERENCES

1. Spiotta AM, Vargas J, Hawk H, et al. **Impact of the ASPECT scores and distribution on outcome among patients undergoing thrombectomy for acute ischemic stroke.** *J Neurointerv Surg* 2015;7:551–58 CrossRef Medline
2. Pfaff J, Herweh C, Pham M, et al. **Mechanical thrombectomy in patients with acute ischemic stroke and lower NIHSS scores: recanalization rates, periprocedural complications, and clinical outcome.** *AJNR Am J Neuroradiol* 2016;37:2066–71 CrossRef Medline
3. Ryu CW, Shin HS, Park S, et al. **Alberta Stroke Program Early CT Score in the prognostication after endovascular treatment for ischemic stroke: a meta-analysis.** *Neurointervention* 2017;12:20–30 CrossRef Medline
4. Powers WJ, Derdeyn CP, Biller J, et al; American Heart Association Stroke Council. **2015 American Heart Association/American Stroke Association Focused Update of the 2013 Guidelines for the Early Management of Patients with Acute Ischemic Stroke Regarding Endovascular Treatment: a Guideline for Healthcare Professionals From the American Heart Association/American Stroke Association.** *Stroke* 2015;46:3020–35 CrossRef Medline
5. Campbell BC, Mitchell PJ, Kleinig TJ, et al; EXTEND-IA Investigators. **Endovascular therapy for ischemic stroke with perfusion-imaging selection.** *N Engl J Med* 2015;372:1009–18 CrossRef Medline
6. Berkhemer OA, Fransen PS, Beumer D, et al; MR CLEAN Investigators. **A randomized trial of intraarterial treatment for acute ischemic stroke.** *N Engl J Med* 2015;372:11–20 CrossRef Medline
7. Goyal M, Demchuk AM, Menon BK, et al; ESCAPE Trial Investigators. **Randomized assessment of rapid endovascular treatment of ischemic stroke.** *N Engl J Med* 2015;372:1019–30 CrossRef Medline
8. Jovin TG, Chamorro A, Cobo E, et al. REVASCAT Trial Investigators. **Thrombectomy within 8 hr after symptom onset in ischemic stroke.** *N Engl J Med* 2015;372:2296–2306 CrossRef Medline
9. Saver JL, Goyal M, Bonafe A, et al; SWIFT PRIME Investigators. **Stent-retriever thrombectomy after intravenous t-PA vs. t-PA alone in stroke.** *N Engl J Med* 2015;372:2285–95 CrossRef Medline
10. Broocks G, Hanning U, Flottmann F, et al. **Clinical benefit of thrombectomy in stroke patients with low ASPECTS is mediated by oedema reduction.** *Brain* 2019;142:1399–1407 CrossRef Medline
11. Sillanpaa N, Saarinen JT, Rusanen H, et al. **Location of the clot and outcome of perfusion defects in acute anterior circulation stroke treated with intravenous thrombolysis.** *AJNR Am J Neuroradiol* 2013;34:100–06 CrossRef Medline
12. Khan M, Baird GL, Goddeau RP Jr, et al. **Alberta Stroke Program Early CT Score infarct location predicts outcome following M2 occlusion.** *Front Neurol* 2017;8:98 CrossRef Medline
13. Sheth SA, Malhotra K, Liebeskind DS, et al. **Regional contributions to poststroke disability in endovascular therapy.** *Interv Neurol* 2018;7:533–43 CrossRef Medline

14. Phan TG, Demchuk A, Srikanth V, et al. **Proof of concept study: relating infarct location to stroke disability in the NINDS rt-PA trial.** *Cerebrovasc Dis* 2013;35:560–65 CrossRef Medline
15. Rangaraju S, Streib C, Aghaebrahim A, et al. **Relationship between lesion topology and clinical outcome in anterior circulation large vessel occlusions.** *Stroke* 2015;46:1787–92 CrossRef Medline
16. Hayden JA, van der Windt DA, Cartwright JL, et al. **Assessing bias in studies of prognostic factors.** *Ann Intern Med* 2013;158:280–86 CrossRef Medline
17. DerSimonian R, Laird N. **Meta-analysis in clinical trials.** *Control Clin Trials* 1986;7:177–88 CrossRef
18. Higgins JP, Thompson SG, Deeks JJ, et al. **Measuring inconsistency in meta-analyses.** *Br Med J* 2003;327:557–60 CrossRef Medline
19. Egger M, Davey Smith G, Schneider M, et al. **Bias in meta-analysis detected by a simple, graphical test.** *Br Med J* 1997;315:629–34 CrossRef Medline
20. Beare R, Chen J, Phan TG; VISTA-Acute Collaboration. **Collaboration VI-A: googling stroke ASPECTS to determine disability—exploratory analysis from VISTA-Acute Collaboration.** *PLoS One* 2015;10:e0125687 CrossRef Medline
21. Fukuda K, Keppetipola K, Davison M, et al. **Utility of aspects region location in predicting stroke thrombectomy outcomes.** In: *Proceedings of the Annual Meeting of the Society of NeuroInterventional Surgery*, Colorado Springs, Colorado. July 24–27, 2017;9Suppl 10:A3–A4
22. Payabvash S, Benson JC, Tyan AE, et al. **Multivariate prognostic model of acute stroke combining admission infarct location and symptom severity: a proof-of-concept study.** *J Stroke Cerebrovasc Dis* 2018;27:936–44 CrossRef Medline
23. Haranhalli N, Mbabuie N, Grewal SS, et al. **Topographic correlation of infarct area on CT perfusion with functional outcome in acute ischemic stroke.** *J Neurosurg* 2019;132:33–41 CrossRef Medline
24. Rosso C, Blanc R, Ly J, et al; ASTER Trial and Pitié-Salpêtrière Investigators. **Impact of infarct location on functional outcome following endovascular therapy for stroke.** *J Neurol Neurosurg Psychiatry* 2019;90:313–19 CrossRef Medline
25. Arnold M, Slezak A, El-Koussy M, et al. **Occlusion location of middle cerebral artery stroke and outcome after endovascular treatment.** *Eur Neurol* 2015;74:315–21 CrossRef Medline
26. Cheng B, Forkert ND, Zavaglia M, et al. **Influence of stroke infarct location on functional outcome measured by the modified Rankin scale.** *Stroke* 2014;45:1695–1702 CrossRef Medline
27. Sheth KN, Terry JB, Nogueira RG, et al. **Advanced modality imaging evaluation in acute ischemic stroke may lead to delayed endovascular reperfusion therapy without improvement in clinical outcomes.** *J Neurointerv Surg* 2013;5(Suppl 1):i62–65 CrossRef Medline
28. McTaggart RA, Jovin TG, Lansberg MG, et al; DEFUSE 2 Investigators. **Alberta stroke program early computed tomographic scoring performance in a series of patients undergoing computed tomography and MRI: reader agreement, modality agreement, and outcome prediction.** *Stroke* 2015;46:407–12 CrossRef Medline
29. Payabvash S, Kamalian S, Fung S, et al. **Predicting language improvement in acute stroke patients presenting with aphasia: a multivariate logistic model using location-weighted atlas-based analysis of admission CT perfusion scans.** *AJNR Am J Neuroradiol* 2010;31:1661–68 CrossRef Medline
30. Payabvash S, Souza LC, Kamalian S, et al. **Location-weighted CTP analysis predicts early motor improvement in stroke: a preliminary study.** *Neurology* 2012;78:1853–59 CrossRef Medline
31. Almekhlafi MA, Hill MD, Roos YM, et al. **Stroke laterality did not modify outcomes in the HERMES meta-analysis of individual patient data of 7 trials.** *Stroke* 2019;50:2118–24 CrossRef Medline
32. Baek BH, Lee YY, Kim SK, et al. **Pretreatment anterior choroidal artery infarction predicts poor outcome after thrombectomy in intracranial ICA occlusion.** *AJNR Am J Neuroradiol* 2019;40:1349–55 CrossRef Medline
33. Tan BY, Kong WY, Ngiam JN, et al. **The role of topographic collaterals in predicting functional outcome after thrombolysis in anterior circulation ischemic stroke.** *J Neuroimaging* 2017;27:217–20 CrossRef Medline
34. Barber PA, Demchuk DM, Zhang J, et al. **Validity and reliability of a quantitative CT score in predicting outcome of hyperacute stroke before thrombolytic therapy: ASPECTS Study Group. Alberta Stroke Programme Early CT Score.** *Lancet* 2000;355:1670–74 CrossRef Medline

Maximum AmbiGuity Distance for Phase Imaging in Detection of Traumatic Cerebral Microbleeds: An Improvement over Current Imaging Practice

K. Nael, J.C. Dagher, M.E. Downs, M.S. Fine, E. Brokaw, and D. Millward



ABSTRACT

BACKGROUND AND PURPOSE: Developed using a rigorous mathematic framework, Maximum AmbiGuity distance for Phase Imaging (MAGPI) is a promising phase-imaging technique that provides optimal phase SNR and reduced susceptibility artifacts. We aimed to test the potential of MAGPI over routinely used SWI in the detection of traumatic cerebral microbleeds in athletes diagnosed with mild traumatic brain injury.

MATERIALS AND METHODS: In this prospective study, 10 athletes (18–22 years of age, 3 women/7 men) diagnosed with mild traumatic brain injury were enrolled. Brain MRIs were performed using 3T MR imaging at 2 days, 2 weeks, and 2 months after head trauma. The imaging protocol included whole-brain T1 MPRAGE, T2 FLAIR, conventional SWI, and the MAGPI multiecho sequence. Phase images from MAGPI were put through a previously described SWI process to generate MAGPI-SWI. Conventional and MAGPI-SWI were assessed independently by a board-certified neuroradiologist for the presence of contusions and cerebral microbleeds. All participants had routine neuropsychological assessment and Visuo-Motor Tests.

RESULTS: At initial assessment, 4 of the participants had visuo-motor performance indicative of mild traumatic brain injury, and 4 participants had a Post-Concussion Symptom Scale score of >21, a threshold that has been used to define moderate impairment. Cerebral microbleeds were identified in 6 participants on MAGPI-SWI, 4 of whom had evidence of concurrent contusions on FLAIR imaging. None of these cerebral microbleeds were identified confidently on conventional SWI due to substantial distortion and susceptibility artifacts.

CONCLUSIONS: Optimal phase unwrapping with reduced susceptibility in MAGPI-SWI can clarify small microbleeds that can go undetected with routinely used conventional SWI.

ABBREVIATIONS: CMB = cerebral microbleeds; ImPACT = Immediate Post-Concussion Assessment and Cognitive Testing; MAGPI = Maximum AmbiGuity distance for Phase Imaging; mTBI = mild traumatic brain injury; PCSS = Post-Concussion Symptom Scale; VMT = Visuo-Motor Test

Approximately 75% of patients who sustain traumatic brain injury have had mild traumatic brain injury (mTBI).¹ Eclipsing the economic cost of mTBI (\$18 billion annually) is the profound health and social damage altering the lives of dynamic

individuals: Of 1.2 million patients with mTBI in the United States each year, 400,000 are children and adolescents, 300,000 are athletes, and 25,000 are members of the military.²

At initial assessment, however, most patients with mTBI have normal neuroimaging findings due to the subtle nature of traumatic changes.³ Typical imaging findings in mTBI include nonhemorrhagic small contusions and cerebral microbleeds (CMB).^{4,5}

Histopathologically, CMB represent focal accumulations of hemosiderin-containing macrophages with paramagnetic properties that can result in susceptibility-related signal loss on MR imaging, best depicted by T2*-weighted sequences or SWI.⁶⁻⁸

The introduction of the SWI sequence has resulted in incremental improvement in the detection of CMB compared with traditional T2*-weighted sequences.^{7,9} SWI combines the MR phase signal, in addition to the magnitude, to improve the contrast in the overall image. Despite these recent advances and improvement in the detection of CMB afforded by the increasing

Received June 3, 2019; accepted after revision July 7, 2020.

From the David Geffen School of Medicine (K.N.), University of California, Los Angeles, Los Angeles, California; Emerging Technologies (J.C.D., M.E.D., M.S.F., E.B.), MITRE Corporation, McLean, Virginia; and Athletics Department (D.M.), University of Arizona, Tucson, Arizona.

This work was supported by internal funding from the MITRE Corporation.

Paper previously presented at: Annual Meeting of the American Society of Neuroradiology, May 18–23, 2019; Boston, Massachusetts; Abstract 2458 and nominated for the ASNR Cornelius Dyke Award 2019.

Please address correspondence to Kambiz Nael, MD, David Geffen School of Medicine at UCLA, Department of Radiological Sciences, 757 Westwood Plaza, Suite 1621, Los Angeles, CA, 90095-7532; e-mail: Kambiznael@gmail.com; @kambiznael

Indicates open access to non-subscribers at www.ajnr.org

<http://dx.doi.org/10.3174/ajnr.A6774>

Table 1: Data collection schedule

Examination, Procedure Description	Duration (Min)	Visit 1 (2–3 Days)	Visit 2 ^a	Visit 3 (2 Weeks)	Visit 4 (1.5 Months)
Informed consent	15	X			
Demographics questionnaire	5	X			
MRI	35	X		X	X
Visuo-Motor tracking	10	X	X	X	X
ImPACT	25 (10 min for questionnaire only)	Questionnaire only	X	Questionnaire only	Questionnaire only
Total time (min)		75	35	55	55

Note:—X indicates task was performed, for example Visuo-motor tracking was performed in visit 1, 2, 3 and 4.

^a Visit 2: additional data collection was performed during a scheduled follow-up at a point in time determined by team of physicians (usually within 1 day from visit 1).

Table 2: Summary of clinical assessment and imaging findings in all 10 participants with presentation of mTBI

Participant No.	ImPACT (at Visit 2) ^a	PCSS	VMT ^c	FLAIR ^d (Contusions)	SWI ^d (CMB)	MAGPI-SWI ^d (CMB)
1	+	19	–	–	–	–
2	+	38 ^b	+	+	–	+
3	–	15	–	+	–	+
4	+	20	–	~	–	+
5	+	63 ^b	–	–	–	–
6	–	4	–	+	–	+
7	–	37 ^b	+	~	–	+
8	–	21	+	–	–	–
9	–	0	–	–	–	–
10	–	34 ^b	+	+	–	+

^a Plus sign in ImPACT indicates performance indicative of traumatic brain injury.

^b Score >21 indicates a threshold that has been used to define moderate impairment.

^c Plus sign in VMT indicates performance indicative of traumatic brain injury.

^d + indicates positive imaging finding (contusion on FLAIR) and (CMB on SWI or MAGPI-SWI). – indicates absence of imaging finding. ~ inconclusive evidence of injury on imaging.

use of high-field-strength MR imaging systems and dedicated imaging sequences such as SWI, our current imaging repertoire significantly underestimates the true number of CMB, with an estimated number of false-negative findings in the range of 50% compared with histopathologic analysis.¹⁰ Therefore, there is a pressing need for tools enabling more sensitive measurement of specific mTBI biologic markers.

One of the limitations of SWI is the inherent trade-off in the choice of the TE, which balances phase-image contrast and susceptibility-induced signal loss. While longer TEs are preferable to improve the sensitivity for detection of CMB, they result in increased susceptibility-induced signal-loss artifacts, which will be problematic near skull base structures. Techniques have been developed to address this concern: Multiecho SWI sequences attempt to provide the advantages of both short and long TEs but have suboptimal phase SNR at shorter TEs, phase wrapping at longer TEs, and increased noise due to the larger readout bandwidths required to accommodate multiple echoes in a TR.¹¹ While magnitude images have better SNR at shorter TEs and decay at longer TEs quasi-exponentially, the trade-off is more complex with phase images. With the MR imaging phase, the phase signal buildup is small at short TEs, thus yielding a poor phase SNR, even in the presence of a modest amount of noise. The phase SNR increases with the TE, reaches a maximum, and falls again as the magnitude of SNR decay increases the noise in the phase signal.¹¹ The maximum phase SNR is attained at TE = T2* of

tissue. Normally, the TE for the best phase SNR is chosen at around TE = 30 ms at 3T.^{11,12}

Recently, Maximum Ambiguity distance for Phase Imaging (MAGPI) has been developed as a promising multiecho phase imaging technique that addresses the trade-offs and concerns above.¹¹ By adopting a rigorous mathematic framework (maximum-likelihood), MAGPI has been shown to provide optimal phase SNR with no phase wrapping and reduced susceptibility artifacts.

We hypothesized that the improved phase image quality of MAGPI has the potential to overcome traditional SNR trade-offs associated with the SWI process. We tested this hypothesis clinically in the context of detection of traumatic CMB in athletes diagnosed with mTBI.

MATERIALS AND METHODS

Study Design

This was a longitudinal single-center prospective study that was approved by the University of Arizona institutional review board. Ten concussed adult athletes from the University's Athletics Department were enrolled after informed consent was obtained. Participants were then referred to the Athletics Department clinical team for postconcussion evaluation. Data collection took place at the following fixed intervals (visits) after head trauma (Table 1): 1) visit 1 within 2–3 days, 2) visit 2, an additional short data collection performed during a scheduled routine follow-up after concussion at a point in time determined by the team of physicians at the University's Athletic Department (usually within 1 day from visit 1), 3) visit 3 at 2 weeks, and 4) visit 4 at 1.5 months. The estimated overall duration for protocol completion per study participant per visit was approximately 75 minutes (Table 1).

Image Acquisition

Image acquisition was performed using a 3T MR imaging scanner (Magnetom Skyra; Siemens) during visits 1, 3, and 4 following head trauma. The imaging protocol included whole-brain T1 MPRAGE, T2 FLAIR, a conventional SWI sequence (TE = 30 ms, TR = 40 ms, flip angle = 15°, matrix size = 336 × 384 × 112, voxel size = 0.57 × 0.57 × 1.2 mm³, readout bandwidths = 80 Hz/pixel,

generalized autocalibrating partially parallel acquisition = 2× acceleration, acquisition time = 8 minutes 30 seconds), and the MAGPI multiecho sequence (TE = 9.34, 17.29, 22.19, 27.09, 32.12, 37.56 ms; TR = 40 ms; flip angle = 15°; matrix size = 552 × 608 × 72; voxel size = 0.37 × 0.37 × 2 mm³; readout bandwidths = 220 Hz/pixel; generalized autocalibrating partially parallel acquisition = 3× acceleration; acquisition time = 8 minutes 25 seconds). Note that MAGPI used a high-readout bandwidth to accommodate reading more echoes in the same TR. The acquisition time was kept the same between the single and multiecho sequences.

MAGPI Postprocessing

MR phase images were reconstructed from channel-uncombined multiecho complex data according to a prescription described previously.^{11,13} The reconstruction process was performed on a Linux computer with a GPU and required about 3 minutes to reconstruct the entire brain volume. The MAGPI phase images were subsequently put through the SWI process as previously described.¹⁴ The MAGPI-SWI process has the following differences: Because MAGPI generates channel-combined, phase-unwrapped, denoised phase images, we were able to apply the high-pass filtering required in SWI directly in the phase domain. Therefore, instead of using the previously homodyne filtering process, we applied a version of the bilateral high-pass-filtering process introduced previously.^{14,15} The advantages of such a filter are reduced blooming artifacts around tissue/bone areas.

Because MAGPI phase images inherently have a higher SNR than traditional phase images, we multiplied the phase mask only twice, instead of 4 times as in prior reports, while achieving contrast similar to that of traditional SWI.¹⁴ Multiplying the mask 4 times increases the contrast to include effects from cortical folds and other deeper gray matter structures. Multiplying the mask a lower number of times reduces the noise amplification associated with this operation.¹⁴

To enable a more direct comparison between the postprocessing steps of MAGPI-SWI and traditional SWI, we performed the following additional experiment: Using raw data from the MAGPI sequence, we created high-pass-filtered phase images according to both the traditional SWI process (as described by Haacke et al¹⁴) and the MAGPI-SWI process (as described above). The overall image quality of phase images in terms of delineation of iron-containing structures such as the red nuclei and substantia nigra was evaluated.

Clinical Assessment

A physician performed routine neuropsychologic assessment including Immediate Post-Concussion Assessment and Cognitive Testing (ImPACT questionnaire) and a novel Visuo-Motor Test (VMT).

ImPACT includes a series of tests used to assess cognitive functioning, including attention span, working memory, sustained and selective attention time, response variability, nonverbal problem-solving, and reaction time. The test also records the severity of 22 symptoms via a 7-point Likert scale (Post-Concussion Symptom Scale [PCSS]). All enrolled athletes also had a baseline (preconcussion) ImPACT test by the University's Athletics Department.

In addition, each participant underwent a VMT during every visit. During this visuomotor task, individuals were asked to modulate their grip force, as measured by a hand dynamometer, to match a variable target force, displayed visually on an iPad (Apple).¹⁶ A horizontal line is the target and moves up and down on the screen in a smooth-but-unpredictable manner. Individuals control the height of the vertical white bar by squeezing the dynamometer. Participants are asked to track the target for 3 minutes. Adequate training was provided to each individual before starting the test. The scores of the ImPACT test and the results of the VMT were recorded for each participant and used for analysis.

Image Analysis

Image analysis was performed by a board-certified neuroradiologist who was blinded to the type of SWI studies (conventional versus MAGPI). FLAIR, MAGPI-SWI, and conventional SWI source images (not the minimum-intensity-projection images)¹⁷ were available for detection of cerebral contusions and CMB. Special attention was paid to common areas for cerebral contusions, including the inferior frontal lobe and temporal poles.

In addition, the overall quality of phase images in terms of delineation of iron-containing structures such as the red nuclei and substantia nigra was evaluated using a typical 5-point Likert scale by the same neuroradiologist.

RESULTS

All study participants (18–22 years of age, 3 women and 7 men) were diagnosed with mTBI by a trained clinician. Participants completed 4 assessments at 2.2 ± 0.8 days (visit 1), 1.7 ± 2.1 days (visit 2), 15.2 ± 3.2 days (visit 3), and 44.3 ± 2.9 days (visit 4) after injury. At the initial assessment, participants had an average PCSS score of 25.1 ± 18.5. Four participants (Nos. 2, 5, 7, and 10) had a PCSS of >21, a threshold that has been used to define moderate impairment.¹⁸ The most commonly encountered symptom (≥3 severity) was fatigue, which was reported by 5 of the participants. At initial assessment, 4 participants (Nos. 2, 7, 8, and 10) had VMT performance indicative of mTBI based on a previously defined threshold.¹⁶ The mean PCSS for these 4 subjects was 32.5 ± 7.85 with 3 having a score of ≥21.

Two weeks postinjury, participants had an average PCSS score of 3.0 ± 6.0 with most (6 of 10) becoming completely asymptomatic at that time. No participants had a PCSS of >21. VMT performance was reduced below the threshold for 2 of the 4 individuals (only Nos. 8 and 10 remained above the threshold). According to the ImPACT scale, participants 1, 2, 4, and 5 showed signs of injury at this time point compared with baseline, with participants 2, 4, and 5 showing visual memory deficits, participants 1, 3, and 5 showing reaction time deficits, and participant 1 also presenting with visual-motor speed impairment.

Four participants had suspect areas of contusions on FLAIR images, evident by small foci of FLAIR hyperintensity (participants 2, 3, 6, and 10) (Fig 1). These findings persisted on all 3 imaging sessions. The same 4 participants also had indications of CMB on MAGPI-SWI, evident by foci of increased susceptibility. Two other participants (4 and 7) had CMB confirmed on MAGPI-SWI without associated contusions on FLAIR images (Fig 2). None of these CMB were noticed confidently on conventional SWI due to

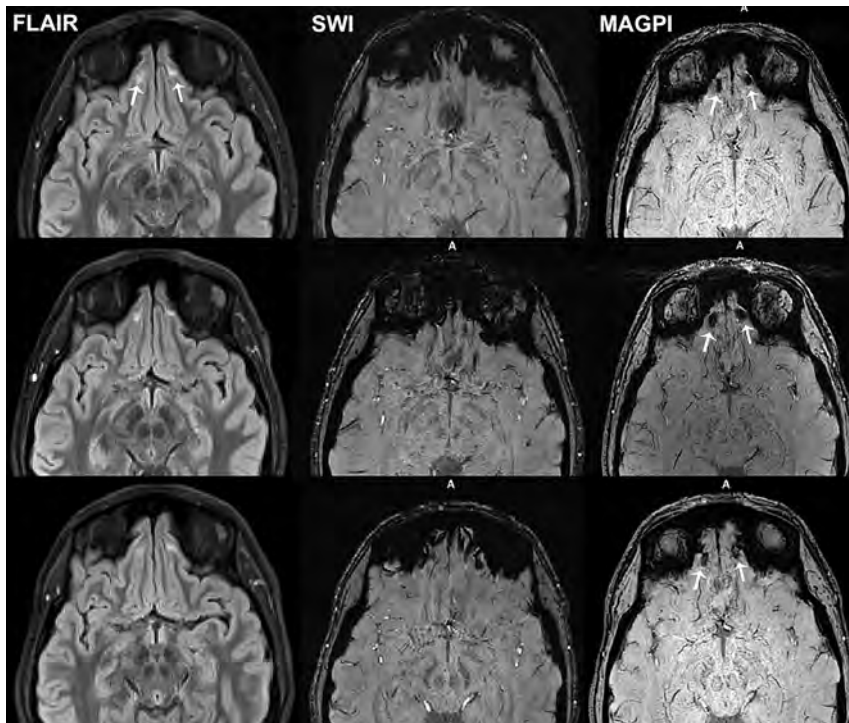


FIG 1. A softball player who had trauma to the forehead and nose (participant 2). The initial Post-Concussion Symptom Scale score was 38. MR images shown are FLAIR, SWI, and MAGPI-SWI obtained at 2 days (*upper row*), 2 weeks (*middle row*), and 6 weeks (*lower row*) after head trauma. There are small contusions in the inferior frontal lobes (*arrows on FLAIR*). In the same region, there are small foci of microbleeds on the MAGPI-SWI persistent on all 3 visits (*arrows on MAGPI*). The susceptibility signal on visit 3 (6 weeks after trauma) has slightly decreased. Please note that these microhemorrhages were exaggerated on the traditional SWI due to skull base–related susceptibility artifacts and thus were unnoticed. The Post-Concussion Symptom Scale score was 0 at 6-week follow-up.

substantial distortion and susceptibility artifacts in the region of the gyrus rectus (Figs 1 and 2). The results of clinical assessment and imaging findings are summarized in Table 2.

The image quality of the high-pass-filtered phase images in terms of delineating iron-containing structures was rated consistently higher (median score = 4) on images generated from MAGPI-SWI versus traditional SWI (median score, 2) ($P = .002$) (Fig 3).

DISCUSSION

To the best of our knowledge, this is the first work in which the advantages of MAGPI over phase-processing methods were evaluated in the context of SWI processing. The advantages of MAGPI over traditional phase-unwrapping and phase-processing algorithms in the raw phase domain have been previously reported.^{11,19} The superior performance of MAGPI in terms of phase SNR over other phase-estimation methods was reported in 2016.¹¹ Recently, MAGPI was shown to produce more repeatable and reproducible results than other methods used for phase unwrapping.¹⁹ Taking advantage of these technical improvements, we showed improved clinical performance of MAGPI-SWI in the detection of CMB compared with the currently used commercially available SWI.

CMB can be seen in roughly 30% of mTBI MR images.⁴ In mTBI, CMB can be seen in the inferior frontal and anterior temporal lobes where contusions can commonly occur due to close proximity to the calvaria and skull base. In cases with a history of more severe head trauma, CMB may be seen in deeper structures such as the corpus callosum and deep white matter tracts, often in association with diffuse axonal injury.^{20,21} Because of the paramagnetic hemosiderin and ferritin content, CMB can be detected by MR imaging as hypointense foci, most notably on T2*-weighted imaging.

Because the phase of the MR signal is much more sensitive than its magnitude to electromagnetic effects induced by CMB and iron deposits,^{22,23} SWI was proposed to use this added sensitivity in the phase domain to increase the contrast in the magnitude images.¹⁴ SWI typically uses a 3D high-spatial-resolution gradient recalled-echo sequence with prolonged TEs to enhance the susceptibility contrast. Postprocessing of SWI involves combining magnitude images with high-pass-filtered (homodyne) phase images to enhance the sensitivity for detecting CMB in comparison with conventional gradient recalled-

echo.^{24,25} Some investigators showed an increase of up to 50% in the detection of CMB using SWI over gradient recalled-echo.^{7,9} Despite the promise of SWI, compared with postmortem histopathologic analysis, at least half of CMB can still be missed with premortem clinical MR imaging.¹⁰

The contrast of SWI is limited by the inherent trade-off between phase noise and phase contrast. Specifically, the SWI phase mask generated from the high-pass-filtered phase image is repeatedly multiplied with the magnitude image. As the number of multiplications increases, the contrast from the phase increases, but so does the noise contribution. A balance between phase noise and phase contrast has been reported with around 4 multiplications.¹⁴ In addition to phase noise, other errors that limit the information with SWI are susceptibility-induced phase-wrapping errors, susceptibility-induced signal loss, phase-combination errors in parallel imaging, and phase-offset errors in multiecho sequences. It has been shown that MAGPI, a recently proposed phase estimation, attains optimal phase SNR because it optimally combines multichannel multiecho data in a maximum-likelihood fashion.¹¹ In fact, in this work, we observed overall improved image quality and better delineation of iron-containing structures on the high-pass-filtered phase images from MAGPI-SWI compared with conventional SWI afforded by a higher SNR and contrast-to-noise ratio obtained with MAGPI as reported by prior work using phantom analysis.^{11,13}

We specifically evaluated the performance of MAGPI in regions with susceptibility-induced signal loss related to the close proximity to the skull base such as the inferior frontal and anterior temporal lobes where contusions can commonly occur, and

we showed that MAGPI was able to recover clinical information in these regions. In 4 participants who had cerebral contusions on FLAIR imaging, we were able to identify CMB with MAGPI-SWI but not with the traditional SWI process (Fig 1). In addition,

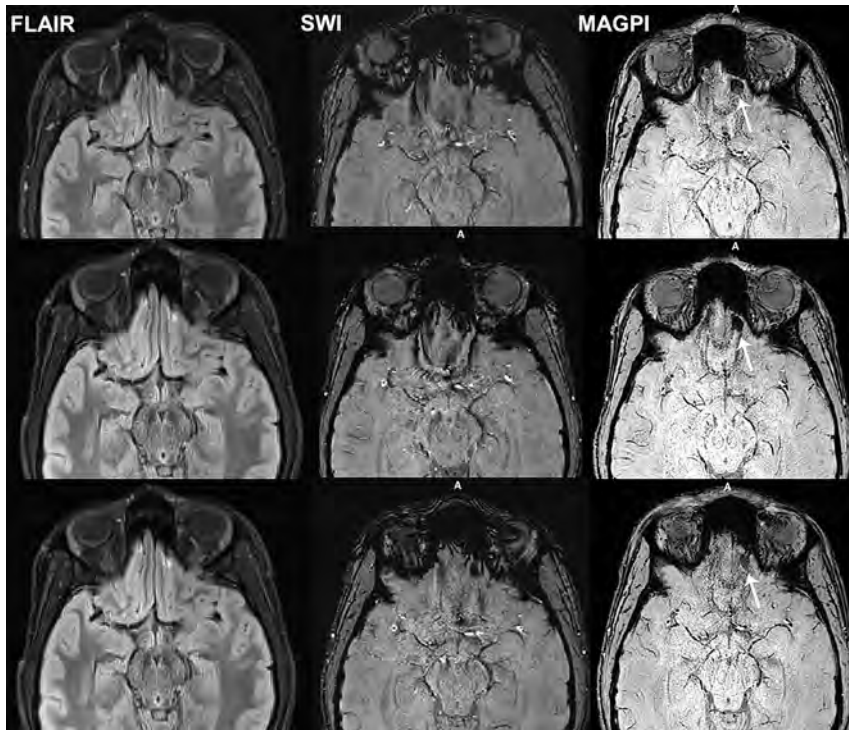


FIG 2. A football player who had helmet-to-helmet frontal trauma (participant 7). The initial postconcussion symptom scale was 37. MR images shown are FLAIR, SWI, and MAGPI-SWI obtained at 2 days (*upper row*), 2 weeks (*middle row*), and 6 weeks (*lower row*) after head trauma. There is a microbleed in the left inferior frontal lobe best seen on MAGPI-SWI (*arrows*). No definitive contusion is visible on FLAIR images. The susceptibility signal on visit 3 (6 weeks after trauma) has slightly decreased in size and intensity. Please note that this microbleed was exaggerated on the traditional SWI due to skull base-related susceptibility artifacts and thus less confidently noticed. The Post-Concussion Symptom Scale score was 0 at 6-week follow-up.

in 2 other individuals without clear evidence of cerebral contusions on FLAIR imaging, CMB were identified on MAGPI-SWI only (Fig 2). Three of 4 individuals who had evidence of brain injury on VMT (Nos. 2, 7, 8, and 10) and 3 of 4 subjects (Nos. 2, 5, 7, and 10) who had evidence of moderate impairment based on PCSS (PCSS > 21) had CMB on MAGPI-SWI. The clinical and prognostic implications of CMB and patients' symptoms in mTBI are still evolving, and future work is needed.^{26,27}

Note that the gains observed with MAGPI-SWI are due not only to improved phase unwrapping in regions of large phases but also to improved phase SNR throughout the image, especially in regions of signal drop. Applying phase-unwrapping methods alone with traditional SWI would have only modest incremental value in terms of improving image quality²⁸ for the following 3 reasons: First, phase-unwrapping algorithms do not recover signal loss due to susceptibility-induced dephasing. The improved SNR of MAGPI in such areas is the fundamental reason behind its improved ability to detect CMB in this study. Second, the homodyne processing used with SWI

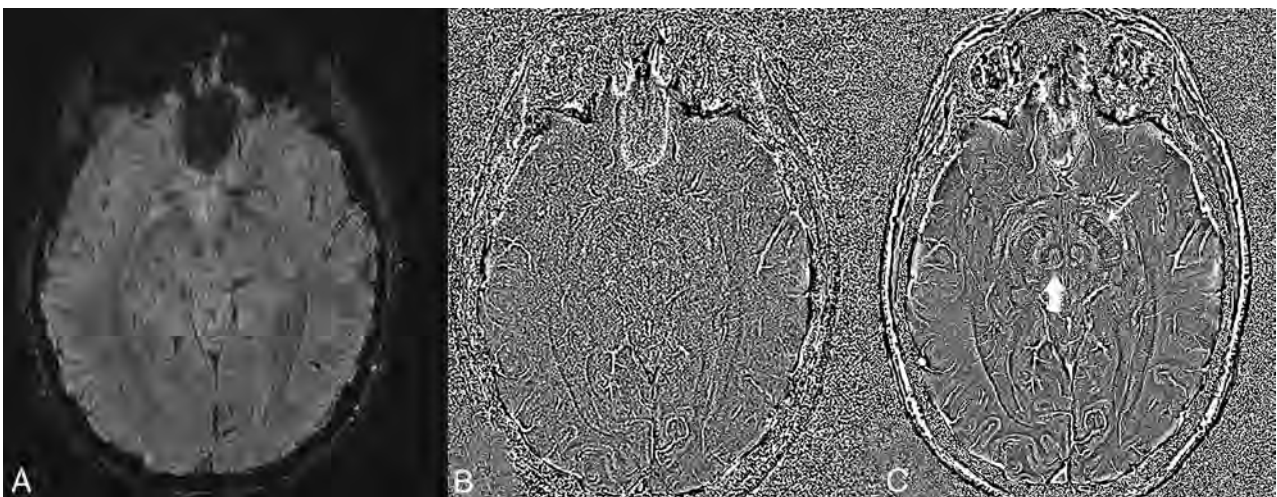


FIG 3. Magnitude (A) and high-pass-filtered phase images obtained from the MAGPI sequence and processed with traditional SWI (B) and MAGPI (C) to highlight the potential of MAGPI processing to capture the optimal phase SNR/contrast-to-noise ratio. Note the overall improved image quality and delineation of structural details seen on MAGPI (C), such as the red nucleus (*vertical arrow*) and substantia nigra (*oblique arrow*).

reduces the need for phase unwrapping because the high-pass-filtering operation applied in complex domains reduces the dynamic range of the underlying phase signal.²⁸ Nevertheless, phase unwrapping can be helpful in regions with a large magnetic susceptibility gradient where the large number of wraps is not resolved with the homodyne-filter operation alone.²⁸ The susceptibility-induced signal loss in those regions reduces the efficacy of phase unwrapping, however. Finally, phase unwrapping often results in inconsistent or incorrect estimates of the underlying phase, with different algorithms often yielding approximate and inconsistent solutions, each with their own advantages and disadvantages.^{11,19}

Our study has several limitations: first, the small sample size that can limit the power and generalizability of our results. Second, due to the study design and inclusion of patients with mTBI, we did not have CMB in deeper structures of the brain that are usually seen with more severe head trauma, often related to diffuse axonal injury. Some of our participants had cerebral contusions near the skull base structures where artifacts are common. However, having a longitudinal design and 3 sequential MR imaging studies helped and allowed the neuroradiologist to resolve any uncertainties about artifacts versus true CMB by examining the longitudinal data. Another potential limitation of this study is the absence of histopathology to confirm the true nature of detected CMB, though this is a common limitation related to a study of this type. The SWI and MAGPI sequences used in this study had slightly different spatial resolutions. The SWI protocol is a standard high-resolution protocol used in clinical scans with a section thickness of 1.2 mm to reduce susceptibility artifacts. However, the SWI still had substantial susceptibility artifacts near the skull base and inferior frontal lobes, which interfered with the diagnostic ability to confidently detect CMB. Despite its thicker section (2 mm), MAGPI-SWI was able to achieve improved susceptibility-induced dephasing artifacts throughout the brain compared with the traditional SWI process.

CONCLUSIONS

Optimal phase unwrapping with reduced susceptibility in MAGPI-SWI can clarify small microbleeds that can go undetected with routinely used conventional SWI.

Disclosures: Kambiz Nael—UNRELATED: Board Membership: Olea Medical, Comments: Medical Advisory Board. Joseph C. Dagher—UNRELATED: Patents (Planned, Pending or Issued): Inventor of the patented MAGPI technology, Comments: patent: MRI with Reconstruction of MR Phase Image; US patent 10,145,925; owner/applicant: Arizona Board of Regents, the University of Arizona. David Millward—RELATED: Grant: University of Arizona, Comments: cost of the MRI use time, research assistant salary to collect data and administer the MRI.*
*Money paid to the institution.

REFERENCES

- Centers for Disease Control and Prevention. Surveillance Report of Traumatic Brain Injury-related Emergency Department Visits, Hospitalizations, and Deaths—United States, 2014. 2019. https://www.cdc.gov/traumaticbraininjury/pdf/TBI-Surveillance-Report-FINAL_508.pdf. Accessed March 29, 2019
- Thurman DJ, Alverson C, Dunn KA, et al. Traumatic brain injury in the United States: A public health perspective. *J Head Trauma Rehabil* 1999;14:602–15 CrossRef Medline
- Xi G, Keep RF, Hoff JT. Mechanisms of brain injury after intracerebral haemorrhage. *Lancet Neurol* 2006;5:53–63 CrossRef Medline
- Hughes DG, Jackson A, Mason DL, et al. Abnormalities on magnetic resonance imaging seen acutely following mild traumatic brain injury: correlation with neuropsychological tests and delayed recovery. *Neuroradiology* 2004;46:550–58 CrossRef Medline
- Scheid R, Preul C, Gruber O, et al. Diffuse axonal injury associated with chronic traumatic brain injury: evidence from T2*-weighted gradient-echo imaging at 3 T. *AJNR Am J Neuroradiol* 2003;24:1049–56 Medline
- Fazekas F, Kleinert R, Roob G, et al. Histopathologic analysis of foci of signal loss on gradient-echo T2*-weighted MR images in patients with spontaneous intracerebral hemorrhage: evidence of microangiopathy-related microbleeds. *AJNR Am J Neuroradiol* 1999;20:637–42 Medline
- Goos JD, van der Flier WM, Knol DL, et al. Clinical relevance of improved microbleed detection by susceptibility-weighted magnetic resonance imaging. *Stroke* 2011;42:1894–1900 CrossRef Medline
- Greenberg SM, Vernooij MW, Cordonnier C, et al; Microbleed Study Group. Cerebral microbleeds: a guide to detection and interpretation. *Lancet Neurol* 2009;8:165–74 CrossRef Medline
- Uetani H, Hirai T, Hashimoto M, et al. Prevalence and topography of small hypointense foci suggesting microbleeds on 3T susceptibility-weighted imaging in various types of dementia. *AJNR Am J Neuroradiol* 2013;34:984–89 CrossRef Medline
- Haller S, Montandon ML, Lazeyras F, et al. Radiologic-histopathologic correlation of cerebral microbleeds using pre-mortem and post-mortem MRI. *PLoS One* 2016;11:e0167743 CrossRef Medline
- Dagher J, Nael K. MAGPI: a framework for maximum likelihood MR phase imaging using multiple receive coils. *Magn Reson Med* 2016;75:1218–31 CrossRef Medline
- Wu B, Li W, Avram AV, et al. Fast and tissue-optimized mapping of magnetic susceptibility and T2* with multi-echo and multi-shot spirals. *Neuroimage* 2012;59:297–305 CrossRef Medline
- Dagher J, Nael K. MR phase imaging with bipolar acquisition. *NMR Biomed* 2017;30: CrossRef Medline
- Haacke EM, Xu Y, Cheng YC, et al. Susceptibility-weighted imaging (SWI). *Magn Reson Med* 2004;52:612–18 CrossRef Medline
- McPhee KC, Denk C, Al-Rekabi Z, et al. Bilateral filtering of magnetic resonance phase images. *Magn Reson Imaging* 2011;29:1023–29 CrossRef Medline
- Fine MS, Lum PS, Brokaw EB, et al. Dynamic motor tracking is sensitive to subacute mTBI. *Exp Brain Res* 2016;234:3173–84 CrossRef Medline
- Cordonnier C, Potter GM, Jackson CA, et al. Improving interrater agreement about brain microbleeds: development of the Brain Observer MicroBleed Scale (BOMBS). *Stroke* 2009;40:94–99 CrossRef Medline
- Chen JK, Johnston KM, Collie A, et al. A validation of the post concussion symptom scale in the assessment of complex concussion using cognitive testing and functional MRI. *J Neurol Neurosurg Psychiatry* 2007;78:1231–38 CrossRef Medline
- Keenan KE, Berman BP, Carnicka S, et al. Validating the acquisition and phase estimation process for magnetic susceptibility measurement. In: *Proceedings of the 5th International Workshop on MRI Phase Contrast & Quantitative Susceptibility Mapping*, Seoul, Korea. September 25–28, 2019
- Schrag M, Greer DM. Clinical associations of cerebral microbleeds on magnetic resonance neuroimaging. *J Stroke Cerebrovasc Dis* 2014;23:2489–97 CrossRef Medline
- Scheid R, Walther K, Guthke T, et al. Cognitive sequelae of diffuse axonal injury. *Arch Neurol* 2006;63:418–24 CrossRef Medline
- Ayaz M, Boikov AS, Haacke EM, et al. Imaging cerebral microbleeds using susceptibility weighted imaging: one step toward detecting vascular dementia. *J Magn Reson Imaging* 2010;31:142–48 CrossRef Medline
- Schweser F, Sommer K, Deistung A, et al. Quantitative susceptibility mapping for investigating subtle susceptibility variations in the human brain. *Neuroimage* 2012;62:2083–2100 CrossRef Medline

24. Tong KA, Ashwal S, Holshouser BA, et al. **Hemorrhagic shearing lesions in children and adolescents with posttraumatic diffuse axonal injury: improved detection and initial results.** *Radiology* 2003;227:332–39 CrossRef Medline
25. Nandigam RN, Viswanathan A, Delgado P, et al. **MR imaging detection of cerebral microbleeds: effect of susceptibility-weighted imaging, section thickness, and field strength.** *AJNR Am J Neuroradiol* 2009;30:338–43 CrossRef Medline
26. Wang X, Wei XE, Li MH, et al. **Microbleeds on susceptibility-weighted MRI in depressive and non-depressive patients after mild traumatic brain injury.** *Neurol Sci* 2014;35:1533–39 CrossRef Medline
27. Huang YL, Kuo YS, Tseng YC, et al. **Susceptibility-weighted MRI in mild traumatic brain injury.** *Neurology* 2015;84:580–85 CrossRef Medline
28. Li N, Wang WT, Sati P, et al. **Quantitative assessment of susceptibility-weighted imaging processing methods.** *J Magn Reson Imaging* 2014;40:1463–73 CrossRef Medline

Dynamic CTA-Derived Perfusion Maps Predict Final Infarct Volume: The Simple Perfusion Reconstruction Algorithm

 C.C. McDougall,  L. Chan,  S. Sachan,  J. Guo,  R.G. Sah,  B.K. Menon,  A.M. Demchuk,  M.D. Hill,  N.D. Forkert,  C.D. d'Esterre, and  P.A. Barber



ABSTRACT

BACKGROUND AND PURPOSE: Infarct core volume measurement using CTP (CT perfusion) is a mainstay paradigm for stroke treatment decision-making. Yet, there are several downfalls with cine CTP technology that can be overcome by adopting the simple perfusion reconstruction algorithm (SPIRAL) derived from multiphase CTA. We compare SPIRAL with CTP parameters for the prediction of 24-hour infarction.

MATERIALS AND METHODS: Seventy-two patients had admission NCCT, multiphase CTA, CTP, and 24-hour DWI. All patients had successful/quality reperfusion. Patient-level and cohort-level receiver operator characteristic curves were generated to determine accuracy. A 10-fold cross-validation was performed on the cohort-level data. Infarct core volume was compared for SPIRAL, CTP–time-to-maximum, and final DWI by Bland-Altman analysis.

RESULTS: When we compared the accuracy in patients with early and late reperfusion for cortical GM and WM, there was no significant difference at the patient level (0.83 versus 0.84, respectively), cohort level (0.82 versus 0.81, respectively), or the cross-validation (0.77 versus 0.74, respectively). In the patient-level receiver operating characteristic analysis, the SPIRAL map had a slightly higher, though nonsignificant ($P < .05$), average receiver operating characteristic area under the curve (cortical GM/WM, $r = 0.82$; basal ganglia = 0.79, respectively) than both the CTP–time-to-maximum (cortical GM/WM = 0.82; basal ganglia = 0.78, respectively) and CTP-CBF (cortical GM/WM = 0.74; basal ganglia = 0.78, respectively) parameter maps. The same relationship was observed at the cohort level. The Bland-Altman plot limits of agreement for SPIRAL and time-to-maximum infarct volume were similar compared with 24-hour DWI.

CONCLUSIONS: We have shown that perfusion maps generated from a temporally sampled helical CTA are an accurate surrogate for infarct core.

ABBREVIATIONS: AUC = area under the curve; EVT = endovascular therapy; mCTA = multiphase CTA; ROC = receiver operating characteristic; SPIRAL = simple perfusion reconstruction algorithm; Tmax = time-to-maximum

Endovascular therapy (EVT) for acute ischemic stroke can lead to remarkable results for improving stroke outcome.¹⁻³ The emphasis on fast treatment decisions for patients with acute ischemic stroke requires simple, quick, and accurate neuroimaging of patients for detection of early ischemic changes. Additionally, image-processing software that can provide this information should be preferably inexpensive and easily accessible to all stroke

centers, both primary and comprehensive, around the world. CT is the most commonly used and practical imaging technique for assessing patients with acute stroke, but sensitivity and reliability are only modest, even in the hands of stroke specialists. Software systems, including perfusion analysis, to identify ischemic tissue using advanced imaging paradigms are now recommended by the American Stroke Association and have been used successfully in several clinical trials, including selection of patients for EVT up to 24 hours after stroke.⁴⁻⁶

Received April 21, 2020; accepted after revision July 7.

From the Department of Clinical Neurosciences (C.C.M., R.G.S., B.K.M., A.M.D., M.D.H., C.D.d., P.A.B.), Calgary Stroke Program; Department of Radiology (C.C.M., B.K.M., N.D.F., C.D.d.E., P.A.B.); Hotchkiss Brain Institute (C.C.M., B.K.M., A.M.D., M.D.H., N.D.F., C.C.d.E., P.A.B.); and Department of Clinical Neurosciences (C.C.M., L.C., S.S., J.G., R.G.S., B.K.M., A.M.D., M.D.H., N.D.F., C.C.d.E.); Alberta Children's Hospital Research Institute (N.D.F.), University of Calgary, Calgary, Alberta, Canada; and Seaman Family Centre (C.C.M., R.G.S., B.K.M., A.M.D., M.D.H., C.D.d.E., P.A.B.), Foothills Medical Centre, Calgary, Alberta, Canada.

This work was supported by the Heart and Stroke Foundation of Canada by a grant-in-aid for the REPERFUSE study.

Please address correspondence to Philip A. Barber, MB, ChB, MD, FRCP (Edinburgh), FRCP(C), Calgary Stroke Program, Department of Clinical Neurosciences, University of Calgary, 3330 Hospital Dr NW, Calgary, AB T2N 4N1, Canada; e-mail: pabarber@ucalgary.ca

 Indicates open access to non-subscribers at www.ajnr.org
<http://dx.doi.org/10.3174/ajnr.A6783>

Infarct core volume measurement using CTP at patient admission is the mainstay for stroke-treatment decision-making.^{4,6,7} CTP improves the detection of ischemia, contributing to the improved accuracy for stroke diagnosis.⁸ Also, there are several potential downsides with cine CTP technology, which include increased radiation dose to the patient; an extra bolus of CT contrast agent, which could cause renal complications; the additional time to acquire and process the perfusion data; the requirement of expensive software and licenses; the lack of standardization across vendor platforms; and limited craniocaudal coverage, to name a few. Therefore, there is a pressing need to improve the accessibility and practicality of brain perfusion imaging while maintaining the diagnostic and prognostic accuracy for radiologic outcome (final infarct volume).

The simple perfusion reconstruction algorithm (SPIRAL) described in this article is a method for analyzing low-temporal-resolution, contrast-enhanced, spiral/helical CT brain scans to obtain perfusion parameter maps of the brain, providing perfusion maps comparable with a cine CTP acquisition for predicting infarct core. Using a group of patients undergoing endovascular treatment with successful reperfusion, we sought to determine the accuracy of SPIRAL perfusion and CT perfusion images for follow-up of infarction confirmed on 24- to 48-hour diffusion-weighted MR imaging.

MATERIALS AND METHODS

Patients

A post hoc analysis was performed using data from the Measuring Collaterals With Multi-phase CT Angiography in Patients With Ischemic Stroke (PROVE-IT) and Endovascular Treatment for Small Core and Proximal Occlusion Ischemic Stroke (ESCAPE) studies from the Calgary Stroke Program.^{1,9} Patients with acute ischemic stroke were included in the study if they presented within 12 hours from last seen healthy. Inclusion criteria for the present study were as follows: 1) older than 18 years of age; 2) known symptom-onset time; 3) any occlusion of the anterior circulation, which could be targeted for EVT; 4) successful reperfusion assessed by digital subtraction angiography at end of the EVT; and 5) next-day follow-up DWI between 2 and 48 hours of admission. A modified TICI score of 2b or 3 was considered successful reperfusion.^{1,2} Demographic and clinical characteristics, medical history, and any relevant workflow time intervals were collected prospectively. The study was approved by the local ethics board of The University of Calgary.

Image Acquisition

At admission, all patients had a standard NCCT scan (5-mm section thickness), a head/neck multiphase CTA (mCTA), and cine CTP with a craniocaudal coverage of 8 cm. The mCTA acquisition has been described previously.⁹ Briefly, 80 mL of an iodinated contrast agent was injected at a rate of 5 mL/s followed by a saline flush of 50 mL at 6 mL/s. For the first phase (7 seconds), the aortic arch-to-vertex helical scan was timed to be in the peak arterial phase by triggering the scan with contrast bolus tracking. The second phase was acquired after a delay of 4 seconds, allowing the table to reposition to the skull base. Scan duration for the next 2 additional phases was 3.4 seconds. Images were reconstructed into 0.625-mm section thickness. For the cine CTP protocol, 45 mL of CT contrast agent (ioversol, Optiray 320; Mallinckrodt) was power-injected at 4.5 mL/s followed by a saline chase of 40 mL at 6 mL/s. Sections of 8-cm

thickness were acquired at 5-mm section thickness. Scanning began after a delay of 5 seconds from contrast injection in up to 2 phases (scanning intervals): the first phase every 2.8 seconds for 60 seconds and an additional second phase every 15 seconds for 90 seconds (total scan time = 150 seconds).

Between 24 and 48 hours of treatment, a clinical DWI scan was acquired using 3T MR imaging (Signa VH/i; GE Healthcare) (flip angle = 90°, single-shot echo-planar sequence, $b = 0$ s/mm⁻² and isotropic $b = 1000$ s/mm⁻², TR = 9000 ms, TE = minimum [80–90 ms], FOV = 240 mm, section thickness = 5.0 mm with a 0- or 2-mm gap).

Image Processing

SPIRAL Perfusion Functional Map Processing. To generate SPIRAL functional images, we registered each phase of the mCTA to the NCCT using a rigid registration. The NCCT was used to determine the baseline Hounsfield unit for each region of the brain in a respective patient. The dynamic series generated from the NCCT and mCTA was postprocessed with the following steps: 1) The skull and ventricles were removed using per-patient Hounsfield unit thresholds on the NCCT (ventricles = 0–12 HU, skull > 60 HU). Time-attenuation curves were created for each voxel after subtraction of the baseline NCCT Hounsfield unit values, a normalization technique common in perfusion processing.⁷ Deconvolution and non-deconvolution approaches were used to generate functional maps of TTP or T0 (time to peak of impulse residue function), CBF, MTT, and CBV.^{7,10} Singular-value decomposition deconvolution was performed for each tissue voxel after selection of an arterial input function from the internal carotid artery.⁷ For the nondeconvolution approach, we created 5 hemodynamic functional maps: 1) TTP = the mCTA phase with the highest magnitude Hounsfield unit; 2) phase 1 blood flow = the slope of the first and second Hounsfield unit magnitudes from the mCTA; 3) phase 2 blood flow = the slope of the second and third Hounsfield unit magnitudes from the mCTA; 4) flow average = the average of 2 and 3; 5) blood volume = integral of the of time-attenuation curves. For all deconvolution and nondeconvolution functional maps, collinearity was determined with a variance inflation factor; any metric with a variance inflation factor of >4 was removed from the analysis. A backward stepwise logistic regression model was trained using the remaining functional maps to create the SPIRAL functional map. The logistic regression coefficients were varied inside an exponential function to iteratively evaluate the discriminatory ability of the model to distinguish infarction and noninfarction at a voxel-level. The equation that is fit to the data is shown below:

$$P = \frac{1}{1 + e^{-(A + BX + CY + DZ + EW)}},$$

where P is the probability of a binomial outcome (between 0 and 1), A is a scaling constant, X and B are the TTP map and the corresponding coefficient, Y and C are the CBF map and the corresponding coefficient, Z and D are the MTT map and the corresponding coefficient, and E and W are the deconvoluted T0 map and associated coefficient.

Perfusion Functional Map Processing. In a subset of 40 patients, CTP functional maps were processed by an expert (C.D.d.E.)

using commercially available deconvolution software (CT Perfusion 4D; GE Healthcare). For each study, the arterial input function was manually selected from the basilar artery or contralateral ICA using a 2 voxel \times 2 voxel (in-section) ROI. For all arterial input functions, baseline-to-peak height Hounsfield unit differences matched those from the respective sagittal sinus. Absolute maps of cerebral blood flow [$\text{mL} \times \text{min}^{-1} \cdot (100 \text{ g})^{-1}$] \times MTT (seconds) start time of the impulse residue function (ie, delay of the tissue time-density curve with respect to the arterial input function) (T_0 ; second) and time-to-maximum ($T_{\text{max}} = T_0 + 0.5 \times \text{MTT}$ (seconds)) were calculated by deconvolution of tissue time-density curves and the arterial input function using a delay-insensitive algorithm (CT Perfusion 4D). Average maps were created by averaging the serial (dynamic) CTP images over the duration of the first pass of contrast; these average maps have suitable anatomic detail for gray/white matter segmentation and as the source image for registration with follow-up imaging. In-plane patient motion was corrected in the x-/y-axis using automated software (CT Perfusion 4D), and in cases with extreme motion, time points were manually removed as needed.⁹

Perfusion Parameter Map Registration. All perfusion parameter maps generated from the mCTA and CT perfusion studies, respectively, were registered to the follow-up DWI dataset. Therefore, the optimal rigid transformation was computed between the follow-up DWI and average CTP or NCCT dataset, respectively, using the mutual-information image-similarity metric within a multiresolution approach.^{11,12} The resulting transformations were then used to transform the perfusion parameter maps to the follow-up DWI dataset using linear interpolation.

Infarct Segmentation and Perfusion Data Extraction. Delineation of the follow-up infarct volume (ROI-1) was performed on the follow-up DWI by applying a single standardized intensity.¹³ A noninfarct ROI (ROI-2) encompassed any brain tissue outside ROI-1, including voxels from the contralateral hemisphere. Subcortical structures (ie, basal ganglia, including the caudate, lentiform, and internal capsule) were manually segmented and analyzed separately from cortical gray/white matter.

Histograms were generated for all ROI-1 and ROI-2 segmentations, respectively, from the SPIRAL perfusion image and CTP T_{max} and CBF maps because these maps have been previously shown by the authors to have the highest accuracy for final infarction.⁷ Patient-level histograms from ROI-1 and -2 were amalgamated to create a single “all patient” ROI-1 and ROI-2 to perform a cohort-level analysis.

An additional analysis was undertaken to evaluate the effect of lesion size on the SPIRAL lesion-detection method described. Lesions at different size intervals were chosen, while larger or smaller lesions were eliminated from the analysis. This interval mean was shifted from 0.015 to 1000 mL, with the upper and lower bounds on the interval being 10% of the mean (ie, 100-mL mean, 90- to 110-mL interval). This analysis was completed to determine whether smaller petechial lesions were not identified by the SPIRAL algorithm.

Statistical Analysis

Clinical data were summarized using standard descriptive statistics. We performed a patient-level analysis and cohort-level

analysis using receiver operating characteristic (ROC) curve analysis. At the patient level, the area under the ROC curve was determined (area under the curve [AUC]) for each patient. At the cohort level, an AUC-ROC was determined for all infarct voxels and noninfarct voxels from all patients in an amalgamated histogram. The Youden method was used to determine these optimal thresholds most associated with follow-up MR imaging infarct volume along with respective sensitivities and specificities for each threshold.¹⁴ AUC values were compared between SPIRAL and CTP-CBF and T_{max} maps. Bland-Altman plots were created to compare SPIRAL, CTP T_{max} , and follow-up DWI lesion volumes using the model/thresholds derived in the cohort-level analysis of 40 patients with both mCTA and CTP acquisitions. T_{max} thresholds were 15.2 and 13.7 seconds for GM/WM and the basal ganglia, respectively. Agreement between the SPIRAL and T_{max} infarct volume and follow-up DWI infarct volume was tested by calculating the systematic error (bias) and the 95% limits of agreement, defined as the bias \pm 1.96 SDs of the individual differences.¹⁵

We also performed a 10-fold cross-validation for the SPIRAL map (derived from our logistic regression). The analysis was performed on the cohort-level histograms using a 10-fold cross-validation to assess the performance and consistency of the SPIRAL map. Each training set formed 90%, with replacement, of the total population and trained the ROC analysis to determine an optimal threshold. That threshold was then applied to the remaining 10% of the total population to assess sensitivity, specificity, AUC, and the optimal threshold. This process was completed 10 times to determine a mean and SD in each of the above metrics.

A 2-sided P value $< .05$ was considered as statistically significant for all statistical tests. All analyses were performed using R (Version 3.2.1; <http://www.r-project.org/>), STATA (Version 13, StataCorp), and Matlab (R2015a, Version 8.5, MathWorks) statistical packages.

RESULTS

Of a total of 80 patients satisfying study inclusion/exclusion criteria, 72 were included in the study. Some patients ($n = 8$) had inadequate registration results due to severe motion in one of the NCCT or mCTA series. Clinical demographics are summarized in Table 1. Median DWI volume was 12 mL (interquartile range, 2.2–41.8 mL). The optimal SPIRAL functional map derived from the logistic regression was generated from the deconvolution T_0 and nondeconvolution TTP, CBF, and MTT. This SPIRAL functional map was used in the patient- and cohort-level analyses as well the cross-validation analysis.

If we compared the ROC-AUC in patients with early and late reperfusion for cortical gray matter + white matter infarction, there was no significant difference at the patient-level (0.83 versus 0.84, respectively), cohort-level (0.82 versus 0.81, respectively), or the cross-validation (0.77 versus 0.74, respectively) (Table 2). When we compared the ROC-AUC in patients with early and late reperfusion for basal ganglia infarction, there was no significant difference at the patient-level (0.82 versus 0.84, respectively), cohort-level (0.81 versus 0.80, respectively), or the cross-validation (0.82 versus 0.78, respectively) (Table 3).

Table 1: Admission demographics, site of occlusion, and workflow metrics

Variables	Total (n = 72 Patients)
Age (median) (minimum-maximum) (yr)	68 (32–89)
Men (No.) (%)	37 (51.4)
Stroke on awakening (No.) (%)	27 (46.6)
Site of occlusion (No.) (%)	
MCA	29 (40.3)
ACA	3 (4.0)
ICA	16 (22.2)
Tandem	5 (6.9)
Affected hemisphere (No.) (%)	
Right	30 (41.7)
Left	39 (54.2)
Coronary artery disease (No.) (%)	12 (16.7)
Congestive heart failure (No.) (%)	6 (8.3)
Valvular disease (No.) (%)	2 (3.4)
Hypertension (No.) (%)	38 (52.8)
Dyslipidemia (No.) (%)	24 (33.3)
Diabetes (No.) (%)	1 (1.4)
Smoking (No.) (%)	20 (27.8)
Statin (No.) (%)	22 (37.9)
EVT treatment (No.) (%)	72 (100)
tPA (alteplase) treatment (No.) (%)	55 (76)
Reperfusion (TICI 2b/3) (No.) (%)	72 (100)
Blood glucose (median) (minimum-maximum) (mmol)	6 (4.4–20.0)
NIHSS baseline (median) (minimum-maximum)	17 (1–29)
NIHSS 24 hours (median) (minimum-maximum)	6 (0–24)
MR spectroscopy baseline (median) (minimum-maximum)	0 (0–3)
MR spectroscopy (median) (minimum-maximum) (90 days)	2 (0–6)
CT to reperfusion time (median) (minimum-maximum) (hh:mm)	1:28 (0:27–3:06)

Note:—hh:mm indicates hours: minutes; ACA, anterior cerebral artery.

In the patient-level ROC analysis, the SPIRAL map had a slightly higher, though nonsignificant ($P < .05$), average ROC-AUC (cortical GM/WM = 0.83; basal ganglia = 0.79, respectively) than both the CTP Tmax (cortical GM/WM = 0.82; basal ganglia = 0.78, respectively) and CTP-CBF (cortical GM/white matter = 0.74; basal ganglia = 0.78, respectively) parameter maps. The same relationship was observed at the cohort level (Table 4).

Bland-Altman plots display the mean difference from zero and limits of agreement (2 SDs) to compare the SPIRAL and CTP Tmax infarct volume and follow-up DWI infarct volume (Fig 1). The Bland-Altman plots for SPIRAL and CTP Tmax infarct core volume show that the bias of agreement was similar when comparing the 2 techniques. Similar agreement was observed for the SPIRAL and GE-CTP Tmax infarct core volume with 24-hour DWI infarct volume: The SPIRAL and Tmax map (cortical GM/WM) infarct core

Table 2: ROC curve AUC for SPIRAL map, stratified by CT-to-reperfusion time for cortical gray and white matter tissue

Statistic	AUC, Patient Level	AUC, Cohort Level	Cross-Validation Sensitivity	Cross-Validation Specificity	Cross-Validation Accuracy
Early reperfusion, <90 minutes (n = 48 patients)					
Mean	0.83	0.82	0.82	0.72	0.77
SD	0.14	NA	0.06	0.03	0.06
Late reperfusion, >90 minutes (n = 24 patients)					
Mean	0.84	0.81	0.79	0.70	0.74
SD	0.11	NA	0.08	0.06	0.07

Note:—NA indicates not applicable.

Table 3: ROC curve AUC for SPIRAL map, stratified by CT-to-reperfusion time for basal ganglia regions

Statistic	AUC, Patient Level	AUC, Cohort Level	Cross-Validation Sensitivity	Cross-Validation Specificity	Cross-Validation Accuracy
Early reperfusion, >90 minutes (21 patients)					
Mean	0.82	0.81	0.82	0.81	0.82
SD	0.11	NA	0.05	0.06	0.06
Late reperfusion, <90 minutes (7 patients)					
Mean	0.84	0.80	0.86	0.71	0.78
SD	0.1	NA	0.08	0.09	0.09

Note:—NA indicates not applicable.

Table 4: ROC curve AUC for SPIRAL map comparison with cine CTP maps for a 40-patient subcohort

Statistic	Cortical GM and White Matter (WM)		Basal Ganglia
	Matter (WM)		
SPIRAL map			
AUC, patient level (mean) (SD)	0.83 (0.14)		0.79 (0.08)
AUC, cohort level (mean)	0.82		0.80
CTP T-max map			
AUC, patient level	0.82 (0.13)		0.78 (0.11)
AUC, cohort level	0.81		0.74
CTP blood flow map			
AUC, patient level	0.74 (0.14)		0.78 (0.09)
AUC, cohort level	0.72		0.77

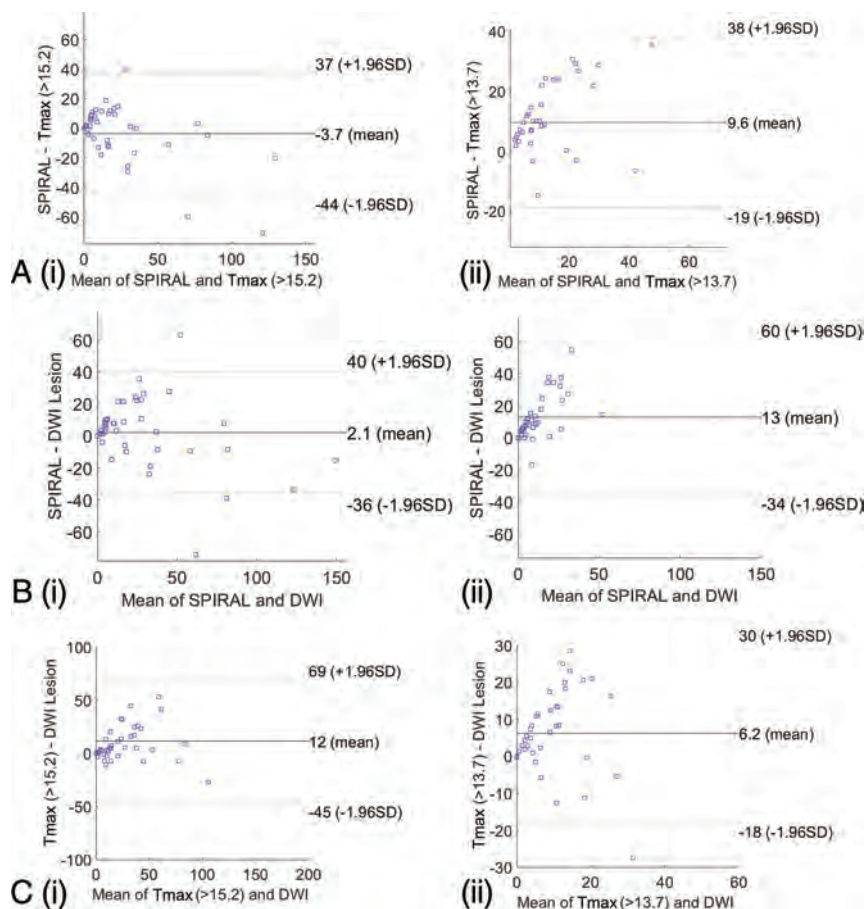


FIG 1. Bland-Altman plots for SPIRAL infarct volume (milliliters) (A) and Tmax infarct volume (milliliters) in cortical gray matter/white matter (i) and basal ganglia (ii). SPIRAL infarct volume (milliliters) (B) and follow-up DWI infarct volume (milliliters) in the cortical gray matter/white matter (i) and basal ganglia (ii). C, Tmax infarct volume and follow-up DWI infarct volume in cortical gray matter/white matter (i) and basal ganglia (ii).

volume mean difference was -3.7 cm^3 (1.96 SDs: $-44-37 \text{ cm}^3$); the SPIRAL and Tmax (basal ganglia) infarct core volume mean difference was 9.6 cm^3 (1.96 SDs: $-19-38 \text{ cm}^3$). Finally, the SPIRAL infarct core volume (cortical GM/WM) and 24-hour DWI volume mean difference was 2.1 cm^3 (1.96 SDs: $-36-40 \text{ cm}^3$); the SPIRAL infarct core volume (basal ganglia) and 24-

hour DWI volume mean difference was 13 cm^3 (1.96 SDs: $-34-60 \text{ cm}^3$).

The SPIRAL map was less accurate in detecting smaller lesions (1–10 mL) while equally as accurate in identifying larger lesions (>100 mL) compared with CTP (Fig 2).

DISCUSSION

Perfusion from low temporally sampled contrast-enhanced imaging has been previously shown in a seminal article by Heinz et al,¹⁶ in 1979. Similarly, we have shown that perfusion parameter maps can be successfully generated from a temporally sampled helical CTA, potentially obviating the need for an additional cine CTP scan in the future. The accuracy, sensitivity, and specificity for follow-up infarct volume is similar to reported values from the CTP literature and the current CTP paradigm available at the authors' institution.⁷ Bland-Altman plots showed good agreement between SPIRAL and CTP infarct core volume and for SPIRAL and CTP comparisons with 24-hour DWI follow-up for cortical gray/white matter. The limits of agreement for SPIRAL and CTP Tmax infarct volume were greater for the basal ganglia threshold. In support of our conclusions from this study, we have recently shown that perfusion measured on mCTA source images can better predict follow-up infarction (quantified by the ASPECTS) and clinical outcomes compared with NCCT and mCTA-rLMC (regional leptomeningeal collateral) (pial collateral scoring), the current paradigm used by the Calgary Stroke Program.^{17,18} Furthermore, the NCCT and CTA collateral score for stroke decision-making requires expert interpretation, contributing diagnostic uncertainty among nonexperts.^{19,20} We now provide an objective, easy-to-interpret, inexpensive, and time-sensitive imaging paradigm to characterize the ischemic lesion at admission with

SPIRAL. Figure 3 provides 3 case study examples of SPIRAL versus CTP Tmax functional maps.

Critical to improving patient outcome in patients with acute stroke is fast treatment, high diagnostic accuracy, and confidence among nonexpert physicians because outcomes of patients with stroke are heavily dependent on these factors.

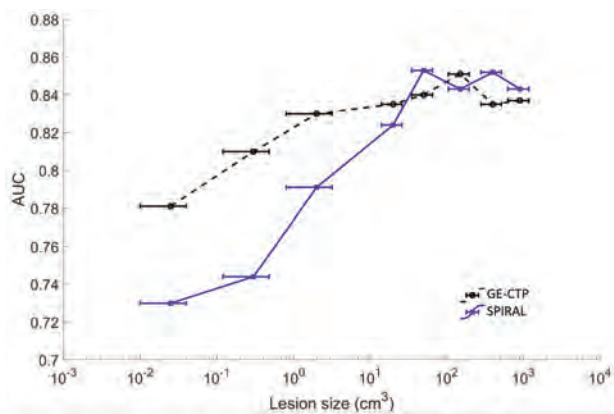


FIG 2. Sensitivity for final infarction on 24-hour MR imaging versus lesion size for SPIRAL and the CTP Tmax map.

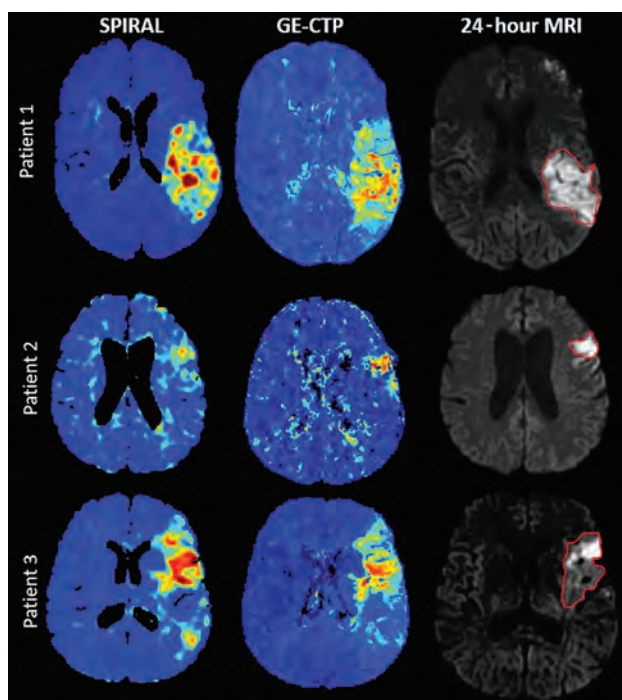


FIG 3. Admission SPIRAL map and CTP Tmax map for 3 patients who underwent EVT for M1 occlusions who had quality/fast reperfusion. The final infarct volume is outlined on the 24-hour DWI.

Brain imaging plays a key role in decision-making that has required expert interpretation,^{9,21-28} but among nonstroke experts, it is a major cause for treatment delays.^{19,29} CTA is required to identify large-vessel occlusion that may be amenable to removal via EVT. Canadian guidelines strongly recommend the use of CTP to select patients with acute ischemic stroke for EVT in the late time window (6–24 hours after symptom onset).³⁰ CTP also has the advantage of improving diagnostic accuracy for the identification of ischemic stroke.³¹ Although, CTP is a required technique for all Comprehensive Stroke Centers, CTP has significant limitations: It requires separate image acquisition and postprocessing (delaying treatment), another contrast injection (increasing risk of acute nephropathy), and additional exposure to ionizing radiation. Finally,

CTP has not been widely adopted in rural stroke centers.^{9,32} In this study, we have shown that SPIRAL functional maps can accurately identify infarct core. In its current state, SPIRAL could be used clinically as part of the “perfusion-derived infarct core/clinical penumbra” paradigm for recanalization decision-making, as was shown useful in the Clinical Mismatch in the Triage of Wake Up and Late Presenting Strokes Undergoing Neurointervention With Trevo (DAWN) trial.⁴ A prospective study to determine whether SPIRAL is a faster, less expensive, and safer technique for obtaining brain blood flow perfusion maps from a time-resolved helical CT angiogram is warranted.

A few important limitations must be acknowledged. This study has a relatively small sample size of highly selected patients with moderate-to-severe stroke symptoms who were treated with EVT and achieved very good and fast reperfusion. The purpose of these selection criteria was to achieve an operational definition of “infarct core,” but we do not know how predictive the SPIRAL map would be in patients with variable reperfusion status and with occlusions in vascular territories other than the anterior circulation. We also had to remove several patients due to the inability to register the images (motion correction to obtain the time-attenuation curve). Nevertheless, the number of patients removed due to this error is consistent with other studies.⁷ We also did not separate our gray and white matter tissue compartments to determine respective accuracies; compared with CTP in which an “average map” provides adequate gray/white differentiation, a low temporally resolved CTA cannot provide this. In the future, mCTA perfusion will need to be assessed in a more heterogeneous stroke cohort to determine the relationship between SPIRAL and other commercialized software. We propose that standardized SPIRAL automation will maintain the diagnostic accuracy of cine CTP-based paradigms, thus providing the potential for supporting significant improvements in stroke triage, both in comprehensive and primary stroke centers.

CONCLUSIONS

We have shown that CT perfusion maps can be generated from a temporally sampled helical CTA, potentially replacing a cine CTP scan for triage of patients with ischemic stroke. SPIRAL has the potential for reducing the time for image acquisition and radiologic interpretation compared with NCCT, CTA collateral scores, and cine CT perfusion techniques.

ACKNOWLEDGMENTS

The authors would like to thank the Calgary Stroke Program and Seaman Family MR Research Centre staff for helping with this study.

Disclosures: Commor McDougall—UNRELATED: Comments: stock ownership in Andromeda Medical Imaging Inc. Andrew M. Demchuk—UNRELATED: Employment: University of Calgary; Patents (Planned, Pending or Issued): Circle NVI, Comments: imaging software; Stock/Stock Options: Circle NVI, Comments: imaging software. Nils Daniel Forkert—UNRELATED: Grants/Grants Pending: Natural Sciences and Engineering Research Council of Canada, Canada Research Chair.* Michael D. Hill—UNRELATED: Board Membership: CNS Foundation, Circle NVI, Comments: unpaid, stock ownership in Circle NVI; Consultancy: NoNo, Comments: unpaid; Grants/Grants Pending: Stryker, Medtronic, NoNo, Boehringer Ingelheim, Comments: grants for clinical trials*; Patents (Planned, Pending or Issued): US Patent office No. 62/

086,077; Stock/Stock Options: Circle NVI; Other: Sun Pharmaceutical Industries. Comments: adjudicator for outcomes in clinical trials, safety monitor, paid position. Christopher d'Este—UNRELATED: Comments: stock ownership in Andromeda Medical Imaging Inc. Philip A. Barber—RELATED: Grant: Canadian Institutes of Health Research grant*; Consulting Fee or Honorarium: Ablynx.* UNRELATED: Comments: stock ownership in Andromeda Medical Imaging Inc. *Money paid to the institution.

REFERENCES

- Goyal M, Demchuk AM, Menon BK, et al; ESCAPE Trial Investigators. **Randomized assessment of rapid endovascular treatment of ischemic stroke.** *N Engl J Med* 2015;372:1019–30. CrossRef Medline
- Saver JL, Goyal M, Bonafe A, et al; SWIFT PRIME Investigators. **Stent-retriever thrombectomy after intravenous t-PA vs. t-PA alone in stroke.** *N Engl J Med* 2015;372:2285–95 CrossRef Medline
- Campbell BC, Mitchell PJ, Kleinig TJ, et al; EXTEND-IA Investigators. **Endovascular therapy for ischemic stroke with perfusion-imaging selection.** *N Engl J Med* 2015;372:1009–18 CrossRef Medline
- Albers GW, Marks MP, Kemp S, et al; DEFUSE 3 Investigators. **Thrombectomy for stroke at 6 to 16 hours with selection by perfusion imaging.** *N Engl J Med* 2018;378:708–18 CrossRef Medline
- Haussen DC, Dehkharghani S, Rangaraju S, et al. **Automated CT perfusion ischemic core volume and noncontrast CT ASPECTS (Alberta Stroke Program Early CT Score): correlation and clinical outcome prediction in large vessel stroke.** *Stroke* 2016;47:2318–22 CrossRef Medline
- Nogueira RG, Jadhav AP, Haussen DC, et al; DAWN Trial Investigators. **Thrombectomy 6 to 24 hours after stroke with a mismatch between deficit and infarct.** *N Engl J Med* 2018;378:11–21 CrossRef Medline
- d'Este CD, Boesen ME, Ahn SH, et al. **Time-dependent computed tomographic perfusion thresholds for patients with acute ischemic stroke.** *Stroke* 2015;46:3390–97 CrossRef Medline
- Naylor J, Churilov L, Chen Z, et al. **Reliability, reproducibility and prognostic accuracy of the Alberta Stroke Program Early CT Score on CT perfusion and non-contrast CT in hyperacute stroke.** *Cerebrovasc Dis* 2017;44:195–202 CrossRef Medline
- Menon BK, d'Este CD, Qazi EM, et al. **Multiphase CT angiography: a new tool for the imaging triage of patients with acute ischemic stroke.** *Radiology* 2015;275:510–20 CrossRef Medline
- Konstas AA, Goldmakher GV, Lee TY, et al. **Theoretic basis and technical implementations of CT perfusion in acute ischemic stroke, Part 2: technical implementations.** *AJNR Am J Neuroradiol* 2009;30:885–92 CrossRef Medline
- Studholme C, Hill DL, Hawkes DJ. **Automated 3D registration of MR and CT images of the head.** *Med Image Anal* 1996;1:163–75 CrossRef Medline
- Gobbi DG, Peters TM. **Generalized 3D nonlinear transformations for medical imaging: an object-oriented implementation in VTK.** *Comput Med Imaging Graph* 2003;27:255–65 CrossRef Medline
- Sah RG, d'Este CD, Hill MD, et al. **Diffusion-weighted MRI stroke volume following recanalization treatment is threshold-dependent.** *Clin Neuroradiol* 2019;29:135–41 CrossRef Medline
- Akobeng AK. **Understanding diagnostic tests 3: receiver operating characteristic curves.** *Acta Paediatr* 2007;96:644–47 CrossRef Medline
- Bland JM, Altman DG. **Statistical methods for assessing agreement between two methods of clinical measurement.** *Lancet* 1986;327:307–10 CrossRef
- Heinz ER, Dubois P, Osborne D, et al. **Dynamic computed tomography study of the brain.** *J Comput Assist Tomogr* 1979;3:641–49 CrossRef Medline
- Reid M, Famuyide AO, Forkert ND, et al. **Accuracy and reliability of multiphase CTA perfusion for identifying ischemic core.** *Clin Neuroradiol* 2019;29:543–52 CrossRef Medline
- Zerna C, Assis Z, d'Este CD, et al. **Imaging, intervention, and workflow in acute ischemic stroke: the Calgary approach.** *AJNR Am J Neuroradiol* 2016;37:978–84 CrossRef Medline
- Shamy MC, Jaigobin CS. **The complexities of acute stroke decision-making: a survey of neurologists.** *Neurology* 2013;81:1130–33 CrossRef Medline
- Moeller JJ, Kurniawan J, Gubitz GJ, et al. **Diagnostic accuracy of neurological problems in the emergency department.** *Can J Neurol Sci* 2008;35:335–41 CrossRef Medline
- Wintermark M, Albers GW, Broderick JP, et al; Stroke Imaging Research (STIR) and Virtual International Stroke Trials Archive (VISTA)-Imaging Investigators. **Acute stroke imaging research roadmap II.** *Stroke* 2013;44:2628–39 CrossRef Medline
- Goyal M, Menon BK, Derdeyn CP. **Perfusion imaging in acute ischemic stroke: let us improve the science before changing clinical practice.** *Radiology* 2013;266:16–21 CrossRef Medline
- Sheth KN, Terry JB, Nogueira RG, et al. **Advanced modality imaging evaluation in acute ischemic stroke may lead to delayed endovascular reperfusion therapy without improvement in clinical outcomes.** *J NeuroIntervent Surg* 2013;5:i62–65 CrossRef Medline
- Menon BK, Almekhlafi MA, Pereira VM, et al; STAR Study Investigators. **Optimal workflow and process-based performance measures for endovascular therapy in acute ischemic stroke: analysis of the Solitaire FR Thrombectomy for Acute Revascularization study.** *Stroke* 2014;45:2024–29 CrossRef Medline
- Kudo K, Sasaki M, Yamada K, et al. **Differences in CT perfusion maps generated by different commercial software: quantitative analysis by using identical source data of acute stroke patients.** *Radiology* 2010;254:200–09 CrossRef Medline
- Bivard A, Levi C, Spratt N, et al. **Perfusion CT in acute stroke: a comprehensive analysis of infarct and penumbra.** *Radiology* 2013;267:543–50 CrossRef Medline
- Nambiar V, Sohn SI, Almekhlafi MA, et al. **CTA collateral status and response to recanalization in patients with acute ischemic stroke.** *AJNR Am J Neuroradiol* 2014;35:884–90 CrossRef Medline
- Mishra SM, Dykeman J, Sajobi TT, et al. **Early reperfusion rates with IV tPA are determined by CTA clot characteristics.** *AJNR Am J Neuroradiol* 2014;35:2265–72 CrossRef Medline
- Barber PA, Zhang J, Demchuk AM, et al. **Why are stroke patients excluded from tPA therapy? An analysis of patient eligibility.** *Neurology* 2001;56:1015–20 CrossRef Medline
- Boulanger JM, Lindsay MP, Gubitz G, et al. **Canadian stroke best practice recommendations for acute stroke management: prehospital, emergency department, and acute inpatient stroke care, 6th edition, update 2018.** *Int J Stroke* 2018;13:949–84 CrossRef Medline
- Hoang JK, Wang C, Frush DP, et al. **Estimation of radiation exposure for brain perfusion CT: standard protocol compared with deviations in protocol.** *AJR Am J Roentgenol* 2013;201:W730–34 CrossRef Medline
- Davenport MS, Khalatbari S, Dillman JR, et al. **Contrast material-induced nephrotoxicity and intravenous low-osmolality iodinated contrast material.** *Radiology* 2013;267:94–105 CrossRef Medline

Comparison of Dynamic Contrast-Enhancement Parameters between Gadobutrol and Gadoterate Meglumine in Posttreatment Glioma: A Prospective Intraindividual Study

J.E. Park, J.Y. Kim, H.S. Kim, and W.H. Shim



ABSTRACT

BACKGROUND AND PURPOSE: Differences in molecular properties between one-molar and half-molar gadolinium-based contrast agents are thought to affect parameters obtained from dynamic contrast-enhanced imaging. The aim of our study was to investigate differences in dynamic contrast-enhanced parameters between one-molar nonionic gadobutrol and half-molar ionic gadoterate meglumine in patients with posttreatment glioma.

MATERIALS AND METHODS: This prospective study enrolled 32 patients who underwent 2 20-minute dynamic contrast-enhanced examinations, one with gadobutrol and one with gadoterate meglumine. The model-free parameter of area under the signal intensity curve from 30 to 1100 seconds and the Tofts model-based pharmacokinetic parameters were calculated and compared intraindividually using paired *t* tests. Patients were further divided into progression (*n*=12) and stable (*n*=20) groups, which were compared using Student *t* tests.

RESULTS: Gadobutrol and gadoterate meglumine did not show any significant differences in the area under the signal intensity curve or pharmacokinetic parameters of K^{trans} , V_e , V_p , or K_{ep} (all *P* > .05). Gadobutrol showed a significantly higher mean wash-in rate (0.83 ± 0.64 versus 0.29 ± 0.63 , *P* = .013) and a significantly lower mean washout rate (0.001 ± 0.0001 versus 0.002 ± 0.002 , *P* = .02) than gadoterate meglumine. Trends toward higher area under the curve, K^{trans} , V_e , V_p , wash-in, and washout rates and lower K_{ep} were observed in the progression group in comparison with the treatment-related-change group, regardless of the contrast agent used.

CONCLUSIONS: Model-free and pharmacokinetic parameters did not show any significant differences between the 2 gadolinium-based contrast agents, except for a higher wash-in rate with gadobutrol and a higher washout rate with gadoterate meglumine, supporting the interchangeable use of gadolinium-based contrast agents for dynamic contrast-enhanced imaging in patients with posttreatment glioma.

ABBREVIATIONS: DCE = dynamic contrast-enhanced; CE = contrast-enhanced; GBCA = gadolinium-based contrast agent; IAUC = initial area under the time-to-signal intensity curve; K_{ep} = rate transfer constant; K^{trans} = volume transfer constant; V_e = extravascular-extracellular space per unit volume of tissue; V_p = blood plasma volume per unit volume of tissue; WHO = World Health Organization

In the evaluation of brain tumors on MR imaging, the interpretation of vascular permeability is important because an insufficient blood supply may be related to resistance to chemotherapy or immunotherapy owing to poor and heterogeneous uptake of the therapeutic agents.^{1,2} Dynamic contrast-enhanced (DCE) T1-weighted perfusion MR imaging, which involves the acquisition

of serial images after the administration of a gadolinium-based contrast agent (GBCA), has demonstrated considerable utility for assessing tumor perfusion, vessel permeability, and the volume of the extravascular-extracellular space.³ DCE imaging is widely used for brain tumor imaging and is a useful noninvasive method for monitoring treatment response.⁴⁻⁶

The relationship between the MR signal intensity of a voxel on DCE-MR imaging and the actual concentration of GBCA is

Received May 17, 2020; accepted after revision July 22.

From the Department of Radiology and Research Institute of Radiology (J.E.P., H.S.K., W.H.S.), University of Ulsan College of Medicine, Asan Medical Center, Seoul, Korea; and Department of Radiology (J.Y.K.), Kangbuk Samsung Hospital, Sungkyunkwan University School of Medicine, Seoul, Korea.

Ji Eun Park and Jung Youn Kim contributed equally to this work.

This work was supported by Bayer Korea and by a National Research Foundation of Korea (Ministry of Education) (grant No. NRF-2020RIA2B5B01001707 and NRF-2020RIA2C4001748). The funders had no role in study design, data collection and analysis, decision to publish, or preparation of the manuscript.

Please address correspondence to Ho Sung Kim, MD, PhD, Department of Radiology and Research Institute of Radiology, University of Ulsan College of Medicine, Asan Medical Center, 88 Olympic-ro 43-gil, Songpa-Gu, Seoul 05505, Korea; e-mail: radhskim@gmail.com

Indicates open access to non-subscribers at www.ajnr.org

<http://dx.doi.org/10.3174/ajnr.A6792>

complex, with the measured tissue relaxivity depending on the flip angle, TR, proton density, and precontrast tissue relaxivity.⁷ To date, both half-molar and one-molar GBCAs have been interchangeably used as DCE imaging agents.⁸⁻¹² The GBCA-induced signal enhancement depends on 3 factors:¹³⁻¹⁶ 1) the T1 relaxivity of GBCA, 2) the concentration of GBCA in the ROI, and 3) certain tissue-specific characteristics such as tissue perfusion and extracellular blood volume. Regarding T1 relaxivity, gadobutrol (gadolinium-DO3A-butrol; Gadovist 1.0; Bayer Schering Pharma) is a 1.0 mmol/mL gadolinium chelate agent with approximately 14%–27% higher T1 relaxivity than half-molar GBCAs on 3T MR imaging.^{17,18} The concentration of GBCA in the ROI is determined by the interactions between the contrast agent molecules and tissues, and the non-ionic property of gadobutrol is thought to affect tissue interactions and accumulation rates in a manner different from those of ionic GBCAs.^{13,14} Glioma is rich in negatively-charged glycosaminoglycans,¹⁹⁻²¹ and differences in ionic properties between gadobutrol and gadoterate meglumine (Dotarem; Guerbet), may affect model-free or quantitative pharmacokinetic DCE parameters; however, there is a lack of studies comparing the 2 types of GBCA in DCE imaging, with the 2 types having been used interchangeably to date.

Thus, the aim of our study was to investigate differences in DCE parameters between one-molar nonionic gadobutrol and half-molar ionic gadoterate meglumine in patients with posttreatment glioma, evaluating both model-free and pharmacokinetic quantifications. On a theoretic basis, the higher T1 relaxivity of gadobutrol may provide excellent wash-in characteristics, and its nonionic nature may enable longer retention of the contrast media in tissue with a high negatively-charged content, resulting in higher contrast-related signal in delayed phases of contrast-enhanced imaging in comparison with ionic half-molar agents. We, therefore, used a prolonged DCE acquisition of 20 minutes to ensure sufficient observation of wash-in and washout patterns.

MATERIALS AND METHODS

Study Patients

This prospective study was designed as an intraindividual comparison within a clinical cohort of patients with posttreatment glioma recruited between March 2017 and March 2019 and was approved by the institutional review board of our tertiary hospital (Asan Medical Center, Seoul, South Korea; institutional review board approval No: 2017-0003). Written informed consent was obtained from each patient. A flow diagram of the recruitment of study participants is shown in Fig 1. Patients with brain gliomas who were allocated for contrast-enhanced (CE) T1-weighted imaging and DCE imaging were potentially eligible. The detailed inclusion criteria for the current study were as follows: 1) histopathologic diagnosis of glioma according to the 2016 World Health Organization (WHO) criteria;²² 2) received standard treatment of radiation and chemotherapy (ie, for glioblastoma, concurrent chemoradiotherapy with temozolomide and 6 cycles of adjuvant temozolomide administered after surgical resection or biopsy); 3) a measurable contrast-enhancing lesion of more than 1 × 1 cm on CE-T1WI; 4) no corticosteroid administration within 1 week before DCE imaging; and 5) an image acquisition deemed to be of adequate quality without motion artifacts. The rationale for avoiding

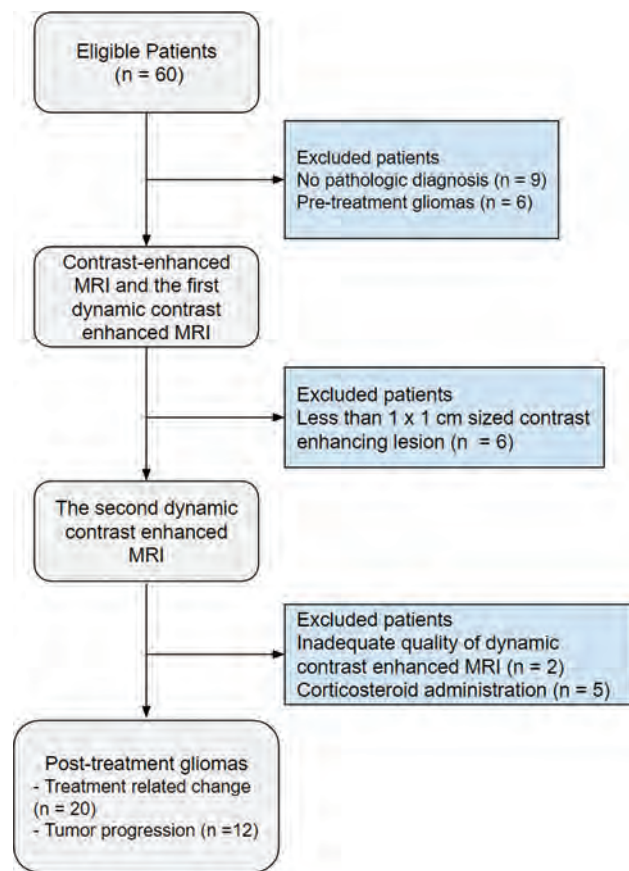


FIG 1. Flow diagram of the participant inclusion process.

a certain period of corticosteroid administration was to avoid the possibility of corticosteroid-induced regression of the tumor.²³

Patients were excluded when there was no pathologic diagnosis ($n = 9$), pre-treatment gliomas ($n = 6$), no visible measurable measurable contrast-enhancing lesion on CE-T1WI ($n = 6$), or when the image quality was deemed inadequate ($n = 2$). Patients who received corticosteroid treatment ($n = 5$) were further excluded. A total of 32 patients (median age, 58 years; age range, 21–76 years; 19 [59.3%] male patients) with posttreatment gliomas were finally included in the study. The clinical characteristics of the patients, including sex, age, extent of surgical treatment for the tumor (gross total resection, partial resection, or biopsy), and pathologic confirmation, were collected from medical records.

MR Imaging Protocol

All MR imaging studies were performed on a 3T unit (Achieva; Philips Healthcare) using an 8-channel head coil. Two DCE imaging examinations were acquired from each patient, with an interval of at least 12 hours between each session. The order of gadobutrol and gadoterate meglumine administration was randomly chosen for each patient. The first session involved acquisition of our dedicated MR imaging protocol for brain tumors, which consisted of T2WI, FLAIR, T1WI, diffusion-weighted imaging, CE-T1WI, and DCE imaging.

DCE imaging was performed using a 3D gradient-echo sequence with 21 slices, with imaging volumes being obtained

after administration of a standard dose of GBCA. Because the one-molar nonionic agent gadobutrol (Gadovist 1.0) is provided at twice the gadolinium concentration of the half-molar ionic gadoterate meglumine (Dotarem), 0.05 mmol (0.1 mL)/kg of body weight (average total volume, 5.8 mL; range, 4–7 mL) of gadobutrol was delivered at a rate of 2 mL/s using an MR imaging-compatible power injector (Spectris; MedRad), whereas 0.1 mmol (0.2 mL)/kg of body weight (average total volume, 13.7 mL; range, 12–15 mL) of gadoterate meglumine was delivered at a rate of 4 mL/s. The temporal resolution was 3.22 seconds, and the contrast material was administered after 10 baseline dynamics. The parameters for the DCE perfusion imaging included section thickness, 4 mm with no gap; TR/TE, 6.4/3.1 ms; flip angle, 15°; FOV, 24 × 24 cm; and matrix, 184 × 186. The total acquisition time for DCE imaging was 18 minutes 40 seconds.

After DCE imaging, CE-T1WI was performed for anatomic reference using a 3D gradient-echo T1-weighted sequence with the following parameters: TR/TE, 9.9/4.6 ms; flip angle, 8°; FOV, 22.4 × 22.4 cm; matrix, 224 × 224; and section thickness, 1 mm with no gap.

Image Registration and Processing

All imaging data were transferred from the MR imaging scanner to an independent computer for quantitative perfusion analysis. For quantitative analysis, contrast-enhancing lesion volumes were segmented on the CE-T1WI using a semiautomated adaptive thresholding technique to select all pixels above a determined threshold value. The resulting segmentation of the entire enhancing tumor was verified by an experienced neuroradiologist (J.E.P., with 7 years of experience in neuro-oncology imaging), who was blinded to the clinical information.

For the DCE imaging, motion correction was performed using rigid-body registration to realign each time point of the time-series. The CE-T1WI was coregistered to the DCE images using an affine transformation with 6 *df* and fourth-degree B-spline interpolation performed using SPM12 (<http://www.fil.ion.ucl.ac.uk/spm/software/spm12>).

The model-free parameters were obtained using Matlab 2019b (MathWorks). The signal intensity was normalized into its percentage change compared with the baseline signal intensity value, and then the initial area under the signal intensity time curve (IAUC) at 30, 100, 200, 300, 400, 500, 600, 700, 800, 900, 1000, and 1100 seconds was calculated for each patient using trapezoidal integration of the normalized signal intensity after the contrast agent arrived in the voxel of interest. Outlier values were automatically removed from the output maps because these can occur due to unstable curve-fitting conditions with a noisy input signal.

The pharmacokinetic parameters were obtained using a dedicated software package (nordicICE; NordicNeuroLab) based on the 2-compartment model proposed by Tofts and Kermode.²⁴ The parameters included volume transfer constant (K^{trans}), rate transfer constant (K_{ep}), blood plasma volume per unit volume of tissue (V_p), and extravascular-extracellular space per unit volume of tissue (V_e). The wash-in rate was calculated as the maximum slope between the time of onset of contrast inflow and the time of peak enhancement on the time-intensity curve. The washout rate was calculated as the negative slope of the late part of the exponential

curve. Each parameter was calculated using a fixed T1 of 1000 ms, because this can contribute to more reliable results and protect the dynamic data from patient movement or inaccurate scaling factors occurring during the DCE imaging acquisition.^{25,26}

The arterial input function was selected by a neuroradiologist (J.Y.K., with 2 years of experience in neuro-oncology imaging), who was blinded to the clinical information of the study subject, using an ROI confined to the vertical portion of the superior sagittal sinus, which avoided problems of feeding veins causing mixed artifacts in the same image section.

Reference Standard for Tumor Progression and Treatment-Related Change

A final diagnosis of tumor progression or treatment-related change was confirmed pathologically in second-look operations when clinically indicated. When second-look operations were not performed, tumor progression on MR imaging was assessed according to the Response Assessment in Neuro-Oncology criteria,²⁷ using serial measures of the product of the 2 largest cross-sectional diameters. The consecutive clinicoradiologic diagnoses were made by consensus between a neuro-oncologist (J.H.K., with 26 years of experience in neuro-oncology practice) and a neuroradiologist (H.S.K., with 21 years of experience in neuro-oncologic imaging) after complete imaging and medical chart review.²⁷

Statistical Analysis

Sample Size. The sample size of our study was determined according to power analysis for paired-means analysis, which was performed using Power Analysis Software (PASS, Version 15.0.7; <https://www.ncss.com/download/pass/updates/pass15/>). We used data on the distribution of the IAUC30 parameter from a previous study,²⁸ which showed mean values of 15.73 ± 2.76 in recurrent glioblastoma and 7.31 ± 3.59 in radiation necrosis, with a meaningful difference between the 2 contrast agents being indicated by a difference of >8.0 . The null hypothesis was that there was no difference in the mean of the paired differences of IAUC30 between the 2 contrast agents. A sample size of 32 would achieve 100% power to detect a mean paired difference of 8.0 with an estimated SD of differences of 7.0 with a significance level (α) of .05 using a 2-sided paired *t* test. This represents significance in a 2-sided *Z*-test ($P < .05$). Thus, the sample size of 32 was sufficient to detect meaningful differences in the 2 contrast agents that would affect the clinical diagnosis of recurrent glioblastoma or radiation necrosis.

DCE parameters were initially assessed for normality using the Shapiro-Wilk test. The DCE parameters were found to be normal and were then expressed as mean \pm SD. Paired *t* tests were used to assess intraindividual differences in the DCE parameters between the 2 GBCAs.

The Student *t* test and χ^2 test were used for comparisons of clinical and demographic characteristics between tumor progression and treatment-related change. Differences in DCE parameters between tumor progression and treatment-related-change groups were assessed using the Student *t* test.

All statistical analyses were performed using SPSS, Version 21 (IBM) and MedCalc, Version 18.2.1 (MedCalc Software). A *P* value $< .05$ was considered statistically significant.

RESULTS

Patient Demographics

Of the 32 study patients, 19 were pathologically confirmed with glioblastoma (WHO grade IV); and 13, with lower-grade astrocytomas (5 with WHO grade II and 8 with grade III; Table 1). There were no differences in age, sex, extent of surgery, and postoperative adjuvant chemotherapy status between the 2 groups.

Comparison of DCE Parameters between Gadobutrol and Gadoterate Meglumine

Table 2 summarizes the comparisons of model-free and pharmacokinetic parameters. When the model-free DCE parameters were compared, gadobutrol showed a trend for a higher rate of relative contrast enhancement compared with gadoterate meglumine, but there was no significant difference in the IAUC 30,

100, 200, 300, 400, 500, 600, 700, 800, 900, 1000, and 1100 seconds (paired *t* test, all *P* > .05).

The pharmacokinetic parameters of K^{trans} , V_e , V_p , and K_{ep} also showed no significant differences between the 2 contrast agents (paired *t* test, all *P* > .05). However, gadobutrol showed a significantly higher mean wash-in rate (0.825 ± 0.644 versus 0.289 ± 0.634 , *P* = .013) and a significantly lower mean washout rate (0.001 ± 0.0001 versus 0.002 ± 0.002 , *P* = .02) than gadoterate meglumine. Figures 2 and 3 show representative cases in patients with tumor progression and treatment-related change, exhibiting differences in wash-in and washout rates.

Subgroup Analysis between Tumor Progression and Treatment-Related Change in DCE Parameters

Table 3 summarizes the comparisons of DCE parameters between the tumor-progression and treatment-related-change groups. The higher wash-in and lower washout rates with gadobutrol compared with gadoterate meglumine were maintained in the tumor-progression and treatment-related-change subgroups, with the higher mean wash-in rate with gadobutrol being especially notable in the treatment-related-change group (0.813 ± 0.521 versus 0.220 ± 0.590 , *P* = .002). The progression group showed trends toward higher areas under the curve, K^{trans} , V_e , V_p , wash-in and washout rates, and lower K_{ep} in comparison with the treatment-related-change group, regardless of the GBCA type, though the differences did not reach statistical significance.

Table 1: Clinical information of the enrolled patients with glioma^a

6-Month Follow-Up	Patients (n = 32)		P Value
	Treatment-Related Change (n = 20)	Tumor Progression (n = 12)	
WHO grade			.71
Grade II	3	2	
Grade III	6	2	
Grade IV	11	8	
No. of male patients	12 (60%)	6 (50%)	.59
Age (yr)	61.5 (36–70)	59.5 (21–69)	.71
Surgical extent (%)			.46
Biopsy or partial resection	14	7	
Gross total resection	6	5	
Postoperative standard radiation therapy or concurrent chemoradiation therapy	19	11	.55

^aData are expressed as the median and range for continuous variables. The χ^2 test was used to test for differences in categorical variables between the 6-month stable and tumor-progression groups.

Table 2: Intraindividual comparison of model-free and pharmacokinetic parameters between gadobutrol and gadoterate meglumine dynamic contrast-enhanced MR imaging^a

DCE Parameter	Gadobutrol	Gadoterate Meglumine	P Value
Model-free method			
IAUC30	3.91 ± 2.38	4.27 ± 2.02	.517
IAUC100	21.50 ± 12.82	23.41 ± 11.28	.530
IAUC200	39.08 ± 23.30	42.53 ± 20.57	.533
IAUC300	56.68 ± 33.77	61.68 ± 29.88	.533
IAUC400	74.25 ± 44.24	80.79 ± 39.17	.534
IAUC500	91.84 ± 54.71	99.91 ± 48.46	.534
IAUC600	109.44 ± 65.19	119.06 ± 57.76	.534
IAUC700	127.04 ± 75.66	138.21 ± 67.07	.535
IAUC800	144.66 ± 86.13	157.37 ± 76.37	.535
IAUC900	166.69 ± 98.74	179.04 ± 83.13	.656
IAUC1000	184.76 ± 109.43	198.43 ± 92.13	.656
IAUC1100	202.85 ± 120.13	217.84 ± 101.13	.657
Pharmacokinetic method			
K^{trans} (min^{-1})	0.016 ± 0.009	0.017 ± 0.008	.592
K_{ep} (min^{-1})	0.127 ± 0.042	0.132 ± 0.041	.594
V_e (%)	17.797 ± 10.057	17.271 ± 7.436	.813
V_p	1.168 ± 0.674	1.263 ± 0.600	.559
Wash-in rate	0.825 ± 0.644	0.289 ± 0.634	.013
Washout rate	0.0010 ± 0.0008	0.0021 ± 0.0025	.024

^aData are means. *P* values are from paired tests when the variables satisfied normality according to the Shapiro-Wilk test or from Wilcoxon-signed rank tests otherwise.

DISCUSSION

We compared gadobutrol with gadoterate meglumine on an intraindividual basis to investigate whether model-free and pharmacokinetic parameters from DCE imaging were affected by differences between one-molar nonionic gadobutrol and half-molar ionic gadoterate meglumine. Gadobutrol had a significantly higher wash-in rate and a lower washout rate compared with gadoterate meglumine. However, neither the model-free parameters obtained from relative signal change nor the pharmacokinetic parameters of K^{trans} , V_e , V_p , or K_{ep} showed any significant difference between the 2 GBCAs. Both GBCAs showed the same trends of higher leakage parameter values, except for the comparison of K_{ep} between the tumor progression group and the treatment-related-change group, though the 2 GBCAs showed no significant difference

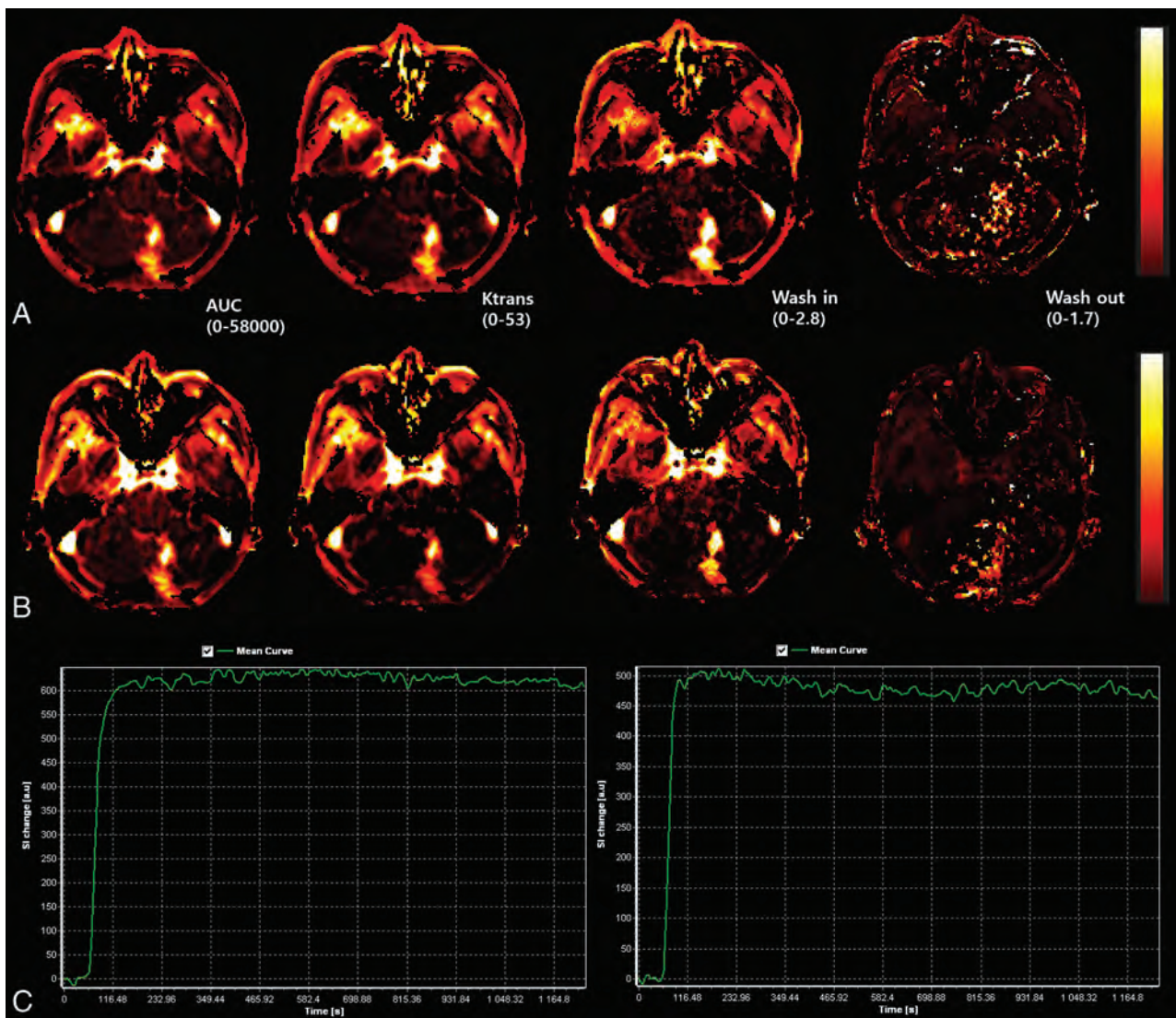


FIG 2. A 62-year-old female patient with posttreatment glioblastoma at 15 weeks after concurrent chemoradiotherapy exhibits a contrast-enhancing mass on DCE imaging with gadobutrol (A, upper row) and gadoterate meglumine (B, lower row). The K^{trans} , IAUC 30, K_{ep} , V_e , V_p , and dynamic curve show similar patterns and values. Wash-in and washout maps show differences between the 2 gadolinium-based contrast agents. The patient was diagnosed with tumor progression. C, The time-to-signal intensity curves (left: gadobutrol and right: gadoterate meglumine) are shown for both contrast agents. SI indicates signal intensity.

between the 2 groups. Our results support the current notion that one-molar nonionic gadobutrol and half-molar ionic gadoterate meglumine can be used interchangeably for DCE imaging in patients with posttreatment gliomas.

Using pharmacokinetic parameters, previous studies found that treatment-related change demonstrated lower K^{trans} , V_e , and V_p than tumor progression, especially in glioblastoma.^{29,30} The diagnostic utility of the model-free parameters of IAUC at 30 and 60 seconds was also previously demonstrated.^{28,31-34} Recently, standardization of the DCE image-processing method has been pursued,¹² with a method involving 2-compartment pharmacokinetic modeling with patient-specific baseline T1 maps and a vascular input function taken from the superior sagittal sinus. Nonetheless, GBCA use has not been standardized, and there are only limited reports comparing DCE patterns between one-molar and half-molar gadolinium-based contrast agents.^{16,35-40}

Whereas some authors reported that gadobutrol resulted in an increase in diagnostic accuracy for detecting prostate cancer in comparison with half-molar GBCAs,⁴¹ other studies^{16,42-44} performed on different organs did not show significant diagnostic benefits with gadobutrol. A recent in vitro study comparing gadobutrol and other half-molar GBCAs in various body regions showed significant differences in signal enhancement among body regions.¹⁵ The highest amplitude of signal enhancement was observed in the blood, followed by well-perfused organs such as the spleen, liver, tongue, and prostate, whereas much lower signal intensity was observed in extremity muscle and only minor signal changes were detected in brain tissue, probably attributable to the blood-brain barrier.¹⁵ Our results indicate that it is unlikely that there would be any significant difference between one-molar nonionic gadobutrol and half-molar ionic gadoterate meglumine when they are used to establish clinical diagnoses or management plans in patients with posttreatment glioma. Our study has value in that it performed a direct head-to-head

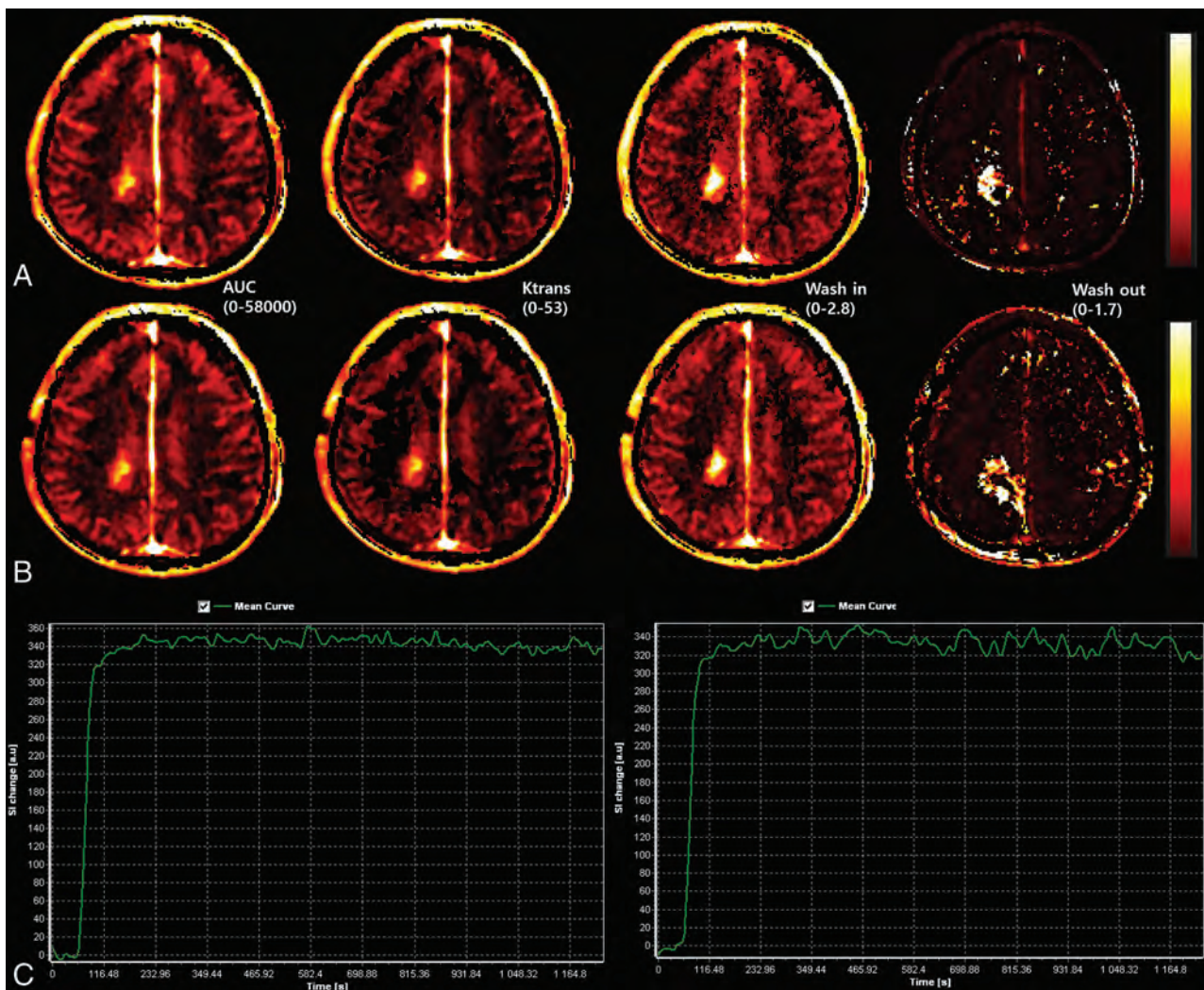


FIG 3. A 55-year-old female patient with posttreatment glioblastoma at 15 weeks after concurrent chemoradiotherapy exhibits a contrast-enhancing mass on DCE imaging with gadobutrol (*A*, upper row) and gadoterate meglumine (*B*, lower row). The K^{trans} , IAUC 30, K_{ep} , V_e , V_p , and dynamic curve show similar patterns and values. Wash-in and washout maps show differences between the 2 gadolinium-based contrast agents. The patient was diagnosed with treatment-related change. *C*, The time-to-signal intensity curves (left: gadobutrol and right: gadoterate meglumine) are shown for both contrast agents. SI indicates signal intensity.

comparison between one- and half-molar GBCA, and our results imply that the 2 GBCA types can be used interchangeably for most of the DCE parameters, thereby supporting the standardization of DCE imaging in patients with posttreatment glioma.

Both gadobutrol and gadoterate meglumine are macrocyclic gadolinium agents and are known to be safer than linear gadolinium agents because of their higher kinetic stability.^{17,45,46} Many studies have shown that contrast agents with higher T1 relaxivity result in stronger contrast enhancement than those with lower T1 relaxivity.^{16,35,36,47} The combined properties of higher gadolinium concentration and T1 relaxivity obtained with gadobutrol could have resulted in a significantly higher wash-in rate calculated by the pharmacokinetic method in comparison with gadoterate meglumine; however, the model-free method with calculation of the IAUC is a robust and simple indicator of tumor vascular characteristics,⁴⁸ and the IAUCs did not show any significant difference between the 2 GBCAs. We, therefore, suggest that the results can be interpreted without having to consider the molarity of the GBCA.

Our finding of a difference in the washout rate is in accord with previous studies in the breast, which demonstrated slower washout of gadobutrol than gadoterate meglumine.^{16,36} The difference might be attributable to the difference in ionic properties between the 2 contrast agents, with the higher washout rate of gadoterate meglumine reflecting its lower accumulation in the extravascular extracellular space compared with gadobutrol. A previous DCE study of cartilage¹⁴ showed that a nonionic neutral agent revealed diffuse contrast enhancement independent of glycosaminoglycan concentration, while a negatively charged ionic agent showed a negative correlation between signal enhancement and the concentration of glycosaminoglycan. This effect was explained by electrostatic repulsion between the ionic contrast agent and the negatively charged glycosaminoglycan-rich extravascular-extracellular space.¹⁴ The extravascular-extracellular space of gliomas is glycosaminoglycan-rich,¹⁹⁻²¹ which may have contributed to the faster washout of the ionic contrast agent compared with the nonionic agent.

Table 3: Intraindividual comparisons of model-free and pharmacokinetic parameters between stable and progression posttreatment glioma groups^a

DCE Parameters	Treatment-Related Change Group			Progression Group			P Value* ^b	P Value † ^b
	Gadobutrol	Gadoterate Meglumine	P Value	Gadobutrol	Gadoterate Meglumine	P Value		
Model-free method								
IAUC30	3.43 ± 1.59	3.90 ± 1.84	.399	4.69 ± 3.24	4.88 ± 2.25	.870	.15	.34
IAUC100	15.82 ± 7.88	17.91 ± 9.21	.446	20.55 ± 13.69	21.20 ± 9.51	.895	.22	.34
IAUC200	15.80 ± 7.87	17.89 ± 9.20	.446	20.54 ± 13.67	21.18 ± 9.49	.896	.22	.34
IAUC300	15.82 ± 7.88	17.91 ± 9.20	.445	20.56 ± 13.67	21.21 ± 9.50	.894	.22	.34
IAUC400	15.79 ± 7.87	17.88 ± 9.18	.445	20.54 ± 13.66	21.17 ± 9.49	.897	.22	.34
IAUC500	15.81 ± 7.87	17.90 ± 9.19	.445	20.55 ± 13.66	21.18 ± 9.50	.898	.22	.34
IAUC600	15.82 ± 7.87	17.91 ± 9.20	.445	20.57 ± 13.66	21.20 ± 9.50	.897	.22	.34
IAUC700	15.83 ± 7.87	17.92 ± 9.20	.445	20.57 ± 13.67	21.21 ± 9.51	.896	.22	.34
IAUC800	15.83 ± 7.87	17.92 ± 9.20	.445	20.58 ± 13.67	21.21 ± 9.51	.896	.22	.34
IAUC900	16.64 ± 8.11	18.29 ± 9.45	.651	19.78 ± 13.43	20.69 ± 8.71	.859	.51	.54
IAUC1000	16.65 ± 8.11	18.30 ± 9.46	.651	19.79 ± 13.43	20.70 ± 8.72	.858	.51	.54
IAUC1100	16.66 ± 8.11	18.31 ± 9.46	.651	19.79 ± 13.44	20.72 ± 8.73	.857	.51	.54
Pharmacokinetic method								
K ^{trans} (min ⁻¹)	0.015 ± 0.007	0.016 ± 0.008	.531	0.017 ± 0.011	0.018 ± 0.007	.921	.45	.66
K _{ep} (min ⁻¹)	0.130 ± 0.041	0.132 ± 0.041	.878	0.121 ± 0.044	0.133 ± 0.044	.528	.58	.95
V _e (%)	16.374 ± 9.615	16.220 ± 6.271	.952	20.169 ± 10.750	19.023 ± 9.085	.780	.31	.31
V _p	1.045 ± 0.508	1.177 ± 0.591	.454	1.374 ± 0.916	1.408 ± 0.611	.915	.20	.29
Wash-in rate	0.813 ± 0.521	0.220 ± 0.590	.002	0.845 ± 0.859	0.404 ± 0.738	.191	.86	.44
Washout rate	0.0009 ± 0.0004	0.0015 ± 0.0016	.107	0.0013 ± 0.0012	0.0031 ± 0.0033	.091	.17	.08

^a Data are means. P values are from paired t-tests.

^b P* values and P† values are from Student t tests between the treatment-related-change and tumor-progression groups for gadobutrol and gadoterate meglumine, respectively.

Several limitations to this study should be noted. First, because of the small sample size of the prospective cohort, the statistical power of our data, especially in the tumor-progression group, might be limited. Second, although our study result does not suggest any recommendations for altering clinical practice or patient management, it may still be important to standardize the MR imaging contrast agent to ensure accurate comparisons in patients with posttreatment glioma undergoing monitoring with serial follow-up MR imaging, especially considering the different T1 relaxivities and ionic properties of the 2 types of GBCA.

CONCLUSIONS

Both one-molar nonionic gadobutrol and half-molar ionic gadoterate meglumine showed the same trends in model-free and pharmacokinetic parameters, except for a higher wash-in rate with gadobutrol and a higher washout rate with gadoterate meglumine. Therefore, our findings support the current interchangeable use of these 2 GBCAs for DCE imaging in patients with posttreatment glioma.

ACKNOWLEDGMENT

The authors would like to thank Jeong Hoon Kim for his assistance in clinicoradiologic diagnoses.

REFERENCES

- Chung SR, Choi YJ, Kim HS, et al. Tumor vascular permeability pattern is associated with complete response in immunocompetent patients with newly diagnosed primary central nervous system lymphoma: retrospective cohort study. *Medicine (Baltimore)* 2016;95:e2624 CrossRef Medline

- Jain RK. Delivery of molecular and cellular medicine to solid tumors. *Adv Drug Deliv Rev* 2001;46:149–68 CrossRef Medline
- Choyke PL, Dwyer AJ, Knopp MV. Functional tumor imaging with dynamic contrast-enhanced magnetic resonance imaging. *J Magn Reson Imaging* 2003;17:509–20 CrossRef Medline
- Nguyen TB, Cron GO, Mercier JF, et al. Diagnostic accuracy of dynamic contrast-enhanced MR imaging using a phase-derived vascular input function in the preoperative grading of gliomas. *AJNR Am J Neuroradiol* 2012;33:1539–45 CrossRef Medline
- Mills SJ, Patankar TA, Haroon HA, et al. Do cerebral blood volume and contrast transfer coefficient predict prognosis in human glioma. *AJNR Am J Neuroradiol* 2006;27:853–58 Medline
- Tofts, PS. T1-weighted DCE imaging concepts: modelling, acquisition and analysis. *Signal* 2010;500(450):400.
- Evelhoch JL. Key factors in the acquisition of contrast kinetic data for oncology. *J Magn Reson Imaging* 1999;10:254–59 CrossRef Medline
- Lemasson B, Serduc R, Maisin C, et al. Monitoring blood-brain barrier status in a rat model of glioma receiving therapy: dual injection of low-molecular-weight and macromolecular MR contrast media. *Radiology* 2010;257:342–52 CrossRef Medline
- Larsen VA, Simonsen HJ, Law I, et al. Evaluation of dynamic contrast-enhanced T1-weighted perfusion MRI in the differentiation of tumor recurrence from radiation necrosis. *Neuroradiology* 2013;55:361–69 CrossRef Medline
- Marine B, Benjamin L, Régine F, et al. Characterization of tumor angiogenesis in rat brain using iron-based vessel size index MRI in combination with gadolinium-based dynamic contrast-enhanced MRI. *J Cereb Blood Flow Metab* 2009;29:1714–26 CrossRef Medline
- Kickingereder P, Sahn F, Wiestler B, et al. Evaluation of microvascular permeability with dynamic contrast-enhanced MRI for the differentiation of primary CNS lymphoma and glioblastoma: radiologic-pathologic correlation. *AJNR Am J Neuroradiol* 2014;35:1503–08 CrossRef Medline
- Anzalone N, Castellano A, Cadioli M, et al. Brain gliomas: multicenter standardized assessment of dynamic contrast-enhanced and dynamic susceptibility contrast MR images. *Radiology* 2018;287:933–43 CrossRef Medline
- Gillis A, Gray M, Burstein D. Relaxivity and diffusion of gadolinium agents in cartilage. *Magn Reson Med* 2002;48:1068–71 CrossRef Medline

14. Wiener E, Woertler K, Weirich G, et al. **Contrast enhanced cartilage imaging: comparison of ionic and non-ionic contrast agents.** *Eur J Radiol* 2007;63:110–09 CrossRef Medline
15. Knobloch G, Frenzel T, Pietsch H, et al. **Signal enhancement and enhancement kinetics of gadobutrol, gadoteridol, and gadoterate meglumine in various body regions: a comparative animal study.** *Invest Radiol* 2020;55:367–73 CrossRef Medline
16. Renz DM, Durmus T, Botcher J, et al. **Comparison of gadoteric acid and gadobutrol for detection as well as morphologic and dynamic characterization of lesions on breast dynamic contrast-enhanced magnetic resonance imaging.** *Invest Radiol* 2014;49:474–84 CrossRef Medline
17. Bellin MF, Van Der Molen AJ. **Extracellular gadolinium-based contrast media: an overview.** *Eur J Radiol* 2008;66:160–07 CrossRef Medline
18. Rohrer M, Bauer H, Mintorovitch J, et al. **Comparison of magnetic properties of MRI contrast media solutions at different magnetic field strengths.** *Invest Radiol* 2005;40:715–24 CrossRef Medline
19. Bertolotto A, Giordana MT, Magrassi ML, et al. **Glycosaminoglycans (GAs) in human cerebral tumors.** *Acta Neuropathol* 1982;58:115–19 CrossRef Medline
20. Bertolotto A, Magrassi ML, Orsi L, et al. **Glycosaminoglycan changes in human gliomas: a biochemical study.** *J Neurooncol* 1986;4:43–48 CrossRef Medline
21. Bourdon MA, Matthews TJ, Pizzo SV, et al. **Immunochemical and biochemical characterization of a glioma-associated extracellular matrix glycoprotein.** *J Cell Biochem* 1985;28:183–95 CrossRef Medline
22. Louis DN, Perry A, Reifenberger G, et al. **The 2016 World Health Organization Classification of Tumors of the Central Nervous System: a summary.** *Acta Neuropathol* 2016;131:803–20 CrossRef Medline
23. Cuoco JA, Klein BJ, Busch CM, et al. **Corticosteroid-induced regression of glioblastoma: a radiographic conundrum.** *Front Oncol* 2019;9:1288 CrossRef Medline
24. Tofts PS, Kermode AG. **Measurement of the blood-brain barrier permeability and leakage space using dynamic MR imaging. 1: fundamental concepts.** *Magn Reson Med* 1991;17:357–67 CrossRef Medline
25. Haacke EM, Filletti CL, Gattu R, et al. **New algorithm for quantifying vascular changes in dynamic contrast-enhanced MRI independent of absolute T1 values.** *Magn Reson Med* 2007;58:463–72 CrossRef Medline
26. Jung SC, Yeom JA, Kim JH, et al. **Glioma: Application of histogram analysis of pharmacokinetic parameters from T1-weighted dynamic contrast-enhanced MR imaging to tumor grading.** *AJNR Am J Neuroradiol* 2014;35:1103–10 CrossRef Medline
27. Wen PY, Macdonald DR, Reardon DA, et al. **Updated response assessment criteria for high-grade gliomas: Response Assessment in Neuro-Oncology working group.** *J Clin Oncol* 2010;28:1963–72 CrossRef Medline
28. Chung WJ, Kim HS, Kim N, et al. **Recurrent glioblastoma: optimum area under the curve method derived from dynamic contrast-enhanced T1-weighted perfusion MR imaging.** *Radiology* 2013;269:561–68 CrossRef Medline
29. Yun TJ, Park CK, Kim TM, et al. **Glioblastoma treated with concurrent radiation therapy and temozolomide chemotherapy: differentiation of true progression from pseudoprogression with quantitative dynamic contrast-enhanced MR imaging.** *Radiology* 2015;274:830–40 CrossRef Medline
30. Thomas AA, Arevalo-Perez J, Kaley T, et al. **Dynamic contrast enhanced T1 MRI perfusion differentiates pseudoprogression from recurrent glioblastoma.** *J Neurooncol* 2015;125:183–90 CrossRef Medline
31. Yoon RG, Kim HS, Koh MJ, et al. **Differentiation of recurrent glioblastoma from delayed radiation necrosis by using voxel-based multiparametric analysis of MR imaging data.** *Radiology* 2017;285:206–13 CrossRef Medline
32. Park JE, Kim HS, Goh MJ, et al. **Pseudoprogression in patients with glioblastoma: assessment by using volume-weighted voxel-based multiparametric clustering of MR imaging data in an independent test set.** *Radiology* 2015;275:792–802 CrossRef Medline
33. Narang J, Jain R, Arbab AS, et al. **Differentiating treatment-induced necrosis from recurrent/progressive brain tumor using nonmodel-based semiquantitative indices derived from dynamic contrast-enhanced T1-weighted MR perfusion.** *Neuro Oncol* 2011;13:1037–46 CrossRef Medline
34. Hamilton JD, Lin J, Ison C, et al. **Dynamic contrast-enhanced perfusion processing for neuroradiologists: model-dependent analysis may not be necessary for determining recurrent high-grade glioma versus treatment effect.** *AJNR Am J Neuroradiol* 2015;36:686–93 CrossRef Medline
35. Haneder S, Attenberger UI, Schoenberg SO, et al. **Comparison of 0.5 M gadoterate and 1.0 M gadobutrol in peripheral MRA: a prospective, single-center, randomized, crossover, double-blind study.** *J Magn Reson Imaging* 2012;36:1213–21 CrossRef Medline
36. Fallenberg EM, Renz DM, Karle B, et al. **Intraindividual, randomized comparison of the macrocyclic contrast agents gadobutrol and gadoterate meglumine in breast magnetic resonance imaging.** *Eur Radiol* 2015;25:837–49 CrossRef Medline
37. Anzalone N, Scarabino T, Venturi C, et al. **Cerebral neoplastic enhancing lesions: multicenter, randomized, crossover intraindividual comparison between gadobutrol (1.0M) and gadoterate meglumine (0.5M) at 0.1 mmol Gd/kg body weight in a clinical setting.** *Eur J Radiol* 2013;82:139–45 CrossRef Medline
38. Maravilla KR, San-Juan D, Kim SJ, et al. **Comparison of gadoterate meglumine and gadobutrol in the MRI diagnosis of primary brain tumors: a double-blind randomized controlled intraindividual crossover study (the REMIND study).** *AJNR Am J Neuroradiol* 2017;38:1681–88 CrossRef Medline
39. Pediconi F, Kubik-Huch R, Chilla B, et al. **Intra-individual randomised comparison of gadobutrol 1.0 M versus gadobenate dimeglumine 0.5 M in patients scheduled for preoperative breast MRI.** *Eur Radiol* 2013;23:84–92 CrossRef Medline
40. Koenig M, Schulte-Altedorneburg G, Piontek M, et al. **Intra-individual, randomised comparison of the MRI contrast agents gadobutrol versus gadoteridol in patients with primary and secondary brain tumours, evaluated in a blinded read.** *Eur Radiol* 2013;23:3287–95 CrossRef Medline
41. Hara T, Ogata T, Wada H, et al. **Prostate cancer detection with multiparametric MRI: a comparison of 1 M-concentration gadobutrol with 0.5 m-concentration gadolinium-based contrast agents.** *Curr Urol* 2018;11:201–05 CrossRef Medline
42. Saake M, Langner S, Schwenke C, et al. **MRI in multiple sclerosis: an intra-individual, randomized and multicentric comparison of gadobutrol with gadoterate meglumine at 3 T.** *Eur Radiol* 2016;26:820–28 CrossRef Medline
43. Maravilla KR, Smith MP, Vymazal J, et al. **Are there differences between macrocyclic gadolinium contrast agents for brain tumor imaging? Results of a multicenter intraindividual crossover comparison of gadobutrol with gadoteridol (the TRUTH study).** *AJNR Am J Neuroradiol* 2015;36:14–23 CrossRef Medline
44. Rahsepar AA, Ghasemiesfe A, Suwa K, et al. **Comprehensive evaluation of macroscopic and microscopic myocardial fibrosis by cardiac MR: intra-individual comparison of gadobutrol versus gadoterate meglumine.** *Eur Radiol* 2019;29:4357–67 CrossRef Medline
45. Frenzel T, Lengsfeld P, Schirmer H, et al. **Stability of gadolinium-based magnetic resonance imaging contrast agents in human serum at 37 degrees C.** *Invest Radiol* 2008;43:817–28 CrossRef Medline
46. Sieber MA, Lengsfeld P, Frenzel T, et al. **Predclinical investigation to compare different gadolinium-based contrast agents regarding their propensity to release gadolinium in vivo and to trigger nephrogenic systemic fibrosis-like lesions.** *Eur Radiol* 2008;18:2164–73 CrossRef Medline
47. Attenberger UI, Runge VM, Morelli JN, et al. **Evaluation of gadobutrol, a macrocyclic, nonionic gadolinium chelate in a brain glioma model: comparison with gadoterate meglumine and gadopentetate dimeglumine at 1.5 T, combined with an assessment of field strength dependence, specifically 1.5 versus 3 T.** *J Magn Reson Imaging* 2010;31:549–55 CrossRef Medline
48. Evelhoch JL, LoRusso PM, He Z, et al. **Magnetic resonance imaging measurements of the response of murine and human tumors to the vascular-targeting agent ZD6126.** *Clin Cancer Res* 2004;10:3650–57 CrossRef

Centrally Reduced Diffusion Sign for Differentiation between Treatment-Related Lesions and Glioma Progression: A Validation Study

P. Alcaide-Leon, J. Cluceru, J.M. Lupo, T.J. Yu, T.L. Luks, T. Tihan, N.A. Bush, and J.E. Villanueva-Meyer



ABSTRACT

BACKGROUND AND PURPOSE: Differentiating between treatment-related lesions and tumor progression remains one of the greatest dilemmas in neuro-oncology. Diffusion MR imaging characteristics may provide useful information to help make this distinction. The aim of the study was to assess the diagnostic accuracy of the centrally reduced diffusion sign for differentiation of treatment-related lesions and true tumor progression in patients with suspected glioma recurrence.

MATERIALS AND METHODS: The images of 231 patients who underwent an operation for suspected glioma recurrence were reviewed. Patients with susceptibility artifacts or without central necrosis were excluded. The final diagnosis was established according to histopathology reports. Two neuroradiologists classified the diffusion patterns on preoperative MR imaging as the following: 1) reduced diffusion in the solid component only, 2) reduced diffusion mainly in the solid component, 3) no reduced diffusion, 4) reduced diffusion mainly in the central necrosis, and 5) reduced diffusion in the central necrosis only. Diagnostic accuracy metrics and the area under the receiver operating characteristic curve were estimated for the diffusion patterns.

RESULTS: One hundred three patients were included (22 with treatment-related lesions and 81 with tumor progression). The diagnostic accuracy results for the centrally reduced diffusion pattern as a predictor of treatment-related lesions ("mainly central" and "exclusively central" patterns versus all other patterns) were as follows: 64% sensitivity (95% CI, 41%–83%), 84% specificity (95% CI, 74%–91%), 52% positive predictive value (95% CI, 37%–66%), and 89% negative predictive value (95% CI, 83%–94%).

CONCLUSIONS: The centrally reduced diffusion sign is associated with the presence of treatment effect. The probability of a histologic diagnosis of a treatment-related lesion is low (11%) in the absence of centrally reduced diffusion.

ABBREVIATION: ROC = receiver operating characteristic

The current standard-of-care treatment for newly diagnosed malignant gliomas is maximal safe resection followed by radiation with concurrent and adjuvant chemotherapy with temozolomide.¹ These therapies often result in inflammation that can mimic tumor progression due to an increase in contrast enhancement on T1 postcontrast MR imaging. Recognizing treatment-related lesions is key for the adequate management of patients with glioma. Multiple advanced MR imaging techniques

including diffusion, perfusion, and MR spectroscopic imaging have been applied to solve this diagnostic challenge.^{2–8}

Diffusion MR imaging is a technique that provides indirect information on the tissue microstructure through the quantification of the Brownian motion of water. The ADC is a measure of the magnitude of diffusion of water within tissue. Many studies have investigated the diagnostic value of the ADC for distinguishing recurrent glioma from treatment-related changes, but the findings have been incongruent, and ADC has been found to have moderate diagnostic performance.⁹ Both recurrent tumors and treatment-related lesions may have a heterogeneous appearance, with solid-enhancing and nonenhancing components as well as necrotic areas. Most studies have focused on the diffusion characteristics of the enhancing component, disregarding the necrotic areas because they were thought to contain no valuable information. However, a recent article by Zakhari et al¹⁰ describes the presence of centrally reduced diffusion in treatment-related necrosis in a small sample of patients. Quantification of ADC in the different lesion components provides

Received December 19, 2019; accepted after revision June 29, 2020.

From the Department of Medical Imaging (P.A.-L.), University Health Network, Toronto, Ontario, Canada; and Departments of Radiology and Biomedical Imaging (J.C., J.M.L., T.J.Y., T.L.L., J.E.V.-M.), Pathology (T.T.), and Neurological Surgery (N.A.B.), University of California, San Francisco, San Francisco, California.

This work was supported by National Institutes of Health grants (P01 CA118816 and P50 CA097257).

Please address correspondence to Javier E. Villanueva-Meyer, Department of Radiology and Biomedical Imaging, UCSF, 505 Parnassus L-352, San Francisco, CA 94143; e-mail: javier.villanueva-meyer@ucsf.edu

Indicates open access to non-subscribers at www.ajnr.org

<http://dx.doi.org/10.3174/ajnr.A6843>

objective measurements, but this approach is often not feasible because tumor segmentation remains time-consuming. In clinical practice, radiologists assess diffusion imaging patterns without ADC quantification. Therefore, a study focusing on imaging pattern more realistically estimates the practical diagnostic accuracy of the centrally reduced diffusion sign.

Our aim was to evaluate the diagnostic accuracy of the centrally reduced diffusion sign for differentiation between treatment-related lesions and true tumor progression in patients with suspected glioma recurrence.

MATERIALS AND METHODS

Subjects

Institutional review board approval was obtained for this single-center retrospective study at the University of California San Francisco. We included patients with an initial pathologically confirmed diagnosis of World Health Organization grade II, III, or IV diffuse glioma treated with chemoradiation and a new or worsening enhancing lesion, undergoing surgery for suspected recurrence. Between October 2007 and November 2018, a total of 231 patients provided written informed consent to participate in a prospective radiologic-pathologic correlative study. A retrospective analysis was performed in this cohort. All patients underwent MR imaging between 1 and 3 days before surgical resection. Patients without macroscopic areas of necrosis were excluded. We considered necrosis a nonenhancing region with fluid signal intensity surrounded by contrast enhancement and showing a sum of biperpendicular diameters of >10 mm. We also excluded patients with susceptibility artifacts in the areas of necrosis to avoid the confounding effect of blood products on the diffusion evaluation.¹¹

MR Imaging Acquisition

MR imaging examinations were performed on a 3T scanner (Discovery 750, GE Healthcare, Waukesha, WI, USA) using an 8-channel phased array head coil. For evaluation of contrast enhancement and central necrosis, we used a volumetric T1-weighted inversion recovery spoiled gradient-echo sequence (TR/TE = 8.86/2.50 ms, matrix = 256 × 256, section thickness = 1.5 mm, FOV = 24 × 24 cm, TI = 400 ms, flip angle = 15°) before and after a 5-mL/s bolus injection of 0.1 mmol/kg body weight of gadopentetate dimeglumine (Magnevist; Bayer HealthCare Pharmaceuticals). For assessment of diffusion lesion characteristics, we used DWI with 6-directional axial diffusion EPI sequences (TR/TE = 7000–12,425/76–89 ms, matrix = 256 × 256 × 120, section thickness = 1.5 mm, FOV = 24 × 24 × 18 cm, $b = 1000$ s/mm², number of excitations = 4) or DWI with 3-directional axial EPI sequences (TR/TE = 13,800/80.2 ms, matrix = 110 × 116, section thickness = 2.5 mm, FOV = 25 × 22.5 cm, $b = 1000$ s/mm², number of excitations = 4). ADC maps were generated from diffusion images. The presence of susceptibility artifacts was assessed on the T2*-weighted angiography sequence (TE = 26 ms, TR = 50 ms, FOV = 256 × 256 cm, matrix size = 300 × 300, resolution = 0.9375 × 0.9375 mm). In the absence of a T2*-weighted angiography sequence, a T2*-weighted EPI sequence was used (TE/flip angle = 25–45 ms/35°, matrix = 256 × 256, section thickness = 5 mm).

Image Interpretation

Screening of patients for inclusion in the study was performed by a neuroradiologist with 9 years of experience (P.A.-L.). Patients lacking presurgical DWI, lacking an area of necrosis, or presenting with susceptibility artifacts due to blood products were excluded. Twenty percent of the potentially eligible patients ($n = 49$) were also assessed by a different neuroradiologist (J.E.V.-M.) for the assessment of interobserver agreement. Disagreements were resolved by consensus. Two neuroradiologists (P.A.-L. and J.E.V.-M.), independently and blinded to the pathology report, evaluated the diffusion images of all patients included in the study. Disagreements were resolved by consensus. We evaluated diffusion characteristics of 2 distinct components of new or worsening lesions, the solid portion, comprising enhancing and nonenhancing signal abnormality, and the central necrotic portion. Diffusion images including $b = 1000$ trace images and ADC maps were interpreted in conjunction with postcontrast T1 images to classify the lesions according to 5 diffusion patterns. We considered areas of reduced diffusion those regions showing hyperintensity on $b = 1000$ trace images with corresponding ADC values lower or equal to those of normal-appearing white matter. On the basis of the results of prior studies,^{10,12} the diffusion patterns were assigned an ordinal scale with a higher score representing a higher probability of a treatment-related lesion and a lower probability of a recurrent tumor. Diffusion patterns were categorized as follows: 1, reduced diffusion in the solid component only; 2, reduced diffusion mainly in the solid component; 3, no reduced diffusion; 4, reduced diffusion mainly in the central necrosis; and 5, reduced diffusion in the central necrosis only.

Histopathology Interpretation

The final diagnosis of a treatment-related lesion or recurrent tumor was assigned on the basis of the pathology report extracted from the electronic medical records. At our institution, pathology in each glioma case is reviewed by an experienced neuropathologist. Cases were assigned to the treatment-related lesion category when treatment-related changes were present and <25% of viable tumor was identified. Cases with ≥25% viable tumor were classified as recurrent tumor regardless of the presence of treatment effect. This threshold was used in a prior study¹³ and is commonly used in clinical decision-making at our institution. When described on the pathology report, percentages of treatment effect and viable tumor were recorded. The histology of cases classified as tumor (>25% of viable tumor) with available slides was re-reviewed by an expert neuropathologist (T.T.) to investigate the impact of mixed lesions in the diagnostic accuracy of the centrally reduced diffusion sign.

Statistical Analysis

The Cohen κ ¹⁴ was calculated to identify the interobserver agreement for the presence of central necrosis and blood. The linearly weighted Cohen κ ¹⁵ was calculated to identify the interobserver agreement for the presence of the different diffusion patterns. A κ value of ≤0.2 indicates slight agreement; 0.21–0.4, fair agreement; 0.41–0.6 moderate agreement; 0.61–0.80, substantial agreement, and 0.81–1.00, almost perfect agreement.¹⁶

Predictive performance of the diffusion patterns was assessed by estimating negative and positive predictive values, sensitivity and specificity, and the area under the receiver operating characteristic

(ROC) curve, with corresponding 95% confidence intervals. We also compared the diagnostic accuracy of the traditional diffusion approach that only considers the diffusion values in the solid regions and the diffusion assessment using the centrally reduced diffusion sign. The McNemar test was used for diagnostic accuracy comparison.

We also investigated the presence of mixed lesions as a cause of false-positive results of the centrally reduced diffusion sign. Within the tumor group (>25% of recurrent tumor), we compared the percentages of treatment effect between patients with predominant centrally reduced diffusion and patients with other diffusion patterns using the Mann-Whitney *U* test. Statistical analyses were performed using GraphPad Prism software, Version 8.2.1 (GraphPad Software).

RESULTS

Baseline Characteristics

A total of 231 patients with glioma with a new-or-worsening enhancing lesion undergoing an operation at our institution were enrolled between October 2007 and November 2018. Patients

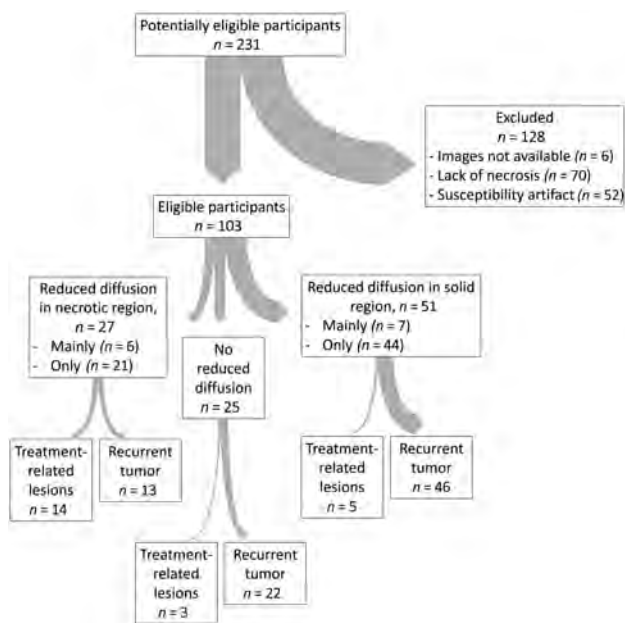


FIG 1. Standards for the Reporting of Diagnostic Accuracy Studies flow diagram. The thickness of the arrows is proportional to the number of subjects.

without areas of visible necrosis ($n = 70$), with susceptibility artifacts ($n = 52$), or without available images ($n = 6$) were excluded. A total of 103 eligible patients (44 women and 59 men) were included for analysis, 81 (79%) with recurrent tumor and 22 (21%) with treatment-related lesions. The mean age at surgery for suspected recurrence was 53 years (range, 25–84 years). The Standards for the Reporting of Diagnostic Accuracy Studies (<https://bmjopen.bmj.com/content/6/11/e012799>) flow diagram is shown in Fig 1. Stereotactic biopsy was performed in 1 patient; gross total resection, in 42 patients; and subtotal resection, in 60 patients. The original tumor histology was oligodendroglioma grade II in 3 cases, oligodendroglioma grade III in 2 cases, oligoastrocytoma grade II in 1 case, oligoastrocytoma grade III in 2 cases, astrocytoma grade II in 1 case, astrocytoma grade III in 13 cases, and glioblastoma/gliosarcoma in 81 cases. Most cases were diagnosed before 2016; therefore, a mix of the World Health Organization classifications of 2007 and 2016 was used. The date of the end of radiation treatment was available in 75/103 patients. The median time from the end of radiation treatment to the pre-operative MR imaging was 7.8 months for the treatment-effect group (95% CI, 3.8–14 months) and 17 months for the recurrent-tumor group (95% CI, 9.4–29 months).

Interobserver Agreement

The κ value was 0.7 (95% CI, 0.5–0.9) for the presence of central necrosis and 0.8 (95% CI, 0.7–1) for the presence of blood products. The linearly weighted κ value for the diffusion patterns was 0.7 (95% CI, 0.6–0.8).

Predictive Value of the Diffusion Patterns

The number of patients showing each diffusion pattern in the recurrent tumor group and in the treatment-related lesions group is shown in the Table and displayed graphically in Fig 2. Figure 3 shows typical diffusion patterns of treatment-related lesions and recurrent tumor.

The diagnostic-accuracy results for the centrally reduced diffusion pattern as a predictor of treatment-related lesions (mainly central and exclusively central patterns versus all other patterns) were as follows: 80% accuracy (95% CI, 71%–87%), 64% sensitivity (95% CI, 41%–83%), 84% specificity (95% CI, 74%–91%), 52% positive predictive value (95% CI, 37%–66%), and 89% negative predictive value (95% CI, 83%–94%). The diagnostic accuracy results for the traditional approach that considers only the presence of reduced diffusion in the solid lesion component as a

Distribution of the different diffusion patterns in the treatment-related lesion and recurrent-tumor groups

Diffusion Pattern	Treatment-Related Lesions	Percentage of Total Cases of Treatment-Related Lesions	Recurrent Tumor	Percentage of Total Cases of Recurrent Tumor
Reduced diffusion in the solid region	3	13.64%	41	50.62%
Reduced diffusion mainly in the solid region	2	9.1%	5	6.17%
No reduced diffusion	3	13.64%	22	27.16%
Reduced diffusion mainly in the necrotic region	3	13.64%	3	3.70%
Reduced diffusion in the necrotic region	11	50%	10	12.35%
All	22	100%	81	100%

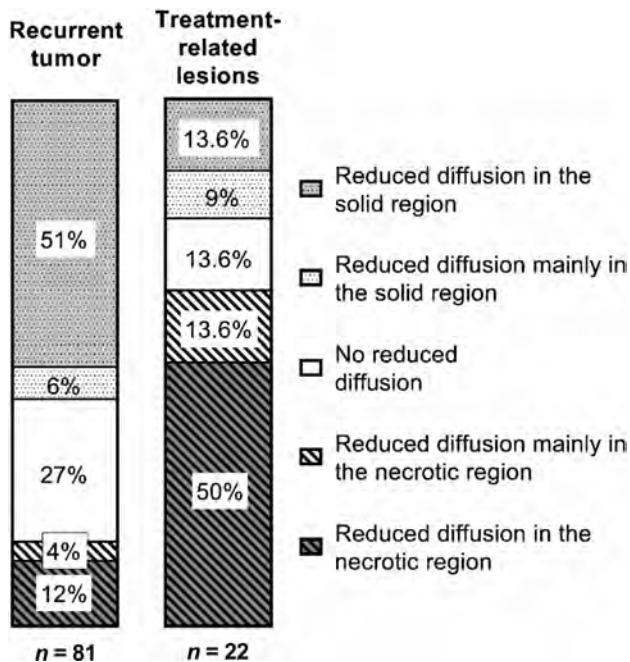


FIG 2. Distribution of the different diffusion patterns in the treatment-related lesion and recurrent-tumor groups.

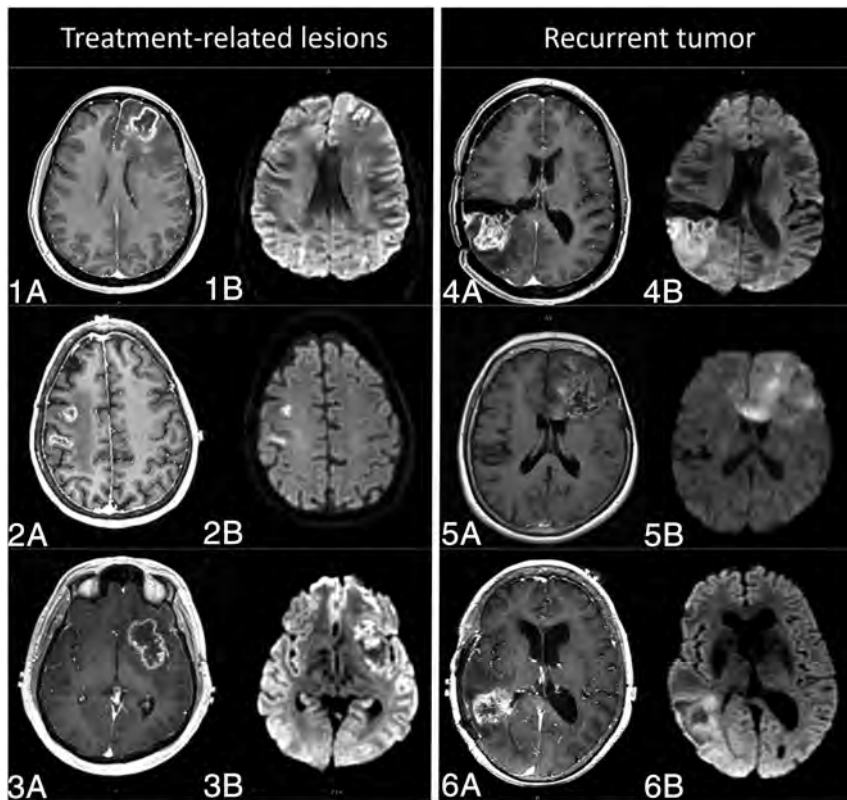


FIG 3. Preoperative MR imaging of 6 patients with suspected glioma recurrence. In 3 cases (1, 2, and 3), histopathology revealed treatment-related lesions, and in the other 3 cases (4, 5, and 6), recurrent tumor. T1-weighted postcontrast (A) and DWI (B) are shown in each case. Treatment-related lesions (1, 2, and 3) show reduced diffusion predominantly in the central necrotic region. Lesions corresponding to progressive tumor (4, 5, and 6), on the other side, show reduced diffusion mainly in the solid-lesion components.

marker of recurrent tumor (mainly solid and exclusively solid diffusion patterns versus all other patterns) were as follows: 61% accuracy (95% CI, 51%–71%), 57% sensitivity (95% CI, 45%–68%), 77% specificity (95% CI, 55%–92%), 90% positive predictive value (95% CI, 81%–95%), and 33% negative predictive value (95% CI, 26%–40%). The diagnostic accuracy of the centrally reduced diffusion sign was significantly higher than that of the traditional diffusion-assessment approach that considers only the reduced diffusion of the solid lesion components ($P < 0.001$).

ROC Analysis of Diffusion Patterns

The ROC curve for the diffusion patterns as a predictor of treatment-related lesions (positive state) or recurrent tumor (negative state) is shown in Fig 4. The area under the ROC curve was 0.77 (95% CI, 0.7–0.9). The best cutoff point for predicting the treatment effect was ≥ 4 . In the ordinal scale assigned to the diffusion patterns, 4 corresponded to reduced diffusion located, mainly but not exclusively, in the necrotic region, whereas 5 corresponded to reduced diffusion present exclusively in the necrotic region.

Subgroup Analysis of False-Positive Cases

Among the patients with recurrent tumor ($n = 81$), the percentage of treatment effect in tissue samples was obtained by pathology re-evaluation for 33 patients with available and sufficient slides. Of the 48 patients without available or sufficient slides, we

were able to find the percentage of treatment effect in the clinical pathology report for 7 additional patients. Percentages of treatment effect were available in a total of 40 patients classified as having recurrent tumor (>25% of viable tumor), combining the re-evaluation of slides and the clinical pathology report. Eleven cases showed a predominant pattern of centrally reduced diffusion, and 29 showed other patterns. In 2 cases, pathologic re-review described >75% of the treatment effect in cases originally classified as recurrent tumor according to initial clinical pathology. In these 2 cases, we decided to keep the clinical diagnosis of recurrent tumor because we cannot confirm that all original slides were available for re-evaluation. The median of the percentage of concurrent treatment effect in patients with tumor recurrence was 30% (95% CI, 20%–45%) in patients with a pattern of centrally reduced diffusion and 40% (95% CI, 30%–75%) in patients with other diffusion patterns. The differences were not statistically significant (Mann-Whitney U test, P value = .076). Figure 5 shows the distribution of the percentages of concurrent treatment effect by diffusion pattern.

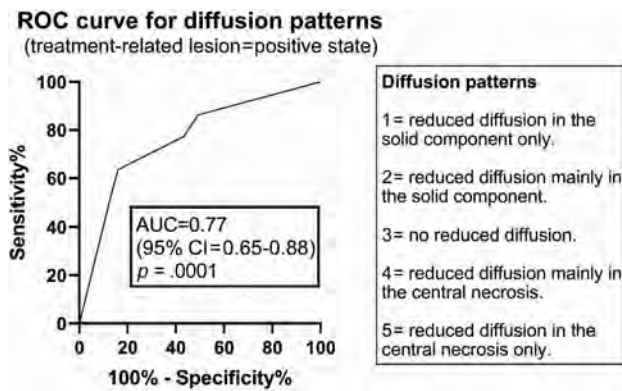


FIG 4. ROC curve for diffusion patterns. AUC indicates area under the curve.

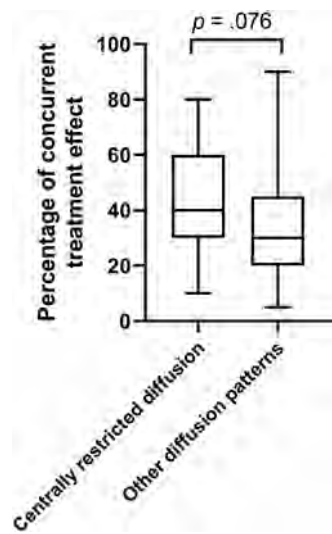


FIG 5. The box-and-whisker plot shows the distribution of the percentages of concurrent treatment effect in patients with recurrent tumor by diffusion pattern. The *whiskers* mark the maximum and minimum values, and the *box edges* indicate the first and third quartiles. The *horizontal line* inside the box corresponds to the median. The median percentage of treatment effect was higher in the group with centrally reduced diffusion than in the group with the other diffusion patterns, but differences were not statistically significant ($P = .076$).

DISCUSSION

The present study found an overall diagnostic accuracy of 80% for the centrally reduced diffusion sign in the differentiation between treatment effect and glioma recurrence. The negative predictive value for a predominantly central reduced diffusion pattern was 89%. The absence of a predominant pattern of centrally reduced diffusion in a ring-enhancing lesion suspicious for glioma recurrence implies only around an 11% chance that the lesion corresponds to treatment effect. When a predominant pattern of centrally reduced diffusion was present, the probability of a lesion being a treatment effect was 51% (positive predictive value). We believe the low positive predictive value of the centrally reduced diffusion sign is likely related to the presence of mixed lesions. In the present study, mixed lesions were more likely to be histologically classified as recurrent tumor because a mixed lesion had to show only >25% of viable tumor tissue to be classified as recurrent tumor. We hypothesized that a number of

mixed lesions with extensive treatment effect and centrally reduced diffusion were classified as recurrent tumor and therefore deemed false-positives. To evaluate this hypothesis, we compared the percentages of concurrent treatment effect in cases classified as recurrent tumor with and without a predominant pattern of centrally reduced diffusion. Unfortunately, the percentage of treatment effect was only available in 40 cases of recurrent tumor, and though the median of the percentages of treatment effect was higher in the patients with recurrent tumor with centrally reduced diffusion than without it (40% versus 30%), the differences were not statistically significant. The diagnostic accuracy of the centrally reduced diffusion sign was significantly higher than that of the traditional diffusion assessment that considers only the solid lesion components. Our results suggest that diffusion restriction in the solid component is a marker of recurrent tumor, whereas the reduced diffusion in the necrotic region is associated with treatment effect. Given the high prevalence of mixed lesions in the context of suspected glioma recurrence, we find the complementary information provided by the diffusion in the solid and necrotic lesion components extremely valuable.

Both the imaging exclusion criteria (lack of necrotic areas and presence of susceptibility) and the diagnostic test (diffusion patterns) showed substantial interobserver reliability ($\kappa = 0.7-0.8$). In the prior study¹⁰ describing the centrally reduced diffusion sign, a single neuroradiologist assessed the images; therefore, interobserver reliability was not evaluated. For a diagnostic sign to be valuable, it must be shown to be reliable when used by different practitioners. Our work not only validates the findings of the prior study but also adds the interobserver reliability assessment.

Diffusion MR imaging has been widely studied for differentiation of recurrent tumor and treatment-related lesions, but prior studies show inconsistent results.^{6,17} One of the reasons for the inconsistency may be methodologic because prior studies differ in the location and method of diffusion measurements. To account for lesion heterogeneity, some studies selected portions of the ADC histogram, either with formal histogram analysis or by manually selecting ROIs with the lowest or highest ADC values. In some studies, the smallest ADC values within the enhancing lesion were the most useful,⁷ whereas others assigned the best discriminative power to the maximum ADC values.³ Most studies focused on the evaluation of the enhancing lesion component exclusively,^{3,5} whereas other studies evaluated the whole lesion.⁷ Inconsistent and even contradictory results of prior studies are not surprising because they do not account for the fact that the central coagulative necrosis in treatment-related lesions can restrict water motion as much as tumor cellularity can.¹⁸

A study using a delayed radiation necrosis model in rats showed significantly lower ADC in the necrotic central zone than in the peripheral zone. Histologic analysis revealed parenchymal coagulative necrosis in the central zone and damaged vessels and reactive astrogliosis in the peripheral zone.¹⁸ Zakhari et al¹⁰ described the presence of centrally reduced diffusion in treatment-related necrosis and the diagnostic accuracy of the central/peripheral ADC ratio for differentiation of radiation necrosis and recurrent glioma. They evaluated a sample of 17 patients including 9 cases of recurrent tumor and 8 cases of radiation necrosis. We believe the proportion of radiation necrosis found in this study was very high, despite it being a prospective study with consecutive patient enrollment; this feature should capture the real prevalence of radiation necrosis and

recurrent tumor. The prevalence of treatment-related lesions in our cohort was 21%. The reason for this mismatch may be the small sample of the prior study and the fact that they excluded patients with equal amounts of treatment effect and recurrent tumor. Using our criteria, those patients would have been classified as having recurrent tumor. The present study evaluates not only a larger but also a more representative sample of patients undergoing an operation for suspected glioma recurrence, which allows positive and negative predictive value estimation. Our results consolidate the presence of centrally reduced diffusion as highly specific for detection of treatment-related lesions in the context of a new or worsening ring-enhancing lesion suspicious for glioma recurrence.

Limitations

The study has some limitations. First, the presence of a concurrent treatment effect was not available in a large portion of patients, precluding a meaningful subanalysis of the false-positive cases. Second, we performed only qualitative evaluation of the diffusion patterns, and we made no distinction among different fractions of reduced diffusion in the solid and necrotic components. We think this is a more broadly applicable approach that better recreates the interpreting physician's clinical practice at the expense of less objective information. Third, the prevalence of treatment-related lesions and, therefore, the predictive values were estimated in a cohort of patients undergoing an operation for suspected glioma recurrence. This assumption may carry an institutional bias because surgical practice patterns in this setting may differ across institutions. Fourth, a few patients with an original diagnosis of low-grade glioma were included in the study together with a majority of patients with higher-grade gliomas. Recurrence in high and low grades may manifest differently, but the low number of patients with low grade gliomas precluded subgroup analysis. Fifth, the radiation dose was not available in all patients; this feature may influence the pretest probability of radionecrosis. Sixth, information on whether treatment effect or tumor recurrence was suspected in each case before the operation was not available for all patients.

CONCLUSIONS

The centrally reduced diffusion sign is highly specific for detecting treatment-related lesions in the context of suspected glioma recurrence. Our findings contradict the traditional assumption that central necrosis contains no valuable information for differentiation of treatment effect and recurrent tumor. Further studies intending to use diffusion or other imaging techniques for differentiating treatment effect and recurrent tumor should also take into account the information extracted from the necrotic portions of the lesions.

ACKNOWLEDGMENTS

The authors wish to acknowledge the generous support of the Slaughter Family Foundation.

Disclosures: Paula Alcaide-Leon—RELATED: Grant: National Institutes of Health.* Janine M. Lupo—RELATED: Grant: National Institutes of Health*; Support for Travel to Meetings for the Study or Other Purposes: National Institutes of Health*; UNRELATED: Grants/Grants Pending: National Institutes of Health, GE Healthcare*; Travel/Accommodations/Meeting Expenses Unrelated to Activities

Listed: National Institutes of Health.* Javier E. Villanueva-Meyer—UNRELATED: Grants/Grants Pending: GE Healthcare.* *Money paid to the institution.

REFERENCES

1. Stupp R, Mason WP, van den Bent MJ, et al. Radiotherapy plus concomitant and adjuvant temozolomide for glioblastoma. *N Engl J Med* 2005;352:987–96 CrossRef Medline
2. Alexiou GA, Zikou A, Tsiouris S, et al. Comparison of diffusion tensor, dynamic susceptibility contrast MRI and 99mTc-Tetrofosmin brain SPECT for the detection of recurrent high-grade glioma. *Magn Reson Imaging* 2014;32:854–59 CrossRef Medline
3. Asao C, Korogi Y, Kitajima M, et al. Diffusion-weighted imaging of radiation-induced brain injury for differentiation from tumor recurrence. *AJNR Am J Neuroradiol* 2005;26:1455–60 Medline
4. Ceschin R, Kurland BF, Abberbock SR, et al. Parametric response mapping of apparent diffusion coefficient as an imaging biomarker to distinguish pseudoprogression from true tumor progression in peptide-based vaccine therapy for pediatric diffuse intrinsic pontine glioma. *AJNR Am J Neuroradiol* 2015;36:2170–76 CrossRef Medline
5. Hein PA, Eskey CJ, Dunn JF, et al. Diffusion-weighted imaging in the follow-up of treated high-grade gliomas: tumor recurrence versus radiation injury. *AJNR Am J Neuroradiol* 2004;25:201–09 Medline
6. Lee WJ, Choi SH, Park CK, et al. Diffusion-weighted MR imaging for the differentiation of true progression from pseudoprogression following concomitant radiotherapy with temozolomide in patients with newly diagnosed high-grade gliomas. *Acad Radiol* 2012;19:1353–61 CrossRef Medline
7. Matsusue E, Fink JR, Rockhill JK, et al. Distinction between glioma progression and post-radiation change by combined physiologic MR imaging. *Neuroradiology* 2010;52:297–306 CrossRef Medline
8. Prager AJ, Martinez N, Beal K, et al. Diffusion and perfusion MRI to differentiate treatment-related changes including pseudoprogression from recurrent tumors in high-grade gliomas with histopathologic evidence. *AJNR Am J Neuroradiol* 2015;36:877–85 CrossRef Medline
9. Zhang H, Ma L, Shu C, et al. Diagnostic accuracy of diffusion MRI with quantitative ADC measurements in differentiating glioma recurrence from radiation necrosis. *J Neurol Sci* 2015;351:65–71 CrossRef Medline
10. Zakhari N, Taccone MS, Torres C, et al. Diagnostic accuracy of centrally restricted diffusion in the differentiation of treatment-related necrosis from tumor recurrence in high-grade gliomas. *AJNR Am J Neuroradiol* 2018;39:260–64 CrossRef Medline
11. Atlas SW, Dubois P, Singer MB, et al. Diffusion measurements in intracranial hematomas: Implications for MR imaging of acute stroke. *AJNR Am J Neuroradiol* 2000;21:1190–94 Medline
12. Alcaide-Leon P, Luks TL, Lafontaine M, et al. Treatment-induced lesions in newly diagnosed glioblastoma patients undergoing chemoradiotherapy and heat-shock protein vaccine therapy. *J Neurooncol* 2020;146:71–73 CrossRef Medline
13. Wang S, Sakai Y, Chawla S, et al. Differentiating tumor progression from pseudoprogression in patients with glioblastomas using diffusion tensor imaging and dynamic susceptibility contrast MRI. *AJNR Am J Neuroradiol* 2016;37:28–36 CrossRef Medline
14. Cohen J. A coefficient of agreement for nominal scales. *Educ Psychol Meas* 1960;20:37–46 CrossRef
15. Cohen J. Weighted kappa: nominal scale agreement with provision for scaled disagreement or partial credit. *Psychol Bull* 1968;70:213–20 CrossRef Medline
16. Landis JR, Koch GG. The measurement of observer agreement for categorical data. *Biometrics* 1977;33:159–74 CrossRef
17. Bobek-Billewicz B, Stasik-Pres G, Majchrzak H, et al. Differentiation between brain tumor recurrence and radiation injury using perfusion, diffusion-weighted imaging and MR spectroscopy. *Folia Neuropathol* 2010;48:81–92 Medline
18. Wang S, Chen Y, Lal B, et al. Evaluation of radiation necrosis and malignant glioma in rat models using diffusion tensor MR imaging. *J Neurooncol* 2012;107:51–60 CrossRef Medline

Monro-Kellie Hypothesis: Increase of Ventricular CSF Volume after Surgical Closure of a Spinal Dural Leak in Patients with Spontaneous Intracranial Hypotension

T. Dobrocky, M. Rebsamen, C. Rummel, L. Häni, P. Mordasini, A. Raabe, C.T. Ulrich, J. Gralla, E.I. Piechowiak, and J. Beck



ABSTRACT

BACKGROUND AND PURPOSE: CSF loss in spontaneous intracranial hypotension disrupts a well-regulated equilibrium. We aimed to evaluate the volume shift between intracranial compartments in patients with spontaneous intracranial hypotension before and after surgical closure of the underlying spinal dural breach.

MATERIALS AND METHODS: In total, 19 patients with spontaneous intracranial hypotension with a proved spinal CSF leak investigated at our institution between July 2014 and March 2017 (mean age, 41.8 years; 13 women) were included. Brain MR imaging–based volumetry at baseline and after surgery was performed with FreeSurfer. In addition, the spontaneous intracranial hypotension score, ranging from 0 to 9, with 0 indicating very low and 9 very high probability of spinal CSF loss, was calculated.

RESULTS: Total mean ventricular CSF volume significantly increased from baseline (15.3 mL) to posttreatment MR imaging (18.0 mL), resulting in a mean absolute and relative difference, +2.7 mL and +18.8% (95% CI, +1.2 to +3.9 mL; $P < .001$). The change was apparent in the early follow-up (mean, 4 days). No significant change in mean total brain volume was observed (1136.9 versus 1133.1 mL, $P = .58$). The mean spontaneous intracranial hypotension score decreased from 6.9 ± 1.5 at baseline to 2.9 ± 1.5 postoperatively.

CONCLUSIONS: Our study demonstrated a substantial increase in ventricular CSF volume in the early follow-up after surgical closure of the underlying spinal dural breach and may provide a causal link between spinal CSF loss and spontaneous intracranial hypotension. The concomitant decrease in the spontaneous intracranial hypotension score postoperatively implies the restoration of an equilibrium within the CSF compartment.

ABBREVIATIONS: CSFVF = CSF venous fistula; MDEFT = modified driven equilibrium Fourier transform; SIH = spontaneous intracranial hypotension

Spontaneous intracranial hypotension (SIH) is an increasingly recognized disorder classically presenting with disabling orthostatic headache, which manifests within minutes after assuming the upright position and subsides after lying down.^{1,2} SIH is widely believed to be triggered by CSF leakage from the intrathecal into the epidural compartment, which is usually due to an osteogenic microspur (calcified disc protrusion or spondylophyte) penetrating the dura or a leaky spinal nerve root diverticulum.^{3,4} Alternatively, a

CSF venous fistula (CSFVF) may be the underlying cause and has been reported in 23% of patients with SIH by Farb et al.⁵⁻⁷

Physiologically, CSF is sealed and circulates within the confines of the dura while a precise balance between production and resorption is maintained. When a dural breach or a CSFVF occurs, perturbation of the system ensues, resulting in a disturbance of the equilibrium. According to the Monro-Kellie hypothesis, the total volume within the confines of the skull is constant and is the sum of the volumes in 3 main compartments: blood, brain parenchyma, and CSF.^{8,9} Volume loss in one compartment is compensated by a reciprocal volume increase in the other compartments. In patients with SIH, the loss of CSF leads to a compensatory volume increase in the other compartments, which may be appreciated on brain imaging and includes meningeal enhancement, venous engorgement, and subdural hygroma.^{10,11} Although the sequelae of CSF loss in patients with SIH are widely recognized, volumetric analysis of the compartments has not yet been reported.

The goal of our study was to evaluate the volume of different intracranial compartments in SIH patients with a confirmed CSF

Received April 15, 2020; accepted after revision July 13.

From the Department of Diagnostic and Interventional Neuroradiology (T.D., C.R., P.M., J.G., E.I.P.), Support Center for Advanced Neuroimaging (M.R., C.R.), and Department of Neurosurgery (L.H., A.R., C.T.U., J.B.), Inselspital, Bern University Hospital, University of Bern, Bern, Switzerland; and Department of Neurosurgery (J.B.), Medical Center–University of Freiburg, Freiburg, Germany.

E.I. Piechowiak and J. Beck contributed equally to this work.

Please address correspondence to Tomas Dobrocky, MD, Institute of Diagnostic and Interventional Neuroradiology, Inselspital, Bern University Hospital, University of Bern, Freiburgstr 8, CH–3010, Switzerland; e-mail: tomas.dobrocky@insel.ch

Indicates open access to non-subscribers at www.ajnr.org

<http://dx.doi.org/10.3174/ajnr.A6782>

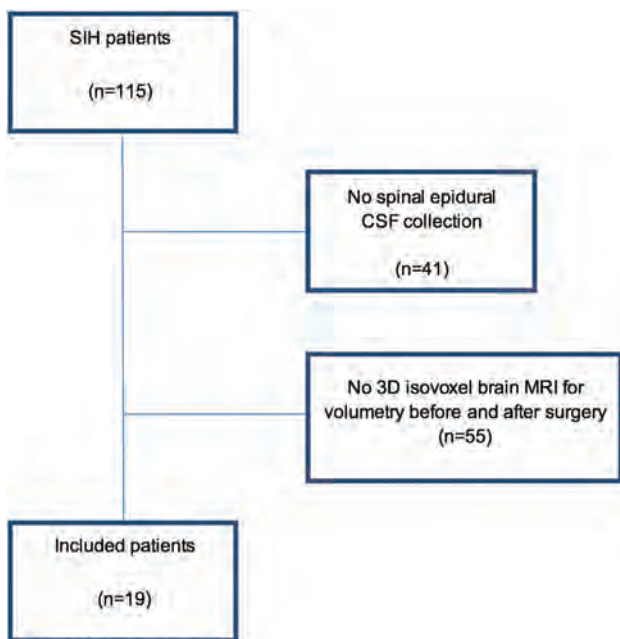


FIG 1. Flow chart of the included patients in our evaluation.

leak based on brain MR imaging before and after surgical closure of the leak.

MATERIALS AND METHODS

Institutional review board approval was obtained, and owing to the retrospective nature of the study, the need for informed consent was waived (Ethikkommission Bern). All consecutive patients with SIH diagnosed according to the International Classification of Headache Disorders,¹² referred to our institution between July 2014 and March 2017, were screened. Subgroups of patients have previously been included in other studies, which have investigated different outcome measures including optic nerve sheath ultrasonography, surgical details of dural closure, CSF dynamics, spinal imaging, and brain MR imaging, but did not report on brain volumetry.^{11,13-16}

Inclusion criteria were the following: 1) positive spinal imaging demonstrating an epidural CSF collection on MR imaging and post-myelography CT; 2) conventional dynamic myelography or dynamic CT myelography demonstrating the level of spinal CSF leakage; 3) surgical exploration and closure of the dural leak; 4) pretreatment brain MR imaging with isotropic, unenhanced T1-weighted sequences performed <7 days before surgery; 5) posttreatment brain MR imaging with isotropic, unenhanced T1-weighted sequences performed <7 days after surgery. Patients with post-lumbar puncture headache, poor-quality MR imaging, or absence of an isotropic T1-weighted sequence were excluded (Fig 1, study flow chart).

The brain and spine imaging of all subjects was assessed by 1 board-certified neuroradiologist (T.D.) with 9 years of experience.

Brain MR Imaging

MR imaging before and after surgical closure of the dural defect was performed on a 1.5T or 3T scanner (Magnetom Avanto and Magnetom Verio; Siemens) with a standard circularly polarized 12-channel phased array head coil.

Routine MRI pulse sequences included precontrast transverse T1-weighted (TR/TE 600/14 ms) spin-echo (SE), transverse T2-weighted (4100/100 ms) turbo SE images: slice thickness 5 mm; field of view (FOV) 192 × 220, and a 294 × 448 matrix size, coronal FLAIR images (8500/89/2440 ms [TR/TE/TI]; slice thickness: 4 mm; FOV 192 × 220 mm; acquisition time 1 minute 51 seconds; 358 × 512 matrix size). Postcontrast sagittal T1-weighted MPRAGE and coronal FLAIR fat-saturated images were acquired.

All patients received gadobutrol, 0.1 mL/kg body weight (1.0 mol/L, Gadovist; Bayer Schering Pharma) with a flow rate of 5 mL/s, followed by 20 mL of sodium chloride with the same flow rate. All patients underwent cranial MR imaging for clinical reasons, and because it was not part of a dedicated study protocol, the acquired sequences were not identical.

Images acquired using an unenhanced T1-weighted 3D modified driven equilibrium Fourier transform (MDEFT) sequence (TR/TE = 7.92/2.48 ms, section thickness = 1 mm, number of averages = 1, FOV = 256 × 256 mm, FOV phase = 50%, flip angle = 16°, acquisition time = 13 minutes and 45 seconds, matrix size = 256 × 256) were used for volumetry.

Brain SIH Score

This 9-point scoring system helps to predict the likelihood of a CSF leak in patients with suspected SIH.¹¹ The score is based on the 6 most relevant imaging findings: 3 major (2 points each), pachymeningeal enhancement, engorgement of the venous sinus, and effacement of the suprasellar cistern (≤ 4.0 mm); and 3 minor findings (1 point each), subdural fluid collection, effacement of the prepontine cistern (≤ 5.0 mm), and mamillopontine distance (≤ 6.5 mm). The SIH score was calculated before and after surgical closure of the dural defect. The total score was used to classify the patient's probability of having a spinal CSF leak: ≤ 2 = low, 3–4 = intermediate, and ≥ 5 = high.

Brain Volumetry

Brain volumetry was performed in patients with an, unenhanced T1-weighted MDEFT sequence acquired before and after surgical closure of the spinal dural breach. The images were run through the recon-all pipeline of the freely available software package FreeSurfer (<https://surfer.nmr.mgh.harvard.edu/>; Version 6.0.0). Briefly, the main processing steps of the FreeSurfer pipeline comprise intensity normalization, affine registration to a template (Talairach), bias field correction, skull-stripping, and nonlinear alignment to the Montreal Neurological Institute 305 atlas followed by a segmentation of tissue classes and subcortical structures using intensity and neighbor constraints. Besides tessellating the cortical surface and estimating morphometric parameters like cortical thickness and surface area,¹⁷ FreeSurfer also segments substructures of the entire brain volume (ventricles, basal ganglia, mesiotemporal structures, brain stem).^{18,19} The following intracranial compartments were segmented and provided in milliliters: ventricular CSF, considering the volume of each ventricle separately (lateral ventricles, third and fourth ventricles); GM and WM; and brain stem. (Fig 2). The choroid plexus was segmented as a separate structure and was not included to the ventricular volume. Each individual case was loaded in free-view in FreeSurfer (https://andysbrainbook.readthedocs.io/en/latest/FreeSurfer/FS_ShortCourse/FS_06_Freeview.html)

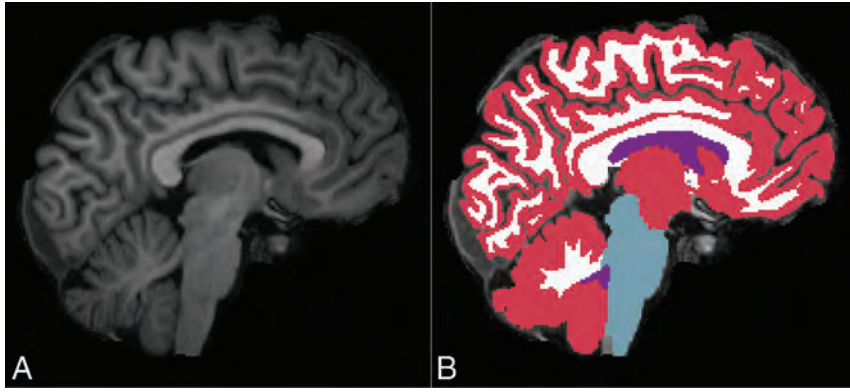


FIG 2. MDEFT sagittal image of a male patient after surgery (A) with the corresponding FreeSurfer segmentation of gray matter (red), white matter (white), brain stem (light blue), and ventricular CSF (purple) (B).

together with the corresponding segmentation for a manual review by M.R., experienced in brain volumetry, to ensure that ventricles were correctly identified and no outliers were erroneously included in the segmentation volume.

Spine Imaging

Our diagnostic technique has previously been described in detail.^{15,20} Briefly, unenhanced and intrathecal gadolinium-enhanced spine MR imaging was performed first. The images were scrutinized for a spinal longitudinal extradural CSF collection or epidural contrast leakage indicative of a spinal CSF leak. Dynamic conventional myelography was then performed with the patient in the prone position when an osteogenic microspur was suspected or in a lateral decubitus position when a spinal nerve root diverticulum was the presumed source of leakage. The level at which the contrast agent exited the intrathecal compartment and started spilling into the epidural space was considered the level of the dural breach. Postmyelography CT was performed immediately thereafter to identify any underlying pathology, eg, a calcified microspur. None of our patients presented with a CSFVF.

Surgical Closure of Dural Breach

This technique has been previously described.^{3,21} In short, after interlaminar fenestration or hemilaminotomy, the ligamentum flavum was removed. In the case of a ventral dural leak, a dorsal durotomy and a spinal cord release maneuver were performed to gain access to the anterior dura. The ventral osseous microspur penetrating the dura was removed, the dura was sutured, and small intra- and epidural patches were placed for augmentation. If a tear was found in the nerve root sleeve, access to the diverticulum was gained via foraminotomy. The diverticulum was reduced and clipped or the dura was sutured before being wrapped with an external dura graft, such as DuraGen (Integra).

Statistics

The statistical analysis was performed using R with the stats package (Version 3.6.2; <http://www.r-project.org/>). Descriptive analysis was performed using frequencies and percentages for categorical variables and mean (\pm SD) or median (interquartile range) for continuous

variables. Differences between pretreatment and follow-up measurements were assessed with paired, 2-sided *t* tests, with a significance threshold of $P < .05$. The relative change of volume was calculated as $100 \times (\text{post} - \text{pre}) / \text{pre}\%$. The differences between baseline and postsurgery volumetry were visualized with Tukey boxplots.

RESULTS

The final study population consisted of 19 patients (mean age, 41.8 ± 12.9 years; range, 25–70 years; 13 women, 6 men). The duration of clinical symptoms varied from a few days to several months. As shown on imaging and verified intraoperatively, the underlying

pathology was a ventral microspur originating from an intervertebral disc or an endplate osteophyte in 14/19 cases (74%) and a tear in the nerve root sleeve diverticulum in 5/19 cases (26%). The median time (interquartile range) from baseline MR imaging to treatment and from treatment to follow-up MR imaging was 1 [\pm 1] day and 4 [\pm 2] days, respectively. The mean brain SIH score in our patients with a confirmed spinal CSF leak was 6.9 ± 1.5 preoperatively, and it decreased to 2.9 ± 1.5 after surgical closure of the dural breach (Fig 3). After surgery, 17 patients demonstrated clinical improvement, 1 patient remained unchanged, and 1 patient was lost to follow-up. The severity of pain was evaluated using the numeric rating scale ranging from 0 to 10. The mean numeric rating scale decreased from 9.5 ± 1.4 before surgery to 2.5 ± 2.3 post-interventionally ($P < 0.001$).

The total mean ventricular CSF volume significantly increased from baseline (15.3 mL) to posttreatment MR imaging (18.0 mL), resulting in a mean absolute and relative difference of +2.7 mL and 18.8% (95% CI, +1.2 to +3.9 mL; $P = .001$) (Fig 4). A decrease in total ventricular CSF volume after the surgery was observed in 1 patient (−0.5%), whereas the remaining 18 patients demonstrated volume increase between 5.9% and 65.4%. The increase in ventricular CSF volume was statistically significant for all compartments: lateral ventricles (+18.7%, $P = .001$), third ventricle (+25.5%, $P = .001$), and fourth ventricle (+20.9%, $P = .008$) (Table and Fig 5). No significant change in mean total brain volume was observed (1136.9 versus 1133.1 mL, mean absolute and relative difference, −3.8 mL and −0.3% [95% CI, 0 to −7.6 mL] $P = .58$); either for GM (652.0 versus 644.8 mL; $P = .18$) or WM (458.7 versus 462.4 mL; $P = .27$).

DISCUSSION

Our data clearly demonstrate a substantial increase in ventricular CSF volume (+18.8%, $P = .001$) after surgical closure of the underlying spinal dural breach and thus may provide a causal link between spinal CSF loss and SIH. While alterations in CSF volume are minuscule and may hardly be appreciated by 2D measurements, volumetric analysis reliably demonstrates the change. The increase in ventricular CSF volume may be demonstrated in the

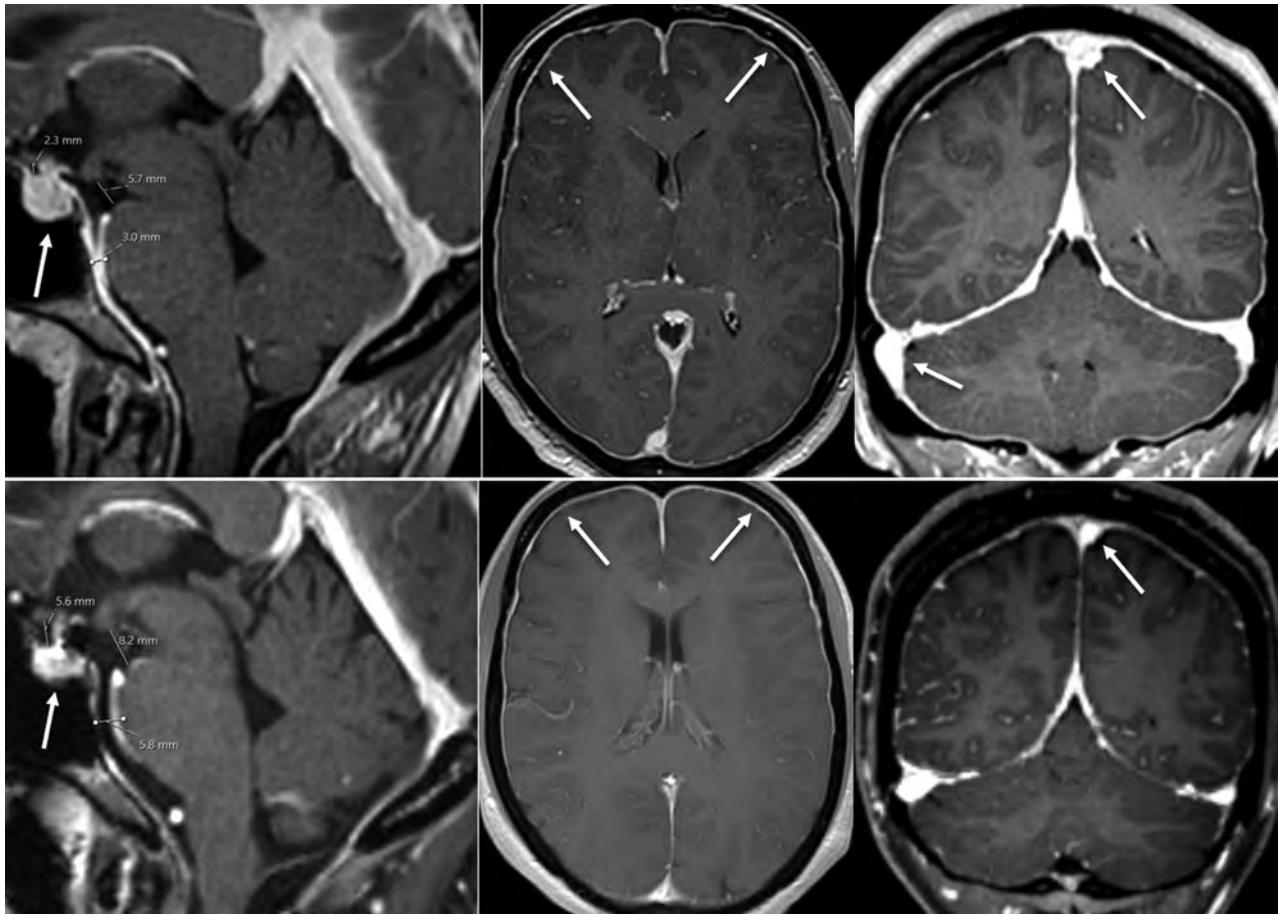


FIG 3. Female patient with a myelographically proved spinal CSF leak (not shown). *Upper row*, MR imaging performed before spinal surgery demonstrates typical findings of intracranial hypotension—SIH score = 8: pachymeningeal enhancement (2 points), engorgement of venous sinus (2 points), effacement of the suprasellar cistern (≤ 4.0 mm, 2 points), no subdural fluid collection (0 points), effacement of the prepontine cistern (≤ 5.0 mm, 1 point), and mamillopontine distance (≤ 6.5 mm, 1 point). *Lower row*, MR imaging performed after surgery demonstrates almost complete resolution of all findings: SIH score 2, due to residual dural enhancement. Note also the decrease in pituitary size (*arrow*).

early postoperative stage (mean, 4 days) and is paralleled by a decrease in the SIH score, which implies the restoration of an equilibrium within the CSF compartment. CSF opening pressure, on the other hand, is an insufficient diagnostic criterion because most patients with a spinal CSF leak present a normal pressure. As reported by Kranz et al,²² only 34% of patients with confirmed SIH had an opening pressure of < 6 cm H₂O.

Although volumetric analysis is time-demanding and usually not available in clinical routine, it may be a helpful tool in selected cases. For instance, in rebound intracranial hypertension, a phenomenon described in SIH patients after surgical closure of the leak, in whom the symptoms may resemble those of intracranial hypotension and make clinical discrimination challenging, however essential, because therapy is contrarious. In these cases, volumetric analysis may help to differentiate both and guide further treatment.

According to the Monro-Kellie doctrine, the sum of the volumes of brain parenchyma, CSF, blood, extracellular fluid, and meninges is constant within the rigid confines of the skull.²³ Thus, CSF loss is compensated by a reciprocal increase of volume in the other compartments to maintain the equilibrium. However, each compartment may not deserve the equal weighting implied by this static concept.⁹

When CSF loss occurs, the CSF production rate is insufficient to maintain an equilibrium within the compartment. Although there is 1 report that speculates that increased CSF production in the early phase of SIH may occur, this mechanism may not be adequate.²⁴ Second, the intracranial blood volume, which averages ~ 100 – 130 mL ($\sim 15\%$ arterial, $\sim 40\%$ venous, and $\sim 45\%$ in the microcirculation), may increase.⁹ The venous structures usually become enlarged and more conspicuous on imaging, leading to sinus distension, pachymeningeal enhancement, or pituitary hyperemia.^{25,26} Third, extra-axial fluid collections to compensate for the volume loss may be observed.²⁷

To depict the change in the blood volume and extraventricular CSF, the SIH score summarizing venous engorgement, dural enhancement, subdural collections, and effacement of the extraventricular CSF compartment (suprasellar, prepontine effacement; decrease in mamillopontine distance) was used in our study. The SIH score ranges from 0 to 9, with 0 indicating very low and 9 indicating a very high probability of spinal CSF loss. We believe that applying the score more appropriate than comparing each imaging sign separately. Furthermore, only imaging signs with high interrater agreement are considered for its calculation, while other imaging signs with low interrater agreement

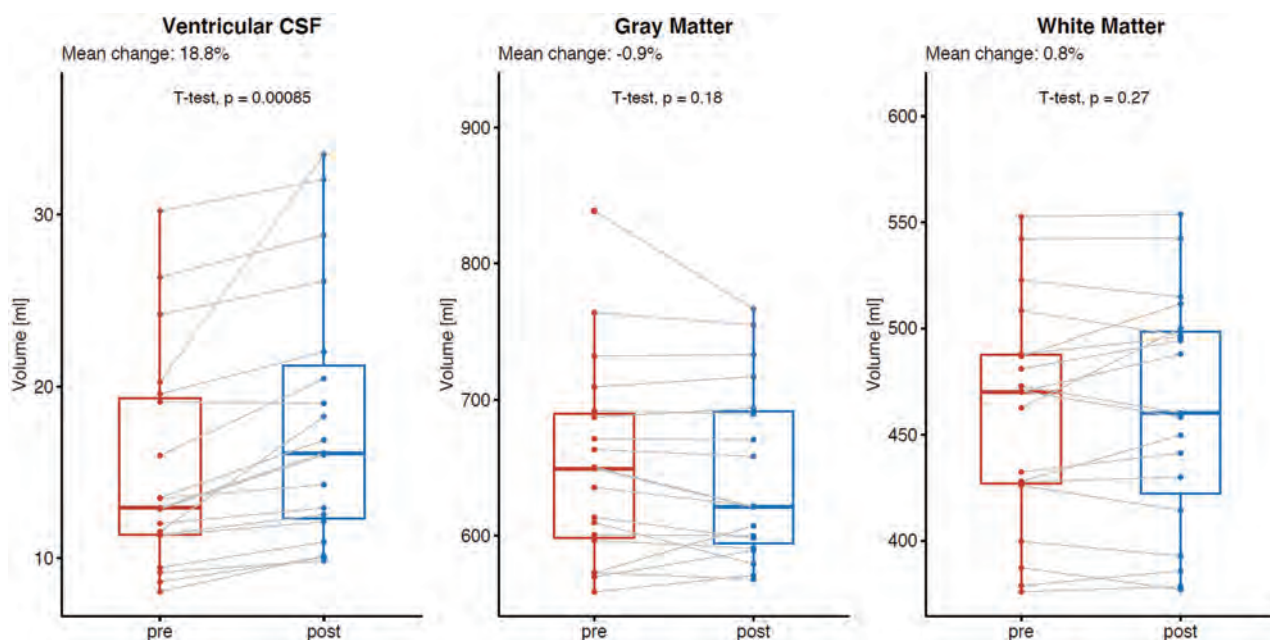


FIG 4. Mean absolute and relative change in volume between baseline and after surgical closure of the dural breach in patients with spontaneous intracranial hypotension: ventricular CSF (left, mean relative change, +18.8%, $P = .001$), total gray matter (middle, mean relative change, -0.9% , $P = .18$), and total white matter (right, mean relative change, $+0.8\%$, $P = .27$).

Volumetry results for different intracranial compartments^a

	Before Surgery	After Surgical Closure of Spinal Dural Tear	Difference: Absolute and Relative	P Value	Measurement Uncertainty
SIH score	6.9 ± 2.2	2.9 ± 1.7		<.001	
Ventricular CSF (mL)	15.3 ± 6.3	18.0 ± 7.4	+2.7 (+18.8%)	<.001	0.2
Lateral ventricle (mL)	12.9 ± 5.9	15.2 ± 6.9	+2.3 (+18.7%)	<.001	0.2
Third ventricle (mL)	0.8 ± 0.4	1.0 ± 0.3	+0.2 (+25.5%)	<.001	0.02
Fourth ventricle (mL)	1.5 ± 0.4	1.8 ± 0.4	+0.3 (+20.9%)	.008	0.05
Total brain parenchyma (mL)	1136.9 ± 116.6	1133.1 ± 111.0	-3.8 (-0.3%)	.58	7.6
Gray matter (mL)	652.0 ± 73.7	644.8 ± 64.3	-7.2 (-0.9%)	.18	7.3
White matter (mL)	458.7 ± 53.0	462.4 ± 54.9	+3.7 (+0.8%)	.27	10.8
Brain stem	22.9 ± 3.6	22.7 ± 3.5	-0.2 (-0.9%)	.34	0.2

^a Measurements show the mean volume in milliliters; the only exception is the SIH score in the first line.

proposed in the literature are not included.¹¹ The mean SIH score was 6.9 ± 1.5 at baseline and decreased to 2.9 ± 1.5 after surgical closure. This outcome translates into less conspicuous venous structures and meningeal enhancement and normalization of the extraventricular CSF compartment postoperatively.

Minor variations of ventricular volume may reflect variations in hydration status. As reported by Dickson et al,²⁸ in a single normally hydrated subject, the mean ventricular volume measured during 4 days showed a variation of 1.63%. Furthermore, in repeated volumetric analysis, an error inherent to the technique itself should be considered. To estimate this error, we refer to Rummel et al,²⁹ who have performed repeat MRIs in healthy subjects within <2 years (31 subjects with a total of brain 87 MRIs) to derive the measurement uncertainty and have reported volume uncertainties of 0.2 mL for the ventricular CSF.

However, the change in intracranial CSF volume presented in our study population clearly outweighs the level of error that could be expected. The ventricular CSF volume after surgery is in line with values reported in healthy individuals.³⁰

Our study did not demonstrate any significant change in the total volume of brain parenchyma after surgical closure of a dural breach. Brain tissue volume is generally considered invariable, and short-term changes are not expected.

Similar results for spinal CSF were reported in a threshold-based spine MR volumetry study in patients with SIH. Chen et al³¹ demonstrated a significant increase in intraspinal CSF between baseline and recovery (72.31 versus 93 mL, $P < .001$). The authors concluded that an increase in intraspinal CSF volume was related to disease recovery.

Limitations of the present study include the low number of patients with SIH with an available MDEFT sequence appropriate for volumetry. Second, only patients with a dural breach were included, not considering those with other etiologies like CSFVF. Third, extraventricular CSF and the intracranial blood volume compartments were not included in our volumetric analysis because they are not provided in FreeSurfer. In the authors' experience, other methods like the FMRIB Automated Segmentation Tool (<http://fsl.fmrib.ox.ac.uk/fsl/fslwiki/fast>),

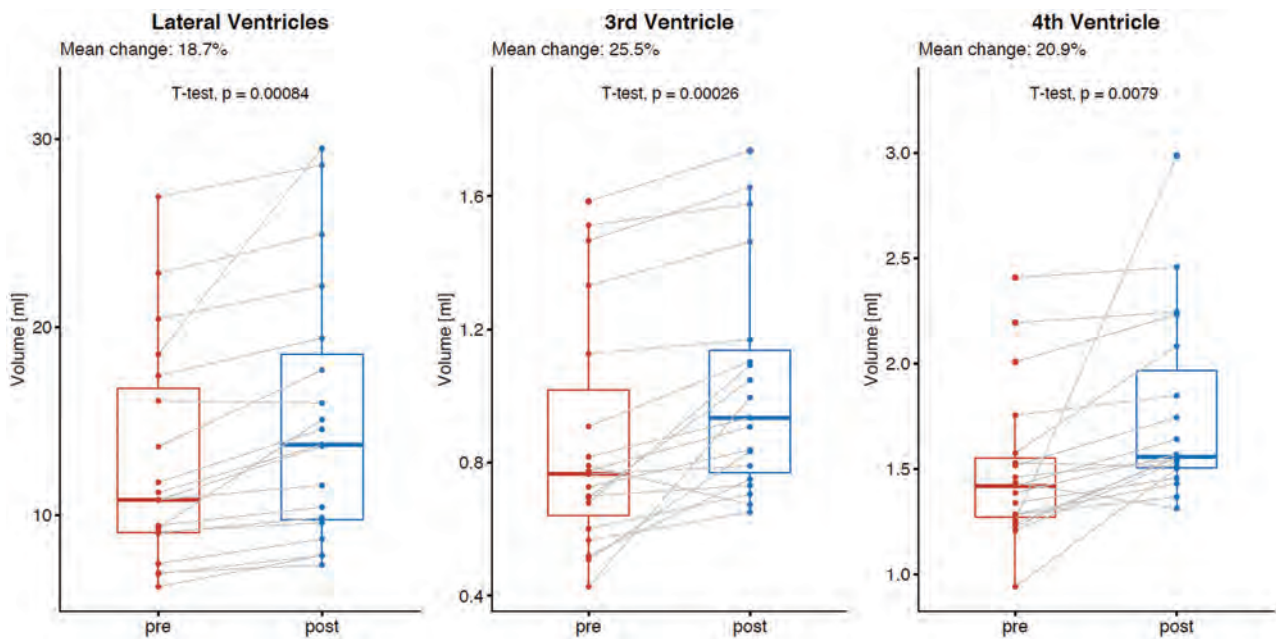


FIG 5. Mean absolute and relative changes in ventricular CSF volume between baseline and after surgical closure of the dural breach in patients with spontaneous intracranial hypotension for each ventricle separately: lateral ventricles (left, mean relative change, +18.7%, $P = .001$), third ventricle (mean relative change, +25.5%, $P = .001$), and fourth ventricle (mean relative change, +20.9%, $P = .008$).

which includes extraventricular CSF, are not reliable due to erroneous outer delineations of the subarachnoid space and variations in skull-stripping.³²

On the other hand, we provide results obtained in a very well-defined cohort of SIH patients SIH with myelographically-proved spinal CSF leak. In addition, the spinal dural breach was verified intraoperatively before being sealed with a suture and an additional patch.

In summary, the continuing research on SIH has increased our understanding of the underlying causes. Our results are in line with the proposed mechanism of CSF depletion leading to compensatory processes. Finally, an increase in total ventricular CSF volume after surgical closure of the spinal breach indicates a restoration of an equilibrium within the CSF compartment that has been perturbed.

CONCLUSIONS

A substantial increase in ventricular CSF volume after surgical closure of the underlying dural breach in patients with SIH may be observed in the early postoperative stage. It may be a valuable indicator of recovery, providing a causal link between the spinal CSF loss and SIH. The concomitant decrease in the SIH score postoperatively implies the restoration of an equilibrium within the CSF compartment and is in line with the Monro-Kellie hypothesis.

Disclosures: Michael Rebsamen—RELATED: Grant: Swiss National Science Foundation, Comments: This work was supported by the Swiss National Science Foundation under grant No.180365.* Jan Gralla—UNRELATED: Consultancy: Global Principal Investigator Swift Direct, Comments: stroke study funded by Medtronic*; Grants/Grants Pending: Swiss National Science Foundation, Comments: stroke MRI study.* *Money paid to the institution.

REFERENCES

1. Schievink WI. Spontaneous spinal cerebrospinal fluid and ongoing investigations in this area. *JAMA* 2006;295:2286–96 CrossRef Medline

2. Kranz PG, Gray L, Amrhein TJ. Spontaneous intracranial hypotension: 10 myths and misperceptions. *Headache* 2018;58:948–59 CrossRef Medline
3. Beck J, Ulrich CT, Fung C, et al. Diskogenic microspurs as a major cause of intractable spontaneous intracranial hypotension. *Neurology* 2016;87:1220–26 CrossRef Medline
4. Kranz PG, Stinnett SS, Huang KT, et al. Spinal meningeal diverticula in spontaneous intracranial hypotension: analysis of prevalence and myelographic appearance. *AJNR Am J Neuroradiol* 2013;34:1284–89 CrossRef Medline
5. Kranz PG, Amrhein TJ, Gray L. CSF venous fistulas in spontaneous intracranial hypotension: Imaging characteristics on dynamic and CT myelography. *AJR Am J Roentgenol* 2017;209:1360–66 CrossRef Medline
6. Kumar N, Diehn FE, Carr CM, et al. Spinal CSF venous fistula: a treatable etiology for CSF leaks in craniocervical hypovolemia. *Neurology* 2016;86:2310–12 CrossRef Medline
7. Farb RI, Nicholson PJ, Peng PW, et al. Spontaneous intracranial hypotension: a systematic imaging approach for CSF leak localization and management based on MRI and digital subtraction myelography. *AJNR Am J Neuroradiol* 2019;40:745–53 CrossRef Medline
8. Harvey C. The third circulation in studies in intracranial physiology and surgery. In: *The Third Circulation in Studies in Intracranial Physiology and Surgery*. Oxford University Press; 1926
9. Wilson MH. Monro-Kellie 2.0: the dynamic vascular and venous pathophysiological components of intracranial pressure. *J Cereb Blood Flow Metab* 2016;36:1338–50 CrossRef Medline
10. Kranz PG, Tanpitukpongse TP, Choudhury KR, et al. Imaging signs in spontaneous intracranial hypotension: prevalence and relationship to CSF pressure. *AJNR Am J Neuroradiol* 2016;37:1374–78 CrossRef Medline
11. Dobrocky T, Grunder L, Breiding PS, et al. Assessing spinal cerebrospinal fluid leaks in spontaneous intracranial hypotension with a scoring system based on brain magnetic resonance imaging findings. *JAMA Neurol* 2019;76:580 CrossRef Medline
12. Headache Classification Committee of the International Headache Society (IHS): the International Classification of Headache Disorders, 3rd edition. *Cephalalgia* 2018; 38:1–211 CrossRef Medline

13. Fichtner J, Ulrich CT, Fung C, et al. **Sonography of the optic nerve sheath diameter before and after microsurgical closure of a dural CSF fistula in patients with spontaneous intracranial hypotension: a consecutive cohort study.** *Cephalalgia* 2019;39:306–15 CrossRef Medline
14. Fichtner J, Ulrich CT, Fung C, et al. **Management of spontaneous intracranial hypotension: transorbital ultrasound as discriminator.** *J Neurol Neurosurg Psychiatry* 2016;87:650–55 CrossRef Medline
15. Dobrocky T, Mosimann PJ, Zibold F, et al. **Cryptogenic cerebrospinal fluid leaks in spontaneous intracranial hypotension: role of dynamic CT myelography.** *Radiology* 2018;289:766–72 CrossRef Medline
16. Beck J, Fung C, Ulrich CT, et al. **Cerebrospinal fluid outflow resistance as a diagnostic marker of spontaneous cerebrospinal fluid leakage.** *J Neurosurg Spine* 2017;27:227–34 CrossRef Medline
17. Fischl B, Dale AM. **Measuring the thickness of the human cerebral cortex from magnetic resonance images.** *Proc Natl Acad Sci U S A* 2000;97:11050–55 CrossRef Medline
18. Fischl B, Salat DH, Busa E, et al. **Whole brain segmentation: automated labeling of neuroanatomical structures in the human brain.** *Neuron* 2002;33:341–55 CrossRef Medline
19. Fischl B, Salat DH, van der Kouwe AJ, et al. **Sequence-independent segmentation of magnetic resonance images.** *Neuroimage* 2004;23 (Suppl 1):S69–84 CrossRef Medline
20. Kranz PG, Luetmer PH, Diehn FE, et al. **Myelographic techniques for the detection of spinal CSF leaks in spontaneous intracranial hypotension.** *AJR Am J Roentgenol* 2016;206:8–19 CrossRef Medline
21. Beck J, Raabe A, Schievink WI, et al. **Posterior approach and spinal cord release for 360° repair of dural defects in spontaneous intracranial hypotension.** *Neurosurgery* 2019;84:E345–51 CrossRef Medline
22. Kranz PG, Tanpitukpongse TP, Choudhury KR, et al. **How common is normal cerebrospinal fluid pressure in spontaneous intracranial hypotension?** *Cephalalgia* 2016;36:1209–17 CrossRef Medline
23. Monro A. *Observations on Structure and Functions of the Nervous System.* Creech and Johnson; 1783
24. Häni L, Fung C, Jesse CM, et al. **Insights into the natural history of spontaneous intracranial hypotension from infusion testing.** *Neurology* 2020;95:e247–55 CrossRef Medline
25. Fishman RA, Dillon WP. **Dural enhancement and cerebral displacement secondary to intracranial hypotension.** *Neurology* 1993;43:609–11 CrossRef Medline
26. Savoirdo M, Armenise S, Spagnolo P, et al. **Dural sinus thrombosis in spontaneous intracranial hypotension: hypotheses on possible mechanisms.** *J Neurol* 2006;253:1197–202 CrossRef Medline
27. Beck J, Gralla J, Fung C, et al. **Spinal cerebrospinal fluid leak as the cause of chronic subdural hematomas in nongeriatric patients.** *J Neurosurg* 2014;121:1380–87 CrossRef Medline
28. Dickson JM, Weavers HM, Mitchell N, et al. **The effects of dehydration on brain volume: preliminary results.** *Int J Sports Med* 2005;26:481–85 CrossRef Medline
29. Rummel C, Aschwanden F, McKinley R, et al. **A fully automated pipeline for normative atrophy in patients with neurodegenerative disease.** *Front Neurol* 2017;8:727 CrossRef Medline
30. Blatter DD, Bigler ED, Gale SD, et al. **Quantitative volumetric analysis of brain MR: normative database spanning 5 decades of life.** *AJNR Am J Neuroradiol* 1995;16:241–51 Medline
31. Chen HC, Chen PL, Tsai YH, et al. **Quantitative measurement of CSF in patients with spontaneous intracranial hypotension.** *AJNR Am J Neuroradiol* 2017;38:1061–67 CrossRef Medline
32. Patenaude B, Smith SM, Kennedy DN, et al. **A Bayesian model of shape and appearance for subcortical brain segmentation.** *Neuroimage* 2011;56:907–22 CrossRef Medline

Sensitive Detection of Infratentorial and Upper Cervical Cord Lesions in Multiple Sclerosis with Combined 3D FLAIR and T2-Weighted (FLAIR3) Imaging

R.E. Gabr, J.A. Lincoln, A. Kamali, O. Arevalo, X. Zhang, X. Sun, K.M. Hasan, and P.A. Narayana



ABSTRACT

BACKGROUND AND PURPOSE: Infratentorial and spinal cord lesions are important for diagnosing and monitoring multiple sclerosis, but they are difficult to detect on conventional MR imaging. We sought to improve the detection of infratentorial and upper cervical cord lesions using composite FLAIR3 images.

MATERIALS AND METHODS: 3D T2-weighted FLAIR and 3D T2-weighted images were acquired in 30 patients with MS and combined using the FLAIR3 formula. FLAIR3 was assessed against 3D T2-FLAIR by comparing the number of infratentorial and upper cervical cord lesions per subject using the Wilcoxon signed rank test. Intrarater and interrater reliability was evaluated using the intraclass correlation coefficient. The number of patients with and without ≥ 1 visible infratentorial/spinal cord lesion on 3D T2-FLAIR versus FLAIR3 was calculated to assess the potential impact on the revised MS diagnostic criteria.

RESULTS: Compared with 3D T2-FLAIR, FLAIR3 detected significantly more infratentorial (mean, 4.6 ± 3.6 versus 2.0 ± 1.8 , $P < .001$) and cervical cord (mean, 1.58 ± 0.94 versus 0.46 ± 0.45 , $P < .001$) lesions per subject. FLAIR3 demonstrated significantly improved interrater reliability (intraclass correlation coefficient = 0.77 [95% CI, 0.63–0.87] versus 0.60 [95% CI, 0.40–0.76] with 3D T2-FLAIR, $P = .019$) and a tendency toward a higher intrarater reliability (0.86 [95% CI, 0.73–0.93] versus 0.79 [95% CI, 0.61–0.89], $P = .23$). In our cohort, 20%–30% (47%–67%) of the subjects with MS had ≥ 1 infratentorial (cervical cord) lesion visible only on FLAIR3.

CONCLUSIONS: FLAIR3 provides higher sensitivity than T2-FLAIR for the detection of MS lesions in infratentorial brain parenchyma and the upper cervical cord.

ABBREVIATION: CNR = contrast-to-noise ratio

Infratentorial brain lesions are commonly present in MS, an inflammatory and demyelinating disease of the CNS that affects 2.5 million individuals worldwide.¹ The current McDonald criteria for diagnosing MS require demonstration of the dissemination of CNS lesions in time and space.² Dissemination in space is established through detection of ≥ 1 T2-hyperintense lesion characteristic of MS in ≥ 2 areas in the CNS: infratentorial (including

the brain stem and cerebellum), periventricular, and juxtacortical brain regions and the spinal cord.²

MR imaging is the primary technique in MS, used for diagnosis, detecting pathology, monitoring the disease course, and patient management. T2-FLAIR MR imaging is currently the most commonly used imaging sequence for identifying brain T2-hyperintense lesions. However, the contrast of infratentorial lesions on T2-FLAIR is suboptimal due to partial T1-weighting and different tissue relaxation properties between supratentorial and infratentorial regions.^{3–5}

3D T2-FLAIR imaging has shown promise in improving the detection of infratentorial lesions,^{6,7} especially with optimized scan parameters.⁸ Combining T2-weighted and proton density-weighted images has also shown improved contrast.⁹ A previous study has shown that an algebraic combination of T2-FLAIR and T2-weighted images,¹⁰ referred to as FLAIR3, can yield substantial improvement in lesion contrast, but the performance for infratentorial lesion detection was not specifically addressed in that publication.

Received March 4, 2020; accepted after revision July 22.

From the Departments of Diagnostic and Interventional Imaging (R.E.G., A.K., O.A., X.S., K.M.H., P.A.N.) and Neurology (J.A.L.), and Center for Clinical and Translational Sciences, (X.Z.), University of Texas Health Science Center at Houston, Houston, Texas.

This work was partially funded by the National Institute of Neurological Disorders and Stroke/National Institutes of Health (grant No. IR56NS105857), the Chair in Biomedical Engineering Endowment, and the Dunn Foundation. The 3T scanner was partially funded by National Institutes of Health (grant No. 1 S10 RR19186-01).

Please address correspondence to Refaat E. Gabr, PhD, Department of Diagnostic and Interventional Imaging, University of Texas Medical School at Houston, 6431 Fannin St, MSE R102D, Houston, TX 77030; e-mail: refaat.e.gabr@uth.tmc.edu

Indicates open access to non-subscribers at www.ajnr.org

<http://dx.doi.org/10.3174/ajnr.A6797>

Table 1: Characteristics of the study participants

Characteristics	
No. of subjects	30
Female/male	24:6
Age (mean) (yr)	43 ± 12
Phenotype	
Relapsing-remitting MS	25
Secondary-progressive MS	5
Disease duration (median) (range) (yr)	6.5 (0.3–43.9)
EDSS (median) (range)	1.75 (0–6.5)

Note:—EDSS indicates Expanded Disability Status Scale.

The primary aim of this prospective study was to test whether the lesion contrast and detectability of MS infratentorial lesions are improved with FLAIR3 imaging compared with 3D T2-FLAIR alone. With the extended FOV offered by 3D acquisitions, we also assessed the performance of these two methods for detecting upper cervical cord lesions.

MATERIALS AND METHODS

Study Subjects

This was a single-center, prospective study that included 30 patients with definite MS. The demographics and clinical characteristics of the study participants are listed in Table 1. The study was approved by our institutional review board, and all volunteers gave written informed consent.

MR Imaging Experiments

All brain MR imaging scans were performed on a 3T Ingenia MR imaging scanner (Philips Healthcare; software version R5.1.7) using a 15-channel head coil. 3D T2-FLAIR and 3D T2-weighted images were acquired in the sagittal plane (frequency-encoding in the foot-head direction with oversampling to reduce aliasing; phase-encoding along the left-right and anterior-posterior directions) with a TSE sequence with refocusing control (volume isotropic turbo spin-echo acquisition). The scan parameters were the following: 3D T2-FLAIR (TR/TI/TE = 4800/1650/300 ms; T2-preparation time = 125 ms; echo-train length = 167; scan time = 5:31 minutes) and 3D T2-weighted (TR/TE = 2500/252 ms; echo-train length = 133; scan time = 4:33 minutes). Both images were acquired with matching spatial coverage and resolution (FOV = 256 × 256 × 180 mm³; voxel size = 1 × 1 × 1 mm³).

FLAIR3 Reconstruction

After acquisition, the 3D T2-FLAIR and 3D T2-weighted images were coregistered with a rigid-body transformation using the Advanced Normalization Tools (ANTs) software¹¹ (<http://stnava.github.io/ANTs/>) and algebraically combined to produce the FLAIR3 image using the following formula: FLAIR3 = FLAIR^{1.55} × T2-weighted^{1.45}. This formula was proposed as a balance between lesion contrast and CSF suppression.¹⁰ To improve the dynamic range of the reconstructed FLAIR3 image, we performed intensity nonuniformity correction using multiplicative intrinsic component optimization, an energy-minimization method for joint bias field estimation and segmentation.¹²

Image Analysis

A board-certified neuroradiologist with 6 years of experience (A.K., rater 1) and an MS neurologist with 15 years of experience in neuroimaging of MS (J.A.L., rater 2) identified all infratentorial and upper cervical lesions seen on 3D T2-FLAIR and FLAIR3 images. Due to the large difference in image contrast between T2-FLAIR and FLAIR3, blind evaluation was not feasible. The 3D T2-FLAIR and FLAIR3 images were reviewed in several sessions during 7 weeks (rater 1) and 8.5 weeks (rater 2), with the raters first analyzing all 3D T2-FLAIR images before starting on FLAIR3 images. There was no specified order for reviewing images in each set. Thus, we did not expect a substantial recall bias. In addition, a neuroradiology fellow (O.A., rater 3) who was not familiar with the imaging protocol or the study objective independently evaluated all images to identify infratentorial and cervical cord lesions. For rater 3, 3D T2-FLAIR and FLAIR3 images from all subjects were pooled and randomized for review. Image evaluation was performed during 1–2 days. Interrater reliability was evaluated using image evaluations by raters 1 and 2, together with the first image evaluation by rater 3. Rater 3 repeated the analysis (with a different randomization) after 3 weeks to assess intrarater reliability.

Lesions were identified as regions with hyperintense signal compared with the background tissue, visible on all 3 planes. ROIs were manually drawn on the identified lesions on an axial section showing the largest extent of the lesion using MRICron software (<https://www.nitrc.org/projects/mricron/>).¹³ The ROIs were carefully placed to minimize partial volume effects from surrounding tissue that could affect contrast computations. Control ROIs were placed in adjacent normal-appearing white matter, and the lesion conspicuity was assessed by the contrast-to-noise ratio (CNR), calculated as $CNR = (S_L - S_B) / SD_N$, where S_L and S_B are the average signal intensities in the lesion and background ROIs, respectively, and SD_N is the estimated SD of the image noise, obtained from histogram analysis of local image variance.¹⁴

To investigate the potential impact of FLAIR3 on the diagnostic criterion in MS, we calculated the number of lesions detected on either or both image sets. We also computed the number of subjects with ($n \geq 1$) and without ($n = 0$) infratentorial or cord lesions on each image.

Statistical Analysis

We constructed histograms to examine distributions of continuous variables. Normality was not satisfied for the difference in the number of lesions. Hence, the number of lesions per subject between 3D T2-FLAIR and FLAIR3 was compared using the Wilcoxon signed rank test. Lesion CNR between T2-FLAIR and FLAIR3 was assessed at the lesion level using the van Elteren test to account for patient clustering. Based on histograms, normality approximately held for the total number (infratentorial + cervical) of lesions only. For the total number of lesions, we fitted the 2-way random-effects models to individual measurements and calculated the intraclass correlation coefficients to measure interrater variability and intrarater reliability. We generated 2000 bootstrap samples to compare the intraclass correlation coefficients for 3D T2-FLAIR and FLAIR3. Pearson correlation analysis and linear regression were performed to visualize the correspondence among the 3 raters for the total number of lesions per subject. A P value < .05 was

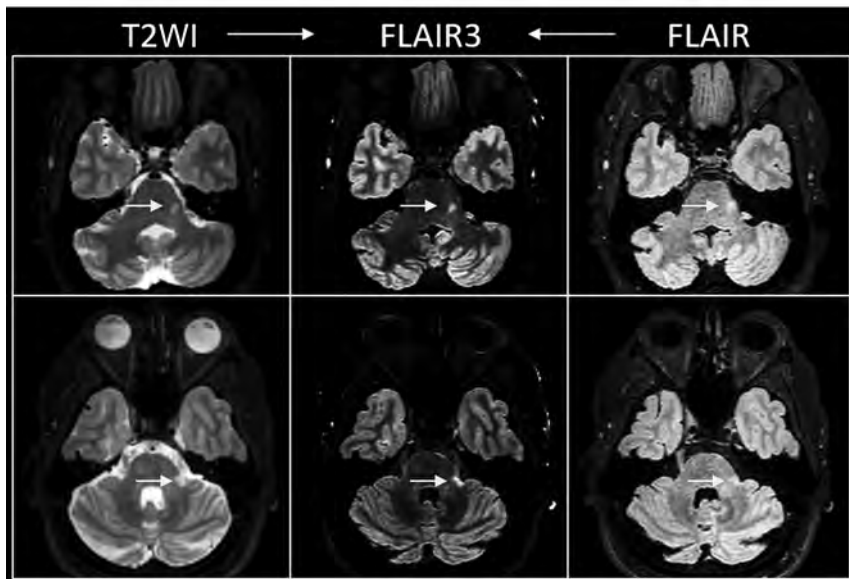


FIG 1. Acquired T2-weighted (left) and FLAIR (right) images and the reconstructed FLAIR3 images (middle) from 2 patients with MS (rows). Note the improved contrast of the infratentorial lesions (arrows) on FLAIR3.

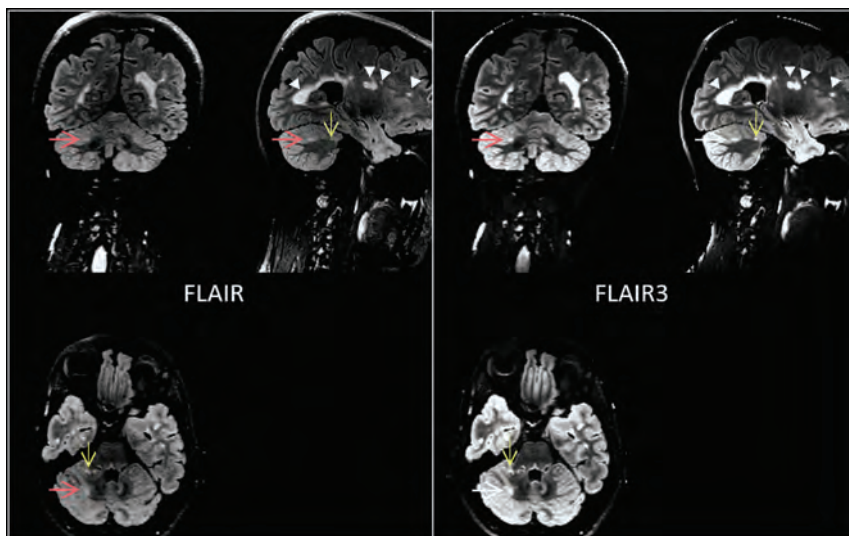


FIG 2. Three-plane view showing the improved contrast of infratentorial lesions (red and yellow arrows) on FLAIR3 compared with FLAIR.

considered statistically significant for all tests. Statistical analysis was performed using the SAS software (Version 9.4; SAS Institute).

RESULTS

Figure 1 shows representative sections from 3D T2-FLAIR, T2-weighted, and reconstructed FLAIR3 images from 2 patients with MS. Note the improved visual lesion contrast in the infratentorial region on FLAIR3. Corresponding 3D T2-FLAIR and FLAIR3 images are shown in subsequent figures, demonstrating the improved lesion contrast with FLAIR3 in infratentorial (Fig 2) and upper cervical cord (Fig 3) lesions.

The number of all lesions per subject by each rater is summarized in Table 2. A larger number of lesions were found using FLAIR3 for both types of lesion by all raters, with a rater average (\pm SD) of 6.2 ± 4.2 total lesions on FLAIR3 versus 2.5 ± 2.0 lesions on 3D T2-FLAIR ($P < .001$). On average, 4.6 ± 3.6 infratentorial lesions and 1.58 ± 0.94 cervical cord lesions were detected on FLAIR3 compared with 2.0 ± 1.8 infratentorial lesions ($P < .01$) and 0.46 ± 0.45 cervical cord lesions ($P < .001$) on 3D T2-FLAIR. Lesions on FLAIR3 showed significantly higher average lesion CNR compared with T2-FLAIR (Table 3).

Good interrater reliability was observed in this study, with a significantly higher intraclass correlation coefficient of 0.77 (95% CI, 0.63–0.87) for all lesions detected on FLAIR3 compared with 3D T2-FLAIR, 0.60 (95% CI, 0.40–0.76) ($P = .019$). Intrarater reliability was also higher for FLAIR3 with the intraclass correlation coefficient of 0.86 (95% CI, 0.73–0.93) compared with 0.79 (95% CI, 0.61–0.89) for 3D T2-FLAIR, but the difference was not statistically significant ($P = .23$). Figure 4 shows the pair-wise Pearson correlation among the 3 raters for the average total number of lesions. The better agreement among the raters using FLAIR3 is evident by the higher correlation coefficients.

The number of infratentorial or upper cervical cord lesions detected on 3D T2-FLAIR alone, FLAIR3 alone, and both 3D T2-FLAIR and FLAIR3 is summarized in Table 4. Table 4 also reports the number of subjects with MS with ($n \geq 1$) and without ($n = 0$) infratentorial or cord lesions detected on either or both images. FLAIR3 identified infratentorial lesions in 20%–30% of the subjects and cervical cord lesions in 47%–67% of the subjects who had normal findings on T2-FLAIR.

DISCUSSION

In this study, on FLAIR3, we detected approximately 2.3 and 3.4 times the number of infratentorial and cervical cord lesions, respectively, compared with 3D T2-FLAIR, with lesion–white matter CNR showing approximately 4- to 5-fold improvement. In addition, higher intra- and interrater agreement was obtained with FLAIR3, suggesting a higher degree of confidence for lesion identification. Most interesting, rater 3, who was blinded to the type of sequence

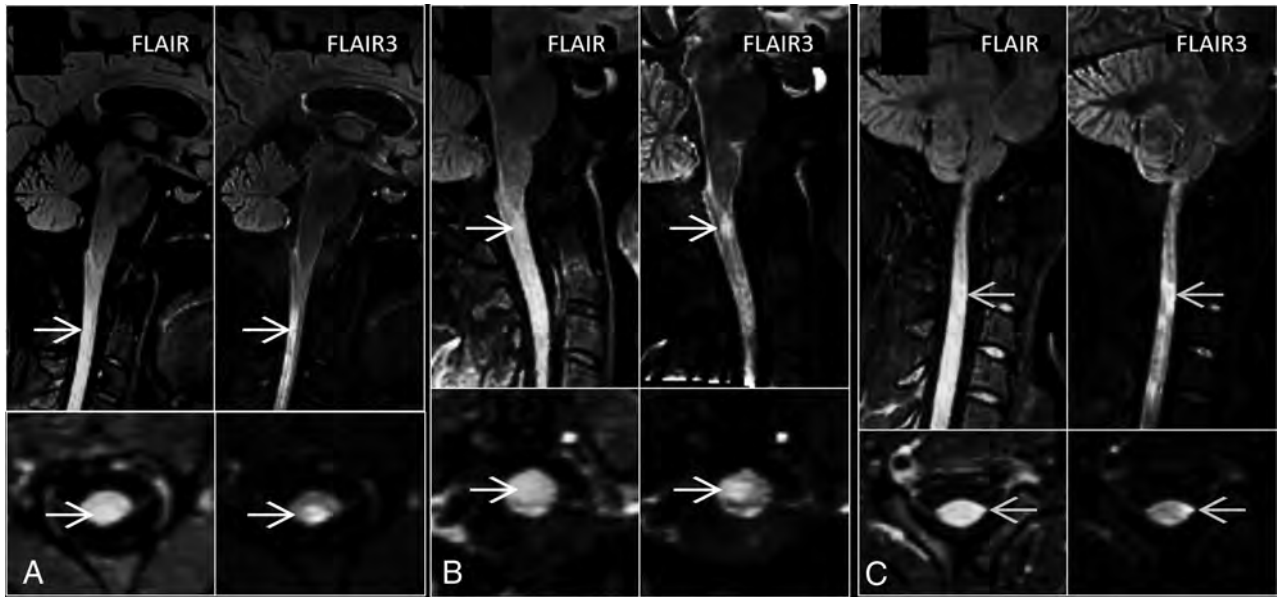


FIG 3. Sagittal (*upper row*) and axial (*lower row*) sections showing improved contrast of cervical cord lesions on FLAIR3 compared with FLAIR in 3 patients with MS. The lesions were detected on both FLAIR and FLAIR3 in case A, but only on FLAIR3 in cases in B and C.

Table 2: Number of lesions per subject detected on 3D T2-FLAIR and FLAIR3

	No. of Lesions per Subject (Mean)					
	Rater 1		Rater 2		Rater 3	
	T2-FLAIR	FLAIR3	T2-FLAIR	FLAIR3	T2-FLAIR	FLAIR3
All lesions	2.3 ± 2.2	6.9 ± 4.7 ^a	2.5 ± 2.2	5.5 ± 3.6 ^a	2.7 ± 2.5	6.1 ± 5.1 ^b
Infratentorial lesions	2.0 ± 1.9	5.4 ± 4.1 ^a	2.0 ± 2.0	3.9 ± 3.3 ^c	2.1 ± 2.4	4.5 ± 4.4 ^c
Cervical cord lesions	0.27 ± 0.58	1.57 ± 1.14 ^a	0.50 ± 0.68	1.60 ± 0.81 ^a	0.60 ± 0.72	1.57 ± 1.17 ^a

^a $P < .001$ compared with T2-FLAIR.

^b $P < .01$ compared with T2-FLAIR.

^c $P < .05$ compared with T2-FLAIR.

Table 3: CNR of lesions detected on 3D T2-FLAIR and FLAIR3^a

	Rater 1				Rater 2			
	T2-FLAIR		FLAIR3		T2-FLAIR		FLAIR3	
	No.	CNR (No. of Lesions)	No.	CNR	No.	CNR	No.	CNR
Infratentorial lesions	61	4.83 ± 2.33	161	23.3 ± 19.9 ^b	59	5.8 ± 2.8	117	27.9 ± 20.3 ^b
Cervical cord lesions	8	13.8 ± 9.1	47	48.2 ± 30.6 ^b	15	9.7 ± 6.2	48	41.9 ± 23.9 ^b

^a Data are means or No.

^b $P < .001$ compared with T2-FLAIR.

and the goal of the study, had a similar number of lesions compared with those obtained with the raters familiar with the imaging protocol. This finding supports the superiority of FLAIR3 in objectively detecting the lesions over 3D T2-FLAIR.

The improved detection of infratentorial and cord lesions can increase the confidence in diagnosing and monitoring patients with MS. In addition to its role in diagnosing MS, a previous study found that the volume of infratentorial lesions correlated with the sensory functional system score.¹⁵ Infratentorial lesions were also found to be predictive of long-term prognosis in patients with initial findings suggestive of MS,¹⁶ and the volume of infratentorial T1-hypointense lesions correlated with the Expanded Disability Status Scale score in patients with MS with chronic cerebellar

ataxia.¹⁷ The high sensitivity of FLAIR3 can, thus, be useful in studies assessing the prognostic value of these lesions.

Our study first focused on imaging infratentorial lesions, but with the extended coverage in the foot-head direction offered by the 3D sagittal TSE protocols, we were able to additionally assess upper cervical cord lesions. Currently, sagittal sequences including conventional T2-weighted, proton density-weighted,¹⁸ STIR,¹⁹ and phase-sensitive inversion recovery²⁰ are recommended for assessing spinal cord lesions.²¹ A comparative study of FLAIR3 with those sequences will be necessary for evaluating the role it can play in spinal cord imaging.

A limitation of FLAIR3, similar to other image-combining methods, is its susceptibility to image registration errors. Executing

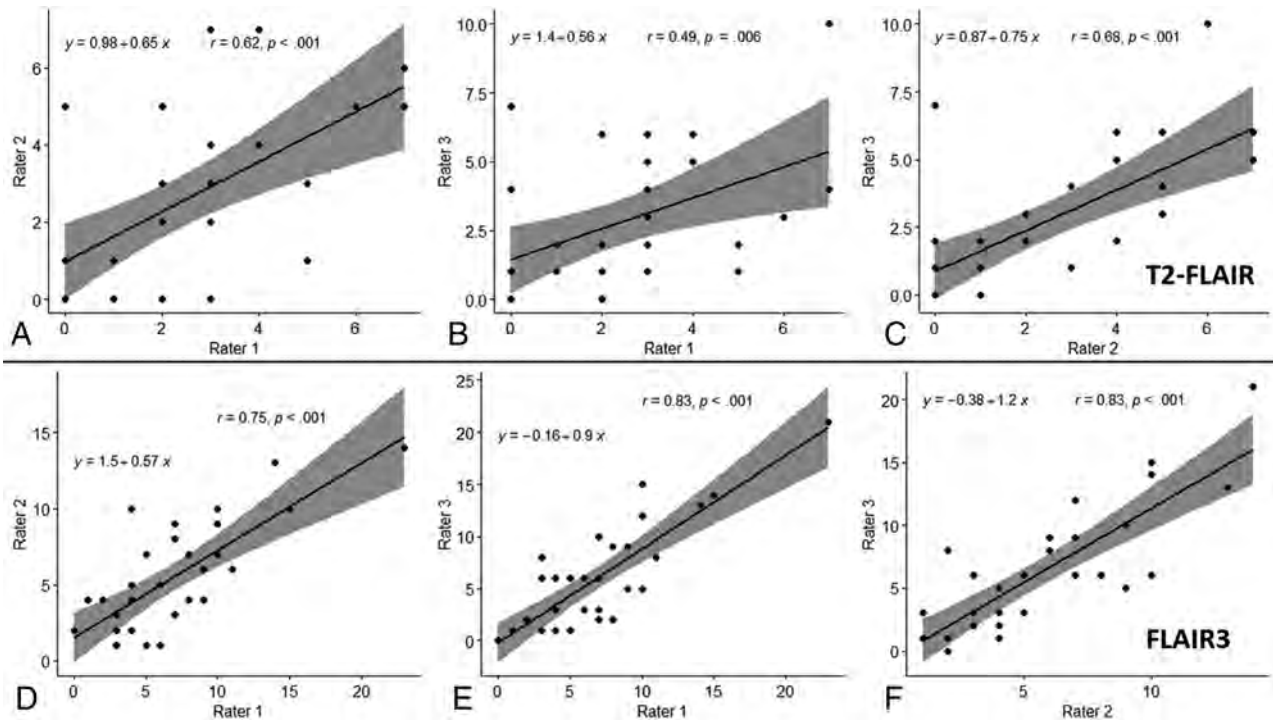


FIG 4. Scatterplot and linear regression with the 95% confidence interval (shaded) between the raters for the average total number of lesions for 3D T2-FLAIR (upper row, A–C) and FLAIR3 (lower row, D–F).

Table 4: Number of lesions detected on 3D T2-FLAIR and/or FLAIR3 images

	Rater 1			Rater 2			Rater 3		
	FLAIR and FLAIR3	FLAIR Only	FLAIR3 Only	FLAIR and FLAIR3	FLAIR Only	FLAIR3 Only	FLAIR and FLAIR3	FLAIR Only	FLAIR3 Only
No. of lesions									
Infratentorial	46	15	115	45	4	72	49	16	89
Cervical cord	7	1	40	13	2	35	14	4	35
No. of subjects with MS with ≥ 1 lesion									
Infratentorial	19	1	9	19	1	7	19	0	6
Cervical cord	6	0	20	13	0	16	14	1	14

the T2-FLAIR and T2-weighted sequences in succession with minimal delay can help minimize these errors. Interleaving the T2-FLAIR and T2-weighted acquisitions in a single pulse sequence, similar to interleaved FLAIR/T2*-weighted imaging,²² can eliminate the need for coregistration and simplify the FLAIR3 reconstruction. However, the longer scan time of the interleaved scan may increase susceptibility to motion. Another limitation of FLAIR3 is the reduced image dynamic range, which results from intensity modulation during reconstruction. This was addressed by applying a non-uniformity correction technique after FLAIR3 reconstruction. In this study, we found visually better results with a joint segmentation and bias field correction method¹² compared with the N4 bias field correction.²³ A FLAIR3-specific nonuniformity correction could theoretically help improve the image quality and will be investigated in future work.

We have thus far evaluated FLAIR3 images reconstructed from 3D FLAIR and 3D T2-weighted images, but generation of FLAIR3 is equally applicable to 2D scans. Volumetric (3D) acquisitions provide

higher spatial resolution, facilitate identification of small lesions, and reduce registration errors. However, motion and aliasing are potential problems in 3D imaging. Our cohort of relatively young subjects with MS appears to have tolerated the 3D scans well, and no substantial motion or aliasing artifacts were observed in this study.

Our study was also limited by the relatively small number of subjects. However, the large gains in lesion contrast and number of lesions detected with FLAIR3 are evident even in this small-sized study. The confidence in the results also reflects the observed high contrast of supratentorial lesions, in concordance with a previous study,¹⁰ which was visually confirmed in this study. Quantitative assessment for supratentorial lesions was not attempted because these lesions are less challenging to identify compared with infratentorial and cord lesions. Another limitation of this work is the lack of correlation of the identified lesion with clinical measures. Further qualitative and quantitative assessment in a larger cohort will be conducted to assess the potential of FLAIR3 in the clinical evaluation of MS.

CONCLUSIONS

FLAIR3 yields substantial gain in lesion contrast and allows detection of more lesions in the infratentorial brain region and in the upper cervical cord. With its simple acquisition and reconstruction protocol, FLAIR3 may provide a sensitive tool for routine clinical application in the diagnosis and follow-up of patients with MS.

ACKNOWLEDGMENTS

We thank Vipulkumar Patel and Corina Donohue for help with the MR imaging studies.

Disclosures: Refaat E. Gabr—RELATED: Grant: National Institutes of Health, Dunn Foundation, Chair in Biomedical Engineering Endowment, Comments: National Institute of Neurological Disorders and Stroke/National Institutes of Health (grant No. 1R56NS105857), Dunn Foundation, Chair in Biomedical Engineering*; UNRELATED: Employment: University of Texas Health Science Center at Houston; Grants/Grants National Institutes of Health, Comments: 2 R01 NS055903-10.* John A. Lincoln—UNRELATED: Grants/Grants Pending: Department of Defense, National Institutes of Health, Comments: current Department of Defense grant; Payment for Lectures Including Service on Speakers Bureaus: Biogen Idec. Ponnada A. Narayana—RELATED: Grant: National Institutes of Health*; UNRELATED: Grants/Grants Pending: SanBio.* *Money paid to the institution.

REFERENCES

1. Tullman MJ. Overview of the epidemiology, diagnosis, and disease progression associated with multiple sclerosis. *Am J Manag Care* 2013;19(2 Suppl):S15–20 Medline
2. Thompson AJ, Banwell BL, Barkhof F, et al. Diagnosis of multiple sclerosis: 2017 revisions of the McDonald criteria. *Lancet Neurol* 2018;17:162–73 CrossRef Medline
3. McGowan JC, Patel RS. Technical issues for MRI examination of the posterior fossa. *J Neurol Sci* 2000;172:S40–42 CrossRef Medline
4. Stevenson V, Parker G, Barker G, et al. Variations in T1 and T2 relaxation times of normal appearing white matter and lesions in multiple sclerosis. *J Neurol Sci* 2000;178:81–87 CrossRef Medline
5. Datta S, Tao G, He R, et al. Improved cerebellar tissue classification on magnetic resonance images of brain. *J Magn Reson Imaging* 2009;29:1035–42 CrossRef Medline
6. Gramsch C, Nensa F, Kastrup O, et al. Diagnostic value of 3D fluid attenuated inversion recovery sequence in multiple sclerosis. *Acta Radiol* 2015;56:622–27 CrossRef Medline
7. Wang KY, Uribe TA, Lincoln CM. Comparing lesion detection of infratentorial multiple sclerosis lesions between T2-weighted spin-echo, 2D-FLAIR, and 3D-FLAIR sequences. *Clin Imaging* 2018;51:229–34 CrossRef Medline
8. Lecler A, El Sanharawi I, El Methni J, et al. Improving detection of multiple sclerosis lesions in the posterior fossa using an optimized 3D-FLAIR sequence at 3T. *AJNR Am J Neuroradiol* 2019;40:1170–76 CrossRef Medline
9. Gaitán MI, Yañes P, Sati P, et al. Optimal detection of infratentorial lesions with a combined dual-echo MRI sequence: “pT2.” *Mult Scler* 2016;22:1367–70 CrossRef Medline
10. Gabr RE, Hasan KM, Haque ME, et al. Optimal combination of FLAIR and T2-weighted MRI for improved lesion contrast in multiple sclerosis. *J Magn Reson Imaging* 2016;44:1293–300 CrossRef Medline
11. Avants BB, Tustison NJ, Stauffer M, et al. The Insight ToolKit image registration framework. *Front Neuroinform* 2014;8:44 CrossRef Medline
12. Li C, Gore JC, Davatzikos C. Multiplicative intrinsic component optimization (MICO) for MRI bias field estimation and tissue segmentation. *Magn Reson Imaging* 2014;32:913–23 CrossRef Medline
13. Rorden CM. MRICron. <https://people.cas.sc.edu/rorden/mricron/index.html>. Accessed October 2016
14. Aja-Fernández S, Tristán-Vega A, Alberola-López C. Noise estimation in single- and multiple-coil magnetic resonance data based on statistical models. *Magn Reson Imaging* 2009;27:1397–409 CrossRef Medline
15. Quattrocchi CC, Cherubini A, Luccichenti G, et al. Infratentorial lesion volume correlates with sensory functional system in multiple sclerosis patients: a 3.0-Tesla MRI study. *Radiol Med* 2010;115:115–24 CrossRef Medline
16. Minneboo A, Barkhof F, Polman CH, et al. Infratentorial lesions predict long-term disability in patients with initial findings suggestive of multiple sclerosis. *Arch Neurol* 2004;61:217–21 CrossRef Medline
17. Hickman SJ, Brierley CMH, Silver NC, et al. Infratentorial hypointense lesion volume on T1-weighted magnetic resonance imaging correlates with disability in patients with chronic cerebellar ataxia due to multiple sclerosis. *J Neurol Sci* 2001;187:35–39 CrossRef Medline
18. Chong AL, Chandra RV, Chuah KC, et al. Proton density MRI increases detection of cervical spinal cord multiple sclerosis lesions compared with T2-weighted fast spin-echo. *AJNR Am J Neuroradiol* 2016;37:180–84 CrossRef Medline
19. Philpott C, Brotchie P. Comparison of MRI sequences for evaluation of multiple sclerosis of the cervical spinal cord at 3 T. *Eur J Radiol* 2011;80:780–85 CrossRef Medline
20. Poonawalla AH, Hou P, Nelson FA, et al. Cervical spinal cord lesions in multiple sclerosis: T1-weighted inversion-recovery MR imaging with phase-sensitive reconstruction. *Radiology* 2008;246:258–64 CrossRef Medline
21. Filippi M, Preziosa P, Banwell BL, et al. Assessment of lesions on magnetic resonance imaging in multiple sclerosis: practical guidelines. *Brain* 2019;142:1858–75 CrossRef Medline
22. Gabr RE, Pednekar AS, Kamali A, et al. Interleaved susceptibility-weighted and FLAIR MRI for imaging lesion-penetrating veins in multiple sclerosis. *Magn Reson Med* 2018;80:1132–37 CrossRef Medline
23. Tustison NJ, Avants BB, Cook PA, et al. N4ITK: improved N3 bias correction. *IEEE Trans Med Imaging* 2010;29:1310–20 CrossRef Medline

MR Imaging Features of Middle Cranial Fossa Encephaloceles and Their Associations with Epilepsy

D.R. Pettersson, K.S. Hagen, N.C. Sathe, B.D. Clark, and D.C. Spencer



ABSTRACT

BACKGROUND AND PURPOSE: Middle cranial fossa encephaloceles are an increasingly recognized cause of epilepsy; however, they are also often encountered on neuroimaging in patients with no history of seizure. We characterized the MR imaging features of middle cranial fossa encephaloceles in seizure and nonseizure groups with the hope of uncovering features predictive of epileptogenicity.

MATERIALS AND METHODS: Seventy-seven patients with middle cranial fossa encephaloceles were prospectively identified during routine clinical practice of neuroradiology at a tertiary care hospital during an 18-month period. Thirty-five of 77 (45%) had a history of seizure, 20/77 (26%) had temporal lobe epilepsy, and 42/77 (55%) had no history of seizures. Middle cranial fossa encephalocele features on MR imaging were characterized, including depth, area, number, location, presence of adjacent encephalomalacia, and degree of associated parenchymal morphologic distortion. MR imaging features were compared between the seizure and nonseizure groups.

RESULTS: No significant difference in MR imaging features of middle cranial fossa encephaloceles was seen when comparing the seizure and nonseizure groups. Comparison of just those patients with temporal lobe epilepsy ($n = 20$) with those with no history of seizure ($n = 42$) also found no significant difference in MR imaging features.

CONCLUSIONS: Anatomic MR imaging features of middle cranial fossa encephaloceles such as size, number, adjacent encephalomalacia, and the degree of adjacent parenchymal morphologic distortion may not be useful in predicting likelihood of epileptogenicity.

ABBREVIATIONS: MCF = middle cranial fossa; MCFE = middle cranial fossa encephalocele; TLE = temporal lobe epilepsy

During the past decade, awareness of aberrant arachnoid granulations and encephaloceles occurring in the middle cranial fossa (MCF) has grown substantially. As of 2010, only 12 cases of middle cranial fossa encephaloceles (MCFEs) had been reported in the literature,¹ and several times that amount has been reported since.²⁻⁴ Patients with encephaloceles involving the sphenoid sinus or temporal bone often come to the attention of otolaryngologists and neurosurgeons when they present with a CSF leak or meningitis.^{2,5,6} Patients with MCFEs can come to the

attention of epileptologists when they present with seizures.⁷ However, recent work in the radiology literature by Benson et al³ has established that MCFEs and arachnoid pits are common asymptomatic incidental findings on neuroimaging using high-resolution T2-weighted imaging. They reviewed 203 consecutive internal auditory canal MR imaging examinations and found MCF arachnoid pits (defects not containing brain parenchyma) in 22% of patients and MCFEs (defects containing brain parenchyma) in another 5% of patients, none of whom had a history of seizure. Campbell et al⁸ investigated the prevalence of MCFEs in 418 patients with refractory epilepsy and found that MCFEs were present in 12% of patients, and they were found more frequently in patients with temporal lobe epilepsy (TLE) than in patients without it. Last, there are several case reports and small case series describing patients with TLE and MCFEs who become seizure-free following resection or disconnection of the cerebral tissue in the MCFE, suggesting a causative association between some MCFEs and epilepsy.^{7,9-14}

Thus, these recent works have demonstrated that MCFEs should no longer be considered rare, are often asymptomatic (ie,

Received May 29, 2020; accepted after revision July 24.

From the Departments of Radiology (D.R.P., B.D.C.), Neurology (K.S.H., D.C.S.), and School of Medicine (N.C.S.), Oregon Health & Science University, Portland, Oregon.

Preliminary data previously presented at: American Epilepsy Society Annual Meeting, December 6-10, 2019; Baltimore, Maryland.

Please address correspondence to David R. Pettersson, MD, Oregon Health & Science University, 3181 SW Sam Jackson Park Rd, Portland, OR, 97239; e-mail: petterss@ohsu.edu

Indicates article with supplemental on-line tables.

Indicates article with supplemental on-line photo.

<http://dx.doi.org/10.3174/ajnr.A6798>

do not cause seizures), and can be the cause of seizures in some patients with epilepsy. These observations can pose a diagnostic dilemma when an MCFE is identified on MR imaging when evaluating a patient with drug-resistant epilepsy for possible surgery. In that scenario, it may be unclear whether the MCFE is the etiology of the epilepsy. While scalp electrographic and semiologic features may help to clarify the relevance of a given MCFE, it remains unclear whether there are specific anatomic MR imaging features of MCFEs associated with epileptogenicity. In the work presented here, we sought to address that knowledge gap by comparing the MR imaging features of MCFEs between 2 groups of patients: those with a history of seizure and those without.

MATERIALS AND METHODS

Patient Selection

Institutional review board approval was obtained for this study. A neuroradiologist with a Certificate of Additional Qualification in the subspecialty of Neuroradiology from the American Board of Radiology, working at a tertiary care teaching hospital, made note of every case of MCFE prospectively encountered during routine clinical neuroradiology practice during an 18-month period. A minority of cases were encountered while reviewing imaging for a fortnightly adult epilepsy multidisciplinary conference. Patients were not excluded on the basis of age, clinical history, type of MR imaging examination, or other findings seen on imaging. Cases were included only if the MCF defect definitively contained brain parenchyma; defects containing only CSF (ie, arachnoid pits, meningoceles) and no brain parenchyma were not included. MCFEs involving the mastoid or petrous portions of the temporal bone or tegmen tympani were also excluded.

Imaging Review

After all cases were collected, the PACS account for each patient was accessed. All available brain MR imaging for each patient was reviewed by the certificated neuroradiologist with the intent of identifying the MR imaging examination and sequences best depicting the MCFE to use for additional imaging review. The type and section thickness of the most informative sequence for each patient were recorded. Additional sequences were used to help with MCFE localization and measurement, typically in planes orthogonal to the primary sequence used for the image review.

Length measurements were made on images from those sequences using the tools embedded in the PACS. A single neuroradiologist with 5 years of post-neuroradiology fellowship experience reviewed each case, making note of MCFE laterality (right, left, bilateral) and number (1, 2, 3, 4, 5, and >5). For each patient, additional measurements were made of the largest single encephalocele present on the scan. These measurements included the 3D size of the osseous defect (3 orthogonal dimensions by caliper measurement, aligned to the plane of the inner table of the calvaria), volume (using the formula for a hemi-ellipsoid, approximating the scalloped morphology of the defects), location (sextant divisions of each MCF, anterior to the mastoid and petrous portions of the temporal bone), degree of brain parenchymal morphologic distortion in or adjacent to the MCFE (subjective 4-point Likert scale of minimal, mild, moderate, and severe distortion; and caliper measurement of the longest single dimension of definitively distorted brain

parenchyma), the presence of encephalomalacia (increased T2 signal and volume loss) of the brain parenchyma in or immediately adjacent to the MCFE, and the presence of punctate or linear CSF-intensity T2 signal within the brain parenchyma in the MCFE. The presence or absence of a subjective asymmetric increase of the intracranial subarachnoid space volume adjacent to the encephalocele was also noted. MCF sextant boundaries (On-line Figure) were approximated by dividing the transverse dimension into equal-length thirds (medial, mid, lateral) and dividing the anterior-posterior dimension into equal halves (polar/anterior, floor/posterior), excluding the petrous and mastoid portions of the temporal bone. The radiologist was not blinded to patient history during the imaging review.

Of the 77 patients included in the study, the primary MR imaging sequences used for the imaging review were 2D STIR ($n = 37$), 2D T2 TSE ($n = 14$), 3D T2 gradient-based sequences ($n = 15$), 3D T2 FSE ($n = 8$), 2D FLAIR ($n = 2$), and 3D FLAIR ($n = 1$). The section thicknesses of the primary sequences used for imaging review were 0.6–1.2 mm ($n = 18$), 2 mm ($n = 31$), 3 mm ($n = 15$), 4 mm ($n = 12$), and 5 mm ($n = 1$). The types of MR imaging protocols of the studies used for the image review included epilepsy ($n = 27$), routine brain ($n = 25$), ear, nose, and throat ($n = 12$), internal auditory canal ($n = 9$), and stereotactic brain protocols ($n = 4$). The magnetic field strength of the scans used for the imaging review included 3T ($n = 49$), 1.5T ($n = 27$), and 1T ($n = 1$).

Clinical Review

Electronic medical records of all patients were retrospectively reviewed by a fellowship-trained epileptologist for any history of seizure or epilepsy, as defined by the International League Against Epilepsy.¹⁵ For those with a history of seizure or epilepsy, all available diagnostic and clinical data were reviewed and patients were categorized by type of epilepsy (TLE, non-TLE, unknown), predominant laterality of seizures (left hemisphere, right hemisphere, bilateral, or unknown), presence of drug-resistant epilepsy at the time of most recent clinical note, and presence of additional seizure risk factors. Of the 35 patients with a diagnosis of either seizure or epilepsy, the medical record included clinical notes from an epileptologist ($n = 24$), clinical notes from a general neurologist ($n = 4$), an epilepsy-monitoring unit admission ($n = 20$), scalp electroencephalogram ($n = 31$), video-electroencephalogram ($n = 6$), stereotactic electroencephalogram ($n = 2$), foramen ovale electrodes ($n = 1$), brain PET scan ($n = 5$), brain SPECT ($n = 1$), or none of the above ($n = 3$).

Statistical Analysis

The Pearson χ^2 test or Fisher exact test was used to examine the statistical significance of categorical MR imaging characteristics of MCFEs between the group of patients with no history of seizures and the group of patients with a history of seizures. The Wilcoxon rank sum test, also known as the Mann-Whitney test, was used to assess whether the difference in the medians of continuous MR imaging characteristics of MCFEs were statistically significantly different between the seizure and nonseizure groups. Some categorical imaging characteristics such as the MCF sextants containing the largest MCFE and the number of bilateral MCFEs were further collapsed to maintain adequate cell sizes. We conducted a sensitivity

Table 1: MR imaging characteristics of encephaloceles compared between patients with a history of seizure and those with no history of seizure^a

Variable	Total (n = 77)	History of Seizure (n = 35)	No History of Seizure (n = 42)	P
Location of encephaloceles				.91
Left	22 (28.6)	10 (28.6)	12 (28.6)	
Right	16 (20.8)	8 (22.9)	8 (19.1)	
Bilateral	39 (50.7)	17 (48.6)	22 (52.4)	
Side of largest encephalocele				.80
Left	43 (55.8)	19 (54.3)	24 (57.1)	
Right	34 (44.2)	16 (45.7)	18 (42.9)	
Total No. of encephaloceles				.12
1	26 (33.8)	15 (42.9)	11 (26.2)	
>1	51 (66.2)	20 (57.1)	31 (73.8)	
Median No. of sextants ^b containing encephaloceles	3 (2)	2 (2)	3 (3)	.21
Largest encephalocele				
Depth (mm)	5 (3)	5 (3)	5.5 (3)	.88
Areal extent (mm ²)	117 (142)	119 (144)	117 (154)	.93
Volume (mm ³)	368 (538)	374 (512)	364 (632)	.76
Morphologic distortion of adjacent brain parenchyma				.51
Minimal	11 (14.3)	4 (11.4)	7 (16.7)	
Mild	21 (27.3)	10 (28.6)	11 (26.2)	
Moderate	32 (41.6)	17 (48.6)	15 (35.7)	
Severe	13 (16.9)	4 (11.4)	9 (21.4)	
Longest single dimension of distorted parenchyma adjacent to largest encephalocele (mm)	13 (11)	14 (13)	13 (11)	.54
Presence of adjacent encephalomalacia	9 (11.7)	2 (5.7)	7 (16.7)	.14

^aData are median (interquartile range) or No. (%).

^bMiddle cranial fossa sextants.

analysis of only those that had TLE and compared MR imaging characteristics of MCFE in this group with the those in the nonseizure group using the same methods as described above. Finally, we descriptively examined seizure characteristics among epileptics. All analyses were performed using STATA, Version 15 (StataCorp, 2017; Stata Statistical Software: Release 15).

RESULTS

MR Imaging Findings

Seventy-seven patients with MCFEs were included in the study (Table 1 and On-line Table 1). MCFEs were seen bilaterally in 39/77 (51%), only on the left in 22/77 (29%), and only on the right in 16/77 (21%). Twenty-six of 77 (34%) had only a solitary MCFE, 29/77 (38%) had between 2 and 5 MCFEs, and the remaining 22/77 (29%) had >5 MCFEs. Regarding the largest MCFE present in each patient, the most common location was the medial polar/anterior sextant (41/77, 53%) followed by the mid-polar/anterior sextant (19/77, 25%), with the remainder of encephaloceles located in the lateral and inferior/floor portions of the MCF. The largest MCFE present in each patient had a mean depth of 5 mm (perpendicular to the inner table of calvaria), a mean area of 117 mm², and a mean volume of 368 mm³. The degree of brain parenchymal distortion in and adjacent to the largest MCFE was subjectively categorized as minimal (14%), mild (27%), moderate (42%), or severe (17%). The mean longest single dimension of definitively distorted parenchyma within or adjacent to the largest MCFE was 13 mm. Encephalomalacia (parenchymal T2 hyperintensity and subjective volume loss) in or adjacent to the largest MCFE was present in only 12% of

patients. The intracranial subarachnoid space adjacent to the largest MCFE was asymmetrically enlarged in 38% of patients. Last, foci of CSF-intensity T2 signal were seen in the parenchyma within the largest encephalocele in 53% of patients.

Clinical Findings

The average patient age at the time of medical record review was 53 years, with an absolute range of 9–96 years and an interquartile range of 33–62 years. Forty-nine of 77 (64%) of patients were female. Of the 77 patients included in the study, 42 (55%) had no history of seizure and 35 (45%) had a history of seizure or epilepsy. Twenty-six of 35 (74%) patients with a history of seizure had a risk factor for seizure other than MCFE. TLE was the most common epilepsy type (20/35, 57%), followed by non-TLE (11/35, 31%) and unknown epilepsy or seizure type (4/35, 11%). For patients with a history of seizure, seizure laterality was left hemisphere (16/35, 46%), right hemisphere (7/35, 20%), bilateral (5/35, 14%), and unknown laterality (7/35, 20%).

Associations

There were no statistically significant differences in the conventional MR imaging features of MCFEs between those patients with a history of seizure and those without (Table 1). Encephalomalacia of the brain parenchyma located within or adjacent to the MCFE was seen almost 3 times more frequently in the nonseizure group (7/42, 17%) compared with the seizure group (2/35, 6%), though this did not meet statistical significance ($P = .14$). The mean volume of the largest MCFE found in each patient also showed no significant difference between the seizure (374 mm³) and nonseizure (364 mm³) groups ($P = .76$). The subjective degree of brain parenchymal

Table 2: MR imaging characteristics of middle cranial fossa encephaloceles compared in patients with a history of temporal lobe epilepsy and those with no history of seizure^a

Variable	Total (n = 62)	History of Temporal Lobe Epilepsy (n = 20)	No History of Seizure (n = 42)	P
Encephalocele side				.86
Left	17 (27.4)	5 (25)	12 (28.6)	
Right	30 (21.0)	5 (25)	8 (19.1)	
Bilateral	32 (51.6)	10 (50)	22 (52.4)	
Side of largest encephalocele				.60
Left	34 (54.8)	10 (50.0)	24 (57.1)	
Right	28 (45.2)	10 (50.0)	18 (42.9)	
Total No. of bilateral encephaloceles				.14
1	20 (32.3)	9 (45.0)	11 (26.2)	
>1	42 (67.7)	11 (55.0)	31 (73.8)	
Median No. of sextants ^b containing encephaloceles	3 (2)	3 (2)	3 (3)	.23
Largest encephalocele				
Depth (mm)	5 (3)	4 (2.5)	5.5 (3)	.43
Areal extent (mm ²)	117 (142)	149 (225.5)	117 (154)	.92
Volume (mm ³)	368 (538)	423 (513)	364 (632)	.74
Morphologic distortion of adjacent brain parenchyma				.83 ^c
Minimal	9 (14.5)	2 (10.0)	7 (16.7)	
Mild	17 (27.4)	6 (30.0)	11 (26.2)	
Moderate	24 (38.7)	9 (45.0)	15 (35.7)	
Severe	12 (19.4)	3 (15.0)	9 (21.4)	
Longest single dimension of distorted parenchyma adjacent to largest encephalocele (mm)	13 (11)	15.5 (15)	13 (11)	.53
Presence of adjacent encephalomalacia	7 (11.3)	0 (0.0)	7 (16.7)	.09 ^c

^a Data are median (interquartile range) or No. (%).

^b Middle cranial fossa sextants.

^c Fisher exact test.

morphologic distortion within and adjacent to the MCFE was also similar between the seizure and nonseizure groups ($P = .51$). Among the 13 patients with “severe” brain parenchymal distortion related to the MCFE, 9 were in the nonseizure group and 4 were in the seizure group. The mean longest single dimension of definitively distorted parenchyma within and adjacent to the MCFE was also similar between the seizure (14 mm) and nonseizure (13 mm) groups ($P = .54$). Likewise, the sextant location of the largest MCFE, laterality of the largest MCFE, the total number of MCFEs, the total number of MCF sextants containing encephaloceles, depth and areal extent of the largest MCFE, the presence of CSF-intensity foci within the parenchyma contained in the MCFE, and increased volume of the intracranial subarachnoid space adjacent to the largest MCFE were all similar between the seizure and nonseizure groups.

A separate-but-similar comparison was made between the subset of patients with TLE ($n = 20$) and the nonseizure patient group ($n = 42$). When all the conventional MR imaging characteristics of MCFEs were compared between the patient group with TLE and the patient group without seizures, no significant difference was found (Table 2 and On-line Table 2).

DISCUSSION

This study found no significant difference between the anatomic MR imaging features of MCFEs found in patients with a history of no seizure, seizure, and TLE. Specifically, we found that MCFE size, location, and number were not predictive of epileptogenicity. Similarly, the presence of encephalomalacia within or adjacent to an MCFE and the subjective degree and measured length of

distorted brain parenchyma within and adjacent to an MCFE were not predictive of epileptogenicity. These results suggest that conventional MR imaging features alone may not be useful in distinguishing between MCFEs that are associated with seizure and those that are not associated with seizure.

Recognition of MCFEs has grown during the past decade, raising questions of their clinical significance. While there is some clarity of the role that MCFEs can play in CSF leak, meningitis, and sphenoid sinus encephalocele development,^{5,16,17} the precise etiologic role of MCFEs in epilepsy syndromes has been less clear. For example, Benson et al³ reviewed 203 consecutive internal auditory canal MR imaging examinations and found arachnoid pits in 22% of scans and MCFEs in 5% of scans, but none of the patients had a history of seizure. In contrast, Gasparini et al⁷ looked at the prevalence of MCFE in different groups and found MCFEs in 5/95 (5%) consecutive patients with TLE of unknown etiology and in 0% of 150 controls. Additionally, 2 of the patients with TLE in their cohort were seizure-free following resection of their MCFEs. Therefore, while it is probable that MCFEs are the cause of seizure in some patients, it is also likely that MCFEs are more commonly an incidental imaging finding, not associated with seizure. The work presented here attempted to identify conventional MR imaging features of MCFEs that are associated with seizure. We found none.

In some patients with epilepsy, MCFEs can be large or numerous and there may be a great deal of morphologic distortion of the brain parenchyma that extends into the MCFE. In these instances, it may be tempting to assume that the MCFE has some etiologic association with the seizures; however, we

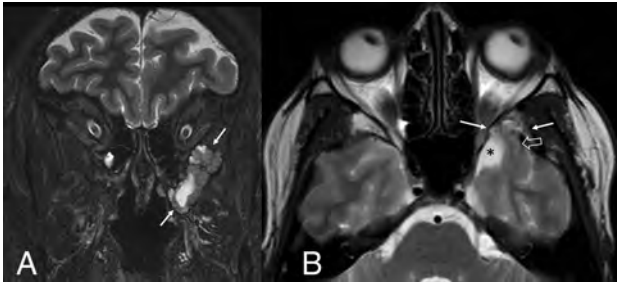


FIG 1. Large left middle cranial fossa encephalocele in a patient with left temporal lobe epilepsy. Coronal STIR image (A, arrows) depicts a focally prominent CSF space and distorted temporal lobe parenchyma surrounded by the scalloped bone margins of the encephalocele. Axial T2 TSE image (B) shows a distorted, stretched appearance of a left temporal lobe gyrus (open arrow) extending into the encephalocele (solid arrows) and asymmetric enlargement of the adjacent intracranial subarachnoid space (asterisk).

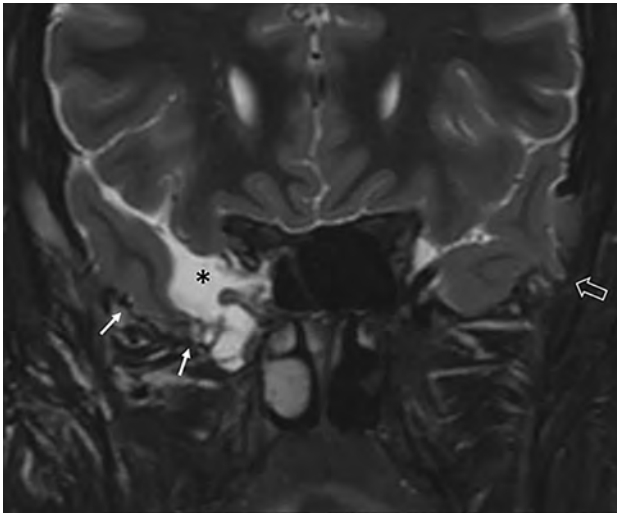


FIG 2. Bilateral middle cranial fossa encephaloceles in a patient with no history of seizure. Coronal STIR image depicts distortion and thinning of temporal lobe parenchyma (solid arrows), which appears adherent to the floor of the encephalocele, and asymmetric enlargement of the adjacent intracranial subarachnoid space (asterisk). A small middle cranial fossa encephalocele is present on the left (open arrow), with associated mild parenchymal distortion.

found no such association. Figures 1 and 2, for example, both depict large MCFEs with associated parenchymal morphologic distortion. Only one of these patients had a history of seizure, and the other did not.

Similarly, it may be tempting to assume that the presence of overt brain parenchymal injury (encephalomalacia) seen in or adjacent to an MCFE would increase the likelihood of epileptogenicity. This is an understandable assumption because neocortical injury due to ischemia is a known risk factor for epilepsy in both pediatric and adult populations. Additionally, the histology of specimens resected from MCFEs in patients who experienced improved seizure frequency following surgery found gliosis to be uniformly present in the MCFE tissue.^{9,10} In our study, the presence of encephalomalacia on MR imaging within or next to MCFEs was not

associated with seizure. In fact, encephalomalacia was seen 3 times more frequently in the nonseizure group than in the seizure group, but this difference did not meet statistical significance.

Given the proximity of the temporal lobe to the middle cranial fossa, it is a logical assumption that MCFEs might be more likely to be causative of seizures in patients with TLE than in patients without TLE, and this assumption is supported in the literature.^{4,8} Working from this assumption, we performed an additional analysis comparing the MR imaging features of MCFEs in the nonseizure patient group with those in the TLE group, excluding cases without TLE. In this analysis, we found no significant difference in the conventional MR imaging appearance of MCFEs between the nonseizure and TLE groups.

The findings presented here may be useful during the work-up of patients with drug-resistant epilepsy of unclear etiology who are found to have an MCFE and are being considered for intracranial diagnostic or therapeutic procedures. Specifically, assumptions about the likelihood of epileptogenicity of an MCFE should not be based on MCFE size or number, the presence or absence of MCFE-related encephalomalacia, or the degree of brain parenchymal morphologic distortion within and adjacent to the encephalocele. In these cases, other methods for localizing the seizure-onset zone should be used. Toledano et al⁴ described a typical seizure semiology in patients with left temporal lobe MCFE-related seizures: “significant deterioration of semantic abilities without impairment of the visual perceptual system.” For patients with epilepsy presenting with bilateral MCFEs, findings from video-electroencephalography and [¹⁸F] FDG-PET have been able to reliably distinguish symptomatic from asymptomatic MCFEs.¹⁰ Perhaps the most accurate means for distinguishing symptomatic from asymptomatic MCFEs is with intraoperative electrocorticography. Panov et al⁹ showed that when intraoperative electrocorticography can localize the seizure-onset zone to the region of MCFE, most patients will have a good surgical outcome following resection or detachment of the parenchyma involved with the MCFE. Future MR imaging studies with larger cohorts of patients with TLE may help to elucidate the potential etiologic significance of various anatomic and functional MR imaging characteristics of MCFEs.

For the radiologist who encounters an MCFE during routine clinical practice and may have minimal knowledge of the patient’s medical history, the findings of this study may also be useful. Specifically, the conventional MR imaging features of MCFE cannot reliably differentiate symptomatic (seizure-related) from asymptomatic MCFEs. Also, when 1 MCFE is encountered, it may be advisable to search for additional and contralateral encephaloceles. In our study, 66% of patients with MCFEs had ≥ 2 MCFEs, and MCFEs were seen bilaterally in 51% of cases. Corroborating the recent work of Benson et al,³ our study shows that MCFEs can be incidentally discovered findings on MR imaging performed in patients with no history of seizure.

Although not the subject of the study presented here, MCFEs and MCF arachnoid pits have known associations with disease processes other than epilepsy. When an MCFE is encountered in clinical practice, radiologists may be able to add diagnostic value by looking for clues to these other associated diseases. For example, CSF leak from MCF defects that involve either the mastoid

portion of the temporal bone or the lateral recess of the sphenoid sinus can result in fluid opacification of those structures, diffuse dural thickening/contrast enhancement from low intracranial pressure, and imaging findings of meningitis. Idiopathic intracranial hypertension also has an association with MCFEs and arachnoid pits and has associated imaging findings including an enlarged and empty sella and stenosis of the lateral portions of the transverse sinuses and protruding optic discs. In our study, there was a slight female preponderance (64%) of patients with MCFE, which is of uncertain clinical significance but may support an association between MCFE and intracranial hypertension.

Much is still unknown about the pathophysiology of encephaloceles. Some clearly have a congenital origin related to genetic disease (eg, occipital encephalocele in Meckel-Gruber syndrome)¹⁸ or problems with closure of the anterior neural pore (eg, frontonasal encephalocele).^{19,20} Other encephaloceles are acquired, arising at the site of skull base fractures or a skull base operation.² However, in the authors' experience, most MCFEs encountered in neuroradiology practice are unrelated to congenital, traumatic, or surgical etiologies and may, instead, fall into the "spontaneous" category. Spontaneous MCFEs appear to be associated with chronically elevated intracranial pressure in a proportion of cases.^{2,21} The MR imaging features described here may provide some clues to their pathophysiology. Some degree of gross parenchymal morphologic distortion was present in all cases, and a subjective asymmetric increase of the intracranial subarachnoid space adjacent to the largest MCFE was present in 38% of patients. Larger MCFEs allowed better depiction of the parenchymal distortion, and a common finding in those cases was parenchymal thinning as it extended into the MCF. The distorted parenchyma was closely approximated with the margins of the MCF defect (Figs 1 and 2).

One possible mechanism to account for these findings is that the brain is somehow drawn into an aberrant arachnoid granulation in the MCF, the pia becomes adherent to the margins of the MCFE, and the displacement of brain parenchyma into the MCFE gives it a stretched appearance and results in ex vacuo enlargement of the adjacent intracranial subarachnoid space. Age-related global cerebral atrophy would accentuate some of these findings in which the cerebrum retracts away from the inner table of the calvaria as it shrinks, leading to further thinning of the pedicle of cerebral tissue extending into the MCFE. Similar imaging findings are seen in association with aberrant arachnoid granulations in the posterior fossa bone and transverse sinuses that can entrain and stretch the cerebellar parenchyma.²² However, there are a few reports of cortical microdysgenesis and laminar disorganization of specimens resected from MCFEs,^{10,13,23,24} which confuse the hypothesis that MCFEs are an acquired phenomenon.

Encephalomalacia of the brain within or immediately adjacent to the MCFE was seen in 12% of patients in this study. A few mechanisms might explain this finding, including local mechanical trauma related to the apparently tethered brain within the MCFE, sequela of prior blunt trauma with head injury, or local gliosis from chronic seizures. Stippled or punctate foci of CSF-intensity T2 signal within the parenchyma located in the MCFE were observed in 53% of our patients and have been described by others.²³ These had an appearance suggestive of clustered dilated perivascular spaces or other CSF-filled parenchymal clefts, but

their etiology was unclear. Notably, this finding was distinct from the confluent regions of T2-hyperintense signal seen with cases of encephalomalacia.

The prospective accrual of patients with MCFEs during routine clinical practice of neuroradiology was a strength of this study in that it formed a patient cohort somewhat representative of cases that might be encountered by practicing neuroradiologists. Many cases of MCFE were undoubtedly missed during the accrual period, however, because clinical practice can be busy, leading to oversight of these often small, inconspicuous lesions. Additionally, there was great variation in the MR imaging protocols included in the study. Another shortcoming of this study was the variability of patient medical histories available for review, leading to possible erroneous assignment of patients with an actual history of seizure to the nonseizure group. It is likely that the MCFEs present in many of the patients in the seizure group were not at all related to their seizures and were instead an unrelated coincidental finding. Indeed, 76% (26/35) of patients in the seizure group were found to have risk factors for seizure other than MCFEs. A larger, case-control study including only patients with epilepsy with definitively epileptogenic MCFEs, confirmed by intracranial monitoring or postsurgical seizure freedom, may have provided a better chance for uncovering etiologically significant MR imaging features of MCFEs. Such a study would be challenging to build due to the paucity of these cases.

CONCLUSIONS

Anatomic MR imaging features alone may not be useful in distinguishing MCFEs associated with seizure from MCFEs not associated with seizure. MCFEs that are large or numerous, MCFEs associated with encephalomalacia, and MCFEs associated with severe morphologic distortion of adjacent brain parenchyma can be seen with similar frequency between patients with and without a history of seizures.

ACKNOWLEDGMENTS

The authors would like to acknowledge Priya Srikanth, MPH, for her thoughtful contributions to the statistical analysis.

Disclosures: Brian D. Clark—UNRELATED: Employment: TRG Medical Imaging, Comments: employed as a radiologist at TRG private practice since August 2019. David C. Spencer—UNRELATED: Board Membership: American Epilepsy Society, Comments: unpaid; Employment: Oregon Health & Science University, VA Portland Health Care System, Comments: salary for my work as a neurologist; Expert Testimony: various, Comments: rare review of legal cases, 1 deposition in last 3 years; Grants/Grants Pending: Eisai Co, Engage Therapeutics, Comments: clinical studies*; Royalties: Oxford University Press, Comments: small amount of royalties for authoring a book several years ago; Payment for Development of Educational Presentations: Neurology Residents Scholar Program, Comments: co-chair of this educational program for residents. *Money paid to the institution.

REFERENCES

1. Byrne RW, Smith AP, Roh D, et al. **Occult middle fossa encephaloceles in patients with temporal lobe epilepsy.** *World Neurosurg* 2010;73:541–46 CrossRef Medline
2. Carlson ML, Copeland WR, 3rd, Driscoll CL, et al. **Temporal bone encephalocele and cerebrospinal fluid fistula repair utilizing the middle cranial fossa or combined mastoid-middle cranial fossa approach.** *J Neurosurg* 2013;119:1314–22 CrossRef Medline

3. Benson JC, Lane J, Geske JR, et al. **Prevalence of asymptomatic middle cranial fossa floor pits and encephaloceles on MR imaging.** *AJNR Am J Neuroradiol* 2019;40:2090–93 CrossRef Medline
4. Toledano R, Jimenez-Huete A, Campo P, et al. **Small temporal pole encephalocele: a hidden cause of “normal” MRI temporal lobe epilepsy.** *Epilepsia* 2016;57:841–51 CrossRef Medline
5. Schuknecht B, Simmen D, Briner HR, et al. **Nontraumatic skull base defects with spontaneous CSF rhinorrhea and arachnoid herniation: imaging findings and correlation with endoscopic sinus surgery in 27 patients.** *AJNR Am J Neuroradiol* 2008;29:542–49 CrossRef
6. Hammer A, Baer I, Geletneký K, et al. **Cerebrospinal fluid rhinorrhea and seizure caused by temporo-sphenoidal encephalocele.** *J Korean Neurosurg Soc* 2015;57:298–302 CrossRef Medline
7. Gasparini S, Ferlazzo E, Pustorino G, et al. **Epileptogenic role of occult temporal encephalomenigocele: case-control study.** *Neurology* 2018;90:e1200–03 CrossRef Medline
8. Campbell ZM, Hyer JM, Lauzon S, et al. **Detection and characteristics of temporal encephaloceles in patients with refractory epilepsy.** *AJNR Am J Neuroradiol* 2018;39:1468–72 CrossRef Medline
9. Panov F, Li Y, Chang EF, et al. **Epilepsy with temporal encephalocele: characteristics of electrocorticography and surgical outcome.** *Epilepsia* 2016;57:e33–38 CrossRef Medline
10. Saavalainen T, Jutila L, Mervaala E, et al. **Temporal anteroinferior encephalocele: an underrecognized etiology of temporal lobe epilepsy?** *Neurology* 2015;85:1467–74 CrossRef Medline
11. Shimada S, Kunii N, Kawai K, et al. **Spontaneous temporal pole encephalocele presenting with epilepsy: report of two cases.** *World Neurosurg* 2015;84:e861.e1–6 CrossRef Medline
12. Abou-Hamden A, Lau M, Fabinyi G, et al. **Small temporal pole encephaloceles: a treatable cause of “lesion negative” temporal lobe epilepsy.** *Epilepsia* 2010;51:2199–02 CrossRef Medline
13. Leblanc R, Tampieri D, Robitaille Y, et al. **Developmental anterobasal temporal encephalocele and temporal lobe epilepsy.** *J Neurosurg* 1991;74:933–39 CrossRef Medline
14. Morone PJ, Sweeney AD, Carlson ML, et al. **Temporal lobe encephaloceles: a potentially curable cause of seizures.** *Otol Neurotol* 2015;36:1439–42 CrossRef Medline
15. Fisher RS, Cross JH, French JA, et al. **Operational classification of seizure types by the International League Against Epilepsy: Position Paper of the ILAE Commission for Classification and Terminology.** *Epilepsia* 2017;58:522–30 CrossRef Medline
16. Settecasse F, Harnsberger HR, Michel MA, et al. **Spontaneous lateral sphenoid cephaloceles: anatomic factors contributing to pathogenesis and proposed classification.** *AJNR Am J Neuroradiol* 2014;35:784–89 CrossRef Medline
17. Shetty PG, Shroff MM, Fatterpekar GM, et al. **A retrospective analysis of spontaneous sphenoid sinus fistula: MR and CT findings.** *AJNR Am J Neuroradiol* 2000;21:337–42 Medline
18. Parelkar SV, Kapadnis SP, Sanghvi BV, et al. **Meckel-Gruber syndrome: A rare and lethal anomaly with review of literature.** *J Pediatr Neurosci* 2013;8:154–57 CrossRef Medline
19. Barkovich AJ, Vandermarck P, Edwards MS, et al. **Congenital nasal masses: CT and MR imaging features in 16 cases.** *AJNR Am J Neuroradiol* 1991;12:105–16 Medline
20. Rojas L, Melvin JJ, Faerber EN, et al. **Anterior encephalocele associated with subependymal nodular heterotopia, cortical dysplasia and epilepsy: case report and review of the literature.** *Eur J Paediatr Neurol* 2006;10:227–29 CrossRef Medline
21. Watane GV, Patel B, Brown D, et al. **The significance of arachnoid granulation in patients with idiopathic intracranial hypertension.** *J Comput Assist Tomogr* 2018;42:282–85 CrossRef Medline
22. Battal B, Castillo M. **Brain herniations into the dural venous sinuses or calvarium: MRI of a recently recognized entity.** *Neuroradiol J* 2014;27:55–62 CrossRef Medline
23. Gasparini S, Ferlazzo E, Villani F, et al. **Refractory epilepsy and encephalocele: lesionectomy or tailored surgery?** *Seizure* 2014;23:583–84 CrossRef Medline
24. Giulioni M, Licchetta L, Bisulli F, et al. **Tailored surgery for drug-resistant epilepsy due to temporal pole encephalocele and microdysgenesis.** *Seizure* 2014;23:164–66 CrossRef Medline

Tumefactive Primary Central Nervous System Vasculitis: Imaging Findings of a Rare and Underrecognized Neuroinflammatory Disease

S. Suthiphosuwana, A. Bharatha, C.C.-T. Hsu, A.W. Lin, J.A. Maloney, D.G. Munoz, C.A. Palmer, and A.G. Osborn



ABSTRACT

SUMMARY: Primary central nervous system vasculitis (PCNSV) is a poorly understood neuroinflammatory disease of the CNS affecting the intracranial vasculature. Although PCNSV classically manifests as a multifocal beaded narrowing of the intracranial vessels, some patients may not have angiographic abnormalities. A rare subset of patients with PCNSV present with masslike brain lesions mimicking a neoplasm. In this article, we retrospectively review 10 biopsy-confirmed cases of tumefactive PCNSV (t-PCNSV). All cases of t-PCNSV in our series that underwent CTA or MRA were found to have normal large and medium-sized vessels. T-PCNSV had a variable MR imaging appearance with most cases showing cortical/subcortical enhancing masslike lesion (70%), often with microhemorrhages (80%). Diffusion restriction was absent in all lesions. In summary, normal vascular imaging does not exclude the diagnosis of t-PCNSV. Advanced imaging techniques including MR perfusion and MR spectroscopy failed to demonstrate specific findings for t-PCNSV but assisted in excluding neoplasm in the differential diagnosis. Biopsy remains mandatory for definitive diagnosis.

ABBREVIATIONS: PCNSV = primary central nervous system vasculitis; t-PCNSV = tumefactive PCNSV; ABRA = amyloid β -associated angiitis; CAA-RI = cerebral amyloid angiopathy-related inflammation; ESR = erythrocyte sedimentation rate; MRP = MR perfusion; CRP = C-reactive protein; PCR = polymerase chain reaction; VWI = vessel wall imaging; PCNSL = primary CNS lymphoma

Primary central nervous system vasculitis (PCNSV) is a poorly understood neuroinflammatory disease involving intracranial vessels.¹⁻⁵ The typical radiologic manifestation of PCNSV is multifocal beading of the large and medium-sized intracranial vessels. An underrecognized and rarer subset of PCNSV, approximately 5%–29%, can present with “masslike” or “tumefactive” lesions mimicking a neoplasm.^{3,4,6-25}

To date, imaging features of tumefactive PCNSV (t-PCNSV) have not been well described and definitive diagnosis can only be made confidently on histopathology.⁵⁻¹⁰ In this article, we

performed a retrospective review of 10 histopathologically proved cases of t-PCNSV and analyzed pertinent imaging features with histopathologic correlation.

CASE SERIES

Case Selection

We performed a retrospective pathology data base search by using the keywords “brain biopsy” and “vasculitis” in histopathology reports from July 2010–December 2018 at a single institution. Exclusion criteria included patients with histopathology findings of amyloid-beta ($A\beta$)-associated angiitis (ABRA) or cerebral amyloid angiopathy-related inflammation (CAA-RI), and infectious CNS vasculitis. Finally, we identified 6 patients who had a final diagnosis of t-PCNSV from this institution. The other 4 patients with t-PCNSV were collected from the imaging and histopathology archives of the contributing authors from 2 other institutions.

All 10 patients presented with masslike brain lesion(s) with provisional radiologic diagnoses of brain neoplasm on initial MR imaging studies, and all patients had eventual histopathologic confirmation of t-PCNSV. Patient records were retrospectively reviewed, and demographic features, clinical presentation, histopathology, laboratory results, and follow-up studies were noted.

Received April 7, 2020; accepted after revision May 26.

From the Departments of Medical Imaging (S.S., A.B., C.C.-T.H., A.W.L.), Surgery (A.B.), and Laboratory Medicine and Pathobiology (D.G.M.), University of Toronto, Toronto, Ontario, Canada; Department of Medical Imaging (C.C.-T.H.), Gold Coast University Hospital, Queensland, Australia; Department of Radiology (J.A.M.), University of Colorado, Aurora, Colorado; and Departments of Pathology (C.A.P.), and Radiology and Imaging Sciences (A.G.O.), University of Utah, Salt Lake City, Utah.

This study was selected as an oral scientific presentation at: 57th Annual Meeting, of the American Society of Neuroradiology, May 2019; Boston, Massachusetts (presentation# 2550).

Please address correspondence to Suradech Suthiphosuwana, MD, FRCR, Neuroradiologist and Assistant Professor, Department of Medical Imaging, Unity Health-St. Michael's Hospital, University of Toronto, 30 Bond St, Toronto, ON, M5B 1W8, CANADA; e-mail: suradech.suthiphosuwana@unityhealth.to

Indicates article with supplemental on-line table.

<http://dx.doi.org/10.3174/ajnr.A6736>

Table 1: Patient clinical and radiologic demographics

Patient Demographics	
Age, median; range (years)	42 (16–68)
Sex, male (%)	7 (70%)
Clinical presentations, <i>n</i> (%)	
Headache	4 (40%)
Seizure	3 (30%)
Hemiparesis	3 (30%)
Confusion	2 (20%)
Visual disturbance	2 (20%)
Cognitive impairment	1 (10%)
Word-finding difficulty	1 (10%)
Location of involvement, <i>n</i> (%)	
Cortex/subcortical white matter	7 (70%)
Deep white matter	6 (60%)
Basal ganglia	4 (40%)
Brain stem	1 (10%)
Enhancement patterns, <i>n</i> (%)	
Patchy enhancement	5 (50%)
Small nodular enhancement	5 (50%)
Ring enhancement	2 (20%)
Linear/perivascular enhancement	1 (10%)
Leptomeningeal enhancement	4 (40%)
Subependymal enhancement	3 (30%)
Microhemorrhages, <i>n</i> (%)	8 (80%)
Patients with available CSF analysis, <i>n</i> (%)	5 (50%)
Abnormal CSF protein (>0.5 g/L)	3 (60%)
CSF leukocytosis (>5 cells/mm ³)	4 (80%)
Patients with available serum inflammatory marker, <i>n</i> (%)	8 (80%)
High ESR (>20 mL/h)	2 (25%)
High CRP (>5 mg/L)	2 (25%)
Surgical procedure	
Stereotactic-guided biopsy	5 (50%)
Tumor resection	4 (40%)
Open wedge biopsy	1 (10%)
Histopathology	
Lymphocytic vasculitis	7 (70%)
Lymphocytic plus necrotizing vasculitis	2 (20%)
Granulomatous vasculitis	1 (10%)
Treatment	
Steroid alone	5 (50%)
Steroid plus immunosuppressive agents	5 (50%)
Total duration follow-up ^a , median (range), months	18 (4–77) ^a

^a Three patients did not have available clinical follow-up detail.

Imaging Analysis

Two neuroradiologists (S.S. and C.C.-T.H.) reviewed all anonymized CT and MR imaging studies in a consensus analysis. Brain MRIs were performed on either 1.5T or 3T scanners. In all studies, MR imaging sequences performed included T1-weighted imaging, T2-weighted imaging, FLAIR, and DWI. Depending on the scanner used, susceptibility-based sequences, either T2*-weighted gradient-echo imaging (GRE-T2*) or susceptibility-weighted imaging, were performed. Gadolinium-enhanced T1WI was acquired in all patients. Location, configuration, signal characteristics, and enhancement pattern of the lesions were recorded. When available, vascular imaging studies including CTA and MRA (9/10) were assessed. In some patients, advanced MR imaging techniques including MR perfusion (MRP) (3/10), MR spectroscopy (2/10), and vessel wall imaging (VWI) (3/10) findings were available.

RESULTS

Clinical Demographics

The 10 patients ranged in age from 16 to 68 years with a mean age of 43.5 years (median, 42 years) at the time of initial diagnosis. There were 7 (70%) males and 3 (30%) females.

Eight patients did not have pre-existing medical conditions. One patient had known alcoholic cirrhosis and hypertension. One patient had known hypoglossal nerve injury from a prior thyroglossal duct cyst resection.

Initial clinical presentations of t-PCNSV were: headaches, 4 (40%); followed by seizures, 3 (30%); hemiparesis, 3 (30%); confusion, 2 (20%); visual disturbance, 2 (20%); cognitive impairment, 1 (10%); and word-finding difficulty 1 (10%).

Five (50%) patients had available CSF analysis. Of these, 4 (80%) had CSF leukocytosis (ranging from 7–47 cells/mm³), and 3 (60%) had abnormal CSF protein (ranging from 0.54–0.71 g/L). Serum inflammatory markers including erythrocyte sedimentation rate (ESR) and C-reactive protein (CRP) were available in 8 (80%) patients. Two had elevated ESR: 22 and 45 mm/h. Two had evaluated CRP: 10 and 32 mg/L.

All patients had available systemic autoimmune and infectious laboratory work-up, some of which included: HIV antibody, HSV1–2, HZV polymerase chain reaction (PCR), hepatitis B and C antibodies, tuberculosis PCR, Venereal Disease Research Laboratory test, antinuclear antibodies, anti-neutrophil cytoplasmic antibodies, C3, C4, and rheumatoid factor; these available results were within normal limits.

Patient clinical demographics, laboratory findings, and treatment are summarized in Table 1 and detailed in the On-line Table.

Imaging Findings

Locations and Multiplicity. Eight (80%) patients presented with a single brain lesion (Figs 1–3). Two (20%) patients presented with multifocal lesions. Lesion locations in the brain included: cortex/subcortical white matter in 7 patients (70%), deep and/or periventricular white matter in 6 patients (60%) (Figs 1 and 2), basal ganglia in 4 patients (40%) (Fig 3), and brain stem in 1 patient (10%).

Signal Characteristics. All lesions had a hypointense signal on T1WI and intermediate to hyperintense signal on T2WI. Marked perilesional T2WI high signal of vasogenic edema was seen in 5 (50%) patients. Five (50%) patients had moderate perilesional vasogenic edema. Diffusion restriction was absent in all lesions (Fig 3B).

Eight (80%) patients had intralesional microhemorrhages, seen as small linear or punctate patterns on either GRE-T2* or SWI (Fig 1E–H). Two (20%) patients did not have evidence of intralesional hemorrhages. Microhemorrhages were not encountered diffusely elsewhere in the brain.

Enhancement Patterns. All 10 patients (100%) demonstrated enhancing lesions. Five patients (50%) demonstrated patchy parenchymal enhancement. Three of them demonstrated “mottled appearance” characterized by multiple small hypoenhancing areas within the patchy enhancing masses (Figs 1A–C). Small nodular

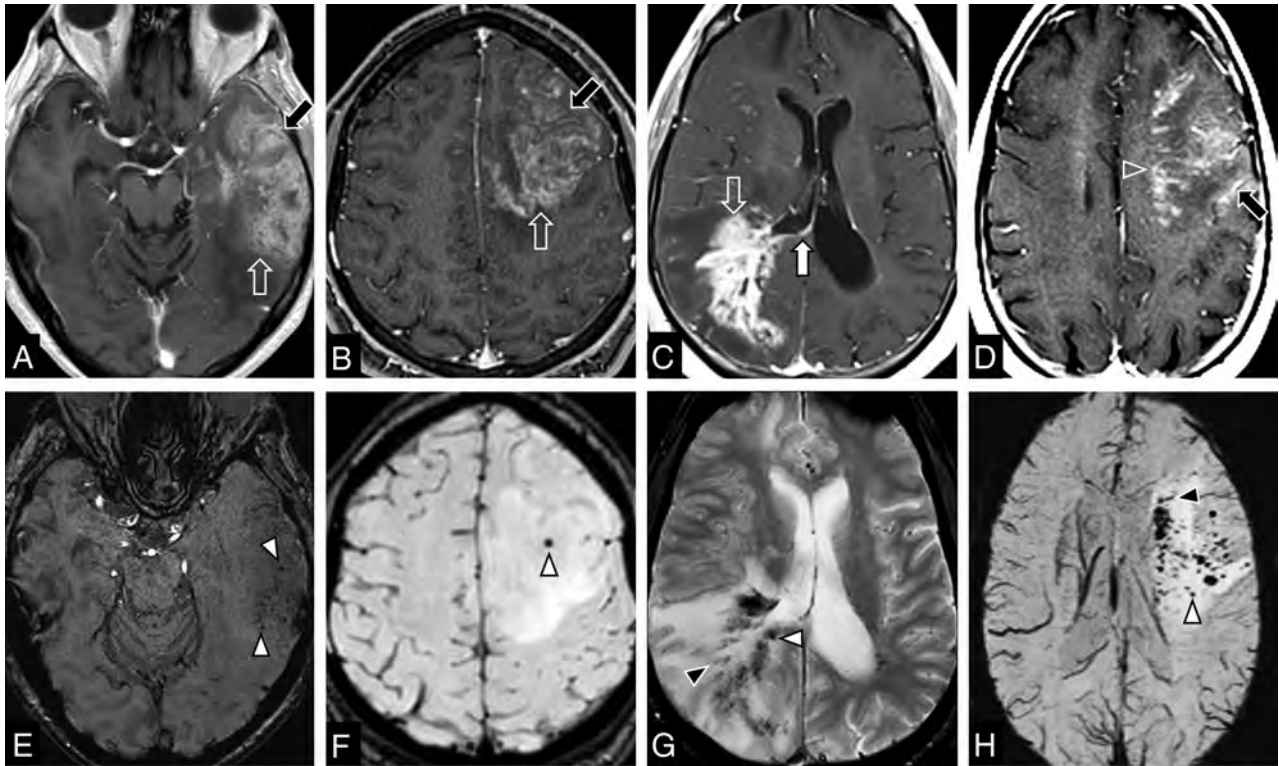


FIG 1. Common MR imaging features of t-PCNSV in 4 different patients. *A* and *E*: 68-year-old man (case 5), *B* and *F*: 16-year-old male adolescent (case 6), *C* and *G*: 42-year-old man (case 8); and *D* and *H*: 55-year-old woman (case 7). Axial postcontrast T1-weighted images (*A–D*) demonstrate lobar masses. The masses have patchy heterogeneous enhancement (mottled appearance) on *A–C* (open arrow) and nodular and linear (perivascular enhancement) on *D* (open arrowhead). Leptomeningeal enhancement is noted on *A*, *B*, and *D* (black arrows). Subependymal enhancement is observed on *C* (white arrow). Axial susceptibility-weighted imaging (*E*, *F*, and *H*) and axial T2*-weighted gradient-echo imaging (*G*) demonstrate microhemorrhages. Punctate microhemorrhages are shown in *E–H* (white arrowheads). Linear microhemorrhages are demonstrated on *G* and *H* (black arrowheads).

enhancement was found in 5 patients (50%) (Figs 1*D* and 2*B*). Two patients (20%) had ring enhancement (Figs 3*A* and *D*). Linear (perivascular) enhancement pattern was found in 1 patient (10%) (Fig 1*D*).

Localized leptomeningeal enhancement adjacent to the dominant/largest lesions was found in 4 patients (40%) (Figs 1*A*, *B*, and *D*). Localized subependymal enhancement adjacent to the lesions was found in 3 patients (30%) (Figs 1*C*, 3*A*, and 3*D*), who had lesions extended to the ventricular margin. No patient had diffuse leptomeningeal enhancement or diffuse subependymal enhancement.

Vascular Imaging: CTA, MRA, and VWI. Nine (90%) of 10 patients had available cerebral CTA and/or MRA. All findings (100%) were normal. None of the patients underwent conventional angiography.

Three patients (30%) had VWI and the imaged proximal large intracranial arteries had no abnormal wall thickening or enhancement.

Advanced MR Imaging: MRP and MR Spectroscopy. Three patients (30%) had available MRP; all demonstrated low relative cerebral blood volume (Fig 3*E*). Two patients (20%) underwent MR spectroscopy, both demonstrated elevated choline peaks compared with the creatine and slightly decreased NAA peak (choline/creatinine ratios were approximately 2.0, and choline/NAA ratios

were approximately 0.9). One patient demonstrated a high lipid-lactate peak while the other did not have a lipid-lactate peak.

Histopathologic Findings

All patients underwent surgery: 5 patients (50%) had a stereotactic-guided biopsy, 4 patients (40%) underwent gross total resection, and 1 patient (10%) had an open wedge biopsy.

Histopathologically, t-PCNSV is characterized by transmural inflammation of small blood vessels in the brain parenchyma and/or leptomeninges, inducing parenchymal ischemic changes of varying ages.²⁶

In 9 patients (90%), the lesions were described as lymphocytic vasculitis, which is characterized by a vasocentric lymphocytic inflammatory infiltrate confirmed on immunohistochemistry staining: CD20 for B-cell lymphocytes (Fig 2*E*) and CD3 for T-cell lymphocytes (Fig 2*F*). Two of the patients with lymphocytic PCNSV had necrotizing vasculitis, characterized by extensive transmural fibrinoid necrosis of the vessel wall confirmed by Martius Scarlet blue staining.²⁶

One patient (10%) had granulomatous t-PCNSV (Fig 3) characterized by vasocentric predominantly mononuclear cell infiltration accompanied by multinucleated giant cells and fibroblasts.²⁶

None of these lesions demonstrated features of amyloid depositions on H&E staining. Confirmatory immunohistochemistry staining for A β and/or Congo red were available in 7 patients

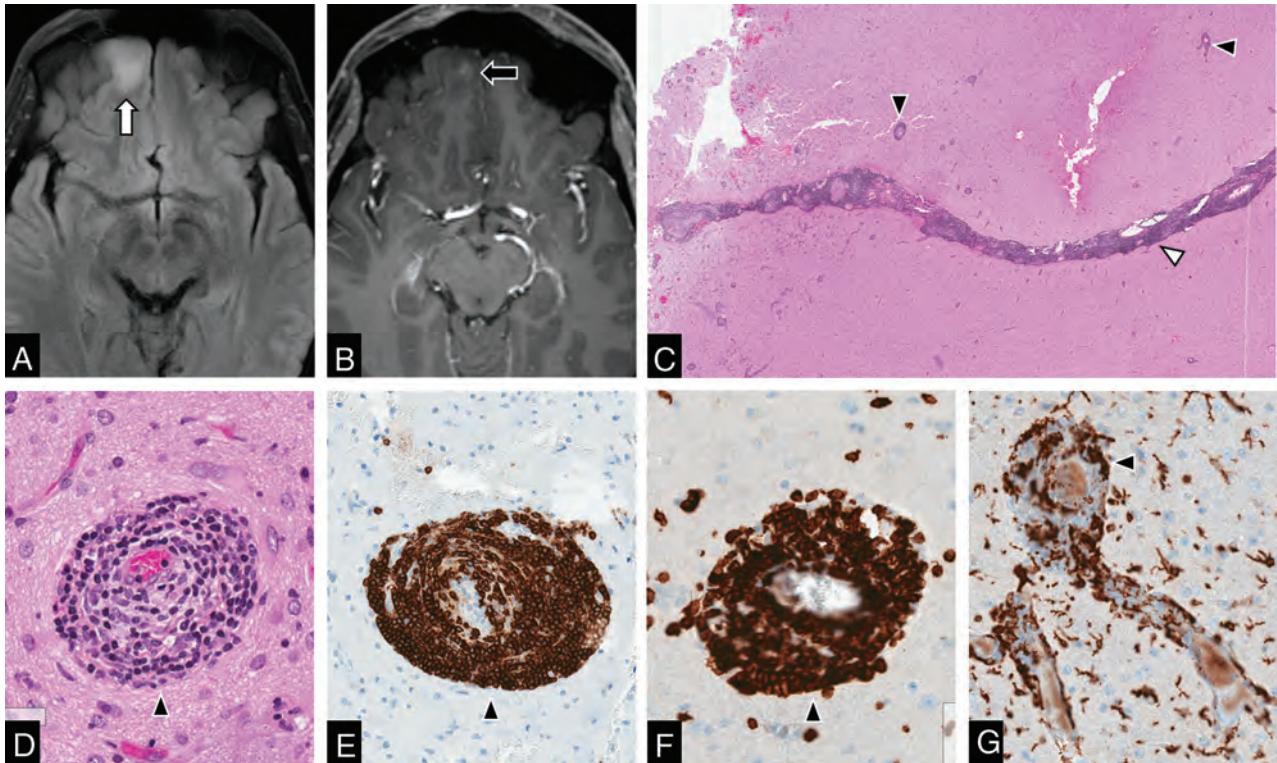


FIG 2. MR imaging findings with histopathologic correlation of t-PCNSV. A 42-year-old man (case 1) presented with first episode seizure. Axial fluid-attenuated inversion recovery (A) shows a hyperintense lesion involving the cortex and subcortical white matter (*white arrow*). Axial post gadolinium T1-weighted imaging (B) demonstrates that the lesion has small nodular enhancement (*black arrow*). The initial imaging diagnosis was glioma. This patient underwent a gross total resection of the mass. Hematoxylin and eosin-stained (C: 2 mm and D: 200 μ m magnifications) demonstrated vasculocentric transmurular lymphocytic infiltration involving the leptomeningeal artery (C, *white arrowhead*) and parenchymal cortical arteries (C and D, *black arrowheads*). Immunohistochemically, the most infiltrating lymphocytic cell is positive for CD20 marker for B-cell lymphocytes (E) and CD3 marker for T-cell lymphocytes (F). The minority of inflammatory cells are macrophages that are positive for CD163 (G).

and were negative. None of these lesions showed nuclear atypia or polymorphic cells. Also, all lesions had Epstein-Barr encoding region in situ hybridization for the detection of the Epstein-Barr virus and were negative.

Medical Treatment and Follow-Up

Five patients received corticosteroid treatment alone and 5 patients had a combination of corticosteroid and immunosuppressive agents that included cyclophosphamide and/or azathioprine. Seven patients had available clinical and imaging follow-up, with a median total duration of follow-up interval of 18 months (range: 4–77 months). Six patients had complete remission on the latest follow-up. One patient had recurrent disease at 48 months after initial treatment and had a remission after repeat treatment with corticosteroid and immunosuppressive therapy (Fig 3).

DISCUSSION

Our study describes and illustrates the spectrum of imaging findings of t-PCNSV, which is a rare disorder manifesting as masslike brain lesions. T-PCNSV seems to preferentially involve small parenchymal and leptomeningeal vessels, usually sparing large to medium-sized intracranial vessels, which may appear unremarkable on commonly performed imaging studies such as CTA or MRA.

Radiologic features of t-PCNSV were not well described or recognized because it is extremely rare entity.⁴ To our knowledge, apart from several case reports^{11–22} and review articles,^{23–25} only a few small case series have been published in the medical literature.^{6–8,10} Molloy et al⁷ reported 8 cases of masslike PCNSV with the proved histopathology including both “A β -related” PCNSV and “non-A β -related” PCNSV from 2 tertiary institutions. In addition, they included a literature review of 30 cases. Lee et al¹⁰ reported 4 cases of biopsy-proved lymphocytic PCNSV mimicking brain tumor on MR imaging. de Boysson et al⁸ described 10 masslike PCNSV cases in their series. Nine cases had histopathology-confirmed PCNSV; 1 case had histopathology negative for PCNSV but had large and medium vessel abnormalities suggestive of PCNSV on both MRA and DSA. In their series, they did not specify the absence or presence of A β on histopathology. Recently, Salvarani et al⁶ have reported a comprehensive analysis of 13 biopsy-proved cases of masslike PCNSV; however, 6 were found to have A β -related PCNSV (or ABRA/CAA-RI), leaving only 7 non-A β -related PCNSV cases. None of these case series identified definitive radiologic features of t-PCNSV. Furthermore, the inclusion of A β -related PCNSV or ABRA/CAA-RI in their sample size may preclude their analysis of the radiologic features of non-A β -related PCNSV. In contrast, our study is exclusively focused on neuroimaging features of t-PCNSV with histopathologic correlation and

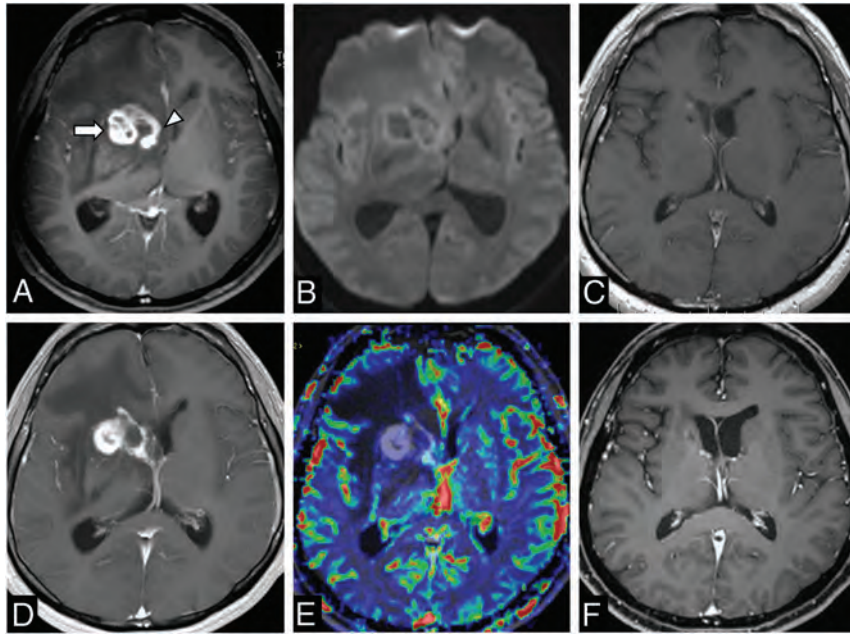


FIG 3. Recurrent granulomatous t-PCNSV. A 30-year-old man presented with headaches (case 4). A and B: Initial brain MR imaging shows conglomerate ring-enhancing mass centered in the right basal ganglia (arrow) with subependymal enhancement (arrowhead) on axial post gadolinium T1-weighted images (Gd-T1WI) (A). This mass does not show diffusion restriction on DWI (B). He underwent stereotactic-guided biopsy and histopathology showed granulomatous t-PCNSV. He was treated with corticosteroid and immunosuppressive agents. C: Follow-up MR imaging at 12 months shows the resolution of the disease. D and E: Follow-up MR imaging at 48 months demonstrates recurrent disease in the same region on Gd-T1WI (D). This mass does not show an increase in relative cerebral blood volume on dynamic susceptibility contrast MR perfusion (E). He was again treated with corticosteroids and an immunosuppressive agent. F: Follow-up Gd-T1WI at 77 months confirms the remission of the disease.

we did not incorporate $A\beta$ -related PCNSV or ABRA/CAA-RI in our analysis because these have recognized characteristic imaging patterns described in prior literature.²⁷⁻³⁰

Our t-PCNSV cohort had a male predominance, which was observed in previous studies.^{3,6,8,25} In our cohort, the most common presentations of patients with t-PCNSV were headaches, seizures, and focal neurologic deficits, which were similar to prior studies.^{6-8,25}

In our study, even though PCNSV had a variety of imaging patterns, we could identify several imaging features shared by many of the patients with t-PCNSV, which may help raise the possible diagnosis of this disease. We found that in t-PCNSV, a single lesion was more common than multiple lesions. The most common location of t-PCNSV was the supratentorial cortex/subcortical areas, as shown in previous studies.²⁵ Deep gray nuclei involvement can be seen occasionally. Only 1 patient had brain stem involvement. All patients with t-PCNSV in our cohort demonstrated enhancement, which had various patterns. Patchy and nodular enhancement patterns were the most common. Less common were ring and linear/perivascular enhancement, respectively. Some patients who demonstrated patchy enhancement had multifocal small hypoenhancing areas within a background of patchy enhancement, resembling a “mottled appearance” (Fig 1A–C). We hypothesized that this unique pattern of enhancement may represent superimposed small infarctions or necrosis within the background of brain parenchymal

inflammatory processes. A minority of the patients showed subependymal or leptomeningeal enhancement associated with the main lesions, thought to represent inflammatory processes involving adjacent leptomeningeal vessels and subependymal vessels, respectively.

Interestingly, in our study, we found that none of the patients with t-PCNSV demonstrated diffusion restriction on DWI (Fig 3B), which several previous studies have reported,^{6,8,10} despite frequent presence of microinfarctions on histopathology.²⁶ We could hypothesize that this may reflect the involvement of very small parenchymal/leptomeningeal vessels (including arterioles, capillaries, and/or venules) found in combination with extensive brain parenchymal inflammation, in contrast to medium or large vessel occlusions causing “bland” acute infarctions (54%–85%).^{4,9}

In our study, we found that most patients with t-PCNSV demonstrated microhemorrhages within the lesions, which can be detected on either GRE-T2* or SWI (Figs 1E–H). The microhemorrhages can appear either punctate or linear. The pathophysiology of parenchymal microhemorrhages in t-PCNSV is not well understood; one proposed mechanism is the alteration

of vessel wall permeability secondary to the vasculitis process itself.⁹

A minority of our patients with t-PCNSV had available advanced MR imaging. Three patients underwent MRP (Fig 3E). There was a low rCBV value that could be due to a lack of neoangiogenesis unlike malignant brain neoplasms, concurring with previous case reports on MRP of t-PCNSV.^{14,17,20} Two patients underwent MR spectroscopy, which showed a nonspecific pattern and did not add specific findings helpful in the exclusion of neoplasm from the diagnosis.^{10,13,14,18,21,25} Three patients had normal vessel wall MR imaging of the large arteries in the circle of Willis.

Our study showed that most t-PCNSV was lymphocytic vasculitis (90%), while only 10% was granulomatous vasculitis. This corresponds to some previous studies.^{8,10,25} However, other previous studies^{6,7} reported that granulomatous vasculitis was more common in PCNSV with a tumorlike presentation. Those studies^{6,7} included patients with ABRA/CAA-RI, which commonly have granulomatous vasculitis and $A\beta$ deposits in the vessel wall.

In our study, we did not include the patient who was diagnosed with ABRA/CAA-RI. Some previous studies^{1,5-7,27,30} have classified ABRA/CAA-RI as a specific subgroup of t-PCNSV. Although ABRA/CAA-RI share similar patterns of angiocentric inflammatory cell infiltrates of vessel walls, the pathophysiologic mechanism is different as it involves $A\beta$ deposition in the walls of small-to-medium vessels mostly arteries in the leptomeninges

and cerebral cortex.^{5,27} It is not fully understood whether the deposition of A β in vessel walls incites the inflammatory response or, conversely, if the inflammation leads to A β deposition. These entities have characteristic imaging patterns described as lobar subcortical edema and cortical/subcortical microhemorrhages associated with predominant leptomeningeal enhancement.²⁷⁻³⁰ ABRA/CAA-RI rarely show parenchymal enhancement seen in our patients with t-PCNSV. The pattern of microhemorrhage is also usually more diffuse in ABRA/CAA-RI as compared with our patients with t-PCNSV, where it was preferentially confined to the areas of signal abnormality and enhancement. An additional reason to exclude ABRA/CAA-RI cases is that ABRA/CAA-RI were commonly seen in older men and those who have other comorbid illnesses and tend to have poorer outcomes compared with t-PCNSV. Furthermore, previous studies in some patients with Alzheimer disease who received amyloid-modifying therapies were found to have amyloid-related imaging abnormalities, which resemble ABRA/CAA-RI on MR imaging.^{31,32} Its potential mechanism is that immunotherapies cause an increase of clearance of parenchymal plaque A β with a transient increase in vascular A β , leading to temporary vascular leakage. This supports the hypothesis that A β plays an important role in the pathomechanism of ABRA/CAA-RI.^{31,32} Therefore, we postulated that ABRA/CAA-RI, where A β deposits are presumed to be the causative factor, could represent an entity different from t-PCNSV, where these deposits are absent.

Differentiation between t-PCNSV and brain neoplasms on imaging alone can be challenging. Advanced imaging techniques such as MRP and MR spectroscopy may aid in the diagnosis. t-PCNSV does not show increased relative CBV, which is a feature of neoangiogenesis seen in high-grade gliomas. Differential diagnosis based on imaging findings would often include primary CNS lymphoma (PCNSL). IntraleSIONAL microhemorrhages are not an uncommon imaging feature of PCNSL.³³ Furthermore, a previous study has shown that systemic lymphoma can occur in about 6% of patients with PCNSV.³⁴ These patients may have a prior history of systemic lymphoma or simultaneous systemic lymphoma detected on PCNSV work-up.³⁴ Radiologically, the lack of diffusion restriction may be helpful in differentiating t-PCNSV from PCNSL. In our cohort, none of our patients had systemic lymphoma, either at the time of the biopsy or on follow-up. The presence of intraleSIONAL microhemorrhages and lack of specific open ring enhancement or peripheral diffusion restriction assisted in differentiating t-PCNSV from tumefactive demyelinating lesions.³⁵ Other unusual atypical infectious conditions such as CNS tuberculosis and fungal infections should also be included in the differential diagnosis of t-PCNSV.

Our study has several limitations; first, as a retrospective study the imaging protocols applied were heterogeneous and some patients did not have complete laboratory tests and follow-up. Second, the extreme rarity of t-PCNSV prevented the undertaking of large-scale studies. We collected cases from different institutions, which may have caused a selection bias. Third, PCNSV has a different disease subtype and multifaceted clinical and histopathologic appearances resulting in difficulty in the grouping of imaging appearances for the diagnosis. Furthermore, we did not have available DSA, which is considered the reference standard for the preoperative diagnosis of PCNSV, because those

patients were thought to have tumors preoperatively. Once the histopathologic diagnosis of PCNSV has been established, DSA is usually not deemed necessary especially in the era of CTA and MRA. It would have been helpful if there were available DSA, though DSA is often negative if the affected vessel diameter is less than 200 μ m in diameter.³⁶ In addition, previous studies have already shown that most patients in this subgroup have normal DSA findings.^{4,6-8}

CONCLUSIONS

T-PCNSV is a distinct subgroup of small vessel vasculitides that can closely mimic brain neoplasm. Pertinent differentiating imaging features include a cortical/subcortical enhancing masslike lesion with intraleSIONAL punctate/linear microhemorrhages, lack of diffusion restriction, and low rCBV. Importantly, absent large-medium vessel involvement on CTA/MRA should not exclude t-PCNSV. Open biopsy and histopathologic examination remain the “gold standard” for definitive diagnosis.

Disclosures: Suradech Suthiphosuwana—UNRELATED: Grants/Grants Pending: Sanofi-Genzyme. Comments: Fellowship educational support by unrestricted educational grant.* Anne Osborn—UNRELATED: Payment for Lectures Including Service on Speakers Bureaus: Bracco Visiting Professor, Stanford University. Comments: Lectures, case conferences March 1–2, 2020; Royalties: Reed-Elsevier. Comments: Author, multiple books and STATdx contributions. *Money paid to the institution.

REFERENCES

- Hajj-Ali RA, Singhal AB, Benseler S, et al. **Primary angitis of the CNS.** *Lancet Neurol* 2011;10:561–72 CrossRef Medline
- Twilt M, Benseler SM. **The spectrum of CNS vasculitis in children and adults.** *Nat Rev Rheumatol* 2011;8:97–107 CrossRef Medline
- Becker J, Horn PA, Keyvani K, et al. **Primary central nervous system vasculitis and its mimicking diseases – clinical features, outcome, comorbidities and diagnostic results – a case control study.** *Clin Neurol Neurosurg* 2017;156:48–54 CrossRef Medline
- Thaler C, Kaufmann-Buhler AK, Gansukh T, et al. **Neuroradiologic characteristics of primary angitis of the central nervous system according to the affected vessel size.** *Clin Neuroradiol* 2019;29:37–44 CrossRef Medline
- Salvarani C, Brown RD, Jr., Christianson T, et al. **An update of the Mayo Clinic cohort of patients with adult primary central nervous system vasculitis: description of 163 patients.** *Medicine (Baltimore)* 2015;94:e738 CrossRef Medline
- Salvarani C, Brown RD, Jr., Christianson TJH, et al. **Primary central nervous system vasculitis mimicking brain tumor: comprehensive analysis of 13 cases from a single institutional cohort of 191 cases.** *J Autoimmun* 2019;97:22–28 CrossRef Medline
- Molloy ES, Singhal AB, Calabrese LH. **Tumour-like mass lesion: an under-recognised presentation of primary angitis of the central nervous system.** *Ann Rheum Dis* 2008;67:1732–35 CrossRef Medline
- de Boysson H, Boulouis G, Dequatre N, et al. **Tumor-like presentation of primary angitis of the central nervous system.** *Stroke* 2016;47:2401–04 CrossRef Medline
- Boulouis G, de Boysson H, Zuber M, French Vasculitis Group, et al. **Primary angitis of the central nervous system: magnetic resonance imaging spectrum of parenchymal, meningeal, and vascular lesions at baseline.** *Stroke* 2017;48:1248–55 CrossRef Medline
- Lee Y, Kim JH, Kim E, et al. **Tumor-mimicking primary angitis of the central nervous system: initial and follow-up MR features.** *Neuroradiology* 2009;51:651–59 CrossRef Medline
- Denny AM, Das SK. **A case of central nervous system vasculitis presenting as a mass-like lesion.** *Childs Nerv Syst* 2019;35:1223–26 CrossRef Medline

12. Killen T, Jucker D, Went P, et al. **Solitary tumour-like mass lesions of the central nervous system: primary angiitis of the CNS and inflammatory pseudotumour.** *Clin Neurol Neurosurg* 2015;135:34–37 CrossRef Medline
13. Kumar PP, Rajesh A, Kandadai RM, et al. **Primary CNS vasculitis masquerading as glioblastoma: a case report and review.** *Asian J Neurosurg* 2017;12:69–71 CrossRef Medline
14. Lee JS, Jung TY, Lee KH, et al. **Primary central nervous system vasculitis mimicking a cortical brain tumor: a case report.** *Brain Tumor Res Treat* 2017;5:30–33 CrossRef Medline
15. Lyra TG, Martin MGM, Carvalho RC, et al. **Pseudotumoral presentation of primary central nervous system vasculitis.** *Arq Neuropsiquiatr* 2013;71:333–35 CrossRef Medline
16. Mabray MC, Cha S. **CNS angiitis as a brain tumor mimic with a branching vascular abnormality on T2* MRI.** *Neurology* 2015;85:1819–20 CrossRef Medline
17. Muccio CF, Di Blasi A, Esposito G, et al. **Perfusion and spectroscopy magnetic resonance imaging in a case of lymphocytic vasculitis mimicking brain tumor.** *Pol J Radiology* 2013;78:66–69 CrossRef Medline
18. Panchal NJ, Niku S, Imbesi SG. **Lymphocytic vasculitis mimicking aggressive multifocal cerebral neoplasm: MR imaging and MR spectroscopic appearance.** *AJNR Am J Neuroradiol* 2005;26:642–45 Medline
19. Sun LI, Zhu L, Zhao T, et al. **A rare case of tumor-mimicking primary angiitis of the central nervous system.** *Mol Clin Oncol* 2016;4:827–29 CrossRef Medline
20. Tanei T, Nakahara N, Takebayashi S, et al. **Primary angiitis of the central nervous system mimicking tumor-like lesion—case report.** *Neurol Med Chir (Tokyo)* 2011;51:56–59 CrossRef Medline
21. Zhang G, Yang C, Chang J, et al. **Primary angiitis of the central nervous system mimicking a cerebellar tumor.** *Br J Neurosurg* 20181–83 CrossRef Medline
22. Zhu DS, Yang XL, Lv HH, et al. **Seizure syndrome as a first manifestation of solitary tumor-like mass lesion of PACNS: two case reports.** *Medicine (Baltimore)* 2017;96:e6018 CrossRef Medline
23. Qu SB, Khan S, Liu H. **Primary central nervous system vasculitis mimicking brain tumour: case report and literature review.** *Rheumatol Int* 2009;30:127–34 CrossRef Medline
24. You G, Yan W, Zhang W, et al. **Isolated angiitis of the central nervous system with tumor-like lesion, mimicking brain malignant glioma: a case report and review of the literature.** *World J Surg Oncol* 2011;9:97 CrossRef Medline
25. Jin H, Qu Y, Guo ZN, et al. **Primary angiitis of the central nervous system mimicking glioblastoma: a case report and literature review.** *Front Neurol* 2019;10:1208 CrossRef Medline
26. Giannini C, Salvarani C, Hunder G, et al. **Primary central nervous system vasculitis: pathology and mechanisms.** *Acta Neuropathol* 2012;123:759–72 CrossRef Medline
27. Salvarani C, Hunder GG, Morris JM, et al. **A β -related angiitis: comparison with CAA without inflammation and primary CNS vasculitis.** *Neurology* 2013;81:1596–1603 CrossRef Medline
28. Salvarani C, Morris JM, Giannini C, et al. **Imaging findings of cerebral amyloid angiopathy, abeta-related angiitis (ABRA), and cerebral amyloid angiopathy-related inflammation: a single-institution 25-year experience.** *Medicine (Baltimore)* 2016;95:e3613 CrossRef Medline
29. Miller-Thomas MM, Sipe AL, Benzinger TL, et al. **Multimodality review of amyloid-related diseases of the central nervous system.** *Radiographics* 2016;36:1147–63 CrossRef Medline
30. Moussaddy A, Levy A, Strbian D, et al. **Inflammatory cerebral amyloid angiopathy, amyloid-beta-related angiitis, and primary angiitis of the central nervous system: similarities and differences.** *Stroke* 2015;46:e210–13 CrossRef Medline
31. Sperling RA, Jack CR, Jr., Black SE, et al. **Amyloid-related imaging abnormalities in amyloid-modifying therapeutic trials: recommendations from the Alzheimer's Association Research Roundtable Workgroup.** *Alzheimers Dement* 2011;7:367–85 CrossRef Medline
32. Barakos J, Sperling R, Salloway S, et al. **MR imaging features of amyloid-related imaging abnormalities.** *AJNR Am J Neuroradiol* 2013;34:1958–65 CrossRef Medline
33. Sakata A, Okada T, Yamamoto A, et al. **Primary central nervous system lymphoma: is absence of intratumoral hemorrhage a characteristic finding on MRI?** *Radiology and Oncology* 2015;49:128–34 CrossRef Medline
34. Salvarani C, Brown RD, Jr, Christianson TJH, et al. **Primary central nervous system vasculitis associated with lymphoma.** *Neurology* 2018;90:e847–55 CrossRef Medline
35. Suh CH, Kim HS, Jung SC, et al. **MRI findings in tumefactive demyelinating lesions: a systematic review and meta-analysis.** *AJNR Am J Neuroradiol* 2018;39:1643–49 CrossRef Medline
36. Brant-Zawadzki M, Gould R, Norman D, et al. **Digital subtraction cerebral angiography by intraarterial injection: comparison with conventional angiography.** *AJNR Am J Neuroradiol* 1982;3:593–99 Medline

Detailed Arterial Anatomy and Its Anastomoses of the Sphenoid Ridge and Olfactory Groove Meningiomas with Special Reference to the Recurrent Branches from the Ophthalmic Artery

M. Hiramatsu, K. Sugiu, T. Hishikawa, J. Haruma, Y. Takahashi, S. Murai, K. Nishi, Y. Yamaoka, Y. Shimazu, K. Fujii, M. Kameda, K. Kurozumi, and I. Date



ABSTRACT

BACKGROUND AND PURPOSE: Detailed arterial anatomy of the sphenoid ridge and olfactory groove meningiomas is complicated due to the fine angioarchitecture and anastomoses between each feeder. Herein, we present details of the arterial anatomy and the relationships of feeders in these lesions.

MATERIALS AND METHODS: This study included 20 patients admitted to our department between April 2015 and March 2020. Conditions of subjects consisted of 16 sphenoid ridge meningiomas and 4 olfactory groove meningiomas. We mainly analyzed arterial anatomy using 3D rotational angiography and slab MIP images of these lesions. We also analyzed the anastomoses of each feeder.

RESULTS: We found that 19 (95%), 15 (75%), and 15 (75%) lesions had feeders from the ophthalmic, internal carotid, and external carotid arteries, respectively. As feeders from the ophthalmic artery, recurrent meningeal arteries were involved in 18 lesions (90%). Fifteen lesions (75%) had anastomoses between each feeder.

CONCLUSIONS: Most of the meningiomas in the sphenoid ridge and olfactory groove had feeders from the ophthalmic and internal carotid arteries. There were various anastomoses between each feeder. This is the first report to demonstrate the detailed arterial anatomy and frequency of recurrent branches from the ophthalmic artery and their anastomoses using detailed imaging techniques.

ABBREVIATIONS: ECA = external carotid artery; EtA = ethmoidal artery; ILT = inferolateral trunk; LSOF = lateral part of the superior orbital fissure; MHT = meningohypophyseal trunk; MMA = middle meningeal artery; MSOF = medial part of the superior orbital fissure; OC = optic canal; OphA = ophthalmic artery; RMA = recurrent meningeal artery; SOF = superior orbital fissure; TOB = transosseous branch; WHO = World Health Organization

The dural arterial anatomy of the sphenoid ridge and anterior skull base is very complicated because there are many fine arteries from not only the external carotid artery (ECA) but also the ICA and ophthalmic artery (OphA).¹ Moreover, there are various anastomoses between each artery.²⁻⁵ In the setting of hypervascular diseases related to the dura, such as meningioma or dural arteriovenous fistula in these regions, the angioarchitecture can be visualized

more clearly. In the present study, we investigated the details of the arterial anatomy of sphenoid ridge and olfactory groove meningiomas with special reference to the recurrent branches of the OphA and anastomoses between each feeder.

MATERIALS AND METHODS

All procedures performed in studies involving human participants were carried out in accordance with the ethical standards of Okayama University Graduate School of Medicine, Dentistry and Pharmaceutical Sciences's institutional research committee (1911-023). Written informed consent was obtained from all patients before DSA and treatment, but written informed consent for this study was not required because of the retrospective and noninvasive study design. Conditions of subjects consisted of 16 sphenoid ridge meningiomas and 4 olfactory groove meningiomas between April 2015 and March 2020. In this study period, we treated 29 patients with meningiomas in these regions, and we excluded 9 cases without 3D rotational DSA

Received May 16, 2020; accepted after revision July 15.

From the Department of Neurological Surgery (M.H., K.S., T.H., J.H., Y.T., S.M., K.N., Y.Y., Y.S., K.F., M.K., K.K., I.D.), Okayama University Graduate School of Medicine, Dentistry and Pharmaceutical Sciences, Okayama, Japan; and Department of Neurosurgery (K.K.), Hamamatsu University School of Medicine, Hamamatsu, Shizuoka, Japan.

Please address correspondence to Masafumi Hiramatsu, MD, Department of Neurological Surgery, Okayama University Graduate School of Medicine, Dentistry and Pharmaceutical Sciences, 2-5-1 Shikata-cho, Kita-ku, Okayama 700-8558, Japan; e-mail: mhiramatsu@okayama-u.ac.jp

Indicates article with supplemental on-line table.

<http://dx.doi.org/10.3174/ajnr.A6790>

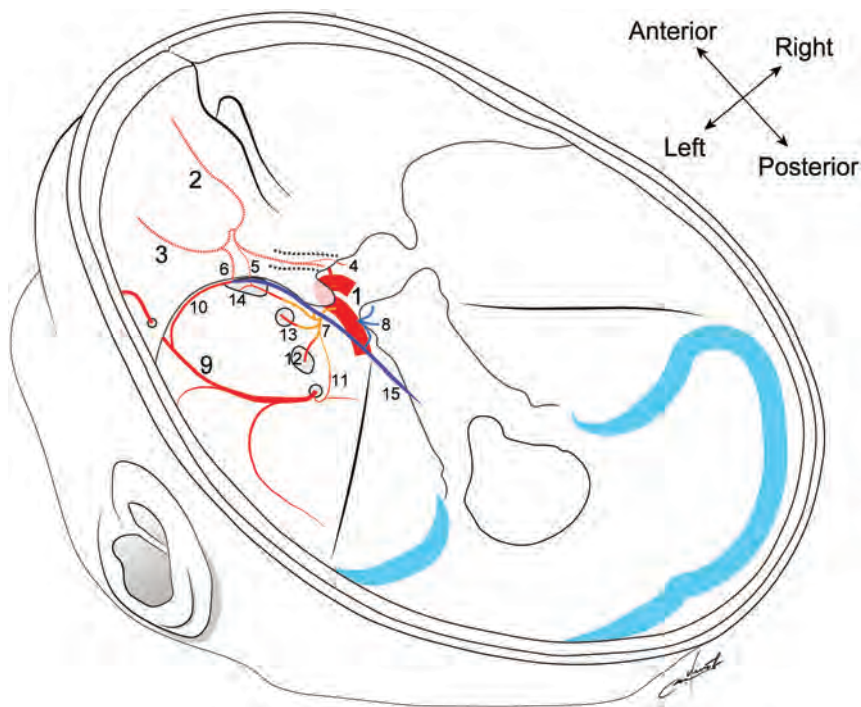


FIG 1. Schematic illustration of dural arterial anatomy and anastomoses among the ophthalmic, internal carotid, and external carotid arteries: 1 indicates the ICA; 2, OphA; 3, lacrimal artery; 4, RMA-OC; 5, RMA-MSOF; 6, RMA-LSOF; 7, ILT; 8, MHT; 9, MMA; 10, sphenoid branch of MMA; 11, cavernous branch of MMA; 12, accessory meningeal artery; 13, artery of the foramen rotundum; 14, artery of the SOF; 15, marginal tentorial artery.

data because we could not analyze the details of the angioarchitecture in these cases.

We examined the meningioma location, tumor invasion, tumor size, histopathologic diagnosis according to World Health Organization (WHO) grade, and arterial anatomy of the feeders. Feeders were divided into branches of the OphA, ICA, and ECA (Fig 1). Branches of the OphA are the recurrent meningeal arteries (RMAs) described below, the ethmoidal artery (EtA), and the transosseous branch (TOB). Branches of the ICA are the inferolateral trunk (ILT) and the meningo-hypophyseal trunk (MHT). Branches of the ECA are the middle meningeal artery (MMA), accessory meningeal artery, deep temporal artery, artery of the foramen rotundum, artery of the superior orbital fissure (SOF), and sphenopalatine artery. We also analyzed the anastomoses of each feeder.

Anatomic Terminology of the Branches of the Ophthalmic Artery

We defined the RMAs as the posteriorly recurrent branches from the OphA or lacrimal artery passing through the SOF or optic canal (OC). We found 2 other types of feeders from the OphA. One of them was the TOB, which originates at the second or third portion of the OphA and courses superiorly, passing through the upper wall of the orbit to reach the dura of the anterior cranial base. Another one was the anterior or posterior EtA, which courses medially, passing through the ethmoidal foramina.

On the basis of the course, we divided feeders from the OphA into 5 types as follows: RMA passing through the OC (RMA-OC), RMA passing through the lateral part of the SOF (RMA-

LSOF), RMA passing through the medial part of the SOF (RMA-MSOF), TOB, and EtA. We distinguished the RMA-LSOF and RMA-MSOF using the coronal section of slab MIP images from rotational angiography data. We present representative cases of the RMA-LSOF (Fig 2), RMA-OC (Figs 3 and 4), TOB (Fig 4), and EtA (Fig 4).

Preoperative Examination

Preoperative DSA was performed with the patient under local anesthesia. After obtaining 2D-DSA of the ECA and ICA, which are ipsilateral to the tumor, 3D-DSA with a 5-second protocol was performed on the branching feeders of the vessels. For 3D-DSA, a 4F diagnostic catheter was inserted into an ICA, and a 100% iodine contrast medium with a 300-mg/mL concentration was infused using an injector (2.5 mL/s flow rate, 1.5- to 2.0-second delay, total 16–18 mL). After obtaining volume-rendered images of 3D-DSA, slab MIP images were derived from rotational angiography data using a workstation to analyze details of the feeder anatomy. An Artis zee biplane (Siemens Healthcare) was used as a flat panel detector, and the syngo X Workplace (Siemens Healthcare) was used as a workstation.

RESULTS

The lesion characteristics and arterial anatomy of meningiomas are summarized in the Table, and details of each case are shown in On-line Table 1. In terms of lesion location, there were 4 sphenoid ridge lateral types, 9 sphenoid ridge medial types, 3 sphenoid ridge diffuse types spreading to the middle and anterior cranial base, and 4 olfactory groove lesions. There were 3 lesions with intraorbital invasion and 1 lesion with invasion to the temporal bone and muscle. The mean maximum diameter was 56 mm. In terms of histopathologic diagnosis, there were 19 WHO grade I meningiomas and 1 WHO grade II meningioma. The 2 most frequent diagnoses were meningothelial ($n=8$) and transitional ($n=8$) meningiomas.

We found that 19 (95%), 15 (75%), and 15 (75%) lesions had feeders from the OphA, ICA, and ECA, respectively. As the feeders from the OphA, there were 7 RMA-OCs in 7 lesions, 14 RMA-LSOFs in 13 lesions, 2 RMA-MSOFs in 2 lesions, 4 TOBs in 4 lesions, and 6 EtAs in 6 lesions. Six of 7 RMA-OCs (86%) originated from the first segment of the OphA. Eleven of 14 RMA-LSOFs (79%) originated from the lacrimal artery. Two RMA-MSOFs originated from the lacrimal artery and the second portion of the OphA. All (4/4) TOBs originated from the second or third segment of the OphA. Four of 6 EtAs (67%) originated from the third segment of the OphA. RMAs from the OphA were involved in 18 lesions (90%). All (7/7) RMA-OCs

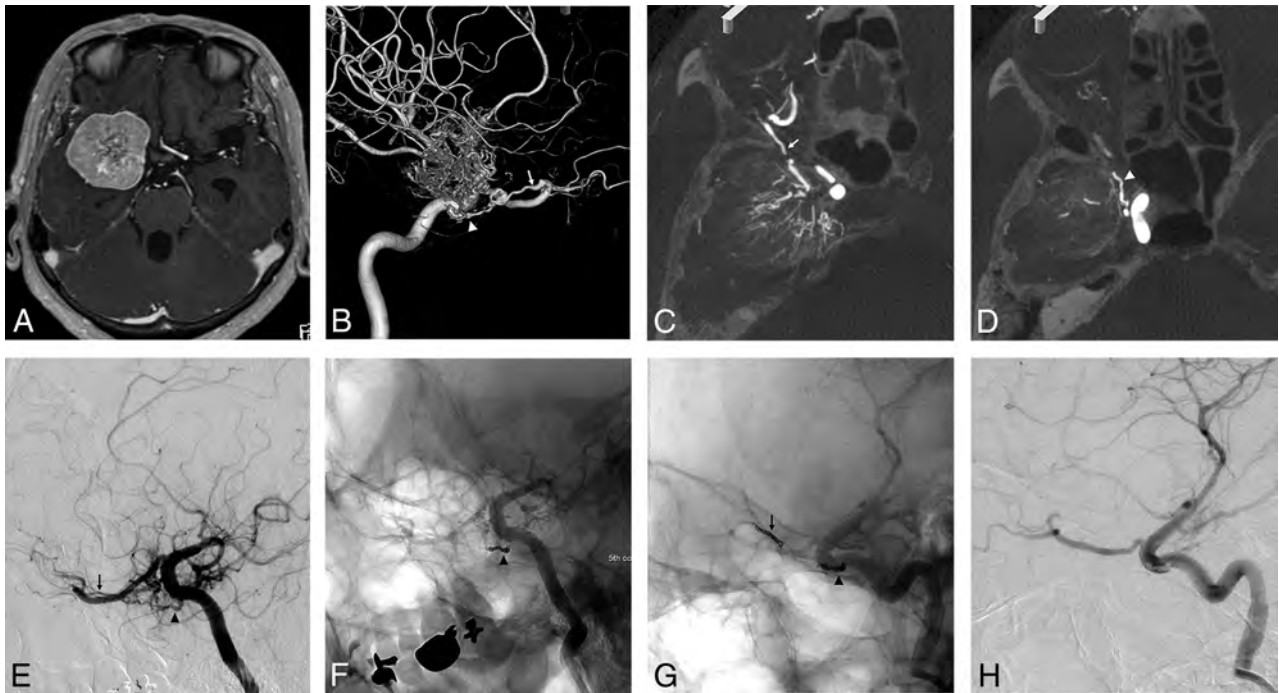


FIG 2. A, Axial view of the gadolinium-enhanced T1-weighted image shows a medial-type sphenoid ridge meningioma. The lateral view of the 3D-DSA (B) and axial views of slab MIP images (C and D) of the right internal carotid angiogram show the feeder of the RMA passing through lateral part of the SOF (arrow) from the lacrimal artery and ILT (arrowhead). There is an anastomosis between the RMA-LSOF and the ILT. E, Oblique view of the internal carotid angiogram before embolization shows both feeders. Internal carotid angiogram after coil embolization of the ILT (F) and RMA-LSOF (G and H). The tumor stain is markedly diminished.

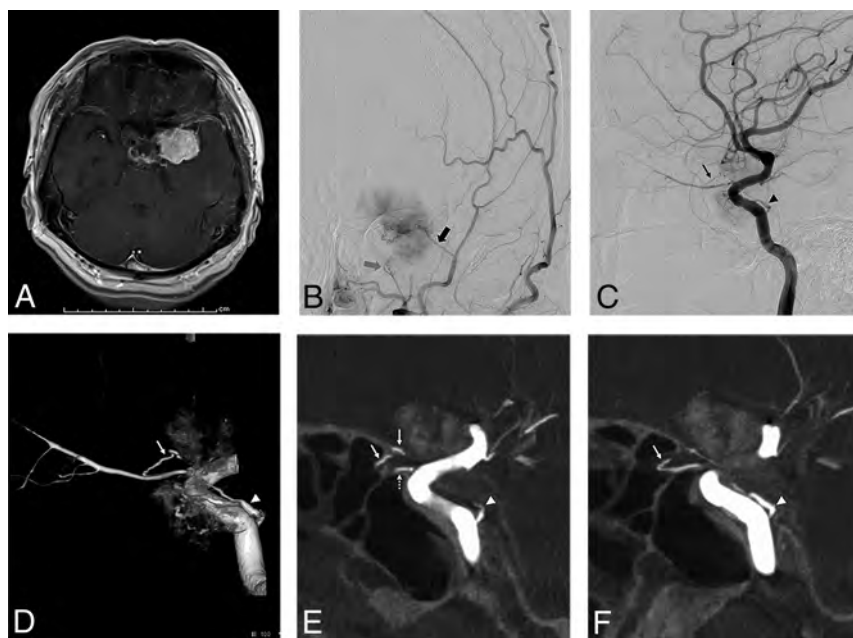


FIG 3. A, The axial view of the gadolinium-enhanced T1-weighted image shows a medial-type sphenoid ridge meningioma. B, Anterior-posterior view of the left external carotid angiogram shows the feeder from the accessory meningeal artery (large gray arrow) and sphenoid branch (large black arrow) of the MMA. The lateral views of the 2D-DSA (C) and 3D-DSA (D) and sagittal views of slab MIP images (E and F) of the left internal carotid angiogram show the feeder of the RMA passing through the OC (arrow) and MHT (arrowhead). The slab MIP images clearly show that the RMA-OC and OphA (dotted arrow) pass through the OC (E and F).

appeared in medial-type sphenoid ridge meningiomas or olfactory groove meningiomas. RMA-LSOFs appeared in all types of sphenoid ridge meningiomas. All sphenoid ridge meningiomas with invasion to other locations (cases 1, 2, 8, 15 in the On-line Table) had multiple feeders from the OphA. One lesion (case 9 in the On-line Table) that had no feeder from the OphA was a psammomatous meningioma (WHO grade I). There were no other relationships between the arterial anatomy and invasion or histopathologic diagnosis.

As the feeders from the ICA, the ILT and MHT were involved in 13 and 9 lesions, respectively. As feeders from the ECA, the sphenoidal branch of the MMA, accessory meningeal artery, artery of the foramen rotundum, and artery of the SOF were involved in 12, 7, 6, and 3 lesions, respectively. Other feeders from the ECA were the petrosal branch of the MMA, deep temporal artery, and sphenopalatine artery. There were 4 lesions with olfactory groove meningiomas. Most of the feeders of

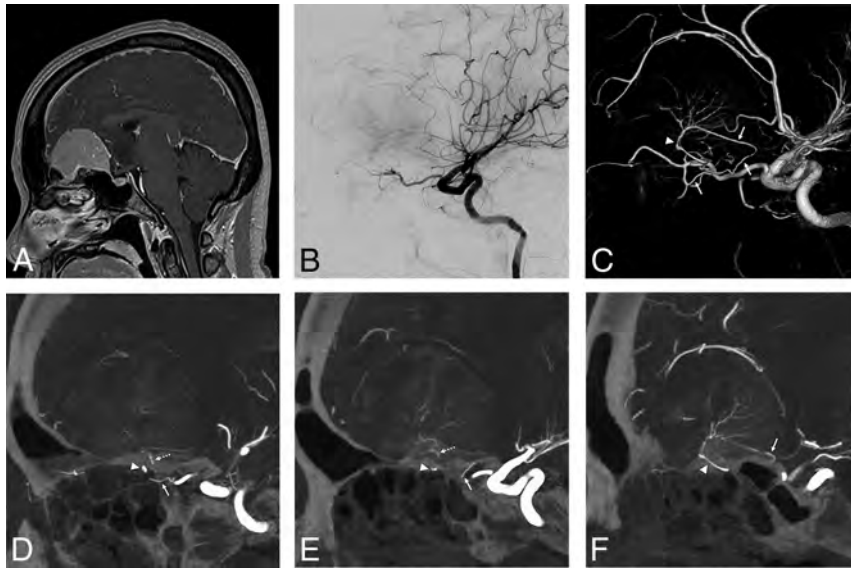


FIG 4. A, Sagittal view of the gadolinium-enhanced T1-weighted image shows an olfactory groove meningioma. The lateral views of the 2D-DSA (B) and 3D-DSA (C) and sagittal views of slab MIP images (D–F) of the right internal carotid angiogram show the feeder from the RMA passing through the OC (arrow) from the third segment of the OphA, posterior EtA, (arrowhead), and TOB (dotted arrow). The slab MIP images show the RMA-OC, and the OphA passes through the OC (E). Feeders from the RMA-OC and EtA configure an arcade shape on the blistering of the planum sphenoidale.

the olfactory groove meningioma were from the OphA, and there was no involvement of the ICA branches and MMA. As the feeders from the OphA, the EtAs, RMA-OCs, and TOBs were involved in 4, 3, and 1 lesion, respectively.

We found that 15 lesions (75%) had anastomoses between each feeder. The most frequent anastomosis was between the OphA and the ICA (eg, RMA-LSOF and ILT). We also found anastomoses between feeders from the ipsilateral OphA (eg, RMA-OC and EtA). Five cases had anastomoses between the OphA or ICA and ECA. Four cases had multiple anastomoses, such as the RMA-ILT-MMA-artery of the SOF. In 3 cases of olfactory groove meningiomas, we found anastomosis between the RMA-OC and the EtA. The mean maximum diameter of the meningiomas that had anastomosis of feeders was 45 ± 13 mm and that of meningiomas without anastomosis was 39 ± 16 mm.

DISCUSSION

Detailed arterial anatomy of the sphenoid ridge and the olfactory groove meningiomas is little understood due to the fine and complicated nature of arterial anatomy in the skull base. It is difficult to differentiate these subtle vessels using conventional 2D-DSA, 3D-CTA, or MR imaging. We demonstrated that the latest imaging technique and slab MIP image of 3D rotational angiography can visualize this fine angioarchitecture. In the present study, we found that 95%, 75%, and 75% of lesions have feeders from the OphA, ICA, and ECA, respectively. Moreover, we demonstrated that 75% of lesions have anastomoses between each feeder. Notably, this is the first report to demonstrate the detailed anatomy and frequency

of recurrent branches from the OphA and their anastomoses using slab MIP images.

Anatomy of the Dural Arteries

Martins et al¹ reported the detailed microsurgical anatomy of dural arteries as follows: The supply to the middle fossa and paracavernous dura derives laterally from the MMA, accessory meningeal artery, and ascending pharyngeal artery and medially from the intracavernous branches (ILT) of the ICA. They also described the contributions to these regions from the recurrent branches of the ophthalmic and lacrimal arteries. There is confusion about the definition of the recurrent ophthalmic arteries. Lasjaunias et al⁶ reported that both the superficial and deep recurrent ophthalmic arteries pass backward through the lateral and medial parts of the SOF, respectively. Meanwhile, Martins et al¹ reported that the superficial recurrent ophthalmic artery, deep recurrent ophthalmic artery, and RMA pass through the optic canal,

the medial part of the SOF, and the lateral part of the SOF, respectively. Therefore, descriptions of both authors were competing. In the present article, we describe the RMA as posteriorly recurrent branches from the OphA passing through the OC or SOF, including the superficial and deep recurrent ophthalmic arteries. Martins et al¹ and Hayreh³ described the recurrent branch passing through the OC. However, to the best of our knowledge, no articles have shown this recurrent artery passing through the OC in imaging or cadaveric studies.

Yamaki et al⁷ reported details of feeding arteries in parasellar meningiomas, including 9 sphenoid ridge meningiomas. In this article, they analyzed 2 lesions (22%) in the sphenoid ridge that were supplied from the superficial recurrent ophthalmic artery or recurrent meningeal artery, respectively. The current imaging technology and slab MIP images provide us with the ability to analyze detailed arterial anatomy. We can demonstrate that RMAs from the OphA were involved in most of the lesions (90%) in the present study.

Anastomosis of Each Feeder

Numerous anastomoses between each artery have been reported.^{2–5} In the setting of hypervascular lesions related to the dura, such as meningiomas or dural arteriovenous fistulas, these feeding arteries can be enlarged and tend to connect.⁸ In the present study, there were various anastomoses in 75% of cases, and 4 cases had multiple anastomoses.

According to the embryologic concepts of the OphA, the connection between the OphA and the ILT is the remnant of the dorsal ophthalmic artery and the connection between the RMA and the MMA is the remnant of the supraorbital artery (branch of the

Lesion characteristics and arterial anatomy of meningiomas

Characteristics/Anatomy	
Total	<i>n</i> = 20
Mean age (yr)	56 ± 14
Male sex (%)	9 (45%)
Location (%)	
Sphenoid ridge (lateral type)	4 (20%)
Sphenoid ridge (medial type)	9 (45%)
Sphenoid ridge (diffuse type)	3 (15%)
Olfactory groove	4 (20%)
Mean maximum diameter (mm)	43 ± 13
Histopathologic diagnosis (%)	
Meningothelial meningioma	8 (40%)
Transitional meningioma	8 (40%)
Other WHO grade I meningioma	3 (15%)
WHO grade II meningioma	1 (5%)
Feeders from OphA (%)	19 (95%)
RMA-OC	7 (35%)
RMA-LSOF	13 (65%)
RMA-MSOF	2 (10%)
EtA	6 (30%)
TOB	4 (20%)
Feeders from ICA (%)	15 (75%)
ILT	13 (65%)
MHT	9 (45%)
Feeders from ECA (%)	15 (75%)
MMA	12 (60%)
Accessory meningeal artery	7 (35%)
Artery of the foramen rotundum	6 (30%)
Artery of the SOF	3 (15%)
Anastomosis of each feeder (%)	15 (75%)
OphA-OphA	4 (20%)
OphA-ICA	5 (25%)
OphA-ECA	2 (10%)
OphA-ICA-ECA	2 (10%)
ICA-ICA	1 (5%)
ICA-ECA	1 (5%)

stapedial artery).⁹⁻¹² De La Torre and Netsky¹³ reported the persistent primitive maxillary artery in the human fetus. They reported that this artery arises from the cavernous portion of the ICA and anastomoses with the lacrimal artery and the anterior branch of the MMA. We can comprehend the complicated anastomoses among the OphA, ICA, and MMA using these findings. Therefore, it is certain that there are various anastomoses among branches of the OphA, ICA, and ECA.

Clinical Implications

Preoperative embolization for meningioma is performed as a standard treatment. Although its usefulness is widely accepted, the embolization of target vessels other than the ECA has been reported as a risk for procedural complications in a nationwide surveillance in Japan.¹⁴ Rosen et al¹⁵ reported their treatment results for preoperative embolization using microparticles to 167 cranial base meningiomas, and 9% of their patients experienced permanent neurologic deficits. They also showed that embolization of the MHT, MMA, and ascending pharyngeal artery involves the risk of a minor or permanent neurologic injury. Meanwhile, Waldron et al¹⁶ reported their treatment results for preoperative embolization using microparticles and coils to 119 cranial base meningiomas, with no complications. Some authors

have reported the usefulness of embolization of the OphA branches.^{17,18} In limited cases, embolization may be performed for branches of the OphA, but it is associated with a risk of visual disturbance due to migration of the embolic material to the central retinal artery.¹⁷ Appropriate knowledge of anatomy, distal catheterization, and the gentle injection of embolic material without reflux are necessary for safe embolization of the OphA.¹⁹

In our opinion, the RMA-OC is inappropriate as the target vessel of preoperative embolization due to the difficulty in catheterization because of its small caliber and short distance from the origin of the OphA with an acute angle. The RMA-LSOF may have a lower risk because of its origins and anastomoses. The RMA-LSOF usually originates from a lacrimal artery and is anastomosed with the sphenoid branch of the MMA. However, if the RMA-LSOF has an anastomosis with the ILT, it involves a risk of the migration of particulate or liquid materials to the ICA. Thus, we recommend embolization of both of the RMA and the ILT using detachable coils in such a case.

Another precaution related to embolization is residual feeding from anastomotic vessels. If there is an anastomosis between each feeder, proximal occlusion of the feeder, which can be easily catheterized, can result in increased blood flow to the tumor from the residual feeder. One should embolize the common trunk of both feeders or the proximal parts of both feeders (Fig 2).

A detailed understanding of arterial microanatomy is also useful in direct surgery. A large sphenoid ridge meningioma requires skull base techniques, such as the transzygomatic approach.^{20,21} Using a skull base technique and extradural drilling of the sphenoid wing to the SOF, we can devascularize the feeder from the ECA and RMA-LSOF/MSOF.²¹ After these procedures, we open the dura mater, and we can debulk the intradural tumor, most of which is already devascularized, whereas, we may not be able to find the feeder from the RMA-OC until identification of the optic nerve. Moreover, coagulation to the RMA-OC involves the risk of optic nerve injury. If we identify all of the feeders using preoperative angiography, we can search for feeders on the basis of the anatomic landmarks of the bone and devascularize them in a safe and efficient manner.

Limitations

The current study has some limitations. First, the number of patients was small. Second, we did not confirm the presented feeding arteries with operative findings. In future studies, we should examine the accuracy of the presented results using operative findings or cadaveric research.

CONCLUSIONS

Sphenoid ridge and olfactory groove meningiomas have feeders from the OphA, ICA, and ECA in 95%, 75%, and 75% of lesions, respectively. Furthermore, 75% of lesions have anastomoses between each feeder.

ACKNOWLEDGMENTS

The authors thank Dr Ryota Ishibashi (Department of Neurosurgery, Kurashiki Central Hospital, Kurashiki, Japan) for his suggestions on the writing of this article.

Disclosures: Masafumi Hiramatsu—UNRELATED: Payment for Lectures Including Service on Speakers Bureaus: Siemens; Travel/Accommodations/Meeting Expenses Unrelated to Activities Listed: Siemens. Kenji Sugiu—UNRELATED: Payment for Lectures Including Service on Speakers Bureaus: Siemens; Travel/Accommodations/Meeting Expenses Unrelated to Activities Listed: Siemens.

REFERENCES

1. Martins C, Yasuda A, Campero A, et al. **Microsurgical anatomy of the dural arteries.** *Neurosurgery* 2005;56(2 Suppl):211–51; discussion 211–51 CrossRef Medline
2. Geibprasert S, Pongpech S, Armstrong D, et al. **Dangerous extracranial-intracranial anastomoses and supply to the cranial nerves: vessels the neurointerventionalist needs to know.** *AJNR Am J Neuroradiol* 2009;30:1459–68 CrossRef Medline
3. Hayreh SS. **Orbital vascular anatomy.** *Eye (Lond)* 2006;20:1130–44 CrossRef Medline
4. Perrini P, Cardia A, Fraser K, et al. **A microsurgical study of the anatomy and course of the ophthalmic artery and its possibly dangerous anastomoses.** *J Neurosurg* 2007;106:142–50 CrossRef Medline
5. Toma N. **Anatomy of the ophthalmic artery: embryological consideration.** *Neurol Med Chir (Tokyo)* 2016;56:585–91 CrossRef Medline
6. Lasjaunias P, Brismar J, Moret J, et al. **Recurrent cavernous branches of the ophthalmic artery.** *Acta Radiology Diagn (Stockh)* 1978;19:553–60 CrossRef Medline
7. Yamaki T, Tanabe S, Sohma T, et al. **Feeding arteries of parasellar meningiomas: angiographic study of medial sphenoid ridge and tuberculum sellae meningiomas.** *Neurol Med Chir (Tokyo)* 1988;28:553–58 CrossRef Medline
8. Kiyosue H, Tanoue S, Hongo N, et al. **Artery of the superior orbital fissure: an undescribed branch from the pterygopalatine segment of the maxillary artery to the orbital apex connecting with the antero-medial branch of the inferolateral trunk.** *AJNR Am J Neuroradiol* 2015;36:1741–47 CrossRef Medline
9. Lasjaunias P, Berenstein A, terBrugge KG. Spinal artery. In: Lasjaunias P, Berenstein A, terBrugge KG. *Surgical Neuroangiography, Volume 1; Clinical Vascular Anatomy and Variations.* 2nd ed. Springer-Verlag; 2001:123
10. Lasjaunias P, Moret J, Mink J. **The anatomy of the inferolateral trunk (ILT) of the internal carotid artery.** *Neuroradiology* 1977;13:215–20 CrossRef Medline
11. Bonasia S, Bojanowski M, Robert T. **Embryology and anatomical variations of the ophthalmic artery.** *Neuroradiology* 2020;62:139–52 CrossRef Medline
12. Padgett DH. **The development of the cranial arteries in the human embryo.** *Contrib Embryol* 1948;32:205–61
13. De La Torre E, Netsky MG. **Study of persistent primitive maxillary artery in human fetus: Some homologies of cranial arteries in man and dog.** *Am J Anat* 1960;106:185–95 CrossRef
14. Sugiu K, Hishikawa T, Murai S, et al. **Treatment outcome of intracranial tumor embolization in Japan: Japanese Registry of NeuroEndovascular Therapy 3 (JR-NET3).** *Neurol Med Chir(Tokyo)* 2019;59:41–47 CrossRef Medline
15. Rosen CL, Ammerman JM, Sekhar LN, et al. **Outcome analysis of preoperative embolization in cranial base surgery.** *Acta Neurochir (Wien)* 2002;144:1157–64 CrossRef Medline
16. Waldron JS, Sughrue ME, Hetts SW, et al. **Embolization of skull base meningiomas and feeding vessels arising from the internal carotid circulation.** *Neurosurgery* 2011;68:162–69 CrossRef Medline
17. Terada T, Kinoshita Y, Yokote H, et al. **Preoperative embolization of meningiomas fed by ophthalmic branch arteries.** *Surg Neurol* 1996;45:161–66 CrossRef Medline
18. Trivelatto F, Nakiri GS, Manisor M, et al. **Preoperative Onyx embolization of meningiomas fed by the ophthalmic artery: a case series.** *AJNR Am J Neuroradiol* 2011;32:1762–66 CrossRef Medline
19. Matsumaru Y, Alvarez H, Rodesch G, et al. **Embolisation of branches of the ophthalmic artery.** *Interv Neuroradiol* 1997;3:239–45 CrossRef Medline
20. Campero A, Villalonga JF, Elizalde RL, et al. **Transzygomatic approach plus mini-peeling of middle fossa for devascularization of sphenoid wing meningiomas: technical note.** *Surg Neurol Int* 2018;9:140 CrossRef Medline
21. González-Darder JM. **Combined extradural and intradural pterional transzygomatic approach to large sphenoid wing meningiomas: operative technique and surgical results.** *J Neurol Surg B Skull Base* 2019;80:244–51 CrossRef Medline

Carotid Stenting and Mechanical Thrombectomy in Patients with Acute Ischemic Stroke and Tandem Occlusions: Antithrombotic Treatment and Functional Outcome

V. Da Ros, J. Scaggiante, F. Sallustio, S. Lattanzi, M. Bandettini, A. Sgreccia, C. Rolla-Bigliani, E. Lafe, G. Sanfilippo, M. Diomedi, M. Ruggiero, N. Haznedari, M. Giannoni, C. Finocchi, and R. Floris



ABSTRACT

BACKGROUND AND PURPOSE: There is no consensus on the optimal antithrombotic medication for patients with acute ischemic stroke with anterior circulation tandem occlusions treated with emergent carotid stent placement and mechanical thrombectomy. The identification of factors influencing hemorrhagic risks can assist in creating appropriate therapeutic algorithms for such patients. This study aimed to investigate the impact of medical therapy on functional and safety outcomes in patients treated with carotid stent placement and mechanical thrombectomy for tandem occlusions.

MATERIALS AND METHODS: A multicenter retrospective study on prospectively collected data was conducted. Only patients treated with carotid stent placement and mechanical thrombectomy for tandem occlusions of the anterior circulation were included. Univariate and multivariate analyses were performed on preprocedural, procedural, and postprocedural variables to assess factors influencing clinical outcome, symptomatic intracranial hemorrhage, stent patency, and successful intracranial vessel recanalization.

RESULTS: Ninety-five patients with acute ischemic stroke and tandem occlusions were included. Good clinical outcome ($mRS \leq 2$) at 3 months was reached by 33 (39.3%) patients and was associated with baseline ASPECTS ≥ 8 (OR = 1.53; 95% CI, 1.16–2.00), ≤ 2 mechanical thrombectomy attempts (OR = 0.71; 95% CI, 0.55–0.99), and the absence of symptomatic intracranial hemorrhage (OR = 0.13; 95% CI, 0.03–0.51). Symptomatic intracranial hemorrhage was associated with a higher amount of intraprocedural heparin, ASPECTS ≤ 7 , and ≥ 3 mechanical thrombectomy attempts. No relationships among types of acute antiplatelet regimen, intravenous thrombolysis, and symptomatic intracranial hemorrhage were observed. Patients receiving dual-antiplatelet therapy after hemorrhagic transformation had been ruled out on 24-hour CT were more likely to achieve functional independence and had a lower risk of symptomatic intracranial hemorrhage.

CONCLUSIONS: During carotid stent placement and mechanical thrombectomy for tandem occlusion treatment, higher intraprocedural heparin dosage (≥ 3000 IU) increased symptomatic intracranial hemorrhage risk when the initial ASPECTS was ≤ 7 , and mechanical thrombectomy needs more than one passage for complete recanalization. Antiplatelets antiplatelets use were safe, and dual-antiaggregation therapy was related to better functional outcomes.

ABBREVIATIONS: AIS = acute ischemic stroke; ICH = intracranial hemorrhage; MT = mechanical thrombectomy; sICH = symptomatic intracranial hemorrhage; TO = tandem occlusion

Tandem occlusions (TOs) occur in up to 16%–20% of patients with acute ischemic stroke of the anterior cerebral circulation and are defined as a combined extracranial-intracranial cervical

ICA lesion (complete occlusion or $\geq 90\%$ stenosis according to the NASCET¹ criteria) and ipsilateral occlusion of proximal intracranial large vessels (ICA, the M1 and/or M2 segment of the middle cerebral artery).²

Acute ischemic stroke (AIS) caused by TOs is generally associated with a poor prognosis when left untreated.³

Received April 21, 2020; accepted after revision July 7.

From the Department of Biomedicine and Prevention (V.D.R., J.S., R.F.), Interventional Neuroradiology Unit, and Comprehensive Stroke Center (F.S., M.D.), Department of Systems Medicine, University of Rome Tor Vergata, Rome, Italy; Neurological Clinic (S.L.), Department of Experimental and Clinical Medicine, Marche Polytechnic University, Ancona, Italy; Neurological Clinic (M.B., C.F.), Department of Neurosciences and Interventional Neuroradiology Unit (A.S., E.L., G.S.), IRCCS Policlinico San Matteo, Pavia, Italy; Department of Diagnostic and Interventional Neuroradiology (C.R.-B.), Policlinico Universitario, San Martino, Italy; Neuroradiology Unit (M.R., N.H.), AUSL Romagna, Cesena, Italy; and Neuroradiological Clinic (M.G.), Department of Radiological Sciences, AOU Ospedali Riuniti, Ancona, Italy.

V.D. Ros and J. Scaggiante contributed equally to the article.

Please address correspondence to Valerio Da Ros, MD, Department of Biomedicine, Interventional Neuroradiology unit, University of Rome Tor Vergata, Viale Oxford 81, Rome, Italy; e-mail: darosvalerio@gmail.com



Indicates article with supplemental on-line tables.

<http://dx.doi.org/10.3174/ajnr.A6768>

Although intravenous thrombolysis with tPA remains part of the criterion standard treatment,⁴ tandem occlusions respond poorly to intravenous thrombolysis alone,⁵ likely due to the poor responsiveness of large thrombi to enzymatic digestion. Because intracranial vessel recanalization is the most powerful predictor of favorable clinical outcome,⁶ endovascular therapy is the standard of care for tandem occlusions.⁷ However, the most appropriate interventional strategy to manage the extracranial carotid disease remains controversial.^{2,7-11}

Systematic reviews¹² and post hoc analyses¹³ reported similar clinical outcomes at 3-month follow-up in patients with acute ischemic stroke and tandem occlusions treated with carotid stent placement or angioplasty. Conversely, a recent meta-analysis,¹⁴ a prospective nonrandomized trial,¹⁵ and the international multicenter Thrombectomy in TANdem Occlusion (TITAN) and Systematic Evaluation of Patients Treated with Stroke Devices for Acute Ischemic Stroke (STRATIS) Registry¹⁶⁻¹⁸ suggested better outcomes and higher recanalization rates for patients undergoing carotid stent placement.

The best antiplatelet/anticoagulant management to reduce the risk of postinterventional symptomatic intracranial hemorrhage (sICH) and prevent stent re-occlusion in these patients remains a matter of ongoing debate. Because emergent carotid stent placement during acute ischemic stroke requires antithrombotic agents, this strategy may be less appealing due to the intracranial hemorrhage (ICH) risk, especially for patients already receiving intravenous thrombolysis.¹⁹ Moreover, as addressed by the TITAN investigators, the use of intraprocedural heparin in tandem occlusions failed to demonstrate better functional, angiographic, or safety outcomes.²⁰ So far, little evidence exists to guide the medical therapy of tandem occlusions treated with carotid stent placement,²¹ and high-quality analyses and randomized controlled trials are needed.²²

This study aimed to investigate the impact of medical therapy on functional and safety outcomes in patients treated with carotid stent placement and mechanical thrombectomy for tandem occlusions.

MATERIALS AND METHODS

Study Design

We retrospectively evaluated all consecutive patients admitted with acute ischemic stroke between January 2018 and December 2019 in 5 Italian neurointerventional centers.

We included in this study only patients treated with emergent carotid stent placement and mechanical thrombectomy for a tandem occlusion, defined as an extracranial ICA lesion (complete occlusion or $\geq 90\%$ stenosis according to the NASCET¹ criteria) and an ipsilateral proximal intracranial large-vessel occlusion (intracranial ICA, the M1 and/or M2 segment of the middle cerebral artery) confirmed at initial cerebral angiography. Eligibility for intravenous thrombolysis and endovascular treatment was evaluated at each center according to the American Heart Association/American Stroke Association guidelines.

Preprocedural, procedural, 24- to 48-hour postprocedural, discharge, and 3-month data were prospectively collected. No ethics committee approval was required for this retrospective observational study.

We evaluated the following variables: demographic characteristics (ie, age, sex), cardiovascular risk factors (ie, atrial fibrillation, arterial hypertension, diabetes mellitus, hypercholesterolemia, smoking, previous cardio-cerebrovascular accidents), clinical and radiologic assessments (ie, mRS,²³ NIHSS score,²⁴ imaging characteristics [ie, ASPECTS]),²⁵ stroke etiology according to the Trial of Org 10172 in Acute Stroke Treatment (TOAST) classification,²⁶ stroke side, hemorrhagic transformation, stent patency, procedural time, (ie, onset-to-groin time, onset-to-recanalization time), number of mechanical thrombectomy (MT) attempts, type of stent (single- or dual-layer), and medical therapy (ie, preprocedural medications, intra- and postprocedural anticoagulant/antiplatelet protocols).

Good clinical outcome was defined as mRS 0–2 at 3-month follow-up, and favorable clinical outcome, as mRS 0–3.

Imaging Evaluation

All CT scans were obtained with 64 slices using a heliocid acquisition (GE LightSpeed VCT 64; GE Healthcare). At each institution, 2 neurointerventional radiologists independently analyzed preprocedural CT scans. Any disagreement was resolved by consensus with a third neuroradiologist (ie, head of the department). The cervical ICA occlusion was included in the TOAST classification on DSA, according to clinical and angiographic imaging characteristics. Successful recanalization was defined as modified TICI 2b–3 on DSA.²⁷

CT angiography was used to assess stent patency within 72 hours from treatment. Acute in-stent occlusion was defined as occlusion of the carotid stent within 72 hours after stent placement.

Symptomatic intracranial hemorrhage (sICH) was defined as parenchymal hematoma type 1 or 2 using the European Cooperative Acute Stroke Study (ECASS) III grading, according to imaging at 24 hours, associated with an increase of at least 4 NIHSS points within 24 hours, or resulting in death.²⁸

Emergent Carotid Stent Placement and MT

There were no technical restrictions to perform cervical ICA stent placement and intracerebral mechanical thrombectomy. Each center independently decided the stent type (ie, single-layer stent or dual-layer stent) and the mechanical thrombectomy technique (ie, aspiration and/or stent retriever) according to their experience.

Anticoagulation/Antiaggregation

For each patient, we assessed preprocedural, intraprocedural, and postprocedural medications, independently decided at each institution.

IV heparin sodium use was administered at the discretion of each center. The total amount of IV heparin was calculated on the basis of the speed of infusion, use of a bolus, and time from first infusion to the end of the procedure.

In patients already receiving antiplatelet medications, a single-antiplatelet therapy was defined as a regular dosage of aspirin (Bayer) (ie, up to 300 mg) or clopidogrel 75 mg. In patients without antiplatelet medication, a dose of 500 mg of intravenous lysine acetylsalicylate administered before deployment of carotid stent placement was considered a regular single dosage. Dual-antiplatelet therapy was defined as a treatment with combined

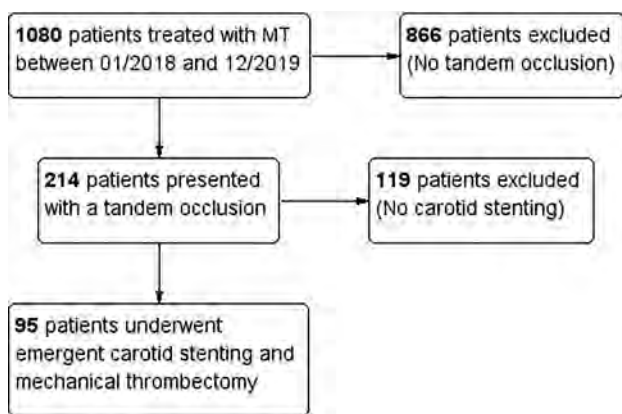


FIGURE. Flow chart of the study population.

Table 1: Overall characteristics of the study population

Characteristics	
Patient characteristics	
Age (mean) (range)	64.6 ± 12.6 (29–86)
Male sex (No./No.) (%)	69/95 (72.6%)
Left-hemisphere stroke (No./No.) (%)	56/95 (58.9%)
Baseline NIHSS (mean) (range)	16.8 ± 5.5; 2–32
Baseline ASPECTS (median) (range)	8; 2–10
Tobacco (No./No.) (%)	35/95 (36.8%)
Diabetes mellitus (No./No.) (%)	7/95 (7.4%)
Dyslipidemia (No./No.) (%)	16/95 (16.8%)
Atrial fibrillation at admission (No./No.) (%)	10/95 (10.5%)
Prestroke antiplatelet therapy (No./No.) (%)	21/95 (22.1%)
Procedural and postprocedural characteristics	
Onset-to-groin time (mean) (range)	284.5 ± 156.4; 70–980 min
Onset-to-recanalization (mean) (range)	376.7 ± 168.3; 110–1075 min
Procedural time (mean) (range)	90.6 ± 58.2; 9–315 min
No. of MT attempts (mean) (range)	2.57 ± 1.7; 1–10
Successful recanalization mTICI ≥2b (No./No.) (%)	58/95 (61.1%)
Intravenous thrombolysis (No./No.) (%)	45/95 (47.4%)
Single-layer carotid stent (No./No.) (%)	87/95 (91.6%)
Dual-layer carotid stent (No./No.) (%)	8/95 (8.4%)
Intraprocedural heparin (No./No.) (%)	40/95 (42.1%)
Intraprocedural single-antiplatelet therapy (No./No.) (%)	46/79 (58.2%)
Intraprocedural dual-antiplatelet therapy (No./No.) (%)	10/43 (23.3%)
Postprocedural single-antiplatelet therapy (No./No.) (%)	25/54 (46.3%)
Postprocedural dual-antiplatelet therapy (No./No.) (%)	30/60 (50%)
Symptomatic ICH	26/94 (27.7%)

Note:—mTICI indicates modified TICI.

medications (eg, aspirin with clopidogrel) or a double regular dose of a single drug (eg, lysine acetylsalicylate, 1000 mg).

Statistical Analysis

Continuous variables were reported as mean ± SD or median with range, and categoric variables, as number and percentage. Contingency analyses for categoric variables were performed using the exact χ^2 test.

Group comparisons were performed with the ANOVA and univariate logistic regression analyses to identify factors influencing clinical outcomes, stent patency, successful revascularization, and sICH. A 2-sided *P* value < .05 indicated statistical significance. The multivariate analysis was performed using a general linear regression model (MANOVA), with a stepwise backward

elimination procedure; a separate ANOVA was conducted for each dependent variable at an α level of .025. Analyses were performed using SPSS, Version 23.0 (IBM).

RESULTS

Study Population

Between January 2018 and December 2019, one thousand eighty patients admitted with acute ischemic stroke underwent mechanical thrombectomy; 214 patients (19.8%) presented with extracranial/intracranial tandem occlusions, of whom 95 patients (44.4%) received emergent carotid stent placement (flow chart in the Figure). The characteristics of the study population are presented in Table 1.

Fifty-six patients (58.9%) presented with a left-hemispheric stroke. Median baseline ASPECTS was 8, and the NIHSS score was

16.8. Forty-five patients (47.4%) were treated with mechanical thrombectomy plus intravenous thrombolysis. The mean onset-to-groin time was 284.5 ± 156.4 minutes, the mean onset-to-recanalization time was 376.7 ± 168.3 minutes, and the mean procedural time was 90.6 ± 58.2 minutes.

Clinical and Angiographic Outcomes

A successful intracranial recanalization (modified TICI 2b–3) was achieved in 58 of 95 patients (61.1%): TICI 3 in 31 (32.6%), TICI 2c in 5 (5.3%), and TICI 2b in 22 (23.2%). The rate of unsuccessful recanalization was 38.9%: TICI 2a in 28 patients (29.5%), TICI 1 in 3 (3.2%), and TICI 0 in 6.3%.

The rate of postprocedural sICH was 27.7%. Parenchymal hematoma type 1 occurred in 12 (12.7%) patients, and parenchymal hematoma type 2, in 14 (14.9%) patients. Clinical follow-up at 3 months from stroke was available in 84 patients: Thirty-three (39.3%) were functionally independent (mRS 0–2), and 47 (56%) achieved a favor-

able outcome (mRS 0–3).

Management of Tandem Lesions

Emergent carotid artery stent placement was performed in all patients. In 87 patients, a single-layer carotid stent was used, and 8 patients were treated with a dual-layer carotid stent.

Factors Influencing Clinical Outcomes: ANOVA, Univariate, and Multivariate Analyses

The subgroup comparison of patients with functional independence (mRS 0–2) and dependence at 3-month follow-up is presented in On-line Table 1. Patients with good clinical outcome were younger (mean age, 61.4 versus 65.9 years), presented with shorter onset-to-recanalization time (median, 317.5 versus

360 minutes), had a higher rate of successful intracerebral recanalization (modified TIC1 ≥ 2 : 75.8% versus 52.9%), were more commonly prescribed postprocedural dual-antiplatelet therapy (67.9% versus 25.9%), and showed lower rates of sICH (9.1% versus 42%). All other cofactors were not statistically different between groups. The univariate logistic regression analysis is presented in On-line Table 2.

Factors associated with a good clinical outcome were higher baseline ASPECTS (OR = 1.53; 95% CI, 1.16–2; $P = .002$), lower rates of sICH (OR = 0.13; 95% CI, 0.37–0.51; $P = .001$), and ≤ 2 MT attempts (OR = 0.71; 95% CI, 0.55–0.99; $P = .04$). Moreover, those patients receiving dual-antiplatelet therapy after hemorrhagic transformation had been ruled out on 24-hour CT had higher chances of functional independence at 3-month follow-up (OR = 6.03; 95% CI, 1.87–19.44; $P = .003$).

All other intraprocedural or postprocedural anticoagulant/antiplatelet protocols were not associated with good clinical outcome.

The multivariate general linear analysis (MANOVA) reported a relevant difference between patients with and without good clinical outcome when considered jointly on the variables of baseline ASPECTS, sICH, postprocedural dual-antiplatelet therapy, and number of MT attempts.

There was a significant difference between patients with and without good clinical outcome on baseline ASPECTS, $F(1-53) = 8.57$, $P = .001$, partial $\eta^2 = 0.14$, with functionally independent patients having higher mean ASPECTS on baseline CT (8.4 ± 0.4 ; 95% CI, 7.9–9.2) versus dependent patients (6.9 ± 0.4 ; 95% CI, 6–7.7).

The multivariate analysis confirmed the association with sICH (negative correlation; $P = .005$) and postprocedural dual-antiplatelet therapy (positive correlation; $P = .003$). Moreover, mean mechanical thrombectomy attempts of 1.9 ± 0.3 (95% CI, 1.3–2.5; $P = .004$) were associated with good clinical outcome versus dependent patients undergoing 3.2 ± 0.3 (95% CI, 2.6–3.9) attempts to recanalize the intracerebral occlusion.

Factors Influencing Successful Recanalization and Stent Patency: ANOVA and Univariate Analysis

The subgroup comparison of patients with successful and unsuccessful intracerebral recanalization is presented in On-line Table 1.

The intracerebral large-vessel occlusion was more often successfully recanalized in patients presenting with left-hemispheric stroke (69% versus 43.2%), higher baseline ASPECTS (median, 8 versus 7), and faster onset-to-groin time (median, 236 versus 275 minutes). Moreover, a trend toward successful recanalization ($P = .052$) was observed for patients receiving intraprocedural heparin. The univariate logistic regression analysis is presented in On-line Table 2.

The only factors associated with a successful recanalization were a left-hemispheric stroke (OR = 2.91; 95% CI, 1.23–6.86; $P = .01$) and ≤ 2 mechanical thrombectomy attempts (OR = 0.69; 95% CI, 0.51–0.93; $P = .01$).

The comparison of the available data on stent patency within 72 hours reported a higher rate of acute in-stent occlusion for dual-layer stent compared with single-layer stent (4/5 patients versus 10/59 patients; 80% versus 16.9%; $P < .001$). A similar result was obtained by univariate logistic regression analysis (On-line Table 2) for dual-layer stent patency (OR = 0.05; 95% CI, 0.005–0.50; $P = .007$).

Factors Influencing Symptomatic Intracerebral Hemorrhage: ANOVA, Univariate, and Multivariate Analyses

The subgroup comparison of patients with and without sICH is presented in On-line Table 1. The only factor associated with sICH was a lower baseline ASPECTS (median, 6.5 versus 8) confirmed by univariate logistic regression analysis (On-line Table 2; $P = .009$). Moreover, those patients receiving dual-antiplatelet therapy after hemorrhagic transformation had been ruled out on 24-hour CT had less chance of sICH (OR = 2.4; 95% CI, 1–5.8; $P = .02$).

The multivariate general linear analysis (MANOVA) reported a significant difference between patients with and without symptomatic ICH when considered jointly on the variables baseline ASPECTS, intraprocedural heparin, and number of mechanical thrombectomy attempts, the Wilk $\Lambda = 0.8$, $F(3,80) = 6.03$, $P = .001$, partial $\eta^2 = 0.18$.

There was a significant difference between patients with and without symptomatic ICH on baseline ASPECTS, $F(1-84) = 12.17$, $P = .001$, partial $\eta^2 = 0.13$, with patients with sICH having lower ASPECTS on baseline CT (mean = 6.6 ± 0.4 ; 95% CI, 5.8–7.4) compared with patients without sICH (8.3 ± 0.2 ; 95% CI, 7.8–8.7).

There was a significant difference between patients with and without sICH in intraprocedural heparin administration, $F(1-84) = 6.4$, $P = .01$, partial $\eta^2 = 0.07$, with patients with sICH in patients receiving higher amounts of heparin (mean = 3547 ± 588 IU; 95% CI, 2377–4718 IU) compared with patients without sICH (1817 ± 339 IU; 95% CI = 1141–2493 IU).

There was a significant difference between patients with and without symptomatic ICH in the number of mechanical thrombectomy attempts, $F(1-84) = 32.14$, $P = .002$, partial $\eta^2 = 0.1$, with sICH in patients treated with a higher number of passes (mean, 3.3 ± 0.3 ; 95% CI, 2.6–4.1) compared with those without sICH (1.9 ± 0.2 ; 95% CI, 1.5–2.4).

DISCUSSION

In this study, we assessed functional outcome and complications in patients with acute ischemic stroke and tandem occlusions treated with emergent carotid stent placement and mechanical thrombectomy. We focused our multicenter retrospective analysis on this specific subgroup of patients with special regard for medical management to respond to the demanding questions raised after the recently reported higher successful recanalization rates and better clinical outcome in tandem occlusions managed with carotid stent placement.¹³⁻¹⁶

We found that a large ischemic core at the initial CT scan (ASPECTS ≤ 7), > 2 mechanical thrombectomy attempts, and ≥ 3000 IU of intraprocedural heparin were significant predictors of sICH (Table 2). Functional independence was related to a small ischemic core (ASPECTS ≥ 8) and with the first-passages effect (ie, successful recanalization obtained with ≤ 2 mechanical thrombectomy attempts) (Table 2). Moreover, both single- and dual-antiplatelet therapy seem safe in emergent carotid stent placement, even if patients receive intravenous thrombolysis. Despite these results differing from those reported by van de Graaf et al,²⁰ they are in accordance with the most recent data from the TITAN registry.²⁹

Table 2: Multivariate analysis of factors influencing symptomatic ICH and functional independence

Factors	Mean	95% CI	P Value
Influencing symptomatic ICH			
Intraprocedural heparin ≥ 3000 IU	3547 \pm 588 IU	2377–4718	.01
ASPECTS ≤ 7	6.6 \pm 0.4	5.8–7.4	.001
MT attempts ≥ 3	3.3 \pm 0.3	2.6–4.1	.002
Influencing functional independence (mRS ≤ 2)			
ASPECTS ≥ 8	8.4 \pm 0.4	7.9–9.2	.001
MT attempts ≤ 2	1.9 \pm 0.3	1.3–2.5	.004

Furthermore, patients receiving dual-antiplatelet therapy after ICH had been ruled out on postprocedural CT had higher chances of functional independence at 3 months from stroke, confirming the safety profile of antiplatelet therapy. This finding is in line with the study by Zhu et al,²⁹ which reported a lower 90-day mortality rate in the antiplatelet therapy group.

Regarding anticoagulation, the intraprocedural heparin dosage influenced the development of sICH. While we did not observe an increased risk of ICH (ie, hemorrhagic infarction or parenchymatous hematoma³⁰) within 24 hours from treatment in patients receiving low-dose intraprocedural heparin (ie, <3000 IU), consistent with previous reports,^{20,31,32} low-dose heparin was not related to higher reperfusion rates.²⁷ On the contrary, a higher dose of intraprocedural heparin (ie, ≥ 3000 IU) was associated with sICH without improvement in the rate of successful recanalization or stent patency.

Heparin is commonly used to reduce the risk of re-occlusion and distal embolization during endovascular treatment,³³ and post hoc analyses from the Thrombectomy REvascularization of Large Vessel Occlusions in Acute Ischemic Stroke (TREVO 2) and Mechanical Embolus Removal in Cerebral Ischemia (MERCII) trials showed its utility in obtaining good functional outcome without increasing the risk of hemorrhagic complications.^{31,34} However, the most recent results from large multicenter registries did not find differences between patients with and without heparin treatment in terms of good outcome³⁵ or successful revascularization rates.^{28,29,36}

In our series, the overall sICH risk seems higher compared with the TITAN registry.^{29,37,38} The explanation of this discrepancy may reside in differences among the study populations. In our analysis, we included only patients who underwent emergent carotid stent placement. Thus, most of the included patients received a mixture of antiplatelet therapy, intravenous thrombolysis, and heterogeneous doses of intraprocedural heparin; in contrast, in the TITAN registry, the analysis of the effect of anticoagulants was based only on patients who received a low dose of heparin.

This multicenter analysis has some limitations. First, the observational and nonrandomized design is subject to methodologic biases inherent in this form of study. Second, although only experienced neuroradiologists assessed data at each institution, we did not confirm our findings using a core lab assessment of brain imaging. Third, despite the effort to establish a comprehensive multicenter registry, there may be a concerning risk of bias due to patients lost to follow-up and missing data in the retrospective dataset. In our study, dual-layer stents represented an independent factor related to in-stent thrombosis, as previously reported by Yilmaz et al;³⁹ however, the

small group of 8 with dual-layer stents did not allow running a powerful subgroup analysis comparing single- and dual-antiplatelet therapy in dual-layer stents.

Finally, the medical treatment strategy was left to the interventionist's discretion with heterogeneous drug dosages and administration times.

CONCLUSIONS

In the literature, there are few data to guide management of tandem occlusions in patients with acute ischemic stroke, and optimal antithrombotic therapy remains to be assessed for patients treated with emergent carotid artery stent placement. In our analysis, regular doses of intraprocedural heparin (≥ 3000 IU) were associated with sICH, antiplatelets were safe, and dual-antiaggregation therapy was related to better functional outcomes. The current findings may inform clinical practice and provide support for a prospective randomized controlled trial aimed at assessing endovascular treatment of patients with tandem occlusions.

REFERENCES

1. Ferguson Gary G, Eliasziw M, Barr Hugh WK, et al. **The North American Symptomatic Carotid Endarterectomy Trial.** *Stroke* 1999;30:1751–58 CrossRef Medline
2. Goyal M, Demchuk AM, Menon BK, et al. **Randomized assessment of rapid endovascular treatment of ischemic stroke.** *N Engl J Med* 2015;372:1019–30 CrossRef Medline
3. Rubiera M, Ribo M, Delgado-Mederos R, et al. **Tandem internal carotid artery/middle cerebral artery occlusion: an independent predictor of poor outcome after systemic thrombolysis.** *Stroke* 2006;37:2301–05 CrossRef Medline
4. Powers WJ, Rabinstein AA, Ackerson T, et al. **Guidelines for the Early Management of Patients with Acute Ischemic Stroke: 2019 Update to the 2018 Guidelines for the Early Management of Acute Ischemic Stroke—A Guideline for Healthcare Professionals From the American Heart Association/American Stroke Association.** *Stroke* 2019;50:e344–418 CrossRef Medline
5. Kim YS, Garami Z, Mikulik R, et al. **Early recanalization rates and clinical outcomes in patients with tandem internal carotid artery/middle cerebral artery occlusion and isolated middle cerebral artery occlusion.** *Stroke* 2005;36:869–71 CrossRef Medline
6. Goyal M, Menon BK, van Zwam WH, et al. **Endovascular thrombectomy after large-vessel ischaemic stroke: a meta-analysis of individual patient data from five randomised trials.** *Lancet* 2016;387:1723–31 CrossRef Medline
7. Bracard S, Ducrocq X, Mas JL, et al; THRACE Investigators. **Mechanical thrombectomy after intravenous alteplase versus alteplase alone after stroke (THRACE): a randomised controlled trial.** *Lancet Neurol* 2016;15:1138–47 CrossRef Medline
8. Berkhemer OA, Fransen PSS, Beumer D, et al; MR CLEAN Investigators. **A randomized trial of intraarterial treatment for acute ischemic stroke.** *N Engl J Med* 2015;372:11–20 CrossRef Medline
9. Campbell BC, Mitchell PJ, Kleinig TJ, et al. **Endovascular therapy for ischemic stroke with perfusion-imaging selection.** *N Engl J Med* 2015;372:1009–18 CrossRef Medline
10. Jovin TG, Chamorro A, Cobo E, et al; REVASCAT Trial Investigators. **Thrombectomy within 8 hours after symptom onset in ischemic stroke.** *N Engl J Med* 2015;372:2296–2306 CrossRef Medline

11. Saver JL, Goyal M, Bonafe A, et al. **Stent-retriever thrombectomy after intravenous t-PA vs. t-PA alone in stroke.** *N Engl J Med* 2015;372:2285–95 CrossRef Medline
12. Wilson MP, Murad MH, Krings T, et al. **Management of tandem occlusions in acute ischemic stroke - intracranial versus extracranial first and extracranial stenting versus angioplasty alone: a systematic review and meta-analysis.** *J Neurointerv Surg* 2018;10:721–28 CrossRef Medline
13. Assis Z, Menon BK, Goyal M, et al. **Acute ischemic stroke with tandem lesions: technical endovascular management and clinical outcomes from the ESCAPE trial.** *J NeuroInterv Surg* 2018;10:429–33 CrossRef Medline
14. Sadeh-Gonik U, Tau N, Friehmann T, et al. **Thrombectomy outcomes for acute stroke patients with anterior circulation tandem lesions: a clinical registry and an update of a systematic review with meta-analysis.** *Eur J Neurol* 2018;25:693–700 CrossRef Medline
15. Li W, Chen Z, Dai Z, et al. **Management of acute tandem occlusions: stent-retriever thrombectomy with emergency stenting or angioplasty.** *J Int Med Res* 2018;46:2578–86 CrossRef Medline
16. Zhu F, Bracard S, Anxionnat R, et al. **Impact of emergent cervical carotid stenting in tandem occlusion strokes treated by thrombectomy: a review of the TITAN collaboration.** *Front Neurol* 2019;10:206 CrossRef Medline
17. Jadhav AP, Zaidat OO, Liebeskind DS, et al. **Emergent management of tandem lesions in acute ischemic stroke.** *Stroke* 2019;50:428–33 CrossRef Medline
18. Papanagiotou P, Haussen DC, Turjman F, et al; TITAN Investigators. **Carotid stenting with antithrombotic agents and intracranial thrombectomy leads to the highest recanalization rate in patients with acute stroke with tandem lesions.** *JACC Cardiovasc Interv* 2018;11:1290–99 CrossRef Medline
19. Jacquin G, Poppe AY, Labrie M, et al. **Lack of consensus among stroke experts on the optimal management of patients with acute tandem occlusion.** *Stroke* 2019;50:1254–56 CrossRef Medline
20. van de Graaf RA, Chalos V, Del Zoppo GJ, et al. **Periprocedural antithrombotic treatment during acute mechanical thrombectomy for ischemic stroke: a systematic review.** *Front Neurol* 2018;9:238 CrossRef Medline
21. Blassiau A, Gawlitza M, Manceau PF, et al. **Mechanical thrombectomy for tandem occlusions of the internal carotid artery: results of a conservative approach for the extracranial lesion.** *Front Neurol* 2018;9:928 CrossRef Medline
22. **Thrombectomy in TANdem Occlusion.** NCT03978988. 2020. clinicaltrials.gov. Accessed April 4, 2020
23. Wilson JT, Hareendran A, Grant M, et al. **Improving the assessment of outcomes in stroke: use of a structured interview to assign grades on the modified Rankin Scale.** *Stroke* 2002;33:2243–46 CrossRef Medline
24. Lyden P. **Using the National Institutes of Health Stroke Scale: a cautionary tale.** *Stroke* 2017;48:513–19 CrossRef Medline
25. Pexman JH, Barber PA, Hill MD, et al. **Use of the Alberta Stroke Program Early CT Score (ASPECTS) for assessing CT scans in patients with acute stroke.** *AJNR Am J Neuroradiol* 2001;22:1534–42 Medline
26. Adams HP Jr, Bendixen BH, Kappelle LJ, et al. **Classification of subtype of acute ischemic stroke: definitions for use in a multicenter clinical trial—TOAST. Trial of Org 10172 in Acute Stroke Treatment.** *Stroke* 1993;24:35–41 CrossRef Medline
27. Zaidat OO, Yoo AJ, Khatri P, et al; STIR Thrombolysis in Cerebral Infarction (TICI) Task Force. **Recommendations on angiographic revascularization grading standards for acute ischemic stroke: a consensus statement.** *Stroke* 2013;44:2650–63 CrossRef Medline
28. Hacke W, Kaste M, Bluhmki E, et al. **Thrombolysis with alteplase 3 to 4.5 hours after acute ischemic stroke.** *N Engl J Med* 2008;359:1317–29 CrossRef Medline
29. Zhu F, Anadani M, Labreuche J, et al; TITAN Investigators. **Impact of antiplatelet therapy during endovascular therapy for tandem occlusions: a collaborative pooled analysis.** *Stroke* 2020;51:1522–29 CrossRef Medline
30. von Kummer R, Broderick JP, Campbell BC, et al. **The Heidelberg Bleeding Classification: classification of bleeding events after ischemic stroke and reperfusion therapy.** *Stroke* 2015;46:2981–86 CrossRef Medline
31. Nahab F, Walker GA, Dion JE, et al. **Safety of periprocedural heparin in acute ischemic stroke endovascular therapy: the multi MERCI trial.** *J Stroke Cerebrovasc Dis* 2012;21:790–93 CrossRef Medline
32. Gory B, Haussen DC, Piotin M; et al; TITAN investigators. **Impact of intravenous thrombolysis and emergent carotid stenting on reperfusion and clinical outcomes in patients with acute stroke with tandem lesion treated with thrombectomy: a collaborative pooled analysis.** *Eur J Neurol* 2018;25:1115–20 CrossRef Medline
33. Nahab F, Kass-Hout T, Shaltoni HM. **Periprocedural antithrombotic strategies in acute ischemic stroke interventional therapy.** *Neurology* 2012;79:S174–81 CrossRef Medline
34. Winningham MJ, Haussen DC, Nogueira RG, et al. **Periprocedural heparin use in acute ischemic stroke endovascular therapy: the TREVO 2 trial.** *J Neurointerv Surg* 2018;10:611–14 CrossRef Medline
35. Zhu F, Piotin M, Steglich-Arnholm H, et al; TITAN (Thrombectomy In TANdem Lesions) Investigators. **Periprocedural heparin during endovascular treatment of tandem lesions in patients with acute ischemic stroke: a propensity score analysis from TITAN registry.** *Cardiovasc Intervent Radiol* 2019;42:1160–67 CrossRef Medline
36. Sallustio F, Motta C, Merolla S, et al. **Heparin during endovascular stroke treatment seems safe.** *J Neuroradiol* 2019;46:373–77 CrossRef Medline
37. Anadani M, Spiotta AM, Alawieh A, et al; on behalf of the TITAN (Thrombectomy In TANdem Lesions) Investigators. **Emergent carotid stenting plus thrombectomy after thrombolysis in tandem strokes: analysis of the TITAN registry.** *Stroke* 2019;50:2250–52 CrossRef Medline
38. Zhu F, Labreuche J, Haussen DC, et al; the TITAN (Thrombectomy in Tandem Lesions) Investigators. **Hemorrhagic transformation after thrombectomy for tandem occlusions: incidence, predictors, and clinical implications.** *Stroke* 2019;50:516–19 CrossRef Medline
39. Yilmaz U, Körner H, Mühl-Benninghaus R, et al. **Acute occlusions of dual-layer carotid stents after endovascular emergency treatment of tandem lesions.** *Stroke* 2017;48:2171–75 CrossRef Medline

Use of Cangrelor in Cervical and Intracranial Stenting for the Treatment of Acute Ischemic Stroke: A “Real Life” Single-Center Experience

A. Cervo, F. Ferrari, G. Barchetti, L. Quilici, M. Piano, E. Boccardi, and G. Pero



ABSTRACT

BACKGROUND AND PURPOSE: In cases of large-vessel-occlusion strokes due to an underlying tandem internal carotid artery occlusion or intracranial atherosclerotic disease, concomitant stent placement may be needed. Immediate platelet inhibition is necessary, but to date, a standardized approach for antiplatelet inhibition in acute settings is still missing. Here we report our single-center experience about the safety and efficacy of periprocedural administration of cangrelor in patients with acute ischemic stroke due to intracranial or cervical artery occlusion undergoing stent placement.

MATERIALS AND METHODS: We retrospectively evaluated all cases of acute ischemic stroke that needed acute stent implantation and were treated with periprocedural administration of cangrelor between January 2019 and April 2020 at our institution. All patients who needed either extracranial or intracranial artery stent placement (in either the anterior or posterior circulation) were included.

RESULTS: We evaluated 38 patients in whom cangrelor was administered IV periprocedurally. Their mean age was 64 years (range, 26–85 years), with 25/38 male subjects and 13/38 female patients. In 26 patients (68.4%), a tandem occlusion was present and was treated with carotid artery stent placement, while 12 patients (31.6%) required an intracranial stent implantation. In 4 subjects (10.5%), an intracerebral hemorrhage occurred after the procedure. All patients in the series were alive 1 week after the procedure.

CONCLUSIONS: Although larger, multicentric randomized studies are strongly warranted, our results support the hypothesis of a possible role of cangrelor as a valuable therapeutic option in the management of platelet inhibition in acute ischemic stroke procedures after intra- or extracranial stent placement.

ABBREVIATIONS: AIS = acute ischemic stroke; DAPT = dual-antiplatelet therapy; GP = glycoprotein; ICH = intracerebral hemorrhage; PCI = percutaneous coronary intervention; STEMI = ST-segment elevation myocardial infarction

Endovascular treatment has become the standard care of acute ischemic stroke (AIS) due to large-vessel occlusion, which results most often from a cardioembolic event (mainly atrial fibrillation).¹ Nevertheless, 15%–20% of large-vessel strokes have an underlying tandem internal carotid artery occlusion or intracranial atherosclerotic disease², with the latter showing a higher incidence in the Asian population.³ Patients with AIS due to an underlying atherosclerotic extracranial or intracranial stenosis

frequently need concomitant stent placement to maintain vessel patency.

Thrombosis is a known and serious complication following stent implantation. Indeed, both bare metal and drug-eluting stents can increase the thrombogenicity of atherosclerotic plaque, inducing platelet adhesion, activation, and thrombus formation directly on or near the stent.⁴ Thus, dual-antiplatelet therapy (DAPT) is long considered mandatory in patients undergoing endovascular stent placement, to reduce the risk of thromboembolic complications.

In emergency settings, when stent placement is required in patients without preadmission DAPT, the choice of the right antiplatelet treatment among all those available could be problematic. Thus, inhibitors of glycoprotein IIb/IIIa (GP IIb/IIIa) are known to be safe and efficient, being widely used in clinical practice.⁵

Nevertheless, in patients with AIS, the risk of intracranial hemorrhage is considerably higher, especially if intravenous fibrinolytic

Received May 6, 2020; accepted after revision July 7.

From the Department of Neuroradiology (A.C., F.F., L.Q., M.P., E.B., G.P.), Azienda Socio-Sanitaria Territoriale Grande Ospedale Metropolitano Niguarda, Milan, Italy; Department of Biology and Biotecnology (F.F.), University of Pavia, Pavia, Italy; and Department of Neuroradiology (G.B.), Sapienza University, Rome, Italy.

Please address correspondence to Guglielmo Carlo Pero, MD, Piazza Ospedale Maggiore, 3 20162 Milan, Italy; e-mail: guglielmocarlo.pero@ospedaleniguarda.it

Indicates article with supplemental on-line table.

<http://dx.doi.org/10.3174/ajnr.A6785>

therapy has been administered, either if oral P2Y12 receptor inhibitors or IV GP IIb/IIIa inhibitors are administered or not.⁶ In the unfortunate case of the occurrence of an intracerebral hemorrhage, the long half-life of these medications may represent a disadvantage in patient management. Nonetheless, this risk is generally outweighed by the potentially more severe consequences of vessel occlusion due to in-stent thrombosis.

Most of the antiplatelet strategies used in neurointerventions come from experience in interventional cardiology. Indeed, the use of DAPT in the emergency department has been extensively investigated in patients with ST-segment elevation myocardial infarction (STEMI) and without it. According to current guidelines,⁷ in patients with STEMI and in subjects referred to percutaneous coronary intervention (PCI), pretreatment with a P2Y12 inhibitor is generally recommended in addition to aspirin (Bayer). In particular, ticagrelor administration is recommended on top of aspirin, regardless of the initial treatment strategy and also in patients already undergoing clopidogrel administration. According to the same guidelines,⁷ when patients undergoing a PCI are not pretreated with a P2Y12 inhibitor, cangrelor can be safely used in the catheterization laboratory and ticagrelor can be administered any time before, during, or at the end of cangrelor infusion.

Although characterized by these valuable features, cangrelor use is still off-label in the setting of neuroendovascular interventions.

Given the relative lack of evidence about cangrelor efficacy in the setting of acute neuroendovascular interventions, the aim of this study was to report a single-center experience about the effects of periprocedural IV administration of this drug in patients with AIS due to intracranial or cervical artery occlusion, who needed stent placement.

MATERIALS AND METHODS

Patient Population

This retrospective study was approved by Niguarda Cà Granda Hospital review board. Informed consent was secured from each patient, if possible, or from his or her next of kin.

At our institution, standard informed consent for emergency endovascular procedures includes consent to use antiplatelet drugs, if needed, even if off-label. Our institution approved the off-label use of cangrelor for neuroendovascular procedures.

Our single-center prospectively maintained data base was searched to evaluate all patients with AIS who underwent an endovascular procedure requiring acute stent implantation and who were treated with periprocedural administration of cangrelor. All patients who needed either extracranial or intracranial stent placement, both in the anterior and posterior circulations between January 2019 and April 2020, were included.

Cangrelor Administration Protocol

Our approach in the presence of AIS due to tandem occlusions is to treat the patient in a “retrograde fashion,” performing intracranial thrombectomy first and stent placement afterward, with the patient under conscious sedation, if possible.

Imaging protocol for patient selection was achieved by the acquisition of a nonenhanced CT scan followed by multiphasic CTA and CT perfusion. Choice of an adequate thrombectomy technique

(ie, a direct aspiration first-pass technique, stent-retriever, or a combination of both) was then made by each neuroradiologist according to the site of the occlusion. Balloon-guided catheters were used only in cases of intracranial ICA or cervical ICA occlusions with no concomitant intracranial occlusions.

The choice to implant a stent was made in the neurointerventional suite if no hemorrhagic complications occurred after thrombectomy and a good recanalization (TICI 2b–3) was achieved, according to the decision process shown in the Figure.

The only exclusion criterion for cangrelor administration was intracranial bleeding, ruled out by a conebeam CT performed in the angiosuite.

As soon as the operator deemed it necessary to implant a stent, in patients with no ongoing antiplatelet therapy and not receiving rtPA administration, a loading dose of 500 mg of aspirin was administered intravenously at the beginning of the procedure. After stent placement, its patency was monitored for about 30 minutes, with the patient remaining in the angiosuite and angiograms were obtained every 10 minutes.

If no intrastent thrombosis occurred, cangrelor administration was avoided. On the other hand, in the case of intrastent thrombosis a 30- μ g/kg bolus of cangrelor was administered, followed by a 4.0- μ g/kg/min IV infusion, until the transition to the

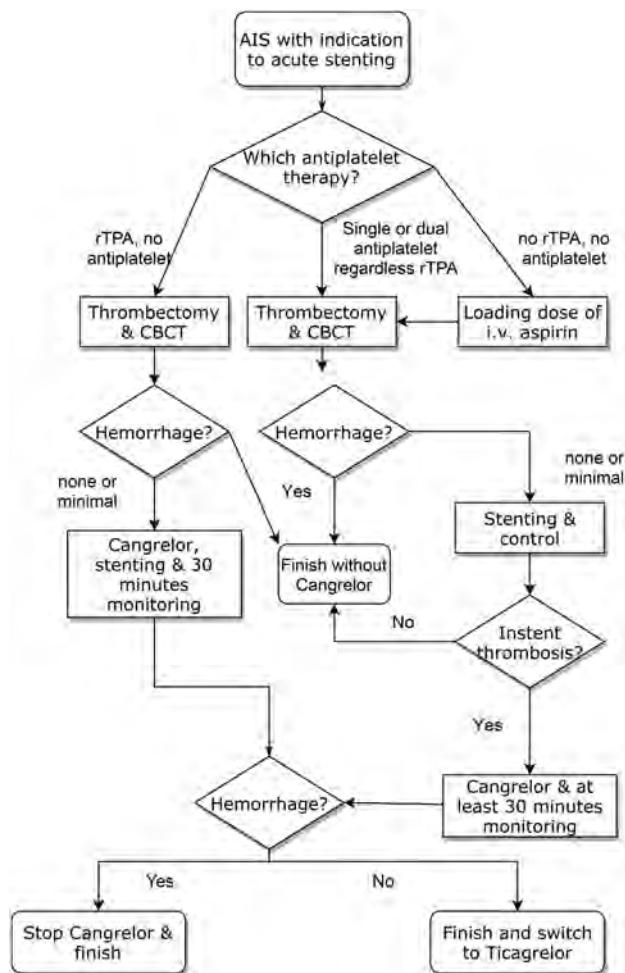


FIGURE. Stent placement and cangrelor administration decision process. CBCT indicates conebeam CT.

oral P2Y₁₂ inhibitor ticagrelor was deemed possible according to the treating physician. A loading dose of ticagrelor, 180 mg, was administered 30 minutes before cangrelor infusion was discontinued. No blood assay was performed to evaluate the effectiveness of antiaggregation, according to our institutional protocol. The postprocedural dual-antiplatelet therapy was performed with ticagrelor, 90 mg twice a day, and aspirin, 100 mg, except for individualized modifications.

In patients who were initially treated with rtPA with no ongoing antiplatelet therapy, after ruling out hemorrhagic complications of the thrombectomy, cangrelor was administered immediately before stent placement, as described above. If during cangrelor infusion, patients showed a clinical deterioration due to hemorrhagic complications, cangrelor administration was stopped and ticagrelor administration was avoided.

Follow-Up and Study Outcomes

All patients received close clinical monitoring in a Stroke Unit or in a Neurologic Intensive Care Unit for at least 24 hours after the procedure. A nonenhanced brain CT scan was scheduled 24 hours after the procedure for all patients in the absence of signs of neurologic deterioration. Cervical carotid artery stent patency was assessed with a Doppler sonographic examination performed 24 hours after the procedure, while intracranial stent patency was assessed with an intracranial CTA. Finally, a brain CT perfusion scan was performed only in selected cases in which doubts about stent patency and/or signs of cerebral ischemia occurred.

The primary outcomes were the occurrence of in-stent thrombosis and the evidence of intracerebral hemorrhage (ICH) both periprocedurally and during the first week after the treatment in in patients stented acutely.

Statistical Analysis

For this report, only descriptive statistics were performed. As for demographic data and baseline patient population characteristics, continuous variables were presented as mean or median, and categorical values, as absolute values and percentages. Statistical analyses were performed using R, Version 3.6.1 (<http://www.r-project.org/>).⁸

RESULTS

Between January 2019 and April 2020, four hundred thirteen endovascular procedures for AIS were performed in our center. Among these, 65 patients, 15.7%, required stent implantation, with 38 subjects (59%) administered IV cangrelor periprocedurally. A complete list of patient demographics, procedural characteristics, and posttreatment complications is presented in the On-line Table.

In this series, the average age was 64 ± 13 years (range, 26–85 years). Five patients received endovascular treatment under general anesthesia, while the remaining 33 were treated under conscious sedation. Furthermore, 10 patients (26.3%) were treated with an aspiration technique and 19 subjects (50%) underwent a combination of aspiration and stent retriever, while in 6 patients (15.8%), both aspiration and a combined technique were used. Finally, in the 3 subjects without intracranial occlusions (7.9%), cervical ICA stent placement was performed.

Six patients were treated during the coronavirus disease 2019 (COVID-19) pandemic, and 1 tested positive for this condition. In 11 patients (28.9%), the onset time of the stroke was unknown, while for the remaining patients, the mean onset-to-groin time was 305 ± 116.8 minutes (range, 120–776 minutes). At the time of the endovascular treatment, 10 patients (26.3%) were under single- or dual-antiplatelet therapy for concomitant pathologies, while only 1 subject (2.6%) was under oral anticoagulation for atrial fibrillation. Of the 38 subjects, 16 patients (42.1%) received IV thrombolysis, while 11 subjects (28.9%) also received intraprocedural aspirin in anticipation of stent placement.

Twenty-six patients (68.4%) presented with tandem occlusions and were treated with cervical or intrapetrous carotid artery stent placement. In this subgroup, 25 Carotid Wallstents (Boston Scientific) were implanted, and only 1 PRO-Kinetic Energy cobalt chromium coronary stent (Biotronik) was implanted for the treatment of a cervical vertebral artery occlusion. The remaining 12 patients (31.6%) required intracranial stent implantation, due to either atherosclerotic disease or dissection of intracranial arteries. In this group, we implanted 7 PRO-Kinetic Energy cobalt chromium coronary stents (Biotronik), 4 Solitaire AB stents (Medtronic), and 1 Neuroform Atlas Stent System (Stryker Neurovascular).

With the exception of a single case (2.6%, TICI 2a), in all patients (97.4%), a good or complete recanalization was achieved (TICI 2b/3).

At the short-term imaging follow-up, no intraprocedural stent occlusion occurred, and no postprocedural stent occlusion occurred within the first 24 hours except for 3 cases (7.9%). Two of these patients, already under oral antiplatelet therapy with clopidogrel, were not switched to ticagrelor and experienced occlusion of the stent when cangrelor infusion was discontinued. One of them underwent a second endovascular procedure during which tirofiban administration and subsequent ticagrelor transition were performed, and the stent was proved patent at 1-week follow-up. The second patient, who was treated with stent placement for an MCA occlusion with an underlying stenosis, did not undergo a second endovascular procedure because he was transferred to a spoke hospital after the procedure; and by the time clinical deterioration was noticed, an ischemic lesion affected the entire MCA territory. The third patient, who underwent basilar artery stent placement for an atherosclerotic stenosis, experienced early postprocedural stent occlusion due to clot progression from the contralateral vertebral artery despite the correct administration of ticagrelor 30 minutes before stopping cangrelor infusion.

During the first week after the procedure, only 1 stent occlusion occurred (2.6%). This patient was under dual-antiplatelet therapy with ticagrelor and aspirin and was switched to ticlopidine and aspirin 24 hours before neurologic symptoms relapsed. The patient underwent a second endovascular procedure, with subsequent cangrelor administration and ticagrelor transition, obtaining stent patency at 1-week follow-up.

In 2 patients (5.2%), a vessel perforation with minimal subsequent subarachnoid hemorrhage occurred, but it was stable after the end of the procedure. In 4 subjects, a small amount of contrast media was found in the Sylvian fissure due to stent retriever traction, without clinical consequences. In such cases, there was no clinical deterioration and no need to stop cangrelor infusion.

Chemical and pharmacokinetic characteristics of P2Y12 receptor inhibitors^a

Compound	Clopidogrel	Prasugrel	Ticagrelor	Cangrelor
Marketed name	Plavix	Effient (US) Efiect (EU)	Brilinta (US) Briquelio or Possia (EU)	Kengreal (US) Kengrexal (EU)
Reversibility	Irreversible	Irreversible	Reversible	Reversible
Administration route	Oral	Oral	Oral	Intravenous
Frequency of administration	Once daily	Once daily	Twice daily	Bolus plus infusion
Onset of effect	2–8 hours	30 min to 4 hours	30 min to 4 hours	Immediate
Duration of effect	5–7 days	7–10 days	3–5 days	30–60 min
Half-life	6 hours	7 hours	8 hours	3–5 min
Apparent volume of distribution	6–72 L	44–68 L	88 L	3.9 L
Plasma protein binding	98%	98%	99.7%	97%–98%
Prodrug	Yes	Yes	No	No
Influenced by genetic variation	Yes	No	No	No

^a Modified from Aguilar-Salinas et al,¹¹ 2019, with permission from BMJ Publishing Group Ltd.

In 4 subjects (10.5%), a basal ganglia reperfusion ICH occurred after the procedure. None of these patients received intravenous thrombolysis, with 1 subject (2.6%) requiring surgical evacuation. The immediate withholding of cangrelor infusion allowed the performance of a safe operation. In the remaining 3 cases, the ICH induced a clinical deterioration, but no surgical evacuation was required, with a subsequent nonenhanced CT scan showing no progression of the ICH after cangrelor discontinuation. All 4 patients were not switched to ticagrelor oral antiplatelet therapy.

All hemorrhagic complications occurred in the ischemic territory. No new hemorrhagic complications, either systemic or intracranial, occurred in the first postprocedural week.

DISCUSSION

This is one of the few reports regarding the intraprocedural use of cangrelor in patients with AIS treated with stent implantation. Although they are being characterized by a descriptive evaluation of data, obtained without a control group, our results seem to suggest that cangrelor could be an effective drug in preventing stent thrombosis, not increasing the risk of hemorrhagic transformation, especially compared with other intraprocedural antiplatelet therapies.^{9,10} Furthermore, the very short half-life of cangrelor could allow an immediate interruption of the antiplatelet action if its discontinuation is needed in case of a hemorrhagic event.

To date, very few studies have been performed to evaluate cangrelor efficacy during emergency neuroendovascular procedures.^{11–14} Indeed, only 27 patients with AIS eligible for stent implantation and subsequently treated with cangrelor administration have been described in literature,^{11–13} and to the best of our knowledge, our study describes, to date, the largest series of patients with AIS undergoing acute stent placement and cangrelor administration.

Until the end of 2018, ReoPro (abciximab) has been the main antiplatelet drug used in our center after stent placement during AIS endovascular procedures. Shortly thereafter, this treatment option was withdrawn from the Italian drug market, and there was a need for a new antiplatelet therapy. Although valuable alternatives to abciximab (namely, tirofiban or eptifibatib, both GP IIb/IIIa inhibitors) were considered at the time, cangrelor gained particular attention due to its promising results in endovascular cardiology procedures.

Cangrelor is a reversible inhibitor of the P2Y12 receptor, being a nonthienopyridine adenosine triphosphate analog. The main pharmacokinetic features of this drug are summarized in the Table.

In particular, compared with other P2Y12 inhibitors, cangrelor has a rapid onset of action, a short half-life, and a predictable pharmacokinetic profile, and it is extensively metabolized by plasma dephosphorylation to inactive metabolites.¹⁵ It has been approved by the Food and Drug Administration for IV periprocedural use in patients undergoing PCI not treated with a P2Y12 platelet inhibitor or glycoprotein IIb/IIIa inhibitors. For this indication, cangrelor is administered as a 30- μ g/kg bolus, followed by a continuous infusion of 4 μ g/kg/min for the PCI duration or at least for 2 hours. The A Clinical Trial Comparing Cangrelor to Clopidogrel Standard of Care Therapy in Subjects Who Require Percutaneous Coronary Intervention (CHAMPION-PHOENIX) trial showed that the occurrence of adverse events at 48 hours (including myocardial infarction, ischemia-driven revascularization, stent thrombosis, and, in some cases, death) is lower in patients treated with cangrelor compared with those receiving clopidogrel.¹⁶

Given the growing evidence supporting the use of this drug in patients with STEMI undergoing PCI, some investigators have started to test its efficacy and safety in neurointerventional procedures.^{11–14}

Our results are in accordance with those reported by Aguilar-Salinas et al¹¹ describing, in a small case series, patients undergoing emergency stent placement for acute ischemic stroke or symptomatic intracranial aneurysms treated with periprocedural cangrelor at half of the standard dose for PCI. Similarly, another study¹⁴ also reported the efficacy of a full dose of this drug in the antiplatelet management of the acute stroke phase in either stent-assisted coiling or flow-diverter treatment of intracranial aneurysms. Furthermore, our results are also in accordance with those reported by 2 other studies^{12,13} describing 2 case series of patients with AIS treated with stent implantation and cangrelor infusion. Finally, and also in line with previous evidence, the very low rate of symptomatic intracranial hemorrhage we found in our cases is similar to those in other reported series using cangrelor after stent placement.^{12,13}

Nevertheless, some degree of heterogeneity exists in the literature regarding the administered cangrelor dose. In this study, we have administered the standard cardiology PCI dose, similar to what happened in most of the previous case series.^{12,13} Nevertheless, another study reported using a half-dose of cangrelor; although only 8 patients were enrolled in their series, the authors reported neither hemorrhagic nor thromboembolic complications.¹¹ In our study, the full-dose decision was made because the vessels of patients with

AIS are likely to have unstable atheromatic plaques, similar to the atheromatous coronary arteries that are PCI targets. On the other hand, ruptured aneurysms (predominantly dissecting if acute stent placement is required) entail an intrinsically higher risk of hemorrhagic complications compared with AIS. Although the main purpose of this study was to report our experience with cangrelor in the treatment of patients with AIS without giving directives about dosage and administration protocol, we think that future studies focusing on different doses of this drug are warranted to find the right balance between efficacy in avoiding thromboembolic complications and reduction of hemorrhagic complications and, in the future, also obtaining tailored drug doses in different patients.

As previously mentioned, cangrelor has a pharmacokinetic profile, especially compared with GP IIb/IIIa inhibitors, that is particularly fitted for its use in acute interventions, when fast, effective treatment and a short half-life are desired. Indeed, its infusion can be started during the procedure and immediately before stent placement without any premedication, a great advantage in neuroendovascular procedures in which a risk of intracranial vessel injury resulting in hemorrhagic complications is present. In fact, due to the fast effect of cangrelor, the operator can rapidly opt for stent placement and antithrombotic therapy up until the end of the intracranial maneuvers, after ruling out any intracranial hemorrhage.

Furthermore, in those few cases in which hemorrhagic complications occur during cangrelor infusion, its short half-life makes the case management easier, given that its antiplatelet activity subsides in less than an hour after the end of the infusion.¹⁶ This feature is of great importance, especially in cases in which a rapid hematoma evacuation is needed, eliminating the need for platelet transfusion. On the other hand, if hemorrhagic complications occur during either GP IIb/or P2Y12 inhibitor treatment, a platelet transfusion may be needed to correct platelet activity, with subsequent time loss and a higher risk of hemorrhage progression.¹⁷

In our series, only 1 patient needed emergency surgical evacuation because of a large basal ganglia hematoma ruled out immediately after the procedure, while cangrelor infusion was still ongoing and promptly discontinued for surgical purposes. A similar case has been recently described,¹³ with a patient who received cangrelor as bridging therapy and required an urgent operation 72 hours after the procedure due to an enlarging infarction. Although some differences between the 2 cases exist (eg, indications or time of surgery), in both cases, the management of the antiplatelet therapy with cangrelor proved to be a safe treatment, avoiding platelet transfusion.

Thus, cangrelor might be a valuable treatment option also as a bridging strategy (also at the low 0.75- $\mu\text{g}/\text{kg}/\text{min}$ dose), as recently reported.¹⁸ Indeed, in a case series recently reported by Godier et al¹⁹ on patients undergoing an unplanned operation after intracranial stent placement, the bridging protocol succeeded in achieving and maintaining platelet inhibition during DAPT discontinuation, with a return to baseline platelet function within 1 hour after cangrelor withdrawal.

Finally, cangrelor might be considered a first-line agent in patients with chronic kidney disease.²⁰ Indeed, it is known that renal function does not alter the pharmacokinetic profile of the drug,²¹ even if clinical studies selectively performed on this population of patients have not been published yet. In this context, in several patients with AIS, there is usually a concomitant presence

of renal dysfunction. Given that these patients usually receive high contrast media doses, both during the diagnostic workflow and the endovascular procedure, having a treatment option that does not affect the renal function is desirable.

Once cangrelor is infused or suspended, ticagrelor (loading dose, 180 mg) has been found to be the safest drug for maintaining antiplatelet activity; it binds competitively to the P2Y12 receptors, thus allowing a continuous and more predictable antiplatelet effect.^{22,23}

Different studies have shown a possible benefit of ticagrelor when switching from cangrelor.^{22,23} In our series, 2 subjects were under clopidogrel treatment at the time of the procedure. Given the lack of studies on patients treated simultaneously with clopidogrel and cangrelor, we refrained from switching to ticagrelor in these 2 patients to avoid an increase in the risk of intracranial hemorrhage. Furthermore, previous studies postulated a competitive effect of cangrelor on clopidogrel antiplatelet activity, thus inducing a blockage of P2Y12, making it unavailable for the active metabolite of clopidogrel itself.^{23,24}

These considerations are also indirectly confirmed and substantiated by some of our results. In particular, in 2 cases of early in-stent thrombosis we experienced, the relapse of neurologic symptoms was documented approximately 50 minutes after the switch from cangrelor to aspirin and clopidogrel, which incidentally appears to be the duration of cangrelor effect.

The 4 patients showing postprocedural ICH in our series had poor blood pressure control following the endovascular treatment. Although there is no clear correlation between poor blood pressure control and hemorrhagic complications, existing data suggest that uncontrolled blood pressure might be a relevant risk factor for ICH development after carotid artery stenosis correction. Strict monitoring of blood pressure (with systolic blood pressure values of <140 mm Hg) is therefore recommended in the angiogram as well as during the first postoperative week to avoid reperfusion hemorrhage.²⁵

On the other hand, if a small and self-limiting subarachnoid hemorrhage suffusion occurs, cangrelor could be safely continued under clinical and imaging monitoring because this complication is often self-limiting.

This study has several limitations, mostly related to its retrospective, single-center nature, with a relatively small number of patients enrolled, with short follow-up, and without comparison with a control group. In addition, we did not perform any test to evaluate the platelet response to P2Y12 inhibition. Finally, in our group, there was a clear under-representation of patients already treated with oral anticoagulants, which usually represent a significant proportion of patients undergoing emergent neuroendovascular procedures, therefore limiting the generalizability of our results.

CONCLUSIONS

Although it is characterized by these limitations, we here report a relatively large case series about periprocedural administration of cangrelor in patients with AIS following the occlusion of an intracerebral or cervical artery and requiring extracranial or intracranial stent placement. Even though larger and randomized studies are recommended, our results are in line with other preliminary observations suggesting that cangrelor might be a valuable therapeutic option in the management of emergency

neuroendovascular interventions, given its efficacy in rapid platelet function inhibition and its fast resolution in cases of hemorrhagic complications.

ACKNOWLEDGMENTS

The authors thank Sirio Coccozza, MD, for his valuable assistance in the revision of the scientific English of this article.

DISCLOSURES: Federica Ferrari—RELATED: Other: scholarship from the Enrico ed Enrica Sovena Foundation, Rome, Italy.

REFERENCES

1. Powers WJ, Rabinstein AA, Ackerson T, et al; American Heart Association Stroke Council. **Guidelines for the Early Management of Patients with Acute Ischemic Stroke: A Guideline for Healthcare Professionals from the American Heart Association/American Stroke Association.** *Stroke* 2018;49:e46–110 CrossRef Medline
2. Grigoryan M, Haussen DC, Hassan AE, et al. **Endovascular treatment of acute ischemic stroke due to tandem occlusions: large multicenter series and systematic review.** *Cerebrovasc Dis* 2016;41:306–12 CrossRef Medline
3. Holmstedt CA, Turan TN, Chimowitz MI. **Atherosclerotic intracranial arterial stenosis: risk factors, diagnosis, and treatment.** *Lancet Neurol* 2013;12:1106–14 CrossRef Medline
4. Windecker S, Meier B. **Late coronary stent thrombosis.** *Circulation* 2007;116:1952–65 CrossRef Medline
5. Farrokh S, Owusu K, Lara LR, et al. **Neuro-interventional use of oral antiplatelets: a survey of neuro-endovascular centers in the United States and review of the literature.** *J Pharm Pract* 2019 Jul 21. [Epub ahead of print] CrossRef Medline
6. Zhu F, Anadani M, Labreuche J, et al; TITAN Investigators. **Impact of antiplatelet therapy during endovascular therapy for tandem occlusions: a collaborative pooled analysis.** *Stroke* 2020;51:1522–29 CrossRef Medline
7. Valgimigli M, Bueno H, Byrne RA, et al; ESC National Cardiac Societies. **2017 ESC focused update on dual antiplatelet therapy in coronary artery disease developed in collaboration with EACTS: the Task Force for dual antiplatelet therapy in coronary artery disease of the European Society of Cardiology (ESC) and of the European Association for Cardio-Thoracic Surgery (EACTS).** *Eur Heart J* 2018;39:213–60 CrossRef Medline
8. R Core Team. **R: A Language and Environment for Statistical Computing.** R Foundation for Statistical Computing. 2019. <https://www.R-project.org/>. Accessed May 5, 2020
9. Al-Mufti F, Amuluru K, Manning NW, et al. **Emergent carotid stenting and intra-arterial abciximab in acute ischemic stroke due to tandem occlusion.** *Br J Neurosurg* 2017;31:573–79 CrossRef Medline
10. Pan X, Zheng D, Zheng Y, et al. **Safety and efficacy of tirofiban combined with endovascular treatment in acute ischaemic stroke.** *Eur J Neurol* 2019;26:1105–10 CrossRef Medline
11. Aguilar-Salinas P, Agnoletto GJ, Brasiliense LBC, et al. **Safety and efficacy of cangrelor in acute stenting for the treatment of cerebrovascular pathology: preliminary experience in a single-center pilot study.** *J Neurointerv Surg* 2019;11:347–51 CrossRef Medline
12. Linfante I, Ravipati K, Starosciak AK, et al. **Intravenous cangrelor and oral ticagrelor as an alternative to clopidogrel in acute intervention.** *J Neurointerv Surg* 2020 May 15. [Epub ahead of print] CrossRef Medline
13. Elhorany M, Lenck S, Degos V, et al. **Cangrelor and stenting in acute ischemic stroke: monocentric case series.** *Clin Neuroradiol* 2020 May 7. [Epub ahead of print] CrossRef Medline
14. Abdennour L, Sourour N, Drir M, et al. **Preliminary experience with cangrelor for endovascular treatment of challenging intracranial aneurysms.** *Clin Neuroradiol* 2019 Jul 15. [Epub ahead of print] CrossRef Medline
15. Storey RF, Sanderson HM, White AE, et al. **The central role of the P (2T) receptor in amplification of human platelet activation, aggregation, secretion and procoagulant activity.** *Br J Haematol* 2000;110:925–34 CrossRef Medline
16. Bhatt DL, Stone GW, Mahaffey KW, et al; CHAMPION PHOENIX Investigators. **Effect of platelet inhibition with cangrelor during PCI on ischemic events.** *N Engl J Med* 2013;368:1303–13 CrossRef Medline
17. Lipinski MJ, Lee RC, Gaglia MA, et al. **Comparison of heparin, bivalirudin, and different glycoprotein IIb/IIIa inhibitor regimens for anticoagulation during percutaneous coronary intervention: a network meta-analysis.** *Cardiovasc Revasc Med* 2016;17:535–45 CrossRef Medline
18. Bhattad VB, Gaddam S, Lassiter MA, et al. **Intravenous cangrelor as a peri-procedural bridge with applied uses in ischemic events.** *Ann Transl Med* 2019;7:408 CrossRef Medline
19. Godier A, Mesnil M, De Mesmay M, et al. **Bridging antiplatelet therapy with cangrelor in patients with recent intracranial stenting undergoing invasive procedures: a prospective case series.** *Br J Anaesth* 2019;123:e2–e5 CrossRef Medline
20. Van Tuyl JS, Newsome AS, Hollis IB. **Perioperative bridging with glycoprotein IIb/IIIa inhibitors versus cangrelor: balancing efficacy and safety.** *Ann Pharmacother* 2019;53:726–37 CrossRef Medline
21. Neumann FJ, Hochholzer W, Pogatsa-Murray G, et al. **Antiplatelet effects of abciximab, tirofiban and eptifibatid in patients undergoing coronary stenting.** *J Am Coll Cardiol* 2001;37:1323–28 CrossRef Medline
22. Schneider DJ, Agarwal Z, Seecheran N, et al. **Pharmacodynamic effects during the transition between cangrelor and ticagrelor.** *JACC Cardiovasc Interv* 2014;7:435–42 CrossRef Medline
23. Steinhubl SR, Oh JJ, Oestreich JH, et al. **Transitioning patients from cangrelor to clopidogrel: pharmacodynamic evidence of a competitive effect.** *Thromb Res* 2008;121:527–34 CrossRef Medline
24. Dovlatova NL, Jakubowski JA, Sugidachi A, et al. **The reversible P2Y12 antagonist cangrelor influences the ability of the active metabolites of clopidogrel and prasugrel to produce irreversible inhibition of platelet function.** *J Thromb Haemost* 2008;6:1153–59 CrossRef Medline
25. Farooq MU, Goshgarian C, Min J, et al. **Pathophysiology and management of reperfusion injury and hyperperfusion syndrome after carotid endarterectomy and carotid artery stenting.** *Exp Transl Stroke Med* 2016;8:7 CrossRef Medline

Transarterial Treatment of Cranial Dural Arteriovenous Fistulas: The Role of Transarterial and Transvenous Balloon-Assisted Embolization

J.O. Zamponi Jr, F.P. Trivelato, M.T.S. Rezende, R.K. Freitas, L.H. de Castro-Afonso, G.S. Nakiri, T.G. Abud, A.C. Ulhôa, and D.G. Abud

ABSTRACT

BACKGROUND AND PURPOSE: Treatment of dural arteriovenous fistulas can be performed by transarterial or transvenous accesses. For those fistulas located at a dural sinus wall, obliteration of the sinus might lead to a substantial risk of complications if the occluded sinus impairs normal venous drainage. For those fistulas with direct leptomeningeal venous drainage, navigation to reach the arteriovenous shunting point of a leptomeningeal vein is usually technically demanding. We report the outcomes of patients with dural AVFs treated by transarterial injection of liquid embolic agents assisted by transarterial double-lumen balloon catheters and/or transvenous balloon catheters.

MATERIALS AND METHODS: This was a retrospective, 3-center study including patients with dural AVFs treated with a balloon-assisted technique in at least 1 treatment session. Angiographic follow-up was performed at 6 months. Clinical assessment was performed at admission and discharge and was reassessed at 30-day and 6-month follow-ups.

RESULTS: Forty-one patients with 43 dural AVFs were treated. Thirty-four fistulas were located at a dural sinus wall. Treatment was performed using only a transarterial approach in 42 fistulas. Only 1 session was needed for complete obliteration of the fistula in 86% of the patients. Immediate complete angiographic occlusion was achieved in 39 fistulas. Of the 41 controlled fistulas, 40 (97.6%) were completely occluded at 6 months. Thirty-nine fistulas (95.1%) were cured without any report of major neurologic events or death during follow-up.

CONCLUSIONS: Transarterial balloon-assisted treatment of dural AVFs with or without transvenous balloon protection was shown to be safe and effective.

ABBREVIATIONS: DAVF = dural arteriovenous fistula; DLB = double-lumen balloon; DLVD = direct leptomeningeal venous drainage; MMA = middle meningeal artery; NALEA = nonadhesive liquid embolic agent; OCC = occipital artery; TAA = transarterial approach; TVA = transvenous approach; TVB = transvenous balloon

Intracranial dural arteriovenous fistulas (DAVFs) are characterized by anomalous shunts located inside the dural leaves between the arterial and the venous systems.¹⁻³ The venous drainage pattern of DAVFs determines their clinical presentation and prognosis and guides their therapeutic management.⁴

Treatment of a DAVF can be performed by transarterial (TAA) or transvenous (TVA) approaches. The TAA has been successfully used to treat DAVFs with direct leptomeningeal

venous drainage (DLVD), while the TVA has been avoided in the treatment of this type of DAVF because navigation to reach the arteriovenous shunting point of a leptomeningeal vein is usually technically demanding and therefore riskier.^{2,3}

For those DAVFs located within the dural sinus wall, transvenous embolization has been classically reported to provide a higher likelihood of cure than arterial embolization. However, complete obliteration of a dural sinus might lead to a substantial risk of complications if the occluded sinus impairs normal venous drainage.^{2,3,5}

The major limitation for curative treatment of DAVFs with DLVD by the TAA is the extension of reflux of the liquid embolic agent along the arterial feeder before it reaches the venous side.⁶ Similarly, the use of a TVA to treat a DAVF of the dural sinus wall poses technical difficulties because there is limited control of the embolic agent penetration into the sinus, exposing it to inadvertent occlusion.¹⁻³

Received May 20, 2020; accepted after revision July 7.

From the Division of Interventional Neuroradiology (J.O.Z., F.P.T., M.T.S.R., A.C.U.), Felício Rocho Hospital, Belo Horizonte, Minas Gerais, Brazil; Division of Interventional Neuroradiology (R.K.F., L.H.d.C.-A., G.S.N., D.G.A.), Hospital das Clínicas, Medical School, University of São Paulo, Ribeirão Preto, São Paulo, Brazil; and Division of Interventional Neuroradiology (T.G.A.), Hospital Israelita Albert Einstein, São Paulo, Brazil.

Please address correspondence to Felipe Padovani Trivelato, MD, PhD, 3616 Timbiras St, Barro Preto, Belo Horizonte, Minas Gerais, Brazil 30320-670; e-mail: felipepadovani@yahoo.com.br; @FelipeTrivelato
<http://dx.doi.org/10.3174/ajnr.A6777>

To overcome these issues, preliminary case series have been published regarding the use of transarterial double-lumen balloons (DLBs) in association, or not, with transvenous balloons (TVBs) to treat DAVFs.⁶⁻¹³ This strategy allows the transarterial injection of embolic material without important reflux because its backflow is retained distal to the inflated balloon at the arterial feeder. The risk of inadvertent occlusion of the dural sinus by transarterial embolization has also been overcome because the possibility of TVB inflation inside the dural sinus ensures lumen protection.⁶⁻¹³ Additionally, the TVB can be inflated or deflated during treatment, according to the desired hemodynamic response intended to redirect the embolic agent toward the fistula.

The aim of this study was to report the clinical and angiographic outcomes of patients with DAVFs treated by transarterial injection of nonadhesive liquid embolic agents (NALEAs) assisted by a transarterial DLB catheter and or TVB.

MATERIALS AND METHODS

Study Design

This was a retrospective, 3-center study that was conducted in accordance with the Strengthening the Reporting of Observational Studies in Epidemiology guidelines (<https://strobe-statement.org/index.php?id=strobe-home>). It was approved by the ethics board of the institutions.

Inclusion criteria were as follows: 1) patients with intracranial DAVFs; 2) dural fistulas located at a sinus wall (Cognard type I or II) or with DLVD (Cognard type III, IV, or V); 3) a DAVF treated by TAA as a first-line therapy; and 4) use of a balloon-assisted technique in at least 1 treatment session.

The exclusion criteria were as follows: 1) a DAVF treated exclusively by TVA, without TAA; and 2) a DAVF for which balloon catheters were not used.

Angiographic Analysis

Occlusion of the DAVF after treatment was reassessed by conventional angiography at 6 months. Complete occlusion was defined as full obliteration of the fistulous zone, with no residual shunt or early venous drainage.

Clinical Analysis

Immediate and late serious clinical events were assessed during follow-up, including death and stroke. Other complications were also registered.

Endovascular Procedure

All 3 centers adopted the same treatment strategy. All interventions were performed with the patient under general anesthesia and systemic heparinization. Cerebral angiography was performed through femoral artery access. If a TVA was planned, venous access was obtained via the femoral vein. When intermittent angiographic control was needed aside from the cervical arterial treatment route (contralateral carotid artery or vertebral artery), contralateral femoral arterial access was obtained.

A 6F guiding catheter was placed in the external carotid artery, giving branches to the DAVF. When a very challenging

anatomy was faced, a triaxial system with a long sheath and guiding catheter with a malleable tip was combined.

The middle meningeal artery (MMA) was used as the primary treatment access route whenever possible because it presents with a commonly enlarged diameter when feeding a DAVF and due to its straight and embedded pathway in the dura. The occipital artery, which is considered a large-diameter vessel and consequently of difficult reflux control during NALEA injection, is even more dilated under hemodynamic stress when supplying a DAVF. Additionally, its tortuous transosseous branches toward the DAVF create higher resistance to NALEA progression. Thus, whenever one of these feeding arteries had a large enough diameter to permit balloon catheter navigation, catheterization was attempted (Fig 1).

A DLB catheter, 4 × 11 mm (Scepter XC; MicroVention) was advanced over a 0.014-inch microguidewire (Transend 14 EX; Stryker) into the branch responsible for the DAVF supply, always trying to reach the fistulous zone or as close as possible to it. In rare cases, when the arterial feeder was very thin and tortuous, only the detachable tip microcatheter was used in association with a TVB.

For those DAVFs within the venous sinus wall, an 8 × 80 mm remodeling balloon (Copernic RC; Balt Extrusion) was navigated over a 0.014-inch microguidewire via the transvenous femoral route through a 6F guiding catheter into the affected sinus covering the fistulous shunt. The balloon was temporarily kept inflated during transarterial injection of the embolic agent for a maximum of 7 minutes. To promote higher inflow of the embolic agent along the sinus wall, we performed transarterial injections intermittently as the balloon was deflated for a few seconds.

Transarterial embolization was performed after the DLB catheter was inflated, and its dead space was filled with dimethyl sulfoxide. Under continuous subtraction fluoroscopy, the NALEA (Onyx-18, Medtronic; or SQUID 18; Emboflu) injections were performed. When 2 arterial accesses were used, double injection was performed, simultaneously or alternately, depending on the penetration of the NALEA inside the fistulous zone (Fig 2).

A control angiography was performed to evaluate occlusion of the fistula, patency of the dural sinus if applicable, and complications.

Data Collection

All data were prospectively collected. Preoperative data included age, sex, clinical presentation, mRS score, DAVF location, Cognard type, feeding arteries, and draining veins or dural sinus involved. Operative data included the treated fistula, accessed vessels, use of balloons and/or microcatheters, embolic agent, and technical complications. Postoperative evaluation included the occlusion rate, complications, and mRS at discharge and at the 6-month follow-up.

Radiologic follow-up included 2 angiographies, immediately after the procedure and at the 6-month follow-up. Angiographic outcome was defined as complete occlusion or partial occlusion. Angiograms were evaluated by an independent neuroradiologist. Clinical outcomes were evaluated at 30-day and 6-month follow-ups by independent neurologists, who examined and interrogated the patients about their own perception of symptom evolution,

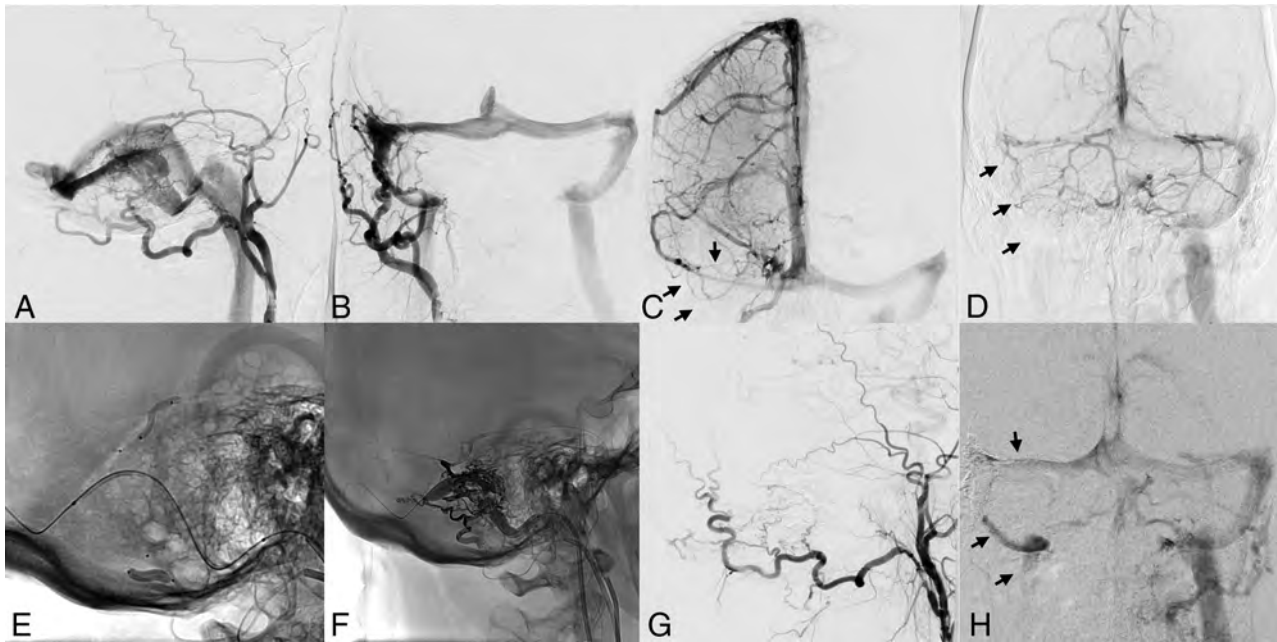


FIG 1. A and B, Angiography shows a transverse-sigmoid sinus DAVF supplied by the OCC and MMA. C and D, Venous phase of ICA and vertebral artery angiograms demonstrates that the right transverse and sigmoid sinuses are nonfunctioning (*arrows*). E, Note the position of the DLB catheters inside the petrosquamous branch of the MMA and inside the mastoid branch of the OCC. F, All 3 balloons are inflated, including the TVB. G, Control angiography reveals total occlusion of the DAVF. H, Venous phase of the ICA control angiogram demonstrates filling of the right transverse and sigmoid sinuses (*arrows*).

categorizing them as asymptomatic (complete resolution of previous symptoms) with clinical improvement or deterioration.

RESULTS

Between January 2016 and July 2019, forty-one patients with 43 DAVFs were treated in accordance with the inclusion criteria.

Patient Demographics

The mean age was 57.3 ± 13.8 years, and 53.7% were men. Four patients were asymptomatic, and 37, symptomatic (Table 1). Before treatment, 9 patients had an mRS score of zero, 21 patients had an mRS score of 1, five patients had an mRS score of 2, and 6 patients had an mRS score >2 .

DAVF Characteristics

Twenty-one (48.8%) fistulas were located at the transverse-sigmoid sinus; 8 (18.6%), at the transverse sinus/torcula region; 7 (16.7%), at the tentorial region; and 7, in other locations.

Of the 34 DAVFs located at a dural sinus wall (79%), the involved sinus was functional in 13 cases and nonfunctional in 21 (61.8%) cases. Three fistulas presented with an isolated sinus (segment of the venous sinus discontinued from the other sinuses, mostly draining through leptomeningeal vein reflux). Nine DAVFs had DLVD. Most DAVFs were supplied by the MMA, followed by the occipital artery (OCC) and ascending pharyngeal artery.

Treatment Characteristics

The interventions were successfully accomplished in all patients. A total of 50 treatment sessions were performed. In 86% of patients, only 1 session was needed for complete obliteration of

the DAVF. One or 2 arterial feeders were embolized in 94% of the cases (Table 2).

Treatment was performed using only TAA in 42 (97.7%) fistulas. In only 1 case, transvenous embolization was necessary in association with the TAA to complete treatment. A transvenous remodeling balloon was used in 44% of sessions. A transarterial DLB catheter for NALEA injection was used in 41 (82%) procedures. Both balloons were used simultaneously in 21 (42%) interventions.

The most frequently used access was the MMA followed by the OCC. The average volume of NALEA injected was almost the same in the MMA and OCC arteries. In 13 procedures, a simultaneous injection was performed through the MMA and OCC.

In 29 (85%) sinus wall DAVFs, the sinus was preserved. In 3 cases, the sinus was occluded through transarterial NALEA injection as planned. In the other 2 DAVFs, the nonfunctioning sinus was nonintentionally occluded but without any clinical impact. In those cases, a TVB was not used.

Angiographic Outcome

Immediate, complete angiographic occlusion was achieved in 39 (90.7%) DAVFs. Of the 41 controlled DAVFs, 40 (97.6%) were completely occluded at 6 months. One patient died before the 6-month follow-up. Another patient whose postprocedural angiography showed complete DAVF occlusion refused angiographic follow-up.

Clinical Outcome

Of the 41 patients enrolled, 39 (95.1%) were treated without major neurologic events or death during follow-up. One patient with a transverse-sigmoid fistula presented with cerebellar ischemia during

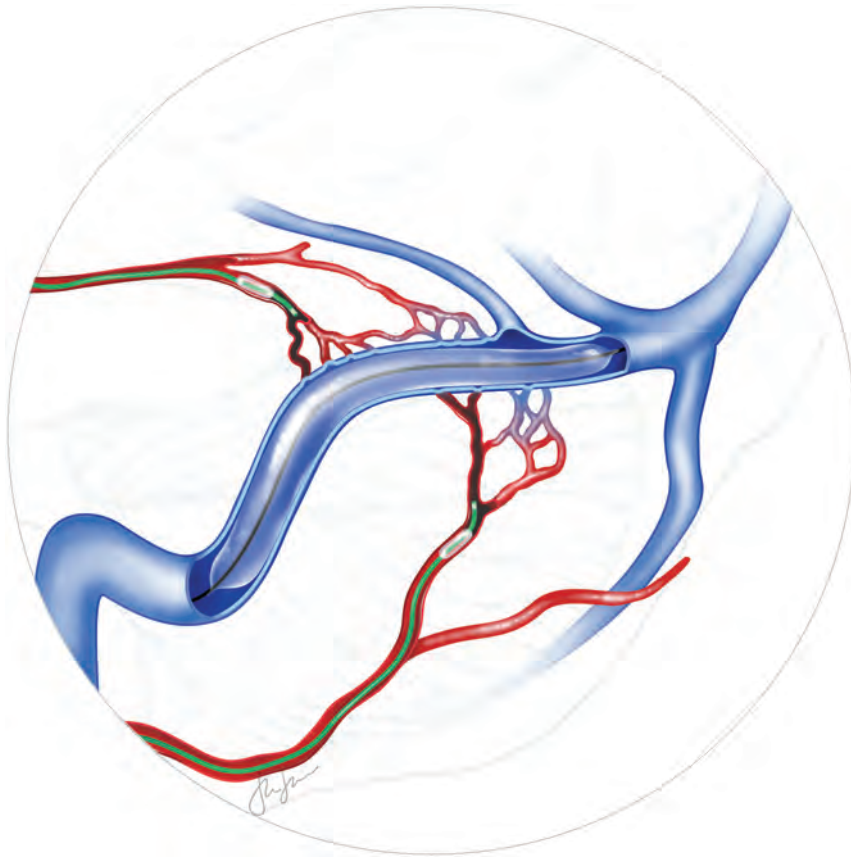


FIG 2. Schematic drawing demonstrates a DAVF of the transverse sinus. A DLB catheter is inside the petrosquamous branch of the MMA, and another DLB catheter is inside the mastoid branch of the OCC. A third balloon catheter is positioned inside the transverse sinus and inflated to protect the sinus lumen. Observe that the DLB catheters avoid liquid embolic agent reflux.

treatment. Total recovery of ataxia was observed after 1 month. The only reported death occurred 3 months after treatment, due to an unrelated cause (complication of a pancreatectomy).

Complications of any kind occurred in 4 (9.7%) patients, including 2 cases of facial palsy, 1 case of alopecia, and 1 case of scalp necrosis. Of the 2 cases of facial palsy, one patient completely recovered and the other patient partially improved. No catheter was retained by the embolic agent.

At the last follow-up, 32 (78%) patients were asymptomatic, 7 (17%) improved, and only 1 (2.4%) deteriorated. One patient died.

DISCUSSION

The present study represents the largest series regarding endovascular treatment of DAVFs assisted by transarterial and/or transvenous balloons. Forty-one patients with 43 DAVFs were included. All patients except 1 were treated solely through a TAA. The treatment strategy was based on flow/pressure control. Injection through an inflated balloon catheter at the arterial feeder improves the penetration of embolic agent because it creates a barrier to reflux backflow, moving the gradient pressure toward the fistula. At the venous side, the mechanical presence of an inflated balloon builds a sinus lumen mold for the embolic agent, protecting it from inadvertent occlusion of the sinus or embolic agent migration.

Endovascular treatment is well-established as the first-line treatment to manage DAVFs.² The TAA for fistulas with DLVD has become the criterion standard since the introduction of NALEAs. It was first reported by Rezende et al,¹⁴ in 2006, when a patient with a lesser sphenoid wing region DAVF was treated by transarterial embolization with Onyx, achieving complete occlusion in a single session. Since then, the safety and effectiveness of NALEAs in the treatment of DAVFs have been consistently reported.²

However, the TAA has some limitations. Considering that the treatment goal for DAVFs with DLVD embolization is to achieve occlusion of the arteriovenous shunt, including the outflow portion of the draining vein, some technical challenges may be encountered to promote proper embolization across tiny arterial feeders up to the venous site of the fistula. Notably, it is difficult to manage the balance between anterograde flow and reflux to predict the progression of the embolic agent toward the fistula.^{2,15} A position close to the fistulous zone, which is the most often intended, is difficult to reach if arterial feeders are very tortuous or have a small caliber. Additionally, in some cases, major embolic agent reflux

along the microcatheter may be observed, compelling the operator to stop the injection to prevent embolization into eloquent arteries or microcatheter retention inside the reflux.^{6,8-10}

On the other hand, DAVFs located at the dural sinus wall are classically treated through a TVA, with sinus sacrifice whenever possible.¹ Some authors advocate the use of the TAA to preserve the sinus lumen, but some controversy exists. Ertl et al¹ showed that sinus-occluding treatment is related to a higher rate of definitive fistula occlusion but was accompanied by a significantly higher complication rate. In contrast, the sinus-preserving approach offered a lower rate of occlusion but a very low complication rate. Most complications are related to an inadvertent occlusion of a functioning sinus. The TAA poses a large challenge because it is essential to occlude all the fistulous connections at the dural sinus wall while avoiding penetration of the embolic agent inside the sinus.⁵

To improve the penetration of NALEAs toward the fistula during the TAA, some strategies have been used, including the pressure-cooker technique using glue or coils and the use of a balloon besides the microcatheter.^{9,16}

The use of a DLB catheter for NALEA injection was described in 2013 and has been expanded since then.¹⁷ The device has 2 lumens: the first lumen is dedicated to the guidewire, and the second lumen is dedicated to balloon inflation. Once the wire is

Table 1: Baseline characteristics of patients and DAVFs^a

Patient Demographics	
Total No. of patients	41
Mean age (yr)	57.3 ± 13.8
Male/female ratio	1.16:1
Clinical presentation	
Asymptomatic	4 (9.8%)
Symptomatic	37 (90.2%)
Headache	27 (65.8%)
Tinnitus	21 (51.2%)
Intracranial hypertension	10 (24.4%)
Hemorrhage	7 (17.1%)
Seizure	4 (9.8%)
Cognitive impairment	3 (7.3%)
DAVF location ^b	
Transverse/sigmoid sinus	21 (48.8%)
Transverse/torcula	8 (18.6%)
Tentorial	7 (16.3%)
Superior sagittal sinus	5 (11.6%)
Lesser sphenoid wing	1 (2.3%)
Convexity	1 (2.3%)
DAVF classification (Cognard) ^b	
I	4 (9.3%)
Ila	8 (18.6%)
Ilb	6 (13.9%)
Ila + b	16 (37.2%)
III	7 (16.3%)
IV	2 (4.6%)
V	0 (0%)
Arterial feeders	
Middle meningeal	40 (93.0%)
Occipital	38 (88.3%)
Ascending pharyngeal	10 (23.2%)
ICA (dural branches)	7 (16.2%)
Vertebral	5 (11.6%)
Superficial temporal	4 (9.3%)
Posterior meningeal	4 (9.3%)
Ophthalmic	3 (6.9%)
Davidoff and Schechter	3 (6.9%)
Posterior auricular	1 (2.3%)
Venous sinus angiographic features ^c	
Isolated sinus	3 (8.8%)
Functional sinus	13 (38.2%)

^a Values are presented as No. (%) unless stated otherwise. Mean values are presented as the mean ± SD.

^b Based on the number of DAVFs (n = 43).

^c Based on the number of DAVFs located at a sinus wall (n = 34).

removed, the NALEA can be injected through the lumen. When the balloon is inflated, it is able to simulate a “wedge and plug” effect, which is mandatory for NALEA anterograde migration. Therefore, it allows a more aggressive embolization, with a prolonged injection time of higher volumes of embolic material without reflux. One of the main disadvantages of this technique is that the navigability of the DLB catheter is poorer than that of other dimethyl-sulfoxide-compatible microcatheters.^{6,10,16}

Deng et al⁹ reported a case series of 8 patients with DAVFs who underwent balloon-assisted transarterial embolization. However, instead of using a DLB catheter, a standard remodeling balloon was placed parallel to a microcatheter. Complete occlusion of the fistula was achieved in all patients without complications.

In 2013, Paramasivam et al¹¹ reported their experience with DLBs in the treatment of 22 patients with different lesions, including intracranial and extracranial arteriovenous malformations,

Table 2: Treatment characteristics and results^a

No. of Treatment Procedures	
Total No. of sessions	50
1 session per DAVF	37 (86.1%)
2 sessions per DAVF	5 (11.6%)
3 sessions per DAVF	1 (2.3%)
No. of arteries embolized per session	
1	22 (44%)
2	25 (50%)
3	3 (6%)
Embolized artery ^b	
Middle meningeal	42 (51.9%)
Occipital	35 (43.2%)
Superficial temporal	3 (3.7%)
Ascending pharyngeal	1 (1.2%)
Volume of NALEA injected per pedicle (mL)	
Middle meningeal	4.48 (0.8–13.4)
Occipital	4.53 (0.7–15.6)
Duration of NALEA injection per pedicle (min)	
Middle meningeal	33.4 (8–110)
Occipital	27.3 (8–62)
Treatment approach per DAVF	
Arterial	42 (97.7%)
Arterial + venous	1 (2.3%)
Balloon use per session	
Only transarterial	20 (40%)
Only transvenous	1 (2%)
Transarterial + transvenous	21 (42%)
None	8 (16%)
Angiographic outcome	
Immediate total occlusion	39/43 (90.7%)
6-Month total occlusion	40/41 (97.6%)
Clinical outcome	
Asymptomatic	32 (78.1%)
Improvement of symptoms	7 (17.1%)
Worsening of symptoms	1 (2.4%)
Death	1 (2.4%)
Complications	
Facial palsy	2
Cerebellar ischemia	1
Alopecia	1
Scalp necrosis	1

^a Values are presented as number (%) unless stated otherwise.

^b Based on the total number of embolized arteries (n = 81).

vein of Galen malformations, and dural fistulas. Among 7 patients with DAVFs, 4 optimal occlusions, 2 suboptimal occlusions, and 1 failed catheterization resulted. In 2 cases, reflux across the balloon was observed, and 1 MMA rupture with extradural hemorrhage occurred.

A nonrandomized study, including only isolated-type DAVFs, compared the results of Onyx embolization using a DLB catheter with those using a nonballoon microcatheter.¹⁰ The balloon group showed complete occlusion of the DAVF in 13 patients and near-complete occlusion in 2 patients, while the nonballoon group showed complete occlusion in 5 patients, near-complete occlusion in 5 patients, and incomplete occlusion in 4 patients. The balloon group presented with a lower mean procedural time, a lower Onyx injection time, and fewer embolized feeders than the nonballoon group. Complication rates were equal in both groups.

The present series achieved 91% and 98% total occlusion rates in immediate and late angiographic follow-up, respectively. Only 1 embolization session was necessary in 86% of the fistulas. Nine

DAVFs with DLVD were treated, with total occlusion in all cases. Considering only sinus wall fistulas, angiographic occlusion was reached in 88% immediately and 97% at the 6-month control.

Two complications, namely alopecia and skin necrosis, resulted from the radiation dose and inadvertent occlusion of the branches supplying the scalp. Facial palsies were related to NALEA penetration in the petrous branch of the MMA during the treatment of DAVFs involving the torcula. In both cases, the balloon was placed inside the OCC while the MMA was embolized using a standard microcatheter. No case of inadvertent reflux in the feeder when the DLB catheter was used occurred. One death was observed in follow-up and was not related to the treatment. Most patients improved.

The use of transosseous branches of the OCC has been reported as poorly suitable for Onyx injection because possible major resistance through these branches limits the embolic agent penetration toward the fistulous point.^{6,13} It seems that the use of the balloons changes this paradigm. Although the MMA remained the feeder of choice in the present series, 35 occipital arteries were embolized, 33 of them with a DLB catheter.

Although the use of transarterial DLB catheters has overcome the reflux issue, unintentional NALEA penetration into the sinus must be managed and avoided. The transvenous balloon can minimize leakage of NALEA into the venous sinus.^{12,13,18} Based on its pathologic origin, multiple abnormal arteriovenous connections are present in the dural sinus wall, not inside the sinus itself. Therefore, occlusion of the connections in the sinus wall seems to be more reasonable than occlusion of the entire lumen, especially when the sinus is used for normal cerebral drainage.^{5,10}

In some cases of dural sinus wall fistulas, the use of TVB is impossible or unnecessary, including isolated sinus, venous sinus thrombosis causing partial occlusion, severe stenosis (>80%), and a very large sinus. The dedicated balloon has a maximum diameter of 10 mm. Although it is possible to use multiple balloons, we decided to not use this technique.

Vollherbst et al¹³ reported a retrospective series of 22 patients with DAVFs treated by a TAA assisted by a TVB; most DAVFs were located at the transverse and/or sigmoid sinus. The affected sinus could be preserved in all patients except 1. The overall complete occlusion rate was 86.4%. In our series, we used both transarterial and transvenous balloons simultaneously to treat 21 DAVFs, with late complete occlusion in all cases. No sinus was inadvertently occluded when the TVB was used. No ischemic or hemorrhagic lesions were observed secondary to transitory balloon occlusion of the sinus.

A major controversy is whether there is a reason for preserving a dural sinus that is nonfunctional. In our series, 6 of 18 nonfunctioning sinuses that were preserved were found to be functioning at the 6-month control angiography. The sinus may be nonfunctioning because of a hemodynamic competition, instead of an anatomic disruption, a true occlusion. Therefore, we believe that the re-establishment of the circulation inside a previously nonfunctioning sinus should be a treatment goal.

In the present series, double arterial simultaneous injection through the MMA and OCC was performed in 13 cases. The reasoning behind this technique is based on a balancing of the pressures.¹⁹ When the balloon is inflated in the OCC or in both the OCC and the MMA, it immediately decreases the pressure inside

the sinus; therefore, the resistance to NALEA flow becomes lower. The balloon inside the sinus can be inflated or deflated according to the dynamics of the injection.

The use of balloons in endovascular treatment of DAVFs is a very promising strategy because it plays an important role in the hemodynamic balance across the fistula, optimizing the embolic agent flow toward the shunting point. Caution must be used regarding the volume of inflation in both balloons.^{12,13}

CONCLUSIONS

Transarterial balloon-assisted treatment of dural arteriovenous fistulas with or without transvenous balloon protection was shown to be safe and very effective. Long-term follow-up and comparative studies are required to provide stronger conclusions regarding the superiority of this technique.

ACKNOWLEDGMENTS

We gratefully acknowledge Lara Laghetto from Visualmedics for preparing the illustration.

REFERENCES

1. Ertl L, Brückmann H, Kunz M, et al. **Endovascular therapy of low- and intermediate-grade intracranial lateral dural arteriovenous fistulas: a detailed analysis of primary success rates, complication rates, and long-term follow-up of different technical approaches.** *J Neurosurg* 2017;126:360–67 CrossRef Medline
2. Abud TG, Nguyen A, Saint-Maurice JP, et al. **The use of Onyx in different types of intracranial dural arteriovenous fistula.** *AJNR Am J Neuroradiol* 2011;32:2185–91 CrossRef Medline
3. Lv X, Jiang C, Li Y, et al. **The limitations and risks of transarterial Onyx injections in the treatment of grade I and II DAVFs.** *Eur J Radiol* 2011;80:e385–88 CrossRef Medline
4. Cognard C, Gobin YP, Pierot L, et al. **Cerebral dural arteriovenous fistulas: clinical and angiographic correlation with a revised classification of venous drainage.** *Radiology* 1995;194:671–80 CrossRef Medline
5. Jittapiromsak P, Ikka L, Benachour N, et al. **Transvenous balloon-assisted transarterial Onyx embolization of transverse-sigmoid dural arteriovenous malformation.** *Neuroradiology* 2013;55:345–50 CrossRef Medline
6. Clarençon F, Di Maria F, Gabrieli J, et al. **Double-lumen balloon for Onyx embolization via extracranial arteries in transverse sigmoid dural arteriovenous fistulas: initial experience.** *Acta Neurochir (Wien)* 2016;158:1917–23 CrossRef Medline
7. Chiu AHY, Grace A, Wenderoth JD. **Double-lumen arterial balloon technique for Onyx embolization of dural arteriovenous fistulas: initial experience.** *J Neurointerv Surg* 2014;6:400–03 CrossRef Medline
8. Dabus G, Linfante I, Galdámez MM. **Endovascular treatment of dural arteriovenous fistulas using dual lumen balloon microcatheter: technical aspects and results.** *Clin Neurol Neurosurg* 2014;117:22–27 CrossRef Medline
9. Deng JP, Zhang T, Li J, et al. **Treatment of dural arteriovenous fistula by balloon-assisted transarterial embolization with Onyx.** *Clin Neurol Neurosurg* 2013;115:1992–97 CrossRef Medline
10. Kim JW, Kim BM, Park KY, et al. **Onyx embolization for isolated type dural arteriovenous fistula using a dual-lumen balloon catheter.** *Neurosurgery* 2016;78:627–36 CrossRef Medline
11. Paramasivam S, Nimi Y, Fifi J, et al. **Onyx embolization using dual-lumen balloon catheter: initial experience and technical note.** *J Neuroradiol* 2013;40:292–302 CrossRef Medline
12. Piechowiak E, Zibold F, Dobrocky T, et al. **Endovascular treatment of dural arteriovenous fistulas of the transverse and sigmoid**

- sinuses using transarterial balloon-assisted embolization combined with transvenous balloon protection of the venous sinus. *AJNR Am J Neuroradiol* 2017;38:1984–89 CrossRef Medline
13. Vollherbst DF, Ulfert C, Neuberger U, et al. **Endovascular treatment of dural arteriovenous fistulas using transarterial liquid embolization in combination with transvenous balloon-assisted protection of the venous sinus.** *AJNR Am J Neuroradiol* 2018;39:1296–302 CrossRef Medline
 14. Rezende MT, Piotin M, Mounayer C, et al. **Dural arteriovenous fistula of the lesser sphenoid wing region treated with Onyx: technical note.** *Neuroradiology* 2006;48:130–34 CrossRef Medline
 15. Cognard C, Januel AC, Silva NA Jr, et al. **Endovascular treatment of intracranial dural arteriovenous fistulas with cortical venous drainage: new management using Onyx.** *AJNR Am J Neuroradiol* 2008;29:235–41 CrossRef Medline
 16. Chapot R, Stracke P, Velasco A, et al. **The pressure cooker technique for the treatment of brain AVMs.** *J Neuroradiol* 2014;41:87–91 CrossRef Medline
 17. Kim ST, Jeong HW, Seo J. **Onyx embolization of dural arteriovenous fistula, using Scepter C balloon catheter: a case report.** *Neurointervention* 2013;8:110–14 CrossRef Medline
 18. Guo F, Zhang Y, Liang S, et al. **The procedure-related complications of transarterial Onyx embolization of dural arteriovenous fistula using transvenous balloon protection.** *World Neurosurg* 2018;116:e203–10 CrossRef Medline
 19. Abud DG, Riva R, Nakiri GS, et al. **Treatment of brain arteriovenous malformations by double arterial catheterization with simultaneous injection of Onyx: retrospective series of 17 patients.** *AJNR Am J Neuroradiol* 2011;32:152–58 CrossRef Medline

Computational Fluid Dynamics Using a Porous Media Setting Predicts Outcome after Flow-Diverter Treatment

M. Beppu, M. Tsuji, F. Ishida, M. Shirakawa, H. Suzuki, and S. Yoshimura



ABSTRACT

BACKGROUND AND PURPOSE: Knowledge about predictors of the outcome of flow-diverter treatment is limited. The aim of this study was to predict the angiographic occlusion status after flow-diverter treatment with computational fluid dynamics using porous media modeling for decision-making in the treatment of large wide-neck aneurysms.

MATERIALS AND METHODS: A total of 27 patients treated with flow-diverter stents were retrospectively analyzed through computational fluid dynamics using pretreatment patient-specific 3D rotational angiography. These patients were classified into no-filling and contrast-filling groups based on the O'Kelly-Marotta scale. The patient characteristics, morphologic variables, and hemodynamic parameters were evaluated for understanding the outcomes of the flow-diverter treatment.

RESULTS: The patient characteristics and morphologic variables were similar between the 2 groups. Flow velocity, wall shear stress, shear rate, modified aneurysmal inflow rate coefficient, and residual flow volume were significantly lower in the no-filling group. A novel parameter, called the normalized residual flow volume, was developed and defined as the residual flow volume normalized by the dome volume. The receiver operating characteristic curve analyses demonstrated that the normalized residual flow volume with an average flow velocity of ≥ 8.0 cm/s in the aneurysmal dome was the most effective in predicting the flow-diverter treatment outcomes.

CONCLUSIONS: It was established in this study that the hemodynamic parameters could predict the angiographic occlusion status after flow-diverter treatment.

ABBREVIATIONS: AIRC = aneurysmal inflow rate coefficient; CF = contrast-filling; CFD = computational fluid dynamics; FD = flow diverter; FV = flow velocity; mAIRC = modified aneurysmal inflow rate coefficient; NF = no-filling; nRFV = normalized residual flow volume; RFV = residual flow volume; SR = shear rate; WSS = wall shear stress

Recanalization and retreatment are frequent even after using stent-assisted coil embolization for large wide-neck internal carotid artery aneurysms. The safety and efficacy of the flow diverter (FD) treatment^{1,2} have been recently demonstrated in many studies. In the large-scale Pipeline for Uncoilable or Failed Aneurysms study, approximately 76% of the patients had complete aneurysm occlusion on 6-month angiography and 93% had complete aneurysm occlusion on 3-year angiography after treatment.^{1,2}

In contrast, some aneurysms need additional treatment and may otherwise rupture. Delayed aneurysm rupture and intraparenchymal hemorrhages are poorly understood and usually lead to fatal complications.^{3,4} Rouchaud et al⁴ reported that 81.3% of patients with delayed ruptures died or had poor neurologic outcomes and 76.6% of the delayed ruptures occurred within 1 month posttreatment. However, predicting whether an aneurysm would be completely occluded or ruptured after the FD treatment is difficult.

In recent times, the development of computational fluid dynamics (CFD) has enabled the evaluation of hemodynamics of cerebral aneurysms. Umeda et al^{5,6} reported the hemodynamic characteristics required to predict the recurrence of coiled aneurysms with CFD using porous media modeling, which can be effective in predicting the postcoiling aneurysm occlusion status. Application of the porous media setting to an intracranial stent may also aid in simulating the hemodynamics after the endovascular treatment with an FD stent.⁷

Received April 11, 2020; accepted after revision July 7.

From the Department of Neurosurgery (M.B., M.S., S.Y.), Hyogo College of Medicine, Hyogo, Japan; Department of Neurosurgery (M.T., F.I.), National Hospital Organization Mie Chuo Medical Center, Tsu, Mie, Japan; and Department of Neurosurgery (H.S.), Mie University Graduate School of Medicine, Tsu, Mie, Japan.

Please address correspondence to Mikiya Beppu, PhD, Department of Neurosurgery, Hyogo College of Medicine, 1-1 Mukogawa, Nishinomiya, Hyogo 663-8501, Japan; e-mail: mikiya.beppu@gmail.com

Indicates open access to non-subscribers at www.ajnr.org

<http://dx.doi.org/10.3174/ajnr.A6766>

The aim of this study was to evaluate the effectiveness of porous media CFD for predicting the angiographic occlusion status after FD treatment.

MATERIALS AND METHODS

This retrospective study was approved by the institutional ethics committee. The patients provided written informed consent for using their data in this study.

Patient Population and Study Protocol

During 2015–2017, thirty-four unruptured internal carotid artery aneurysms were treated with FD using a Pipeline Embolization Device (Covidien) after 3D rotational angiography.

We evaluated the angiographic occlusion status during follow-up DSA at 6–12 months postprocedure. The DSA findings were classified into 2 groups using the O’Kelly-Marotta classification.⁸ We classified the O’Kelly-Marotta classes A (A1, A2, A3), B (B1, B2, B3), and C (C1, C2, C3) as the contrast-filling (CF) group and D as the no-filling (NF) group. Two independent observers who were blinded to the hemodynamic results evaluated and classified the O’Kelly-Marotta grading.

Investigators who were unaware of the occlusion status performed CFD analyses independently. We compared the morphologic variables and hemodynamic parameters of the CF group with those of the NF group. We also evaluated the effectiveness of the CFD analysis for predicting the angiographic occlusion status after FD treatment.

Morphologic Variables

As previously described, the morphologic variables were measured on stereolithographic models generated from preoperative 3D rotational angiography using ImageJ (National Institutes of Health) and CFX-post (CFX CFD19.2; ANSYS).

CFD Analysis

The patient-specific geometries were generated from the DICOM datasets of preoperative 3D rotational angiography that were obtained using Artis zee dBA Twin (Siemens). The surface reconstruction of the computational model was obtained by segmenting the lumen boundary from 3D rotational angiography images using an analytic software (Mimics 16.0; Materialise). The stereolithography was re-meshed to improve the surface triangle quality (3-matic 8.0; Materialise). The 3D neck part was created using a Boolean subtraction between the original geometry and aneurysm-deleted models. A 3D stent domain was obtained by a transformation, in which the 3D neck part was offset by a thickness of 0.048 mm, which corresponded to the diameter of the strut of the Pipeline. The computational hybrid meshes were generated with tetrahedral and prism elements (ICEM CFD19.2; ANSYS). The size of the tetrahedral elements was 0.1–1.2 mm for the fluid domain and 0.05 mm for 3D stent domain. Five prismatic boundary layers with a total thickness of 0.15 mm covered the surface to ensure an accurate definition of the velocity gradient. The average mesh number we used in this study was about 3.8 million. Volumetric meshes were used to ensure sufficient mesh resolution around the 3D stent domain. The effect of mesh density on 3D stent domain controls (the mesh independence study) showed that the mesh size did not remarkably affect

hemodynamic parameters evaluated in this study. A straight inlet extension was added to the inlet section to obtain a completely developed laminar flow.

For the fluid domain, the 3D incompressible laminar flow fields were obtained by solving the continuity and Navier–Stokes equations. Numeric modeling was performed using a commercially available CFD package (CFX 19.2; ANSYS). Blood was assumed to be an incompressible Newtonian fluid with a blood density of 1056 kg/m³ and a blood dynamic viscosity of 0.0035 Pa × s. The typical flow waveform of phase-contrast MR imaging was scaled to achieve the physiologic wall shear stress (WSS).^{9,10}

Traction-free boundary conditions were applied at all outlets. When there were several outlets, we set the outlets at a certain distance and height from the aneurysm to prevent uneven distribution of blood flow. The steady-state analysis was performed using the mean flow-volume rate. We used the typical flow waveform of phase-contrast MR imaging to achieve the physiologic WSS based on the Murray law. We used the blood flow rate set by the vessel diameter of the inlet. Thus, the steady flow analysis was assumed to use the mean flow-volume rate.

We conducted the 2-pattern CFD simulations, which involved the simulation of an untreated stent-free aneurysm as the preoperative status (control model) and assuming an aneurysm with a simple placement of an FD stent (FD model) (Fig 1).

FD Model

In this study, we applied the 2 numeric models in the fluid and porous domains. The flow in the fluid domain was simulated using the Navier–Stokes equation and equation of continuity as follows:

$$\nabla \cdot v = \text{div} \cdot v = 0,$$

$$\frac{\partial v}{\partial t} + (v \cdot \nabla)v = -\frac{1}{\rho} \nabla p + \frac{\mu}{\rho} \nabla^2 v + F,$$

where v is the velocity of the flow, p is the pressure, ρ is the density, μ is the viscosity of the fluid, and F is the body force.

Control model

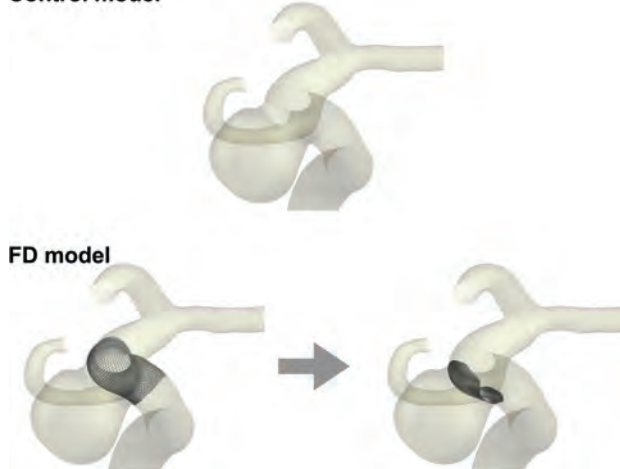


FIG 1. Images of porous media modeling for FD treatment. The control model enables the simulation of preoperative status, whereas the FD model enables the simulation of simple deployment of an FD stent.

Table 1: Comparison of patient characteristics^a

	CF Group (n = 11)	NF Group (n = 16)	P Value ^b
Patient characteristics			
Age (yr)	68.6 ± 9.9 (52–83)	61.8 ± 9.7 (40–75)	.09 ^b
Male sex	1 (9.1)	1 (6.3)	1.00 ^c
Aneurysm characteristics			
Location (cavernous)	2 (18.2)	9 (56.3)	.11 ^c
Symptomatic	2 (18.2)	6 (37.5)	.41 ^c
Treatment characteristics			
No. of Pipelines	1.0 (1)	1.1 ± 0.3 (1–2)	.42 ^b
Coil	0	0	
PTA	1 (9.1)	1 (6.3)	1.00 ^c

Note:—CF indicates contrast filling; NF, no filling; PTA, percutaneous transluminal angioplasty.

^a Data are expressed as mean ± SD (range) or number of cases (% of cases).

^b P values were estimated using the Welch t test between CF and NF groups.

^c P values were estimated using Fisher exact tests or χ^2 tests between CF and NF groups.

The flow in the stent regimes was simulated using porous media modeling that follows the Darcy law. In these flow regimes, pressure was locally balanced with resistance forces, such that

$$0 = -\nabla p - K\nu,$$

where K is a constant of porous resistance. This was assumed to be a quasilinear function of the magnitude of velocity,

$$K = \alpha v + \beta,$$

where α and β are coefficients, for which the values are determined using the Ergun equation as follows:

$$\alpha = \frac{1.75\rho(1 - \kappa)}{\kappa^3 D_p}$$

$$\beta = \frac{150\mu(1 - \kappa)^2}{\kappa^3 D_p^2},$$

where D_p is the average particle diameter.¹¹ It was set to 0.048 mm, which corresponded to the diameter of the strut of the Pipeline.

The volume coverage ratio is defined as the ratio of the volume of the stent strut to the stent volume. The variable κ ¹² denotes the porosity of the porous media stent.

$$\text{Volume Coverage Ratio (\%)} = \frac{\text{Volume of Stent Strut}}{\text{Stent Volume}} \times 100$$

$$\kappa(\text{Stent}) = 1 - \frac{\text{Volume Coverage Ratio}}{100}.$$

The metal coverage ratio is defined as the ratio of the area of the stent strut to the stent area. The relationship between the volume coverage ratio and metal coverage ratio is defined using the following formula:

$$\text{Volume Coverage Ratio} = \frac{\pi}{6} \times \text{Metal Coverage Ratio}.$$

The metal coverage ratio of the Pipeline was considered to be approximately 30%. Thus, we estimated the volume coverage ratio as 15%. In an aneurysm treated by overlapping 2 FDs, the

volume coverage ratio was assumed to be 30% for aneurysmal flow reduction. To simulate the hemodynamics in an occlusion status, we calculated hemodynamic parameters under steady-state conditions. The aneurysmal inflow rate coefficient (AIRC) was used as a predictor of recanalization after coil embolization in basilar tip aneurysms.¹³ The original AIRC is the proportion of the aneurysmal inflow rate to the basilar artery flow rate. We modified this parameter for internal carotid artery aneurysms, and the modified AIRC (mAIRC) denoted the proportion of the aneurysmal inflow

rate to the proximal parent artery flow rate.

The residual flow volume (RFV) was calculated to predict the postcoiling angiographic results in unruptured cerebral aneurysms.^{5,6} The RFV was the volume of fluid domain in the aneurysmal dome and was defined as the volume with more than the following mean flow velocity (FV): Tested thresholds included 4, 6, 8, 10, 12, 14, 16, 18, and 20 cm/s. Because RFV was affected by the volume of aneurysmal dome, we developed a novel parameter, the normalized residual flow volume (nRFV), which is defined as RFV normalized by the dome volume. The nRFV α denoted nRFV with an average FV of over α cm/s. We calculated the mAIRC in the control model, RFV in the FD model, and FV, WSS, and shear rate (SR) in both models.

Statistical Analysis

All values were expressed as mean ± SD. Statistical analyses were performed using the software environment R (Version 3.3.3; <http://www.r-project.org/>). We compared the variables between the CF and NF groups using the Welch t test. P values < .05 were considered statistically significant, while the area under the receiver operating characteristic curve was used to determine the diagnostic accuracy of predicting intra-aneurysmal thrombosis.

RESULTS

Among the 34 patients, 7 were excluded because of the difficulty in reconstructing the vascular geometry from 3D rotational angiography. Therefore, 27 patients with 27 unruptured aneurysms, which were treated endovascularly with an FD stent, fulfilled the criteria and constituted the study population. The patients' characteristics, aneurysm characteristics, and treatment characteristics in the 2 groups are summarized in Table 1.

Differences between the NF and CF Groups on Univariate Analyses

Patient Characteristics and Aneurysmal Morphologic Variables. No significant differences were observed in terms of patient characteristics and aneurysmal morphologic variables between the NF and CF groups (Tables 1 and 2).

Aneurysmal Hemodynamic Factors. Among the hemodynamic parameters in the control CFD, FV (0.16 m/s versus 0.28 m/s;

Table 2: Comparison of morphologic variables^a

Morphologic Variables	CF Group (n = 11)	NF Group (n = 16)	P Value ^b
Aneurysm depth (mm)	6.72 ± 2.26 (3.52–11.04)	6.33 ± 2.28 (3.45–11.87)	.67
Projection length (mm)	6.79 ± 2.29 (3.60–11.25)	6.84 ± 2.31 (3.50–11.96)	.96
Maximum size (mm)	12.67 ± 4.60 (9.41–25.49)	12.98 ± 4.97 (7.74–23.27)	.87
Neck width (mm)	11.72 ± 4.07 (9.14–23.32)	11.56 ± 4.84 (6.14–22.61)	.93
Parent artery diameter (mm)	5.13 ± 0.50 (4.14–5.89)	5.06 ± 0.61 (4.02–6.56)	.74
Aspect ratio	0.59 ± 0.16 (0.37–0.91)	0.61 ± 0.27 (0.31–1.11)	.79
Projection ratio	0.59 ± 0.16 (0.38–0.91)	0.65 ± 0.25 (0.33–1.12)	.50
Size ratio	2.51 ± 1.00 (1.67–5.17)	2.59 ± 1.02 (1.52–4.92)	.83
Neck area (cm ²)	0.99 ± 0.76 (0.56–3.21)	0.92 ± 0.69 (0.27–2.51)	.80
Dome area (cm ²)	2.57 ± 1.84 (1.05–7.47)	2.29 ± 1.46 (0.90–5.11)	.68
Dome volume (cm ³)	0.58 ± 0.68 (0.13–2.51)	0.46 ± 0.43 (0.10–1.35)	.61
VOR (mm)	5.13 ± 2.36 (2.32–9.38)	4.96 ± 2.65 (2.04–11.00)	.86

Note.—VOR indicates volume-to-osmium area ratio.

^aData are expressed as mean ± SD (range).

^bP values were estimated using the Welch t test between CF and NF groups.

Table 3: Comparison of hemodynamic parameters^a

Hemodynamic Parameters	CF Group (n = 11)	NF Group (n = 16)	P Value ^b
Control model			
FV _{aneurysm} (m/s)	0.27 ± 0.08 (0.12–0.43)	0.16 ± 0.08 (0.03–0.31)	.003
WSS (Pa)	4.66 ± 1.89 (1.27–7.89)	2.92 ± 1.87 (0.40–7.16)	.03
SR (× 10 ² /s)	12.83 ± 5.2 (2.78–21.68)	8.12 ± 5.10 (1.13–19.22)	.03
mAIRC	0.29 ± 0.19 (0.11–0.70)	0.14 ± 0.09 (0.02–0.34)	.04
FD model			
FV _{aneurysm} (m/s)	0.16 ± 0.03 (0.10–0.23)	0.10 ± 0.05 (0.01–0.20)	.002
WSS (Pa)	1.00 ± 0.31 (0.52–1.59)	0.67 ± 0.45 (0.01–1.39)	.03
SR (1/s)	10.55 ± 3.1 (5.73–16.60)	7.22 ± 4.74 (0.14–14.70)	.03

Note.—FV_{aneurysm} indicates average flow velocity in the aneurysmal dome.

^aData are expressed as mean ± SD (range).

^bP values were estimated using the Welch t test between CF and NF groups.

Table 4: Comparison of RFV and nRFV^a

Parameters	CF Group (n = 11)	NF Group (n = 16)	P Value ^b
RFV ₄ (mm ³)	553.4 ± 616.5 (128.4–2264.0)	358.9 ± 358.5 (0–1307.0)	.42
RFV ₆ (mm ³)	526.3 ± 552.9 (123.5–2036.0)	331.8 ± 338.0 (0–1230.0)	.31
RFV ₈ (mm ³)	495.8 ± 486.9 (118.6–1800.0)	262.5 ± 290.1 (0–1070.0)	.18
RFV ₁₀ (mm ³)	454.9 ± 406.1 (111.0–1519.0)	210.8 ± 259.9 (0–913.2)	.10
RFV ₁₂ (mm ³)	399.5 ± 304.1 (103.6–1174.0)	175.2 ± 229.6 (0–753.6)	.05
RFV ₁₄ (mm ³)	329.7 ± 201.5 (93.9–833.0)	140.1 ± 196.3 (0–586.2)	.02
RFV ₁₆ (mm ³)	250.6 ± 119.5 (82.7–463.3)	110.2 ± 159.8 (0–526.4)	.02
RFV ₁₈ (mm ³)	181.5 ± 99.2 (67.7–406.4)	84.4 ± 124.6 (0–432.3)	.03
RFV ₂₀ (mm ³)	142.9 ± 106.7 (27.7–382.3)	58.3 ± 85.8 (0–292.0)	.04
nRFV ₄	0.97 ± 0.02 (0.90–0.99)	0.84 ± 0.27 (0–0.99)	.07
nRFV ₆	0.95 ± 0.05 (0.81–0.98)	0.77 ± 0.29 (0–0.97)	.02
nRFV ₈	0.92 ± 0.07 (0.72–0.97)	0.64 ± 0.33 (0–0.96)	.004
nRFV ₁₀	0.88 ± 0.10 (0.61–0.96)	0.54 ± 0.37 (0–0.95)	.002
nRFV ₁₂	0.82 ± 0.14 (0.47–0.94)	0.46 ± 0.37 (0–0.93)	.001
nRFV ₁₄	0.74 ± 0.20 (0.33–0.92)	0.37 ± 0.34 (0–0.90)	.001
nRFV ₁₆	0.64 ± 0.26 (0.19–0.90)	0.29 ± 0.31 (0–0.85)	.004
nRFV ₁₈	0.53 ± 0.30 (0.07–0.87)	0.24 ± 0.28 (0–0.79)	.02
nRFV ₂₀	0.43 ± 0.31 (0.03–0.82)	0.17 ± 0.23 (0–0.71)	.03

Note.—RFV₄, RFV₆, RFV₈, RFV₁₀, RFV₁₂, RFV₁₄, RFV₁₆, RFV₁₈, and RFV₂₀ indicate intra-aneurysmal RFV with an average flow velocity of >4, 6, 8, 10, 12, 14, 16, 18, and 20 cm/s, respectively; and nRFV₄, nRFV₆, nRFV₈, nRFV₁₀, nRFV₁₂, nRFV₁₄, nRFV₁₆, nRFV₁₈, and nRFV₂₀ indicate intra-aneurysmal nRFV with an average flow velocity of >4, 6, 8, 10, 12, 14, 16, 18, and 20 cm/s, respectively.

^aData are expressed as mean ± SD (range).

^bP values were estimated using the Welch t test between CF and NF groups.

P = .003), WSS (2.92 Pa versus 4.66 Pa; *P* = .03), SR (8.12 × 10² 1/s versus 12.83 × 10² 1/s; *P* = .03), and the mAIRC (0.14 versus 0.29; *P* = .04) were significantly lower in the NF group (Table 3).

The porous media CFD showed that FV (0.10 m/s versus 0.16 m/s; *P* = .002), WSS (0.67 Pa versus 1.00 Pa; *P* = .03), SR (7.22 × 10² 1/s versus 10.55 × 10² 1/s; *P* = .03), RFV₁₄ (140.1 mm³ versus 329.7 mm³; *P* = .02), RFV₁₆ (110.2 mm³ versus 250.6 mm³; *P* = .02), RFV₁₈ (84.4 mm³ versus 181.5 mm³; *P* = .03), and RFV₂₀ (58.3 mm³ versus 142.9 mm³; *P* = .04) were significantly lower in the NF group than in the CF group (Tables 3 and 4). Similar findings were observed for nRFV₆ (0.77 versus 0.95; *P* = .02), nRFV₈ (0.64 versus 0.92; *P* = .004), nRFV₁₀ (0.54 versus 0.88; *P* = .002), nRFV₁₂ (0.46 versus 0.82; *P* = .001), nRFV₁₄ (0.37 versus 0.74; *P* = .001), nRFV₁₆ (0.29 versus 0.64; *P* = .004), nRFV₁₈ (0.24 versus 0.53; *P* = .02), and nRFV₂₀ (0.17 versus 0.43; *P* = .03) (Table 4).

Receiver Operating Characteristic Curve Analyses of Possible Determinants for Intra-Aneurysmal Thrombosis after FD Treatment

Among the parameters that demonstrated significant differences between the CF and NF groups on univariate analyses, nRFV₈ demonstrated the highest area under the receiver operating

Table 5: ROC curve analysis for hemodynamic parameters that had significant differences between the CF and NF groups on univariate analyses to predict intra-aneurysmal thrombosis after FD treatment

	AUC	95% CI	Sensitivity	Specificity	Cutoff Value
Control model					
FV _{aneurysm}	0.82	0.66–0.98	0.81	0.73	0.24 m/s
WSS	0.77	0.58–0.95	0.75	0.73	3.76 Pa
SR	0.76	0.56–0.95	0.75	0.73	1053.0 1/s
mAIRC	0.77	0.59–0.95	0.50	1.00	0.10
FD model					
FV _{aneurysm}	0.82	0.66–0.98	0.75	0.82	0.14 m/s
WSS	0.71	0.51–0.91	0.44	1.00	0.42 Pa
SR	0.71	0.51–0.91	0.44	1.00	449.0 1/s

Note:—AUC indicates area under the ROC curve; ROC, receiver operating characteristic.

Table 6: ROC curve analysis for RFV and nRFV that had significant differences between the CF and NF groups on univariate analyses to predict intra-aneurysmal thrombosis after FD treatment

	AUC	95% CI	Sensitivity	Specificity	Cutoff Value
RFV ₁₄	0.81	0.64–0.99	0.81	0.82	141.0 mm ³
RFV ₁₆	0.81	0.64–0.99	0.75	0.91	100.9 mm ³
RFV ₁₈	0.76	0.57–0.95	0.56	1.00	23.8 mm ³
RFV ₂₀	0.79	0.62–0.96	0.56	1.00	15.7 mm ³
nRFV ₆	0.84	0.69–0.99	0.75	0.82	0.95
nRFV ₈	0.85	0.71–1.00	0.88	0.73	0.93
nRFV ₁₀	0.83	0.67–0.99	0.81	0.73	0.86
nRFV ₁₂	0.82	0.65–0.98	0.81	0.82	0.76
nRFV ₁₄	0.82	0.66–0.99	0.81	0.82	0.66
nRFV ₁₆	0.82	0.65–0.98	0.81	0.82	0.58
nRFV ₁₈	0.79	0.62–0.96	0.63	0.82	0.19
nRFV ₂₀	0.78	0.61–0.96	0.50	1.00	0.03

Note:—RFV₁₄, RFV₁₆, RFV₁₈, and RFV₂₀ indicate intra-aneurysmal RFV with an average flow velocity of >14, 16, 18, 20 cm/s, respectively; and nRFV₆, nRFV₈, nRFV₁₀, nRFV₁₂, nRFV₁₄, nRFV₁₆, nRFV₁₈, and nRFV₂₀ indicate intra-aneurysmal nRFV with an average flow velocity of >6, 8, 10, 12, 14, 16, 18, and 20 cm/s, respectively.

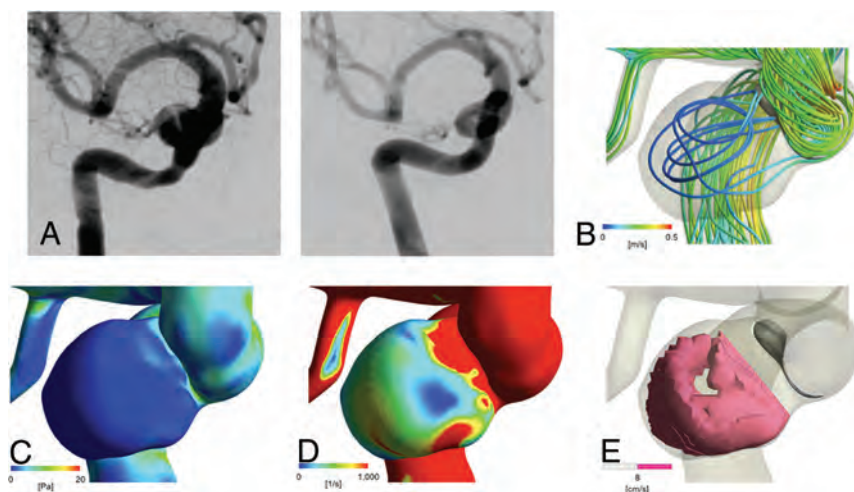


FIG 2. Representative no-filling case. A 58-year-old woman with an asymptomatic aneurysm. A, Digital subtraction angiography shows a large wide-neck aneurysm located at the left cavernous portion of the internal carotid artery (left), which completely disappeared 6 months after the FD treatment (right). B, Streamline of FV in the FD model. The mean FV at the dome is 0.06 m/s. C, Contour line of wall shear stress in the FD model (mean value at the dome is 0.37 Pa). D, Contour line of the shear rate in the FD model (mean value at the dome is 3.96×10^2 1/s). E, Intra-aneurysmal nRFV of 0.38 with an average flow velocity of >8 cm/s.

characteristic curve value of 0.85 (95% CI, 0.71–1.00). The cutoff value was 0.93 with a sensitivity of 0.88 and a specificity of 0.73 (Tables 5 and 6).

Representative Cases

Case 1: NF. A 58-year-old woman had a left cavernous portion aneurysm (Fig 2). The maximum size and neck width were 10.1 and 7.7 mm, respectively. In the control model, FV, WSS, SR, and the mAIRC were 0.08 m/s, 1.13 Pa, 3.20×10^2 1/s, and 0.02, respectively. In the FD model, FV, WSS, and SR were 0.06 m/s, 0.37 Pa, and 3.96×10^2 1/s, respectively. RFV₁₆ and nRFV₈ were 11.1 mm³ and 0.38, respectively. We treated this aneurysm with FD using a Pipeline Embolization Device (4.5 × 20 mm). DSA at 6 months after treatment showed complete disappearance of the aneurysm.

Case 2: CF. A 73-year-old woman had a left paracavernous portion aneurysm (Fig 3). The maximum size and the neck width were 12.4 and 11.7 mm, respectively. In the control model, the values of FV, WSS, SR, and the mAIRC were 0.43 m/s, 7.89 Pa, 21.68×10^2 1/s, and 0.54, respectively. In the FD model, FV, WSS, and SR were 0.22 m/s, 1.25 Pa, and 12.8×10^2 1/s, respectively. RFV₁₆ and nRFV₈ were 429.0 mm³ and 0.96, respectively. We treated this aneurysm with a FD using a Pipeline Embolization Device (4.75 × 25 mm). The DSA at 6 months after treatment showed an incomplete disappearance of the aneurysm.

DISCUSSION

In this study, we demonstrated that the hemodynamic parameters using both control CFD and porous media CFD could predict the angiographic occlusion status at 6 months after the FD treatment. In addition, nRFV₈ was the strongest predictor. These results indicated that preoperative CFD could be effective in decision-making during the treatment of large wide-neck internal carotid artery aneurysms.

A previous CFD study with high-fidelity virtual stent placement showed that posttreatment aneurysmal flow reduction, including the average FV, WSS, inflow rate, and turnover time,

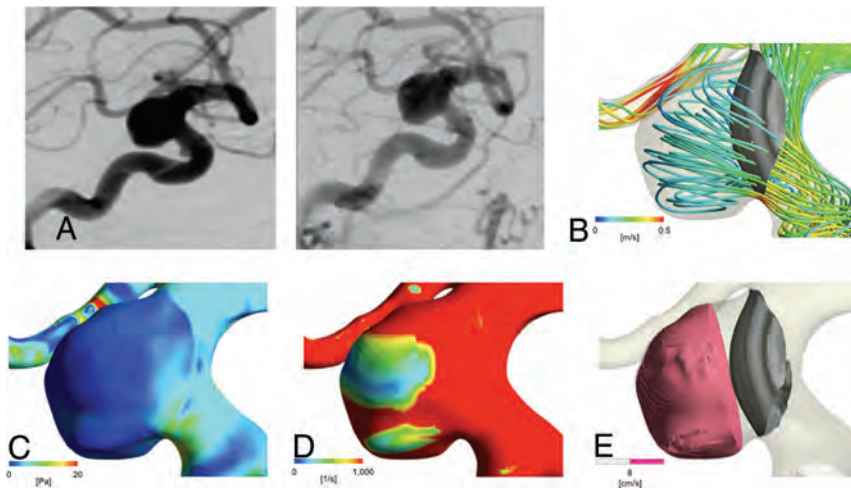


FIG 3. Representative contrast-filling case. A 73-year-old woman with an asymptomatic aneurysm. A, Digital subtraction angiography shows a large wide-neck aneurysm located at the left paraclinoid portion of internal carotid artery (*left*), which does not disappear at 6 months after the FD treatment (*right*). B, Streamline of FV in the FD model. The mean FV at the dome is 0.22 m/s. C, Contour line of wall shear stress in the FD model (mean value in the dome is 1.25 Pa). D, Contour line of the shear rate in the FD model (mean value in the dome is 12.8×10^2 1/s). E, Intra-aneurysmal nRFV of 0.96 with an average flow velocity of >8 cm/s.

could be correlated with aneurysmal occlusion outcomes.¹⁴ In the *in vivo* studies, local FV and SR were significantly smaller and the mean transit time was higher in occluded aneurysms than in the rest of the cases.¹⁵ These results suggested that hemodynamic reduction in terms of FV, SR, and WSS is the most important mechanism to induce intra-aneurysmal thrombosis. Corbett et al¹⁶ reported that flow-induced thrombosis occurred under an SR threshold of 54 seconds⁻¹ or a specific WSS threshold of 0.41 Pa. These *in vivo* and *in vitro* results support the findings of the present study.

We also demonstrated that the NF group had significantly lower mAIRC and RFV values. These results were similar to those reported by Sugiyama et al¹³ and Umeda et al.^{5,6} Sugiyama et al stated that the AIRC was an independent and significant predictor for recanalization after coil embolization. Umeda et al reported that RFV was an effective parameter in predicting the recurrence of coiled aneurysms. It was suggested that mAIRC and RFV could be good predictors for the angiographic occlusion status after the FD treatment, as in the case of coil embolization.^{5,6,13} In this study, the receiver operating characteristic curve analyses demonstrated that nRFV_{8,0} had the strongest predictive capability among all studied parameters.

The clinical implication of the present study is the ability to predict whether the FD treatment is effective for every individual case. Mut et al¹⁷ demonstrated that the aneurysms in the fast occlusion group demonstrated a lower mean FV, inflow rate, and SR. However, these values were determined under posttreatment hemodynamic conditions. Therefore, it remains unknown whether their findings could be used for treatment decision-making. In contrast, the FV at an aneurysm dome using a porous media setting can simulate the outcomes of selected reconstructive treatments, such as direct operations with respect to trapping of an aneurysm and parent artery with high-flow bypass and FD treatment with/without coils.

To treat an aneurysm with insufficient FV reduction by endovascular treatment, we considered the following 2 treatments to increase the reduction of FV. The first approach involves FD stent placement with coils. In a previous study, it was demonstrated that the FD treatment with coils further reduced FV and WSS and increased the low wall shear area.¹⁸ Double-porous media CFD can be used to predict the post-treatment angiographic aneurysmal occlusion status preoperatively.¹⁹ The other approach involves overlapping FD stents or performing compacted FD stent placement. Some reports showed that overlapped or compacted FD stents reduced the values of hemodynamic parameters, including the mean intra-aneurysmal FV, WSS, and inflow rate.²⁰ Therefore, FD stent placement with coils, overlapped FD stent placement, and compacted FD stent placement can be considered as treatment options for

aneurysms with insufficient FV reduction.

The present study has several limitations. First, this study is simple and retrospective. A prospective larger cohort study that includes all types of aneurysms is required to establish the effectiveness of hemodynamic simulation for predicting the outcome of the FD treatment. Second, all the patients who participated in the study were Japanese. Some studies indicated that there was a racial difference in platelet function.²¹ They suggested that ethnicity might be an important factor in determining the outcome of the FD treatment. Third, other factors could influence the outcome of the FD treatment, including body forces such as blood viscosity and blood pressure, anti-platelet effect, aneurysm location, branching artery, and incomplete FD expansion. It is difficult for this model to accurately reflect the stent-placement conditions that can influence the hemodynamic factors, but this model makes a distribution of stent uniform.

In addition, we cannot overlook the limitations of the CFD studies. The vessel walls were assumed to be rigid, and blood was modeled as a Newtonian fluid in this study. Newtonian fluids may overestimate WSS and SR at the aneurysmal dome.²² Therefore, our quantitative CFD results might have some bias. Further studies are thus necessary to validate the results under different simulations.

CONCLUSIONS

All studied hemodynamic factors were significantly lower in the NF group, and nRFV₈ was observed to be the strongest predictor of aneurysmal occlusion status after the FD treatment. It was shown that CFD could be useful in pretreatment planning, thereby contributing to more reliable and effective FD treatments for cerebral aneurysms.

ACKNOWLEDGMENTS

We thank Editage (www.editage.jp) for English language review of the manuscript.

Disclosures: Manabu Shirakawa—UNRELATED: Payment for Lectures Including Service on Speakers Bureaus: Stryker, Comments: lecture fee. Shinichi Yoshimura—RELATED: Consulting Fee or Honorarium: Medtronic, Comments: lecture fee; UNRELATED: Consultancy: Kaneka Medix; Payment for Lectures Including Service on Speakers Bureaus: Boehringer Ingelheim, Daiichi Sankyo, Bayer Yakuhin, Ltd. Bristol-Meyers Squibb, Stryker, Sanofi, Otsuka Pharmaceutical, Johnson & Johnson, MicroVention Terumo, Biomedical Solutions.

REFERENCES

1. Beckske T, Potts MB, Shapiro M, et al. **Pipeline for uncoilable or failed aneurysms: 3-year follow-up results.** *J Neurosurg* 2017;127:81–88 CrossRef Medline
2. Beckske T, Brinjikji W, Potts MB, et al. **Long-term clinical and angiographic outcomes following Pipeline embolization device treatment of complex internal carotid artery aneurysms: five-year results of the Pipeline for Uncoilable or Failed Aneurysms Trial.** *Neurosurgery* 2017;80:40–48 CrossRef Medline
3. Cruz JP, Chow M, O'Kelly C, et al. **Delayed ipsilateral parenchymal hemorrhage following flow diversion for the treatment of anterior circulation aneurysms.** *AJNR Am J Neuroradiol* 2012;33:603–08 CrossRef Medline
4. Rouchaud A, Brinjikji W, Lanzino G, et al. **Delayed hemorrhagic complications after flow diversion for intracranial aneurysms: a literature overview.** *Neuroradiology* 2016;58:171–77 CrossRef Medline
5. Umeda Y, Ishida F, Tsuji M, et al. **Computational fluid dynamics (CFD) analysis using porous media modeling predicts angiographic occlusion status after coiling of unruptured cerebral aneurysms: preliminary study.** *Journal of Neuroendovascular Therapy* 2015;9:69–77 CrossRef
6. Umeda Y, Ishida F, Tsuji M, et al. **Computational fluid dynamics (CFD) using porous media modeling predicts recurrence after coiling of cerebral aneurysms.** *PLoS One* 2017;12:e0190222 CrossRef Medline
7. Li Y, Zhang M, Verrelli DI, et al. **Numerical simulation of aneurysmal haemodynamics with calibrated porous-medium models of flow-diverting stents.** *J Biomech* 2018;80:88–94 CrossRef Medline
8. O'Kelly CJ, Krings T, Fiorella D, et al. **A novel grading scale for the angiographic assessment of intracranial aneurysms treated using flow diverting stents.** *Interv Neuroradiol* 2010;16:133–37 CrossRef Medline
9. Murray CD. **The physiological principle 1 of minimum work applied to the angle of branching of arteries.** *J Gen Physiol* 1926;9:835–41 CrossRef Medline
10. Ford MD, Alperin N, Lee SH, et al. **Characterization of volumetric flow rate waveforms in the normal internal carotid and vertebral arteries.** *Physiol Meas* 2005;26:477–88 CrossRef Medline
11. Akgiray Ö, Saatçı AM. **A new look at filter backwash hydraulics.** *Water Science & Technology: Water Supply* 2001;1:65–72 CrossRef
12. Derdeyn CP, Chimowitz MI, Lynn MJ, et al; Stenting and Aggressive Medical Management for Preventing Recurrent Stroke in Intracranial Stenosis Trial Investigators. **Aggressive medical treatment with or without stenting in high-risk patients with intracranial artery stenosis (SAMMPRIS): the final results of a randomised trial.** *Lancet* 2014;383:333–41 CrossRef Medline
13. Sugiyama S, Niizuma K, Sato K, et al. **Blood flow into basilar tip aneurysms: a predictor for recanalization after coil embolization.** *Stroke* 2016;47:2541–47 CrossRef Medline
14. Xiang J, Damiano RJ, Lin N, et al. **High-fidelity virtual stenting: modeling of flow diverter deployment for hemodynamic characterization of complex intracranial aneurysms.** *J Neurosurg* 2015;123:832–40 CrossRef Medline
15. Chung B, Mut F, Kadirvel R, et al. **Hemodynamic analysis of fast and slow aneurysm occlusions by flow diversion in rabbits.** *J Neurointerv Surg* 2015;7:931–35 CrossRef Medline
16. Corbett SC, Ajdari A, Coskun AU, et al. **In vitro and computational thrombosis on artificial surfaces with shear stress.** *Artif Organs* 2010;34:561–69 CrossRef Medline
17. Mut F, Raschi M, Scrivano E, et al. **Association between hemodynamic conditions and occlusion times after flow diversion in cerebral aneurysms.** *J Neurointerv Surg* 2015;7:286–90 CrossRef Medline
18. Jing L, Zhong J, Liu J, et al. **Hemodynamic effect of flow diverter and coils in treatment of large and giant intracranial aneurysms.** *World Neurosurg* 2016;89:199–207 CrossRef Medline
19. Tsuji M, Kishimoto T, Tomoyuki K, et al. **Double porous media modeling in computational fluid dynamics for hemodynamics of stent-assisted coiling of intracranial aneurysms: A technical case report.** *Brain Hemorrhages* 2020;1:85–88 CrossRef
20. Damiano RJ, Tutino VM, Paliwal N, et al. **Compacting a single flow diverter versus overlapping flow diverters for intracranial aneurysms: a computational study.** *AJNR Am J Neuroradiol* 2017;38:603–10 CrossRef Medline
21. Edelstein LC, Simon LM, Montoya RT, et al. **Racial differences in human platelet PAR4 reactivity reflect expression of PCTP and miR-376c.** *Nat Med* 2013;19:1609–16 CrossRef Medline
22. Xiang J, Tremmel M, Kolega J, et al. **Newtonian viscosity model could overestimate wall shear stress in intracranial aneurysm domes and underestimate rupture risk.** *J Neurointerv Surg* 2012;4:351–57 CrossRef Medline

Efficacy of Asahi Fubuki as a Guiding Catheter for Mechanical Thrombectomy: An Institutional Case Series

L. Rinaldo, H. Cloft, and W. Brinjikji

ABSTRACT

SUMMARY: Treatment outcomes of mechanical thrombectomy for acute stroke secondary to large-vessel occlusion in which the Asahi Fubuki was used as a guide catheter were reviewed. Among 154 patients treated with mechanical thrombectomy, the Fubuki was successfully delivered to the cervical ICA in 151 cases (98.1%) and the lesion was successfully crossed in 150 cases (97.4%). Median times to lesion crossing and revascularization were 9 and 19 minutes, respectively.

ABBREVIATION: MT = mechanical thrombectomy

Mechanical thrombectomy (MT) is now an established therapy for treatment of acute ischemic stroke secondary to large-vessel occlusion.¹ Essential to timely MT performance is navigation of a guiding catheter to a location allowing delivery of interventional devices to the site of vessel occlusion, typically the cervical ICA in instances of anterior circulation occlusion. For the past few years at our institution, we have used the Fubuki catheter (Asahi Intecc) as a first-line guide catheter for MT. Herein, we report on the efficacy of the Fubuki when used for this procedure.

MATERIALS AND METHODS

Patient Selection

After institutional review board approval, we retrospectively reviewed the radiology reports of patients undergoing MT for acute ischemic stroke secondary to large-vessel occlusion at our institution between November 2015 and January 2020. Patients were included for analysis if the Fubuki was used as the initial guide catheter for the procedure. The catheter is 90 cm in length, with inner and outer diameters of 2.28 mm (0.090 inches) and 2.70 mm (0.106 inches), respectively. The Fubuki was used in 2 acute stroke cases between 2015 and 2016 and was subsequently used in most mechanical thrombectomies performed at our institution starting in February 2017. Between February 2017 and January 2020, 196 MTs were performed at our institution, and the Fubuki was selected as the guide catheter for 152 (77.6%) of

these procedures. Guide catheters used in the remaining procedures included the 6F Neuron MAX (Penumbra, $n = 22$), 8F FlowGate² (Stryker Neurovascular, $n = 17$), 6F Benchmark (Penumbra, $n = 2$), 6F Shuttle (Cook, $n = 2$), and the Mo.MA proximal balloon protection device (Medtronic, $n = 1$). The FlowGate² and Mo.Ma were preferentially selected for cases of acute stroke secondary to tandem cervical internal carotid artery and intracranial large-vessel occlusions. Two cases were performed via a radial approach, and for both of these cases, the Benchmark guide catheter was used. Otherwise guide catheters were selected according to the physician's preference and not on the basis of specific patient anatomic characteristics.

Patient and Treatment Characteristics

Collected patient demographic information included sex and age at the time of stroke. Anatomic information included laterality and the site of large-vessel occlusion, aortic arch configuration, and the presence or absence of bovine anatomy. The aortic arch configuration was categorized as type I, II, or III based on preprocedural neck CT angiography according to standard criteria.² Treatment characteristics included the method of Fubuki insertion into the femoral artery and type of revascularization device used.

Outcome measures of interest included whether the Fubuki was delivered to the cervical ICA, whether the lesion was crossed with the Fubuki as a guide catheter, whether there was herniation of the Fubuki into the aortic arch during interventional device delivery, and whether crossover to another guide catheter was necessary due to failure of the Fubuki. Whether revascularization was achieved was also noted and characterized as a TICI score of $<2b$ or $\geq 2b$ according to established criteria.³ Times to lesion

Received April 14, 2020; accepted after revision June 21.

From the Departments of Neurosurgery (L.R., W.B.), and Radiology (H.C., W.B.), Mayo Clinic, Rochester, Minnesota.

Please address correspondence to Lorenzo Rinaldo, MD, PhD, Mayo Clinic, 200 1st St SW, Rochester, MN 55902; e-mail: Rinaldo.Lorenzo@mayo.edu
<http://dx.doi.org/10.3174/ajnr.A6748>

Table 1: Patient characteristics

Characteristics	
No. of Patients	154
Age (mean) (SD) (yr)	67.6 (15.1)
Range	21–94
Sex (No.) (%)	
Female	74 (48.1)
Male	80 (51.9)
Site of large-vessel occlusion (No.) (%)	
M1	65 (42.2)
SC-ICA	29 (18.8)
M2	28 (18.2)
Tandem cervical ICA and M1	19 (12.3)
Basilar artery	7 (4.5)
P1	4 (2.6)
Cervical ICA	2 (1.3)
Laterality (No.) (%) ^a	
Right	63 (42.9)
Left	84 (57.1)
Arch configuration (No.) (%) ^b	
I	84 (62.7)
II	35 (26.1)
III	15 (11.2)
Bovine anatomy (No.) (%) ^b	
No	110 (82.1)
Yes	24 (17.9)

Note:—SC-ICA indicates supraclinoid internal carotid artery.

^a Excludes patients with a basilar occlusion.

^b Preprocedural CTA was not available for 20 patients.

crossed and revascularization in minutes from the time of femoral access were also recorded. We also recorded the incidence of significant access site complications. The incidence of self-limited groin hematomas not requiring imaging evaluation or further intervention was not recorded.

Statistical Analysis

Descriptive statistics for continuous and categorical variables are reported as means and SDs and frequency and percentage, respectively. Descriptive statistics for times to lesion crossed and revascularization are provided as median and range. Predictors of failure to deliver the Fubuki to the cervical ICA were identified using logistic regression analysis. The α level for statistical significance was set at .05. Analyses were performed using commercially available software (JMP; SAS Institute).

RESULTS

Patient Characteristics

There were 154 patients who underwent MT between November 2015 and January 2020 and met the inclusion criteria for analysis. The mean age of patients was 67.6 ± 15.1 years, and a slight majority of patients were men (51.9%). The site of large-vessel occlusion was most often the M1 segment (42.2%), followed in frequency by the internal carotid artery terminus (18.8%). Most large-vessel occlusions occurred on the patient's left side (57.1%). The frequencies of type I, II, and III aortic arch configurations were 62.7%, 26.1%, and 11.2%, respectively, and there were 24 patients with bovine anatomy. A complete summary of patient characteristics is presented in Table 1.

Table 2: Treatment characteristics and outcomes

Characteristics	
Access mode (No.) (%)	
Primary insertion	148 (96.1)
Sheath	6 (3.9)
Fubuki delivered to ICA? (No.) (%)	
Yes	151 (98.1)
No	3 (1.9)
Lesion crossed with Fubuki as guide? (No.) (%)	
Yes	150 (97.4)
No	4 (2.6)
Herniation of Fubuki into aortic arch? (No.) (%)	
Yes	1 (0.6)
No	153 (99.4)
Crossover to another guide catheter? (No.) (%)	
Yes	1 (0.6)
No	153 (99.4)
Mechanism of embolectomy (No.) (%)	
Aspiration	111 (72.1)
Stent retriever	4 (2.6)
Combined aspiration and stent retriever	34 (22.1)
Failure	5 (3.2)
\geq TICI 2b revascularization? (No.) (%)	
Yes	128 (83.1)
No	26 (16.9)
Time to lesion crossed (median) (min)	9
Range	4–102
Time to revascularization (median) (min)	17
Range	3–96
Major access site complications? (No.) (%)	
Yes	3 (1.9)
No	151 (98.1)

Treatment Outcomes

Insertion of the Fubuki directly into the femoral artery was performed in a large majority cases (96.1%). The Fubuki was delivered to the cervical ICA, and the occlusive lesion was successfully crossed with the Fubuki as the guide catheter in 98.1% and 97.4% of cases, respectively. Herniation of the Fubuki into the aortic arch was noted in a single case (0.6%), and crossover to another guide catheter was necessary in 1 case (0.6%). The mechanism of revascularization was most often aspiration (72.1%), followed by aspiration in combination with a stent retriever (22.1%). An interventional device could not be delivered to the site of occlusion in 5 cases (3.2%). TICI 2b revascularization was achieved in 83.1% of cases. Median times to lesion crossed and revascularization were 9 and 17 minutes, respectively (Table 2). For comparison, herniation of the guide catheter from the carotid artery into the aortic arch occurred in 3 of the 22 cases (13.6%) in which the 8F FlowGate² was used and 1 of 17 cases (5.9%) in which the 6F Neuron MAX was used. Procedural outcomes for the other guiding catheters were not included due to the small sample size.

There were 3 instances (1.9%) of major access site complications. One patient experienced a painful femoral pseudoaneurysm that ultimately resolved without intervention. A second patient experienced persistent bleeding from the femoral access site after the procedure, requiring surgical femoral cutdown and repair of the artery. The final patient experienced occlusion of a previously placed femoropopliteal graft, resulting in limb ischemia; this patient also required surgical femoral cutdown and arterial revascularization.

Table 3: Logistic regression identifying predictors of failure to deliver the Fubuki to the ICA

Variable	OR (95% CI)	P Value
Age (yr)	2.04 (0.66–6.36) ^a	.22
Male sex	0.46 (0.04–5.13)	.52
Left-sided occlusion	0.36 (0.03–4.15)	.42
Bovine anatomy	2.35 (0.20–27.00)	.49
Bovine and left-sided occlusion	4.54 (0.38–53.54)	.23
Type III aortic arch	18.15 (1.54–214.16)	.021 ^b

^a Unit odds ratios denoting effect on risk for every decade of age.

^b Statistically significant.

Predictors of failure to deliver the Fubuki to the cervical ICA were determined using logistic regression analysis. A type III aortic arch was the only variable significantly associated with a reduced likelihood of Fubuki delivery to the ICA (OR, 18.15; 95% CI, 1.54–214.16; $P = .021$; Table 3).

DISCUSSION

While previous studies have assessed the efficacy of specific guide catheters for the performance of MT,⁴ to our knowledge, our study is unique in that its focus was on the navigability of the Fubuki as determined by the frequency of failure to deliver the catheter to the cervical ICA. The reported rate of failure in tandem with our relatively low median time to lesion crossed of 9 minutes suggests that the Fubuki is highly efficacious at reaching the cervical ICA in a timely fashion and maintaining a stable position. On logistic regression analysis, a type III aortic arch was the only patient characteristic associated with Fubuki failure, which was unsurprising given previous studies associating complicated arch anatomy with the inability to perform MT.⁵ Nevertheless, as depicted in our representative case, the Fubuki was able to cross relatively tortuous arch anatomy while providing adequate support to complete the MT. In the future, more in-depth anatomic analyses of MT cases may allow improved

quantification of guide catheter performance and facilitate comparison among different catheters.

Limitations

Our study is limited by the single-center, retrospective methodology; thus, it is possible that our results are not completely generalizable. Similar efficacy of the Fubuki should be confirmed in multi-institutional series.

CONCLUSIONS

Our results indicate that the 6F Fubuki is highly effective when used for MT to treat acute ischemic stroke secondary to large-vessel occlusion. These results may serve as a benchmark when assessing the performance of other guide catheters used for this procedure.

REFERENCES

1. Berkhemer OA, Fransen PS, Beumer D, et al; MR CLEAN Investigators. **A randomized trial of intra-arterial treatment for acute ischemic stroke.** *N Engl J Med* 2015;372:11–20 CrossRef Medline
2. Bhatt CT. *Guide to Peripheral and Cerebrovascular Intervention.* Remedica; 2004
3. Zaidat OO, Yoo AJ, Khatri P, et al; STIR Thrombolysis in Cerebral Infarction (TICI) Task Force. **Recommendations on angiographic revascularization grading standards for acute ischemic stroke: a consensus statement.** *Stroke* 2013;44:2650–63 CrossRef Medline
4. Yi HJ, Sung JH, Lee MH, et al. **Experience of the new FlowGate² device as a balloon guide catheter for ischemic stroke intervention.** *World Neurosurg* 2019;126:736–42 CrossRef Medline
5. Knox JA, Alexander MD, McCoy DB, et al. **Impact of aortic arch anatomy on technical performance and clinical outcomes in patients with acute ischemic stroke.** *AJNR Am J Neuroradiol* 2020;41:268–73 CrossRef Medline

Percutaneous CT-Guided Core Needle Biopsies of Head and Neck Masses: Technique, Histopathologic Yield, and Safety at a Single Academic Institution

T.J. Hillen, J.C. Baker, J.R. Long, M.V. Friedman, and J.W. Jennings



ABSTRACT

BACKGROUND AND PURPOSE: CT-guided head and neck biopsies can be challenging due to the anatomy and adjacent critical structures but can often obviate the need for open biopsy. A few studies and review articles have described approaches to biopsy in the head and neck. This retrospective study evaluated technical considerations, histopathologic yield, and safety in CT-guided head and neck core needle biopsies.

MATERIALS AND METHODS: A retrospective review of head and neck biopsies performed from January 2013 through December 2019 was conducted. Clinical diagnosis and indication, patient demographics, mass location and size, biopsy needle type, technical approach, dose-length product, sedation details, complications, diagnostic histopathologic yield, and the use of iodinated contrast were recorded for each case.

RESULTS: A total of 27 CT-guided head and neck core needle biopsies were performed in 26 patients. The diagnostic sample rate was 100% (27/27). A concordant histopathologic diagnosis was obtained in 93% (25/27) of cases. There was a single complication of core needle biopsy, a small asymptomatic superficial hematoma.

CONCLUSIONS: Percutaneous CT-guided biopsy of deep masses in the head and neck is safe and effective with careful biopsy planning and has a high diagnostic yield that can obviate the need for open biopsy.

ABBREVIATION: CTCAE = Common Terminology Criteria for Adverse Events

In the United States, >60,000 new cases of head and neck cancer will be diagnosed in 2020, comprising approximately 4% of new cancer cases in men.¹ Many of these cancers that arise within the oropharynx are diagnosed by an otolaryngologist using direct visualization by laryngoscopy. Most of the superficial soft-tissue masses in the neck are biopsied either by palpation² or sonographic guidance.³⁻⁶ The masses within the deep spaces of the neck are most commonly biopsied using CT guidance. In the past, many of these deep head and neck biopsies were performed using CT guidance and fine-needle aspiration techniques.⁷⁻¹⁰ More recent articles have described the use of CT guidance and spring-loaded core biopsy needles.¹¹⁻¹⁵

Compared with other biopsies, deep head and neck masses are difficult to biopsy safely and effectively due to the critical anatomy in the region of the biopsies, including nerves, vessels, and salivary glands. Despite the critical anatomy, there are few reported serious complications in head and neck soft-tissue biopsies.¹⁶

In general, the demand for percutaneous CT-guided biopsies continues to increase due to the evolving requirements of clinical treatment and study protocols. The well-published safety, efficacy, and high histopathologic yield obviates the need for open biopsies; however, there are relatively few publications addressing CT-guided soft-tissue core biopsies of the head and neck.

The purposes of this retrospective original research are to describe and expand technical considerations, including the use of CT angiography, and to demonstrate the high histopathologic yield and safety of CT-guided head and neck soft-tissue core biopsies.

MATERIALS AND METHODS

Patient Selection and Study Enrollment

Approval from the institutional review board was granted with a waiver of informed consent for this Health Insurance Portability and Accountability Act-compliant retrospective study. Correlating

Received April 30, 2020; accepted after revision July 7.

From the Mallinckrodt Institute of Radiology (T.J.H., J.C.B., M.V.F., J.W.J.), Musculoskeletal Section, Washington University School of Medicine, St. Louis, Missouri; and Musculoskeletal Radiology (J.R.L.), Mayo Clinic Arizona, Phoenix, Arizona.

Please address correspondence to Travis J. Hillen, MD, Washington University School of Medicine, Mallinckrodt Institute of Radiology, Musculoskeletal Section, Campus Box 8131, 510 S Kingshighway Blvd, St. Louis MO 63110; e-mail: tjhillen@wustl.edu; @travisjhillen
<http://dx.doi.org/10.3174/ajnr.A6784>

data were collected for all CT-guided head and neck biopsies performed at Washington University in St. Louis from January 2013 to December 2019 included in this study. These data were acquired by searching the radiology information system for neck biopsy cases using a combination of Current Procedural Terminology codes for neck/thorax biopsy (21550), soft-tissue mass biopsy (20206), and CT guidance (77012) and using the following search terms: “neck biopsy,” “parapharyngeal space,” “masticator space,” “carotid space,” and “paraspinal.” Inclusion criteria were CT guidance, suspicion of

either benign or malignant tumor, soft-tissue mass, core needle biopsy, and follow-up available in the electronic medical record. CT-guided biopsies for infection or superficial neck lymph nodes were excluded. For each case, we collected and evaluated the following data: patient demographics, clinical diagnosis and indication, mass size and location, biopsy needle type/gauge, technical approach, number and length of each soft-tissue biopsy, CT dose-length product, sedation details, and diagnostic histopathologic yield. Procedural complications were documented according to the Common Terminology Criteria for Adverse Events (CTCAE), Version 5.0.¹⁷ Patients were clinically monitored for at least 1 hour after each procedure for evidence of acute complications such as hematoma formation or neurologic injury. A short-term follow-up phone call between 1 and 3 days following the procedure was used to document any additional short-term complications. The electronic medical records were also reviewed for evidence of delayed complications within 30 days of the biopsy.

Table 1: Biopsy needles by size and brand used for 27 biopsies

Size and Brand	No.
Biopsy needle gauge	
14-ga	14
16-ga	6
18-ga	6
20-ga	1
Needle brand	
Bard Mission	13
Achieve	9
Unknown	5
Arrow OnControl	2 ^a

^a The OnControl needle used for access in 2 cases followed by coaxial placement of a soft-tissue needle.

Biopsy Procedure

All procedures were performed by 1 of 4 board-certified fellowship-trained musculoskeletal radiologists with 12, 10, 7, and 6 years of experience. Twenty-three of the 27 procedures were

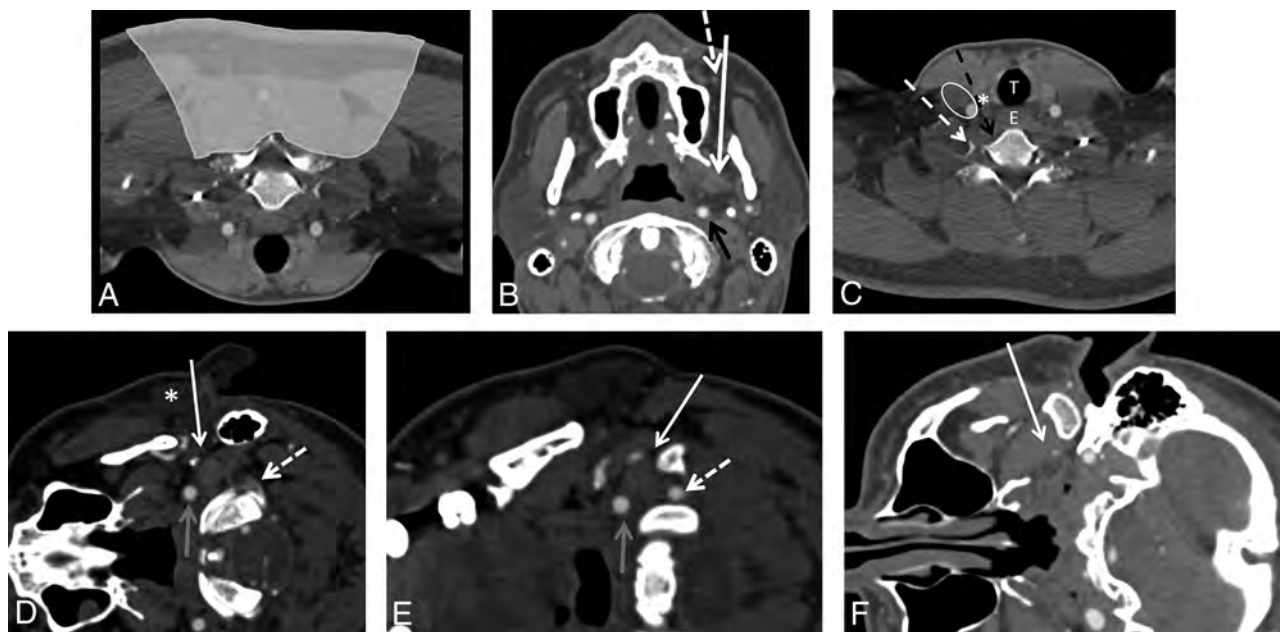


FIG 1. CT-guided neck biopsies can be performed using multiple different approaches depending on the location of the lesion. In almost all approaches, there are critical neural and vascular structures adjacent to the needle tract. A, CT angiogram of the neck flipped vertically to depict prone positioning for a posterior-approach neck biopsy. Neck biopsies in the shaded region would commonly be performed using a posterior approach. In the shaded region, there are no critical neurovascular structures. B, CT angiogram soft-tissue-windowed image of the neck with the patient in a supine position for the paramaxillary approach (white arrow). The needle course is between the maxillary sinus and the mandible adjacent to the facial artery (dashed arrow) through the buccal space. This approach can be used for lesions in the buccal, masticator, parapharyngeal, retropharyngeal, and carotid sheath spaces. The critical structures to avoid include the facial artery (dashed arrow) and the internal carotid artery (black arrow). C, CT angiogram of the neck with the patient in a supine position for anterior-approach biopsies, which can be either medial (black dashed arrow) or lateral (dashed white arrow) to the carotid and jugular vasculature (white oval). These approaches can be used for lesions in the infrahyoid neck and lower cervical vertebrae. The critical structures to avoid include the carotid artery, jugular vein, and vagus nerve (white oval); the trachea (white T); the esophagus (white E); and the thyroid gland (white asterisk). CT angiograms of the neck with the patient in a decubitus position: This positioning will be used for the retromandibular (D), submastoid (E), and subzygomatic (F) approaches denoted by white arrows. Note that the needle will sometimes pass through a portion of the parotid gland for the retromandibular approach (white asterisk). Critical structures to avoid include the carotid (gray arrows) and vertebral arteries (dashed white arrows) with the retromandibular and submastoid approaches and the retromandibular vein in the retromandibular approach because of its proximity to the facial nerve. These approaches can be used for lesions in the deep parotid, parapharyngeal, pharyngeal, and retropharyngeal spaces.

Table 2: Neck biopsy approach

Approach	No.
Anterior	7
Paramaxillary	2
Posterior	5
Retromandibular	2
Submastoid	8
Subzygomatic/sigmoid notch	3

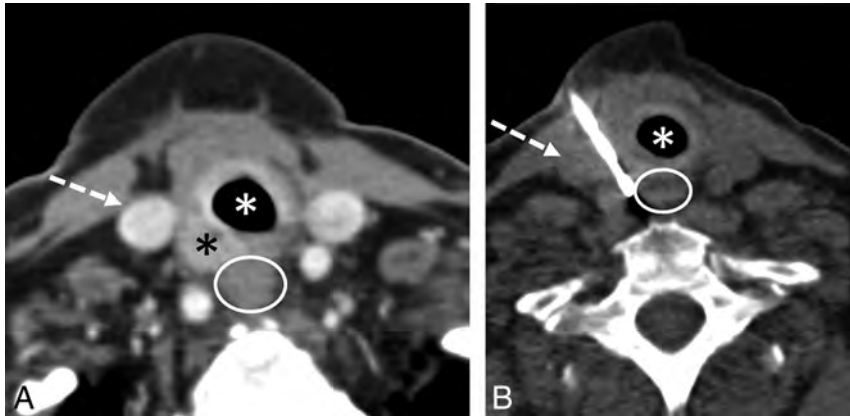


FIG 2. A 74-year-old woman with a previously excised papillary thyroid carcinoma also treated with radioactive iodine who has a new mass in the right visceral space of the neck adjacent to the thyroidectomy bed. Axial contrast-enhanced CT image (A) from a neck CT demonstrates an enhancing mass (*black asterisk*) in the right visceral space abutting the trachea (*white asterisk*), the esophagus (*white oval*), and the right internal jugular vein (*dashed white arrow*). Intraprocedural axial CT soft-tissue-windowed image (B) with the core biopsy needle in place. An anterior approach was chosen to pass just medial to the internal jugular vein (*dashed white arrow*), just lateral to the trachea (*white asterisk*), and stopping short of the esophagus (*white oval*). The histopathology from the biopsy was recurrent papillary thyroid carcinoma.

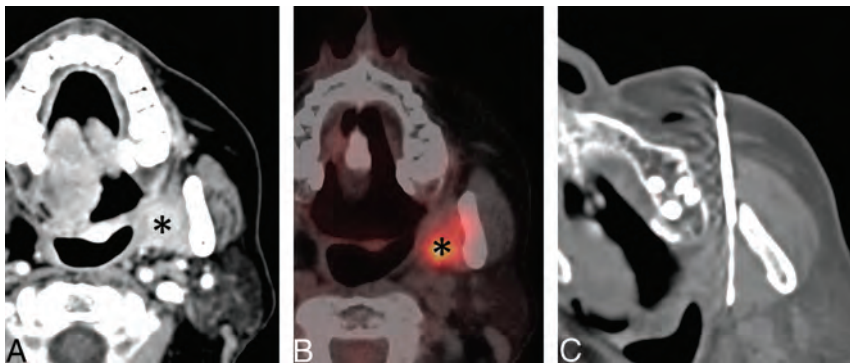


FIG 3. A 75-year-old woman with previously excised and re-excised left base-of-tongue and retromolar squamous cell carcinoma. Axial contrast-enhanced neck CT (A) and fused PET/CT (B) images demonstrate an enhancing FDG avid mass (*black asterisk*) in the left masticator space. A paramaxillary approach was chosen to perform the biopsy (C). The histopathology from the biopsy was recurrent squamous cell carcinoma. With this biopsy, the facial artery is medial to the needle-entry site just anterior to the maxilla and is not problematic for the needle path.

performed with conscious sedation; 2/27, with general anesthesia; and 2/27, with local anesthetic only. In most cases, a 1:1 mixture of bupivacaine 0.25% and lidocaine 1% was first administered for subcutaneous and deep anesthesia. The average sedation time for the conscious sedation cases was 43 minutes. The average intravenous

fentanyl and midazolam dosages for the conscious sedation cases were 159.8 μ g and 2.6 mg, respectively. For the biopsies, Bard Mission (Bard Peripheral Vascular) or Achieve (CareFusion) spring-loaded coaxial biopsy needle systems were used. The choice of needle gauge was based on the relative proximity of the lesion to important neurovascular structures, the space available to avoid those structures, and the ability to maneuver the needle into the lesion without injuring those structures.

For lesions with minimal clearance between the needle path and a critical neurovascular structure, a smaller gauge needle was chosen, either 18 or 20 ga. The outer introducer needle was placed just proximal to the target mass followed by the coaxial placement of the spring-loaded biopsy needle into the mass. In 2 cases, the Arrow OnControl battery-powered bone biopsy system (Teleflex) was used to access the soft-tissue lesions. Table 1 describes in detail the different biopsy needles used for lesion biopsy. The most common needle used was 14 gauge in 14/27 biopsy procedures. The average number of biopsy cores acquired was 4.4 (range, 2–9). Patient positioning on the table was dependent on the location of the head and neck lesion and the approach used to perform the biopsy.

There are multiple described approaches for biopsies in the head and neck, depending on the locations of the masses.^{18–21} A brief description and the approximate needle course for the different biopsy approaches are presented in Fig 1. Biopsy approaches for the patients in our group included the following: anterior 7/27, paramaxillary 2/27, posterior 5/27, retromandibular 2/27, submastoid 8/27, and subzygomatic/sigmoid notch 3/27 (Table 2). The anterior approach was used for lesions in the perivertebral, anterior cervical, prevertebral, visceral (Fig 2), and pharyngeal spaces. The paramaxillary approach was used for lesions in the masticator and parapharyngeal spaces (Fig 3). The posterior approach was used for posterior perivertebral lesions. The retromandibular approach was used for parapharyngeal space lesions (Fig 4). The submastoid approach was used for lesions in the perivertebral, parapharyngeal, and carotid spaces (Fig 5). The subzygomatic approach was used for lesions in the masticator space.

CT angiography was performed immediately before the biopsy when the pathway to the soft-tissue mass included important

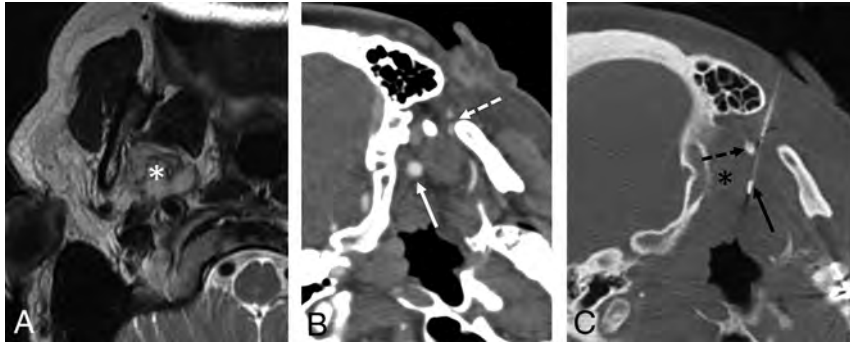


FIG 4. A 69-year-old woman with an incidentally found right-neck mass on a cervical spine MR imaging. Axial T2-weighted MR image (A) from a cervical spine MR imaging demonstrates an indeterminate T2-hyperintense mass (*white asterisk*) at the deep margin of the parotid gland, centered within the parapharyngeal space posterior to the masticator space. Intraoperative contrast-enhanced soft-tissue-windowed CT image (B) with the patient in the left lateral decubitus position. Note the internal carotid artery (*white arrow*) and other vascular structures including the retromandibular vessels adjacent to the mandibular ramus (*white dashed arrow*). Intraoperative axial CT bone-windowed image (C) with the core biopsy needle in place (*black arrow*). A retromandibular course with the entry point posterior to the ear was chosen to access the mass. The needle path is to avoid the vascular structures adjacent to the mandibular ramus, including the retromandibular vein, but anterior to the styloid process (*black dashed arrow*) and internal carotid artery (approximately at the site of the *black asterisk* but occult on noncontrast CT). The pathology was adenoid cystic carcinoma.

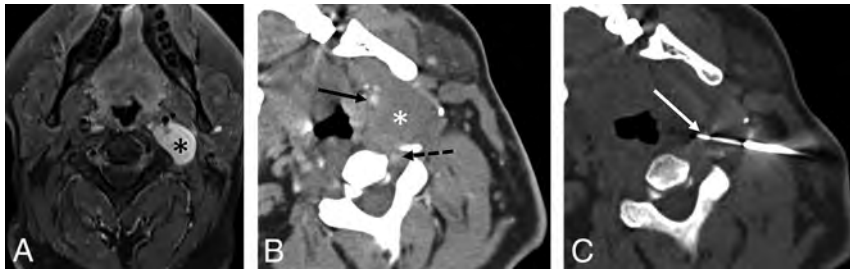


FIG 5. A 25-year-old man with neurofibromatosis type 1, new vagus nerve-related symptoms, and an enlarging painful left carotid space mass. Axial T1-weighted fat-suppressed postcontrast MR image (A) from a neck MR imaging demonstrates an enhancing carotid space mass (*black asterisk*). Intraoperative contrast-enhanced soft-tissue-windowed CT image (B) with the patient supine but with the head turned to the right. Note that the mass (*white asterisk*) is located between the internal carotid (*black arrow*) and vertebral (*black dashed arrow*) arteries and is pushing the carotid artery anteriorly. Intraoperative axial CT soft-tissue-windowed image (C) with the core biopsy needle in place (*white arrow*). A submastoid approach was chosen to avoid the carotid and vertebral arteries. The histopathology from the biopsy was neurofibroma. Given the progressive symptoms, concern for sampling error, and the high risk given the diagnosis of type neurofibromatosis 1, the mass was excised and final pathology was plexiform neurofibroma containing focal areas of low-grade malignant peripheral nerve sheath tumor.

vascular structures, to better delineate the vascular anatomy and plan the safest biopsy route while minimizing the risk of vascular injury. Of the 27 biopsy procedures, 10 had corresponding CT angiograms with a dose average of 80 mL of ioversol contrast (Optiray 350; Mallinckrodt) given intravenously (Figs 4 and 5).

RESULTS

Patient Characteristics

A total of 26 patients underwent 27 CT-guided head and neck soft-tissue biopsies. Fifty-four percent of the patients were men,

and 46% were women. The age range of the patients was from 3 months to 77 years of age, with an average age of 54.7 years. The clinical concern in these cases was for primary tumor in 52% (14/27), locoregional recurrent disease in 33% (9/27), or metastatic disease in 15% (4/27). One complication of core needle biopsy occurred. This was a small intraprocedural hematoma (CTCAE grade 1), which was asymptomatic and required no further treatment or follow-up. Additionally, there was an adverse event in which the patient developed new asymptomatic atrial fibrillation with a rapid ventricular response (CTCAE grade 3) during positioning and the initial contrast-enhanced CT scan for localization of tumor. This was before administration of sedation medications and beginning the biopsy procedure. This patient was transported to the emergency department for heart rate control, and the biopsy was performed at a later date without complications.

Lesion Characteristics and Histopathology

The average size of the biopsied masses measured in the longest axis of each lesion was 33 mm, ranging between 14 and 71 mm. The locations of the lesions were the following: the anterior cervical space, 11% (3/27); carotid space, 11% (3/27); masticator space, 19% (5/27); parapharyngeal space, 22% (6/27); perivertebral space, 26% (7/27); pharyngeal space, 4% (1/27); prevertebral space, 4% (1/27); and visceral space, 4% (1/27) (Table 3).

A sufficient sample was obtained for histopathologic diagnosis in 100% (27/27) of the biopsies. The pathology obtained was malignant in 16/27 biopsies and benign in 11/27 biopsies. Two

of the 11 benign biopsies were found to be discordant with the clinical impression and repeat biopsy results were subsequently found to be malignant. One was initially diagnosed as fibrosis with a foreign body giant cell reaction and was later found to be recurrent squamous cell carcinoma on a repeat CT-guided biopsy 6 weeks later. The second was initially diagnosed as benign neurofibroma, but at excision, it was found to have areas of malignant peripheral nerve sheath tumor within the lesion. The remaining 9 benign lesion biopsies either demonstrated no concerning change on imaging follow-up in 56% (5/9) or were confirmed benign by excision in the remaining 44% (4/9). The most

Table 3: Anatomic location of the target mass in 27 biopsy procedures

Target Lesion	No.
Anterior cervical	3
Carotid space	3
Masticator space	5
Parapharyngeal	6
Perivertebral	7
Pharyngeal	1
Prevertebral	1
Visceral space	1

Table 4: Histopathologic results of CT-guided head and neck biopsies

Histopathology	No.
Acute on chronic inflammation	1
Adenoid cystic carcinoma ^a	1
Atypical melanin rich neoplasm ^a	1
Benign fibrocollagenous tissue	1
Chondroid lesion	1
Fibrosis with foreign body giant cell reaction	1 ^b
Granulation tissue	1
Metastatic myxoid liposarcoma ^a	1
Malignant peripheral nerve sheath tumor ^a	2
Myxoma	1
Neurofibroma	1 ^b
Papillary thyroid cancer ^a	1
Pleomorphic adenoma	1
Round cell sarcoma ^a	1
Schwannoma	2
Spindle cell neoplasm ^a	1
Squamous cell carcinoma ^a	8
Synovial cyst	1

^a Malignant.

^b Two cases with discordant histopathology. The fibrosis with foreign body giant cell reaction was found to be recurrent squamous cell carcinoma on repeat CT-guided biopsy. The neurofibroma was found to have components of malignant peripheral nerve sheath tumor when excised.

common malignant lesion was squamous cell carcinoma, found in 8 patients (Table 4). The overall concordance of the biopsies was 93%.

CT Radiation Dose

The dose-length product ranged from 76 to 2790 mGy × cm, with an average of 533 mGy × cm. When we considered the most recent biopsies, specifically from January 2015 to December 2019, which account for 89% (24/27) of all biopsies performed, there was a decreased average dose-length product of 455 mGy × cm. The highest dose-length product recorded was 2790 mGy × cm. This was performed before increased awareness of scanning parameters, advanced scanner technology, as well as institutional emphasis on decreasing diagnostic and procedural radiation doses.

DISCUSSION

Masses in the head and neck arise in multiple different anatomic spaces and have a wide variety of tumor histopathologies. Diagnosis and treatment require a multidisciplinary approach, which is constantly evolving.²²⁻²⁴ Often, the tissue required for diagnosis is acquired by a subspecialty-trained radiologist, particularly when the

mass is located within a deep neck space requiring CT guidance for biopsy access.

Multiple publications have demonstrated the safety and utility of soft-tissue biopsies in general, but few have focused specifically on the deep head and neck.⁷⁻¹⁵ Most complications reported in the literature in these studies are minor, including small hematoma, pain, vasovagal reaction, and minor infection.⁷⁻¹⁵ Another more rarely described complication is seeding of tumor along the biopsy needle tract. A MEDLINE data base search between 1970 and 2014 found 7 reported cases of tumor seeding, 5 with fine-needle aspiration and 2 with core needle biopsy, in the 610 articles reviewed.²⁵ These findings are similar to those in our study in which we report 1 minor complication of the biopsy procedure, no tumor seeding complications, and 1 adverse event before beginning the biopsy procedure, which was unlikely related to the procedure, given that this occurred before a needle was placed in the neck. The only reported major complication related to a CT-guided head and neck biopsy in the literature was an internal maxillary artery pseudoaneurysm presenting 3 months after the CT-guided fine-needle aspiration. This was thought to be due to an increased risk from prior radical neck surgery and radiation therapy, leading to abnormal neoangiogenic vascularity or large-vessel vasculopathy.¹⁶

Given the relatively high-stakes anatomy in the head and neck, choosing the appropriate anatomic approach to safely perform the biopsy is of the utmost importance. There are multiple described approaches to head and neck masses, with some overlap in the ability to access a deep neck space.¹⁸⁻²¹ For example, pathways to reach the parapharyngeal, masticator, and pharyngeal spaces may include paramaxillary, retromandibular, submassoid, and subzygomatic approaches. Thus, it is important to fully evaluate the preprocedural imaging for the location of vessels, nerves, salivary glands, and salivary ducts to find the safest and most direct needle course. The CT angiography technique increases the certainty and safety of the needle path chosen for the procedure, particularly when positioning for the procedure is different from the standard supine position typically used for CT imaging and when there are arteries in or directly adjacent to the targeted mass. This technique has been previously described in cervical spine biopsies,²⁶ but not in biopsies of head and neck masses. All except 2 of the 27 cases were performed with either conscious sedation or local anesthesia, increasing the safety of the biopsy in this patient population, which is typically considered at higher risk for general anesthesia.

The choice of biopsy technique, fine-needle aspiration versus core needle biopsy, is often dependent on the institution. At our institution, core needle biopsies are preferred by the pathologist when feasible for increased diagnostic certainty. In previous clinical series, the yield of both CT-guided fine-needle aspiration and core biopsy of the head and neck soft tissues is varied. In the largest study of 216 patients who underwent CT-guided fine-needle aspiration, a diagnostic sample was obtained in 90% of patients, with a concordant diagnosis in 88% of cases.⁹ Studies of CT-guided core biopsies have reported diagnostic yields ranging from 73% to 96%.¹²⁻¹⁵ Compared with these prior CT-guided soft-tissue mass biopsy series, our diagnostic yield is similar-to-slightly higher, with 100% of samples sufficient for histopathologic diagnosis and a concordant diagnosis in 93% (25/27) of all biopsies. This result may be

due to the larger average needle gauge used in our study, most commonly 14 gauge, and the higher average number of core specimens obtained of 4.4.

CONCLUSIONS

This original research demonstrates the safety and efficacy of CT-guided percutaneous core biopsy for deep soft-tissue masses in the head and neck, obviating the need for open biopsies and their associated risks in locations not easily accessible by palpation, sonography, or laryngoscopy. It also describes the use of CT angiography for vessel localization and mapping before needle placement following patient positioning on the procedural table to reduce the risk of vascular injury.

Disclosures: Travis J. Hillen—UNRELATED: Consultancy: Medtronic, SI BONE, Ultragenyx Pharmaceutical, ERT, Comments: paid consultant for studies not related to published work. Jack W. Jennings—RELATED: Consulting Fee or Honorarium: Bard/BD and Stryker, Comments: Both are for consultation for the bone biopsy system and nothing to do with this article; UNRELATED: Consultancy: Merit, Medtronic, Comments: Merit contract ended June 30, 2020, Medtronic monitoring for OPuS 1 spine ablation trial.

REFERENCES

1. American Cancer Society. **Cancer Facts and Figures 2020**. <https://www.cancer.org/content/dam/cancer-org/research/cancer-facts-and-statistics/annual-cancer-facts-and-figures/2020/cancer-facts-and-figures-2020.pdf>. Accessed April 13, 2020
2. Nyquist GG, Tom WD, Mui S. **Automatic core needle biopsy: a diagnostic option for head and neck masses**. *Arch Otolaryngol Head Neck Surg* 2008;134:184–89 CrossRef Medline
3. Pfeiffer J, Kayser G, Technau-Ihling K, et al. **Ultrasound-guided core-needle biopsy in the diagnosis of head and neck masses: indications, technique, and results**. *Head Neck* 2007;29:1033–40 CrossRef Medline
4. Novoa E, Gurtler N, Arnoux A, et al. **Role of ultrasound-guided core-needle biopsy in the assessment of head and neck lesions: a meta-analysis and systematic review of the literature**. *Head Neck* 2012;34:1497–1503 CrossRef Medline
5. Douville NJ, Bradford CR. **Comparison of ultrasound-guided core biopsy versus fine-needle aspiration biopsy in the evaluation of salivary gland lesions**. *Head Neck* 2013;35:1657–61 CrossRef Medline
6. Pfeiffer J, Ridder GJ. **Diagnostic value of ultrasound-guided core needle biopsy in patients with salivary gland masses**. *Int J Oral Maxillofac Surg* 2012;41:437–43 CrossRef Medline
7. Gatenby RA, Mulhern CB, Strawitz J. **CT guided percutaneous biopsies of head and neck masses**. *Radiology* 1983;146:717–19 CrossRef Medline
8. DelGaudio JM, Dillard DG, Albritton FD, et al. **Computed tomography-guided needle biopsy of head and neck lesions**. *Arch Otolaryngol Head Neck Surg* 2000;126:366–70 CrossRef Medline
9. Sherman PM, Yousem DM, Loevner LA. **CT-guided aspirations in the head and neck: assessment of the first 216 cases**. *AJNR Am J Neuroradiol* 2004;25:1603–07 Medline
10. Sack MJ, Weber RS, Weinstein GS, et al. **Image-guided fine-needle aspiration of the head and neck: five years' experience**. *Arch Otolaryngol Head Neck Surg* 1998;124:1155–61 CrossRef Medline
11. Mukherji SK, Turetsky D, Tart RP, et al. **A technique for core biopsies of head and neck masses**. *AJNR Am J Neuroradiol* 1994;15:518–20 Medline
12. Connor SEJ, Chaudhary N. **CT-guided percutaneous core biopsy of deep face and skull-base lesions**. *Clin Radiol* 2008;63:986–94 CrossRef Medline
13. Wu EH, Chen YL, Wu YM, et al. **CT-guided core needle biopsy of deep suprahyoid head and neck lesions**. *Korean J Radiol* 2013;14:299–306 CrossRef Medline
14. Wu EH, Chen YL, Toh CH, et al. **CT-guided core needle biopsy of deep suprahyoid head and neck lesions in untreated patients**. *Interv Neuroradiol* 2013;19:365–69 CrossRef Medline
15. Cunningham JD, McCusker MW, Power S, et al. **Accessible or inaccessible? Diagnostic efficacy of CT-guided core biopsies of head and neck masses**. *Cardiovasc Intervent Radiol* 2015;38:422–29 CrossRef Medline
16. Walker AT, Chaloupka JC, Putman CM, et al. **Sentinel transoral hemorrhage from a pseudoaneurysm of the internal maxillary artery: a complication of CT-guided biopsy of the masticator space**. *AJNR Am J Neuroradiol* 1996;17:377–81 Medline
17. US Department of Health and Human Services. **Common terminology criteria for adverse events (CTCAE), Version 5.0**. https://ctep.cancer.gov/protocolDevelopment/electronic_applications/docs/CTCAE_v5_Quick_Reference_8.5x11.pdf. Accessed April 14, 2020
18. Gupta S, Henningsen JA, Wallace MJ, et al. **Percutaneous biopsy of head and neck lesions with CT guidance: various approaches and relevant anatomic and technical considerations**. *Radiographics* 2007;27:371–90 CrossRef Medline
19. McKnight CD, Glastonbury CM, Ibrahim M, et al. **Techniques and approaches for safe, high-yield CT-guided suprahyoid head and neck biopsies**. *AJR Am J Roentgenol* 2017;208:76–83 CrossRef Medline
20. Abrahams JJ. **Mandibular sigmoid notch: a window for CT-guided biopsies of lesions in the peripharyngeal and skull base regions**. *Radiology* 1998;208:695–99 CrossRef Medline
21. Tu AS, Geyer CA, Mancall AC, et al. **The buccal space: a doorway for percutaneous CT-guided biopsy of the parapharyngeal region**. *AJNR Am J Neuroradiol* 1998;19:728–31 Medline
22. Gibson MK, Forastiere AA. **Multidisciplinary approaches in the management of advanced head and neck tumors: state of the art**. *Curr Opin Oncol* 2004;16:220–24 CrossRef Medline
23. Chin D, Boyle GM, Porceddu S, et al. **Head and neck cancer: past, present and future**. *Expert Rev Anticancer Ther* 2006;6:1111–18 CrossRef Medline
24. Bradford CR. **The care of the head and neck cancer patient is a team sport**. *JAMA Otolaryngol Head Neck Surg* 2013;139:337–39 CrossRef Medline
25. Shah KS, Ethunandan M. **Tumour seeding after fine-needle aspiration and core biopsy of the head and neck: systematic review**. *Br J Oral Maxillofac Surg* 2016;54:260–65 CrossRef Medline
26. Wiesner EL, Hillen TJ, Long J, et al. **Percutaneous CT-guided biopsies of the cervical spine: technique, histopathologic and microbiologic yield, and safety at a single academic institution**. *AJNR Am J Neuroradiol* 2018;39:981–85 CrossRef Medline

Image-Guided Biopsies in the Head and Neck: Practical Value and Approach

The authors of “Percutaneous CT-Guided Core Needle Biopsies of Head and Neck Masses: Technique, Histopathologic Yield, and Safety at a Single Academic Institution” have shown the efficacy and safety of image-guided core needle biopsy in the head and neck (H&N) at their institution. A H&N image-guided biopsy service adds immense value to patient care by offering an accurate and less invasive histopathologic diagnosis than a surgical biopsy, facilitating radiologic-pathologic correlation and growing a more management-driven radiology service. Three important points will underscore and highlight the practical value of the authors’ work on image-guided core biopsy.

1. Head and neck fine-needle aspiration (FNA) versus core needle biopsy (CNB): When will FNA suffice and when is CNB likely to be needed?
2. The value of imaging biopsy versus surgical biopsy.
3. The value of the H&N radiologist performing the biopsy.

In our head and neck biopsy service, we routinely do both ultrasound (US)-guided and CT-guided biopsies and both FNA and CNB. The referring clinician will request a biopsy; then, it comes to us for vetting. In general, US biopsies are more commonly requested and used for most superficial targets (<3 cm deep). CT-guided biopsies are usually reserved for deeper targets, most frequently near the skull base or in parapharyngeal or retropharyngeal spaces, which are not easily accessible with US.

The first choice in planning will be US versus CT:

US

- Targets <3 cm deep
- Most lateral and supraclavicular lymph nodes
- Most parotid masses
- Thyroid and thyroid bed masses

CT

- Targets >3 cm deep
- Lesions near the skull base/clivus

- Parapharyngeal space mass (often minor salivary tumors)
- Deep lobe of the parotid
- Retropharyngeal nodes
- Pterygopalatine fossa lesion

Some common indications for image-guided biopsy include a new palpable mass/node, staging nodes in a patient with known H&N cancer including thyroid cancer, evaluating recurrence in nodes after treatment for H&N cancer, and parotid or submandibular masses.

H&N FNA versus Core Biopsy: When Will FNB Suffice and When Is CNB Needed?

- FNA: Usually narrow-gauge 22- to 25-ga needle (23 ga most commonly)
 - 1) A US guided FNA: 3.5 cm 23 ga needle for most at our institution
 - 2) Coaxial technique for CT-guided FNA, a 6-cm, 19-ga introducer and 10-cm, 22-ga needle for FNA
- CNB: Usually larger gauge needles (16-20 ga); SuperCore 18 ga for most at our institution (<https://www.argonmedical.com/products/supercore-semi-automatic-biopsy-instrument/>).

The next important consideration is FNA versus CNB. The major benefit of FNA is safety, especially with small targets but also preliminary cytologic assessment by an on-site cytopathologist, allowing real-time feedback regarding the adequacy of the sample. The main disadvantage of FNA is the small sample size, which can lead to nondiagnostic results. FNAs are generally performed with narrow-gauge needles (22–25 ga), and core needle biopsies are performed with larger gauge needles (16–20 ga). The main advantage of CNB is the increased diagnostic yield compared with FNA of salivary gland lesions and cervical lymph nodes.^{1,2}

There will be some circumstances when the referring team (or the radiologist) will request a core upfront. Some reasons would include a previous non-diagnostic FNA, a suspected diagnosis that is difficult to make on FNA alone or enrollment in a clinical trial which needs core tissue. In addition, if asked to biopsy a lesion with a less typical leading diagnosis, it is often helpful to

discuss the case ahead of time with your cytopathologists to understand their comfort level making that particular diagnosis with FNA vs CNB. At our institution, most biopsies will start with FNA and then progress to core on the basis of the real-time feedback of the cytopathologist. At some institutions, a CNB may also be chosen over FNA because of the preference of the radiologists or availability and expertise of the cytopathologists. However, it is useful for radiologists to have a general concept of which diagnoses can be easily made with FNA and which will likely require core. This is important to understand before starting a biopsy.

In our experience, FNA alone will usually suffice to diagnose squamous cell carcinoma (SCC), papillary thyroid carcinoma (with thyroglobulin assay), melanoma, and other carcinomas, particularly in patients who already have a confirmed head and neck primary. Other histopathologic diagnoses are more difficult to make with FNA. For example, salivary gland neoplasms and infiltrative soft-tissue masses around the skull base (with a differential of lymphoma, lymphoma mimics, immunoglobulin G4, sarcoidosis, chronic infection, etc.) and are all examples of lesions which can be difficult to diagnose on FNA.

In general, FNA has a high diagnostic yield for SCC often in the setting of tumor recurrence, thyroid carcinoma, and melanoma. It is often our choice for small lesions in this category. In fact, a retrospective review of our preliminary institutional experience with a H&N biopsy service in 2010 found that 88/102 (87%) FNAs (mean target size = 1.6 cm) performed in the non-thyroid neck were diagnostic.³ The clinical indications for US-guided FNA included an initial diagnosis of a nonthyroid gland neck mass ($n = 13$), initial cervical lymph node staging in the setting of known malignancy ($n = 3$), suspected abscess ($n = 4$), and suspected persistence or recurrence of a known malignancy ($n = 75$). The latter category was clearly the most common indication, with the most common histopathology being thyroid carcinoma, squamous cell carcinoma, and melanoma in descending order.

FNA has a higher non-diagnostic rate and limited sensitivity for malignancy in salivary gland neoplasms. FNA can also be more challenging with lymphoma and rare inflammatory diagnoses as noted above. CNB of salivary gland lesions has emerged as the preferred method to overcome the limitations of FNA. In 3 studies directly comparing FNA and CNB of salivary lesions, the nondiagnostic rate was 19%–56% for FNA and 4%–5% for CNB, while the sensitivity for malignancy was 60%–76% for FNA and 89%–93% for CNB, with only minor complications such as hematoma and no major complication such as facial nerve injury.^{1–5} Compared with FNA alone, CNB has also been shown to increase the diagnostic yield for lymphoma and decrease the need for excisional biopsy.⁶

At our institution, we often begin with FNA for both salivary neoplasms and suspected lymphoma, but we have a lower threshold to add CNB if there is a sufficient-size solid component and preliminary FNA is nondiagnostic. We use a SuperCore 18-ga core biopsy gun with an adjustable specimen notch for either 1- or 2-cm core specimens. The needle has an echogenic tip on the outer cannula to promote accurate placement under ultrasound guidance.

What is the Value of Image-Guided Biopsy versus Surgical Biopsy?

Many patients with head and neck cancer have other comorbidities, which make open biopsy under general anesthesia a higher risk. In addition, patients who have already undergone complex resection, reconstruction, and/or radiation also have tissue distortion and scarring, which complicates a re-operation. Finally, most of these deep abnormalities are detected by imaging only. Therefore, image-guided biopsy ensures radiologic-pathologic correlation. In other words, image-guided biopsy ensures that the suspicious lesion on imaging is actually the tissue that is correctly sampled. In a deep resection bed with extensive scarring/granulation and flap reconstruction, it is not a simple task for the surgeon to confirm that he or she is sampling the imaging abnormality, and this issue can lead to false-negatives.

What is the Value of a Diagnostic H&N Radiology Group Performing the Biopsies for the Studies They Interpret?

Divorcing the interpreting radiologists from the radiologist performing the biopsies can affect both the accuracy of the original image interpretations and the accuracy of the biopsies (confusion over target/exact area of concern in some cases). Diagnostic radiologists who do not perform procedures and/or communicate with colleagues performing the procedures may overcall imaging abnormalities which are difficult to access. An imaging abnormality with an unclear risk assessment that cannot easily be biopsied can lead to frustration for the referring clinician and stress for the patient. Radiologists who routinely perform their own biopsies quickly develop an understanding of whether they can safely reach the target, whether an abnormality can be successfully biopsied, whether a CT abnormality will translate to a viable US target, whether the target is reproducible, and so forth. It can be very beneficial to think like an interpreting radiologist and a procedure-vetting radiologist at the time of your original dictation.

There are many potential advantages to having a neuroradiologist or dedicated head and neck radiologist perform the image-guided biopsy. Thorough knowledge of the neck imaging anatomy, normal and abnormal appearance of the postoperative/postradiotherapy neck, and specific patterns of nodal spread for various head and neck malignancies are major advantages. The neuroradiologist often interprets the imaging or participates in multidisciplinary tumor boards that prompt FNA, leading to familiarity with the case and deliberation on the advantages and disadvantages of US-guided FNA, CT-guided FNA, and core or follow-up imaging. This scenario is particularly important in complex cases with >1 potential target. The true risk category of an imaging abnormality may be at the crossroads of multiple modalities (CT, PET, MR imaging) and multiple time points. Thus, the accuracy of biopsies can also be adversely affected if the interpreting radiologist is not performing the biopsy. There is also an opportunity to reconcile radiologic-pathologic discordance on site during the procedure, so that mismatches can be discussed and additional passes/alternative targets selected during the procedure. This interaction also facilitates a collegial relationship among the head and neck surgeon, neuroradiologist, and cytopathologist, which is the key to optimal multidisciplinary patient care.

In summary, image-guided biopsies have replaced surgical biopsies for most head and neck lesions, with increased safety and efficacy. Furthermore, the many potential advantages of having a neuroradiologist or dedicated head and neck radiologist perform the image-guided biopsy include thorough knowledge of the neck anatomy, normal and abnormal appearance of the postoperative/ postradiotherapy neck, and specific patterns of nodal spread for various head and neck malignancies. While FNA will usually suffice to establish cervical nodal metastasis or nodal recurrence for common pathologies such as SCC, thyroid carcinoma, and melanoma, CNB may be needed for increased accuracy for salivary gland masses and suspected lymphoma. In the end, the decision to use FNA versus CNB is often based on the unique presentation of each case, the operator's experience, institutional preference, and real-time cytopathologic evaluation.

REFERENCES

1. Eom HJ, Lee JH, Ko MS, et al. **Comparison of fine-needle aspiration and core needle biopsy under ultrasonographic guidance for detecting malignancy and for the tissue-specific diagnosis of salivary gland tumors.** *AJNR Am J Neuroradiol* 2015;36:1188–93 CrossRef Medline
2. Novoa E, Gurtler N, Arnoux A, et al. **Role of ultrasound-guided core-needle biopsy in the assessment of head and neck lesions: a meta-analysis and systematic review of the literature.** *Head Neck* 2012;34:1497–1503 CrossRef Medline
3. Lorenzo G, Saindane AM, Aiken A, Lewis M, Hollis B, Hudgins PA. **Diagnostic utility of ultrasound-guided fine needle aspiration in the (non-thyroid gland) neck.** American Society of Head and Neck Radiology, Houston, TX, October 2010 (oral presentation).
4. Pratap R, Qayyum A, Ahmed N, et al. **Ultrasound-guided core needle biopsy of parotid gland swellings.** *J Laryngol Otol* 2009;123:449–52 CrossRef Medline
5. Haldar S, Mandalia U, Skelton E, et al. **Diagnostic investigation of parotid neoplasms: a 16-year experience of freehand fine needle aspiration cytology and ultrasound-guided core needle biopsy.** *Int J Oral Maxillofac Surg* 2015;44:151–57 CrossRef Medline
6. Ryu YJ, Cha W, Jeong WJ, et al. **Diagnostic role of core needle biopsy in cervical lymphadenopathy.** *Head Neck* 2015;37:229–33 CrossRef Medline

© A.H. Aiken

Departments of Radiology and Imaging Sciences and
Otolaryngology-Head and Neck Surgery
Emory University
Atlanta, Georgia

<http://dx.doi.org/10.3174/ajnr.A6855>

Diagnostic Yield and Therapeutic Impact of Face and Neck Imaging in Patients Referred with Otolgia without Clinically Overt Disease

E. Ainsworth, I. Pai, M. Kathirgamanathan, and S.E.J. Connor



ABSTRACT

BACKGROUND AND PURPOSE: Otolgia may be secondary to serious pathology, such as upper aerodigestive tract malignancies, and CT or MR imaging of the skull base, face, and neck is often performed to detect clinically occult lesions. The diagnostic yield, management impact, and therapeutic impact of imaging in this clinical scenario, however, have yet to be elucidated.

MATERIALS AND METHODS: CT and MR imaging in patients who presented with otalgia without clinically overt disease was retrospectively analyzed from a single center over a 9-year period. The cohort was subdivided into groups, depending on the presence of additional symptoms and a history of head and neck cancer. Relevant diagnostic outcome findings were categorized, and the diagnostic yield and impact of imaging on management and therapy were calculated for each group.

RESULTS: In our study cohort of 235 patients, the diagnostic yield of imaging for otalgia, with or without other symptoms, in patients who lacked a history of head and neck cancer was negligible for upper aerodigestive tract malignancy (1%), abnormalities related to otalgia (2%), and other moderate or major findings (2%). Although equivocal or unimportant findings occasionally resulted in additional investigations, the therapeutic impact was also very low (2%). The diagnostic yield for upper aerodigestive tract malignancy (34%) and therapeutic impact increased (34%) when there was a history of head and neck cancer.

CONCLUSIONS: The diagnostic yield and therapeutic impact of imaging for otalgia without clinically overt disease are very low, unless there is a history of head and neck cancer.

ABBREVIATIONS: FNE = fiberoptic nasendoscopy; UAT = upper aerodigestive tract

The causes of otalgia (earache) are diverse and can be categorized as primary and secondary. Primary causes of otalgia are pathologies that affect the ear itself,¹ with common causes that include otitis externa, otitis media,² trauma, and foreign bodies. Primary otalgia often presents with overt clinical signs and can be managed without imaging studies. Secondary (referred) otalgia is caused by pathologies in locations outside the ear and results from shared pathways of sensory innervation.¹⁻⁷ Some etiologies may also be diagnosed on the basis of additional clinical findings and supported by targeted imaging (eg, temporomandibular joint or dental).

Upper aerodigestive tract (UAT) malignancies are a potential cause of secondary otalgia, and it is a clinical feature that prompts rapid referral for head and neck cancer investigation in most clinical networks⁸; therefore, fiberoptic nasoendoscopy (FNE) is usually performed in the early diagnostic work-up in these patients. Even in the presence of a normal FNE, clinicians may remain concerned that a submucosal UAT lesion or other clinically occult pathology may be present, so cross-sectional imaging is frequently proposed. Despite this common clinical practice, to our knowledge, the diagnostic value of face and neck imaging in patients referred with otalgia has not been documented. We, therefore, performed a single-center retrospective study that analyzed the diagnostic yield, management impact, and therapeutic impact of imaging with CT and MR of the skull base, face, and neck in patients referred with otalgia but without clinically overt disease over a 9-year period.

MATERIALS AND METHODS

We performed a retrospective search of all CT and MR imaging requests on the radiology information systems, for requests and reports that contained the specific terms “otalgia,” “earache,” or

Received April 29, 2020; accepted after revision July 7.

From the Departments of Radiology (E.A., M.K., S.E.J.C.) and Otolaryngology (I.P.), Guy's and St. Thomas' Hospital, London, United Kingdom; School of Biomedical Engineering and Imaging Sciences Clinical Academic Group (I.P., S.E.J.C.) and Department of Neuroradiology (S.E.J.C.), King's College Hospital, London, United Kingdom.

Please address correspondence to Dr Steve E. J. Connor, Department of Neuroradiology, Ruskin Wing, Kings College Hospital, Denmark Hill, London SE5 9RS, United Kingdom; e-mail: steve.connor@nhs.net; @SEJConnor



Indicates article with supplemental on-line photos.

<http://dx.doi.org/10.3174/ajnr.A6760>

“ear pain” between January 2009 and September 2017. Cases in which dedicated CT or MR imaging was performed for targeted anatomic regions (eg, skull base, intracranial, temporomandibular joint, and paranasal sinus) were excluded. Also excluded were cases in which clinical examination, including FNE, identified the cause of otalgia before imaging (eg, middle ear and external ear inflammation, foreign body in the external ear, peritonsillar abscess, palpable nodal metastases in the neck, and previously identified mandibular osteochondroma). Routine contrast-enhanced imaging protocols for CT and MR imaging encompassed the whole face and neck. The imaging was reported by dedicated head and neck radiologists.

The clinical and imaging data were interrogated by using electronic patient record, PACS, and radiology information systems. For the remaining cases, demographic information, type of imaging, laterality of otalgia, clinical examination findings (including FNE), imaging findings, subsequent clinical management, and final diagnoses were recorded. Presenting symptoms were divided into 4 categories: pure otalgia, otalgia with UAT symptoms, otalgia with other symptoms, and otalgia in patients with a history of head and neck cancer. Imaging findings were classified as important, indeterminate, or unimportant abnormality. Important abnormalities included those that may be etiologies for otalgia or that were deemed major or moderate unrelated imaging findings.⁹ Imaging findings that potentially cause otalgia were defined as those pathologies that occur in ipsilateral locations that are recognized to cause referred pain to the ear; these were assessed by a combined clinicrodiology team. Unrelated imaging findings were categorized as major, moderate, or minor, according to previous guidelines on incidental imaging findings from the Royal College of Radiologists.⁹ Major findings were defined as those that always required further investigation and were likely to have adverse health effects, whereas moderate findings were those that usually required further investigation but health effects were unclear. Minor findings were defined as those that did not require further investigations or have adverse health effects (eg, degenerative cervical spine disease, generalized or mild sinonasal or dental disease, thyroid nodules that do not require biopsy, venous malformation, and thymic hyperplasia). For the purpose of this study, minor findings with no important abnormality were grouped together for subsequent analysis of the diagnostic yield, management impact, and therapeutic impact.⁹

The final diagnostic outcomes were considered important if they were in 1 of the following 3 groups: UAT malignancies, new abnormalities that potentially cause ipsilateral otalgia, and other new major or moderate findings unrelated to otalgia.

Patients in whom malignancy had been identified on FNE before imaging were recorded separately because imaging was used for staging rather than diagnosis. For the remaining patients, the “diagnostic yield” (the number of studies with a new or major finding divided by the total number of studies) was used as an indicator of the value of the study in assisting diagnosis. The term “management impact” (the number of studies that result in a change in clinical management divided by the total number of studies) was used as an indicator of the influence on the patient’s clinical management.^{10,11} The term “therapeutic impact” (the number of studies that result in subsequent directed therapy for detected pathology divided by the total number of

studies) was used as an indicator of truly beneficial impact of imaging. The diagnostic yield, management impact, and therapeutic impact of CT/MR imaging of the skull base, face, and neck were calculated for the detection of UAT malignancy, abnormalities that potentially cause ipsilateral otalgia, and other major or moderate findings unrelated to otalgia.

The data were described and summarized according to each of the categories of pure otalgia, otalgia with UAT symptoms, otalgia with other symptoms, and otalgia in patients with a history of head and neck cancer. The percentage incidence of UAT malignancy, any other cause of otalgia, and other moderate and/or major findings unrelated to otalgia were calculated for each category. The diagnostic yield, management impact, and therapeutic impact were also analyzed for each category.

RESULTS

A total of 787 relevant imaging requests were identified on the initial search. Exclusions were dedicated imaging studies (skull base, intracranial, temporomandibular joint, and paranasal sinus) ($n = 516$), patients with clinically overt disease and diagnoses on clinical examination other than FNE ($n = 20$), diagnosis of malignancy on FNE ($n = 13$), and incorrect clinical information about the presence of otalgia after review of the electronic patient record ($n = 3$).

Of the remaining 235 patients who were included in the analysis, 65% were female and 35% male patients (female to male, 152 to 83). The mean \pm standard deviation age at the time of imaging was 52 ± 15.2 years (range, 8–90 years), and this included 4 patients <16 years old. All were referrals from secondary care, with 89% of requests from ear, nose, and throat specialists; head and neck surgeons; or oral and maxillofacial surgeons ($n = 210$). The remaining 11% of the requests came from other specialties, such as oncology, oral medicine, audiovestibular clinic, neurology, and rheumatology ($n = 25$). With regards to imaging modality, 54% of the patients underwent MR imaging ($n = 126$) and 46% underwent CT ($n = 109$) of the face and neck.

Otalgia Symptom Categories

The study cohort was grouped into 4 main categories: pure otalgia (20% [47/235]), otalgia with UAT symptoms (32% [76/235]), otalgia with other symptoms (35% [83/235]), and otalgia with a history of previous head and neck malignancy (13% [29/235]). Imaging was performed for bilateral otalgia in 8% (17/235), left-sided otalgia in 40% (95/235), and right-sided otalgia in 51% (120/235). No information on laterality was provided in 1% (3/235). The details of associated symptoms are provided in Tables 1 and 2. FNE findings were provided in 67% of the cases (156/235) and were categorized into normal or benign, indeterminate, or diagnostic, as illustrated in Table 3.

Analysis by Subgroup

Pure Otalgia. The pure otalgia group accounted for 20% of the total study cohort (47/235). Of these, 66% (31/47) had FNE as part of their clinical examination before imaging, which was indeterminate in 7 patients. No important abnormality was found on imaging in 98% (46/47). In 1 patient who had indeterminate findings on initial FNE (2%), the imaging outcome was also indeterminate

Table 1: Otolgia with UAT symptoms—Symptom type and number

UAT Symptoms	No.	Percentage
Total	87	100
Odynophagia	64	74
Dysphagia	7	8
Globus	6	7
Voice change	5	6
Nasal blockage	2	2
Epistaxis	2	2
Anosmia	1	1

Table 2: Otolgia with other symptoms—Symptom type and incidence

Other Symptoms	No.	Percentage
Total	84	100
Neck pain and/or swelling	31	37
Facial pain	16	19
Headache	11	13
Tinnitus	8	9
Hearing loss	6	7
Vertigo	4	5
Facial weakness and/or numbness	4	5
Trismus	3	4
Contralateral neck pain	1	1

Table 3: Categories of FNE findings

Benign	Indeterminate	Diagnostic
Reinke edema, candida, presbylaryngitis, interarytenoid edema, laryngopharyngeal reflux, rhinitis, lingual hyperplasia	Pooling in pyriform fossae, foci of soft-tissue prominence, asymmetry within the nasopharynx and/or larynx, shallow ulceration	Masses; ulcerated lesions; fixed, edematous vocal cords

and repeated FNE was subsequently performed, which was normal. The diagnostic yield of head and neck imaging for those who presented with pure otalgia, therefore, was 0%, and the management impact figure was 1% (normal repeated FNE), whereas the overall therapeutic impact of imaging was 0%. The details of this subgroup are illustrated in On-line Fig 1.

Otolgia with UAT Symptoms. The otalgia with UAT symptoms group accounted for 32% of the total study cohort (76/235). The FNE findings were normal or benign in 67% (51/76) and indeterminate in 20% (15/76). There was no documentation of FNE in the other 13% (10/76). No important abnormality was found on imaging in 79% (60/76). There was no imaging finding of UAT malignancy, whereas in 1 patient (1%) imaging demonstrated ipsilateral tonsillar enlargement, considered to be the cause of otalgia. In another patient (1%), imaging identified a moderate or major new finding unrelated to otalgia of a pituitary nodule, which, subsequently, was managed conservatively with MR imaging surveillance. There were 15 patients (20%) with indeterminate imaging findings, which then led to further investigations (panendoscopy, biopsy, tonsillectomy, 11; further imaging with MR and PET, 2; fine needle aspiration cytology, 1; repeated FNE, 1), but none revealed UAT malignancy. The details of this subgroup are illustrated in On-line Fig 2.

The total diagnostic yield of imaging in otalgia with UAT symptoms in the absence of overt malignancy detected on FNE, therefore, was 0% for UAT malignancy, 1% for any other cause of otalgia, and 1% for any other moderate or major findings unrelated to otalgia. With 16 patients in total undergoing further investigations based on the imaging findings, the management impact was 21%, but the total therapeutic impact was 0%.

Otolgia with Other Symptoms. The otalgia with other symptoms group accounted for 35% of the total study cohort (83/235). The FNE findings were normal or benign in 58% (48/83) and indeterminate in 5% (4/83). There was no documentation of FNE in the other 37% (31/83). No important abnormality was found on imaging in 88% (73/83). Two patients were found to have UAT malignancy on imaging (2%), neither of whom had undergone FNE as part of a clinical examination before being referred for imaging; 1 patient found to have a neck mass had refused to have FNE despite the medical recommendation, and the other patient, with trismus as an associated symptom, had been seen in a specialty setting in which FNE could not be offered as part of a clinical examination.

In another 4 patients (5%), imaging identified the underlying cause of otalgia, which included pathologic fracture of the cervical spine, ipsilateral severe sinonasal disease, ipsilateral tonsillar enlargement (subsequently confirmed reactive hyperplasia on histology), and Warthin tumor of the parotid. In a further 3 patients (4%), imaging detected moderate or major new findings unrelated to otalgia, including neck vein thrombosis, thyroglossal duct cyst, and calcified mediastinal thymus. In the remaining patient, the imaging outcome was indeterminate but further investigations

confirmed a benign pathology unrelated to otalgia (calcified thyroid nodule). All but 1 patient with indeterminate or important imaging findings had further investigations ($n = 2$), monitoring ($n = 1$), and/or surgical intervention ($n = 6$). The details of this subgroup are illustrated in On-line Fig 3.

The total diagnostic yield of imaging in otalgia with other symptoms in the absence of overt malignancy detected on FNE, therefore, was 2% for UAT malignancy, 5% for any other cause of otalgia, and 4% for any other moderate or major findings unrelated to otalgia. With 9 patients in total undergoing further investigation, monitoring, or intervention based on the imaging findings, the management impact was 11%. Overall, 5 patients who presented with otalgia with other symptoms underwent definitive therapeutic interventions, which led to a total therapeutic impact figure of 6%.

Otolgia with a History of Head and Neck Cancer. The otalgia with a history of head and neck cancer group accounted for 13% of the total study cohort (29/235). The FNE findings were normal or benign in 28% (8/29). In the other 72% (21/29), there was no documentation of FNE before imaging, a clear reason for this being recorded in only 3 patients (seen by a specialist unable to perform FNE, 2; no endoscope was available on day 1). No important abnormality was found on imaging in 48% (14/29). Ten

patients were found to have UAT malignancy on imaging (34%), 9 of whom had recurrences and the other had a new UAT primary. Of note, only 3 of these 10 patients had undergone FNE before imaging. In another patient (3%), imaging identified mandibular osteoradionecrosis as the underlying cause of otalgia. No other moderate or major findings were identified on imaging. There were 4 patients (14%) with indeterminate imaging findings, which then led to further investigations (further imaging with MR/PET, 2; biopsy, 1; FNE, 1), but none revealed UAT malignancy. The details of this subgroup are illustrated in On-line Fig 4.

The total diagnostic yield of imaging in otalgia with a history of head and neck cancer, therefore, was 34% for UAT malignancy and 3% for any other cause of otalgia. With 15 patients in total undergoing further investigations, monitoring, or interventions based on the imaging findings, the management impact was 52%. All 10 patients with UAT malignancy detected on imaging received further treatment, which led to a total therapeutic impact figure of 34%.

Summary Comparison of Significant Outcomes with and without a History of Head and Neck Cancer. The diagnostic yield of imaging for otalgia, with or without other symptoms, of patients who lacked a history of head and neck cancer, was 1% for UAT malignancy (2/206), 2% for abnormalities related to otalgia (5/206), and 2% for other moderate or major findings (4/206). This compared with 34% for UAT malignancy (10/29), 3% for abnormalities related to otalgia (1/29), and 0% for other moderate or major findings (0/29) in those with a history of head and neck cancer. The therapeutic impact increased from 2% in patients without head and neck cancer (5/206) to 34% in patients with head and neck cancer (10/29).

DISCUSSION

In almost 50% of patients, ear pain may be arising from disease distant to the ear.^{12,13} The mechanism of this secondary otalgia is still poorly understood. The “convergence-projection theory” is the most widely accepted potential pathophysiologic mechanism, whereby multiple nerves converge into a shared neural pathway, which results in the CNS being unable to distinguish the origin of the nociceptor stimulation.¹⁴ Sensory innervation of the peri-auricular region, external ear, and middle ear is derived from a range of cutaneous and cranial nerves, including branches of the trigeminal, facial, glossopharyngeal, and vagus nerves, as well as the cervical plexus and autonomic fibers. Sources of such referred pain, therefore, include the entire UAT, retro- and parapharyngeal regions, major salivary glands, thyroid gland, teeth, sinonasal region, temporomandibular joint, cervical spine, and thorax.^{1,5,15,16} Although the underlying cause of secondary otalgia is benign in most cases,^{6,15,17,18} the possibility of severe pathology such as UAT malignancy must always be considered.

When a patient presents with otalgia in the absence of clinically overt disease, CT or MR imaging of the face and neck has been proposed to evaluate for pathologies remote to the ear.^{1,19,20} However, there has been no previous study that addressed the overall diagnostic yield and impact on management decisions in this clinical scenario. It, therefore, is not surprising that there are currently no national imaging guidelines for otalgia.

Furthermore, otalgia is not represented as a clinical feature in either the UK iRefer²¹ or the American College of Radiology Appropriateness Criteria.²² Clinical reviews on the subject vary in their emphasis of imaging and at which point in the clinical pathway it should be considered.^{19,23-26} Some investigators have considered imaging to be appropriate after specialist review and in the presence of “red flag” clinical features (eg, weight loss and other UAT symptoms), particularly with prolonged and unilateral symptoms,^{17,23-26} though others state that it would be indicated in all patients who present with otalgia and a negative ear, nose, and throat examination.¹⁹

This issue has become of increasing importance in the context of guidelines and targets for rapid imaging turnaround required for patients with suspected head and neck cancer. This approach has been supported by evidence for a shorter time to diagnosis being associated with more favorable outcomes.²⁷ The 2005 iteration of the United Kingdom National Institute of Clinical Care Excellence guidelines²⁸ identified unexplained otalgia with normal otoscopy as a clinical presentation that required fast-track referral. Although otalgia was removed from the subsequent, more evidence-based 2015 United Kingdom National Institute of Clinical Care Excellence guidelines,²⁹ it remains a clinical criterion for rapid assessment within a number of clinical networks.⁸ A recent study of 5000 patients demonstrated a statistically significant association between prolonged otalgia with normal otoscopy and head and neck cancer, and the investigators argue for inclusion of this clinical presentation in future guidelines. The NHS England and NHS Improvement³⁰ 28-day faster diagnosis standard will further increase pressures on the imaging department to rapidly image and report for patients referred on these pathways.

Previous studies have addressed the final presumptive diagnosis in patients with otalgia and normal otoscopy being referred for specialist evaluation, with the subsequent diagnostic yield for UAT malignancy varying between 6% and 18%.^{15,31} However, it should be borne in mind that these figures represented the overall incidence of UAT malignancy and did not describe what proportion of the cancer diagnoses was made on imaging rather than on clinical assessment, including FNE. Because clinical pathways usually indicate that full specialist examination should be performed before imaging, what has yet to be elucidated is the true value of imaging of the face and neck in patients who present with otalgia but a normal clinical examination. Although a single case series has described infratemporal fossa malignancy in 2% of patients who presented with otalgia and normal ear, nose, and throat examination,²⁰ there has been no systematic approach to the imaging yield for all pathologies.

To the best of our knowledge, our study is the first to address the question of appropriateness of CT and MR imaging of the face and neck in patients with otalgia in the absence of clinically overt disease. Our results show that the contribution of imaging is negligible in those who present with pure otalgia, no other associated symptoms, and no history of head and neck cancer. The diagnostic yield and therapeutic impact of imaging are similarly very low in cases of otalgia with associated UAT or other symptoms, especially when there is no important finding on FNE. The situation in which imaging plays a significant role seems to be in the context of otalgia in patients with a history of

head and neck cancer. However, the figures obtained from our study cohort should be interpreted with caution, given the low rates of FNE being performed before referral for imaging. It may be that, if FNE had been carried out in all the cases, then the proportion of UAT malignancy detected on imaging because of new findings would have been lower. It was noted that a high proportion of patients (62%) with previous head and neck cancer proceeded straight to imaging without a clear reason for the lack of documented FNE outcomes. Clinicians should be reminded that, especially in this high-risk group, imaging should complement clinical findings rather than replace them.

Another area that is worth further discussion is how to interpret the management impact of imaging. Although it would seem at first glance that imaging had a relatively significant management impact in the otalgia with UAT symptoms group (21%), every patient in this group proceeded to further investigations on the basis of indeterminate imaging findings, with an ultimate diagnostic yield and therapeutic impact figures of 0% and 1%, respectively. The incidence of unrelated or “incidental” imaging findings in our cohort is not an unexpected phenomenon. Incidental findings have been found to be common in healthy volunteers in research studies, being documented in 3%–12% of neuroimaging studies and 30% of body imaging studies.⁹

Incidentally detected pathologies may become more prevalent relative to the symptomatic pathologies when there is a lower threshold for imaging patients. The implications of such discoveries will not always be positive and may cause the patient unnecessary anxiety. Furthermore, asymptomatic incidental abnormalities may trigger further investigations with potential risks and financial costs but without clear clinical benefit. We, therefore, would propose that, when evaluating increased requirements for imaging services, management impact figures should be analyzed not in isolation but in conjunction with diagnostic yields and therapeutic impact.

It is recognized that there are additional potential drivers and perceived benefits of imaging patients with otalgia that extend beyond the diagnostic yield. Such factors may relate to the clinician’s intolerance of uncertainty, fear of legal action, or perception that imaging is required to complete the patient episode. Patient expectation and the need for reassurance may also result in increased imaging requests. However, a systematic review of 5 randomized controlled trials, which included >1500 patients, showed little value of imaging in the reassurance of patients in primary care.³² The lack of data on the diagnostic yield of imaging in otalgia without clinically overt disease, combined with the aforementioned factors and cancer imaging targets, has led to increased demand on imaging services in recent years. It is hoped that the outcomes from our study will help establish a more evidence-based approach and efficient use of resources.

Limitations

We acknowledge that our study had a number of limitations. First, the retrospective design and the lack of current imaging guidelines for patients with otalgia led to some heterogeneity of the data available and likely variation in the approach to imaging these patients. Potential bias may have been introduced by the retrospective selection of the study group. Second, we did not follow those patients with otalgia and no clinically overt disease who had

not undergone imaging. Third, in excluding cases of targeted imaging studies, we made an assumption that they had specific clinical features of skull base, intracranial, temporomandibular joint, or paranasal sinus disease. Fourth, the variable use of either CT or MR imaging also may have led to bias because the imaging modalities vary in their diagnostic strengths; however, the dataset was equally divided between the 2 imaging modalities. Fifth, the availability of data on FNE findings before imaging was inconsistent, but we aimed to overcome this shortcoming by analyzing the documentation of imaging outcomes in both those patients with and without FNE having been performed.

CONCLUSIONS

To our knowledge, our study is the first to address the diagnostic yield, management impact, and therapeutic impact of imaging in otalgia without clinically overt disease. The diagnostic yield of imaging was extremely low for otalgia, with and without associated symptoms, but increased markedly when there was a history of head and neck cancer. Similarly, the therapeutic impact is very limited unless there is a history of head and neck cancer or when FNE cannot be performed. Analysis of this data will help rationalize imaging guidelines for patients with otalgia in the context of increasing demands on imaging services.

Disclosures: Steve E. J. Connor—UNRELATED: Grants/Grants Pending: Guy’s and St Thomas Charity, Comments: Grant awarded 2012 (last payment >24 months ago) for a research project on the use of DWI MRI in head and neck cancer follow up.* *Money paid to the institution.

REFERENCES

1. Chen RC, Khorsandi AS, Shatzkes DR, et al. **The radiology of referred otalgia.** *AJNR Am J Neuroradiol* 2009;30:1817–23 CrossRef Medline
2. Ely J, Hansen MR, Clark EC. **Diagnosis of ear pain.** *Am Fam Physician* 2008;77:621–28 Medline
3. Greenall C, Rhys R. **Radiology of Referred Otalgia.** *ENT and Audiology News* 2009;23:37–40
4. Kuttilla SJ, Kuttilla MH, Niemi PM, et al. **Secondary otalgia in an adult population.** *Arch Otolaryngol Head Neck Surg* 2001;127:401–05 CrossRef Medline
5. Weissman JL. **A pain in the ear: the radiology of otalgia.** *AJNR Am J Neuroradiol* 1997;18:1641–51 Medline
6. Jaber J, Leonetti J, Lawrason A, et al. **Cervical spine causes for referred otalgia.** *Otolaryngol Head Neck Surg* 2008;138:479–85 CrossRef Medline
7. Hersh S, Hersh JN. **Referred otalgia: a diagnostic conundrum in an aging population.** *Consultant* 2005;55:516–23
8. Pan-London Suspected Cancer Referral Guide - Head & Neck. <https://l-nelh-uks-wp05-wa.azurewebsites.net/wp-content/uploads/2019/04/Pan-London-Suspected-Cancer-Referral-Guide-Head-and-Neck.pdf>. Accessed November 24, 2019
9. The Royal College of Radiologists. *Management of Incidental Findings Detected During Research Imaging.* London: The Royal College of Radiologists; 2011
10. Fakhran S, Alhilali L, Branstetter BF IV. **Yield of CT angiography and contrast-enhanced MR imaging in patients with dizziness.** *AJNR Am J Neuroradiol* 2013;34:1077–81 CrossRef Medline
11. Loop J, Lusted LE. **American College of Radiology diagnostic efficacy studies.** *AJR Am J Roentgenol* 1978;131:173–79 CrossRef Medline
12. Yanagisawa K, Kveton JF. **Referred otalgia.** *Am J Otolaryngol* 1992;13:323–27 CrossRef Medline
13. Thaller S, De Silva A. **Otalgia with a normal ear.** *Am Fam Physician* 1987;36:129–36 Medline

14. Wright EF. **Referred craniofacial pain patterns in patients with temporomandibular disorder.** *J Am Dent Assoc* 2000;131:1307–15 CrossRef Medline
15. Fenton JE, Uzomefuna V, O'Rourke C, et al. **Applying the Ts of referred otalgia to a cohort of 226 patients.** *Clin Otolaryngol* 2018;43:937–40 CrossRef Medline
16. Scarbrough T, Day T, Williams T, et al. **Referred otalgia in head and neck cancer.** *Am J Clin Oncol* 2003;26:e157–62 CrossRef Medline
17. Rerucha C. **What is the differential diagnosis of otalgia in an adult with a normal ear examination?** *Evidence-Based Practice* 2016;19:15–16 CrossRef
18. Al-Sheikhli A. **Pain in the ear-with special reference to referred pain.** *J Laryngol Otol* 1980;94:1433–40 CrossRef Medline
19. Visvanathan V, Kelly G. **12 minute consultation: an evidence-based management of referred otalgia.** *Clin Otolaryngol* 2010;35:409–14 CrossRef Medline
20. Leonetti J, Li J, Smith PG. **Otalgia. An isolated symptom of malignant infratemporal tumors.** *Am J Otol* 1998;19:496–98 Medline
21. RCR iRefer guidelines. <https://www.rcr.ac.uk/clinical-radiology/being-consultant/rcr-referral-guidelines/about-irefer/irefer-england>. Accessed January 10, 2020
22. American College of Radiology ACR Appropriateness Criteria. <https://acsearch.acr.org/docs/69509/Narrative>. Accessed January 10, 2020
23. Harrison E, Cronin M. **Otalgia.** *Aust Fam Physician* 2016;45:493–97 Medline
24. Charlett S, Coatesworth A. **Referred otalgia: a structured approach to diagnosis and treatment.** *Int J Clin Pract* 2007;61:1015–21 CrossRef Medline
25. Earwood J, Rogers T, Rathjen N. **Ear pain: diagnosing common and uncommon causes.** *Am Fam Physician* 2018;97:20–27 Medline
26. Finnikin S, Mitchell-Innes A. **Recurrent otalgia in adults.** *BMJ* 2016;354:i3917 CrossRef Medline
27. Neal RD, Tharmanathan P, France B, et al. **Is increased time to diagnosis and treatment in symptomatic cancer associated with poorer outcomes? Systematic review.** *Br J Cancer* 2015;112(suppl 1):S92–107 CrossRef Medline
28. National Institute for Health and Care Excellence. *Referral Guidelines for Suspected Cancer.* London: National Institute for Health and Care Excellence; 2005. <http://www.nice.org.uk/guidance/cg27chapter/guidance#head-and-neck-cancer-including-thyroid-cancer>. Accessed January 10, 2020
29. National Institute for Health and Care Excellence. *Referral Guidelines for Suspected Cancer.* London: National Institute for Health and Care Excellence; 2015. <https://www.nice.org.uk/guidance/ng12/chapter/1-Recommendations-organised-by-site-of-cancer#head-and-neck-cancers>. Accessed January 10, 2020
30. NHS England and NHS Improvement. **Diagnosing cancer earlier and faster.** <https://www.england.nhs.uk/cancer/early-diagnosis/>. Accessed January 10, 2020
31. Tikka T, Pracy P, Paleri V. **Refining the head and neck cancer referral guidelines: a two-centre analysis of 4715 referrals.** *Clin Otolaryngol* 2016;41:66–75 CrossRef
32. van Ravesteijn H, van Dijk I, Darmon D, et al. **The reassuring value of diagnostic tests: a systematic review.** *Patient Educ Couns* 2012;86:3–8 CrossRef Medline

Diagnostic Value of Model-Based Iterative Reconstruction Combined with a Metal Artifact Reduction Algorithm during CT of the Oral Cavity

Y. Kubo, K. Ito, M. Sone, H. Nagasawa, Y. Onishi, N. Umakoshi, T. Hasegawa, T. Akimoto, and M. Kusumoto



ABSTRACT

BACKGROUND AND PURPOSE: Metal artifacts reduce the quality of CT images and increase the difficulty of interpretation. This study compared the ability of model-based iterative reconstruction and hybrid iterative reconstruction to improve CT image quality in patients with metallic dental artifacts when both techniques were combined with a metal artifact reduction algorithm.

MATERIALS AND METHODS: This retrospective clinical study included 40 patients (men, 31; women, 9; mean age, 62.9 ± 12.3 years) with oral and oropharyngeal cancer who had metallic dental fillings or implants and underwent contrast-enhanced ultra-high-resolution CT of the neck. Axial CT images were reconstructed using hybrid iterative reconstruction and model-based iterative reconstruction, and the metal artifact reduction algorithm was applied to all images. Finally, hybrid iterative reconstruction + metal artifact reduction algorithms and model-based iterative reconstruction + metal artifact reduction algorithm data were obtained. In the quantitative analysis, SDs were measured in ROIs over the apex of the tongue (metal artifacts) and nuchal muscle (no metal artifacts) and were used to calculate the metal artifact indexes. In a qualitative analysis, 3 radiologists blinded to the patients' conditions assessed the image-quality scores of metal artifact reduction and structural depictions.

RESULTS: Hybrid iterative reconstruction + metal artifact reduction algorithms and model-based iterative reconstruction + metal artifact reduction algorithms yielded significantly different metal artifact indexes of 82.2 and 73.6, respectively (95% CI, 2.6–14.7; $P < .01$). The latter algorithms resulted in significant reduction in metal artifacts and significantly improved structural depictions ($P < .01$).

CONCLUSIONS: Model-based iterative reconstruction + metal artifact reduction algorithms significantly reduced the artifacts and improved the image quality of structural depictions on neck CT images.

ABBREVIATIONS: IR = iterative reconstruction; hybrid-IR+MAR = combination of hybrid iterative reconstruction and metal artifact reduction algorithms; MAR = metal artifact reduction algorithms; MBIR = model-based iterative reconstruction; MBIR+MAR = combination of model-based iterative reconstruction and metal artifact reduction algorithms; U-HRCT = ultra-high-resolution CT

Many patients have metallic dental fillings or implants, which are highly attenuating objects that often cause metal artifacts on CT and thus limit the diagnostic value of these data by reducing the image quality.¹ On CT, these artifacts comprise

areas of low or high density that appear as streaks or radial foci with variable levels of brightness.² Metal artifacts can also cause areas of whiteout, where CT numbers around the metallic object exceed the maximum CT number range, or blackout, where no image data are visible. Consequently, several artifact reduction methods have been developed to improve the quality of images produced by modern CT systems.

Iterative reconstruction (IR) was initially developed to preserve the quality of a CT image while reducing the level of noise.³ Although iterative reconstruction methods have been available since 1970, the limited computational power available at that time meant that this option was not feasible in clinical settings due to the overly long duration of image reconstruction. Therefore, a simpler approach (filtered back-projection) was used because it allowed faster processing and greater feasibility in clinical settings. Iterative reconstruction did not reappear until 2009.⁴

Received April 13, 2020; accepted after revision July 7.

From the Department of Diagnostic Radiology (Y.K., K.I., M.S., H.N., Y.O., N.U., T.H., M.K.), National Cancer Center Hospital, Tokyo, Japan; Department of Cancer Medicine (Y.K., T.A.), Jikei University Graduate School of Medicine, Tokyo, Japan; and Division of Radiation Oncology and Particle Therapy (T.A.), National Cancer Center Hospital East, Kashiwa, Japan.

The study was supported by a grant from Canon Medical Systems.

Paper previously presented, in part, at: Annual Meeting of the European Society of Head and Neck Radiology, October 3–5, 2019; Palermo, Italy.

Please address correspondence to Yuko Kubo, MD, 5-1-1 Tsukiji, Chuo-ku, Tokyo, 104-0045 Japan; e-mail: yukkubo@ncc.go.jp

Indicates open access to non-subscribers at www.ajnr.org

<http://dx.doi.org/10.3174/ajnr.A6767>

Unlike conventional filtered back-projection, which is based on simpler mathematic assumptions of the tomographic imaging system,⁵ IR is used to generate a set of synthesized projections by accurately modeling the data-collection process in CT. Hybrid iterative reconstruction (hybrid-IR) approaches apply some noise-reduction techniques to sinograms and image spaces. Hybrid-IR provides much better image quality and potentially enables reductions in radiation doses.⁶⁻⁸ Recently, the evolution of hybrid-IR led to model-based iterative reconstruction (MBIR). This fully iterative algorithm minimizes the difference between the measured original sinogram and the sinogram reproduced by forward projection and uses a more complex system of prediction models that account for scanner hardware parameters, the conebeam trajectory, and the photoelectric trajectory.^{9,10} Compared with earlier hybrid-IR techniques, MBIR provides superior image resolution at lower radiation doses.¹¹⁻¹⁷ MBIR has also been reported to constitute a useful approach for metal artifact reduction.¹⁸⁻²¹

Another approach for the reduction of metal artifacts involves the use of dedicated metal artifact reduction algorithms (MAR). With time, researchers have described the remarkable ability of MAR to enhance the visualization of various target lesions by reducing metallic artifacts.^{18,22-29} Therefore, the intended effect of MAR has been established, and the use of CT with MAR comprises the current clinical standard.

Recent advances have made possible the combination of MBIR and MAR. This study aimed to clarify differences in the degree of metal artifact reduction and depiction of oral cavity structures between hybrid-IR and MBIR when both techniques were combined with MAR and to evaluate the ability of the latter to improve image quality and diagnostic value.

MATERIALS AND METHODS

This retrospective single-institution study was approved by the institutional review board of the National Cancer Center Hospital, Tokyo, Japan. The institutional review board waived the requirement for written informed consent from patients due to the design of the study and the use of anonymized patient records and data.

Patient Characteristics

The inclusion criteria were the diagnosis of oral or oropharyngeal carcinoma with tumors of >2 cm (longest diameter) and evaluation by contrast-enhanced ultra-high-resolution CT (U-HRCT) at our hospital between October 2017 and August 2018. The exclusion criteria were as follows: 1) a history of an oral cavity operation, 2) a lack of dental fillings or implants, and 3) a lack of raw CT data required for reconstruction.

For all patients, the age, sex, tumor location, histopathologic cancer type, and the number and sites of dental fillings or implants were determined. In cases involving the placement of dental fillings on multiple adjacent teeth, such as dental bridges, the number of originally treated teeth was counted. The size of the dental fillings or implants was not considered because these were ≤ 12 mm per tooth and thus equal to or less than the size of the original tooth.

CT

All images were acquired on a U-HRCT scanner (Aquilion Precision, Canon Medical Systems) in super-high-resolution

mode (1792 channels/detector row, 0.25×160 rows; matrix size, 1024). The scanning parameters were a rotation time of 0.5 seconds, pitch factor of 0.569, scanning FOV of 24 cm, and voltage of 120 kV. Automatic tube current modulation was used in all examinations, resulting in a mean tube current of 272.4 ± 38.2 mA, mean CT dose index of 14.5 ± 1.3 mGy, and mean dose-length product of 511.9 ± 57.4 mGy. A body weight-adapted volume of iodinated contrast medium (iopromide, Ultravist, 370 mg/mL; Bayer HealthCare) was administered intravenously at a flow rate of 1.6–2.0 mL/s for 50 seconds. The scan was acquired at a delay of 80 seconds after the commencement of contrast injection.

Axial images of the neck were reconstructed from helical scan data using the following algorithms: hybrid-IR (Adaptive Iterative Dose Reduction 3D [AIDR3D]; Canon Medical Systems) and MBIR (Forward projected model-based Iterative Reconstruction SoluTion [FIRST]; Canon Medical Systems); then, MAR (Single Energy Metal Artifact Reduction [SEMAR]; Canon Medical Systems) was applied to all images. Finally, hybrid-IR+MAR and MBIR+MAR were performed. A total of 80 image sets (40 patients) were obtained by reconstruction. AIDR3D reconstructions of areas of soft tissue were created using the standard reconstruction FC13 kernel. FIRST was reconstructed using a BODY kernel equivalent to a standard reconstruction kernel. The following parameters were identical across the reconstruction algorithms: z-axis range, frontal sinus to cricoid cartilage; section thickness, 3.0 mm; section interval, 3.0 mm; and reconstruction FOV, 24 cm.

Quantitative Image Analysis

The quantitative image analyses were performed by a board-certified radiologist (Y.K., with 14 years of experience). Circular ROIs were placed over the tongue apex in an area containing metal artifacts (~ 400 mm²) and over the nuchal muscle at the level of the hyoid bone in an area without metal artifacts (~ 100 mm²). The copy-paste function was used to ensure that the sizes and locations of the ROIs were identical across both reconstruction algorithms applied to data from a single patient. The mean CT attenuation value (Hounsfield units) and SD of all ROIs were measured twice, and the average value of the 2 corresponding measures was applied.

The SD of the ROI is a widely used measure of noise on radiographic images.³⁰ When used in biologic tissue, the SD represents a combination of the tissue heterogeneity and noise (which may also be caused by metal). In a section containing a metal object, the SD is affected by both the image noise and the metal artifacts. Calculating the index between the SDs of the muscle (no metal artifacts) and tongue (metal artifacts) reduces the influence of tissue heterogeneity, though this assumes a consistent level of tissue heterogeneity. According to previous studies,^{31,32} the artifact index (AI) used to quantify the severity of metal artifacts is defined as

$$AI = [(SD_{\text{TONGUE}})^2 - (SD_{\text{MUSCLE}})^2]^{1/2},$$

where SD_{TONGUE} and SD_{MUSCLE} denote the SD of the tongue apex and nuchal muscle, respectively.

The number of reconstructed CT slices was counted, and the time required per CT section reconstructed by hybrid-IR+MAR or MBIR+MAR was measured.

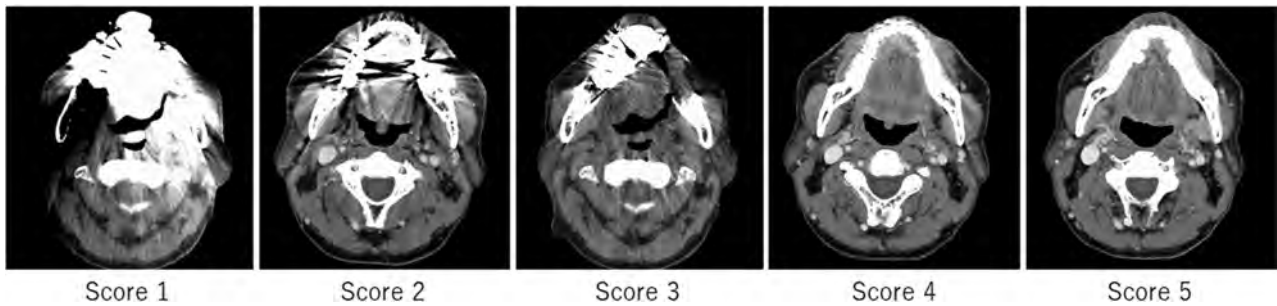


FIG 1. Representative CT images of the degree of metal artifact reduction. The image quality of metal artifact reduction was scored using the following 5-point scale: 1, severe metal artifacts in a large area; 2, severe metals artifact in a small area; 3, moderate metal artifacts; 4, minimal metal artifacts; and 5, no metal artifacts.

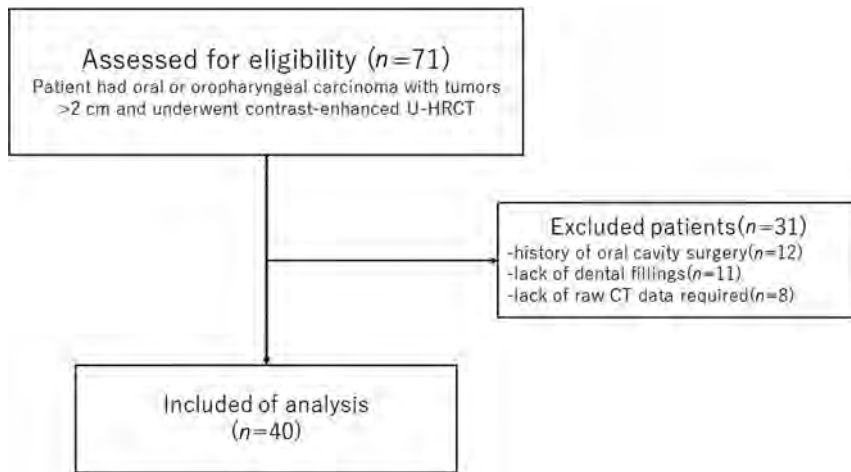


FIG 2. Flow diagram of the inclusion of potentially eligible patients.

Qualitative Analyses

Three board-certified radiologists (N.U., T.H., and Y.O., with 3, 8, and 9 years of experience, respectively) performed a qualitative analysis of the CT images in consensus. All readers were blinded to the patient demographics and CT parameters and given standardized instructions and training on image sets from 5 patients not included in this study. The readers used the same monitor (RadiForce RX440; EIZO), and the study images were presented in random order on a preset soft-tissue window (window width and level, 325 and 60 HU, respectively).

The readers evaluated the image-quality scores of metal artifact reduction and the depictions of representative structures (apex and base of the tongue, parapharyngeal space, superior portion of the internal jugular chain, parotid gland) on a 5-point scale (5, no artifacts/excellent visualization; 4, minimal artifacts/good visualization; 3, moderate metal artifacts/acceptable visualization for diagnosis; 2, severe metal artifacts in a small area/poor visualization; and 1, severe metal artifacts in a large area/no visualization), as shown in Fig 1. Finally, the readers assigned a diagnostic tumor stage according to the criteria of the American Joint Committee on Cancer, *Cancer Staging Manual*, 8th edition³³ and examined the correlation between the qualitative metal artifact reduction score and the number of dental fillings or implants in each patient.

Statistical Analysis

The SPSS Statistics 25 software package (IBM) was used to perform the statistical analyses. The paired Student *t* test was used to assess quantitative differences among the CT images reconstructed using hybrid-IR+MAR and MBIR+MAR. The Wilcoxon signed rank test was used to evaluate qualitative differences in image-quality scores between the 2 reconstruction algorithms. In the qualitative analysis, we calculated each of the weighted κ statistics for all combinations of the 2 readers to assess the degree of agreement among the 3 readers (ie, interobserver agreement). κ statistics of 0.81–1.00, 0.61–0.80, 0.41–0.60, 0.21–0.40, or 0.00–0.20 were interpreted as excellent, substantial, moderate, fair, or poor agreement, respectively.³⁴

The relationship between the number of dental fillings or implants and the metal artifact reduction image-quality score in the qualitative analysis was analyzed by calculating the Spearman rank correlation coefficient. Specifically, using Excel 2016 (Microsoft), we created an approximation curve by plotting the mean scores of the 3 readers that corresponded to the number of dental fillings or implants on a scatter diagram. The level of statistical significance was set at $P < .05$.

RESULTS

Patient Characteristics

Figure 2 presents the flow diagram used to determine the inclusion of potentially eligible patients. Overall, 40 patients were included. Table 1 presents the additional demographic and clinical characteristics of the study population. The number of metallic dental fillings or implants per patient ranged from 1 to 23 (median, 11). These fillings or implants were bilateral, right-sided, and left-sided in 37, 2, and 1 patient, respectively.

Quantitative Analyses

Table 2 presents the findings from quantitative image analyses. At the apex of the tongue and nuchal muscle, the mean CT

Table 1: Characteristics of the study population

Variable	Value
Age (mean) (yr)	62.9 ± 12.3
Sex (male/female)	31:9
Tumor location	
Oral tongue	11
Tonsil	11
Floor of mouth	6
Palate	4
Base of tongue	4
Gingiva	3
Buccal mucosa	1
Histopathologic type	
Squamous cell carcinoma	32
Malignant lymphoma	3
Clear cell carcinoma	2
Adenocarcinoma	1
Adenosquamous cell carcinoma	1
Mucoepidermoid carcinoma	1

Table 2: Quantitative evaluation of CT attenuation (HU) of the apex of the tongue and nuchal muscle

	Hybrid-IR+MAR (Mean)	MBIR+MAR (Mean)	Difference	
			95% CI	P Value ^a
Mean of apex of the tongue (HU)	103.7 ± 52.5	91.9 ± 50.6	8.2–15.4	<.01 ^b
Mean of nuchal muscle (HU)	64.9 ± 6.7	64.0 ± 6.7	0.1–1.5	.025 ^b
SD of apex of the tongue (HU)	82.9 ± 56.0	74.1 ± 64.1	2.7–14.8	<.01 ^b
SD of nuchal muscle (HU)	8.9 ± 1.6	7.5 ± 2.0	1.1–1.7	<.01 ^b

^a Paired t test.^b Significant difference.

attenuation value and SD from MBIR+MAR were significantly lower than those from hybrid-IR+MAR ($P < .01$). At the apex of the tongue, hybrid-IR+MAR and MBIR+MAR yielded mean metal artifact index values of 82.2 (95% CI, 64.2–100.2) and 73.6 (95% CI, 53.0–94.1), respectively, and these values differed significantly between the 2 algorithms (95% CI, 2.6–14.7; $P < .01$). Notably, MBIR+MAR led to a reduction of 11% in the metal artifact index relative to hybrid-IR+MAR (Fig 3).

The median number of CT slices reconstructed was 102 (range, 83–118). The reconstruction times by hybrid-IR+MAR and MBIR+MAR were 2.1 and 37.6 seconds per section, respectively. In other words, MBIR+MAR required a reconstruction time >17 times longer than that of hybrid-IR+MAR.

Qualitative Analyses

The weighted κ statistic revealed excellent interobserver agreement among the 3 readers (κ range, 0.88–0.98). A comparison of the metal artifact reduction image-quality scores revealed that MBIR+MAR yielded significant reductions in metal artifacts compared with hybrid-IR+MAR ($P < .01$). Figure 4 demonstrates that MBIR+MAR improved the delineation of the oral structures and oral cavity cancers by significantly reducing metal artifacts relative to those produced by hybrid-IR+MAR.

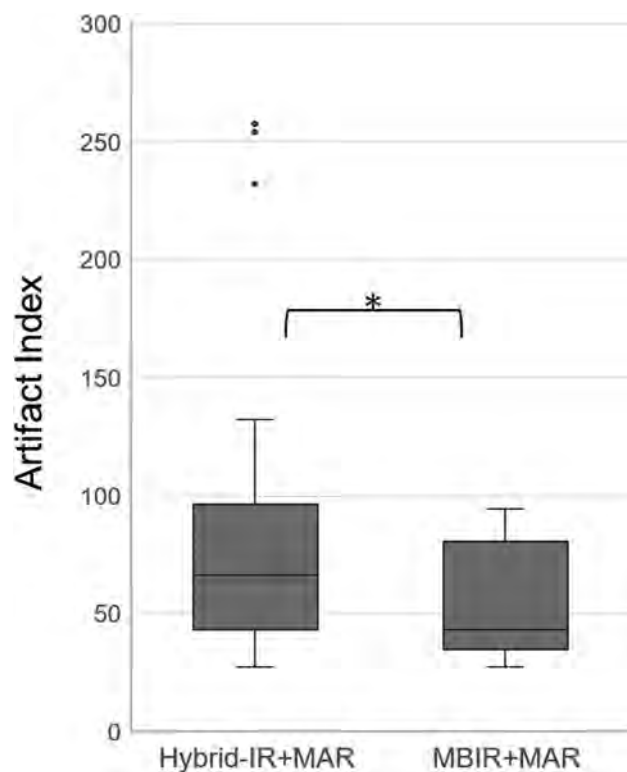
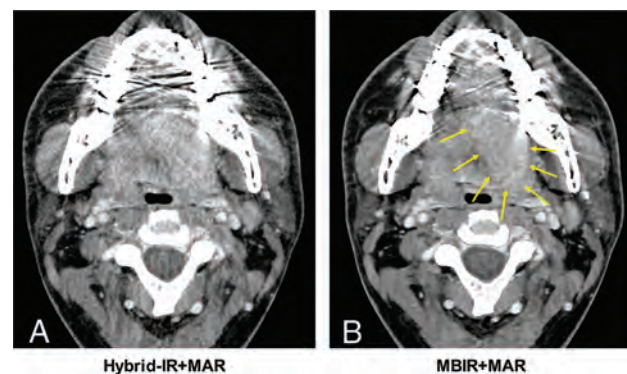
**FIG 3.** Boxplot comparison of the artifact index values calculated using the 2 reconstruction algorithms: hybrid-IR+MAR and MBIR+MAR. The asterisk indicates a significant difference ($P < .01$).**FIG 4.** Axial CT images of a 32-year-old man with left-tongue cancer. Reconstruction was performed using hybrid-IR+MAR (A) and MBIR+MAR (B). As shown, MBIR+MAR provided superior reduction of dental artifacts and a better depiction of the tumor (arrows).

Table 3 presents the image-quality scores of the depicted neck structures. All representative structures except the apex of the tongue had a mean score of ≥ 3 , which was within the identifiable visual level; the apex of the tongue only had a score of ≥ 3 using MBIR+MAR. Comparisons revealed significant differences in the average scores obtained using the 2 reconstruction algorithms. MBIR+MAR yielded higher average scores for all representative structural depictions compared with hybrid-IR+MAR.

Finally, the approximate power curve indicated a negative relationship between the number of dental fillings or implants and the metal artifact reduction image-quality score, regardless of

Table 3: Qualitative evaluation of image-quality scores of representative structures

Representative Structures	Hybrid-IR+MAR (Mean)	MBIR+MAR (Mean)	P Value ^a
Apex of the tongue	2.78 ± 0.72	3.02 ± 0.75	<.01 ^b
Base of the tongue	4.11 ± 0.29	4.27 ± 0.41	<.01 ^b
Parapharyngeal space	4.58 ± 0.33	4.68 ± 0.27	<.01 ^b
Superior portion of internal jugular vein	4.77 ± 0.24	4.88 ± 0.18	<.01 ^b
Parotid gland	4.50 ± 0.40	4.67 ± 0.37	<.01 ^b

^a Wilcoxon signed rank test.

^b Significant difference.

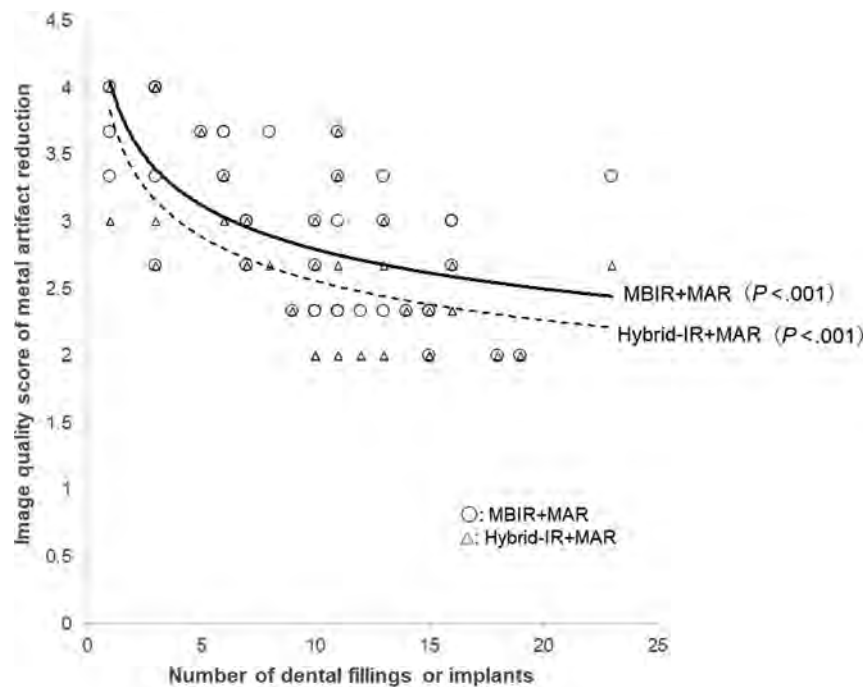


FIG 5. Analysis of the correlation between the image-quality score of artifact reduction and the number of dental fillings or implants between the 2 reconstruction algorithms: hybrid-IR+MAR and MBIR+MAR.

the reconstruction algorithm used. Higher scores were achieved with MBIR+MAR than with hybrid-IR+MAR (Fig 5). The cancer tumor stage diagnoses did not differ significantly with respect to the type of reconstruction algorithm.

DISCUSSION

This study aimed to compare the CT image quality achieved using a combination of MBIR and MAR versus that achieved with a combination of hybrid-IR and MAR in a sample of patients with oral or oropharyngeal cancer. Our quantitative analysis demonstrated that MBIR+MAR significantly reduced both the mean CT attenuation at the apex of the tongue and the metal artifact index compared with hybrid-IR+MAR. Also, our qualitative analysis demonstrated that MBIR+MAR yielded a more significant reduction of metal artifacts in the oral cavity than hybrid-IR+MAR. In other words, objective and subjective *in vivo* evaluations revealed significantly better artifact reduction and image quality with MBIR+MAR relative to hybrid-IR+MAR.

CT is considered a first-line diagnostic technique for oral cancer because of its broad availability, capacity for whole-body tumor staging, and good overall detection of sensitivity and specificity.³⁵ However, it is essential to achieve an excellent image quality with minimal artifacts despite the presence of metal dental fillings or implants. Prior studies indicated a superior reduction of dental artifacts caused by dental hardware or diverse maxillofacial metal implants when several MAR algorithms from major vendors were used, compared with standard reconstruction.²⁴⁻²⁹ However, MAR algorithms may introduce new artifacts into the image. These new artifacts can appear as defects or blurring around metal hardware in the bone window.^{26,27} Recently, several clinical studies reported that the combination of spectral detector CT (or dual-energy CT) with virtual monoenergetic images and MAR provided optimal artifact reduction and improved diagnostic imaging assessments in patients with dental implants and bridges or metallic dental prostheses.^{36,37}

As noted previously, the MBIR algorithm is a revolutionary reconstruction technology that uses various models and repeats the subtraction of original raw data after forward projection to yield a reconstructed image that differs minimally from the raw data. In addition to reducing image noise, only the MBIR algorithm reduces streak and beam-hardening artifacts, respectively.¹⁹ In a previous study, MBIR similarly reduced metal artifacts in the pelvis, spine, oral cavity, and extremities, which was to a greater extent than filtered back-projection or hybrid-IR.¹⁸⁻²⁰ Previous reports indicated a better reduction of metal artifacts when hybrid-IR+MAR was used, compared with MBIR without MAR.^{21,38} These results suggest that both MBIR and MAR can effectively reduce metal artifacts. Therefore, this *in vivo* study investigated the usefulness of MBIR+MAR for reducing metal artifacts in the oral cavity. We found that compared with hybrid-IR+MAR, MBIR+MAR provided better representations of normal neck structures and reduced metal artifacts. We attribute the improved image quality achieved with MBIR+MAR to the incorporation of MBIR settings such as the focus size, detector size, and voxel size, which would improve the spatial resolution. In previous analyses, Wellenberg et al³⁹ and Neroladaki et al⁴⁰ reported that MBIR+MAR significantly reduced orthopedic metal artifacts on pelvic CT images produced by other vendors. Although the results of those studies were consistent with our findings, the

methods differed from ours in that either phantoms or small numbers of large orthopedic metal implants were used.

A previous phantom study observed that the metal artifacts increased and the CT image accuracy decreased as the number of metal implants in the oral cavity increased.⁴¹ From in our vivo study, we also concluded that the metal artifacts worsened as the number of dental fillings increased. MBIR+MAR was relatively less affected by an increased number of dental fillings or implants. Overall, our results demonstrate the specific clinical impact of the combination of MBIR and MAR, even though the metallic artifacts could not be removed completely. Specifically, this in vivo study revealed a reduction of metal artifacts on CT images of the neck region when using MBIR+MAR.

Our study had some limitations: First, U-HRCT, which first became commercially available in 2017, uses smaller detector elements equivalent to a quarter of the area of the elements in a conventional CT detector. In a previous report, U-HRCT with improved spatial resolution was shown to reduce the artifacts associated with calcified lesions in coronary arteries.⁴² Theoretically, U-HRCT with small detector elements would affect metal artifact reduction by improving the spatial resolution. In our study, however, all patients were scanned using U-HRCT; therefore, we could not evaluate the specific reduction of metal artifacts by U-HRCT. Second, in addition to dental fillings or implants, metal plates and screws used in postoperative applications are a major cause of image degradation and a main obstacle to the follow-up of local recurrence in patients with oral cancer. However, these devices were set as an exclusion criterion in this study. Third, the patient population was relatively small and derived from a single institution, and the study design was retrospective. Further studies with much larger samples are needed to reject null hypotheses with clinically negligible differences.⁴³ Fourth, the inclusion of only patients with oropharyngeal and oral cancers with solid tumors of >2 cm might have led to selection bias. Ideally, we would have included early cancers because these would be most susceptible to metal artifacts. Finally, although MBIR+MAR has some advantages over hybrid-IR+MAR, as demonstrated in our study, it is also disadvantaged by significant computational requirements. Consequently, a longer reconstruction period is required. Future studies should aim to reduce the reconstitution time and increase the practical application of MBIR+MAR.

CONCLUSIONS

The combination of MBIR and MAR enabled the significant reduction of metal artifacts during oral cavity CT. Moreover, this reconstruction algorithm improved the depiction of structures in the neck with a minimal dependence on the number of dental fillings or implants.

Disclosures: Yuko Kubo—RELATED: Grant: Canon Medical Systems.* Masahiko Kusumoto—RELATED: Grant: Canon Medical Systems*; UNRELATED: Payment for Lectures Including Service on Speakers Bureaus: Ono Pharmaceutical, AstraZeneca KK, MSD KK. Comments: I received honoraria for lecture fees from Ono Pharmaceutical, AstraZeneca KK, and MSD KK. Miyuki Sone—RELATED: Grant: Canon Medical Systems.* *Money paid to the institution.

REFERENCES

1. Goerres GW, Hany TF, Kamel E, et al. **Head and neck imaging with PET and PET/CT: artefacts from dental metallic implants.** *Eur J Nucl Med Mol Imaging* 2002;29:367–70 CrossRef Medline
2. Barrett JF, Keat N. **Artifacts in CT: recognition and avoidance.** *Radiographics* 2004;24:1679–91 CrossRef Medline
3. Ravishankar S, Ye JC, Fessler JA. **Image reconstruction: from sparsity to data-adaptive methods and machine learning.** *Proc IEEE Inst Electr Electron Eng* 2020;108:86–109 CrossRef Medline
4. Willemink MJ, Noel PB. **The evolution of image reconstruction for CT: from filtered back projection to artificial intelligence.** *Eur Radiol* 2019;29:2185–95 CrossRef Medline
5. Herman GT. *Fundamentals of computerized tomography: image reconstruction from projections.* Springer-Verlag: London, 2009 CrossRef
6. Singh S, Kalra MK, Hsieh J, et al. **Abdominal CT: comparison of adaptive statistical iterative and filtered back projection reconstruction techniques.** *Radiology* 2010;257:373–83 CrossRef Medline
7. Gervaise A, Osemont B, Lecocq S, et al. **CT image quality improvement using adaptive iterative dose reduction with wide-volume acquisition on 320-detector CT.** *Eur Radiol* 2012;22:295–301 CrossRef Medline
8. Martinsen ACT, Sæther HK, Hol PK, et al. **Iterative reconstruction reduces abdominal CT dose.** *Eur J Radiol* 2012;81:1483–87 CrossRef Medline
9. Yu Z, Thibault JB, Bouman CA, et al. **Fast model-based X-ray CT reconstruction using spatially nonhomogeneous ICD optimization.** *IEEE Trans Image Process* 2011;20:161–75 CrossRef Medline
10. Fleischmann D, Boas FE. **Computed tomograph: old ideas and new technology.** *Eur Radiol* 2011;21:510–17 CrossRef Medline
11. Chang W, Lee JM, Lee K, et al. **Assessment of a model-based, iterative reconstruction algorithm (MBIR) regarding image quality and dose reduction in liver computed tomography.** *Invest Radiol* 2013;48:598–606 CrossRef Medline
12. Goodenberger MH, Wagner-Bartak NA, Gupta S, et al. **Computed tomography image quality evaluation of a new iterative reconstruction algorithm in the abdomen (adaptive statistical iterative reconstruction-V): a comparison with model-based iterative reconstruction, adaptive statistical iterative reconstruction, and filtered back projection reconstructions.** *J Comput Assist Tomogr* 2018;42:184–90 CrossRef Medline
13. Noda Y, Goshima S, Koyasu H, et al. **Renovascular CT: comparison between adaptive statistical iterative reconstruction and model-based iterative reconstruction.** *Clin Radiol* 2017;72:901.e913–19 CrossRef Medline
14. Smith EA, Dillman JR, Goodsitt MM, et al. **Model-based iterative reconstruction: effect on patient radiation dose and image quality in pediatric body CT.** *Radiology* 2014;270:526–34 CrossRef Medline
15. Taguchi N, Oda S, Imuta M, et al. **Model-based iterative reconstruction in low-radiation-dose computed tomography colonography: preoperative assessment in patients with colorectal cancer.** *Acad Radiol* 2018;25:415–22 CrossRef Medline
16. Yasaka K, Katsura M, Akahane M, et al. **Model-based iterative reconstruction and adaptive statistical iterative reconstruction: dose-reduced CT for detecting pancreatic calcification.** *Acta Radiol Open* 2016;5:205846011662834 CrossRef Medline
17. Yuki H, Oda S, Utsunomiya D, et al. **Clinical impact of model-based type iterative reconstruction with fast reconstruction time on image quality of low-dose screening chest CT.** *Acta Radiol* 2016;57:295–302 CrossRef Medline
18. De Crop A, Casselman J, Van Hoof T, et al. **Analysis of metal artifact reduction tools for dental hardware in CT scans of the oral cavity: kVp, iterative reconstruction, dual-energy CT, metal artifact reduction software—does it make a difference?** *Neuroradiology* 2015;57:841–49 CrossRef Medline
19. Boudabbous S, Arditi D, Paulin E, et al. **Model-based iterative reconstruction (MBIR) for the reduction of metal artifacts on CT.** *AJR Am J Roentgenol* 2015;205:380–85 CrossRef Medline

20. Kuya K, Shinohara Y, Kato A, et al. **Reduction of metal artifacts due to dental hardware in computed tomography angiography: assessment of the utility of model-based iterative reconstruction.** *Neuroradiology* 2017;59:231–35 CrossRef Medline
21. Yasaka K, Kamiya K, Irie R, et al. **Metal artefact reduction for patients with metallic dental fillings in helical neck computed tomography: comparison of adaptive iterative dose reduction 3D (AIDR 3D), forward-projected model-based iterative reconstruction solution (FIRST) and AIDR 3D with single-energy metal artefact reduction (SEMAR).** *Dentomaxillofac Radiol* 2016;45:20160114 CrossRef Medline
22. Li H, Noel C, Chen H, et al. **Clinical evaluation of a commercial orthopedic metal artifact reduction tool for CT simulations in radiation therapy.** *Med Phys* 2012;39:7507–17 CrossRef Medline
23. Brook OR, Gourtsoyianni S, Brook A, et al. **Spectral CT with metal artifacts reduction software for improvement of tumor visibility in the vicinity of gold fiducial markers.** *Radiology* 2012;263:696–705 CrossRef Medline
24. Lell MM, Meyer E, Kuefner MA, et al. **Normalized metal artifact reduction in head and neck computed tomography.** *Invest Radiol* 2012;47:415–21 CrossRef Medline
25. Kidoh M, Nakaura T, Nakamura S, et al. **Reduction of dental metallic artefacts in CT: value of a newly developed algorithm for metal artefact reduction (O-MAR).** *Clin Radiol* 2014;69:e11–16 CrossRef Medline
26. Diehn FE, Michalak GJ, DeLone DR, et al. **CT dental artifact: comparison of an iterative metal artifact reduction technique with weighted filtered back-projection.** *Acta Radiol Open* 2017;6:205846011774327 CrossRef Medline
27. Hakim A, Slotboom J, Lieger O, et al. **Clinical evaluation of the iterative metal artefact reduction algorithm for post-operative CT examination after maxillofacial surgery.** *Dentomaxillofac Radiol* 2017;46:20160355 CrossRef Medline
28. Weiß J, Schabel C, Bongers M, et al. **Impact of iterative metal artifact reduction on diagnostic image quality in patients with dental hardware.** *Acta Radiol* 2017;58:279–85 CrossRef Medline
29. Niehues SM, Vahldiek JL, Tröltzsch D, et al. **Impact of single-energy metal artifact reduction on CT image quality in patients with dental hardware.** *Comput Biol Med* 2018;103:161–66 CrossRef Medline
30. Lubner MG, Pickhardt PJ, Tang J, et al. **Reduced image noise at low-dose multidetector CT of the abdomen with prior image constrained compressed sensing algorithm.** *Radiology* 2011;260:248–56 CrossRef Medline
31. Lin XZ, Miao F, Li JY, et al. **High-definition CT Gemstone spectral imaging of the brain: initial results of selecting optimal monochromatic image for beam-hardening artifacts and image noise reduction.** *J Comput Assist Tomogr* 2011;35:294–97 CrossRef
32. Wang Y, Qian B, Li B, et al. **Metal artifacts reduction using monochromatic images from spectral CT: evaluation of pedicle screws in patients with scoliosis.** *Eur J Radiol* 2013;82:e360–66 CrossRef Medline
33. Lydiatt WM, Patel SG, O'Sullivan B, et al. **Head and neck cancers: major changes in the American Joint Committee on Cancer Eighth Edition Cancer Staging Manual.** *CA Cancer J Clin* 2017;67:122–37 CrossRef Medline
34. Svanholm H, Starklint H, Gundersen HJ, et al. **Reproducibility of histomorphologic diagnoses with special reference to the kappa statistic.** *APMIS* 1989;97:689–98 CrossRef Medline
35. Blatt S, Ziebart T, Krüger M, et al. **Diagnosing oral squamous cell carcinoma: How much imaging do we really need? A review of the current literature.** *J Craniomaxillofac Surg* 2016;44:538–49 CrossRef Medline
36. Cha J, Kim HJ, Kim ST, et al. **Dual-energy CT with virtual monochromatic images and metal artifact reduction software for reducing metallic dental artifacts.** *Acta Radiol* 2017;58:1312–19 CrossRef Medline
37. Laukamp KR, Zopfs D, Lennartz S, et al. **Metal artifacts in patients with large dental implants and bridges: combination of metal artifact reduction algorithms and virtual monoenergetic images provides an approach to handle even strongest artifacts.** *Eur Radiol* 2019;29:4228–38 CrossRef Medline
38. Toso S, Laurent M, Lozeron ED, et al. **Iterative algorithms for metal artifact reduction in children with orthopedic prostheses: preliminary results.** *Pediatr Radiol* 2018;48:1884–90 CrossRef Medline
39. Wellenberg RH, Boomsma MF, van Osch JA, et al. **Computed tomography imaging of a hip prosthesis using iterative model-based reconstruction and orthopaedic metal artefact reduction: a quantitative analysis.** *J Comput Assist Tomogr* 2016;40:971–78 CrossRef Medline
40. Neroladaki A, Martin SP, Bagetakos I, et al. **Metallic artifact reduction by evaluation of the additional value of iterative reconstruction algorithms in hip prosthesis computed tomography imaging.** *Medicine* 2019;98:e14341 CrossRef Medline
41. Tsuchida Y, Takahashi H, Watanabe H, et al. **Effects of number of metal restorations and mandibular position during computed tomography imaging on accuracy of maxillofacial models.** *J Prosthodont Res* 2019;63:239–44 CrossRef Medline
42. Motoyama S, Ito H, Sarai M, et al. **Ultra-high-resolution computed tomography angiography for assessment of coronary artery stenosis.** *Circ J* 2018;82:1844–51 CrossRef Medline
43. Faber J, Fonseca LM. **How sample size influences research outcomes.** *Dental Press J Orthod* 2014;19:27–29 CrossRef Medline

Characterization of MR Imaging–Visible Perivascular Spaces in the White Matter of Healthy Adolescents at 3T

J. Piantino, E.L. Boespflug, D.L. Schwartz, M. Luther, A.M. Morales, A. Lin, R.V. Fossen, L. Silbert, and B.J. Nagel



ABSTRACT

BACKGROUND AND PURPOSE: Perivascular spaces play a role in cerebral waste removal and neuroinflammation. Our aim was to provide data regarding the burden of MR imaging–visible perivascular spaces in white matter in healthy adolescents using an automated segmentation method and to establish relationships between common demographic characteristics and perivascular space burden.

MATERIALS AND METHODS: One hundred eighteen 12- to 21-year-old subjects underwent T1- and T2-weighted 3T MR imaging as part of the National Consortium on Alcohol and Neurodevelopment in Adolescence. Perivascular spaces were identified in WM on T2-weighted imaging using a local heterogeneity approach coupled with morphologic constraints, and their spatial distribution and geometric characteristics were assessed.

RESULTS: MR imaging–visible perivascular spaces were identified in all subjects (range, 16–287). Males had a significantly higher number of perivascular spaces than females: males, mean, 98.4 ± 50.5 , versus females, 70.7 ± 36.1 , ($P < .01$). Perivascular space burden was bilaterally symmetric ($r > 0.4$, $P < .01$), and perivascular spaces were more common in the frontal and parietal lobes than in the temporal and occipital lobes ($P < .01$). Age and pubertal status were not significantly associated with perivascular space burden.

CONCLUSIONS: Despite a wide range of burden, perivascular spaces are present in all healthy adolescents. Perivascular space burden is higher in adolescent males than in females, regardless of age and pubertal status. In this population, perivascular spaces are highly symmetric. Although widely reported as a feature of the aging brain, awareness of the presence of perivascular spaces in a cohort of healthy adolescents provides the foundation for further research regarding the role of these structural variants in health and disease.

ABBREVIATIONS: CF = count fraction; NCANDA = National Consortium on Alcohol and Neurodevelopment in Adolescence; PVS = perivascular space; VF = volume fraction

A recent resurgence in interest in the perivascular space (PVS) in the brain, particularly as a route for waste clearance, has primarily focused on its relationship with neurodegenerative diseases marked by waste accumulation. Such disorders include Alzheimer disease, cerebral amyloid angiopathy, cerebrovascular or small-vessel disease, neuroinflammation (eg, multiple sclerosis), or acute insult, as in traumatic brain injury.^{1–4} Perhaps due to the positive correlation between MR imaging–visible PVS burden and senescence (PVS burden remains static during childhood

and adolescence^{5,6}), information regarding the pediatric prevalence of these spaces is sparse and generally focused on groups of clinical import, such as those with headache and migraines, developmental delay, autism, and epilepsy.^{5–10} However, abnormal findings of very large tumefactive and/or numerous PVSs are consistently reported in rarer pediatric diseases, such as adrenoleukodystrophy and mucopolysaccharidoses.¹¹ There are only 2 studies of the prevalence of MR imaging–visible PVSs in large pediatric populations: Two reported that approximately 3%–4% of

Received May 19, 2020; accepted after revision July 17.

From the Department of Pediatrics (J.P., M.L.), Division of Child Neurology, Doernbecher Children's Hospital; Department of Neurology (E.L.B., D.L.S., L.S.), Layton Aging and Alzheimer's Disease Center; Advanced Imaging Research Center (D.L.S.); Departments of Psychiatry (A.M.M., R.V.F., B.J.N.), and Emergency Medicine (A.L.), Center for Policy and Research in Emergency Medicine; Oregon Health & Science University, Portland, Oregon; and Department of Neurology (L.S.), Portland Veterans Affairs Medical Center, Portland, Oregon.

This work was supported by the National Heart, Lung, and Blood Institute, K23HL150217-01 and K12HL133115; the National Institute on Aging, K01AG059842 and P30 AG008017; and the National Institute on Drug Abuse, K01DA046649.

Please address correspondence to Juan A. Piantino, MD, 707 SW Gaines St., Portland, OR 97239; e-mail: piantino@ohsu.edu

Indicates open access to non-subscribers at www.ajnr.org

Indicates article with supplemental on-line tables.

Indicates article with supplemental on-line photos.

<http://dx.doi.org/10.3174/ajnr.A6789>

subjects presented with visible PVSs, and one reported that dilated PVSs were visible in 64%.^{5,6} This wide variability is likely due to the MR imaging instruments used to image PVSs in vivo, historically variable definitions of “normal” and “dilated” PVSs, and inconsistent methods of quantifying visible PVS burden.

It is possible that these spaces may be visible in many more youth than previously thought; that they are almost entirely a phenomenon of the aging brain is unlikely. Perhaps due to these many factors, little is known about the timing of MR imaging-visible PVS appearance and its relation to age, pubertal status, sex differences, or spatial distribution in childhood and adolescence. Finally, a normative benchmark for the spatial distribution of these spaces may be particularly important because left-right symmetry in MR imaging-visible white matter PVSs has been broadly reported at all levels of PVS burden; frank asymmetry, along with PVS size, has been noted as clinically relevant.¹²⁻¹⁴

The primary objective of this study was to update existing literature describing normative data regarding MR imaging-visible PVS burden in white matter, including the number, volume fraction, and morphology, in a well-characterized cohort of healthy adolescents using high-field 3T MR imaging with T2-weighted imaging and manually inspected results from a fully automated segmentation algorithm.¹⁵ The secondary objective was to examine the relationship between demographic variables such as age, sex, and pubertal status on the number and morphology of PVSs in these subjects. Finally, the prevalence and degree of asymmetry was assessed and reported. These data will provide clinicians and researchers with a survey of normative data in a well-characterized clinically healthy adolescent population. This report aims to be an essential informant for future studies aimed at understanding the potential role and etiology of MR imaging-visible WM PVSs in pediatric health and disease.

MATERIALS AND METHODS

Study Design

The subjects included in this study represent a subset of the cohort enrolled in the National Consortium on Alcohol and Neurodevelopment in Adolescence (NCANDA). NCANDA is a multisite, cohort-sequential, longitudinal neuroimaging study of adolescents.¹⁶ All NCANDA subjects participated in an informed-consent process. The institutional review board at Oregon Health & Science University approved the use of de-identified data for this study.

Participants

Subjects recruited for NCANDA at a single site ($n = 148$) were eligible for inclusion in this study. Adolescents (12–21 years of age) were eligible to participate. Exclusion criteria were the following: inability to understand English; residence of >50 miles from the assessment site; MR imaging contraindications; current use of medications affecting brain function or blood flow (eg, antidepressants, stimulants); history of a serious medical problem that could affect MR imaging (eg, diabetes, recurrent migraine, traumatic brain injury with loss of consciousness for >30 minutes); mother who drank >2 drinks in a week or used nicotine >10 times per week, marijuana >2 times per week, or other drugs during pregnancy; prematurity (<30 weeks' gestation); low birth weight or other perinatal complications requiring intervention; a current diagnosis of

an Axis I psychiatric disorder (including psychosis) that would interfere with valid completion of the protocol (mild depression, simple phobia, social phobia, and attention deficit/hyperactivity disorder are not exclusionary); substance dependence; history of learning disorders; and pervasive developmental disorder or any other condition requiring specialized education. Thirty subjects with any history of injury to the head or neck—even those with no loss of consciousness—were further excluded, and the remaining 118 subjects made up the final cohort for this study. Demographic variables included sex, age, height, weight, and ethnicity. Pubertal stage was characterized using the self-assessment Pubertal Development Scale.¹⁷ The Pubertal Development Scale categories were dichotomized into early-mid pubertal and late-post pubertal.

MR Imaging Acquisition and Review

A 3D T1-weighted magnetization prepared rapid acquisition of gradient echo sequence (TR = 1900 ms, TE = 2.92 ms, TI = 900 ms, flip angle = 9°, imaging matrix = 256 × 256, FOV = 24 cm, voxel dimensions = 1.2 × .9375 × 0.9375 mm, 160 contiguous slices) and a 3D T2-weighted turbo spin-echo with variable excitation pulse sequence (TR/TE = 3200/404 ms, imaging matrix = 256 × 256, FOV = 24 × 24 cm, voxel dimensions = 1.2 × .9375 × 0.9375 mm, 160 contiguous slices) were performed. MR imaging volumes were collected in the sagittal plane on a 3T Tim Trio scanner (Siemens) equipped with a 12-channel head coil. T1-weighted MR images were read by a board-certified neuroradiologist.¹⁸ These reports were manually reviewed, and information about incidental findings was noted.

Imaging Preprocessing

T1-weighted images were segmented into tissue types using FreeSurfer (Version 5.1; <http://surfer.nmr.mgh.harvard.edu>) to yield masks of white matter, cortical gray matter, subcortical gray matter, and ventricular CSF. FreeSurfer-generated parcellations were also used to create a mask that included the cerebellum, basal ganglia, and midbrain. The T1-weighted volume was registered to the T2-weighted volume (FMRIB Linear Image Registration Tool, FLIRT; <http://www.fmrib.ox.ac.uk/fsl/fslwiki/FLIRT>), and the same transformation matrix was applied to the T1-derived FreeSurfer masks described above. T2-weighted images were first up-sampled to 0.6-mm isotropic voxels (3dresample, Analysis of Functional Neuro Images [AFNI]; <http://afni.nimh.nih.gov/afni>), skull-stripped (FSL Brain Extraction Tool; <http://fsl.fmrib.ox.ac.uk/fsl/fslwiki/BET>), and submitted to a 5 class K-means-based tissue segmentation in SPM5 (<https://www.fil.ion.ucl.ac.uk/spm/doc/>), which produces a homogenized image in preprocessing (Fig 1B). The tissue class corresponding to WM was thresholded at >50% likelihood (3dcalc, AFNI; Fig 1C), holes in the resulting mask were filled (Fig 1D), and the entire mask was eroded by 2 voxels (3dmask_tool, AFNI; Fig 1E) to avoid the possibility of mis-segmented parts of neocortical gray matter being misidentified as PVS in WM. Finally, any voxels that shared membership between the resultant WM mask and the cerebellar/basal ganglia/midbrain mask were eliminated from the WM mask (3dcalc).

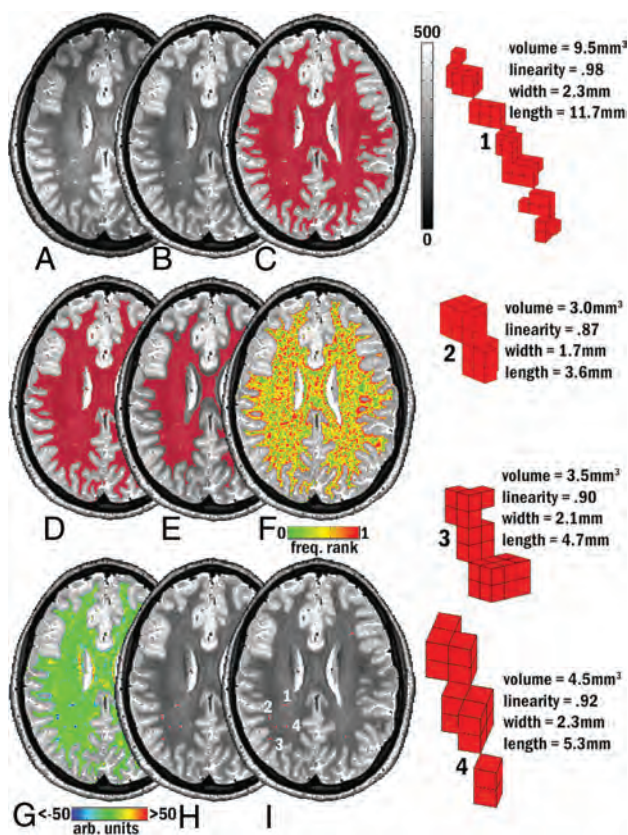


FIG 1. Examples of MR imaging-visible PVSs on T2-based images and PVS segmentation method. *A*, Acquired T2. *B*, After intensity normalization. *C–H*, Intermediate steps in the algorithm. *C*, WM tissue mask with holes filled (*D*) and eroded by 2 voxels (*E*). *F*, Frequency rank map. *G*, Map of local-intensity difference. *H*, Segmented objects submitted to morphologic constraint. *I*, Final segmentation mask. 1–4, Morphologic characteristics of 4 of the final segmented PVSs visible on this axial section (see *I*).

PVS Segmentation

A similar methodology to that used in a previous study was used for PVS identification (Fig 1).¹⁵ Preprocessed homogenized T2-weighted images were subjected to a 2-part, local heterogeneity assessment. The sphere of a radius of 3 mm was constructed around each voxel within the eroded WM mask, and the voxels within that sphere were ranked-based on their intensity (ie, a voxel was marked as 0.5 if its intensity fell into the 50th percentile of surrounding voxels, Fig 1*F*). Next, the sphere of a radius of 4 mm was constructed around a voxel, and the average of the difference in intensity between that voxel and surrounding voxels was calculated and that voxel was marked with the result (3dLocalstat, AFNI; Fig 1*G*). Finally, if a voxel did not reside in the cerebellum/basal ganglia/midbrain mask, did reside in the eroded WM mask, had an average difference in intensity from surrounding voxels that was >15% of its own intensity, and had an intensity that fell into the top fifth percentile of its neighbors, it was considered for morphologic analysis (3dcalc, AFNI; Fig 1*H*). All clusters of >1 mm³ (~5 voxels, 3D corner-to-corner connectivity, 3dclust type 3, AFNI) were passed to the morphology constraint. Linearity, width, length, and total volume of each cluster were calculated in Matlab (MathWorks) (Fig 1*I* and Fig 1, parts 1–4); a cluster was retained

as a putative PVS if the segmented object was <16.41-mm wide and had a linearity of at least 0.8. Each PVS detected by the automated algorithm was assessed by a trained researcher (M.L.); false alarms were removed from further analysis. See the RESULTS section for a summary of error counts and rates.

Spatial Distribution of PVS

Delineation of WM into lobar regions (left and right frontal, temporal, parietal, and occipital) was accomplished, in part, using standard ROI output from FreeSurfer via recon-all (e.g., frontal_R_GM.nii.gz and frontal_L_GM.nii.gz). Periventricular and other deep WM regions are not marked by FreeSurfer; however, some WM PVSs exist in these unmarked WM regions, so it is necessary to classify unmarked voxels into lobes. Every voxel in the total WM mask that was not marked by FreeSurfer as belonging to juxtacortical WM was subjected to the following procedure: An integer-based (1–8, describing the 8 juxtacortical WM lobar regions above) histogram was constructed for every voxel that fell within the sphere of a radius of 7.5 mm from each unmarked voxel. After dividing the count of each juxtacortical WM region (1–8) by the volume of that region to account for differently sized lobes (eg, frontal >> occipital), we marked each voxel as a member of the lobe and hemisphere of the maximum normalized frequency of the histogram by a winner-take-all method (On-line Fig 1). This process failed at the FreeSurfer WM parcellation stage for 3/118 subjects (2 females and 1 male); all WM lobar PVS distributions are described in the remaining 115 subjects. Probability maps of PVS incidence in this cohort were generated using nonlinear registrations. All subjects' skull-stripped and homogenized T2-weighted images were affine-registered to Montreal Neurological Institute space (FLIRT, FSL, and 3dAllineate, AFNI; mni_icbm152_t2_relx_tal_nlin_sym_09a.nii.gz was used as an initial template). The resulting datasets were simultaneously submitted to template construction (antsMultivariateTemplateConstruction.sh, Advanced Normalization Tools software package [ANTS], affine + 2-step nonlinear transform, <https://github.com/ANTsX/ANTs/issues/553>). The initial affine transformation and all subsequent transformations were combined and applied to single-subject native space PVS masks with false alarms removed (antsApplyTransforms; ANTS). The mean of all transformed PVS masks was calculated; the result was voxelwise-thresholded at 0.5% likelihood and cluster-thresholded at 43.2 mm³ (two hundred 0.6-mm isotropic voxels) for ease of viewing.

Statistical Analysis

Statistical analyses were performed using STATA/MP 15 (StataCorp). Descriptive statistics were used to analyze the demographic characteristics of the cohort. Sex regression models were implemented with the total PVS number and volume as outcomes of interest; sex and age differences were analyzed using 2-sample *t* tests. Multivariate linear regression models were implemented with total PVS number and volume as outcomes of interest; sex, age, and pubertal stage were used as covariates. PVS volume fraction (VF) and count fraction (CF) were calculated as the total volume of PVSs (cubic millimeters) or PVS count within the volume of the WM search field (cubic centimeters), respectively. The interaction of sex and age on PVS characteristics was tested with linear regression models. A

secondary analysis included multiple linear regression with cluster characteristics (width, length, and volume) as individual outcomes and the same covariates indicated above. Differences in PVS number and volume across lobes were obtained using Pearson regression and paired and unpaired t-tests, as appropriate. An asymmetry index was created by calculating the absolute value of the log of the left divided by the right CF and VF so that departure from zero (ie, symmetric) indicated asymmetry; subjects were identified as outliers if asymmetry indices were ≥ 2.5 SDs from the population mean. Regression diagnostics for all models were examined for model fit. All reported *P* values are 2-sided, and the threshold for statistical significance set to an α of .05.

Data Availability Statement

The data that support the findings of this study are available from the NCANDA study on request. The statistical code used to analyze these data is available on request.

RESULTS

Table 1 provides demographic information and characteristics of the study cohort. Fifty-six subjects in the cohort (47%) were male. The median age was 16 years (interquartile range, 14.1–18.3 years) for males, and 16.7 years (interquartile range, 14.3–18.4 years) for females. In order to study a diverse cohort, both Hispanic and Non-Hispanic subjects were included. Seven subjects in the cohort (6%) identified themselves as Hispanic. Nine subjects had incidental intracranial findings noted by a neuroradiologist (3 instances of mega cisterna magna; 2 pineal cysts; 1 tonsillar ectopia; 1 gray matter heterotopia; 1 large vein; 1 large prepontine cistern). None of the subjects had prominent perivascular spaces noted by a neuroradiologist. After adjusting for age, the male brain volume was

145.2 cm³ larger than that of females (95% CI, 108.5–182 cm³; *P* < .01), and male white matter volume was 58.5 cm³ larger than that of females (95% CI, 41–76 cm³; *P* < .01, On-line Table 1). In this cohort, age was not significantly associated with brain volume or total white matter volume (On-line Fig 1). Plots of residuals versus predicted values, QQ plots, partial regression plots, and outlier and leverage statistics indicated a good model fit. The total error rate (of 12,274 detected objects) of the PVS segmentation algorithm in this dataset was 19.4% (2372). Most false alarms were attributable to hypointense WM voxels other than PVS (1696 or 13.8%). The remaining false alarms were attributable to partial inclusion of GM in the basal ganglia (676 or 5.5%) (On-line Fig 3).

PVS Characteristics

Examples of MR imaging-visible PVSs detected by the segmentation algorithm can be seen in Fig 1I. PVSs were observed in the supratentorial white matter of all 118 subjects in the cohort (Table 2). Males had a significantly higher absolute number of PVSs than females (mean, 98.4 \pm 50.5 and 70.7 \pm 36.1, respectively; *P* < .01). Males also had a higher total volume of PVSs than females (mean, 334.8 \pm 192.4 mm³ and 241.2 \pm 134 mm³, respectively; *P* < .01). After adjusting for white matter volume, males had higher PVS number per cubic centimeter of white matter than females (CF mean, 0.2 \pm 0.1 and 0.1 \pm 0.07, respectively; *P* = .02). Males also had a higher PVS volume per cubic centimeter of white matter than females (VF mean, 0.7 \pm 0.4 and 0.5 \pm 0.3, respectively; *P* = .04). The morphologic characteristics of PVS (ie, length, width, and volume) were not statistically different between males and females (*P* > .35). After we adjusted for sex, no effect of age or pubertal stage was observed on total PVS volume, total PVS count, and PVS VF or CF (*P* > .3, On-line Table 2 and On-line Fig 4).

There were no significant interactions between age and sex on any of the above-mentioned PVS characteristics (*P* = .68–.94).

PVS Location by Lobe

PVS volume, count, VF, and CF were significantly positively correlated across hemispheres in each lobe (Pearson *r* > 0.4, *P* < .01, Fig 2). Significant asymmetry in this population was defined as 1 hemisphere having approximately 225%

Table 1: Cohort characteristics

Patient Characteristics (Median) (IQR)	Males (n = 56)	Females (n = 62)
Age (yr)	16 (14.1–18.3)	16.7 (14.3–18.4)
Weight (kg)	63.5 (56.2–81.6)	57.6 (52.1–63.5)
Height (cm)	169 (163.8–180.3)	162.5 (157.4–167.6)
BMI (kg/m ²)	22 (19.3–26.1)	21.8 (19.5–24)
PDS score	3.1 (2.6–3.6)	3.6 (2.6–3.6)
Ethnicity (No.) (%)		
Hispanic	5 (9)	2 (3)
Non-Hispanic	51 (91)	60 (97)

Note:—BMI indicates body mass index; PDS, Pubertal Development Scale; IQR, interquartile range.

Table 2: Characteristics of PVS identified with the automated algorithm

Characteristic	<i>P</i> Value ^a	Females (n = 62)		Males (n = 56)	
		Mean (SD)	Range	Mean (SD)	Range
PVS whole brain					
PVS total No.	<.01	70.7 (36.1)	20–153	98.4 (50.5)	16–287
PVS total volume (mm ³)	<.01	241.2 (134)	74.7–617	334.8 (192.4)	43–1103.3
PVS WM (No./cm ³)	.02	0.1 (0.07)	0.04–0.36	0.2 (0.1)	0.04–0.6
PVS volume WM (mm ³ /cm ³)	.04	0.5 (0.3)	0.16–1.3	0.7 (0.4)	0.1–2.3
Individual PVS cluster					
Individual cluster length (mm)	.75	3.6 (0.2)	3.3–4.5	3.6 (0.2)	3–4.3
Individual cluster width (mm)	.35	2 (0.07)	1.8–2	2 (0.08)	1.7–2
Individual cluster volume (mm ³)	.80	2.9 (0.3)	2.1–3.8	2.8 (0.3)	2–3.6
Cluster volume (mm ³) by total cluster (No.)	.80	0.05 (0.02)	0.02–0.16	0.03 (0.02)	0.01–0.14

^a Two-sample *t* test.

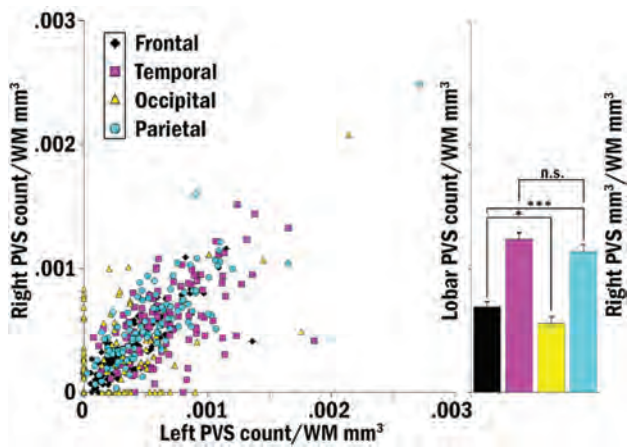


FIG 2. PVS burden in the right and left hemispheres. PVS count and white matter volume are correlated between hemispheres in all lobes. Barplots illustrate significantly different PVS count/white matter volume by lobe across hemispheres. Asterisk indicates $P < .05$; triple asterisks, $P < .001$.

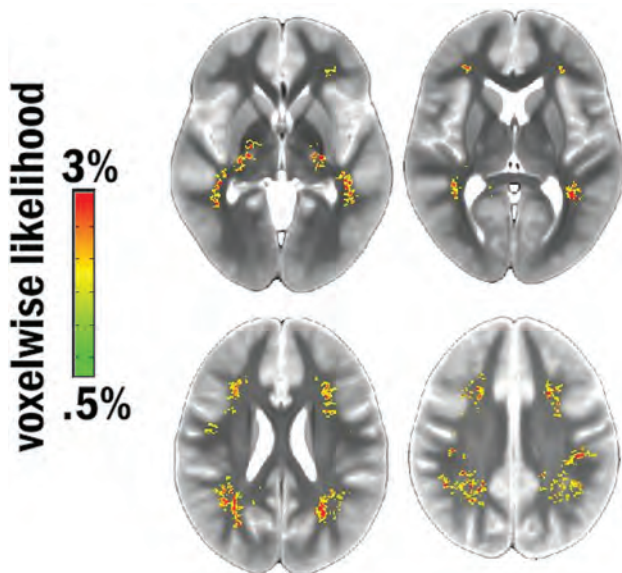


FIG 3. Map of the likelihood of a segmented PVS at a given voxel across all subjects.

of the burden of the other hemisphere (asymmetry index ≈ 0.34 , approximately 2.5 SDs above the mean). One male and 2 females (1.7% and 3.7%) had asymmetry indices for VF that exceeded this cutoff; CF asymmetry was similarly distributed across the population (2 [3.3%] and 2 [3.7%] for males and females, respectively). There was no difference in asymmetry indices between males and females (VF or CF, $P > .1$) nor was there an association between CF or VF asymmetry and age ($P > .1$). Over both hemispheres, PVS CF was significantly higher in the parietal and temporal lobes than the frontal lobe; the frontal lobe bore a significantly higher PVS CF than the occipital lobe (all $P < .01$, bar graphs in Fig 2). The same relationships were true of PVS VF. There were more PVSs in the parietal than frontal lobes, more in frontal than temporal lobes, and more in temporal than occipital lobes; the same relationships were true of

lobar PVS volume (all $P < .001$, data not shown). PVS CF was also compared within lobes between sexes (male $>$ female, $P < .05$ in the temporal lobe; all other lobes were nonsignificant) and across sexes within lobes between hemispheres (the burden was higher in the left temporal lobe than in the right, $P < .01$; On-line Fig 5, center column). The same relationships were observed for VF (data not shown). A brain-wide map of voxelwise probability for a detected PVS can be found in Fig 3.

DISCUSSION

In this study, we quantify the number and morphology of white matter PVSs in a cohort of healthy adolescents under rigorous study-entry criteria. Using 3T MR imaging scans and objective quantitative methods, we demonstrate that PVSs are seen in this population in a much larger proportion of subjects than previously described in the literature.^{5,6} We provide normative PVS morphologic characteristics, including total number, volume, and individual length, width, and diameter of PVSs in this age group and the distribution of lobar locations of PVS burden. We show that male adolescents have a higher total number and volume of PVSs per unit of white matter than females. We show that in adolescents, individual PVS morphology (length, width, and diameter) is not associated with age, sex, or increasing white matter volume. Finally, we report the incidence rate of asymmetric burden. These findings support the notion that PVSs are seen in MRIs of healthy individuals.

In adults, the presence of PVSs has been mainly linked to the aging process⁹ and to vascular and Alzheimer dementias.^{19,20} Two studies in youth concluded that in this population, PVSs were either absent or a rare finding, present in $<5\%$ of subjects.^{5,6} These early studies, although considered the first attempts at quantifying PVS in children, have limitations. Counts were performed on MRIs obtained using a 1.5T field strength, introducing a floor effect for small structures with limited contrast to surrounding tissue due to partial volume effects. Early studies used subjective visual ratings, which are subject to interrater variability and differences in interpretation and do not provide morphologic details about each individual PVS. Although children were labeled as “healthy,” MRIs were performed in subjects with entities such as benign epilepsy, headaches, or behavioral problems, which limit their generalizability.⁵ Early studies did not adjust for other important covariates such as sex or total cerebral white matter. The results presented here expand this previous work by filling existing gaps in the limited literature addressing this phenomenon. NCANDA participants met rigorous study entry criteria that provided us with important baseline clinical and demographic information on each subject. NCANDA participants underwent 3T MR imaging, which provided adequate visualization of PVSs. By incorporating objective PVS quantification, we minimized visual rater irregularities. We were also able to provide details about the morphology of each PVS, including important characteristics such as width, length, and volume.

In this cohort, males had a higher number of morphologically similar PVSs than females. Most important, age and pubertal stage were not significantly associated with PVS number or total volume. Furthermore, there was no interaction between age and sex on PVS burden. A higher prevalence of “large” (>2 mm in diameter) PVSs in males than in females has been reported in subjects aged

0–99 years using a visual rating scale.⁹ The authors, however, did not provide an analysis of sex differences across age groups. A separate study using a volumetric approach in an adult population also identified higher burden volumes in males over females in control subjects.¹ The timing and etiology of sex differences are yet to be elucidated. However, the fact that sex differences are already present in early-pubertal individuals argues in favor of a much earlier etiology than previously established. These differences may be present at birth or develop during childhood.

In agreement with previous work, PVS burden in this cohort was highest in the frontal and parietal lobes.^{5,6} However, PVSs were also found in the temporal and, more rarely, the occipital lobes. The appearance of PVSs in the temporal and occipital lobes could be, in part, attributed to the better resolution of the 3T scans and the objective measurements used in our study, resulting in a higher sensitivity for PVS detection. In our cohort, PVS burden was bilaterally symmetric, and a high burden in 1 hemisphere, regardless of the measure used for burden or of the lobar location, is indicative of a high burden in the contralateral side. It is certain that the high likelihood of burden symmetry across hemispheres is a reflection of the symmetry of cerebral vasculature. However, the high interindividual variability in overall MR imaging–visible PVSs (approximately an 8-fold difference) remains unexplained. In our cohort, pubertal status and age were not associated with PVS burden. It is possible that other variables not included in this analysis may affect PVS burden. For example, sleep efficiency has been shown to affect PVS burden in adults, and it may play a role in PVS burden variability in adolescents.²¹ Last, the incidence rate of a significantly asymmetric burden in healthy adolescents should be considered 1%–3%, according to these data. This suggests that an asymmetric burden, defined as approximately >225% of PVS count or volume between hemispheres, is a rare occurrence, though the clinical significance of such a finding remains unclear.

Finally, we observed a difference in burden per unit WM between lobes. It is unlikely that WM is perfused by nearly twice as many vessels in the temporal and parietal lobes than in the frontal and occipital lobes per unit tissue; if the interpretation of a difference in burden between lobes is predicated on an uneven distribution of lobar vasculature, then the most parsimonious explanation is that these spaces are organized about the venous system. Therefore, the finding may arise from either an uneven lobar distribution of venous architecture in WM or because the parietal and temporal lobes are more susceptible to the underlying cause of PVS expansion, or both. Given that the identity, artery or vein, of the vessels in WM around which these spaces are visible remains an open question, this report may serve to inform this debate considerably, and strongly suggests that venous return is the primary system around which these spaces expand in WM. Another possibility is that the temporal and parietal lobes contain some characteristic that makes a member voxel more likely to be a PVS; in either case, the finding provides a clue to the underlying cause of the fact that some of these spaces are large enough to view on a standard clinical MR imaging instrument and some are not.

Previous studies have found no correlation between the number of PVSs and age in young individuals.^{5,6} While a strong relationship between MR imaging–visible PVSs and age has been noted in patients older than 60 years,⁹ other studies suggest that

the relationship may be regionally dependent²² or dependent on the resolution of the images acquired.²³ Future studies that objectively address the evolution of age- and sex-related differences in PVS burden across the life span, especially ones with longitudinal designs, are needed to further elucidate the potential clinical relevance of these findings.

This study has several limitations. The cross-sectional design of this analysis precludes the possibility of determining individual longitudinal changes in PVS burden. Future investigations, including longitudinal data from this cohort, should be conducted to better understand individual differences in the development of this phenomenon. Second, the present methodology is limited to white matter. Given evidence that PVSs do occur in other regions, including the thalamus, midbrain, cerebellum, insular cortex, extreme capsule, optic tract, and hippocampus, future studies evaluating these regions in an adolescent cohort are certainly warranted.^{24,25}

CONCLUSIONS

Using objective measurements in a rigorously selected cohort, we conclude that PVSs are seen in clinically healthy adolescents, that males have higher PVS burden than females, and that while overall burden varies widely, burden symmetry across hemispheres is preserved. These differences are not related to age, total white matter volume, or pubertal status. These findings establish a baseline from which PVS burden can be investigated in different disease processes and present the foundation for further research in the physiology and pathology of these structures in youth.

Disclosures: Juan Piantino—RELATED: Grant: National Institutes of Health, Comments: National Heart, Lung, and Blood Institute, K23HL150217-01. Erin Boespflug—RELATED: Grant: National Institutes of Health, Comments: research salary support from National Institutes of Health grants K01AG059842 and P30AG008017.* Amber Lin—RELATED: Grant: National Institutes of Health K12 training grant, Comments: This grant supports my time (biostatistical support) for a number of investigators, including the primary author of this article. Lisa Silbert—UNRELATED: Grants/Grants Pending: National Institutes of Health, Comments: Principal Investigator on a National Institutes of Health R01 and Co-Investigator on several National Institutes of Health grants, not directly related to this article.* Bonnie J. Nagel—RELATED: Grant: National Institute on Alcohol Abuse and Alcoholism, Comments: This work was supported by NIH U01 AA02169.* *Money paid to the institution.

REFERENCES

1. Ramirez J, Berezuk C, McNeely AA, et al. **Visible Virchow-Robin spaces on magnetic resonance imaging of Alzheimer's disease patients and normal elderly from the Sunnybrook Dementia Study.** *J Alzheimers Dis* 2014;43:415–44 CrossRef Medline
2. Potter GM, Chappell FM, Morris Z, et al. **Cerebral perivascular spaces visible on magnetic resonance imaging: development of a qualitative rating scale and its observer reliability.** *Cerebrovasc Dis* 2015;39:224–31 CrossRef Medline
3. Patankar TF, Mitra D, Varma A, et al. **Dilatation of the Virchow-Robin space is a sensitive indicator of cerebral microvascular disease: study in elderly patients with dementia.** *AJNR Am J Neuroradiol* 2005;26:1512–20 Medline
4. Charidimou A, Jaunmuktane Z, Baron JC, et al. **White matter perivascular spaces: an MRI marker in pathology-proven cerebral amyloid angiopathy?** *Neurology* 2014;82:57–62 CrossRef Medline
5. Groeschel S, Chong WK, Surtees R, et al. **Virchow-Robin spaces on magnetic resonance images: normative data, their dilatation, and a review of the literature.** *Neuroradiology* 2006;48:745–54 CrossRef Medline

6. Rollins NK, Deline C, Morriss MC. **Prevalence and clinical significance of dilated Virchow-Robin spaces in childhood.** *Radiology* 1993;189:53–57 CrossRef Medline
7. Schick S, Gahleitner A, Wober-Bingol C, et al. **Virchow-Robin spaces in childhood migraine.** *Neuroradiology* 1999;41:283–87 CrossRef Medline
8. Edvinsson L, Haanes KA, Warfvinge K. **Does inflammation have a role in migraine?** *Nat Rev Neurol* 2019;15:483–90 CrossRef Medline
9. Heier LA, Bauer CJ, Schwartz L, et al. **Large Virchow-Robin spaces: MR-clinical correlation.** *AJNR Am J Neuroradiol* 1989;10:929–36 Medline
10. Liu C, Habib T, Salimeen M, et al. **Quantification of visible Virchow-Robin spaces for detecting the functional status of the glymphatic system in children with newly diagnosed idiopathic generalized epilepsy.** *Seizure* 2020;78:12–17 CrossRef Medline
11. Murata R, Nakajima S, Tanaka A, et al. **MR imaging of the brain in patients with mucopolysaccharidosis.** *AJNR Am J Neuroradiol* 1989;10:1165–70 Medline
12. Austein F, Langguth P, Lindner T. **Extreme widening of asymmetric giant cystic Virchow-Robin spaces.** *Neuroradiology* 2018;60:3–5 CrossRef Medline
13. Ogawa T, Okudera T, Fukasawa H, et al. **Unusual widening of Virchow-Robin spaces: MR appearance.** *AJNR Am J Neuroradiol* 1995;16:1238–42 Medline
14. Sawada M, Nishi S, Hashimoto N. **Unilateral appearance of markedly dilated Virchow-Robin spaces.** *Clin Radiol* 1999;54:334–36 CrossRef Medline
15. Schwartz DL, Boespflug EL, Lahna DL, et al. **Autoidentification of perivascular spaces in white matter using clinical field strength T1 and FLAIR MR imaging.** *Neuroimage* 2019;202:116126 CrossRef Medline
16. Brown SA, Brumback T, Tomlinson K, et al. **The National Consortium on Alcohol and NeuroDevelopment in Adolescence (NCANDA): a multisite study of adolescent development and substance use.** *J Stud Alcohol Drugs* 2015;76:895–908 CrossRef Medline
17. Petersen AC, Crockett L, Richards M, et al. **A self-report measure of pubertal status: reliability, validity, and initial norms.** *J Youth Adolesc* 1988;17:117–33 CrossRef Medline
18. Sullivan EV, Lane B, Kwon D, et al. **Structural brain anomalies in healthy adolescents in the NCANDA cohort: relation to neuropsychological test performance, sex, and ethnicity.** *Brain Imaging Behav* 2017;11:1302–15 CrossRef Medline
19. MacLullich AM, Wardlaw JM, Ferguson KJ, et al. **Enlarged perivascular spaces are associated with cognitive function in healthy elderly men.** *J Neurol Neurosurg Psychiatry* 2004;75:1519–23 CrossRef Medline
20. Weller RO, Subash M, Preston SD, et al. **Perivascular drainage of amyloid-beta peptides from the brain and its failure in cerebral amyloid angiopathy and Alzheimer's disease.** *Brain Pathol* 2008;18:253–66 CrossRef Medline
21. Berezuk C, Ramirez J, Gao F, et al. **Virchow-Robin spaces: correlations with polysomnography-derived sleep parameters.** *Sleep* 2015;38:853–58 CrossRef Medline
22. Dubost F, Yilmaz P, Adams H, et al. **Enlarged perivascular spaces in brain MRI: automated quantification in four regions.** *Neuroimage* 2019;185:534–44 CrossRef Medline
23. Zong X, Park SH, Shen D, et al. **Visualization of perivascular spaces in the human brain at 7T: sequence optimization and morphology characterization.** *Neuroimage* 2016;125:895–902 CrossRef Medline
24. Jungreis CA, Kanal E, Hirsch WL, et al. **Normal perivascular spaces mimicking lacunar infarction: MR imaging.** *Radiology* 1988;169:101–04 CrossRef Medline
25. Hirabuki N, Fujita N, Fujii K, et al. **MR appearance of Virchow-Robin spaces along lenticulostriate arteries: spin-echo and two-dimensional fast low-angle shot imaging.** *AJNR Am J Neuroradiol* 1994;15:277–81 Medline

Prognostic Accuracy of Fetal MRI in Predicting Postnatal Neurodevelopmental Outcome

M. Wilson, K. Muir, D. Reddy, R. Webster, C. Kapoor, and E. Miller



ABSTRACT

BACKGROUND AND PURPOSE: The superior diagnostic accuracy of fetal MR imaging in detecting fetal brain abnormalities has been previously demonstrated; however, the ability of fetal MR imaging to prognosticate postnatal outcome is not well-studied. We performed a retrospective analysis to determine the prognostic accuracy of fetal MR imaging in predicting postnatal neurodevelopmental outcome.

MATERIALS AND METHODS: We identified all fetal MR imaging performed at the Children's Hospital of Eastern Ontario during a 10-year period and assessed agreement between prenatal prognosis and postnatal outcome. Prenatal prognosis was determined by a pediatric neurologist who reviewed the fetal MR imaging report and categorized each pregnancy as having a favorable, indeterminate, or poor prognosis. Assessment of postnatal neurodevelopmental outcome was made solely on the basis of the child's Gross Motor Function Classification System score and whether the child developed epilepsy. Postnatal outcome was categorized as favorable, intermediate, or poor. We also assessed the diagnostic accuracy of fetal MR imaging by comparing prenatal and postnatal imaging diagnoses.

RESULTS: We reviewed 145 fetal MR images: 114 were included in the assessment of diagnostic accuracy, and 104 were included in the assessment of prognostic accuracy. There was 93.0% agreement between prenatal and postnatal imaging diagnoses. Prognosis was favorable in 44.2%, indeterminate in 50.0%, and poor in 5.8% of pregnancies. There was 93.5% agreement between a favorable prenatal prognosis and a favorable postnatal outcome.

CONCLUSIONS: A favorable prenatal prognosis is highly predictive of a favorable postnatal outcome. Further studies are required to better understand the role of fetal MR imaging in prognosticating postnatal development, particularly in pregnancies with indeterminate and poor prognoses.

ABBREVIATIONS: feMRI = fetal MRI; GA = gestational age; GMFCS = Gross Motor Function Classification System; VM = ventriculomegaly

Fetal MR imaging (feMRI) is emerging as an important supplement to ultrasound in pregnancy. Many studies have demonstrated that feMRI provides superior diagnostic accuracy to antenatal ultrasound, with postnatal imaging findings used as the outcome reference diagnosis.¹⁻⁴ The role of feMRI in prognosticating the neurodevelopmental outcome of the child, however, has not been thoroughly investigated. Until recently, there have been only scattered studies, limited to mostly studies of cases of

isolated ventriculomegaly (VM) and posterior fossa abnormalities, which have assessed the role of feMRI in predicting postnatal outcome.⁵⁻⁸ The Magnetic Resonance Imaging to Enhance the Diagnosis of Fetal Developmental Brain Abnormalities in Utero (MERIDIAN) study is a large multicenter prospective study that assessed the utility of feMRI in diagnosing fetal brain abnormalities.⁹ One component of this study, published in 2019, assessed the prognostic accuracy of feMRI versus ultrasound in predicting postnatal neurodevelopment.¹⁰ The authors concluded that neither feMRI nor ultrasound was able to accurately predict abnormal development, but they did report that feMRI was better than ultrasound at ruling out abnormal development. While the MERIDIAN study is very robust, it is currently the only study to date to assess concordance between feMRI-based prognosis and postnatal outcome; thus, further studies are required. We therefore retrospectively assessed concordance between the prognosis

Received April 30, 2020; accepted after revision July 6.

From the Departments of Medical Imaging (M.W., C.K., E.M.) and Pediatric Neurology (K.M.) and Research Institute (D.R., R.W.), Children's Hospital of Eastern Ontario, University of Ottawa, Ottawa, Ontario, Canada; and Department of Neurology (M.W.), Beth Israel Deaconess Medical Center, Harvard Medical School, Boston, Massachusetts.

Please address correspondence to Elka Miller, MD, FRCP, Department of Medical Imaging, CHEO, University of Ottawa, 401 Smyth Rd, Ottawa, ON, Canada, K1H 8L1; e-mail: EMiller@cheo.on.ca

<http://dx.doi.org/10.3174/ajnr.A6770>

of the fetal brain based on prenatal MR imaging and the neurodevelopmental outcome of the child. Additionally, we measured the diagnostic accuracy of feMRI with an assessment of concordance between prenatal diagnosis by feMRI and the postnatal imaging diagnosis.

MATERIALS AND METHODS

Demographic Data

This retrospective study was approved by the institutional review board of Children's Hospital of Eastern Ontario, Canada. All referrals for feMRI followed a dedicated fetal neurosonographic study. No written informed consent was obtained at the Medical Imaging Department, but feMRI requisitions were discussed with a multidisciplinary team before booking the MR imaging, as per departmental practice. A search of the Medical Imaging Department data base was performed to identify feMRI studies performed with a 3T system (Magnetom Skyra; Siemens) and a 1.5T MR imaging system (Signa HD; GE Healthcare) from January 1, 2008, to November 30, 2018. We examined the final radiology report of all the feMRIs identified during this time and included only those that had dedicated imaging of the fetal brain. A total of 145 pregnancies with at least 1 feMRI scan were found. In the assessment of diagnostic accuracy, we excluded cases that did not have postnatal imaging ($n = 31$).

In cases of termination of pregnancy or fetal death, we reviewed postmortem imaging, if available. In the assessment of prognostic accuracy, patients were excluded if they lacked sufficient documented postnatal clinical follow-up to assess the postnatal neurodevelopmental outcome (ie, there was no postnatal clinical follow-up or there was follow-up but the Gross Motor Function Classification System [GMFCS; <https://cerebralpalsy.org.au/our-research/about-cerebral-palsy/what-is-cerebral-palsy/severity-of-cerebral-palsy/gross-motor-function-classification-system/>]) score and epilepsy status could not be determined ($n = 36$) or if there was termination of pregnancy ($n = 5$) because the clinical postnatal assessment could not be performed. In pregnancies with multiple feMRIs, we included only the feMRI performed at the latest gestational age (GA). For assessments of both diagnostic and prognostic accuracy of feMRI, we repeated our analyses after dividing patients into 2 groups, GA <25 weeks and GA \geq 25 weeks, because decisions regarding termination of pregnancy in our institution are preferable earlier during the second trimester.

Image Analysis

For assessment of the diagnostic accuracy between feMRI and postnatal imaging, each of the fetal MR imaging report impressions was reviewed by a medical student (M.W.) and compared with the final radiology impression from the postnatal MR imaging brain report or, alternatively, if a postnatal MR imaging was not performed, the postnatal ultrasound brain report. For each pregnancy, concordance was reported as the following: 1) agreement (comparable results) between prenatal and postnatal final diagnosis, or 2) disagreement between the prenatal and postnatal final diagnosis.

Cases that were initially deemed to have disagreement between prenatal and postnatal diagnoses underwent further review by a

pediatric neuroradiologist (E.M., 19 years of experience in fetal imaging), which included an examination of both the prenatal MR imaging and postnatal images and associated reports. The initial assessment of discordance of the case was amended if the radiologist determined that there was actually agreement between the prenatal and postnatal diagnoses.

The fetal MR imaging reports were reviewed (M.W.) to determine the predominant type of brain abnormality of each fetus. Each fetal MR imaging of the brain was classified as one of the following: VM (mild, moderate, or severe), corpus callosum abnormalities, posterior fossa abnormalities, sulcation/migration, space-occupying lesion, vascular anomaly, hemorrhage, or normal brain. When there was >1 brain abnormality identified, we reported the most severe abnormality.

Assessment of Prenatal Prognosis

Prenatal prognosis was determined by a pediatric neurologist (K.M., with 1 year of experience as an attending pediatric neurologist) who reviewed all feMRI reports and categorized each pregnancy as having either a favorable, indeterminate, or poor prognosis based on her clinical experience, to replicate what would occur in clinical practice. The neurologist was blinded to postnatal outcome. For a small number of cases in which the feMRI findings were difficult to interpret, the neurologist received input from the radiologist, again replicating what would occur in clinical practice. When available ($n = 36$), prenatal consult notes produced by fetal-maternal medicine, genetics, and neurology were examined to verify that the prognosis provided by our neurologist was concordant with the prognosis provided by experts at the time of pregnancy.

Assessment of Postnatal Outcome

Postnatal neurodevelopmental status was assessed by reviewing the clinical notes of the children corresponding to the pregnancies included in the study. This assessment was performed by a pediatric neurologist (K.M.) and a medical student (M.W.) who were blinded to the prenatal prognosis of the child. The most recent report in the child's medical history to document gross motor function and seizure status was reviewed. Reports produced before 12 months of age were not reviewed. Reports produced by neurologists and geneticists were prioritized. If the reports produced by these specialists did not provide sufficient information to assess neurodevelopmental status or were non-existent, we then reviewed reports produced by other allied health professionals. If after review of all available medical reports, there was insufficient information to grade the neurodevelopmental outcome, then the patient was excluded.

For each child, the postnatal neurodevelopmental outcome was categorized as either favorable, intermediate, or poor. The postnatal outcome was determined by a combination of the following: gross motor function measured using the GMFCS score¹¹ of the child and the presence or absence of epilepsy. For GMFCS, a score of either 0 or I was considered favorable, a score of either II or III was considered intermediate, and a score of IV or V was considered poor. For epilepsy, having no diagnosis of epilepsy was considered favorable, a diagnosis of epilepsy controlled by medication was considered intermediate, and a diagnosis of intractable epilepsy (failing to respond to 2 antiepileptic drugs) was considered

Table 1: Characteristics of participants included in image analysis

Characteristic	All GA (n = 114)	GA <25 Weeks (n = 56)	GA ≥25 Weeks (n = 58)
GA at fetal MR imaging (range) (median) (IQR) (wk)	19.00–39.43 (25.9 [21.9–32.3])	19.00–24.43 (21.8 [21.0–23.1])	25.86–39.43 (32.2 [29.1–34.1])
Maternal age at fetal MR imaging (range) (median) (IQR) (yr)	16.00–41.00 (31.0 [28.0–34.0])	16.00–41.00 (31.0 [28.8–35.0])	17.00–41.00 (31.0 [27.2–34.0])
Brain region (No.) (%)			
Ventriculomegaly	39 (34.2%)	20 (35.7%)	19 (32.8%)
Mild	23 (21.9%)	14 (25.0%)	9 (15.5%)
Moderate	7 (4.4%)	4 (3.6%)	3 (5.1%)
Severe	9 (7.9%)	2 (3.6%)	7 (12.1%)
Posterior fossa	26 (22.8%)	12 (21.4%)	14 (24.1%)
Corpus callosum	13 (11.4%)	3 (5.4%)	10 (17.2%)
Sulcation/migration	15 (13.2%)	9 (16.1%)	6 (10.3%)
Normal brain	15 (13.2%)	11 (19.6%)	4 (6.9%)
Space-occupying lesion	4 (3.5%)	1 (1.8%)	3 (5.2%)
Vascular anomaly	1 (0.9%)	0 (0.0%)	1 (1.7%)
Hemorrhage	1 (0.9%)	0 (0.0%)	1 (1.7%)

Note:—IQR indicates interquartile range.

Table 2: Image analysis—concordance between fetal MR imaging and postnatal imaging

	No. (%)	GA <25 Weeks (No.) (%)	GA ≥25 Weeks (No.) (%)
Agreement	106 (93.0%)	50 (89.3%)	56 (96.6%)
Disagreement	8 (7.0%)	6 (10.7%)	2 (3.4%)

poor. The overall neurodevelopmental outcome of the child was reported as the least favorable outcome between the GMFCS and epilepsy scores. Death due to a brain abnormality in the postnatal period and stillbirth were also considered a poor outcome. Researchers were blinded to the prenatal prognosis.

An overall assessment of concordance was made by comparing the prenatal prognosis with the neurodevelopmental outcome of the child. Additionally, we specifically tested concordance between the prenatal prognosis and the postnatal development of epilepsy in all children who survived to at least 1 year of age.

RESULTS

Image Analysis

Of 145 patients in the study sample who underwent feMRI, 31 were removed from the image analysis because they did not have any documented postnatal imaging. For the group of 114 patients included in this analysis, the gestational age range was 19.0–39.4 weeks (median, 25.9 weeks; interquartile range, 21.9–32.3 weeks). The maternal age range was 16–41 years (median, 31 years; interquartile range, 28–34 years). In 15.8% (18/114) of pregnancies, there were multiple brain abnormalities noted on feMRI. Table 1 summarizes the participants' characteristics and abnormalities found on feMRI. There was agreement between the prenatal diagnosis by feMRI and the postnatal imaging diagnosis in 93% (106/114) of cases (Table 2). After the prenatal and postnatal imaging reports were reviewed by the medical student, there were 9 cases of disagreement between prenatal and postnatal imaging; however, after these 9 cases were reviewed by the radiologist, it was determined that there was disagreement in only 8 cases. A list of the 8 cases in which there was disagreement between prenatal and postnatal imaging is provided in Table 3.

Concordance between Prenatal Prognosis and Postnatal Neurodevelopmental Outcome

A total of 104 patients with feMRI met the study criteria and were included in the final study group for analysis. The gestational age range was 19–39.4 weeks (median, 26.1 weeks; interquartile range, 21.8–31.9 weeks). The maternal age range was 16–41 years (median, 31 years; interquartile range, 28–33 years). In 11.5% (12/104) of pregnancies, there were multiple brain abnormalities noted on the feMRI. The range of ages for postnatal follow-up was 1.0–10.4 years (median, 3 years; interquartile range, 1.9–5.9 years). For the assessment of postnatal outcome, clinic notes from neurologists or geneticists were available in 69.2% (72/104) of cases. Table 4 summarizes the participants' characteristics and abnormalities found on feMRI. There were 36 pregnancies in which prenatal consult notes were available. In all 36 of these pregnancies, the prognosis generated by the neurologist was the same as the prognosis provided in the prenatal consult notes.

Of all pregnancies with a prenatal and postnatal assessment, the prenatal prognosis was favorable in 44.2% (46/104), indeterminate in 50.0% (52/104), and poor in 5.8% (6/104); the postnatal outcome was favorable in 74.0% (77/104), intermediate in 11.5% (12/104), and poor in 14.4% (15/104) (Table 5). Of the 15 with a poor postnatal outcome, 7 died in the postnatal period and 1 was stillborn.

Of the pregnancies with a favorable prenatal prognosis, 93.5% (43/46) had a favorable postnatal outcome, while 2.2% (1/46) had a poor postnatal outcome. Of the pregnancies with a poor prenatal prognosis, 16.7% (1/6) had a favorable postnatal outcome. For pregnancies with an indeterminate prognosis, 46% (24/52) had a prenatal diagnosis of VM, 19.2% (10/52) had corpus callosum abnormalities, 13.5% (7/52) had posterior fossa abnormalities, and 13.5% (7/52) had sulcation/migration abnormalities.

There were 96 pregnancies with children surviving to at least 1 year of age. Of those with a favorable prognosis, 97.8% (45/46) did not develop epilepsy in the postnatal period, while 2.2% (1/46) developed intractable seizures (Table 6). There were 47 pregnancies with an indeterminate prognosis, of which 3 developed intractable seizures. Fetal and postnatal imaging is provided for 1 of these cases in Fig 1C. There were 3 pregnancies with a poor prognosis, 2 of which did not develop seizures while 1 developed intractable seizures.

Table 3: List of prenatal and postnatal imaging diagnoses in cases of disagreement

GA (wk)	Prenatal Diagnosis	Postnatal Diagnosis
24	Macrocephaly with moderate asymmetric VM	Healthy
22	Vermis and cerebellum slightly small for GA	Healthy
27	Moderate VM (Fig 2A)	Mild VM and 3 subependymal heterotopias
20	Mild VM and moderate pericardial effusion	Cystic encephalomalacia
24	Mild VM (Fig 2B)	Microcephaly with severe VM
24	Flattening of inferior surface of cerebellum (Fig 2C)	Extensive lissencephaly with band heterotopia
19	Twin A, healthy	Congenital CMV
19	Twin B, healthy	Congenital CMV

Note:—CMV indicates cytomegalovirus.

Table 4: Characteristics of participants included in the assessment of concordance between prenatal prognosis and postnatal neurodevelopmental outcome

Characteristic	(n = 104)	GA <25 Weeks (n = 50)	GA ≥25 Weeks (n = 54)
GA at fetal MR imaging (range) (median) (IQR) (wk)	19.00–39.43 (26.1 [21.8, 31.9])	19.00–24.43 (21.7 [21.0, 23.0])	25.00–39.43 (31.9 [29.6–34.0])
Maternal age at fetal MR imaging (range) (median) (IQR) (yr)	16.00–41.00 (31.0 [28.0–33.0])	16.00–41.00 (30.0 [28.0–32.0])	17.00–41.00 (31.0 [28.0–34.0])
Age at postnatal visit (range) (median) (IQR) (yr)	1.00–10.42 (3.0 [1.9–5.9])	1.00–8.92 (2.8 [1.7–5.1])	1.00–10.42 (3.8 [2.0–6.0])
Brain region (No.) (%)			
Ventriculomegaly	32 (30.8%)	17 (34.0%)	15 (27.8%)
Mild	20 (19.2%)	12 (24.0%)	8 (14.8%)
Moderate	5 (4.8%)	3 (6.0%)	2 (3.7%)
Severe	7 (6.7%)	2 (4.0%)	5 (9.3%)
Posterior fossa	19 (18.3%)	7 (14.0%)	12 (22.2%)
Corpus callosum	11 (10.6%)	2 (4.0%)	9 (16.7%)
Sulcation/migration	8 (7.7%)	5 (10.0%)	3 (5.6%)
Normal	28 (26.9%)	18 (36.0%)	10 (18.5%)
Space	4 (3.8%)	1 (2.0%)	3 (5.6%)
Vascular anomaly	1 (1.0%)	0 (0.0%)	1 (1.9%)
Hemorrhage	1 (1.0%)	0 (0.0%)	1 (1.9%)

Table 5: Prenatal prognosis and postnatal outcome for all gestational ages (n = 104)

Prenatal Prognosis (No.) (%)	Postnatal Outcome, Favorable (n = 77)	Postnatal Outcome, Intermediate (n = 12)	Postnatal Outcome, Poor (n = 15)
Favorable (n = 46)	43 (93.5%)	2 (4.3%)	1 (2.2%)
Indeterminate (n = 52)	33 (63.5%)	10 (19.2%)	9 (17.3%)
Poor (n = 6)	1 (16.7%)	0 (0.0%)	5 (83.3%)

Table 6: Prenatal prognosis and postnatal development of epilepsy (n = 96)

Prenatal Prognosis (No.) (%)	Absence of Epilepsy (n = 84)	Medically Controlled Epilepsy (n = 7)	Intractable Epilepsy (n = 5)
Favorable (n = 46)	45 (97.8%)	0 (0.0%)	1 (2.2%)
Indeterminate (n = 47)	37 (78.7%)	7 (14.9%)	3 (6.4%)
Poor (n = 3)	2 (66.7%)	0 (0.0%)	1 (33.3%)

FeMRI Prognostication by GA

The distribution of prenatal prognosis and postnatal outcome for GA <25 weeks and GA ≥25 weeks is presented in Tables 7 and 8. The proportion of pregnancies given a favorable prognosis that resulted in favorable development was similar between groups (92.0% GA <25 weeks versus 95.2% GA ≥25 weeks).

DISCUSSION

Our study demonstrated a high level of agreement between prenatal diagnosis by feMRI and postnatal imaging diagnosis, with agreement observed in 93% (106/114) of cases. Our findings are comparable with prior diagnostic-accuracy studies of feMRI^{1–4} and further highlight the strength of feMRI in accurately diagnosing fetal brain abnormalities. In 7% (8/114) of cases, there was disagreement between prenatal and postnatal imaging. The prenatal and postnatal imaging diagnoses for each of these 8 cases are listed in Table 3, with representative images provided for 3 of these cases in Fig 2.

An example of discordant imaging diagnoses is that of the fetus whose feMRI was reported as having slight flattening of the inferior surface of the cerebellum with no note made of any lissencephaly (Table 3). The postnatal MR imaging, however, demonstrated extensive lissencephaly with subcortical band heterotopia (Fig 2C). On retrospective review of the feMRI, there was a subtle, thin, T2-hypointense cerebral

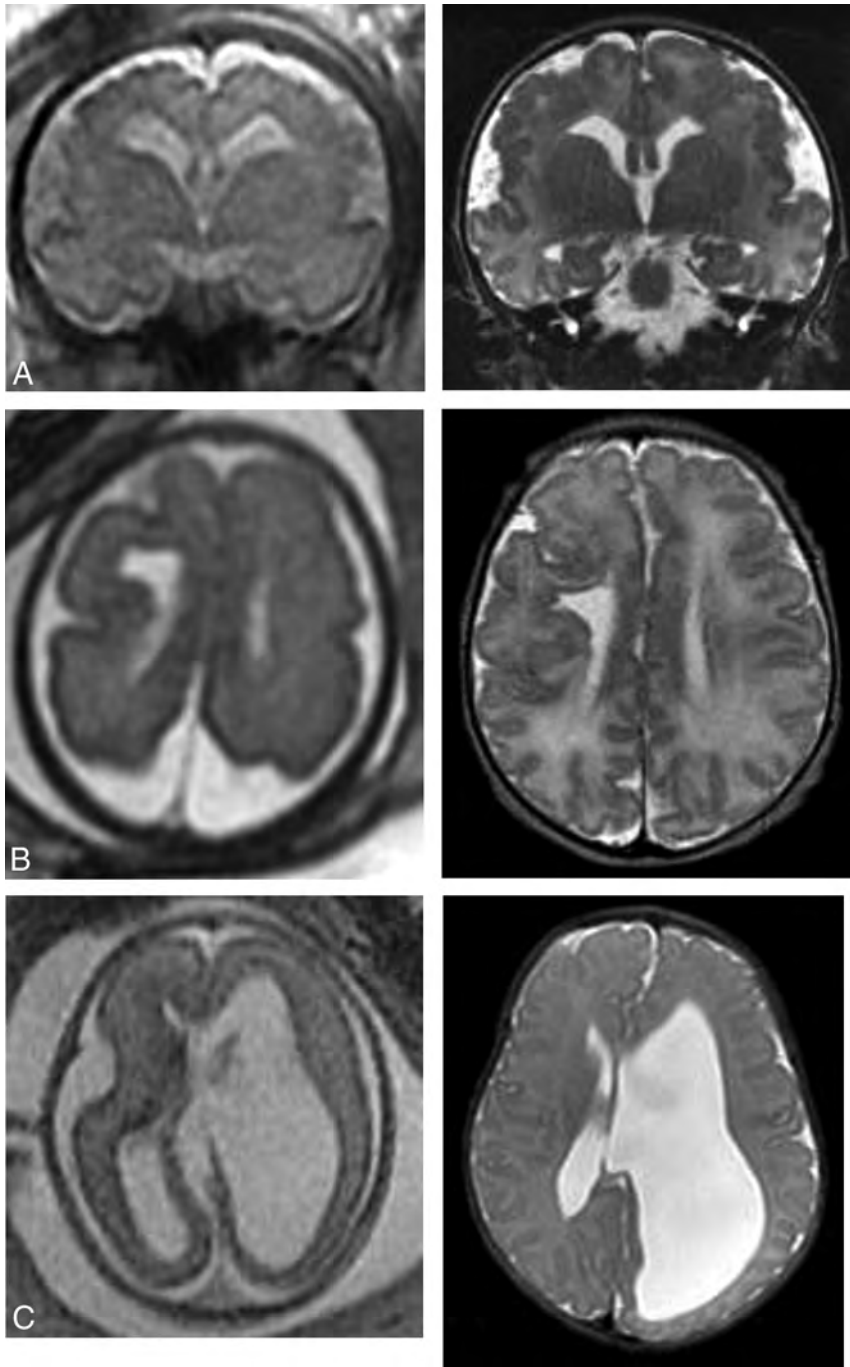


FIG 1. Prenatal and postnatal imaging examples of cases in which an indeterminate prognosis was associated with a poor outcome. *A*, Coronal single-shot fast spin-echo at 33 weeks with extensive bilateral polymicrogyria (peri-Sylvian, frontal, and parietal). Coronal T2 at 2 days of age confirms diffuse polymicrogyria. *B*, Axial single-shot fast spin-echo at 30 weeks shows a small right cerebral hemisphere with associated abnormal sulcation. There is right-sided polymicrogyria, a left subependymal nodule, and a large middle cystic structure (not shown) inferior to the corpus callosum and extending to the posterior fossa. Axial T2 at 2 days of age confirmed the fetal MR imaging findings. *C*, Axial FIESTA at 23 weeks demonstrates left unilateral VM. Axial T2 at 3 weeks of age confirms the left VM. The patient later required ventriculoperitoneal shunt due to complications of hydrocephalus and further disconnection surgery without resolution of seizures.

line that can be appreciated in the frontal lobes. This antenatal diagnosis, however, could only be made retrospectively in light of the available postnatal imaging data.

It is often difficult to predict and explain discordant imaging diagnoses. After reviewing the images of the 8 discordant cases, we are confident that the imaging findings reported are accurate and that the changes seen on postnatal imaging would have been very difficult if not impossible to predict. In reality, there are changes in the fetal brain that can occur in the prenatal period after the feMRI and also in the brain of the child in the postnatal period. Fortunately, novel imaging techniques are emerging to facilitate more accurate and earlier prenatal imaging diagnoses.¹²⁻¹⁴ For example, the use of myo-inositol in MR spectroscopy shows promise as an early marker of congenital cytomegalovirus infection.¹⁴ This technique may have aided in the detection of congenital cytomegalovirus in the twins in our study, who had normal brains on feMRI but were both subsequently diagnosed with congenital cytomegalovirus infection postnatally (Table 3).

The principal aim of this study was to retrospectively assess the ability of feMRI to prognosticate the neurodevelopment of the child. The key finding of our study was the strong association between a favorable prognosis and favorable postnatal outcome, with 93.5% (43/46) of pregnancies assigned a favorable prognosis resulting in a favorable outcome. Similar results were observed when comparing the prognosis with the postnatal development of epilepsy, with 97.8% (45/46) of favorable pregnancies resulting in children without a postnatal diagnosis of epilepsy. Poor prognosis and poor outcome were also highly concordant, albeit in a small sample, with 83.3% (5/6) of pregnancies assigned a poor prognosis resulting in a poor outcome. Of all pregnancies with a prenatal prognosis and postnatal assessment, 50.0% (52/104) were given an indeterminate prognosis. It has previously been reported that an advantage of feMRI compared with antenatal ultrasound is that fewer indeterminate prognoses are

made.¹ Many identified brain abnormalities, however, have an unknown outcome regardless of when they are discovered or who is generating the prognosis; thus, an outcome cannot be predicted

Table 7: Prenatal prognosis and postnatal outcome at GA <25 weeks (n = 50)

Prenatal Prognosis (No.) (%)	Postnatal Outcome, Favorable (n = 36)	Postnatal Outcome, Intermediate (n = 7)	Postnatal Outcome, Poor (n = 7)
Favorable (n = 25)	23 (92.0%)	1 (4.0%)	1 (4.0%)
Indeterminate (n = 25)	13 (52.0%)	6 (24.0%)	6 (24.0%)
Poor (n = 0)	0 (0.0%)	0 (0.0%)	0 (100.0%)

Table 8: Prenatal prognosis and postnatal outcome at GA ≥25 weeks (n = 50)

Prenatal Prognosis (No.) (%)	Postnatal Outcome, Favorable (n = 41)	Postnatal Outcome, Intermediate (n = 5)	Postnatal Outcome, Poor (n = 8)
Favorable (n = 21)	20 (95.2%)	1 (4.8%)	0 (0.0%)
Indeterminate (n = 27)	20 (74.1%)	4 (14.8%)	3 (11.1%)
Poor (n = 6)	1 (16.7%)	0 (0.0%)	5 (83.3%)

regardless of the accuracy of the imaging test. For pregnancies with an indeterminate prognosis, 63.5% (33/52) had a favorable outcome, 19.2% (10/52) had an intermediate development, and 17.3% (9/52) had a poor outcome. An indeterminate prognosis is not predicting an intermediate neurodevelopmental outcome. Rather, an indeterminate prognosis implies that a range of outcomes is possible, which could be favorable, intermediate, or poor. We have included representative imaging for 3 cases in which an indeterminate prognosis was associated with a favorable outcome (Fig 3) and 3 cases in which an indeterminate prognosis was associated with a poor outcome (Fig 1).

The most common prenatal diagnosis for pregnancies with an indeterminate prognosis was VM, which accounted for 46% (24/52) of the prenatal diagnoses. Of these 24 fetuses with VM given an indeterminate prognosis, 12 had mild VM, 5 had moderate VM, and 7 had severe VM. In our study, VM was a challenging prenatal diagnosis to prognosticate as demonstrated by the 75% (24/32) of all fetuses with VM and 100% (12/12) of fetuses with moderate (n = 5) or severe (n = 7) VM given an indeterminate prognosis. The large proportion of indeterminate prognoses given to pregnancies with a diagnosis of VM appears justified because the 24 pregnancies with VM given an indeterminate prognosis resulted in a wide range of outcomes, including 15 children with a favorable outcome, 5 with an intermediate outcome, and 4 with a poor outcome (including 3 deaths).

The MERIDIAN diagnostic accuracy study is currently the most exhaustive study of feMRI and its ability to aid in the prenatal diagnosis of fetal brain abnormalities.⁹ One component of this study compared prognostication of postnatal neurodevelopmental outcome between feMRI and antenatal ultrasound.¹⁰ Prenatal prognosis was categorized as either normal, favorable, intermediate, poor, or unknown. Postnatal neurodevelopment was assessed at 2–3 years of age and was categorized as either normal, at risk, or abnormal and was assessed using primarily the Bayley Scales of Infant and Toddler Development, Third Edition, and the Ages & Stages Questionnaire, Third Edition, as well as the Strength and Difficulties Questionnaire, GMFCS, and whether the child developed cerebral palsy. They concluded that neither feMRI nor ultrasound was able to accurately predict abnormal development, but they did report that feMRI was better than ultrasound at ruling out

abnormal development. Unlike our study, this study did not report the proportion of pregnancies with a favorable prognosis based on feMRI that resulted in a child with favorable development. However, they did report that in children who developed normally, 72% (71/99) were given a favorable or healthy prognosis based on feMRI. Furthermore, they reported that in surviving children with abnormal development, 39% (21/54) were given a favorable or normal prognosis based on feMRI, and in nonsurviving infants, 15% (11/73) were given a favorable or normal prognosis. In this respect, the study by Hart et al¹⁰ suggested that a

favorable prognosis based on feMRI is less predictive of normal development than it was in our retrospective study. This suggestion could be explained by numerous factors, including differences in the prognosis categories, outcome assessment, clinical thresholds for indicating a feMRI, and likely different practices in providing prognoses.

We also compared feMRI prognostication between 2 GA groups: <25 weeks and ≥25 weeks. We found that the ability of feMRI to predict favorable development in pregnancies with a favorable prenatal prognosis was not influenced by GA, with 92.3% (23/25) agreement for GA <25 weeks versus 95.2% (20/21) for GA ≥25 weeks. Providing accurate prognoses to patients is particularly important in the earlier stages of pregnancy because decisions regarding termination of pregnancy may be based on these fetal scans. It is, therefore, encouraging to note that feMRI performed at GA <25 weeks provides a high level of prognostic accuracy that is not inferior to feMRI performed at GA ≥25 weeks.

In our study, there was 1 pregnancy assigned a favorable prenatal prognosis that resulted in a poor postnatal outcome. This was a twin pregnancy with the feMRI for the fetus in question being unremarkable apart from a fluid-filled cavity above the tentorium believed to be an arachnoid cyst. This fetus was given a favorable prenatal prognosis; however, the child had a poor outcome with GMFCS II–III and intractable seizures. Postnatal MR imaging findings at 4 months were unremarkable. The most likely explanation is that this child had a predisposition to seizures without any associated intracranial abnormality demonstrated on feMRI. A large portion of children with seizures do not have any evidence of intracranial abnormality on postnatal imaging.¹⁵ We therefore do not believe that this poor outcome could have been predicted on the basis of findings of the feMRI.

A concerning scenario is when the prognosis of a fetus is determined to be poor and the child has a favorable postnatal outcome. There was 1 case like this in our study. The fetus had a vein of Galen aneurysmal malformation seen on feMRI. A poor prenatal prognosis was made retrospectively from the feMRI report and images; however, the child's postnatal development was favorable, with the vein of Galen malformation redemonstrated on postnatal MR imaging. Many interventional procedures were

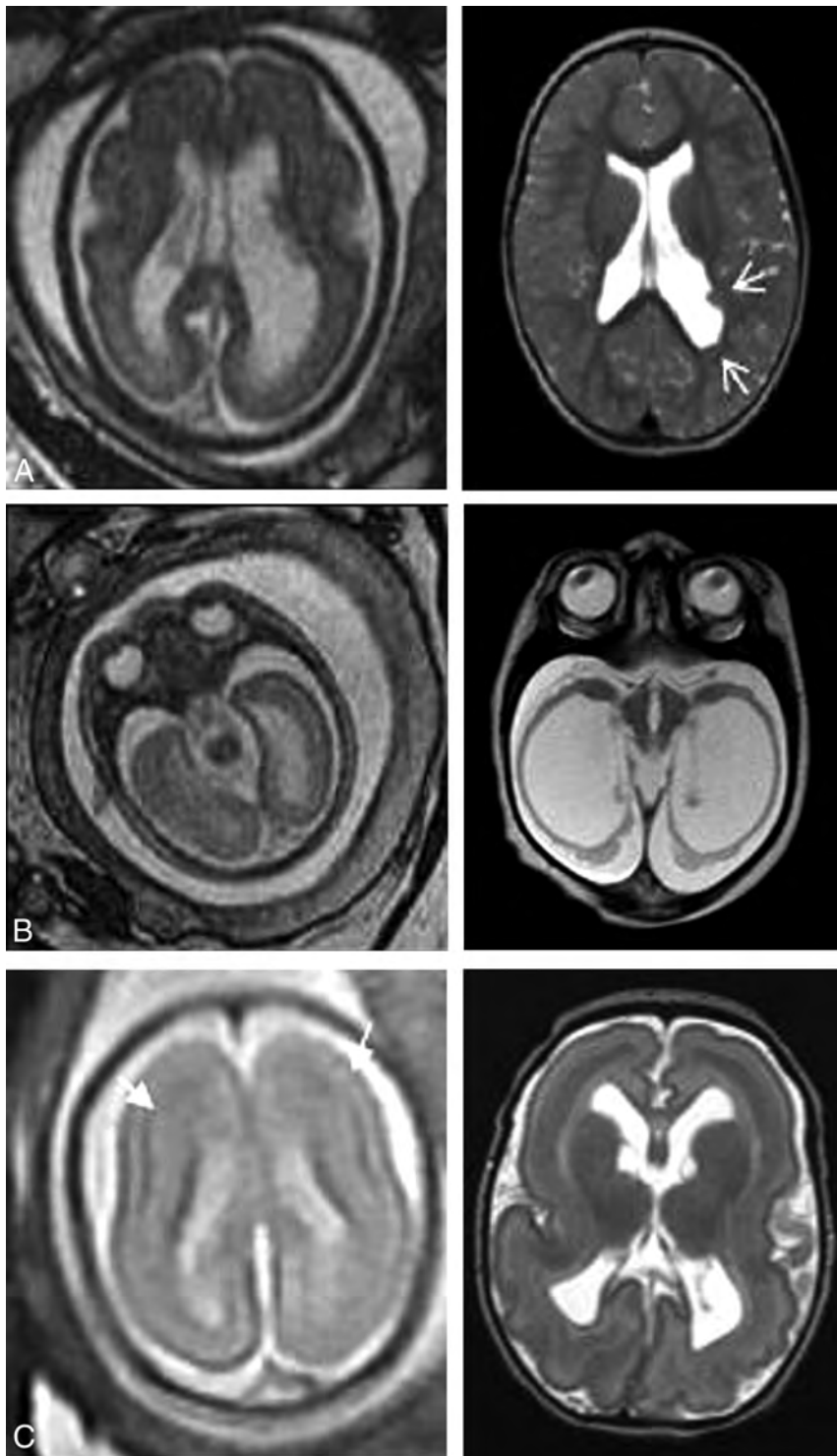


FIG 2. Prenatal and postnatal images showing examples of discordant imaging findings. *A*, Axial T2 feMRI at 27 weeks shows moderate VM, and postnatal axial T2 MRI shows mild VM with subependymal heterotopia (*arrows*). *B*, feMRI at 24 weeks shows mild VM and a preserved cerebral mantle, and postnatal MRI shows microcephaly and severe ventriculomegaly with thinning of the cerebral mantle. *C*, feMRI at 24 weeks shows a thin T2-hypointense cerebral line in the frontal lobes (*arrows*) that was overlooked. Postnatal MRI confirmed subcortical band heterotopia.

completed to render the malformation nonhemodynamically significant, and apart from decreased endurance and some fine motor difficulties, the child has been developing normally. Vein of Galen

malformations are known to have variable outcomes, which could explain why this child developed favorably despite a poor prognosis by feMRI. Furthermore, while this child did meet our criteria for a favorable postnatal outcome, he did require several embolizations in the postnatal period; thus, the postnatal outcome was not as benign as in another child with a favorable outcome who did not require such an extensive follow-up.

One of the main limitations of our study, inherent in its retrospective design, was that in most pregnancies (68/104), the prenatal prognosis was established solely on the basis of the feMRI report and imaging, without any clinical data that would otherwise be available in the real world. In the 36 pregnancies for which prenatal consult notes were available, we demonstrated that the prognosis determined by the neurologist was the same as the prognosis provided in the prenatal consult notes. We can therefore be fairly confident that the prognoses retrospectively determined by our neurologist likely represent the prognoses that would be provided by our institution for all 104 pregnancies included in the prognostic arm of the study. Nonetheless, it is difficult to distinguish whether the prognosis was established purely on the basis of feMRI or if the prognosis represents the combined efforts of feMRI coupled with the interpretation of clinical information by our pediatric neurologist. Even in the 36 cases for which a prognosis had already been established, it is entirely possible that factors beyond the findings of the feMRI influenced the prognosis that was generated at the time.

In the postnatal period, our neurodevelopmental assessments were limited to the GMFCS score and the presence/absence of seizures because these were the only outcomes that could be accurately assessed in our retrospective chart review. We therefore did not perform any assessment of language or social or cognitive skills. Furthermore, using the GMFCS score, originally designed to evaluate children with cerebral palsy, in our cohort that was

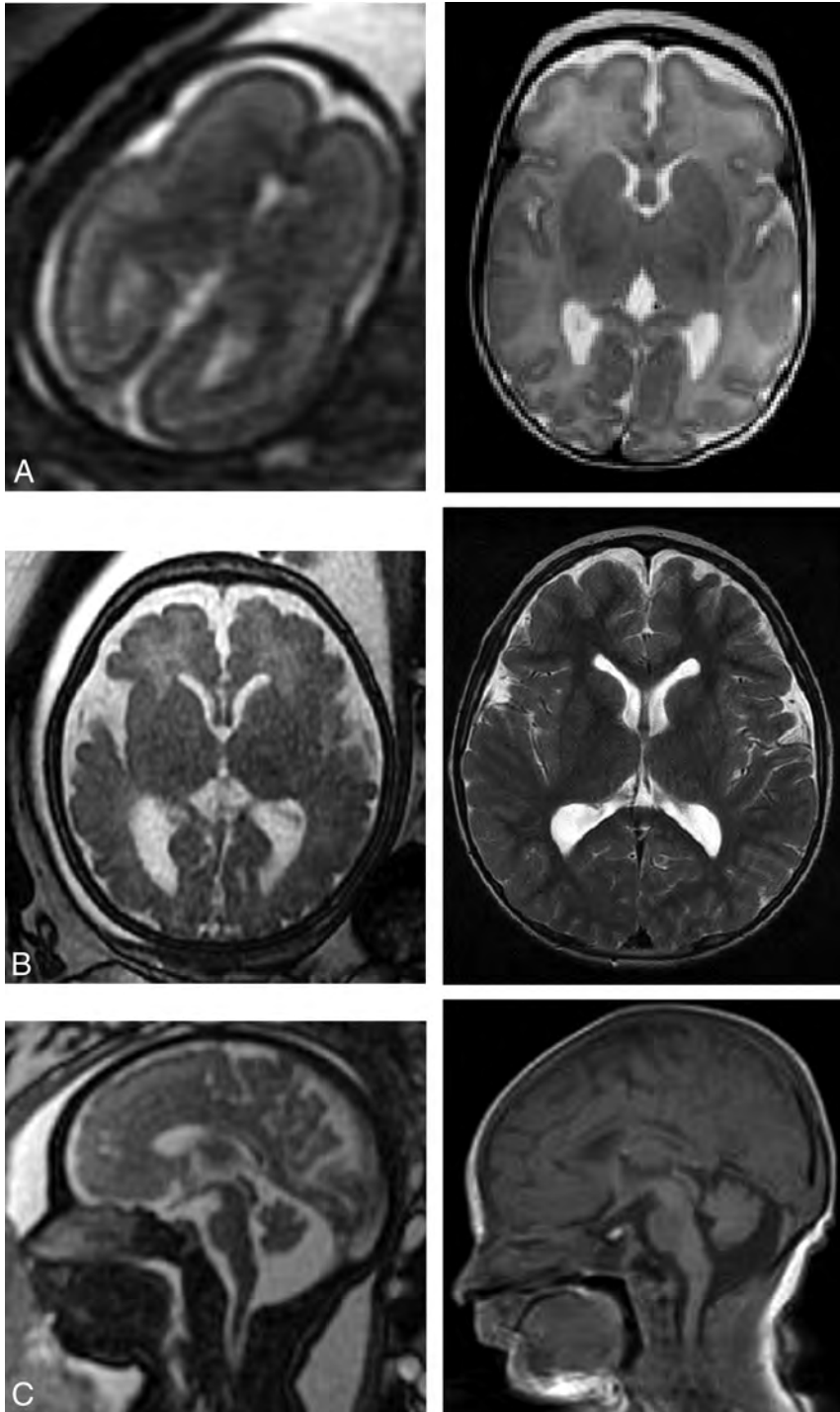


FIG 3. Prenatal and postnatal imaging examples of cases in which an indeterminate prognosis was associated with a favorable outcome. A, Axial single-shot fast spin-echo at 23 weeks with primitive sulcation and oligohydramnios. Axial T2 at 2 months of age shows normal brain MRI findings. B, Axial single-shot fast spin-echo at 35 weeks with VM (left 13 and right 12 mm). MRI at 6 years of age shows persistent prominent VM similar to findings on the ultrasound after birth (not shown). The patient has normal neurologic examination findings. C, Sagittal single-shot fast spin-echo at 35 weeks with a large cisterna magna versus vermian hypoplasia. Sagittal T1 at 3 days of life shows a prominent cisterna magna without other abnormalities.

not limited to children with cerebral palsy, has its limitations. We also assessed developmental outcomes at a wide range of ages (1–10 years of age). Our sample size was relatively small, particularly

the number of pregnancies that had a poor prognosis. This size limits our ability to provide any definitive guidance for pregnancies given a poor prognosis. Last, our retrospective study summarizes feMRI data during a 10-year period from 2008 to 2018; therefore, we may not have captured improvements in imaging techniques in terms of resolution and the applicability of advanced techniques during this time. feMRI continues to be an evolving technology, and novel imaging methods such as FLAIR, DWI, and DTI may further increase both diagnostic and prognostic accuracy.^{12–14}

CONCLUSIONS

Our study confirmed that feMRI provides a high level of diagnostic accuracy (93.0%), which is comparable with that in previous studies of diagnostic accuracy. The principal finding of our retrospective study was that a favorable prenatal prognosis based on feMRI is highly predictive of a favorable neurodevelopmental outcome in the child (93.5% agreement). A large portion of the pregnancies in our study were given indeterminate prognoses (50%), of which a large proportion had a prenatal diagnosis of VM (46%). The pregnancies given an indeterminate prognosis resulted in a wide range of outcomes, 63.5% of which were favorable. Last, our study found no differences in prognostication between feMRI completed at GA <25 weeks and GA ≥25 weeks.

Our study adds to the growing body of literature examining the utility of feMRI, particularly the work by Hart et al,¹⁰ who were the first to publish a prospective cohort study comparing prognoses based on feMRI and postnatal neurodevelopmental outcome. Moving forward, more large, prospective studies are required to better understand the role of feMRI in prognosticating neurodevelopment, particularly in cases in which the prognosis is indeterminate. These may eventually allow clinicians to provide

prognoses for these patients with greater certainty of postnatal outcome. Future studies should also aim to recruit large numbers of pregnancies with poor prognoses on feMRI because prognostication

of outcome in these cases has only been studied in small samples to date.

Disclosures: Elka Miller—UNRELATED: Board Membership: I am on the Board at my hospital as a representative of the medical staff. I do not receive payment for this.

REFERENCES

1. Griffiths PD, Bradburn M, Campbell MJ, et al; MERIDIAN collaborative group. **Use of MRI in the diagnosis of fetal brain abnormalities in utero (MERIDIAN): a multicentre, prospective cohort study.** *Lancet* 2017;389:538–46 CrossRef Medline
2. Jarvis D, Mooney C, Cohen J, et al. **A systematic review and meta-analysis to determine the contribution of MR imaging to the diagnosis of foetal brain abnormalities in utero.** *Eur Radiol* 2017;27:2367–80 CrossRef Medline
3. Rossi A, Prefumo F. **Additional value of fetal magnetic resonance imaging in the prenatal diagnosis of central nervous system anomalies: a systematic review of the literature.** *Ultrasound Obstet Gynecol* 2014;44:388–93 CrossRef Medline
4. van Doorn M, Oude Rengerink K, Newsum EA, et al. **Added value of fetal MRI in fetuses with suspected brain abnormalities on neurosonography: a systematic review and meta-analysis.** *J Matern Fetal Neonatal Med* 2016;29:2949–61 CrossRef Medline
5. Winkler A, Tölle S, Natalucci G, et al. **Prognostic features and long-term outcome in patients with isolated fetal ventriculomegaly.** *Fetal Diagn Ther* 2018;44:210–20 CrossRef Medline
6. Li Z, Lv Y, He P, et al. **Clinical value of prenatal MRI for diagnosis of isolated ventriculomegaly and prediction of early postnatal developmental outcomes.** *Prenat Diagn* 2019;39:124–29 CrossRef Medline
7. Patek KJ, Kline-Fath BM, Hopkin RJ, et al. **Posterior fossa anomalies diagnosed with fetal MRI: associated anomalies and neurodevelopmental outcomes.** *Prenat Diagn* 2012;32:75–82 CrossRef Medline
8. Limperopoulos C, Robertson RL, Estroff JA, et al. **Diagnosis of inferior vermian hypoplasia by fetal magnetic resonance imaging: potential pitfalls and neurodevelopmental outcome.** *Am J Obstet Gynecol* 2006;194:1070–76 CrossRef Medline
9. Griffiths PD, Bradburn M, Campbell MJ, et al. **MRI in the diagnosis of fetal developmental brain abnormalities: the MERIDIAN diagnostic accuracy study.** *Health Technol Assess* 2019;23:1–144 CrossRef Medline
10. Hart AR, Embleton ND, Bradburn M, et al. **Accuracy of in-utero MRI to detect fetal brain abnormalities and prognosticate developmental outcome: postnatal follow-up of the MERIDIAN cohort.** *Lancet Child Adolesc Health* 2020;4:131–40 CrossRef Medline
11. Palisano R, Rosenbaum P, Walter S, et al. **Development and reliability of a system to classify gross motor function in children with cerebral palsy.** *Dev Med Child Neurol* 1997;39:214–23 CrossRef Medline
12. Diogo MC, Prayer D, Gruber GM, et al. **Echo-planar FLAIR sequence improves subplate visualization in fetal MRI of the brain.** *Radiology* 2019;292:159–69 CrossRef Medline
13. Kasprian G, Del Río M, Prayer D. **Fetal diffusion imaging: pearls and solutions.** *Top Magn Reson Imaging* 2010;21:387–94 CrossRef Medline
14. Diogo MC, Glatter S, Binder J, et al. **The MRI spectrum of congenital cytomegalovirus infection.** *Prenat Diagn* 2020;40:110–24 CrossRef Medline
15. Dayan PS, Lillis K, Bennett J, et al. **Prevalence of and risk factors for intracranial abnormalities in unprovoked seizures.** *Pediatrics* 2015;136:e351–60 CrossRef Medline

Diffuse Leptomeningeal Glioneuronal Tumor of Childhood

D.A. Lakhani, K. Mankad, S. Chhabda, P. Feizi, R. Patel, A. Sarma, and S. Pruthi



ABSTRACT

SUMMARY: Diffuse leptomeningeal glioneuronal tumor is a newly defined entity under the neuronal and mixed neuronal-glia tumors category in the 2016 World Health Organization classification of brain tumors. In this series, we report clinical, radiologic, and histologic findings in 7 cases of diffuse leptomeningeal glioneuronal tumor. Our cases and literature review indicate that the most characteristic imaging finding is diffuse intracranial and intraspinal nodular leptomeningeal thickening and enhancement. This is often associated with small cyst-like, nonenhancing lesions. It should be noted that tumors sometimes bear nontypical features, for example, presenting as a solitary spinal cord mass without leptomeningeal involvement or with a dominant intracranial mass. In children with characteristic imaging findings and without clinical features of infection, the radiologist has an opportunity to promptly raise the possibility of diffuse leptomeningeal glioneuronal tumor, and thereby, affect streamlined diagnostic evaluation.

ABBREVIATIONS: DL-GNT = diffuse leptomeningeal glioneuronal tumor; WHO = World Health Organization

Diffuse leptomeningeal glioneuronal tumor (DL-GNT) is a newly defined neuronal and mixed neuronal-glia tumor described in the 2016 World Health Organization (WHO) classification of brain tumors.¹ This entity has previously been described as disseminated oligodendroglial-like leptomeningeal tumor, dysembryoplastic neuroepithelial tumor-like neoplasm, meningeal gliomatosis, diffuse leptomeningeal neurocytoma, diffuse leptomeningeal gangliocytoma, and diffuse leptomeningeal oligodendrogliomatosis.²

DL-GNT is a rare neoplasm that is more common in male children. Adult cases are rare.¹ The exact incidence is unknown, as only limited cases have been reported in the published literature. Most of these tumors show slow progression and have been

managed by surgical resection, radiation therapy, and/or chemotherapy. Given the rarity of this tumor, an optimal evidence-based management strategy has yet to be developed.

Predominant diffuse abnormal nodular leptomeningeal growth without evidence of a primary intraparenchymal focus is the most common imaging feature.^{3,4} Characteristic diffuse abnormal leptomeningeal enhancement is most commonly seen in the basal cisterns and posterior fossa, and along the spinal cord. Small, nodular T2-hyperintense leptomeningeal lesions resembling cysts are sometimes seen. Though discrete intraparenchymal lesions are unusual, they have been most commonly described in the spinal cord.^{4,5} The wide spectrum of histologic, radiologic, and clinical features often mimicking chronic infection or leptomeningeal carcinomatosis, along with very low incidence rate can make prospective tumor identification by imaging challenging.¹⁻⁴

Here, we report the clinical characteristics, imaging features, and histopathologic findings of DL-GNT in 7 patients with emphasis on imaging in hopes of increasing awareness of this entity and facilitating rapid diagnosis in affected patients.

CASE SERIES

Institutional review board approval was waived and not required for this retrospective case series. Seven cases were identified from 3 different institutions: Vanderbilt University Medical Center in Nashville; Great Ormond Street Hospital in London; and McGovern Medical School, The University of Texas Health

Received April 8, 2020; accepted after revision June 1.

From the Department of Radiology (D.A.L., P.F.), School of Medicine, West Virginia University, Morgantown, West Virginia; Department of Neuroradiology (D.A.L., P.F.), Rockefeller Neuroscience Institute, West Virginia University, Morgantown, West Virginia; Division of Internal Medicine (D.A.L.), Vanderbilt University Medical Center, Nashville, Tennessee; Department of Neuroradiology (K.M., S.C.), Great Ormond Street Hospital (GOSH), London, UK; Department of Diagnostic and Interventional Imaging, Section of Neuroradiology (R.P.), The University of Texas Health Science Center at Houston, McGovern Medical School, Houston, Texas; and Department of Radiology and Radiological Sciences (A.S., S.P.), Monroe Carell Jr. Children's Hospital, Vanderbilt University Medical Center, Nashville, Tennessee.

Previously presented in part at: Annual Meeting of the American Society of Pediatric Neuroradiology 2019, January 18–21; Los Angeles, California.

Please address correspondence to Sumit Pruthi, MD, Associate Professor of Radiology and Pediatrics, Chief of Pediatric Neuroradiology, Vanderbilt University Medical Center, Nashville, TN 37235; e-mail: sumit.pruthi@vumc.org; @sumsnets



Indicates article with supplemental on-line tables.

<http://dx.doi.org/10.3174/ajnr.A6737>

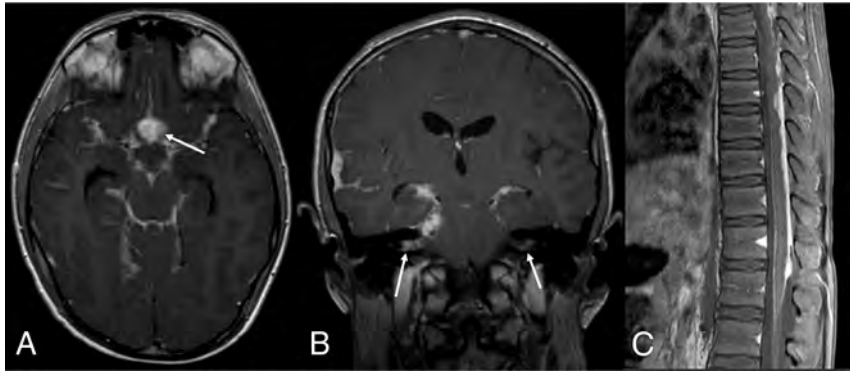


FIG 1. DL-GNT with diffuse leptomeningeal disease. Axial and coronal postcontrast T1-weighted (A and B) MR images demonstrate diffuse intracranial nodular/mass-like leptomeningeal enhancement. This is most prominent within the basilar cisterns, with masslike enhancement at the level of the optic chiasm (*arrow*). Also seen is abnormal enhancement extending along both cranial nerve VII/VIII complexes (*arrows*). Abnormal enhancement extending along cranial nerves is not uncommon in this entity. Sagittal T1-weighted postcontrast fat-suppressed image of the thoracic spine (C) shows thick, nodular leptomeningeal enhancement predominantly along the dorsal thoracic cord. The constellation of imaging findings seen in this case is the most commonly described in DL-GNT.

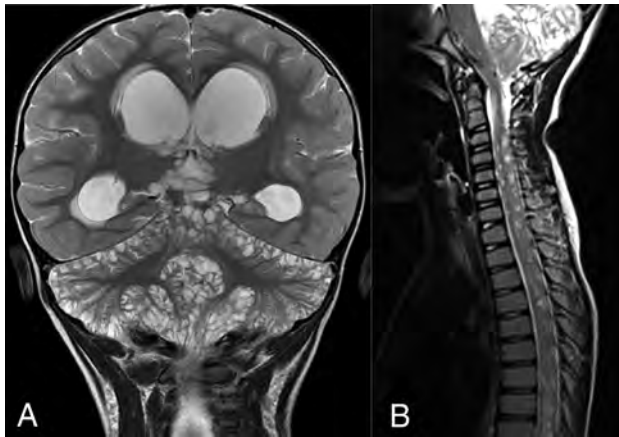


FIG 2. DL-GNT with diffuse "cyst-like" foci of T2 prolongation involving the brain and spine. Coronal T2-weighted image of the brain (A) demonstrates numerous foci of T2 prolongation located predominantly along the leptomeningeal surfaces of the cerebellum. These did not enhance after contrast administration or suppress on FLAIR (not shown). Also seen is hydrocephalus with transependymal edema as evidenced by abnormal periventricular T2 prolongation. Sagittal T2-weighted image of the cervicothoracic spine (B) in a different patient shows numerous small cervicothoracic intramedullary cyst-like lesions expanding the spinal cord. These cyst-like lesions are very suggestive of DL-GNT.

Science Center at Houston between October 2015 and December 2019.

Electronic medical record review yielded age, clinical presentation, and histopathologic diagnosis. All patients underwent brain and spinal cord imaging at either 1.5 or 3T with the following key sequences obtained in all cases: T2-weighted, FLAIR, postgadolinium T1-weighted, and diffusion-weighted. All MR imaging studies were reviewed independently by 2 fellowship-trained pediatric neuroradiologists (S.P., A.S.).

Clinical data are summarized in On-line Table 1. All patients were male. Patients presented between 3 and 14 years of age with

chronic headaches ($n = 4$), new onset seizure ($n = 2$), and gait imbalance ($n = 1$). Detailed infectious work-up including CSF analysis for infection was negative in all patients. All 7 patients underwent biopsy.

On MR imaging, diffuse nodular intracranial leptomeningeal thickening was present in 5 of 7 (72%) cases (On-line Table 1, Fig 1A, -B). One of the 5 (20%) cases had infratentorial predominance, while the other 4 (57%) cases demonstrated diffuse intracranial involvement with all demonstrating basilar cisterns involvement. Of note, the remaining 2 (29%) cases showed minimal to no intracranial leptomeningeal disease. Multiple intracranial lesions that did not enhance or suppress on FLAIR ("cystic-appearing") were noted in 2 of

7 (29%) cases (On-line Table 1, Fig 2A). Hydrocephalus was noted in 5 of 7 (71%) cases. A dominant intracranial parenchymal mass lesion was noted in 1 of 7 (15%) cases (On-line Table 1, Fig. 3A-C).

The patterns of spinal involvement included: diffuse, dorsal-predominant nodular leptomeningeal thickening (On-line Table 1, Fig 1C) in 5 of 7 (72%) cases, intramedullary spinal cord mass (On-line Table 1, Fig. 4A-C) in 2 of 7 (29%) cases, and multifocal cystic spinal cord lesions (On-line Table 1, Fig 2B) in 2 of 7 (29%) cases. Interestingly, 1 patient with cystic-appearing spinal cord lesions and another patient with a large intramedullary mass were the ones without associated nodular leptomeningeal spinal disease.

All the cases underwent biopsy and histopathologic analysis. Biopsy samples were obtained from cystic lesions in 2 of 7 (29%) cases, isolated spinal cord masses in 2 of 7 (29%) cases, and leptomeningeal nodular lesions in 2 of 7 (29%) cases. Histopathology demonstrated strong reactivity for *OLIG2*, *MAP2*, and *S-100*, with variable expression of glial fibrillary acidic protein and synaptophysin. *BRAF* fusion was noted in 2 of 7 (29%) cases, and deletion of chromosome arm 1p was noted in 2 of 7 (29%) cases. We did not see co-deletion of chromosome 1p19q in any cases (On-line Table 1).

DISCUSSION

This series describes the clinical, pathologic, and radiologic features in 7 cases of DL-GNT. Most existing publications on this topic have been presented in the pathology and oncology literature, and we believe that this imaging-focused series is the largest in the radiology literature to date. This is important because many tumors previously classified otherwise (eg, disseminated oligodendroglial-like leptomeningeal tumor) are now known to represent DL-GNT, and this tumor may not be as rare as once suspected. Furthermore, despite its somewhat distinctive imaging presentation, the diagnosis frequently remains unsuspected early in the patient's clinical course, sometimes resulting in excessive diagnostic testing for other entities with increased cost and

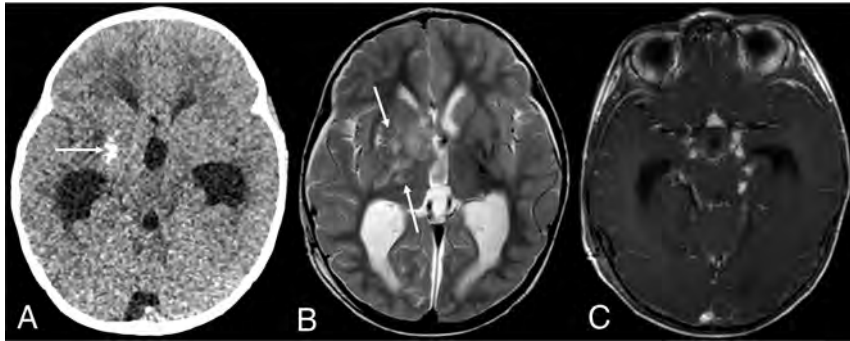


FIG 3. DL-GNT with dominant intracranial parenchymal mass. Axial noncontrast head CT in a patient with findings of hydrocephalus (A) shows ill-defined calcification within the right basal ganglia (arrow). Basal ganglia germinoma was initially considered in the differential diagnosis. Axial T2-weighted MR imaging (B) shows an ill-defined, slightly expansile area of T2 prolongation within the right putamen, thalamus, and caudate head overlapping with the calcified region demonstrated on CT (arrows). Minimal enhancement was seen in the right anterior thalamus (not shown). Axial T1-weighted postcontrast image (C) shows numerous foci of nodular supratentorial leptomeningeal enhancement lining the basilar cisterns. Despite the atypical-appearing mass involving central gray matter, the presence of characteristic diffuse supra- and infratentorial nodular deposits led to prospective consideration of DL-GNT in the differential diagnosis.

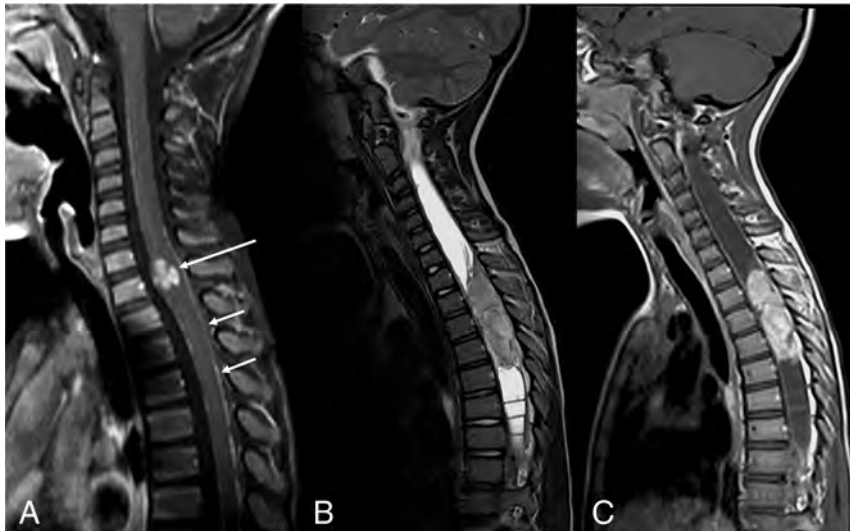


FIG 4. DL-GNT with isolated spinal cord mass. Sagittal T1-weighted postcontrast image of the cervical spine (A) demonstrates a small focal enhancing mass (long arrow) expanding the lower cervical spinal cord. Scattered areas of linear leptomeningeal enhancement are also seen along the dorsal (short arrows) and ventral aspects of the cord. Sagittal T2-weighted and T1-weighted postcontrast images of the spine (B and C) in another patient demonstrate a large hypointense, enhancing intramedullary mass extending from T2 to T5, with associated large, septated syrinx. These 2 examples highlight that intramedullary masses in DL-GNT can exhibit different appearances.

delayed diagnosis. In expeditiously raising suspicion for DL-GNT when the characteristic appearance is encountered in a patient without clinical findings of infection, the radiologist has an opportunity to facilitate rapid biopsy, diagnosis, and treatment of affected patients.

Histopathologically, tumor consists of 2 cell populations, neuronal and glial. The neuronal component consists of synaptophysin-positive neurocytes, while the glial component features glial fibrillary acidic protein-positive astrocytes.⁴ Histologically, DL-GNTs are low- to moderate-cellularity lesions consisting of relatively monomorphous oligodendrocyte-like cells with a

“glioneural commitment,” embedded in a desmoplastic or myxoid leptomeningeal stroma. Immunohistochemical features of the tumor cells include strong reactivity for *OLIG2*, *MAP2*, and S-100, with variable expression of glial fibrillary acidic protein and synaptophysin. Tumors commonly harbor *BRAF* fusions as well as deletions of chromosome arm 1p, either alone or occasionally combined with 19q deletion (hence previous use of the descriptor “oligodendroglioma-like”). Immunostaining is negative for NeuN, epithelial membrane antigen, and mutant *IDH1*, distinguishing DL-GNT from adult oligodendrogliomas (R132H).¹⁻⁴ In summary, histopathologically, DL-GNTs are low-grade neoplasms with primarily oligodendroglioma-like features, neuronal differentiating capacity, and tendency toward extensive leptomeningeal dissemination.

Based on the literature review of published DL-GNT cases, the median age at presentation is approximately 4 years and there is a male predilection (58 of 91) (64%).^{2,6-8} In our case series, all patients were male, with a median age of 6 years.

On-line Table 2 summarizes features of cases previously reported in the literature. Our case series was similar to those reported in the literature in terms of percentage of cases with diffuse intracranial nodular leptomeningeal thickening (72% in our series, 73% in the literature); diffuse intraspinal nodular leptomeningeal thickening (72% of cases, 62% in the literature); and intramedullary spinal cord mass (29% of cases, 20% in the literature). Our series had a smaller number of cases with multiple intracranial nonenhancing lesions with T2 prolongation (29% in our series, 43% in the literature); and more cases with hydrocephalus (71% in our series, 29% in the literature).

Although extensive intracranial leptomeningeal tumor has been considered a defining feature of DL-GNT, 29% of the cases in our series demonstrated minimal to no obvious intracranial leptomeningeal involvement (compared with 19% in the literature). Compared with previously reported studies, our series had a smaller percentage of cases with multifocal nonenhancing intramedullary spinal cord lesions with T2 prolongation (29% of cases, 43% in the literature). A single case in our series was

associated with extensive intracranial and spinal leptomeningeal tumor deposits with an ill-defined, minimally-enhancing, calcified mass involving the right putamen, thalamus, and caudate nucleus; a similar finding has previously been reported by Gardiman et al.⁹

The imaging presentation of DL-GNT is not well-understood. The key MR imaging findings of DL-GNT based on our case series and literature review include diffuse leptomeningeal thickening and multifocal cystic-appearing lesions in both the brain and spinal cord. These findings may be present in conjunction with or without isolated spinal cord mass.

Based on our literature review, DL-GNT was frequently misdiagnosed as tuberculosis, especially in cases from Europe and the Asia-Pacific region.¹⁰ The broad imaging differential diagnosis includes infection (eg, bacterial or tuberculous meningitis, neurocysticercosis), other CNS tumors including disseminated high-grade and low-grade neoplasms (eg, atypical teratoid/rhabdoid tumor, high-grade glioma, primary diffuse leptomeningeal gliomatosis, medulloblastoma, pilomyxoid astrocytoma), leukemia or leptomeningeal lymphomatosis, phakomatosis (eg, neurocutaneous melanosis, Sturge-Weber syndrome), and neurosarcooidosis.

Correlation with clinical features of infection and evaluation of the character of leptomeningeal involvement can help to differentiate DL-GNT from infection. Bacterial meningitis tends to have smooth rather than nodular sulcal-cisternal enhancement, and tuberculous meningitis more often causes confluent basilar enhancement. The vesicular stage of neurocysticercosis may present with multiple cysts with internal characteristic scolex “dots” deep within deep sulci, with intense inflammatory reaction in the adjacent parenchyma, that is not typical of DL-GNT.

Apart from noninfectious CSF findings, the key in differentiating DL-GNT from other entities is identification of diffuse leptomeningeal involvement of the brain and spinal cord, with or without multifocal cystic-appearing changes, or the presence of a solitary solid spinal mass.

CONCLUSIONS

Given the recent changes in classification by the WHO, as well as the rarity of this neoplasm, many radiologists may not yet be aware of DL-GNT. Furthermore, this condition may be unexpected by referring clinicians caring for patients with a newly discovered leptomeningeal disease process. In recognizing the various imaging patterns illustrated in this series, the radiologist may be the first member of the clinical team to suspect this rare diagnosis.

There should be a high index of suspicion for DL-GNT when the characteristic findings are observed in the absence of clinical and laboratory signs of infection, and when a dominant neural axis mass is absent or disproportionately small or indolent-appearing relative to the marked degree of leptomeningeal disease. While these imaging findings are typical, it should be noted that DL-GNT can also present as a solitary spinal cord mass without leptomeningeal involvement. When the diagnosis is suspected, prompt biopsy should

be performed to reduce the time to definitive diagnosis and appropriate treatment.

Disclosures: Kshitij Mankad—UNRELATED: Expert Testimony: Medicolegal reporting in UK; Payment for Lectures Including Service on Speakers Bureaus: Speaker honoraria – Novartis, Siemens. Asha Sarma—UNRELATED: Royalties: Cambridge University Press, Comments: Unrelated textbook.

REFERENCES

1. Louis DN, Perry A, Reifenberger G, et al. **The 2016 World Health Organization classification of tumors of the central nervous system: a summary.** *Acta Neuropathol* 2016;131:803–20 CrossRef Medline
2. Karlowee V, Kolakshyapati M, Amatya VJ, et al. **Diffuse leptomeningeal glioneuronal tumor (DLGNT) mimicking Whipple's disease: a case report and literature review.** *Childs Nerv Syst* 2017;33:1411–14 CrossRef Medline
3. Louis DN, Ohgaki H, Wiestler OD, et al. **The 2007 WHO classification of tumours of the central nervous system.** *Acta Neuropathol* 2007;114:97–109 CrossRef Medline
4. Gardiman MP, Fassan M, Orvieto E, et al. **Diffuse leptomeningeal glioneuronal tumors: a new entity?** *Brain Pathol* 2010;20:361–66 CrossRef Medline
5. Chiang JCH, Harreld JH, Orr BA, et al. **Low-grade spinal glioneuronal tumors with BRAF gene fusion and 1p deletion but without leptomeningeal dissemination.** *Acta Neuropathol* 2017;134:159–62 CrossRef Medline
6. Lyle MR, Dolia JN, Fratkin J, et al. **Newly identified characteristics and suggestions for diagnosis and treatment of diffuse leptomeningeal glioneuronal/neuroepithelial tumors: a case report and review of the literature.** *Child Neurol Open* 2015;2:2329048X14567531. CrossRef Medline
7. Pellerino A, Rudà R, Bertero L, et al. **Successful use of bevacizumab in an adult primary diffuse leptomeningeal glioneuronal tumor.** *J Neurosurg Sci* 2018;62:229–32. CrossRef Medline
8. Rodriguez FJ, Perry A, Rosenblum MK, et al. **Disseminated oligodendroglial-like leptomeningeal tumor of childhood: a distinctive clinicopathologic entity.** *Acta Neuropathol* 2012;124:627–41 CrossRef Medline
9. Gardiman MP, Fassan M, Nozza P, et al. **Diffuse leptomeningeal glioneuronal tumours: clinico-pathological follow-up.** *Pathologica* 2012;104:428–31 CrossRef Medline
10. Lee JK, Ko HC, Choi JG, et al. **A case of diffuse leptomeningeal glioneuronal tumor misdiagnosed as chronic tuberculous meningitis without brain biopsy.** *Case Rep Neurol Med* 2018;2018:1391943 CrossRef Medline
11. Deng MY, Sill M, Chiang J, et al. **Molecularly defined diffuse leptomeningeal glioneuronal tumor (DLGNT) comprises two subgroups with distinct clinical and genetic features.** *Acta Neuropathol* 2018;136:239–53 CrossRef Medline
12. Schniederjan MJ, Alghamdi S, Castellano-Sanchez A, et al. **Diffuse leptomeningeal neuroepithelial tumor: 9 pediatric cases with chromosome 1p/19q deletion status and IDH1 (R132H) immunohistochemistry.** *Am J Surg Pathol* 2013;37:763–71 CrossRef Medline
13. Aguilera D, Castellino RC, Janss A, et al. **Clinical responses of patients with diffuse leptomeningeal glioneuronal tumors to chemotherapy.** *Childs Nerv Syst* 2018;34:329–34 CrossRef Medline
14. Preuss M, Christiansen H, Merckenschlager A, et al. **Disseminated oligodendroglial-like leptomeningeal tumors: preliminary diagnostic and therapeutic results for a novel tumor entity [corrected].** *J Neurooncol* 2015;124:65–74 CrossRef Medline
15. Cho HJ, Myung JK, Kim H, et al. **Primary diffuse leptomeningeal glioneuronal tumors.** *Brain Tumor Pathol* 2015;32:49–55 CrossRef Medline
16. Schwetye KE, Kansagra AP, McEachern J, et al. **Unusual high-grade features in pediatric diffuse leptomeningeal glioneuronal tumor:**

- comparison with a typical low-grade example. *Hum Pathol* 2017;70:105–12 CrossRef Medline
17. Yamasaki T, Sakai N, Shinmura K, et al. **Anaplastic changes of diffuse leptomeningeal glioneuronal tumor with polar spongionblastoma pattern.** *Brain Tumor Pathol* 2018;35:209–16 CrossRef Medline
 18. Fiaschi P, Badaloni F, Cagetti B, et al. **Disseminated oligodendroglial-like leptomeningeal tumor in the adult: case report and review of the literature.** *World Neurosurg* 2018;114:53–57 CrossRef Medline
 19. Tiwari S, Yadav T, Pamnani J, et al. **Diffuse leptomeningeal glioneuronal tumor: a unique leptomeningeal tumor entity.** *World Neurosurg* 2020;135:297–300 CrossRef Medline

Variability of T2-Relaxation Times of Healthy Lumbar Intervertebral Discs is More Homogeneous within an Individual Than across Healthy Individuals

A. Sharma, R.E. Walk, S.Y. Tang, R. Eldaya, P.J. Owen, and D.L. Belavy



ABSTRACT

BACKGROUND AND PURPOSE: When one uses T2 relaxometry to classify lumbar intervertebral discs as degenerated, it is unclear whether the normative data should be based on other intervertebral discs from the same individual or from a pool of extraneous controls. This study aimed to explore the extent of intra- versus intersubject variation in the T2 times of healthy intervertebral discs.

MATERIALS AND METHODS: Using prospectively acquired T2-relaxometry data from 606 intervertebral discs in 101 volunteers without back pain (47 men, 54 women) in a narrow age range (25–35 years), we calculated intra- and intersubject variation in T2 times of intervertebral discs graded by 2 neuroradiologists on the Pfirrmann scale. Intrasubject variation of intervertebral discs was assessed relative to other healthy intervertebral discs (Pfirrmann grade, ≤ 2) in the same individual. Multiple intersubject variability measures were calculated using healthy extraneous references ranging from a single randomly selected intervertebral disc to all healthy extraneous intervertebral discs, without and with segmental stratification. These variability measures were compared for healthy and degenerated (Pfirrmann grade ≥ 3) intervertebral discs.

RESULTS: The mean T2 values of healthy (493/606, 81.3%) and degenerated intervertebral discs were 121.1 ± 22.5 ms and 91.5 ± 18.6 ms, respectively ($P < .001$). The mean intrasubject variability for healthy intervertebral discs was 9.8 ± 10.7 ms, lower than all intersubject variability measures ($P < .001$), and provided the most pronounced separation for healthy and degenerated intervertebral discs. Among intersubject variability measures, using all segment-matched healthy discs as references provided the lowest variability ($P < .001$).

CONCLUSIONS: Normative measures based on the T2 times of healthy intervertebral discs from the same individual are likely to provide the most discriminating means of identifying degenerated intervertebral discs on the basis of T2 relaxometry.

ABBREVIATIONS: I, X, Xs, Xc, Xcs = various measures of variability in T2 times of intervertebral discs; IVD = intervertebral disc; np = used as a suffix to indicate measures assumed to represent nucleus pulposus

Loss of signal intensity of the central part of intervertebral discs (IVDs) on T2-weighted MR images is a well-established indicator of underlying degenerative changes.^{1–4} Visual recognition of the extent of this loss of signal intensity also forms the basis of grading the extent of disc degeneration on frequently used grading schemes such as one proposed by Pfirrmann et al.⁵ To overcome the subjectivity of visual assessment, T2 relaxometry provides a reliable, objective, and

continuous measure of IVD health, the T2 time.^{6–9} Previous studies have used this technique to identify differences in IVDs from cohorts differing in their Pfirrmann grade, age, and presence of back pain.^{7,9–12}

Theoretically, T2 relaxometry should be able to indicate pathologic changes in the IVDs before these become evident to human readers. However, this inherently requires a definition of a normative range against which the T2 time of a given IVD should be measured. At present, categorization of a given IVD into healthy or degenerated cannot be done with reasonable certainty simply on the basis of its T2 time. The existing literature not only lacks a normative definition, but it also fails to establish whether such a definition should be based on other IVDs from the same individual or from a pool of extraneous controls. While it has been shown that the segmental level influences the T2 times of the IVDs,¹³ it remains unclear whether these intersegmental variations between cohorts of IVDs from different subjects are larger or smaller than

Received May 17, 2020; accepted after revision July 20.

From the Mallinckrodt Institute of Radiology (A.S., R.E.) and Departments of Biomedical Engineering (R.E.W., S.Y.T.), and Orthopaedic Surgery (S.Y.T.), Washington University in St. Louis, St. Louis, Missouri; and School of Exercise and Nutrition Sciences (P.J.O., D.L.B.), Institute for Physical Activity and Nutrition, Deakin University, Geelong, Australia.

This work was supported by Deakin University School of Exercise and Nutrition Sciences (to D.L. Belavy 2014–2017).

Please address correspondence to Aseem Sharma, MD, Mallinckrodt Institute of Radiology, Washington University in St. Louis, Campus Box 8131, 510 S. Kingshighway Blvd, St. Louis, MO 63110; e-mail: aseemsharma@wustl.edu
<http://dx.doi.org/10.3174/ajnr.A6791>

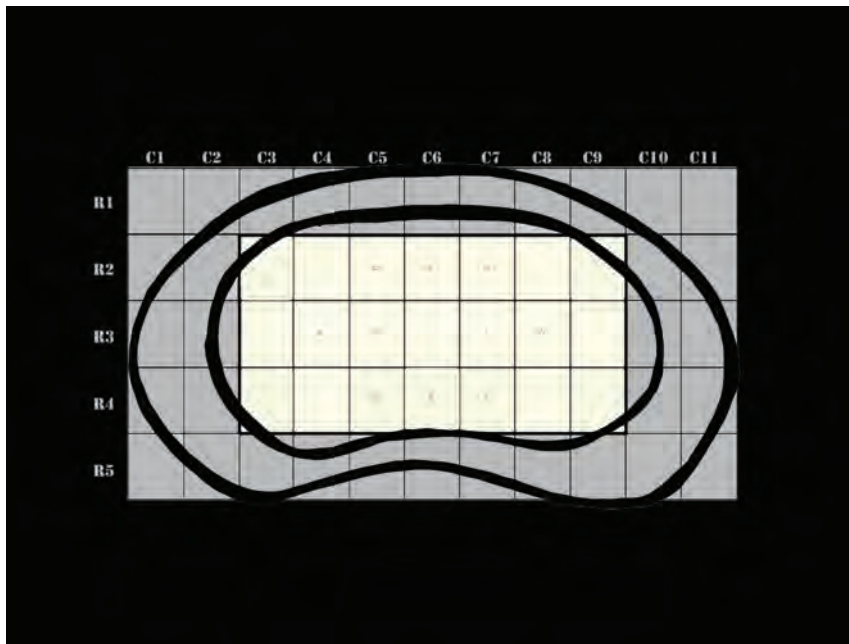


FIG 1. Artistic rendering of a fixed-sized intervertebral disc to which T2 values of all individual discs were interpolated. For each disc, T2 values of 55 equally sized regions were available that could be represented by a grid with 11 (left-to-right) columns (C1–C11) and 5 anterior-to-posterior rows (R1–5). To exclude the influence of the outer annulus fibrosus, we used the mean T2 time of the central 21 regions (shaded yellow) indicated by rows R2–4 and columns C3–9 to represent the T2 time of any given disc. Of these 21 regions, 11 regions with the highest T2 values were assumed to represent the core of the disc (*asterisk*), which would be least affected by the inner annulus fibrosus. Mean T2 value of these 11 pixels was assumed to represent the mean T2 time of the nucleus pulposus of the disc.

the intrasubject variation in T2 times between lumbar IVDs at different segmental levels.

In this study of pain-free volunteers within a narrow age range (25–35 years) who were scanned on the same scanner using identical scan parameters, we aimed to explore the extent of intrasubject-versus-intersubject variation in T2 times of healthy IVDs.

MATERIALS AND METHODS

Participants

This study represents a secondary analysis of the data collected for a previously reported study performed on 101 participants (47 men, 54 women; age range, 25–35 years) without spine disease. Exclusion criteria included current spinal pain, history of spinal surgery, history of traumatic injury to the spine, known scoliosis for which prior medical consultation was sought, current or prior smoker, known claustrophobia, and possible pregnancy.^{14–16}

MR Imaging

All studies were performed on the same 3T scanner (Ingenia; Philips Healthcare). For T2 mapping, a sagittal spin-echo multiecho technique was used with 8 TEs (15.75, 36.75, 57.75, 78.75, 99.75, 120.75, 141.75, and 162.75 ms). Additional scanning parameters were a section thickness of 3 mm, an interslice distance of 1.5 mm, TR of 2000 ms, FOV of 281 × 281 mm, and image resolution of 0.366 mm per pixel. In addition, sagittal T2-weighted TSE images were obtained across the lumbar spine with

a slice thickness of 3 mm, interslice distance of 1.5 mm, TR of 2600 ms, and TE of 70 ms.

Image Analysis

Two board-certified neuroradiologists with 1 and 16 years of practice experience independently evaluated sagittal T2-weighted images and graded T12 through S1 IVDs in each participant according to the Pfirrmann grading system.⁵ Differences were resolved by consensus. Only healthy (Pfirrmann grade 2 or 3) or degenerated (Pfirrmann grade ≥ 3) IVDs accepted by both neuroradiologists were included for subsequent analysis for this study.

For T2 mapping, each IVD was initially segmented manually on each image using the native polygon selections tool in the off-line software ImageJ (National Institutes of Health). A custom plug-in (ROI Analyzer; <https://sites.google.com/site/daniellbelavy/home/roianalyser>) was then used to calculate the T2 time in 5 anterior-posterior regions across the IVD in each sagittal image. These values were then interpolated to a fixed-sized IVD so that each IVD, when viewed in an axial

plane, could be represented by a grid of 55 regions represented by 11 columns (left to right) and 5 rows (anterior to posterior) (Fig 1). T2 times were then calculated for each of these regions. Of these, 2 columns on both sides and 1 row each at the anterior and posterior margins of the IVD were excluded from analyses because these regions were likely to include the outer annulus fibers (Fig 1). An average of T2 times of the remaining central 21 (7 × 3) regions was obtained to represent the T2 time of a given disc (Fig 1). Because the distinction between the inner annulus and nucleus pulposus cannot be made visually on T2-weighted images, to try to minimize the influence of the inner annulus or the abnormal regions within the nucleus pulposus that could have been too small to affect categorization of the disc as degenerated on the basis of the Pfirrmann grading, we calculated an additional parameter (T2np) that represented the average of 11/21 regions with the highest T2 values (Fig 1).

Parameters for Intrasubject and Intersubject Variation

For each IVD, we assessed the intrasubject variation (I) of the T2 time by calculating the difference between the T2 time of that IVD and the average T2 time of other healthy IVDs within T12 through S1 segments from the same participant. Another measure of the intrasubject variation, Inp, was calculated similarly using the T2np time instead.

A number of different measures of intersubject variation were calculated for each disc. X (and Xnp) represented the difference

Variation of T2 times of central aspect of lumbar IVDs from various normative reference T2 times^a

	Mean (ms)	SD (ms)	I ^b	Inp ^b	X ^b	Xnp ^b	Xs ^b	Xsnp ^b	Xc ^b	Xcnp ^b	Xcs ^b	Xcsnp ^b
I	9.8	10.7										
Inp	11.7	13.4	<.001									
X	15.8	16.0	<.001	<.001								
Xnp	18.6	19.3	<.001	<.001	<.001							
Xs	15.5	15.3	<.001	<.001	.123	<.001						
Xsnp	18.3	18.6	<.001	<.001	<.001	.27	<.001					
Xc	17.2	17.3	<.001	<.001	<.001	.003	<.001	.027				
Xcnp	20.2	20.9	<.001	<.001	<.001	.001	<.001	<.001	<.001			
Xcs	21.8	20.7	<.001	<.001	<.001	.002	<.001	<.001	<.001	.031		
Xcsnp	25.7	25.2	<.001	<.001	<.001	<.001	<.001	<.001	<.001	<.001	<.001	

^a Variability parameters represent the difference between T2 times of the central aspect of the index IVD from the mean T2 times of the other healthy IVDs from same individual (I), the mean of T2 times of all other healthy lumbar IVDs (X), the mean T2 times of all other healthy lumbar IVDs at the same segmental level as the index IVD (Xs), T2 time of a randomly selected healthy IVD from a different individual but at the same segmental level as the index IVD (Xcs), the mean T2 times of 6 randomly selected healthy discs from different individuals (Xc), each representing a particular segmental level between the T12 through S1 levels. Inp, Xnp, Xsnp, Xcnp, and Xcsnp indicate corresponding values calculated using 52.4% of the central IVD regions with highest T2 values.

^b P values based on a paired Student t test.

between the T2 (or T2np) time of a given disc and the average T2 (or T2np) times of all other IVDs with same Pfirrmann grade as that disc. Xs and Xsnp represented similar calculations restricted to the same segmental level as a given disc. Additional measures assessed intersubject variation with respect to a single randomly selected healthy IVD from the same segmental level or an average of 6 randomly selected healthy IVDs representing the T12–S1 segments (Table).

Statistical Analysis

Interobserver reliability of Pfirrmann grading was tested for the 2 readers, and the Cohen κ was calculated. Mean and SDs were calculated for each measure of T2 variability. A paired 2-tailed Student *t* test was used to assess differences between various measures of variability. A nonpaired Student *t* test was used to assess differences between the variability measures of IVDs that were categorized as healthy and degenerated on the basis of the Pfirrmann grading system. A *P* value < .05 was considered significant. A Bonferroni correction was applied to correct for multiple comparisons.

RESULTS

Of 606 IVDs, 493 (81.4%) were deemed healthy after a consensus read by 2 radiologists and were included for subsequent analysis. Of these, 489/493 (99.2%) were assigned grade 2 on the Pfirrmann scale. Individual reader agreement was excellent ($\kappa = 0.84$; 95% CI, 0.78–0.89) for categorization of IVDs as healthy or degenerated and good ($\kappa = 0.73$; 95% CI, 0.67–0.79) for a specific Pfirrmann grade. Readers disagreed on the grading of 61/606 (10.1%) IVDs. Readers were able to reach a consensus on all except 2 IVDs, which were excluded from subsequent analysis.

Mean T2 and T2np values for all IVDs were 115.5 ± 24.6 ms and 131.5 ± 30.0 ms, respectively. IVDs graded healthy (Pfirrmann grades 1 and 2) had higher T2 (121.1 ± 22.5 ms) and T2np (138.6 ± 26.8 ms) values compared with corresponding T2 and T2np values of 91.5 ± 18.6 ms and 101.0 ± 23.3 ms, respectively, for degenerated IVDs (*P* < .001 for both).

Intrasubject variability measures (I and Inp) were significantly lower than any of the corresponding intersubject variability measures (*P* < .001 for all, Table and Fig 2). Inp, while being

significantly lower than all of the intersubject variability measures (*P* < .001 for all), was significantly higher than I (*P* < .001).

Intersubject variability was higher when a single or 6 randomly selected IVDs were used as a comparison rather than all healthy IVDs in all participants without or with stratification for the segmental level (*P* < .001 for all, Table and Fig 2).

Stratification based on the segmental level did not impact the variability, with no significant difference observed between X and Xs (*P* = .12) or between Xnp and Xsnp (*P* = .27).

DISCUSSION

Many previous studies have suggested that T2-relaxometry can provide a reliable, objective, and continuous quantitative measure of the health of lumbar IVDs. Despite these advantages, this technique has failed to replace traditional subjective assessment of the signal intensity of IVDs on T2-weighted images for categorization of a given IVD as healthy or degenerated. The current literature is also deficient in providing either a T2 value or a measure based on such a value that could be used to determine normalcy of a given IVD. Our study was not designed to develop such a measure. Instead, it aimed to take the first step toward establishing the most appropriate reference standard. By showing that the T2 time of a given healthy IVD most closely matched that of other healthy lumbar IVDs from the same individual (Fig 2), our results suggest that that other healthy IVDs within an individual, if available, are likely to provide the most optimal basis of the definition of normal against which a given IVD should be compared. This suggestion is further highlighted because the differences between healthy and degenerated IVDs were most stark when compared with internal rather than extraneous healthy IVDs (Fig 2). Using internal healthy IVDs as a reference would also have the advantage of circumventing the potential of variation in measured T2 times of discs scanned on different scanners.

A recent study highlighted the role of level stratification in MR imaging–quantification studies using T2 data.¹³ Our analysis of the same data demonstrated that while the level of stratification might be important when cohorts of IVDs are being compared, T2 times of healthy IVDs at other levels in the same individual are likely to provide a better measure of the health of a given IVD

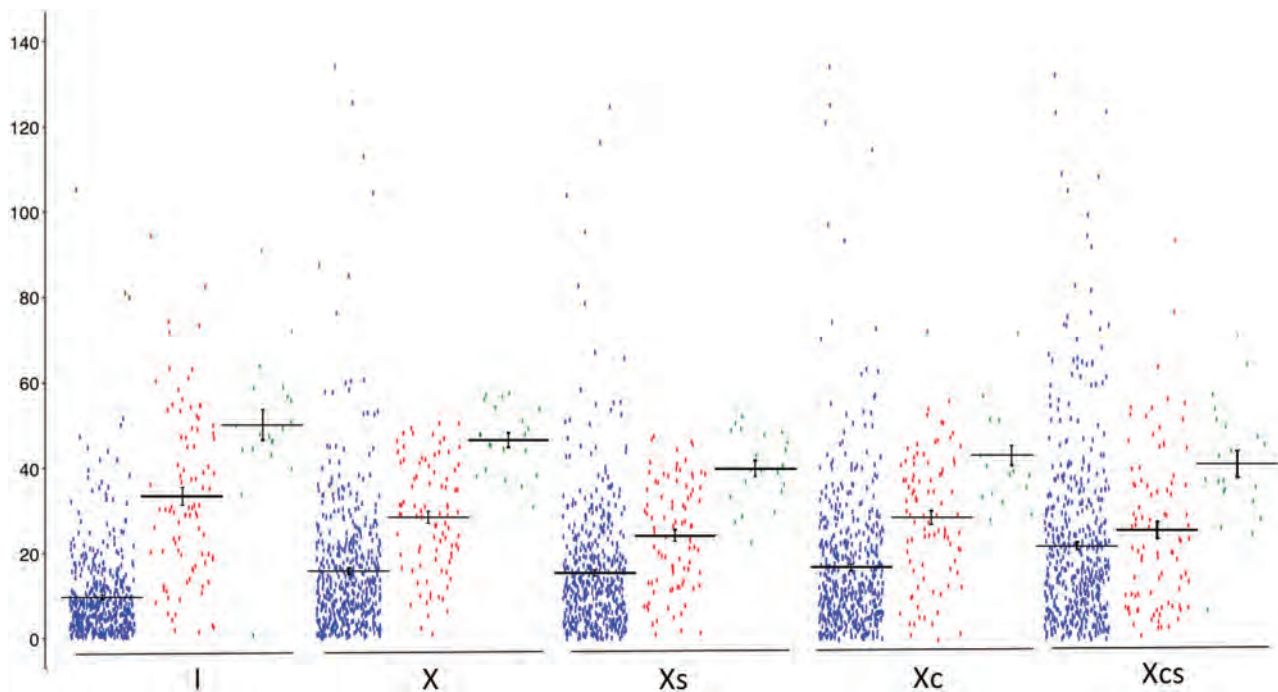


FIG 2. Plots of differences of T2 time in milliseconds (y-axis) of 604 lumbar IVDs with Pfirrmann grades of ≤ 2 (blue), 3 (red), and 4 (green) relative to mean T2 time (or T2 time when single) of other healthy lumbar IVDs from same individual (I), all other healthy IVDs in 101 study participants without (X) and with (Xs) stratification for the segmental level, 6 randomly selected healthy IVDs representing T12–S1 segments (Xc), and a single randomly selected IVD from same segmental levels (Xcs). Horizontal bars show means with standard errors. The variation in T2 times of healthy IVDs, as represented by the spread along the y-axis, is least for healthy IVDs with Pfirrmann grade of ≤ 2 . Notice that the measure I provides the most and the measure Xcs provides the least discrimination between healthy and degenerated IVDs with Pfirrmann grades of 3 or 4, as indicated by separation of means along the y-axis.

than T2 times of a healthy IVD at the same segmental level from any other given individual or even an average T2 time of a large number of the same segmental-level IVDs from many other healthy controls. The reason may be both due to genetic similarities between IVDs from the same individual and the fact that placement of any given individual within the MR imaging scanner is likely to produce somewhat unique subtle variations in the magnetic environment that may affect T2 calculations even under identical scanning equipment and parameters. In addition, comparison with other IVDs within the same scan can help overcome many other confounding factors such as disc hydration status, time of the day, and loading of the spine, which would be difficult to control in comparison across individuals but are known to affect the T2 time of IVDs.^{17,18}

Of all comparison scenarios studied, T2 values of any given healthy IVD differed most from a randomly selected healthy IVD from a different individual but from the same segmental level. It is likely that the variation in T2 times in healthy IVDs in the population are a combination of both the underlying true differences in T2 times of healthy IVDs across subjects and systematic effects due to the noise encountered during the process of measuring the T2 times using MR imaging. While the true underlying variability in T2 times cannot be changed, a greater number of samples can minimize the contributions of the noise. This feature likely explains why the interobserver variability decreased as the number of control discs increased from 1 (Xcs) to 6 (Xc), with a further significant reduction when a much larger number of control discs

were used, as was the case for calculation of X and Xs (Table). This benefit of using a larger number of IVDs to define the T2 value of healthy IVDs remained irrespective of whether the IVDs were used from the same segmental level or not. However, despite a relatively small number of intrasubject control discs, such discs provide a T2 value that may be expected to be most similar to that of a given healthy IVD.

Certain methodologic details of our experiment merit explanation of the rationale. As opposed to measuring the T2 time of the entire IVD, as in a previous study,¹³ we chose to investigate that of a central aspect of the IVD, deliberately trying to exclude the outer annulus. While the central portion of the IVD is known to undergo loss of T2 signal in the presence of pathology, the T2 time of the abnormal annulus (annular fissures) may be expected to increase. Given that annular fissures often accompany and perhaps precede the appearance of IVD desiccation,^{19,20} we propose that given the opposing effects of degenerative changes in these components of IVDs, it would be reasonable to exclude the outer annulus from T2 calculations if the T2 value is to be used to define the degenerated status of the disc. For the sake of simplicity, some previous studies have used a central hyperintense zone of IVDs as being representative of the nucleus pulposus.^{9,10,21} The nucleus pulposus is not readily identifiable on T2-weighted MR imaging as a distinct structure from the inner annulus.²² While the central hyperintense region on T2-weighted images that represents a combination of the nucleus pulposus and the inner annulus fibrosus shows a loss of signal intensity with disc

degeneration in its entirety, it is possible that there are underlying subtle differences in the rate of signal loss in these 2 components of IVDs that are not fully understood. Assuming that the nucleus pulposus might have inherently higher T2 times given its higher hydration level relative to that of inner annulus fibrosus, which slowly decreases from the central to outer aspect of the inner annulus,^{23,24} we explored the possibility that a smaller number of regions with higher intensity might be more representative of the nucleus pulposus of the IVDs (Fig 1). Accordingly, we analyzed variability only on the basis of regions skewed toward higher intensity. Notably, variability increased when a smaller number of regions from the IVDs were used (Table).

The mechanisms for this consistent difference remain unclear. It is possible that an increase in variation when dealing with a smaller sample of pixels is simply a function of the increasing influence of noise that would be expected to be minimized by averaging a higher number of pixels. It is also possible that this amplified variation results from the fact that the number of regions selected as possible representations of the nucleus pulposus was arbitrary and not necessarily restricted to the size of the nucleus pulposus, which itself is difficult to establish.^{22,25} Inclusion of the nucleus pulposus and variable parts of the inner annulus fibrosus in T2 calculations, therefore, could have resulted in a higher degree of variation observed in our study. When it becomes technologically feasible to allow a reliable segmentation of the nucleus pulposus, it would be interesting to study the variation among T2 values of the nucleus pulposus alone in healthy lumbar IVDs.

Our study has some limitations. First, it was restricted to participants in a narrow age range. While this was critical in allowing us to test our hypothesis free from the confounding effects of age, it does not ensure generalizability of these results to other age groups. It is known that T2 times of IVDs are affected by age. In the absence of any previous studies indicating segmental variations in these effects, we expect our results to be similar in other age groups. Additional studies would be needed however to test this expectation. Second, the area of IVDs taken into consideration to represent IVDs free of the outer annulus was somewhat arbitrary. However, by demonstrating similar results even when the analysis was restricted to central pixels skewed toward higher T2 values, we think that our results were able to overcome this limitation. While all the participants were free of back pain, we do not think this to be a significant limitation of the study. Previous studies have shown that despite a varying burden of overall disc degeneration in individuals with varying predispositions, disc degeneration remains a disc-specific process that follows a remarkably similar natural history irrespective of the presence of symptoms.²⁰ Furthermore, despite the absence of back pain, a number of IVDs in our patient population demonstrated evidence of overt disc degeneration as indicated by their Pfirrmann grades.

CONCLUSIONS

By demonstrating a significantly higher variation in the T2 times of IVDs across subjects, our study suggests that normative measures based on the T2 times of healthy lumbar IVDs from the same individual are likely to provide the most discriminating means of identifying degenerated IVDs on the basis of T2 relaxometry. If such a measure could be developed on the basis of a relatively small

number of healthy IVDs, T2 relaxometry has the potential to become valuable not only for comparisons of cohorts but also as a reliable and objective means of identifying early degeneration of individual IVDs. While using a large pool of extraneous discs would be the next-best option, such a measure is likely to lack widespread utility due to potential variations in T2 quantification on different scanner types. Further studies are needed to ensure that these results remain valid across different age groups.

Disclosures: Aseem Sharma—UNRELATED: Patents (Planned, Pending or Issued): Method for Medical Image Analysis and Manipulation, US patent No. 9,846,937; Stock/Stock Options: Founder, Correlative Enhancement LLC. Simon Y. Tang—RELATED: Grant: National Institutes of Health, Comments: grants K01AR069116 and R01AR074441.* *Money paid to the institution.

REFERENCES

1. Haughton VM. **MR imaging of the spine.** *Radiology* 1988;166:297–301 CrossRef Medline
2. Yu SW, Haughton VM, Ho PS, et al. **Progressive and regressive changes in the nucleus pulposus, Part II: the adult.** *Radiology* 1988;169:93–97 CrossRef Medline
3. Yu S, Haughton VM, Sether LA, et al. **Criteria for classifying normal and degenerated lumbar intervertebral disks.** *Radiology* 1989;170:523–26 CrossRef Medline
4. Pfirrmann CW, Metzdorf A, Zanetti M, et al. **Magnetic resonance classification of lumbar intervertebral disc degeneration.** *Spine* 2001;26:1873–78 CrossRef Medline
5. Pfirrmann CW, Metzdorf A, Zanetti M, et al. **Magnetic resonance classification of lumbar intervertebral disc degeneration.** *Spine (Phila Pa 1976)* 2001;26:1873–78 Medline
6. Antoniou J, Pike GB, Steffen T, et al. **Quantitative magnetic resonance imaging in the assessment of degenerative disc disease.** *Magn Reson Med* 1998;40:900–07 CrossRef Medline
7. Boos N, Dreier D, Hilfiker E, et al. **Tissue characterization of symptomatic and asymptomatic disc herniations by quantitative magnetic resonance imaging.** *J Orthop Res* 1997;15:141–49 CrossRef Medline
8. Boos N, Wallin A, Schmucker T, et al. **Quantitative MR imaging of lumbar intervertebral disc and vertebral bodies: methodology, reproducibility, and preliminary results.** *Magn Reson Imaging* 1994;12:577–87 CrossRef Medline
9. Watanabe A, Benneker LM, Boesch C, et al. **Classification of intervertebral disk degeneration with axial T2 mapping.** *AJR Am J Roentgenol* 2007;189:936–42 CrossRef Medline
10. Marinelli NL, Haughton VM, Anderson PA. **T2 relaxation times correlated with stage of lumbar intervertebral disk degeneration and patient age.** *AJNR Am J Neuroradiol* 2010;31:1278–82 CrossRef Medline
11. Marinelli NL, Haughton VM, Munoz A, et al. **T2 relaxation times of intervertebral disc tissue correlated with water content and proteoglycan content.** *Spine (Phila Pa 1976)* 2009;34:520–24 CrossRef Medline
12. Menezes-Reis R, Salmon CE, Carvalho CS, et al. **T1rho and T2 mapping of the intervertebral disk: comparison of different methods of segmentation.** *AJNR Am J Neuroradiol* 2015;36:606–11 CrossRef Medline
13. Hebelka H, Lagerstrand K, Brisby H, et al. **The importance of level stratification for quantitative MR studies of lumbar intervertebral discs: a cross-sectional analysis in 101 healthy adults.** *Eur Spine J* 2019;28:2153–61 CrossRef Medline
14. Belavy DL, Quittner MJ, Ridgers N, et al. **Running exercise strengthens the intervertebral disc.** *Sci Rep* 2017;7:45975 CrossRef Medline
15. Belavy DL, Quittner MJ, Ridgers ND, et al. **Specific modulation of vertebral marrow adipose tissue by physical activity.** *J Bone Miner Res* 2018;33:651–57 CrossRef Medline
16. Belavy DL, Quittner M, Ling Y, et al. **Cervical and thoracic intervertebral disc hydration increases with recumbency: a study in 101 healthy volunteers.** *Spine J* 2018;18:314–20 CrossRef Medline

17. Hebelka H, Toren L, Lagerstrand K, et al. **Axial loading during MRI reveals deviant characteristics within posterior IVD regions between low back pain patients and controls.** *Eur Spine J* 2018;27:2840–46 CrossRef Medline
18. Paajanen H, Lehto I, Alanen A, et al. **Diurnal fluid changes of lumbar discs measured indirectly by magnetic resonance imaging.** *J Orthop Res* 1994;12:509–14 CrossRef Medline
19. Sharma A, Lancaster S, Bagade S, et al. **Early pattern of degenerative changes in individual components of intervertebral discs in stressed and nonstressed segments of lumbar spine: an in vivo magnetic resonance imaging study.** *Spine (Phila Pa 1976)* 2014;39:1084–90 CrossRef Medline
20. Sharma A, Parsons M, Pilgram T. **Temporal interactions of degenerative changes in individual components of the lumbar intervertebral discs: a sequential magnetic resonance imaging study in patients less than 40 years of age.** *Spine (Phila Pa 1976)* 2011;36:1794–1800 CrossRef Medline
21. Niu G, Yang J, Wang R, et al. **MR imaging assessment of lumbar intervertebral disk degeneration and age-related changes: apparent diffusion coefficient versus T2 quantitation.** *AJNR Am J Neuroradiol* 2011;32:1617–23 CrossRef Medline
22. Pech P, Haughton VM. **Lumbar intervertebral disk: correlative MR and anatomic study.** *Radiology* 1985;156:699–701 CrossRef Medline
23. Adams MA, Hutton WC. **The effect of posture on the fluid content of lumbar intervertebral discs.** *Spine (Phila Pa 1976)* 1983;8:665–71 Medline
24. Antoniou J, Steffen T, Nelson F, et al. **The human lumbar intervertebral disc: evidence for changes in the biosynthesis and denaturation of the extracellular matrix with growth, maturation, ageing, and degeneration.** *J Clin Invest* 1996;98:996–1003 CrossRef Medline
25. O'Connell GD, Vresilovic EJ, Elliott DM. **Comparison of animals used in disc research to human lumbar disc geometry.** *Spine (Phila Pa 1976)* 2007;32:328–33 CrossRef Medline

Cauda Equina and Filum Terminale Arteriovenous Fistulas: Anatomic and Radiographic Features

K. Namba, Y. Niimi, T. Ishiguro, A. Higaki, N. Toma, and M. Komiyama



ABSTRACT

SUMMARY: Intradural AVF below the conus medullaris may develop either on the filum terminale or the cauda equina (lumbosacral and coccygeal radicular nerves). Although not a few filum terminale AVFs are found in the literature, only 3 detailed cauda equina AVFs have been reported. Here, we analyze the angiographic and MR imaging findings of our cauda equina and filum terminale AVF cases, supplemented with literature research to characterize the radiologic features of the 2 entities. On angiography, filum terminale AVFs were invariably supplied by the extension of the anterior spinal artery accompanied by a closely paralleling filum terminale vein. Cauda equina AVFs were fed by either a radicular or a spinal artery or both arteries, often with a characteristic wavy radicular-perimedullary draining vein. On thin-section axial MR imaging, the filum terminale AVF draining vein joined the spinal cord at the conus medullaris apex, but that of the cauda equina AVF joined above the conus medullaris apex.

ABBREVIATIONS: ASA = anterior spinal artery; FT = filum terminale

The spinal canal below the conus medullaris accommodates lumbar, sacral, or coccygeal nerve roots (ie, the cauda equina)¹ and the filum terminale (FT). Intradural vascular lesions in this region may affect the cauda equina or the FT. Since the pioneering work by Djindjian et al,² the FT AVF has gained wide recognition, but the cauda equina AVF is scarcely known.³⁻⁵ As such, few radiologic findings differentiating the 2 diseases are known.⁵

We present our cauda equina and FT AVF cases supplemented by previous reports and discuss the angiographic and MR imaging features of the 2 diseases.

CASE SERIES

Patients and Imaging Features

The study followed the policies of each institution's Research Ethics Committee. The cases were retrieved from a prospectively collected spinal vascular malformation database between November 2012 and April 2017. Four patients with cauda equina or FT AVF were identified. All patients underwent spinal angiography, including bilateral internal iliac and all appropriate segmental arteries.

To observe the ascending draining vein, a precontrast axial T2-weighted turbo spin-echo (section thickness, 4 mm; TE, 105 ms; TR, 5000 ms) sequence and postcontrast axial T1-weighted turbo spin-echo (section thickness, 4 mm; TE, 9.30 ms; TR, 650 ms) sequence 5 minutes after a 10-mL IV injection of gadobutrol (Gadovist; Bayer Schering Pharma) were studied on a 3T scanner (Magnetom Skyra; Siemens). Whereas the radicular vein accompanies a nerve root that is apart from the spinal cord at the conus medullaris apex, the FT vein anastomoses with the anterior spinal vein at the apex. Therefore, a draining vein off the spinal cord at the conus medullaris apex was interpreted as radicular, whereas the vein on the cord was an FT vein.

Literature Review

A PubMed search on May 1, 2019, was performed using the following terms: "cauda equina AND arteriovenous fistula," "cauda equina AND arteriovenous malformation," "filum terminale AND arteriovenous fistula," or "filum terminale AND arteriovenous malformation." The research yielded 36, 62, 50, and 72

Received March 22, 2020; accepted after revision June 1.

From the Center for Endovascular Therapy (K.N., A.H.), Division of Neuroendovascular Surgery, Jichi Medical University, Tochigi, Japan; Department of Neuroendovascular Therapy (Y.N.), St. Luke's International Hospital, Tokyo, Japan; Department of Neurointervention (T.I., M.K.), Osaka City General Hospital, Osaka, Japan; and Department of Neurosurgery (N.T.), Mie University Graduate School of Medicine, Mie, Japan.

Previously presented in part at: 9th Meeting of the Niche Neuro-Angiology Conference, Osaka, Japan, May 30, 2015; 31st Annual Meeting of the Japanese Society for Neuroendovascular Therapy, Okayama, Japan, November 20, 2015; and 33rd Annual Meeting of the Japanese Society for Neuroendovascular Therapy, Tokyo, Japan, November 25, 2017.

Please address correspondence to Katsunari Namba, Center for Endovascular Therapy, Division of Neuroendovascular Surgery, Jichi Medical University, 3311-1 Yakushiji, Shimotsuke, Tochigi 329-0498, Japan; e-mail: knamba@jichi.ac.jp



Indicates article with supplemental on-line table.

<http://dx.doi.org/10.3174/ajnr.A6813>

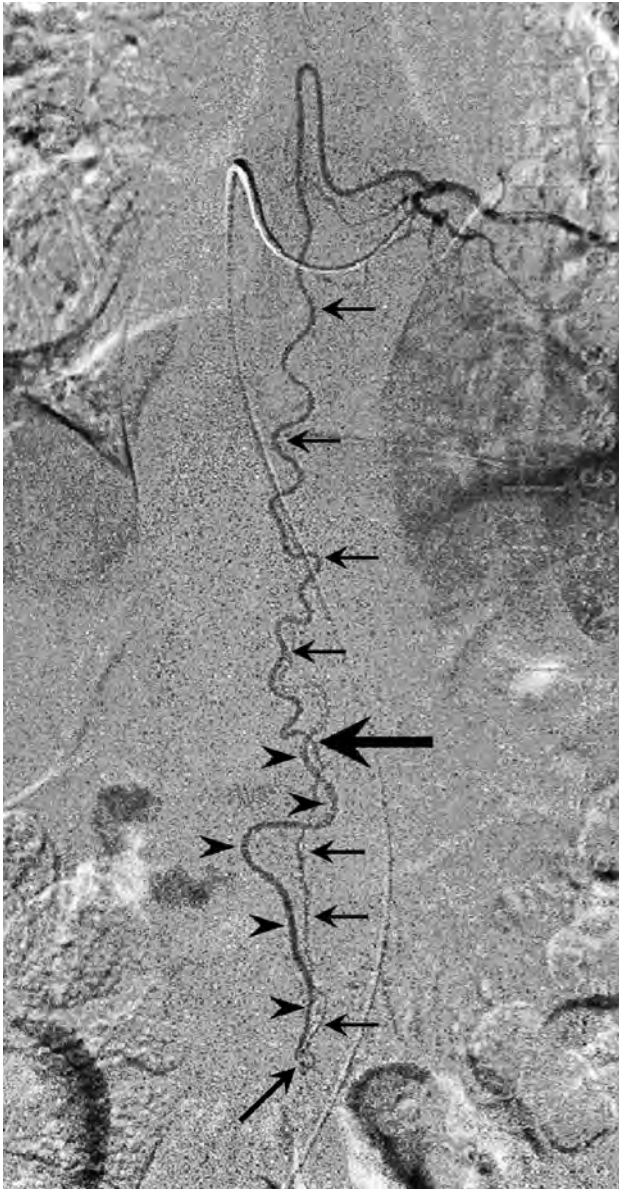


FIG 1. Left T9 intercostal artery angiogram in anteroposterior view shows the extension of the anterior spinal artery (arrows) traveling caudally to form an AVF at the L2 level (oblique arrow). The ascending draining vein shows a characteristic wavy pattern (arrowheads). Note the change in the course and caliber of the ASA at the conus medullaris apex (large arrow), suggesting a change of the feeding artery to a radicular artery. Reprinted with permission from Figure 2c in Tanioka S, Toma N, Sakaida H, et al. A case of AVF of the cauda equina fed by the proximal radicular artery: anatomical features and treatment precautions. *Eur Spine J* 2018;27(suppl 3):281–86.

articles, respectively. Only the articles containing both angiographic figures and surgical confirmation of the fistula were included. Three cauda equina^{3,5} and 31 FT^{2,4,6-25} AVF cases were eligible, including 1 patient in this study (case 3).⁵

RESULTS

Patient demographics, angiographic and MR imaging characteristics, and treatment outcomes are listed in the On-line Table. We diagnosed 3 cauda equina AVFs (cases 1, 2, 3) and 1 FT AVF

(case 4). The FT and 2 cauda equina AVFs were treated by endovascular embolization and 1 cauda equina AVF by direct surgery. All the procedures were completed without clinical sequelae. One embolized cauda equina AVF (case 1) resulted in residual fistula, but the patient declined further treatment (case 1).

Spinal Angiography

Spinal angiography detected all the AVFs between the L2 and L4 vertebral levels. In 2 AVFs, caudal extension of the anterior spinal artery (ASA) was the single feeder (cases 3 and 4, Figs 1 and 2A), and a single right S1 radicular artery was the feeder in 1 (case 2, Fig 3A). Both the extension of the ASA and left S1 radicular artery were the feeders in 1 (case 1, Fig 4A, -B). In cases 1 and 3, the ASA made changes in the course and caliber at the conus medullaris apex (Figs 1 and 4, large arrow), whereas in case 4, the ASA made a straight descent without changing its caliber.

The ascending draining vein showed a wavy pattern not paralleling the feeding artery in 2 cases (cases 1 and 3, Figs 4A and 1) and a straight ascent in 1 (case 2, Fig 3A) and closely paralleled the feeding artery in 1 (case 4, Fig 2A).

Case 2 was complicated by multiple AVFs described in detail in Fig 3.

MR Imaging Features

Thin-section axial T2WI and enhanced T1WI detected the ascending draining vein in cases 1, 2, and 4 (Figs 4C, 3C, and 2B, arrows). In cases 1 and 2, the vein was off the spinal cord at the conus medullaris apex (Figs 4C and 3C, arrowhead) and joined it at the L1 level (Figs 4C and 3C, large horizontal arrow) and thus was interpreted as radicular. In case 4, the vein united with the cord at the conus medullaris apex (Fig 2B, arrowheads) and hence was an FT vein. In case 3, the MR imaging failed to detect the vein.

DIAGNOSIS

Based on the angiographic and MR imaging findings, the diagnosis of cauda equina AVF was made in cases 1 and 2 and FT AVF in case 4. In case 3, surgical findings confirmed the diagnosis of cauda equina AVF.⁵

Literature Review

The literature review yielded 3^{3,5} and 31^{2,4,6-25} surgically confirmed cauda equina and FT AVF cases, respectively. In all the 3 cauda equina AVF cases, the fistula was fed by a single extension of the ASA without radicular artery involvement. The ASA changed its course and caliber at the conus medullaris apex. In 2 cases, the draining vein showed a wavy pattern, but the other case paralleled the feeding artery.³

In the 31 FT AVF cases, the ASA invariably fed the fistula and maintained its straight course and robust caliber at the conus medullaris apex. All FT AVF draining veins showed the parallel feeder–drainer pattern. To date, only 4 surgically proved cases with additional radicular artery supply have been reported,^{4,10,16,24} and no FT AVF with exclusive radicular artery supply is known.

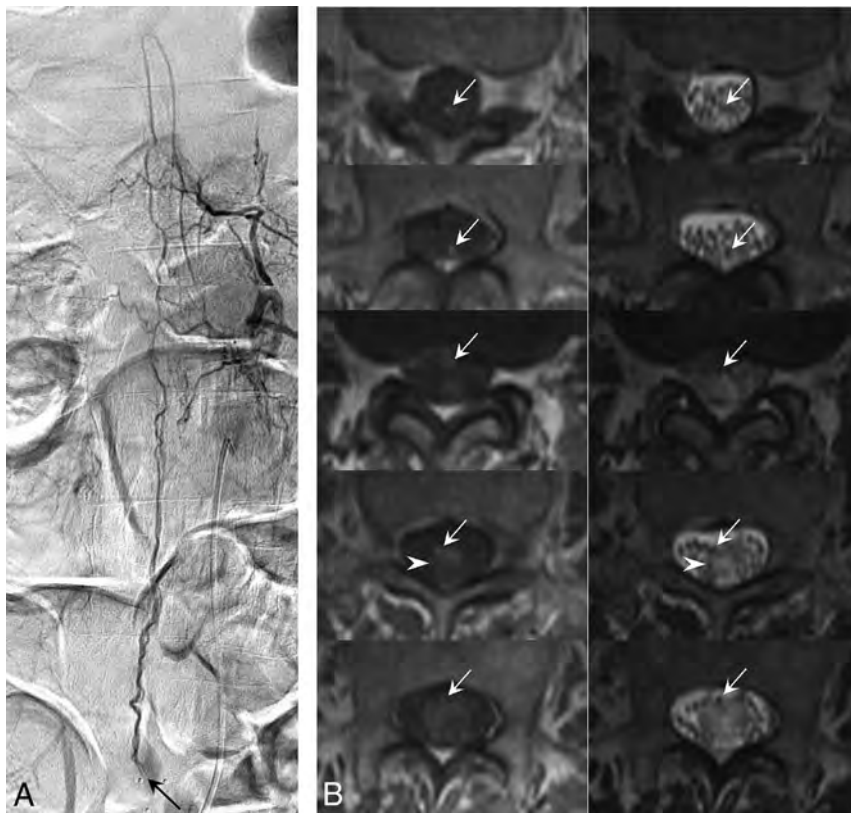


FIG 2. A, Angiogram of the left L1 lumbar artery in anteroposterior projection demonstrates a filum terminale AVF at the L4 level. The fistula (*oblique arrow*) is supplied by the caudal extension of the anterior spinal artery, which is the artery of the filum, and drained by the vein of the filum. The ASA does not change its course or caliber at the conus medullaris and maintains its robust caliber down to the fistula site. Note the parallel feeder and drainer pattern. B, Serial thin-section gadolinium enhanced T1WI (*left column*) and T2WI (*right column*) arranged in caudal (*upper*) to cranial (*lower*) order show the draining vein (*arrows*) merging with the spinal cord at the apex of the edematous conus medullaris (*arrowhead*). This finding suggests that this is the vein of FT.

DISCUSSION

The main findings in the present study were 1) in the FT AVF, the ASA maintained its course and caliber at the conus medullaris apex, 2) the FT AVF showed a parallel feeder–drainer pattern, 3) the cauda equina AVF had variable feeding arteries, 4) the extension of the ASA involved in the cauda equina AVF changed its course and caliber at the conus medullaris apex, 5) the cauda equina AVF showed a wavy draining vein in 3 of 5 cases, and 6) thin-section axial MR imaging detecting the draining vein may aid in differentiating cauda equina and FT AVFs.

Vascular Anatomy of the Filum Terminale and Filum Terminale AVF and Diagnostic Considerations

Anatomically, the FT artery is the direct caudal continuation of the ASA,²⁶ and embryologically, the FT is a remnant of the spinal cord.^{27,28} Therefore, it is reasonable that the cardinal feeder of the FT AVF should be the extension of the ASA (FT artery), and the ASA maintained a straight course and robust caliber at the conus medullaris apex.

Normal and pathologic AVF sections of the FT showed the FT artery and vein existing side by side throughout the length of the

FT.^{21,26} These findings may explain the characteristic parallel feeder–drainer pattern observed in all the FT AVF cases.^{2,4,6–25}

Vascular Anatomy of the Cauda Equina and Cauda Equina AVF and Diagnostic Considerations

The cauda equina is supplied from the segmental radicular arteries originating from the medial and lateral sacral arteries, or the iliolumbar artery. Importantly, Parke et al²⁹ demonstrated that the proximal one-third of the radicular nerve was supplied by the spinal artery, mainly the vasa corona, and the peripheral two-thirds was supplied by the radicular artery. Consequently, the cauda equina AVF feeder could be radicular, spinal, or both.

In the literature, only 3 surgically proved and 7 angiographic cauda equina AVF cases have been reported.^{3–5} All 7 angiographic AVFs were reported by Hong et al⁴ based on the findings that the feeder was a radicular artery and the fistula was located off the midline. No spinal artery involvement was noted in their series. In contrast, in all 3 surgically proven AVFs, extension of the ASA was the sole feeder.^{3,5} Our results demonstrated mixed results as may be expected from the cauda equina vascular anatomy.

In cauda equina AVFs, the ASA showed changes in the caliber and course at the conus medullaris apex. These changes may reflect the transition of the ASA into a radicular artery and were observed only in the cauda equina AVF and thus may be pathognomonic findings.

The radicular arteries are bound loosely to their nerve filaments by filmy pia arachnoid,³⁰ and this may be similar for the veins. This loose connection may explain the wavy drainage vein pattern seen in 3 of the 5 cauda equina AVF cases. Because the feeder–drainer is always parallel in the FT AVF, the wavy drainer pattern may also be pathognomonic for cauda equina AVF.

Thin-section axial MR imaging detected the draining vein in 3 of 4 cases. A draining vein joining the spinal cord above the conus medullaris apex (Figs 4C and 3C) was especially suggestive of a radicular vein. In case 3, in which the MR imaging failed in vein detection, the examination was conducted within 1 month after a transient paraparesis. We presume that the lesion was premature for MR imaging detection.

CLINICAL RELEVANCE

Accurate fistula diagnosis is crucial in treating spinal AVFs. This prevents disorientation during surgical exploration and incomplete

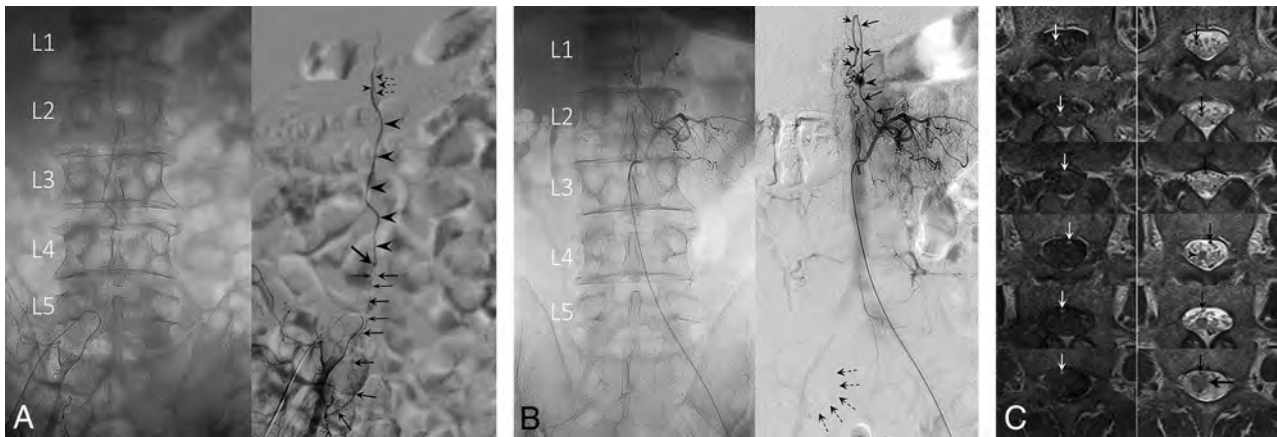


FIG 3. A, Unsubtracted (*left*) and subtracted (*right*) angiograms of the right internal iliac artery. A radicular artery (*large arrows*) originating from the right S1 lateral sacral artery forms a fistula (*oblique arrow*) at the L4 level. Note a second small feeder contributing to the fistula (*small arrows*). The straight ascending draining vein (*arrowheads*) opens into the perimedullary vein at the L1 level (*small arrowhead*), demonstrated by the opacification of superficial pial veins (*dashed arrows*). This finding suggests that the draining vein is a radicular vein. The ASA had no contribution to the fistula (not shown). B, A coexisting L1 level perimedullary AVF supplied from the left L2 radiculopial artery (*arrows*). An aneurysm (*arrowhead*) is seen at the fistulous site (*small arrow*). Note the faint opacification of the right S1 lateral sacral artery, identical to that seen in A, supplying the L4 level fistula (*dashed arrows*). Note the descending, then ascending draining vein that is separate from the right S1 radicular AVF. C, Serial thin-section gadolinium-enhanced T1WI (*left column*) and T2WI (*right column*) arranged in caudal (*upper*) to cranial (*lower*) order show the draining vein (*arrows*) is off the cord at the apex of the conus medullaris (*arrowhead*). The draining vein eventually merges with the spinal cord at a higher level (*large horizontal arrow*). This finding suggests that the draining vein is a radicular vein.

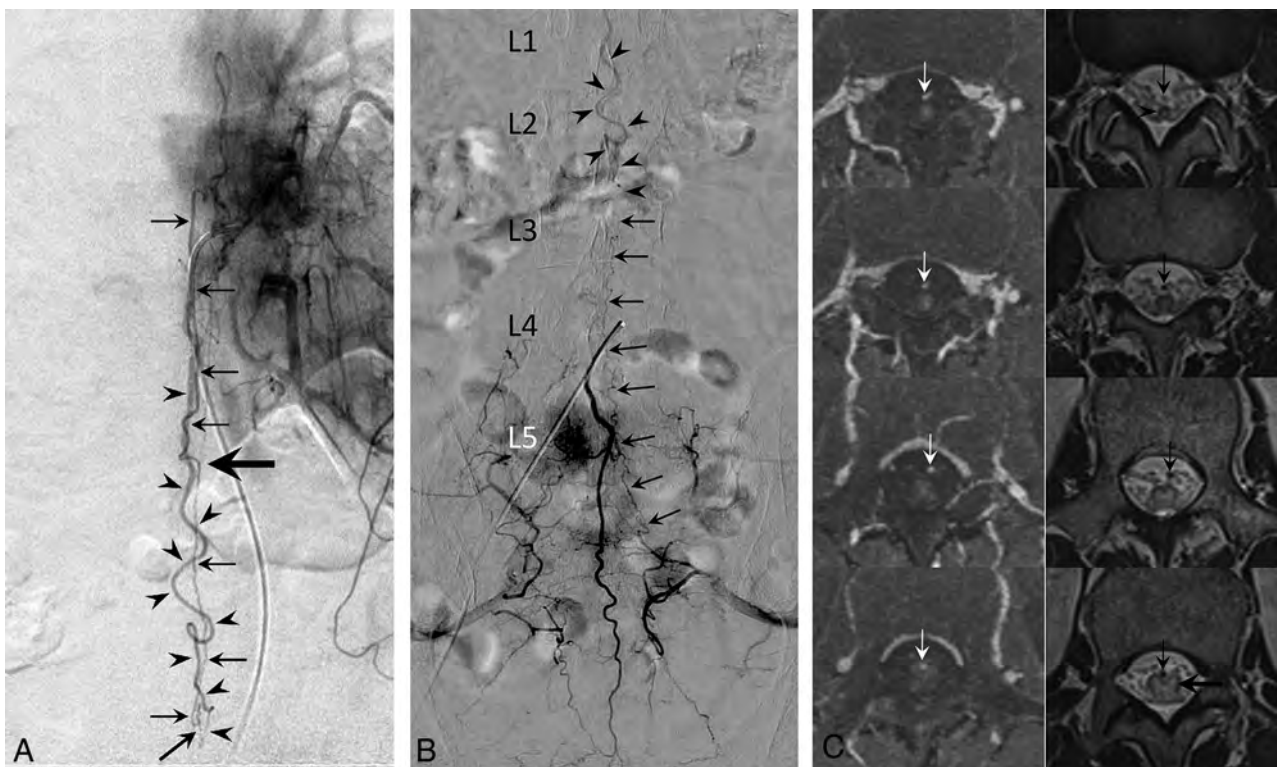


FIG 4. A, Angiogram of the left T11 intercostal artery in anteroposterior view demonstrates a posterior spinal artery supplying the anterior spinal artery (ASA) via the vasa corona. The ASA extends caudally to form a fistula at the L3 level (*oblique arrow*). The ascending draining vein shows a characteristic wavy pattern (*arrowheads*). Note the change in course and caliber of the descending ASA at the apex of the conus medullaris, suggesting a switch in the ASA to a radicular artery (*large horizontal arrow*). B, Medial sacral artery angiogram in anteroposterior view demonstrates anastomotic opacification of the radicular artery (*arrows*) from the left S1 lateral sacral artery supplying the L3 level AVF. The same draining vein seen in A is detected in this study (*arrowheads*). The L3 AVF in this patient has a dual supply from the ASA and an S1 radicular artery. C, Serial thin-section gadolinium-enhanced T1WI (*left column*) and T2WI (*right column*) arranged in caudal (*upper*) to cranial (*lower*) order show the draining vein (*arrows*) is off the cord at the apex of the conus medullaris (*arrowhead*). The draining vein eventually merges with the spinal cord at the L1 level (*large horizontal arrow*). This finding suggests that the draining vein is a radicular vein.

embolization. Also, the vascular anatomy may prefer direct surgery over an endovascular approach because of a long and narrow feeding artery. More important, treatment to a radicular nerve carries a higher risk of neuronal damage than a functionally dormant FT. Therefore, embolization of a cauda equina AVF should be carried out with discretion.

LIMITATIONS

The small case number and lack of surgically confirmed AVF except in 1 case prevent us from reaching definitive conclusions. To overcome these shortcomings, we recruited definitive AVF cases from the literature and added the venous information by thin-section axial MR imaging studies. Nevertheless, surgically confirmed cauda equina and FT AVFs were limited to 3 and 31 cases, respectively. Although the number was limited, MR imaging seemed a promising method that may be added to the existing diagnostic technique in the future.

CONCLUSIONS

Cauda equina AVF and FT AVF may be radiologically differentiated by combining the characteristic arterial and venous features.

Disclosures: None.

REFERENCES

1. Olry R, Haines DE. **Between André Du Laurens' horse tail and William Cadogan's pony tail.** *J Hist Neurosci* 2012;21:327–31 CrossRef Medline
2. Djindjian M, Djindjian R, Rey A, et al. **Intradural extramedullary spinal arterio-venous malformations fed by the anterior spinal artery.** *Surg Neurol* 1977;8:85–93 Medline
3. Ohtonari T, Ota S, Nishihara N, et al. **Arteriovenous fistula in a nerve root of the cauda equina fed by a proximal radiculo-medullary artery: a report of two cases.** *Interv Neuroradiol* 2011;17:217–23 CrossRef Medline
4. Hong T, Park JE, Ling F, et al. **Comparison of 3 different types of spinal arteriovenous shunts below the conus in clinical presentation, radiologic findings, and outcomes.** *AJNR Am J Neuroradiol* 2017;38:403–09 CrossRef Medline
5. Tanioka S, Toma N, Sakaida H, et al. **A case of arteriovenous fistula of the cauda equina fed by the proximal radicular artery: anatomical features and treatment precautions.** *Eur Spine J* 2018;27:281–86 CrossRef Medline
6. Gueguen B, Merland JJ, Riche MC, et al. **Vascular malformations of the spinal cord: intrathecal perimedullary arteriovenous fistulas fed by medullary arteries.** *Neurology* 1987;37:969–79 CrossRef Medline
7. Meisel HJ, Lasjaunias P, Brock M. **Modern management of spinal and spinal cord vascular lesions.** *Minim Invasive Neurosurg* 1995;38:138–45 CrossRef Medline
8. Tender GC, Vortmeyer AO, Oldfield EH. **Spinal intradural arteriovenous fistulas acquired in late adulthood: absent spinal venous drainage in pathogenesis and pathophysiology. Report of two cases.** *J Neurosurg Spine* 2005;3:488–94 CrossRef Medline
9. Mitha AP, Murphy EE, Ogilvy CS. **Type A intradural spinal arteriovenous fistula. Case report.** *J Neurosurg Spine* 2006;5:447–50 CrossRef Medline
10. Jin YJ, Kim KJ, Kwon OK, et al. **Perimedullary arteriovenous fistula of the filum terminale: case report.** *Neurosurgery* 2010;66:E219–20 CrossRef Medline
11. Kumar A, Deopujari CE, Mhatre M. **Misdiagnosis in a case of non-compressive myelopathy due to a lumbar spinal intradural fistula supplied by the artery of Adamkiewicz.** *Surg Neurol Int* 2011;2:12 CrossRef Medline
12. Witiw CD, Fallah A, Radovanovic I, et al. **Sacral intradural arteriovenous fistula treated indirectly by transection of the filum terminale: technical case report.** *Neurosurgery* 2011;69:E780–84 CrossRef Medline
13. Trinh VT, Duckworth EA. **Surgical excision of FT arteriovenous fistulae after lumbar fusion: Value of indocyanine green and theory on origins (a technical note and report of two cases).** *Surg Neurol Int* 2011;2:63 CrossRef Medline
14. Lim SM, Choi IS, David CA. **Spinal arteriovenous fistulas of the filum terminale.** *AJNR Am J Neuroradiol* 2011;32:1846–50 CrossRef Medline
15. Takami T, Yamagata T, Mitsunashi Y, et al. **Direct surgery for spinal arteriovenous fistulas of the filum terminale with intraoperative image guidance.** *Spine* 2012;37:E1524–28 CrossRef Medline
16. Fischer S, Aguilar Perez M, Bassiouni H, et al. **Arteriovenous fistula of the filum terminale: diagnosis, treatment, and literature review.** *Clin Neuroradiol* 2013;23:309–14 CrossRef Medline
17. Chanthanaphak E, Pongpech S, Jiarakongmun P, et al. **Filum terminale arteriovenous fistulas: the role of endovascular treatment.** *J Neurosurg Spine* 2013;19:49–56 CrossRef Medline
18. Krishnan P, Banerjee TK, Saha M. **Congestive myelopathy (Foix-Alajouanine syndrome) due to intradural arteriovenous fistula of the filum terminale fed by anterior spinal artery: case report and review of literature.** *Ann Indian Acad Neurol* 2013;16:432–36 CrossRef Medline
19. Takeuchi M, Niwa A, Matsuo N, et al. **Pathomorphological description of the shunted portion of a filum terminale arteriovenous fistula.** *Spine J* 2014;14:e7–10 CrossRef Medline
20. Sharma P, Ranjan A, Lath R. **Arteriovenous fistula of the filum terminale misdiagnosed and previously operated as lower lumbar degenerative disease.** *Asian Spine J* 2014;8:365–70 CrossRef Medline
21. Ding D, Law AJ, Scotter J, et al. **Lumbar disc herniation exacerbating venous hypertension from a spinal perimedullary arteriovenous fistula of the filum terminale.** *J Neurol Sci* 2016;369:276–77 CrossRef Medline
22. Li J, Li G, Bian L, et al. **Concomitant lumbosacral perimedullary arteriovenous fistula and spinal dural arteriovenous fistula.** *World Neurosurg* 2017;105:1041.e7–1041.e14 CrossRef Medline
23. Hong T, Yu JX, Liu W, et al. **Filum terminale arteriovenous fistulas with multiple shunt points: a report of two exceptional cases.** *World Neurosurg* 2018;118:235–39 CrossRef Medline
24. Takai K, Komori T, Taniguchi M. **Angioarchitecture of filum terminale arteriovenous fistulas: relationship with a tethered spinal cord.** *World Neurosurg* 2019;122:e795–804 CrossRef Medline
25. Scullen T, Mathkour M, Amenta PS, et al. **Arteriovenous fistula of the filum terminale: a case report and review of the literature.** *World Neurosurg* 2019;130:42–49 CrossRef Medline
26. Djindjian M, Ribeiro A, Ortega E, et al. **The normal vascularization of the intradural filum terminale in man.** *Surg Radiology Anat* 1988;10:201–09 CrossRef Medline
27. Streeter GL. **Factors involved in the formation of the filum terminale.** *Am J Anat* 1919;25:1–12 CrossRef
28. Kunitomo K. **The development and reduction of the tail and of the caudal end of the spinal cord in the human embryo.** In: *Contributions to Embryology.* Carnegie Institution of Washington; 1918:8
29. Parke WW, Gammell K, Rothman RH. **Arterial vascularization of the cauda equina.** *J Bone Joint Surg Am* 1981;63:53–62 Medline
30. Crock HV, Yamagishi M, Crock MC. *The Conus Medullaris and Cauda Equina in Man. An Atlas of the Arteries and Veins.* Springer-Verlag; 1986:2

Celebrating 35 Years of the AJNR

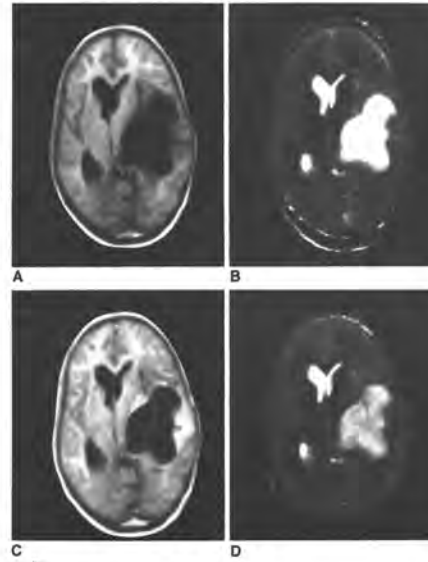
November 1985 edition

Contrast-Enhanced MR Imaging of Malignant Brain Tumors

Meche Graf¹
Graeme M. Bydder¹
Robert E. Steiner¹
Peter Niendorf²
David G. T. Thomas³
Ian R. Young⁴

Magnetic resonance (MR) imaging was performed before and shortly after intravenous injection of 1 mmol/kg gadolinium-DTPA (Schering) in 17 patients with clinical and histologic diagnoses of malignant cerebral tumors. There was a decrease of 1% in T1 and 10% in T2 in normal white matter and a decrease of 8% in T1 and 14% in T2 in normal gray matter. Contrast enhancement was observed in 16 of the 17 tumors. In the region of maximal enhancement a mean decrease of 18% in T1 was observed in low-grade gliomas, a mean decrease in T1 of 29% was seen in high-malignancy gliomas, and a mean decrease in T1 of 33% was observed in metastases. The decreases in T1 persisted for at least 50 min. In one case the central cystic region of the tumor displayed a decrease in T1 and T2. Measurements of signal intensity displayed maximal contrast enhancement with an IR 1500/300/44 sequence, much less with SE 1500/44, and least with SE 1500/80. Edema was observed on precontrast images in 14 cases, but satisfactory definition of the tumor-edema margin was only possible in four cases. After contrast enhancement this margin was defined in 10 cases. In four of the 17 cases areas of apparent "edema" seen before administration of Gd-DTPA displayed significant contrast enhancement and probably represented tumor infiltration. Comparison with CT showed a greater degree of contrast enhancement on MR images in eight cases, an equal degree in eight cases, and greater enhancement on CT in one case. Definition of the tumor-edema interface was better with MR in six cases and equal to CT in four cases. No significant toxic effects were found with the contrast agent. Gd-DTPA provided significant additional information over unenhanced MR imaging and enhanced CT.

The value of contrast enhancement was recognized soon after the introduction of cranial CT [1, 2]. The situation with magnetic resonance (MR) imaging is more complex. A greater level of soft-tissue contrast is available without contrast enhancement, and, unlike CT, no contrast agents suitable for parenteral use were available when the technique was first introduced. Nevertheless, particular situations have been defined, such as differentiation between tumor and edema, where contrast enhancement might be useful [3, 4], and recently the paramagnetic contrast agent gadolinium-DTPA has been tested in animals [5, 6] and used in clinical pilot studies [7-9]. In this report we extend our earlier clinical studies by



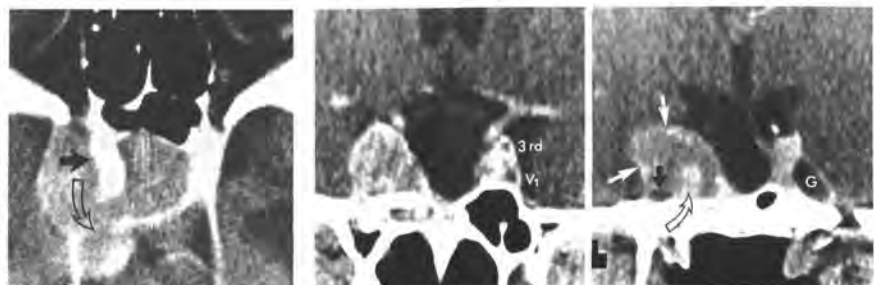
Received March 6, 1985; accepted after revision June 12, 1985.
This work was supported in part by Schering AG, Berlin (Gd-DTPA), and Medical Research Council, Department of Health and Social Security.
¹Department of Diagnostic Radiology, Royal Postgraduate Medical School, Hammersmith Hospital, Du Cane Rd., London W12 0HG, United Kingdom. Address reprint requests to M. Graf, MRM Unit.
²Schering AG, Berlin, West Germany.
³Department of Neurosurgery, Maida Vale Hospital, Maida Vale, London W9, United Kingdom.
⁴Robert Hooke Medical Research Centre, Westbury, Wiltshire, United Kingdom.
AJNR 6:885-892, November/December 1985
0195-9574/85/060885-08\$02.00
© American Roentgen Ray Society

Cavernous Sinus Invasion by Pituitary Adenomas

Jamhid Ahmad¹
Charles M. North¹
Hervey D. Segall¹
Chi-Shing Zee²
Martin H. Weiss³

One hundred ninety-eight surgically explored pituitary adenomas were evaluated preoperatively by high-resolution computed tomography (CT). At surgery, evidence of direct cavernous sinus invasion was demonstrated in 19. CT findings in these cases included cavernous sinus expansion (17 patients) and visible encasement of the internal carotid artery (14 patients). The invasive tumor often enhanced to a lesser degree than the cavernous sinuses and ipsilateral internal carotid artery. Intracavernous cranial nerve compression, obliteration, or displacement (14 patients), invasion of the lateral wall of the cavernous sinus (seven patients), and diffuse bone destruction (seven cases) were other findings. Magnetic resonance imaging in three patients provided excellent demonstration of intracavernous internal carotid artery encasement, but displacement and obliteration of intracavernous cranial nerves was not shown as well as it was with CT. Histologically, only three patients showed anaplastic features and only one of them had distant metastases. There was no correlation between histologic features, hormone assays, and invasiveness. This experience indicates any type of pituitary adenoma, regardless of its endocrinologic activity, can invade the cavernous sinus. Cavernous sinus involvement makes complete surgical removal difficult. Preoperative recognition of invasive behavior of these tumors has prognostic value and aids in designing appropriate management. CT is the most useful technique generally available for evaluation and follow-up.

This article appears in the November 1985 issue of AJNR and is issue of AJNR.
Received December 12, 1984; revision May 14, 1985.
¹Department of Radiology, St. Luke's, University of Southern California, Los Angeles, CA 90033.
²Department of Neurology, LAC-USC, Box 2, 1250 N. State St., Los Angeles, CA 90033.
³Department of Neurology, University of Southern California School of Medicine, Los Angeles, CA 90033.
AJNR 6:893-898, November/December 1985
0195-9574/85/060893-06\$02.00
© American Roentgen Ray Society



Chest CT Scanning in Suspected Stroke: Not Always Worth the Extra Mile



We read with interest the article by Kwee et al¹ entitled “CT Scanning in Suspected Stroke or Head Trauma: Is it Worth Going the Extra Mile and Including the Chest to Screen for COVID-19 Infection?” In this study, the authors retrospectively analyzed 27 patients with suspected stroke or head trauma who underwent head CT with routine addition of a chest CT in a coronavirus disease 2019 (COVID-19)–endemic region in the Netherlands. Most of these patients had suspected stroke, and 7 (26%) patients were positive on reverse transcriptase polymerase chain reaction (RT-PCR) for COVID-19. The authors appropriately concluded that suspicious chest CT findings needed to be interpreted with clinical history and confirmed by RT-PCR testing.

Although the article title implies that using chest CT to screen for COVID-19 in this patient population may add value, we believe that the routine addition of a chest CT for patients with suspected stroke undergoing neuroimaging may not be worth the extra mile because of the low potential diagnostic yield. We retrospectively investigated patients with acute stroke with large-vessel occlusions at our institution for COVID-19 status (study exempted by the institutional review board). From March 1, 2020, to April 30, 2020, at the Massachusetts General Hospital (Boston, Massachusetts), a comprehensive stroke center, a total of 34 admitted patients had large-vessel occlusions on neuroimaging. This time period includes the rise and peak of the COVID-19 pandemic in Massachusetts, with a cumulative total of nearly 67,000 COVID-19–positive cases reported during those 2 months,² greater than the number of cases in the Netherlands.³ In addition, our hospital saw the largest number of hospitalized patients with COVID-19 in Massachusetts.

Of the 34 patients with large-vessel occlusions, only 1 (3%) was positive for COVID-19 by RT-PCR. Of the remaining patients, 20 (59%) tested negative for COVID-19 by RT-PCR (average, 2.2 negative tests per patient) and 13 did not undergo testing. The patients who did not undergo testing were all patients

admitted in March without clinical findings suspicious for COVID-19. In April, our institution mandated COVID-19 testing for all hospitalized patients. Given the low prevalence of COVID-19 infection among these patients with stroke, the routine addition of chest CT at the time of neuroimaging would have had a low diagnostic yield in this cohort. These findings contrast with the study of Kwee et al,¹ in which 26% of patients with suspected stroke or head trauma were positive for COVID-19, suggesting a higher possible yield. A possible explanation for this difference is that although Kwee et al found that 20 of 27 patients (74%) had symptoms of possible COVID-19 infection (fever, cough, and/or dyspnea), we found that only 4 of 34 (12%) patients in our cohort had such symptoms at the time of hospital admission. This difference in symptom prevalence could be because our cohort included only patients with large-vessel occlusions, but Kwee et al included any patient with suspected stroke or head trauma.

Because the diagnostic yield appears to be associated with symptom prevalence, we advocate for the targeted use of chest CT informed by clinical history, as opposed to the routine addition of chest CT to all patients with suspected stroke undergoing neuroimaging. Given the low positive predictive value of chest CT for COVID-19 infection as reported by Kwee et al¹ (54.6%), the incidental detection of lung parenchymal findings could lead to additional infection control precautions, diagnostic testing, and personal protective equipment consumption. Nevertheless, in a multi-institutional study of 118 patients with stroke during the height of the COVID-19 pandemic in New York City (with greater COVID-19 case numbers than Massachusetts or the Netherlands³), 26% of patients were positive for COVID-19 by RT-PCR.⁴ Thus, it remains possible that a screening chest CT could be worthwhile in regions of very high disease prevalence.

We thank the authors for sharing their experience, which provides valuable data for how we can optimize imaging protocols during the COVID-19 pandemic.

Indicates open access to non-subscribers at [www.ajnr.org](http://dx.doi.org/10.3174/ajnr.A6763)
<http://dx.doi.org/10.3174/ajnr.A6763>

Disclosures: William Mehan Jr—UNRELATED: Consultancy: Kura Oncology, Comments: independent image reviewer for head and neck clinical trial; Expert

Testimony: CRICO and other medical insurance companies; expert opinion for medicolegal cases involving neuroimaging.

REFERENCES

1. Kwee RM, Krdzalic J, Fasen B, et al. **CT scanning in suspected stroke or head trauma: is it worth going the extra mile and including the chest to screen for COVID-19 infection?** *AJNR Am J Neuroradiol* 2020;41:1165–69 CrossRef Medline
2. Commonwealth of Massachusetts. **COVID-19 response reporting.** www.mass.gov/info-details/covid-19-response-reporting. Accessed June 6, 2020
3. Dong E, Du H, Gardner L. **An interactive web-based dashboard to track COVID-19 in real time.** *Lancet Infect Dis* 2020;20:533–54 CrossRef Medline
4. Kihira S, Schefflein J, Chung M, et al. **Incidental COVID-19 related lung apical findings on stroke CTA during the COVID-19 pandemic.** *J Neurointerv Surg* 2020;12:669–72 CrossRef Medline

 M.D. Li

 M. Lang

 B.C. Yoon

 B.P. Applewhite

 K. Buch

 S.P. Rincon

Department of Radiology

 T.M. Leslie-Mazwi

Department of Neurology and Neurosurgery

 W.A. Mehan Jr

Department of Radiology

Massachusetts General Hospital

Harvard Medical School

Boston, Massachusetts

REPLY:



I thank Li and colleagues for their interest in our article “CT Scanning in Suspected Stroke or Head Trauma: Is it Worth Going the Extra Mile and Including the Chest to Screen for COVID-19 Infection?”¹ Our article title is a question, which does not imply that using chest CT to screen for coronavirus disease 2019 (COVID-19) in this patient population may add value. The Fleischner Society’s position article on the use of chest imaging during the COVID-19 pandemic² did not specifically address whether additional chest CT should be performed to detect COVID-19 in patients who undergo extrathoracic CT in regions of high COVID-19 prevalence. Our study¹ provides new scientific information, and we address the possible pros and cons of performing additional chest CT for COVID-19 detection in patients who undergo head CT for suspected stroke or head trauma in a COVID-19–endemic region. We clearly stated that the data from our study may be used to weigh the potential advantages and disadvantages of performing additional chest CT. This is up to the readers of our article. However, I certainly appreciate that Li and colleagues are sharing their valuable thoughts. They relied on reverse transcription polymerase chain reaction (RT-PCR) testing for diagnosing COVID-19 infection. Unfortunately, RT-PCR is an imperfect test, with a reported pooled sensitivity of 89% (95%

CI, 81%–94%).³ Even repeat RT-PCR testing may yield a false-negative result in patients with COVID-19.⁴ Li and colleagues did not perform chest CT. Therefore, from a scientific point of view, it remains speculative whether chest CT would truly have had a low diagnostic yield in their stroke population during the rise and peak of the COVID-19 pandemic.

REFERENCES

1. Kwee RM, Krdzalic J, Fasan BA, et al. **CT scanning in suspected stroke or head trauma: is it worth going the extra mile and including the chest to screen for COVID-19 infection?** *AJNR Am J Neuroradiol* 2020;41:1165–69 CrossRef Medline
2. Rubin GD, Ryerson CJ, Haramati LB, et al. **The role of chest imaging in patient management during the COVID-19 pandemic: a multinational consensus statement from the Fleischner Society.** *Chest* 2020;158:106–16 CrossRef Medline
3. Li D, Wang D, Dong J, et al. **False-negative results of real-time reverse-transcriptase polymerase chain reaction for severe acute respiratory syndrome coronavirus, 2: role of deep-learning-based CT diagnosis and insights from two cases.** *Korean J Radiol* 2020;21:505–08 CrossRef Medline
4. Kim H, Hong H, Yoon SH. **Diagnostic performance of CT and reverse transcriptase-polymerase chain reaction for coronavirus disease 2019: a meta-analysis.** *Radiology* 2020 Apr 17. [Epub ahead of print] CrossRef Medline

Indicates open access to non-subscribers at www.ajnr.org
<http://dx.doi.org/10.3174/ajnr.A6787>

R.M. Kwee
Department of Radiology
Zuyderland Medical Center
Heerlen/Sittard/Geleen, the Netherlands

Hemorrhagic Neurologic Manifestations in COVID-19: An Isolated or Multifactorial Cause?



We read with great interest the article by Nicholson et al¹ that described 4 patients with coronavirus disease 2019 (COVID-19) presenting with parenchymal hemorrhages during their critical care admission. We agree with the authors' proposal that a thrombotic microangiopathy may cause hemorrhagic neurologic manifestations in COVID-19. This is supported by imaging features of coagulopathy and endothelial dysfunction in multiple organ systems observed in such patients. However, there remains a degree of uncertainty with regard to potentially shared underlying pathophysiologic mechanisms in the critically ill COVID-19 cohort.

Herein, we present 2 male patients with COVID-19 (48 and 65 years of age) with CT findings of isolated intraventricular hemorrhage (IIVH) during their prolonged critical care admission. Both patients were treated for COVID-19-related respiratory failure, requiring mechanical ventilation, and were placed on Continuous Venovenous Hemofiltration (CVVH; <https://www.massgeneral.org/medicine/nephrology/treatments-and-services/cvvh>). Neither patient required extracorporeal membrane oxygenation. The platelet count, prothrombin level, and activated partial thromboplastin times were within the normal referenced ranges. At least 2 weeks into the admission, CT of the head was performed due to reduced consciousness levels despite a sedation hold. CT revealed a dependent hyperdense fluid level in the occipital horn, consistent with IIVH. Noninvasive angiography (CT/MR imaging) did not reveal any underlying vascular abnormality. Findings of MR imaging of the head (48-year-old patient) showed cerebral microbleeds (CMB) in the splenium of the corpus callosum and subcortical white matter (Figure). Transient T2-weighted hyperintensity (resolved on subsequent MR imaging 2 weeks later) was evident in the splenium of the corpus callosum without diffusion restriction or pathologic enhancement. A transthoracic echocardiogram excluded features of infective endocarditis. Both patients recovered from their acute respiratory illness sufficiently for hospital discharge.

IIVH as a presenting feature on CT imaging is a comparatively rare entity in adults, accounting for about 3% of all

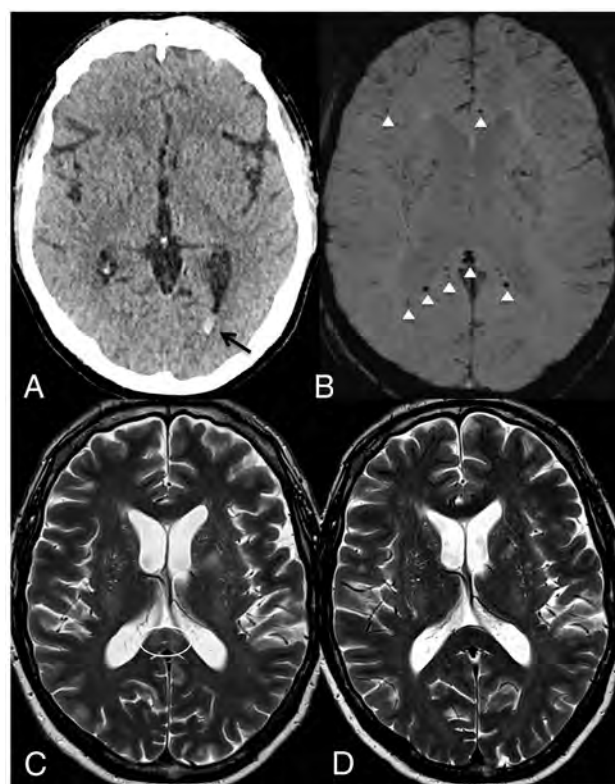


FIGURE Axial images of the 48-year-old male patient. A, Unenhanced CT demonstrates isolated intraventricular hemorrhage (black arrow). B, Susceptibility-weighted imaging shows microbleeds in the subcortical white matter, splenium, and genu of the corpus callosum (white arrowhead). C, T2-weighted image shows the splenial hyperintense lesion (white circle). D, T2-weighted imaging shows resolution after 2 weeks.

intracranial hemorrhages, with coagulopathy as a known risk factor. No underlying cause may be identified in up to 25%–46% of patients.² Most interestingly, both patients with IIVH had normal coagulation parameters. The hyperinflammatory syndrome or “cytokine storm” strongly associated with severe COVID-19 infection could explain the transient splenial lesion demonstrated.³ The observed CMBs are atypical

Indicates open access to non-subscribers at www.ajnr.org

<http://dx.doi.org/10.3174/ajnr.A6795>

for hypertensive or amyloid angiopathy causes. Instead, thrombotic microangiopathy and endotheliitis, also described in relation to COVID-19, may be contributory factors in sepsis/critical illness-related CMBs. However, corpus callosum CMBs have been reported in patients with acute respiratory distress syndrome with a resemblance seen in CMB-related high-altitude exposure, sharing a common underlying etiology of hypoxemia.⁴ This resemblance could similarly explain the findings in our case. Other variables that may influence the presence and/or extent of microhemorrhage in patients with COVID-19 include therapeutic anticoagulation (for pulmonary embolus or renal support) and raised cerebral venous pressure due to ventilator measures to optimize alveolar recruitment and patient oxygenation.

The exact etiology of the presented cryptogenic IIVH and CMB demonstrated in patients with COVID-19 remains unclear. Indeed, it is likely that shared pathophysiologic mechanisms are responsible for the various neurologic manifestations of COVID-19, particularly in the critically unwell.

Disclosures: Robert Lenthal—UNRELATED: Payment for Development of Educational Presentations: The European Course in Minimally Invasive Neurological Therapy (ECMINT) faculty, Comments: lecturer in the ECMINT course, multiple talks not on coronavirus disease 2019 (COVID-19) as yet; Other: equipment manufacturers, Comments: I have received support to attend educational meetings from multiple device manufacturers on multiple occasions for 20 years.

REFERENCES

1. Nicholson P, Alshafai L, Krings T. **Neuroimaging findings in patients with COVID-19.** *AJNR Am J Neuroradiol* 2020;41:1380–83 CrossRef Medline
2. Weinstein R, Ess K, Sirdar B, et al. **Primary intraventricular hemorrhage: clinical characteristics and outcomes.** *J Stroke Cerebrovasc Dis* 2017;26:995–99 CrossRef Medline
3. Mehta P, McAuley DF, Brown M, et al; HLH Across Speciality Collaboration, UK. **COVID-19: consider cytokine storm syndromes and immunosuppression.** *Lancet* 2020;395:1033–34 CrossRef Medline
4. Fanou EM, Coutinho JM, Shannon P, et al. **Critical illness-associated cerebral microbleeds.** *Stroke* 2017;48:1085–87 CrossRef Medline

P.S. Dhillon

Neuroradiology Department
Queen's Medical Centre
Nottingham University Hospitals National Health Service Trust
Nottingham, UK

Radiological Sciences, Division of Clinical Neuroscience
University of Nottingham
Nottingham, UK

A. Chattopadhyay

Neuroradiology Department
Queen's Medical Centre
Nottingham University Hospitals National Health Service Trust
Nottingham, UK

R.A. Dineen

Radiological Sciences, Division of Clinical Neuroscience
University of Nottingham
Nottingham, UK
National Institute for Health Research Nottingham Biomedical Research Centre
Nottingham, UK

R. Lenthal

Neuroradiology Department
Queen's Medical Centre
Nottingham University Hospitals National Health Service Trust
Nottingham, UK

REPLY:



We thank the authors for their comments and for their interest in our paper. We completely agree that although the underlying pathomechanism of hemorrhagic manifestations in critically ill patients with coronavirus 2019 (COVID-19) remains uncertain, it is likely multifactorial. We have expanded on this series of patients in a larger cohort (currently under submission), and as the authors suggest, a few broad imaging themes have begun to allude to some of these potential underlying mechanisms. These imaging features include cerebral microhemorrhages, venular thrombosis, arterial infarcts, subarachnoid hemorrhage, petechial or juxtacortical microhemorrhages, leukoencephalopathy, and catastrophic large-volume hemorrhages (including intraventricular hemorrhages). These myriad imaging findings could all result from downstream pathophysiological outcomes resulting from hypoxemia, hypercoagulability, and endotheliitis, all of which seem to be more common in patients with COVID-19. As the authors have correctly stated, the addition of systemic anticoagulation may also be an additional factor leading to hemorrhage in some of these patients.

Although there is much uncertainty regarding the cause of these findings at present, with the literature being populated with relatively small-series single-center studies (such as our own), we eagerly await the results of several ongoing large-cohort

studies to help clarify imaging findings and neurologic outcomes in these patients. For example, the C-VASC COVID-19 study is a prospective, pragmatic, longitudinal multicenter Canadian cohort study looking at stroke outcomes in these patients. Data sharing from many of these trials is also being harmonized through collaborations with organizations such as the Neurocritical Care Society and other international partners, pointing to the strengths of the collaborations that arose as a result of the COVID-19 pandemic. It is becoming increasingly clear that far from being “just a respiratory disease,” COVID-19 is, in fact, a multisystem illness that can have serious consequences for a certain subset of patients. We therefore look forward to the results of these larger studies to help us to get a better picture regarding both short- and long-term neurologic outcomes in these patients.

P. Nicholson

Division of Neuroradiology
Joint Department of Medical Imaging
Toronto Western Hospital
University Health Network, University of Toronto, Canada

L. Alshafai

Division of Neuroradiology
Joint Department of Medical Imaging
Mount Sinai Hospital
University Health Network, University of Toronto, Canada

T. Krings

Division of Neuroradiology
Joint Department of Medical Imaging
Toronto Western Hospital
University Health Network, University of Toronto, Canada

Indicates open access to non-subscribers at www.ajnr.org

<http://dx.doi.org/10.3174/ajnr.A6827>

Risk of Acute Cerebrovascular Events in Patients with COVID-19 Infection



Neurologic symptoms are reported in patients with coronavirus disease 2019 (COVID-19) with a higher prevalence in more severe cases; these symptoms can include altered mental status, dizziness, headache, and anosmia.¹ Coagulopathy and vascular endothelial injury in COVID-19 infection are also reported and may contribute to multiorgan dysfunction.^{2,3} The risk of acute cerebrovascular events (CVE), however, is poorly defined.^{1,4} A group from Union Hospital, Tongji Medical College in China detailed in their single-center experience that the risk of acute CVE, including hemorrhagic and ischemic stroke, was approximately 5% (11 of 219 patients).⁴ Here, we report a similar risk of acute CVE at a large academic institution in the United States.

During a 2-week period between March 27 and April 10, 2020, four hundred sixty-eight patients hospitalized at our institution tested positive for COVID-19 by real-time polymerase chain reaction: 105 underwent neuroimaging (CT or MR imaging). The most common indication was altered mental status, followed by head trauma and clinical concern of stroke (Table). Six cases were found to have acute CVE on imaging; 4 cases were hemorrhagic in nature (lobar intracranial hemorrhage in 2, subarachnoid hemorrhage in 1, and multifocal microhemorrhages in 1); and 2 were ischemic in nature (internal capsule infarct in 1 and subcortical frontal lobe infarct in 1). The acute CVE risk was 5.7% for all patients with COVID-19 who underwent neuroimaging in our study, similar to the 5% acute CVE risk reported by the Tongji Medical College group from China.⁴ If all patients with COVID-19 without neuroimaging were presumed to be negative for CVE, however, the risk would decrease to 1.3%. A challenge with acute CVE estimates in the general COVID-19 population, however, is the possibility of missing clinically silent strokes, especially given the difficulty in clinical detection of stroke in critically ill patients. A high proportion of patients in our cohort with acute CVE were critically ill, with 4 of the 6 patients with acute CVE (67%) admitted to the intensive care unit, 3 of whom required intubation. Furthermore, 2 of the 6 (33%) patients with acute CVE in our study died. Overall, these findings are consistent with the current literature suggesting a potentially dysfunc-

tional inflammatory response, coagulopathy, and endothelial damage in critically ill patients with COVID-19 infection.^{2,3,5}

In contrast to previous reports, we found no significant differences in age and comorbidities between patients with COVID-19 with and without acute CVE (Table).⁴ This finding suggests that the risk of acute CVE may be increased in general for critically ill patients with COVID-19 infection and attention should not be limited to older patients with cerebrovascular risk factors as previously proposed. This is further supported by a case series reporting large-vessel stroke in 5 patients with COVID-19 younger than 50 years of age.³ Further research on this topic is needed.

COVID-19 infection appears, therefore, to be associated with a more diffuse pattern of vascular abnormalities with multiorgan involvement. Acute CVE should be considered in critically ill patients with COVID-19 with new neurologic deficits, and despite the logistical challenges posed by this population, there should be a relatively low threshold for obtaining neuroimaging when clinically indicated.

Disclosures: Matthew Li—UNRELATED: Grants/Grants Pending: Radiological Society of North America Research & Education Foundation Resident/Fellow Research Grant recipient. William A. Mehan, Jr.—UNRELATED: Consultancy: Kura Oncology, Comments: independent reviewer of head and neck images for a clinical trial; Expert Testimony: CRICO and other medical insurance companies, Comments: expert opinion for medicolegal cases involving neuroimaging.

REFERENCES

1. Mao L, Jin H, Wang M, et al. **Neurologic manifestations of hospitalized patients with coronavirus disease 2019 in Wuhan, China.** *JAMA Neurol* 2020;77:683 CrossRef Medline
2. Zhou F, Yu T, Du R, et al. **Clinical course and risk factors for mortality of adult inpatients with COVID-19 in Wuhan, China: a retrospective cohort study.** *Lancet* 2020;395:1054–62 CrossRef Medline
3. Oxley TJ, Mocco J, Majidi S, et al. **Large-vessel stroke as a presenting feature of Covid-19 in the young.** *N Engl J Med* 2020;382:e60 CrossRef Medline
4. Li Y, Li M, Wang M, et al. **Acute cerebrovascular disease following COVID-19: a single center, retrospective, observational study.** *Stroke Vasc Neurol* 2020;382:e60 CrossRef Medline
5. Ricardo J, Jose AM. **COVID-19 cytokine storm: the interplay between inflammation and coagulation.** *Lancet Respir Med* 2020;8:e46–47 CrossRef Medline

Indicates open access to non-subscribers at [www.ajnr.org](http://dx.doi.org/10.3174/ajnr.A6796)
<http://dx.doi.org/10.3174/ajnr.A6796>

Summary of patient characteristics

Characteristics	Patients with COVID-19 with Acute CVE (<i>n</i> = 6)	Patients with COVID-19 without Acute CVE (<i>n</i> = 99)	<i>P</i> value
Mean age (yr)	62 ± 14	66 ± 17	0.41 ^a
< 50 yrs, <i>n</i> (%)	1 (17)	14 (14)	>0.99 ^b
≥ 50 yrs, <i>n</i> (%)	5 (83)	85 (86)	
Sex, <i>n</i> (%)			0.40 ^b
Male	5 (83)	57 (58)	
Female	1 (17)	42 (42)	
Indication for neuroimaging, <i>n</i> (%)			0.08 ^c
Altered mental status	1 (17)	47 (47)	
Trauma	1 (17)	24 (24)	
Stroke symptoms	4 (67)	14 (14)	
Headache	0 (0)	7 (7)	
Seizure	0 (0)	3 (3)	
Syncope	0 (0)	3 (3)	
Dizziness	0 (0)	1 (1)	
Comorbidities, <i>n</i> (%)			
Current smoker	0 (0)	7 (7)	>0.99 ^b
Ex-smoker	1 (17)	8 (8)	0.42 ^b
Hypertension	3 (50)	62 (63)	0.67 ^b
Diabetes	2 (33)	38 (38)	>0.99 ^b
Obesity	3 (50)	20 (20)	0.12 ^b
COPD/asthma/OSA	2 (33)	18 (18)	0.32 ^b
Malignancy	0 (0)	11 (11)	>0.99 ^b
Cardiovascular disease	1 (17)	11 (11)	0.53 ^b
Cerebrovascular disease	0 (0)	7 (7)	>0.99 ^b
Requiring ICU admission, <i>n</i> (%)	4 (67)	47 (47)	0.43 ^b
With intubation	3 (50)	42 (42)	>0.99 ^b
Discharged, <i>n</i> (%)	2 (33)	46 (46)	0.69 ^b
Deceased, <i>n</i> (%)	2 (33)	11 (11)	0.16

Note:—COPD indicates chronic obstructive pulmonary disease; OSA, obstructive sleep apnea; ICU, intensive care unit.

^a Two-tailed t-test.

^b Fisher's exact test.

^c Chi-squared test.

 M. Lang

 M.D. Li

 K. Buch

 B.C. Yoon

 B.P. Applewhite

Department of Radiology

 T.M. Leslie-Mazwi

Departments of Neurosurgery and Neurology

 S. Rincon

 W.A. Mehan, Jr.

Department of Radiology

Massachusetts General Hospital, Harvard Medical School

Boston, Massachusetts

Break Out the World's Smallest Violin for an Overwhelmed Neuroradiologist

When the world seemingly stopped turning in early March 2020, I anticipated many life changes, most involving isolation and a slowing of routine activities, both professional and personal. As my husband and I transported my (astoundingly) heavy Barco monitor and workstation to our weekend place at the shore, I knew that the sort of elective and semi-elective head and neck imaging that has made up the bulk of my practice would likely slow significantly. I am (and sincerely hope I am still) at a relatively late stage of my career and had been thinking a lot about how I needed to slow down and carve out some more time for myself. I imagined extricating myself from all academic activities that didn't "spark joy" and spending more time looking at cases and talking to referrers, my first and primary love in radiology. Maybe I'd finish up the case series manuscript I had started (mumbles into hand) a number of years ago. I'd certainly catch up on my reading and exercise. We had been talking a lot about retiring to the shore and figured that the time spent here during quarantine would give us an opportunity to see if the local offerings would be enough stimulation for us city folk. In short, I imagined that this episode would be great practice for upcoming retirement.

Turns out I could not have been more wrong. Although neuroimaging volumes plummeted, my colleagues and I, who now spoke more via text and Microsoft Teams than we ever did in person, started to think about COVID-19 and how we could explain some of the things we were seeing. Where have all the stroke codes gone? Why can't people smell—should we look at the olfactory bulbs? This prompted furious races (with every other academic physician on the planet) to apply for institutional review boards, collect data, and start constructing manuscripts. Never mind that I previously hated writing data-driven papers; this was something entirely new and completely fascinating!

Then professional societies started calling. How will we turn our annual meeting virtual? Will we need to do so for next year as well? How can we prepare our society for vast changes in its activities and finances and, hey, how about some webinars? The proliferation of webinars may be the most simultaneously rewarding and vexing change in our professional landscape. How does Zoom work? How do I record my lectures in PowerPoint? How many times do I need to re-record given this annoying hiss and that choppy transition? Who knew people talked so much between slides?

In addition to death and taxes, there are some things that you can always count on, such as on-line training modules for infection control (ironic), fire safety, information technology phishing, and so on. Then the medical staff office comes calling with your recertification packet. There are physician time studies and resident reviews. Somehow, the consults kept coming in despite the absence of elective surgery (wishful thinking?). When the volumes finally started increasing again, you felt like you never really had a break. All this on top of shopping and meal prep for 3 meals a day, a challenge for New Yorkers used to eating out as often as in, and, of course, all that cleaning. So, so much cleaning.

I am, of course, eternally grateful that my loved ones and I are safe, that I have a wonderful job, that I wake every morning to the sunrise over the beach and end each day watching the sun set over our leafy town. Alas, we are only human. We need to acknowledge that although we may have the best intentions, we may occasionally succumb to small and sometimes petty annoyances, like the ones listed above. Can you eke out a little sympathy and play me a tune on the world's smallest violin?

I'd like to acknowledge my husband Doug Phillips both for his help with edits and for putting up with me during quarantine.

©D.R. Shatzkes

Department of Radiology

Lenox Hill Hospital, Zucker School of Medicine at Hofstra/Northwell

New York, New York

<http://dx.doi.org/10.3174/ajnr.A6786>